IUTAM Bookseries

Marian Wiercigroch
Giuseppe Rega *Editors*

IUTAM Symposium on Nonlinear Dynamics for Advanced Technologies and Engineering Design

Proceedings of the IUTAM Symposium on Nonlinear Dynamics for Advanced Technologies and Engineering Design, held Aberdeen, UK, 27–30 July 2010

Springer

IUTAM Symposium on Nonlinear Dynamics for Advanced Technologies and Engineering Design

IUTAM BOOKSERIES

VOLUME 32

Aims and Scope of the Series

The IUTAM Bookseries publishes the proceedings of IUTAM symposia under the auspices of the IUTAM Board.

For further volumes:
http://www.springer.com/series/7695

Marian Wiercigroch • Giuseppe Rega
Editors

IUTAM Symposium on Nonlinear Dynamics for Advanced Technologies and Engineering Design

Proceedings of the IUTAM Symposium on Nonlinear Dynamics for Advanced Technologies and Engineering Design, held Aberdeen, UK, 27–30 July 2010

Springer

Editors
Prof. Marian Wiercigroch
Centre for Applied Dynamics Research
School of Engineering
College of Physical Sciences
University of Aberdeen
Aberdeen, Scotland
United Kingdom

Prof. Giuseppe Rega
Department of Structural
and Geotechnical Engineering
Sapienza University of Rome
Rome
Italy

ISSN 1875-3507
ISBN 978-94-007-5741-7
DOI 10.1007/978-94-007-5742-4
Springer Dordrecht Heidelberg New York London

ISSN 1875-3493 (electronic)
ISBN 978-94-007-5742-4 (eBook)

Library of Congress Control Number: 2012952086

Printed on acid-free paper

Springer is part of Springer Science+Business Media (www.springer.com)

Introduction to *N*DATED

Marian Wiercigroch and Giuseppe Rega

Abstract In this introduction, we briefly outline the origins behind organizing the IUTAM Symposium on Nonlinear Dynamics of Advanced Technologies and Engineering Design. We also give our view how the advancements of nonlinear dynamics can be implemented into the engineering world and report on the structure of the proceedings.

Keywords Nonlinear dynamics • New technologies • Engineering design

The IUTAM Symposium on Nonlinear Dynamics for Advanced Technologies and Engineering Design (NDATED) held between 27 and 30 July 2010 in Aberdeen was a part of the series of IUTAM Symposia focused on nonlinear dynamics and chaos.

The series originated at the end of the 1980s (Stuttgart, 1989) when the International Union of Theoretical and Applied Mechanics realized the importance of complex phenomena in applied mechanics and engineering. Starting with that meeting, mechanics community began to think of nonlinear vibrations within a wider and more modern context of nonlinear dynamics, where classical analytical techniques are meaningfully paralleled by the development and use of computational, geometrical and experimental methods. Successive IUTAM Symposia in the same area (London, 1993; Ithaca, NY, 1997) dealt with a variety of ever intriguing problems in nonlinear and chaotic dynamics of engineering systems, where the

M. Wiercigroch (✉)
Centre for Applied Dynamics Research, School of Engineering, University of Aberdeen, Kings College, Aberdeen AB24 3UE, UK
e-mail: m.wiercigroch@abdn.ac.uk

G. Rega
Department of Structural and Geotechnical Engineering, Sapienza University of Rome, via A. Gramsci 57, 00197 Rome, Italy
e-mail: giuseppe.rega@uniroma1.it

complementary use of those approaches allows to gain overall more complete understanding of the tacked problems.

Further Symposia in the series (Eindhoven, 1996; Rome, 2003; Nanjing, 2006) highlighted the importance of the interaction between nonlinear dynamics and control, which plays an important role in securing desired dynamic behaviour and improved reliability of advanced engineering systems undergoing complex phenomena, possibly in a stochastic environment.

Overall, the last Symposia highlighted the need to overcome the limitations inherent in the archetypal single- or few-degrees-of-freedom systems considered in the past, to develop more reliable models for the analysis of high-dimensional systems and processes, and to explore implications of complexity in design and operating conditions of advanced systems.

The Aberdeen (2010) IUTAM Symposium, from which this Proceedings volume evolves, was mostly dedicated to applications, as described in the paragraphs below, and aimed at making a meaningful step forward towards addressing real engineering systems.

Indeed, upon enjoying for nearly four decades a vast development resulting in a range of well established theory, nonlinear dynamics has now the potential to significantly enhance performance, effectiveness, reliability and safety of physical systems as well as to offer novel design and technologies. Although the research programme for the Aberdeen Symposium was tuned to engineering, the applications of the proposed approach are much more generic and similar nonlinear interactions can be exploited in biology, genetics, finance, medicine, earth sciences and others.

It is believed that fundamental understanding of various nonlinear physical phenomena producing bifurcations and of the ensuing complex response has reached a critical mass and now there is time to develop basic technology, which could take advantage of the natural richness of behaviour offered by nonlinear systems or being a product of nonlinear interactions.

The basic philosophy of this approach is to investigate conditions that naturally optimise the behaviour of systems and/or processes in such a way that nonlinear interactions will generate favourable operation. The nonlinearities may arise either as inherent characteristics of the system/process, or may be artificially created, for example in a control system. This approach should radically influence the current design, control and exploitation paradigms, in a magnitude of contexts, which because of their incremental nature are often only able to produce marginal improvements in performance of technological systems.

The main aim of the Aberdeen meeting was to stimulate engineering science research to develop the technology for new generation products/processes operating on principles of nonlinear interaction and in the nonlinear regimes, leading to more effective, sensitive, accurate, and durable operations than are currently available. This can be achieved by addressing the following five specific objectives:

1. To establish a basis for a unified framework harnessing nonlinear interactions by critically appraising the state of the art and by exploiting the existing knowledge to develop new theoretical tools and advanced practical and numerical techniques for nonlinear analysis.

2. To systematically classify various nonlinear phenomena and to investigate their potential for appropriate applications in engineering design. To investigate how various nonlinearities can be introduced to engineering systems and processes to produce improved responses.
3. To set in progress a raft of high quality inter- and multidisciplinary activities at the applied nonlinear systems/engineering interface, with emphasis on projects in mechanical and electronic engineering, solid/structural mechanics, acoustics and optics, with a high degree of coherence and collaboration with experts in these areas.
4. To evaluate and demonstrate the viability of the undertaken approach in a series of benchmark systems (demonstrators).
5. To synthesise the obtained methodologies and results into unified strategies, criteria and procedures for design of new processes, devices, sensors, machines for control, manufacturing and remote sensing, and for exploitation of natural resources.

For the Symposium, an International Scientific Committee was appointed by the Bureau of IUTAM with the following members: M. Wiercigroch (Aberdeen, Chair), G. Rega (Rome, Co-Chair), F.L. Chernousko (Moscow), E. Kreuzer (Hamburg), F.C Moon (Ithaca, NY), M.P. Paidoussis (Montreal), J.M. Thompson (Cambridge), D.H. van Campen (Eindhoven). The Committee selected the papers to be presented at the Symposium in lecture and poster-discussion sessions.

The Symposium gathered international experts from 20 different countries including Austria (1), Brazil (5), Canada (1), China (3), Denmark (1), France (2), Germany (3), India (2), Israel (2), Italy (3), Japan (4), Malaysia (1), Poland (3), Portugal (1), Russia (4), Spain (1), The Netherlands (1), UK (21), Ukraine (1), and USA (10).

Besides reviewing the state of the art and fostering future directions for the development of engineering technologies and design using robust nonlinear dynamics modelling and analysis, the meeting put a strong emphasis on employing experimentally calibrated and validated models, which reflect engineering realism. Such models can provide a powerful vehicle for development of new (i) more effective technologies and designs and (ii) robust controllers and condition monitoring systems enhancing performance of existing technologies and design.

In this volume we have included 32 contributed papers, among those presented at the Symposium, which have been peer reviewed. The volume is divided into the four following parts:

I. New Nonlinear Dynamics Methods and Theories
II. Smooth Engineering Systems
III. Non-smooth Engineering Systems
IV. Nonlinear Control of Engineering Systems

where Parts, I, II, III and IV contain 7, 13, 6 and 6 contributions, respectively. At this point we would like to thank both the participants to the Symposium and the authors of the papers for their valuable contributions.

The Symposium was held in the Kings College Conference Centre of the Old Aberdeen Campus. The opening remarks were given by Professor Ian Diamond (The Principal and Vice-Chancellor, University of Aberdeen), Professor Dick van Campen (IUTAM Representative), Professor Giuseppe Rega (Symposium Co-Chair), Professor Marian Wiercigroch (Symposium Chair), and Sir Duncan Michael(Symposium Honorary Chair).

The success of the Symposium would not have been possible without the work of the local Organizing Committee established at the Centre for Applied Dynamics Research, School of Engineering, University of Aberdeen, whose members were Marian Wiercigroch (Chair), Marko Keber, Marcos Silveira, and Anna Najdecka.

The financial support of IUTAM, ARUP, and Aberdeen City Council is most gratefully acknowledged.

Finally, we would like to express our gratitude to Springer, especially to Ms. Nathalie Jacobs and Ms. Anneke Pot, for their support, patience and efficient cooperation in producing this Proceedings volume.

Contents

Part I
New Nonlinear Dynamics Methods and Theories

Noise-Induced Jumping Prior to a Fold: Applied to Climate Tipping Predictions

J. Michael T. Thompson and Jan Sieber

Abstract We present a scheme of analysis for predicting the approach to a fold in the noisy time series of a slowly evolving system. It provides estimates of the evolution rate of the control parameter, the variation of the stability coefficient, the path itself, and the level of noise in the time series. Finally, it gives probability estimates of the future time at which the system will jump to a remote (dangerous) steady state. We apply the technique, first, to the output of a *computer simulation* from a model for sudden cooling of the Earth. Second, we use the algorithms to give probabilistic tipping estimates for the end of the most recent glaciation of the Earth using actual *geological data* from the Vostok ice core.

Keywords Noisy time series • Dangerous bifurcations • Climate tipping prediction

1 Introduction

Geologists have accumulated, over a long period, many time series relating to the Earth's paleo-climate, using data derived from ice-cores, sediments, isotope concentrations, etc. These provide a comprehensive picture of climatic changes over millions of years of the Earth's history, and some sample results are shown

J.M.T. Thompson (✉)
School of Engineering, Aberdeen University, Aberdeen, Scotland

Department of Applied Mathematics & Theoretical Physics, Cambridge University, Centre for Mathematical Sciences, Wilberforce Road, Cambridge, CB3 0WA, UK
e-mail: jmtt@ucl.ac.uk

J. Sieber
Department of Mathematics, University of Portsmouth, Portsmouth, PO1 3HF, UK
e-mail: Jan.Sieber@port.ac.uk

M. Wiercigroch and G. Rega (eds.), *IUTAM Symposium on Nonlinear Dynamics for Advanced Technologies and Engineering Design*, IUTAM Bookseries (closed) 32, DOI 10.1007/978-94-007-5742-4_1,

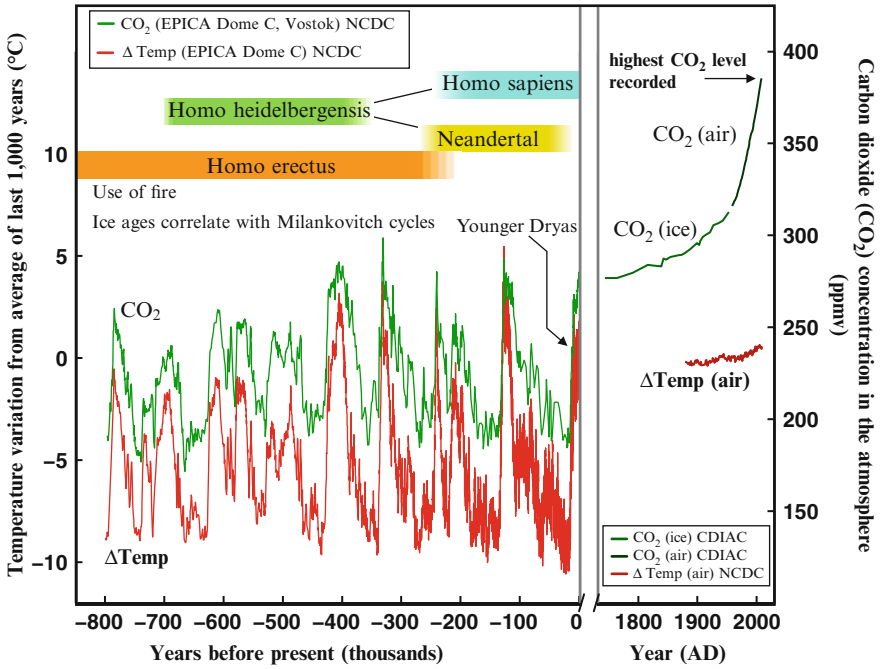

Fig. 1 Past climates and ice ages as deduced from geological data. The main time axis shows years before the present

in Fig. 1. Here the time scale includes the four latest ice ages (between −500 and 0 on the main time scale of the graph) with proxies for both temperature and carbon dioxide; and we have summarized human evolution on the figure, with the bronze age of *homo sapiens* appearing quite close to the end of the main time scale. These ice ages are thought to correlate with the Earth's orbital variations in eccentricity, spin axis and perihelion as first postulated by Milankovitch (1920, 1941). In terms of the closely correlated temperature and carbon dioxide graphs, the start-up of each ice age is rather gradual: but each age ends with a quite sudden jump to warmer conditions in what we would now call a climate tipping point.

A much earlier event that happened about 34 million years ago was a sudden *cooling* of the Earth in what is called the green-house to ice-house tipping. This is illustrated in Fig. 2 which displays the calcium carbonate ($CaCO_3$) content from Pacific sediment cores which were laid down some 30–40 million years ago. In this paper we shall be making prediction studies of, firstly, a computer simulation of a model cooling event, and secondly *ice-core data* for the end of the most recent glaciation of the Earth.

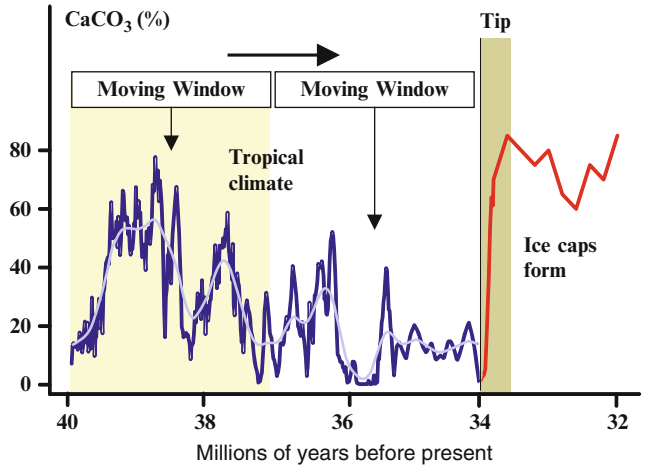

Fig. 2 The sudden cooling of the Earth from tropical conditions to a state with ice caps that is captured in the calcium carbonate percentage of oceanic sediment cores. The time series is the calcium carbonate content from tropical Pacific sediment cores, laid down 30 to 40 million years ago

2 Recent Prediction Studies

Given the current concerns about global warming (IPCC 2007), and even the precautionary examination of massive geo-engineering interventions Launder and Thompson (2010), there is currently much interest in examining climatic tipping points to see if it is feasible to predict them in advance. This recent work looks for a slowing down of the intrinsic transient responses, which is predicted to occur before an instability is encountered (Thompson and Stewart 2002; Thompson and Sieber 2010). This is done, for example, by determining the short-term autocorrelation coefficient ARC(1) which examines to what extent a current point is correlated to its preceding point based on averaging over a sliding window of the time series. This stability coefficient (a mapping eigenvalue) should increase to unity at tipping. Such studies have been made both on climatic computer models and on real paleo-climate data preceding ancient tipping events.

The paper by Livina and Lenton (2007) is particularly noteworthy because it presents the first bifurcational predictions using real geological data (as opposed to data from a computer simulation), namely the Greenland ice-core data spanning the time from 50,000 years ago to the present. The unevenly spaced data comprised 1,586 points and their DFA-propagator, analogous to ARC(1), was calculated in sliding windows of length 500 data points. The results are shown in Fig. 3, and the rapid warming at the end of the last ice age, around 11,500 years before the present is anticipated by an upward trend in the propagator, which is heading towards its critical value of unity at about the correct time. The sliding window that ends near the tipping is highlighted, and we note that from a prediction point of view, the

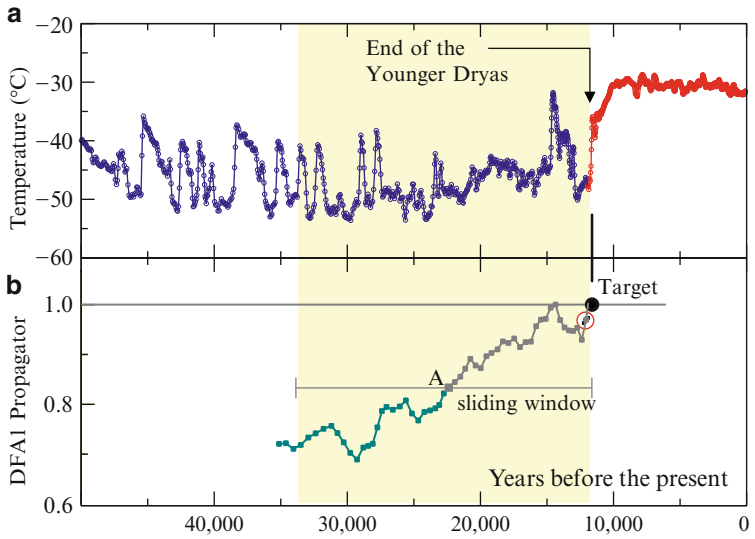

Fig. 3 The prediction study of Livina and Lenton (2007) of the tipping point at the end of the last ice age, using ice-core data from Greenland. The *small grey trace* within a *red circle* summarizes a much more localised study by Dakos et al. (2008) focused on the ending of the Younger Dryas event

propagator estimates would end at point A. The grey propagator curve beyond A uses time-series points beyond the tipping point, which would not normally be available: in any event, they should not be used, because they contaminate the grey results with data from a totally different climatic state. In a second paper, Dakos et al. (2008) systematically estimated the slowing of transients for real data in their analysis of eight ancient tipping events via reconstructed time series. These were:

(a) The end of the greenhouse Earth about 34 million years ago when the climate tipped from a tropical state (which had existed for hundreds of millions of years) into an icehouse state with ice caps, using data from tropical Pacific sediment cores,
(b) The end of the last glaciation, and the ends of three earlier glaciations, drawing data from the Antarctica Vostok ice core,
(c) The Bølling-Alleröd transition which was dated about 14,000 years ago, using data from the Greenland GISP2 ice core,
(d) The end of the Younger Dryas event about 11,500 years ago when the Arctic warmed by 7 ° in 50 years, drawing on data from the sediment of the Cariaco basin in Venezuela. This examines at a much shorter time scale, and with different data, the transition of Fig. 3.
(e) The desertification of North Africa when there was a sudden shift from a savanna-like state with scattered lakes to a desert about 5,000 years ago, using the sediment core from ODP Hole 658C, off the west coast of Africa.

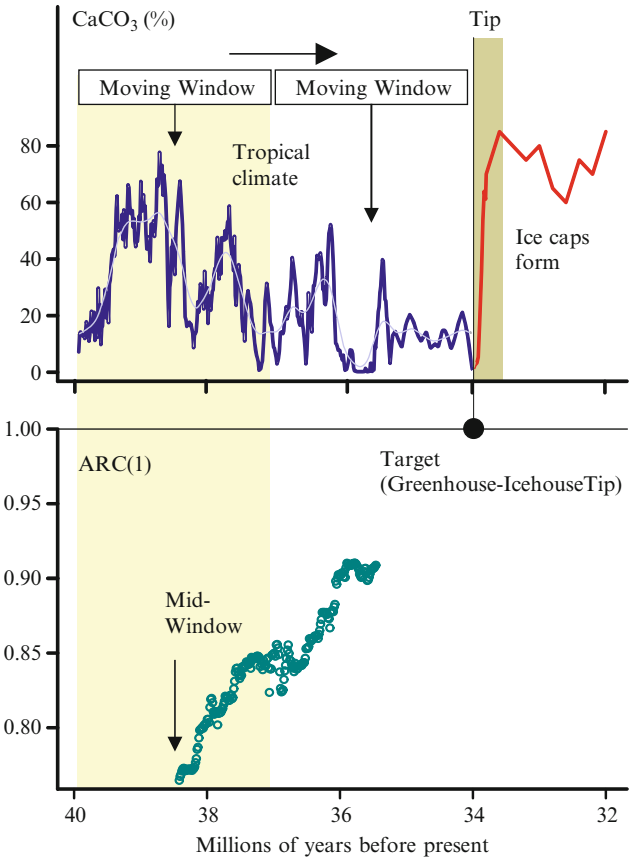

Fig. 4 The prediction results of Dakos et al. (2008) for the green-house to ice-house tipping that occurred about 34 million years ago, using the calcium carbonate ($CaCO_3$) content from Pacific sediment cores

In all of these ancient tippings, the dynamics of the system were shown to slow down before the transition as revealed by the significant increase of the short-term autocorrelation coefficient, ARC(1). An example of Dakos's results, for the transition shown in Fig. 2, is shown in Fig. 4. Here the upper time-series data is the calcium carbonate ($CaCO_3$) content from tropical Pacific sediment cores. The smooth central line is the Gaussian kernel function used to filter out slow trends.

The lower graph shows the plot of ARC(1) based on the *centre* of the sliding window (see discussion in Thompson and Sieber (2010)) and we notice that the projection is heading fairly accurately towards the target, namely the known tipping point from the paleo-data where ARC(1) should reach unity. Note, though, that other studies by Dakos et al were often much less convincing, as we might expect from the sparseness of much of the data.

3 Thermohaline Circulation (THC)

The thermohaline circulation is a global oceanic flow, illustrated in Fig. 5, which aids the burial of carbon in the deep ocean. The circulation is driven by the sinking of cold salty surface waters near the poles, and an increase of fresh-water melt from glaciers, etc., can disrupt this sinking. Such disruption has in the past shutdown the THC, and such a shutdown can give less carbon burial, thereby increasing any warming of the planet.

As a well-defined sub-system of the Earth's climate which can suddenly tip into an alternative steady state (namely a tipping element in the terminology of Lenton et al. (2008)) the THC has been extensively studied over many years. Figure 6, adapted from Rahmstorf (2000), summarizes the behaviour under a slow control sweep of the freshwater forcing. We should note that the subcritical pitchfork bifurcation will be observed in very simple models, but will be replaced by a fold in more elaborate ones.

A prediction study, based on the *simulation* from a more realistic model of the THC, is due to Held and Kleinen (2004) and is illustrated in Fig. 7. This study was the archetype on which the later works of Livina and Lenton (2007) and Dakos et al. (2008) were based. It uses the local decay rate as the diagnostic variable that Held and Kleinen thought is most directly linked to the distance from a bifurcation threshold. They demonstrated its use to predict the shutdown of the circulation using the oceanic output of CLIMBER2, a predictive coupled model of intermediate complexity. They made a 50,000 years transient run with a linear increase in atmospheric CO_2 from 280 to 800 parts per million (ppm), which generates within the model an increase in the fresh water forcing. This run results in the eventual collapse of the THC as illustrated.

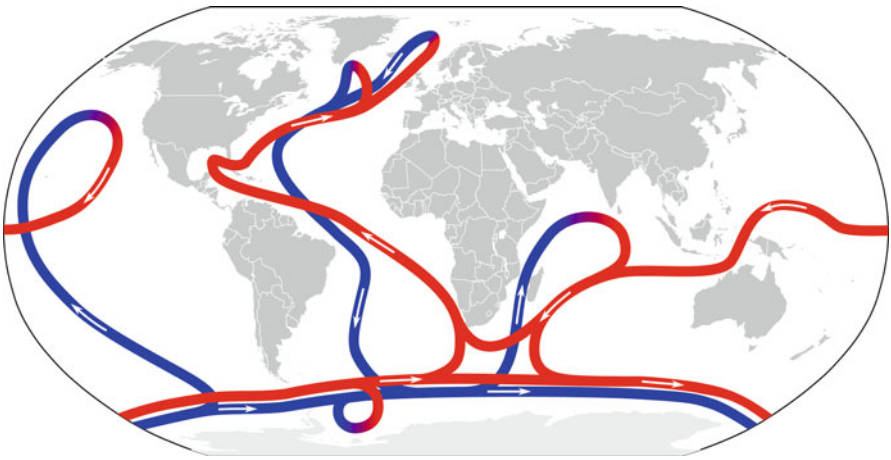

Fig. 5 A schematic over-view of the thermohaline circulation. Warm surface currents are shown in *red*, while cold deep currents are shown in *blue* (Map by Robert Simmon, NASA)

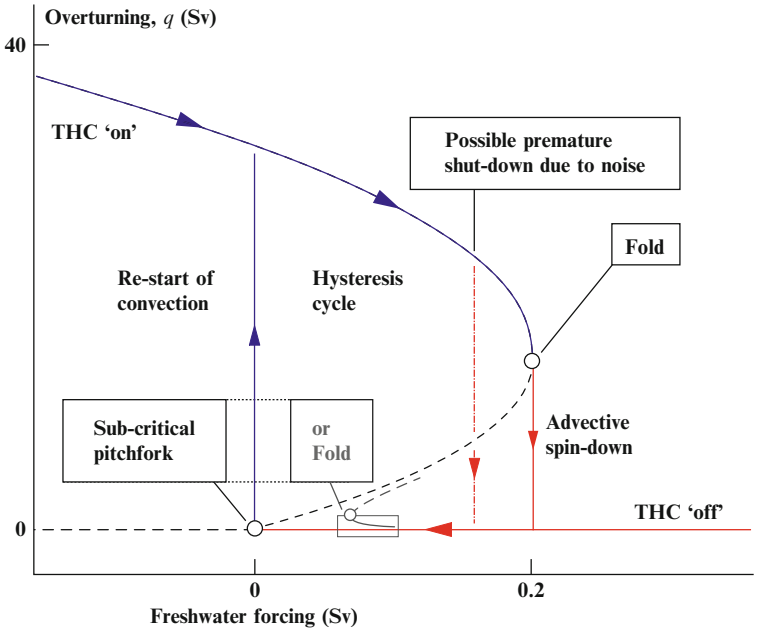

Fig. 6 A schematic diagram of the response of the THC showing two bifurcations and the associated hysteresis cycle. Note that 1 Sv is 10^6 m^3/s, which is roughly the combined flow rate of all the rivers on Earth

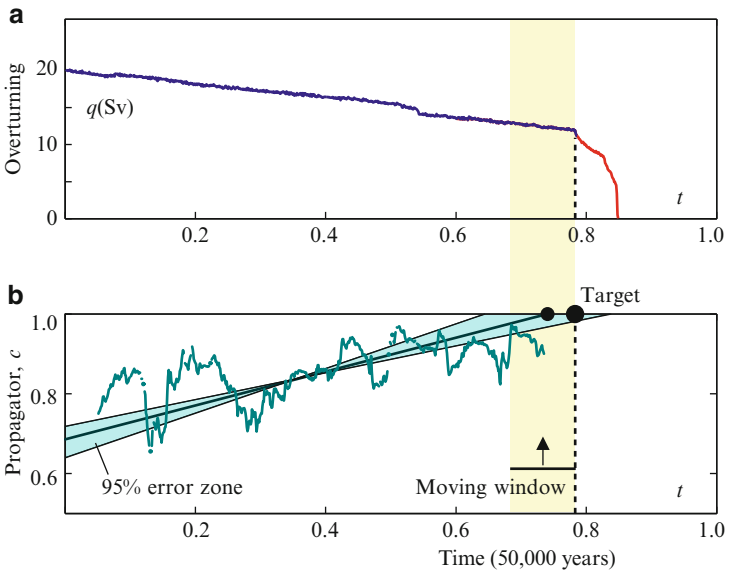

Fig. 7 The results of Held and Kleinen (2004) give a good prediction of the collapse of the thermohaline circulation induced by a four-fold linear increase of CO_2 over 50,000 years in a model simulation. Collapse present at $t \approx 0.8$ is predicted to occur when the propagator, c = ARC(1) reaches +1

The top graph in Fig. 7 corresponds approximately to the schematic diagram of Fig. 6. It is fairly linear over much of the timescale, and there is no early prediction of the fold bifurcation in terms of path curvature. The lower graph shows the variation of the *first-order autoregressive coefficient* or *propagator*, $c = \mathrm{ARC}(1)$. Unlike the upper response diagram, the time-series of ARC(1), although noisy, allows a fairly good prediction of the imminent collapse using the linear fit drawn. The fairly steady rise of ARC(1) towards its critical value of $+1$ is indeed seen over a very considerable time scale. Note that the linear fit is surrounded by a 95% zone, giving probability bounds to the collapse time.

4 Slowing of Transients and ARC Analysis

A precursor of many bifurcational instabilities is a slowing of transients, and this is exploited in the auto-regressive techniques that are used in the afore-mentioned prediction studies. The transients that we have in mind here are the 'internal transients' that are generated intrinsically within a complex dynamical system when localized fast motions act as noisy disturbances on the slower overall dynamics.

Since a slowly evolving system, such as the Earth's climate, can be expected to encounter only codimension-one bifurcations, we list in Table 1 the known

Table 1 List of all co-dimension-1 bifurcations of continuous dissipative dynamics, with notes on their precursors. Here *S*, *E* and *D* are used to signify the safe, explosive and dangerous events respectively. *LDR* is the local decay rate, measuring how rapidly the system returns to its steady state after a small perturbation

Name	Type	Precursor of codim-1 bifurcations
Supercritical Hopf	S: point to cycle	LDR$\rightarrow$ 0 linearly with control
Supercritical Neimark	S: cycle to torus	LDR$\rightarrow$ 0 linearly with control
Supercritical flip	S: cycle to cycle	LDR$\rightarrow$ 0 linearly with control
Band merging	S: chaos to chaos	Separation decreases linearly
Flow explosion	E: point to cycle	Path folds. LDR$\rightarrow$ 0 linearly along path
Map explosion	E: cycle to torus	Path folds. LDR$\rightarrow$ 0 linearly along path
Intermittency explosion: flow	E: point to chaos	LDR $\rightarrow$ 0 linearly with control
Intermittency explosion: map	E: cycle to chaos	LDR$\rightarrow$ 0 as trigger (fold, flip, Neimark)
Regular interior crisis	E: chaos to chaos	Lingering near impinging saddle cycle
Chaotic interior crisis	E: chaos to chaos	Lingering near impinging chaotic saddle
Static fold	D: from point	Path folds. LDR$\rightarrow$ 0 linearly along path
Cyclic fold	D: from cycle	Path folds. LDR$\rightarrow$ 0 linearly along path
Subcritical Hopf	D: from point	LDR$\rightarrow$ 0 linearly with control
Subcritical Neimark	D: from cycle	LDR$\rightarrow$ 0 linearly with control
Subcritical flip	D: from cycle	LDR$\rightarrow$ 0 linearly with control
Saddle connection	D: from cycle	Period of cycle tends to infinity
Regular exterior crisis	D: from chaos	Lingering near impinging saddle cycle
Chaotic exterior crisis	D: from chaos	Lingering near impinging accessible saddle

codimension-one events of dissipative nonlinear dynamics (Thompson et al. 1994; Thompson and Stewart 2002; Thompson and Sieber 2010). We indicate in the table those events that are preceded by a well-defined vanishing of the local decay rate (LDR), and we see that the majority of the listed bifurcations do have this property. For a more extensive review of the slowing of transients, and the related ARC analyses see our reviews (Thompson and Sieber (2010, 2011a,b)).

5 Fold for Incipient Tipping (FIT)

Suppose we have reason to believe (as in the THC) that a fold is incipient. Under this condition we can augment the ARC analysis to extract the fold normal form parameters and their drift speed to estimate when a collapse is likely to occur. A dynamical system near a fold bifurcation behaves like an overdamped particle at position x in a gradually disappearing potential well (see Fig. 8a). Tipping then corresponds to an escape of the particle from the well to $-\infty$. Generically the potential well has the form

$$U(x) = x^3/3 - ax$$

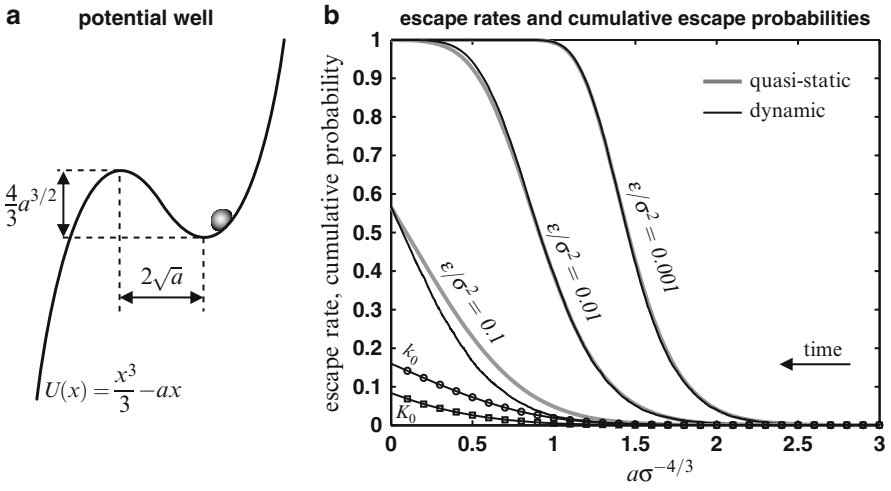

Fig. 8 (**a**) Overdamped particle in a potential well close to a fold. The displayed particle in the well is shown slightly flattened to indicate "sliding" rather than "rolling" to convey an intuition about the dynamical behaviour. (**b**) Static escape rate and cumulative escape probabilities (dynamic and quasi-static) for fold normal form at various ratios between drift speed ε and noise amplitude σ. For example, if $\sigma = 1$ and the drift speed of a is $\varepsilon = 0.001$ then the probability of escape before a reaches 1.5 is 50%. The static escape rate $k_0(a)$ and its integral $K_0(a)$ have been used to obtain the quasi-static approximation of the cumulative escape probability. The dynamic probabilities have been computed by integrating the stochastic normal form with drifting a

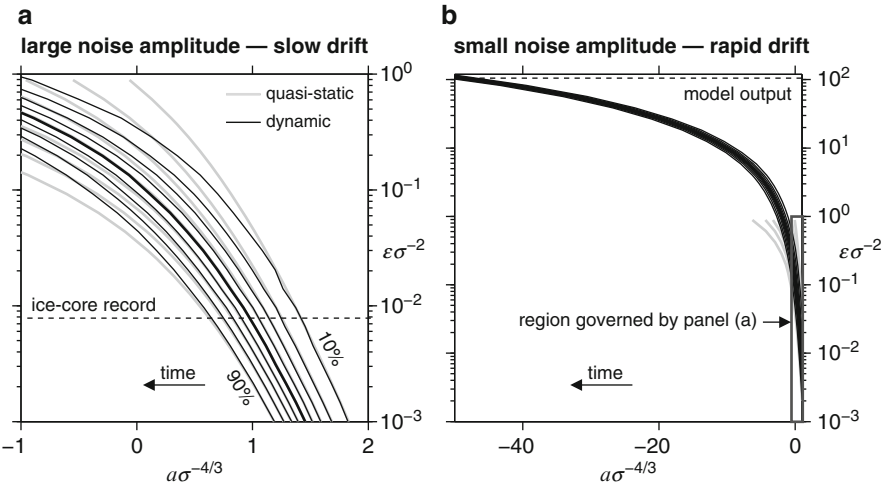

Fig. 9 Percentiles of cumulative escape probabilities for small ratio between drift speed ε and noise variance σ^2, (**a**), and large ratio ε/σ^2, (**b**). The median is highlighted as a *thick curve*. The *grey curves* correspond to the quasi-static approximation, which is valid only in panel (**a**)

where a is a system parameter that is gradually decreasing. If we assume that the system is affected by Gaussian white noise then the dynamics of the particle is governed by the stochastic differential equation

$$\mathrm{d}x = -\partial_x U(x)\mathrm{d}t + \sigma \mathrm{d}W_t = [a - x^2]\mathrm{d}t + \sigma \mathrm{d}W_t,$$

where σ is the noise amplitude and W_t is a Wiener process (that is, W_t has a normal distribution of variance t and increments such that $W_{t+s} - W_s$ (for $t, s > 0$) are independent from each other. With a gradually decreasing at a non-zero rate the equation for x must be augmented by

$$\mathrm{d}a = -\varepsilon \mathrm{d}t,$$

where ε is the drift speed of a. One expects that the balance between noise and drift governs the statistics of the escape process. At the extremes we have two cases. Without noise but with drift ($\sigma = 0$, $\varepsilon > 0$) the escape to infinity will be slightly delayed (that is, it will not happen at $a = 0$). More precisely, x will escape to infinity when a reaches $\varepsilon^{2/3} a_\infty$ where $a_\infty \approx -2.35$. At the other extreme end, with noise but without drift ($\sigma > 0$, $\varepsilon = 0$) the particle will escape almost surely for every positive a. Now, for any given a at fixed σ one can determine the *escape rate* k_0, that is, the probability of escape per unit time once 'steady conditions' are achieved. This rate is shown in Fig. 8b as a graph (curve with circles). For $a \gg \sigma^{4/3}$ an analytical expression for k_0 is known as Kramers' rate (Hänggi et al. 1990). If drift and noise amplitude are both non-zero, early and delayed escape partly 'balance' each other resulting in the cumulative escape probabilities shown in Figs. 8b and 9.

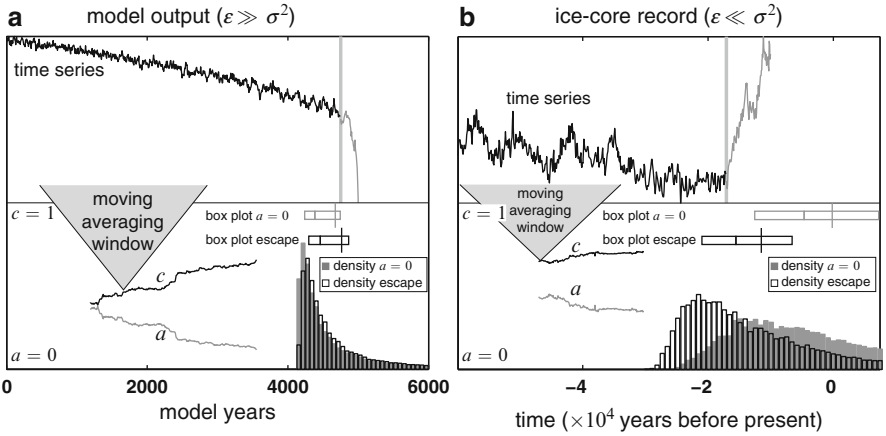

Fig. 10 Estimate of early or delayed escape from time series: (**a**) output of a transition model, (**b**) ice-core record by Petit et al. (1999). The *grey* histogram shows the probability for the first crossing of the critical value $a = 0$ for the estimated normal form parameter. The *black*-and-*white* histogram shows the probability of escape corresponding to this normal form parameter estimate (details in Sieber and Thompson (2012) and Thompson and Sieber (2011b)). The *box plots* show the quartiles and the mean of the respective density

For slow drift or large noise level ($\varepsilon \ll \sigma^2$) $P_{\text{esc}}(a)$ for the particle to escape before the drifting parameter reaches the value a can be approximated analytically using k_0 (a quasi-static approximation, see Miller et al. (2010) and Thompson and Sieber (2011b) for details). If we re-scale variables and time such that $\sigma = 1$ the probability of escape is approximately

$$P_{\text{esc}}(a) = 1 - \exp(-K_0(a)/\varepsilon) \quad \text{where} \quad K_0(a) = \int_a^{a(0)} k_0(a')\mathrm{d}a',$$

provided that $a(0) \gg 1$. The integral K_0 is also shown in Fig. 8b along with the resulting P_{esc} for various ratios of ε/σ^2 (grey curves). Note that a decreases over time as indicated by the arrow. For comparison the results of an integration of the stochastic differential equation are given in black. Figure 9 gives an overview of the percentiles of the cumulative escape probability over a range of drift-to-noise ratios. In the rapid-drift (or small-noise) regime in Fig. 9b the percentiles (and, thus, the escape probability densities) are concentrated near the curve given by the escape value of the deterministic trajectory: $a = \varepsilon^{2/3} a_\infty$. In both panels the horizontal coordinate changes in time along trajectories with a speed determined by the vertical coordinate. The two dotted lines (ice-core record in Fig. 9a and model output in Fig. 9b) are examples which will be discussed below.

Figure 10 demonstrates how one can estimate if escape will be early or delayed for two time series. Figure 10a shows the output of a model by Fraedrich (1978) for a transition to an icehouse Earth, taken from a paper by Dakos et al. (2008). Time series (b) is a snapshot of temperatures before the end of the last glaciation,

20,000 years ago. The data is taken from a paper by Petit et al. (1999) and is available at ftp.ncdc.noaa.gov. The window of the snapshot is identical to Fig. 1I in Dakos et al. (2008).

The lower parts of Fig. 10 show the AR(1) coefficient c as extracted by least-squares fitting the linear recursion $x_{n+1} = cx_n$ to the de-trended time series in a moving window. Each point in the time series c is the result of a fit in a window as indicated in the figure. For both time series the propagator increases. The critical value $c = 1$ is indicated in the figure but the distance of c to the critical value is in arbitrary units because this distance depends on the density of measurement points taken. Correspondingly, the drifting normal form parameter a decreases toward its critical value 0. Extrapolating the time series of the estimated normal form parameter we get a probability for the first crossing of $a = 0$ (histograms shown in grey in Fig. 10). The least-squares fit of the AR(1) coefficient also provides an estimate of the noise amplitude σ such that we can apply the normal form analysis from Fig. 9 to estimate when the trajectory will escape (see Sieber and Thompson 2012; Thompson and Sieber 2011b for details of the procedure). The resulting histogram is shown in Fig. 10 in black-and-white. The box plots in Fig. 10 show the quartiles and means corresponding to the first crossing of the critical parameter value (grey) and escape (black). That is, the vertical edges of the boxes correspond to the times $t_{0.25}$, $t_{0.5}$ and $t_{0.75}$ determined such that the probability of crossing the critical value before $t_{0.5}$ is 0.5 (for the grey box plot, similar for $t_{0.25}$ and $t_{0.75}$). The mean is indicated by the longer vertical line. We conclude that the time series (a) is from a system in the small-noise (or rapid-drift) regime ($\varepsilon \gg \sigma^2$). Thus, the escape is likely to have been slightly delayed. The time series of the ice-core record is in the large-noise (or slow-drift) regime such that the escape is likely to have occurred early. The estimated ratios ε/σ^2 are also indicated in Fig. 9.

6 Conclusion

Lenton et al. (2008) have proposed that bifurcations of climate subsystems may be the underlying mechanism for climate tipping in the foreseeable future. Similarly, Dakos et al. (2008) have identified a slowing-down near rapid transitions in paleo-climate time series that would hint at underlying fold bifurcations. Recent research into early-warning signals estimates this slowing down via short term autocorrelation or de-trended fluctuation analysis. A typical feature of dynamical systems near dangerous bifurcations with slowly drifting system parameters and noise is that the jump (escape) from the current attractor may occur early or delayed, depending on the balance between drift speed and noise and the properties of the noise (Baer et al. 1989; Kuske 1999; Miller et al. 2010; Thompson and Sieber 2011b). We have determined the probability distribution for escape over time for the fold normal form subject to Gaussian white noise of constant amplitude depending on drift speed and noise amplitude. Based on an estimate of the normal form

parameters we demonstrated for two example time series how early escape affects the early-warning signals and the prediction of tipping. In a more recent paper (Sieber and Thompson 2012), we have incorporated nonlinear features into climate-prediction studies.

References

Baer, S.M., Erneux, T., Rinzel, J.: The slow passage through a Hopf bifurcation: delay, memory effects, and resonance. SIAM J. Appl. Math. **49**(1), 55–71 (1989)

Dakos, V., Scheffer, M., van Nes, E.H., Brovkin, V., Petoukhov, V., Held, H.: Slowing down as an early warning signal for abrupt climate change. Proc. Natl. Acad. Sci. U. S. A. **105**, 14308–14312 (2008)

Fraedrich, K.: Structural and stochastic analysis of a zero-dimensional climate system. Q. J. R. Meteorol. Soc. **104**, 461–474 (1978)

Hänggi, P., Talkner, P., Borkovec, M.: Reaction-rate theory: fifty years after Kramers. Rev. Mod. Phys. **62**, 251–341 (1990)

Held, H., Kleinen, T.: Detection of climate system bifurcations by degenerate fingerprinting. Geophys. Res. Lett. **31**, L23207 (2004)

IPCC (2007) Climate Change: Contribution of Working Groups I–III to the fourth assessment report of the intergovernmental panel on climate chang. In: Solomon, S., Qin, D., Manning, M., Chen, Z., Marquis, M., Averyt, K.B., Tignor, M., Miller, H.L. (eds.) I The Physical Science Basis, II Impacts, Adaptation and Vulnerability, III Mitigation of Climate Change. Cambridge University Press, Cambridge (2007)

Kuske, R.: Probability densities for noisy delay bifurcations. J. Stat. Phys. **96**(3), 797–816 (1999)

Launder, B., Thompson, J.M.T. (eds.): Geo-Engineering Climate Change: Environmental necessity or Pandora's Box? Cambridge University Press, Cambridge (2010)

Lenton, T.M., Held, H., Kriegler, E., Hall, J.W., Lucht, W., Rahmstorf, S., Schellnhuber, H.J.: Tipping elements in the Earth's climate system. Proc. Natl. Acad. Sci. U. S. A. **105**, 1786–1793 (2008)

Livina, V.N., Lenton, T.M.: A modified method for detecting incipient bifurcations in a dynamical system. Geophys. Res. Lett. **34**, L03712 (2007)

Milankovitch, M.: Theorie Mathematique des Phenomenes Thermiques produits par la Radiation Solaire. Gauthier-Villars, Paris (1920)

Milankovitch, M.: Kanon der Erdbestrahlungen und seine Anwendung auf das Eiszeitenproblem Belgrade. New English Translation, 1998, Canon of Insolation and the Ice Age Problem. With Introduction and Biographical Essay by Nikola Pantic, 636pp. Alven Global (1941). ISBN 86-17-06619-9

Miller, N., Burgner, C., Dykman, M., Shaw, S., Turner, K.: Fast estimation of bifurcation conditions using noisy response data. Proc. SPIE **7647**(1), 764700–764712 (2010)

Petit, J.R., Jouzel, J., Raynaud, D., Barkov, N.I., Barnola, J.-M., Basile, I., Bender, M., Chappellaz, J., Davis, M., Delaygue, G., Delmotte, M., Kotlyakov, V.M., Legrand, M., Lipenkov, V.Y., Lorius, C., Pépin, L., Ritz, C., Saltzman, E., Stievenard, M.: Climate and atmospheric history of the past 420,000 years from the Vostok ice core, Antarctica. Nature **399**, 429–436 (1999)

Rahmstorf, S.: The thermohaline ocean circulation: a system with dangerous thresholds? Clim. Change **46**, 247–256 (2000)

Sieber, J., Thompson, J.M.T.: Nonlinear softening as a condition for early climate tipping. Philos. Trans. R. Soc. A **370**(1962), 1166–1184 (2012)

Thompson, J.M.T., Stewart, H.B.: Nonlinear Dynamics and Chaos, 2nd edn. Wiley, Chichester (2002)

Thompson, J.M.T., Sieber, J.: Predicting climate tipping points. In: Launder, B., Thompson, J.M.T. (eds.) Geo-Engineering Climate Change: Environmental Necessity or Pandora's Box? Cambridge University Press, Cambridge (2010)

Thompson, J.M.T., Sieber, J.: Predicting climate tipping points as a noisy bifurcation: a review. Int. J. Bifurc. Chaos **21**(2), 399–423 (2011a)

Thompson, J.M.T., Sieber, J.: Climate tipping as a noisy bifurcation: a predictive technique. IMA J. Appl. Math. **76**(1), 27–46 (2011b)

Thompson, J.M.T., Stewart, H.B., Ueda, Y.: Safe, explosive, and dangerous bifurcations in dissipative dynamical systems. Phys. Rev. E **49**, 1019–1027 (1994)

Computation of the Basins of Attraction in Non-smooth Dynamical Systems

Ugo Galvanetto and Alessandro Colombo

Abstract The paper discusses several issues related to the numerical computation of the stable manifold of saddle-like periodic cycles in piecewise smooth dynamical systems. Results are presented for a particular stick–slip system. In the second part of the paper the same mechanical model is used to briefly describe the interaction between fold and adding-sliding bifurcations.

Keywords Non-smooth dynamical systems • Stable manifolds • Computational methods

1 Introduction

Engineering systems affected by some form of nonlinearity can exhibit multiple stable solutions under steady state conditions of the external forces. If the system is dynamic it is common to express this concept by saying that there are coexisting attractors. Usually only one of them represents the normal working mode of the system from an engineering point of view, whereas the others are conditions to be avoided because the system is too deformed or cannot function (safely) if it reaches them. A classical problem of engineering mechanics is to determine whether the normal working mode of the system is robust with respect to perturbations. These can often be represented as variations in the positions or the velocities of the system.

U. Galvanetto (✉)
Department of Structural and Transportation Engineering, University of Padua, 35131 Padova, Italy
e-mail: ugo.galvanetto@unipd.it

A. Colombo
Department of Electronics and Information, Politecnico di Milano, 22100 Como, Italy
e-mail: alessandro.colombo@polimi.it

M. Wiercigroch and G. Rega (eds.), *IUTAM Symposium on Nonlinear Dynamics for Advanced Technologies and Engineering Design*, IUTAM Bookseries (closed) 32, DOI 10.1007/978-94-007-5742-4_2,

They are acceptable as long as they do not bring the system far from its normal working mode, or unacceptable otherwise. In simple smooth systems, it is possible to adopt a new design approach aiming at defining, within the basin of attraction, a "safety set" of all initial conditions which do not compromise the integrity of the system (Cruck et al. 2001; Barreiro et al. 2002). In these cases, the overall size of the basin can provide a measure of the safety or robustness of an engineering system. Another measure could be provided by the distance between the attractor and its basin's boundaries, that would provide an indication of the size or the duration of the perturbation needed to bring the system out of the safety basin. Since engineering systems may be subjected to pulse loads of finite duration, attention should be given to both the absolute basins, related to steady external forcings, and transient basins corresponding to transient excitations. Similar ideas have been proposed in the past, for example in (Soliman and Thompson 1989; Thompson and Soliman 1990). Therefore one of the classical problems in nonlinear dynamics, the computation of the basins boundaries, which separate safe initial conditions from the unsafe ones, could in the future become a standard step in the design of systems of engineering relevance. In particular in smooth dynamical systems the boundaries of the basins of attraction of coexisting attractors consist of stable manifolds of saddle limit sets. The numerical computation of invariant manifolds has interested several researchers in the past (Parker and Chua 1989) and has been practically solved for the case of smooth dynamical systems. In the present work some properties of the stable manifolds of equilibria or cycles of saddle type are discussed for the case of piecewise smooth dynamical systems (Galvanetto 2008; Colombo and Galvanetto 2009). Our results can in principle be applied to systems of any dimension, but the details reported here concern in particular three-dimensional systems, where the computation of invariant manifold is of practical use and it is easier to visualize the concepts. In particular, a crucial ingredient for the application of the method is the understanding of the geometric constraints that the piecewise nature of the flow imposes on the shape of the manifold (Colombo and Galvanetto 2009). The final part of the paper presents a few results regarding transitions and bifurcations of the piecewise smooth steady state motions investigated in earlier sections of the paper.

2 The Forced Friction Oscillator

The non-smooth dynamics investigated in the present work is generated by the system sketched in Fig. 1, that was presented in reference (Oestreich et al. 1996): a block of mass m is supported by a belt moving with constant velocity V_{dr}. The block is connected to a fixed support by a linear elastic spring of stiffness k, which assumes its unstretched length for $x = 0$, and is subjected to an external harmonic force of magnitude a and frequency ω. While the block rides on the belt with no relative motion between them, the motion is in a stick phase described by the two states of the system position x and time t in the following equation:

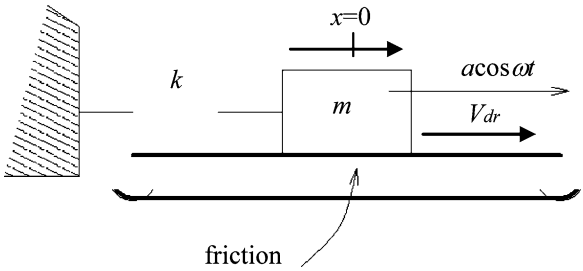

Fig. 1 The mechanical model under investigation

$$x(t) = x(t_0) + V_{\mathrm{dr}}(t - t_0) \tag{1}$$

where $x(t_0)$ is the position of the block a time $t = t_0$. The block can stick if $\dot{x} = V_{\mathrm{dr}}$ and the following conditions are simultaneously true:

$$-\frac{F_{sf}}{k} + \frac{a}{k}\cos\omega t \le x \tag{2a}$$

$$x \le \frac{a}{k}\cos\omega t + \frac{F_{sf}}{k} \tag{2b}$$

where F_{sf} is the magnitude of the maximum static friction force. The two sinusoidal functions of time $x(t) = [(a/k)\cos\omega t \pm F_{sf}/k]$ are the boundaries in the plane (x, t) of the stick zone. Once either of the two inequalities (2) is satisfied as equality an accelerated motion starts, called slip phase, which can be of two types:

$$\textit{forward slip phase} \quad m\ddot{x} + kx = a\cos\omega t - F_{kf}, \quad \textit{if} \quad \dot{x} > V_{dr} \tag{3a}$$

$$\textit{backward slip phase} \quad m\ddot{x} + kx = a\cos\omega t + F_{kf}, \quad \textit{if} \quad \dot{x} < V_{dr} \tag{3b}$$

where F_{kf} is the magnitude of the kinetic friction force which will be defined later. The motion described by Eq. (3a) starts when the equality in (2a) is verified, and the speed of the block is greater than V_{dr}; otherwise if the equality in (2b) is verified then the dynamics given by Eq. (3b) starts, and the speed of the block is less than V_{dr}. During a slip phase the system is described by three states, x, t and velocity $\dot{x}$.

The static friction force can assume any value in the range between $-F_{sf} = -\mu_s mg$ and $F_{sf} = \mu_s mg$; where $\mu_s(=\alpha+\beta)$ is the coefficient of static friction and mg is the weight of the block. The magnitude of the kinetic friction force is a function of the relative velocity and is defined as $F_{kf} = \mu_k mg$, where μ_k is the coefficient of kinetic friction defined as (Fig. 2):

$$\mu_k = \frac{\alpha}{1 + \gamma|\dot{x} - V_{dr}|} + \beta + \eta(\dot{x} - V_{dr})^2 \tag{4}$$

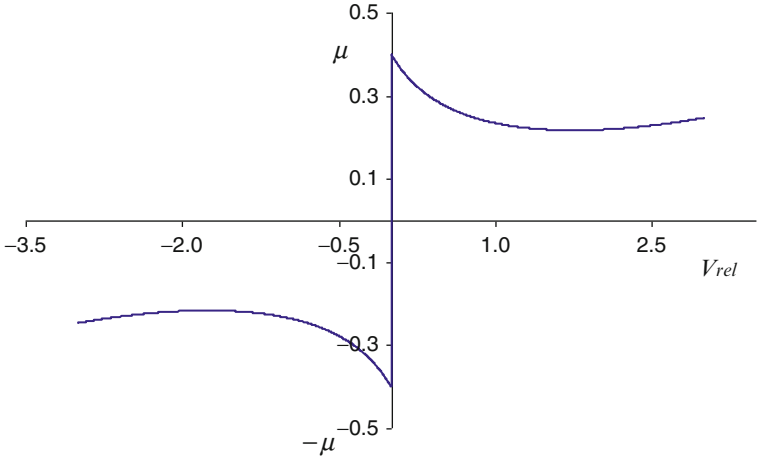

Fig. 2 Example of a commonly adopted friction characteristic, $V_{rel} = V_{dr} - \dot{x}$

If during an accelerated motion governed by either of Eqs. (3) the velocity of the block coincides with that of the belt and the position of the block is within the boundaries of the sticking region, then the block sticks to the belt and its motion is described again by Eq. (1) in which t_0 is the instant of re-attachment.

In the formalism usually adopted in the literature on non-smooth dynamical systems (Di Bernardo et al. 2007) Eqs. (3), written in a way familiar to most engineers, are recast in the following form:

$$\dot{x} = f(x) = \begin{cases} f_1(x) & \text{if } h(x) > 0 \\ f_2(x) & \text{if } h(x) < 0 \end{cases} \tag{5}$$

Where $x = (x_1, x_2) = (x, \dot{x})$, $h(x) = x_2 - V_{dr}$ and

$$f_1(x) = \left\{ \frac{-k x_1 + a \cos(\omega t)}{m} - g \left(\frac{\overset{x_2}{\alpha}}{1 + \gamma (x_2 - V_{dr})} + \beta + \eta (x_2 - V_{dr})^2 \right) \right. \tag{6a}$$

$$f_2(x) = \left\{ \frac{-k x_1 + a \cos(\omega t)}{m} + g \left(\frac{\overset{x_2}{\alpha}}{1 - \gamma (x_2 - V_{dr})} + \beta + \eta (x_2 - V_{dr})^2 \right) \right. \tag{6b}$$

In the paper the parameter values are fixed:

$$\begin{array}{lllll} m = 1 & k = 1 & a = 3.5 & \omega = 1.0 & g = 10 \quad V_{dr} = 1 \\ \alpha = 0.3 & & \beta = 0.1 & \mu_s = 0.4 & \gamma = 1.42 \quad \eta = 0.01 \end{array}$$

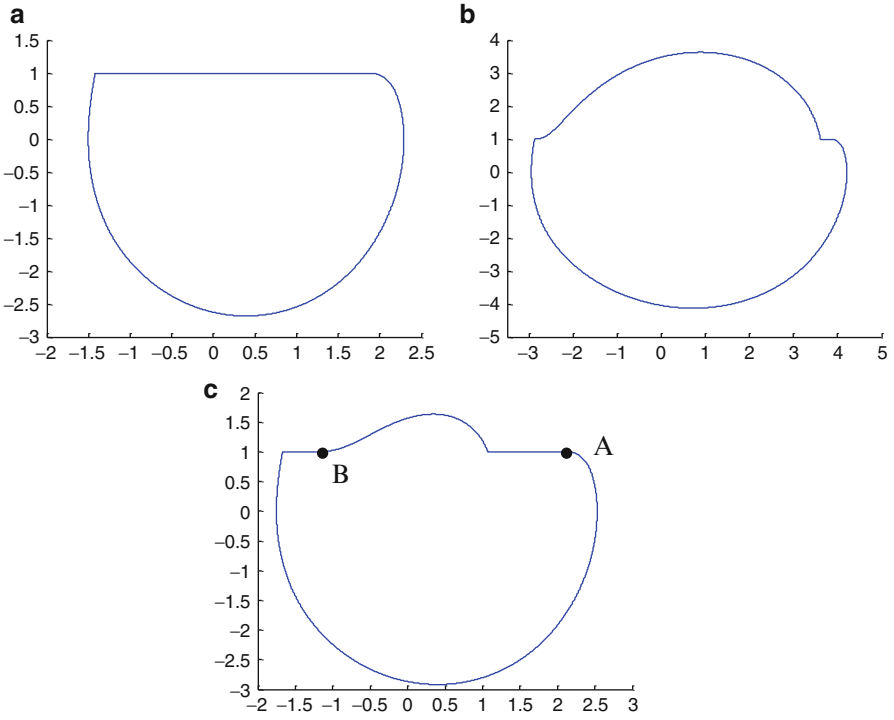

Fig. 3 (**a**) motion-1s, (**b**) motion-2s, (**c**) motion-2u. The scales of the figures are not the same

The friction characteristic adopted is the same presented in (Oestreich et al. 1996) and is considered a good approximation of physically observed friction behaviours.

The mechanical system under investigation with the above parameter values posses (at least) three steady states: two attractors and a saddle cycle as shown in Fig. 3. The nature of the stability of the steady states and the algorithms adopted to accurately locate unstable stick–slip motions have been described elsewhere (Galvanetto 2000, 1999). The three steady states are called motion-1s, motion-2s and motion-2u where the numbers 1 or 2 indicate how many stick phases are present and the letter s or u indicate respectively the stable or unstable nature of the steady state. In the plane of initial conditions $(x, \dot{x})$ at time zero the stable manifold of the saddle cycle forms the boundary between the basins of the two coexisting attractors. Figure 4 shows the basin of motion-2s (and of motion-1s) computed with a cell-mapping type algorithm (Hsu 1987).

In Fig. 3c the saddle cycle of a stick–slip system is characterised by two portions of sticking branch, the horizontal segments; points A and B on the orbit indicate where the stick–slip transitions take place: the stick–slip transitions appear smoother than the slip–stick transitions, this fact is related with the degree of continuity in the friction force. If $\dot{x} = V_{dr}$ in Eq. (4) then $\mu_s = \mu_k = \alpha + \beta$ therefore the transition

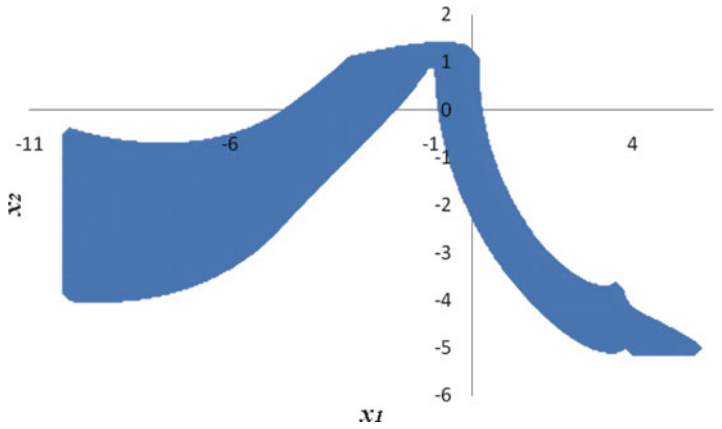

Fig. 4 The *blue area* is the basin of attraction of motion-2s in the window $-10 < x < 5$, $-5 < \dot{x} < 2$

from the static friction force to the kinetic friction force is continuous, although it is non smooth as shown in Fig. 2. Vice versa the transition between kinetic and static friction is in general associated to a jump in the forces applied to the block and therefore in its acceleration (Galvanetto 1999). At a transition from kinetic to static friction the friction force usually jumps from one of the two the extreme values $\pm(\alpha + \beta)mg$ to a value within the range $-(\alpha + \beta)mg \div +(\alpha + \beta)mg$ defined by the following equilibrium equation:

$$F_s = kx - a\cos\omega t$$

in which the value of x is that of the slip–stick transition provided by the numerical integration.

3 Reconstruction of the Stable Manifold

Figure 5 is a sketch of the flow around any of the two sticking branches of motion-2u: if $\dot{x} > V_{dr}$ the trajectories intersect transversally the line $\dot{x} = V_{dr}$ from above; in a similar way in the half-plane $\dot{x} < V_{dr}$ the trajectories intersect transversally the line $\dot{x} = V_{dr}$ from below. Every point of the sticking phase can be thought to belong simultaneously to three trajectories: the sticking-trajectory, the trajectory converging to it from above and the trajectory converging from below. The main idea of the method proposed in (Galvanetto 2008; Colombo and Galvanetto 2009) to compute the stable manifold of a saddle cycle, is that the stable manifold can be numerically reconstructed by integrating backwards in time all trajectories that in forward time converge to the saddle limit set, thus, in the case of the cycle in Fig. 3c,

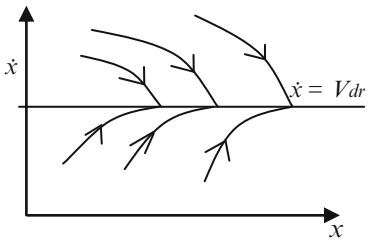

Fig. 5 Sketch of the flow near a sticking branch

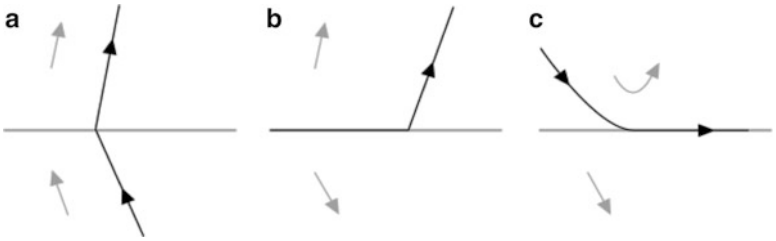

Fig. 6 Geometry of a single trajectory on the stable manifold at a generic intersection with a discontinuity surface. In the figure, *arrows* on the orbits indicate the positive direction of time, while *grey arrows* sketch the vector field above and below the switching surface

all trajectories that converge to the sticking branches of the cycle. Once a single trajectory of the stable manifold is found, the whole manifold can be constructed by numerical continuation, following the trajectory as its end point is changed along the manifold. This idea has been successfully used in smooth systems and is explained for example in (Krauskopf et al. 2005). To apply it to a piecewise smooth dynamical system, a first and fundamental step is to understand how the orbits, and the families of orbits that constitute a stable manifold, intersect the surfaces of discontinuity of the system, taking into account the non-reversibility introduced by the non-smooth nature of the flow. A careful look at the generic geometries of intersection of families of orbits with smooth discontinuity surfaces, casted into the framework of singularity theory, allows to conclude that a generic orbit belonging to a stable manifold intersects a discontinuity boundary in one of the three scenarios in Fig. 6, while a one-parameter family of orbits, that is, a two dimensional stable manifold, may contain some of the seven singular points depicted in Fig. 7. Additionally, certain conditions that have been identified, give place to some more singular points, analogous to the one in Fig. 7g, where however the complex interplay of vector fields with the discontinuity boundary cause a breakup of the manifold. The geometries and consequences of these cases are subject of ongoing research. Although, as shown in this short discussion, the geometry of these manifold can be rather intricate, the picture is, in most applications, quite simpler.

As long as all sticking branches are stable, meaning that slipping trajectories converge to the branch, rather than diverging, only scenarios (b) and (e) in Fig. 7 are possible, since all others include unstable sticking branches. Many mechanical and engineering systems admit only stable sticking phases, and in these cases scenarios

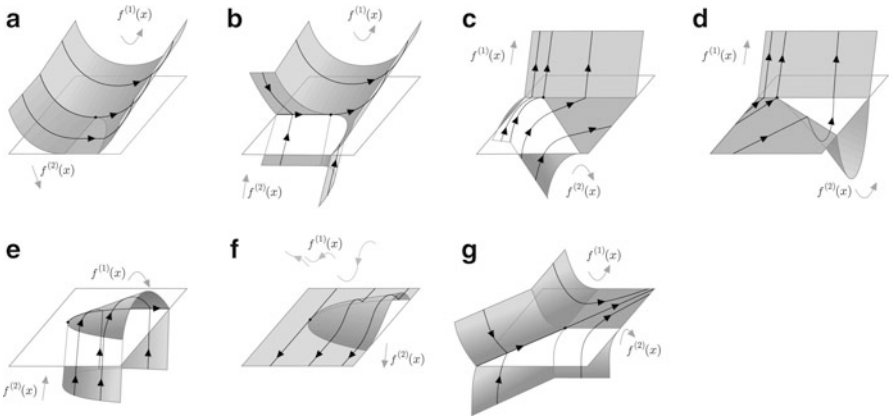

Fig. 7 Geometry of the stable manifold around each one of the seven singular points, [7]

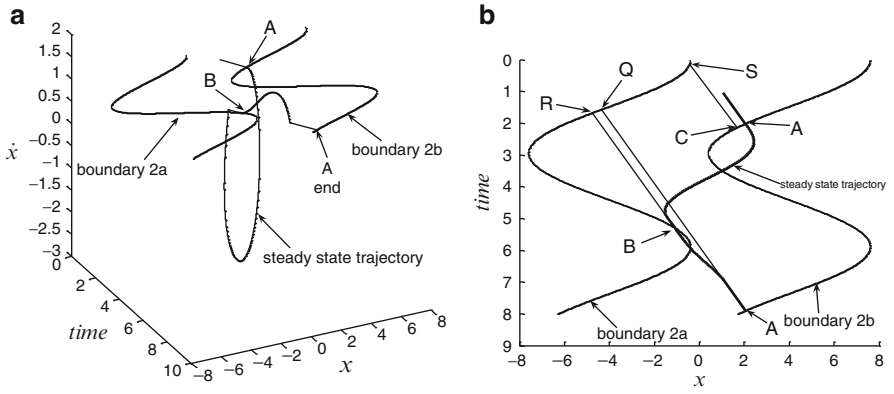

Fig. 8 (**a**) Three-dimensional phase portrait; the *thick line* is the trajectory of the unstable steady state and the *thin lines* are the boundaries of the stick zone. (**b**) Projection of figure (**a**) on the plane displacement-time; [6]

(b) and (e) are sufficient for the analysis (as long as the stable manifold is two-dimensional). They represent respectively the end and start points of a sticking phase.

Figure 8a is a three-dimensional view of the unstable limit cycle of Fig. 3c in its phase space. Thick lines indicate the steady states, thin sinusoidal lines in the plane (x, V_{dr}, t) show the boundaries of the stick zone. Since the saddle cycle has (two) sticking segments, all orbits of its stable manifold must eventually converge to these segments, each one of which can therefore be chosen as the family of end points to generate the whole manifold. The stick phase ending at point A required by the new method, is not only the portion belonging to the steady state trajectory shown in Fig. 8a; it is the whole stick phase shown by the thin straight line AQ in Fig. 8b, since it is apparent that all points belonging to such line will be attracted to the unstable limit cycle. The stick phase AQ is found by starting from the end point

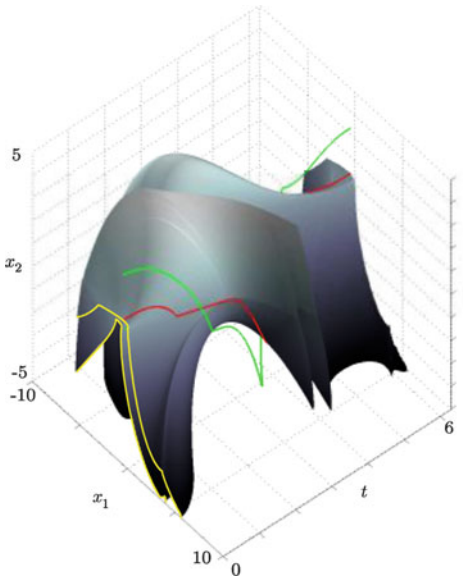

Fig. 9 Stable manifold of motion-2u; the *green lines* represent attractors and the *red line* the saddle-cycle. The *yellow lines* are the basin boundary to be compared with that of Fig. 4

A and integrating backward in time along the stick trajectory to the first intersection (point Q) with one of the boundaries of the stick phase. The same concept applies to the other stick phase ending at B. The two portions of straight lines AQ and BR are stick phases partially belonging to the unstable limit cycle and partially attracted by it. They are not necessarily all the stick phases attracted by the unstable limit cycle, transient stick phases could exist (and do exist!) which generate slip trajectories eventually attracted by motion-2u. Infinitely many of these transient stick phases could exist, as shown in (Galvanetto 2008). In the example examined in the present paper only one transient stick-phase exists, which is indicated by the line CS in Fig. 8b.

In Fig. 8b a transient slip trajectory could be drawn to connect point C with a point of the line AQ, but it is not shown for clarity reasons. Points A, B, C of Fig. 8 are singular points of the stable manifold of the type shown in Fig. 7b, whereas points R, Q, S are singular points such as the one sketched in Fig. 7e. It is worth observing that the knowledge of only one of the stick phases (for example AQ) is sufficient to reconstruct computationally the whole manifold, since all others stick phases are connected to it, either backward or forward in time. The algorithm adopted for the computation of the stable manifold is fully described elsewhere (Colombo and Galvanetto 2009).

Figure 9 shows part of the non-smooth stable manifold computed with the method presented above. All orbits that, departing from the saddle cycle backward in time, remain between the surfaces $|\dot{x}| > 5$, are represented. The intersection of the manifold with the plane $t = 0$ is marked in yellow, and corresponds to the boundary of the basin shown in Fig. 4. Moreover Fig. 10 shows two projections of the same manifold on the planes $\dot{x} = 0$ and $x = 0$.

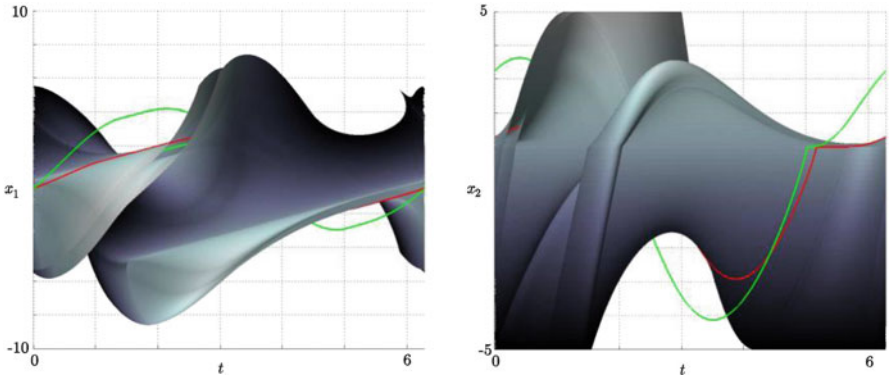

Fig. 10 Projections of the stable manifold on the planes $\dot{x} = 0$, *left*, and $x = 0$, *right*. *Green orbits* are attractors, the *red orbit* is the saddle cycle

4 Remarks on Transitions and Bifurcations

In this last section of the paper we briefly describe how bifurcations and transitions can interact in the evolution of the dynamics as a parameter is changed. For the given set of parameter values there exist three steady state motions: motion-1s, motion-2s and motion-2u, as already explained above. In reference (Merillas 2006) a smooth co-dimension-two cusp bifurcation was presented. As can be seen in Fig. 11, taken from the same reference, from the cusp point B_2, two branches of fold bifurcation, which we shall denote by Γ_{f1} and Γ_{f2}, merge (tangentially). The resulting wedge divides the parameter plane into two regions. In region 1, inside the wedge, there are the three solutions shown in Fig. 3, while in the other region, outside the wedge, there is a single solution, which is stable. Varying ω and crossing either Γ_{f1} or Γ_{f2} away from the cusp point we find a non-degenerate fold bifurcation. Along a third bifurcation curve (not depicted in Fig. 11) inside the wedge, motion-1s gains one more sticking segment, becoming topologically equivalent to motion-2u. This is known in the literature as adding sliding bifurcation (Di Bernardo et al. 2007).

These bifurcations might be better understood by looking at the 1-d map induced by the system, see (Oestreich et al. 1996) on how to obtain the map, which shows some features of the dynamics of the system itself. Motion-1s has only one stick phase, motion-2s and motion-2u have two stick phases, for that reason motion-1s can be seen in the first-iterated map and in the second-iterated map as a fixed point of the map. Motion-2s and motion-2u can only be seen as fixed points of the second-iterated map shown in Fig. 12.

If the force frequency is reduced to $\omega = 0.95$ only motion-2s survives, as shown in Fig. 13a. Motion-1s and motion-2u do not exist because there is no intersection between the map and the bisection line at 45°. The sudden disappearance of motion-1s can be understood looking at the second iterated map of Fig. 13a, b.

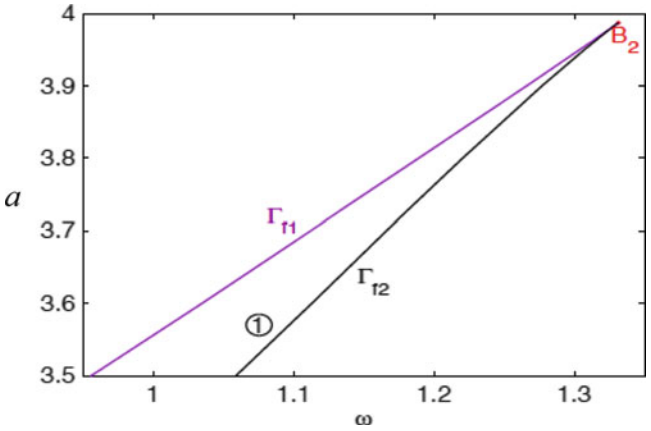

Fig. 11 Bifurcation diagram taken from page 99 of Merillas (2006)

Fig. 12 Second iterated map showing motion-1s, motion-2s and motion-2u for $\omega = 1$

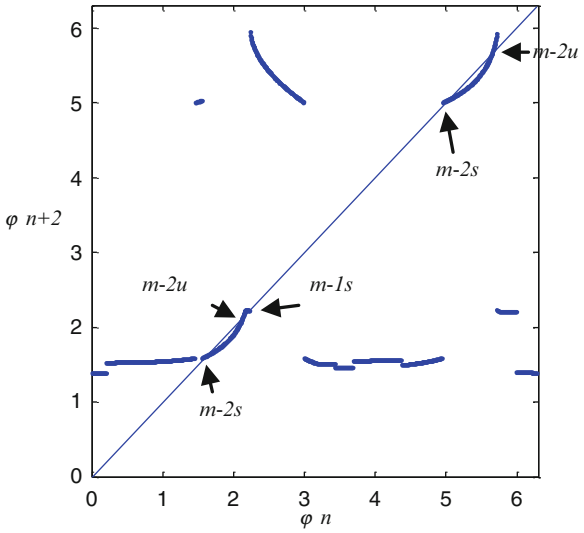

Motion-1s and motion-2u have collided in what appears to be a non-degenerate fold bifurcation which takes place after a transition has affected motion-1s: before the fold occurs the trajectory of motion-1s changes so that a second branch of stick phase appears. Once the transition has taken place the fold involves two motions with the same topological structure. Figure 13b shows the second-iterated map for an intermediate value of the parameter ω for which all three steady states are characterized by two stick phases. Summarizing: for the parameter values defined above the system possess the three steady states shown in Fig. 3. If the value of the parameter ω is reduced below 1, an adding-sliding bifurcations adds a stick phase to motion-1s, which is then shown in Fig. 13b as motion-1sa and -1sb. A further

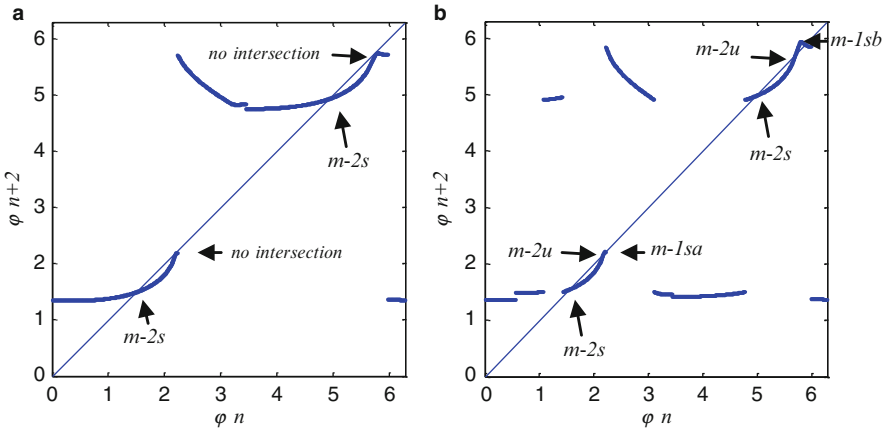

Fig. 13 (**a**) $\omega = 0.95$: second iterated map showing only one, period-2 motion for the map, corresponding to motion-2s. (**b**) $\omega = 0.975$: second iterated map showing three period-2 steady states for the map corresponding to motion-2u, motion-2s, and the motion generated at the adding-sliding bifurcation from motion-1s

reduction of ω causes a standard fold bifurcation in which motion-2u disappears colliding with motion-1s. Several adding-sliding bifurcation lines exist in the wedge of Fig. 11.

5 Conclusions

The paper presents the main ideas of a method to compute the stable manifolds of saddle-like periodic cycles in piece-wise smooth dynamical systems. They represent the basin boundaries of the relevant coexisting attractors. The method is applied to a mechanical system affected by dry friction in which three steady states, two stable and one of saddle-type, exist. In the second part of the paper the evolution of the three steady states is followed as a parameter is varied. It is shown how standard bifurcations and non-smooth bifurcations can interact; in particular an example described in the paper shows that adding-sliding bifurcations may be required before fold bifurcations can take place.

References

Barreiro, A., Aracil, J., Pagano, D.: Detection of attraction domains of nonlinear systems using bifurcation analysis and Lyapunov functions. Int. J. Control **75**, 314–327 (2002)

Colombo, A., Galvanetto, U.: Stable manifolds of saddles in piecewise smooth systems. CMES **53**, 235–254 (2009)

Cruck, E., Moitie, R., Seube, N.: Estimation of basins of attraction for uncertain systems with affine and Lipschitz dynamics. Dyn. Control **11**, 211–227 (2001)

Di Bernardo, M., Budd, C.J., Champneys, A.R., Kowalzyk, P.: Piecewise-Smooth Dynamical Systems: Theory and Applications. Springer, New York (2007)

Galvanetto, U.: Nonlinear dynamics of multiple friction oscillators. Comp. Method Appl. Mech. Eng. **178**(3–4), 291–306 (1999)

Galvanetto, U.: Numerical computation of Lyapunov exponents in discontinuous maps implicitly defined. Comput. Phys. Commun. **131**, 1–9 (2000)

Galvanetto, U.: Computation of the separatrix of basins of attraction in a non-smooth dynamical system. Phys. D **237**, 2263–2271 (2008)

Hsu, C.S.: Cell-to-cell mapping: a method of global analysis for nonlinear systems. Springer, New York (1987)

Krauskopf, B., Osinga, H.M., Doedel, E.J., Henderson, M.E., Guckenheimer, J., Vladimirsky, A., Dellnitz, M., Junge, O.: A survey of methods for computing (un)stable manifolds of vector fields. Int. J. Bifurc. Chaos **14**, 763–791 (2005)

Merillas, I.: Modeling and numerical study of nonsmooth dynamical systems. Ph.D. thesis, Dept. Matematica Aplicada IV, Universitat Politècnica de Catalunya (2006)

Oestreich, M., Hinrichs, N., Popp, K.: Bifurcation and stability analysis for a non-smooth friction oscillator. Arch. Appl. Mech. **66**, 301–314 (1996)

Parker, T.S., Chua, L.O.: Practical Numerical Algorithms for Chaotic Systems. Springer, Berlin (1989)

Soliman, M.S., Thompson, J.M.T.: Integrity measures quantifying the erosion of smooth fractal basins of attraction. J. Sound Vib. **135**, 453–475 (1989)

Thompson, J.M.T., Soliman, M.S.: Fractal control boundaries of driven oscillators and their relevance to safe engineering design. Proc. R. Soc. Lond. A **428**, 1–13 (1990)

Two Formulations of Nonlinear Normal Vibration Modes and Their Applications

Yuri V. Mikhlin

Abstract Two formulations of nonlinear normal vibration modes (NNMs) in conservative and near conservative systems are considered. Construction of the NNMs and their applications in some mechanical problems are presented. Namely, the nonlinear vibro-absorption problem, the cylindrical shell nonlinear dynamics and the vehicle suspension nonlinear dynamics are analyzed.

Keywords Nonlinear normal modes • Vibration absorber • Cylindrical shells • Vehicle dynamics

1 Introduction

Nonlinear normal vibration modes (NNMs) are a generalization of normal (or principal) vibrations in conservative linear systems. In the normal vibration mode a finite dimensional system behaves like a conservative one having a single degree of freedom.

Kauderer (1958) became a forerunner in developing quantitative methods for analyzing NNMs in some two-DOF conservative system. Rosenberg (1962, 1966) defined NNMs as "vibrations in unison", i.e., synchronous periodic motions during which all coordinates of the system vibrate equiperiodically, reaching their maximum and minimum values at the same instant of time. He selected broad classes of essentially nonlinear systems allowing NNMs with rectilinear trajectories (modal lines) in a configuration space. The first formulation of the NNMs can be named **the Kauderer-Rosenberg concept**. In general, the NNM modal lines are curvilinear.

Y.V. Mikhlin (✉)
National Technical University "Kharkov Polytechnic Institute", 21 Frunze str, Kharkov 61002, Ukraine
e-mail: muv@kpi.kharkov.ua

M. Wiercigroch and G. Rega (eds.), *IUTAM Symposium on Nonlinear Dynamics for Advanced Technologies and Engineering Design*, IUTAM Bookseries (closed) 32, DOI 10.1007/978-94-007-5742-4_3,

The power series method to construct these trajectories is proposed in Manevich and Mikhlin (1972), Manevich et al. (1989), Mikhlin (1996).

Shaw and Pierre (1991, 1993) proposed the other formulation of NNMs for a general class of nonlinear discrete conservative or non-conservative systems. This analysis is based on the computation of invariant manifolds on which the NNM oscillations take place. This NNMs formulation can be named **the Shaw-Pierre concept**.

Different problems of the NNMs theory are studied in Vakakis and Rand (1992), Vakakis and Cetinkaya (1993), Pilipchuk (2001). The Rauscher method was first used for analyses of normal vibrations in some non-autonomous systems in Kinney and Rosenberg (1966). Rauscher's idea and the power-series method for trajectories in a configuration space are used in construction of resonance solutions in Mikhlin (1974). NNMs in self-excited systems are analyzed in Mikhlin and Morgunov (2001). Generalization of the NNMs concepts to continuous systems is made in King and Vakakis (1993), Shaw and Pierre (1994), Nayfeh and Nayfeh (1994). Basic results on NNMs are presented in the book (Vakakis et al. 1996) where quantitative and qualitative analyses of NNMs in conservative and non-autonomous systems, as well in distributed systems, are considered. Development of the NNMs theory during last years is presented in Vakakis et al. (2008), where problems of the energy transfer and localization in mechanical systems are analyzed in details. Generalization of the NNMs concept to systems with non-smooth characteristics is presented in Pilipchuk (2010). General concepts and a development of the nonlinear normal modes theory is described in Mikhlin and Avramov (2011). The nonlinear normal modes theory has been used last years to solve different applied problems some of them are presented in this paper.

The paper is organized as follow. In Sect. 2 the Kauderer-Rosenberg concept of the nonlinear normal modes is presented. Equations and boundary conditions in the finite-DOF conservative systems to obtain the NNMs trajectories in configuration space are obtained. Construction of the modal lines in power series is described. In Sect. 3 a generalization of the Kauderer-Rosenberg concept to non-conservative systems is considered. The principal idea of the Shaw-Pierre concept for the nonlinear normal modes is shown in Sect. 4. Then some applications of the NNMs theory are presented. In Sect. 5 it is shown that the snap-through truss can be used as effective vibration absorber. In Sect. 6 the NNMs theory is used to investigate nonlinear dynamics of cylindrical shells with initial imperfections, in the supersonic flow. In Sect. 7 the 7-DOF model of the nonlinear vehicle dynamics is considered by using the NNMs approach.

2 The NNMs Concept by Kauderer and Rosenberg

The normal vibrations of the conservative systems can be presented by trajectories in the configuration space. Equations of motion of the finite-DOF conservative system are the following:

$$m_i \ddot{x}_i + \Pi_{x_i} = 0, \tag{1}$$

where $\Pi = \Pi(x)$ is the system potential energy, which is a positive definite analytical function. One introduces the next change of variables: $\sqrt{m_i}x_i \to x_i$.

Equations to obtain trajectories of motion in the system configuration space can be obtained as the Euler equations for the Jacobi variation principle. If some generalized coordinate is chosen as the independent one, for example, $x_1 \equiv x$, then the following functions must be obtained:

$$x_i = p_i(x); \quad (i = 2, 3, \ldots, n) \tag{2}$$

The last relations define the NNMs by Kauderer-Rosenberg and describe some synchronous periodic motions. The new independent variable x is introduced instead of t. By using the energy integral, we can derive equations to obtain trajectories (modal lines) in the system configuration space of the form:

$$2x_i''(h - \Pi) \Big/ \left(1 + \sum_{k=2}^{n} x_k'^2\right) + x_i'(-\Pi_x) = -\Pi_{x_i} \quad (i = 2, 3, \ldots, n) \tag{3}$$

Here and later the prime means a differentiation by the variable x. The Eq. (3) are convenient to construct rectilinear, or nearly rectilinear, trajectories of the NNMs (Rosenberg 1966; Manevich and Mikhlin 1972; Manevich et al. 1989; Mikhlin 1996; Vakakis et al. 1996). These equations have singular points on the maximal equipotential surface $\Pi(x_1, \ldots, x_n) = h$. An analytical continuation of the NNMs trajectories to the surface is possible if the next boundary conditions are satisfied (Rosenberg 1966; Manevich and Mikhlin 1972; Manevich et al. 1989; Mikhlin 1996; Vakakis et al. 1996), namely,

$$x'_i(X)\,[-\Pi_x(X, x_2(X) \ldots, x_n(X))] = -\Pi_{x_i}(X, x_2(X) \ldots, x_n(X)) \ (i = 2, 3, \ldots, n) \tag{4}$$

Here $x = X$, $x_i(X)$ are the trajectory return points lying on the maximal equipotential surface $\Pi(x_1, \ldots, x_n) = h$.

Let's the modal line (2) is obtained from the boundary problem (3), (4), and the functions $p_i(x)$ are single-valued and analytical. Then the law of motion in time t can be found by using the equation

$$\ddot{x} + \Pi_x(x_1, p_2(x), \ldots, p_n(x)) = 0. \tag{5}$$

The periodic solution $x(t)$ can be found as inversion of the corresponding integral. So, the NNMs are two-parametric (by energy and phase of the motion) family of periodic solutions with smooth trajectories in the configuration space.

Note that the energy and amplitudes of the obtained single-DOF nonlinear system are connected by the following relation: $h = V(X)$.

It is interesting that the number of NNMs in the nonlinear case can exceed the number of degrees of freedom. This remarkable property has no analogy in general linear systems, excepting some degenerate cases.

One considers the dynamical system with the potential energy, $\Pi^{(0)} + \varepsilon\Pi^{(1)}$, where $\varepsilon \ll 1$; one assumes that the unperturbed system (for $\varepsilon = 0$) allows the rectilinear modal lines. The dynamical system can be written as

$$\ddot{x}_i + \tilde{\Pi}^{(0)}_{x_i}(x_1, \ldots, x_n) + \varepsilon\tilde{\Pi}^{(1)}_{x_i}(x_1, \ldots, x_n) = 0;\ i = \overrightarrow{1, n}. \tag{6}$$

To construct the NNM close to the rectilinear NNM it can use the following power series:

$$x_i = \sum_{k=0} \varepsilon^k x_{ik}(x);\ x \equiv x; \quad x_{ik} = \sum_{l=1} a^{(l)}_{ik} x^l \tag{7}$$

A determination of coefficients of the power series (7) from the Eqs. (3) and (4) is described in Manevich and Mikhlin (1972), Manevich et al. (1989), Mikhlin (1996), Vakakis et al. (1996). Conditions of solvability and a convergence of the power series are discussed in these publications. Analytical continuation of obtained local expansions for large vibration amplitudes can be made by using the rational diagonal Pade' approximants (Manevich et al. 1989; Mikhlin 1995).

3 NNMs in Near-Conservative Systems

The perturbation methodology is utilized to the analysis of NNMs in broad classes of finite-dimensional non-autonomous and self-excited systems close to conservative ones. One considers the following near-conservative system:

$$\ddot{x}_i + \Pi_{x_i}(x_1, x_2, \ldots, x_n) + \varepsilon\, f_i(x_1, \dot{x}_1, x_2, \dot{x}_2, \ldots, x_n, \dot{x}_n, t) = 0;\ \left(i = \overrightarrow{1, n}\right) \tag{8}$$

Here ε is a small parameter; Π is a potential energy of the unperturbed conservative system; the functions f_i may be periodical with respect to time. This system may involve friction of any physical nature.

It is considered such vibration modes when all positional coordinates of the finite-dimensional non-conservative system are linked. In these modes, the system behaves like a single-DOF conservative one. The periodic solutions could be called ***Nonlinear normal modes of the non-conservative nonlinear system***.

One considers a solution that all phase coordinates are defined as single-valued and analytical functions of some selected coordinate $x \equiv x_1$. Besides, it is assumed that within a semi-period of the periodic solution one can express t as a single-values function of the displacement x. This idea was first introduced by Rausher (1938). It means that along the NNM trajectory the non-conservative system behaves like to some ***pseudo-autonomous system*** (Kinney and Rosenberg 1966; Mikhlin 1974; Kubenko et al. 1984).

Then, eliminating a time and introducing a new independent variable x, one obtains equations governing trajectories of the NNMs in the system configuration space and the additional boundary conditions which guarantee an absence of singularities in these equations. These equations and boundary conditions, which are not presented here, are similar to ones previously presented for the conservative systems. The NNM modal line can be determined as power series by ε and x (Kinney and Rosenberg 1966; Mikhlin 1974; Kubenko et al. 1984; Nayfeh and Nayfeh 1994). In case of the non-autonomous system a determination of the steady-state resonance motions in form of the NNMs must be completed by condition of periodicity. In a case of the self-excited system one has the additional condition that the work of all forces over the period is equal to zero (Nayfeh and Nayfeh 1994).

4 The NNMs Concept by Shaw and Pierre

Shaw and Pierre (1991, 1993) reformulated the method of NNMs for a general class of quasilinear dissipative systems. Their analysis is based on the computation of invariant manifolds of motion on which the NNMs take place.

To use this approach the mechanical system must be presented of the next standard vector form:

$$dx/dt = y,\ dy/dt = f\,(x, y) \tag{9}$$

One chooses a couple of new independent variables (u, v), where u is some ***dominant generalized coordinate,*** and ***v is the corresponding generalized velocity***. By the Shaw-Pierre formulation, the nonlinear normal mode is such regime when all phase coordinates are univalent functions of the selected couple of variables. Choosing the coordinate and velocity with the index 1 as the selected couple of variables, one writes the nonlinear normal mode as

$$x_1 = u,\ y_1 = v,\ x_2 = X_2\,(u, v)\,,\ y_2 = Y_2\,(u, v)\,, \ldots, x_N = X_N\,(u, v)\,,\ y_N = Y_N\,(u, v) \tag{10}$$

Computing derivatives of all variables in the relations (10), and taking into account that $u = u(t)$ and $v = v(t)$, then substituting the obtained expressions to the system (9), one has the following system of partial differential equations:

$$\begin{aligned} &\frac{\partial X_i}{\partial u} v + \frac{\partial X_i}{\partial v} f_1\,(x, y) = Y_i\,(u, v), \\ &\frac{\partial Y_i}{\partial u} v + \frac{\partial Y_i}{\partial v} f_1\,(x, y) = f_i\,(x, y),\ (i = 1, 2, \ldots, N) \end{aligned} \tag{11}$$

It is possible to obtain the system (11) solution in power series by new independent variables u and v.

5 Snap-Through Truss as Vibration Absorber

Numerous scientific publications contain a description and analysis of different devices for the vibration absorption. The NNMs in a system considering an essentially nonlinear oscillator as absorber is studied in Mikhlin and Reshetnikova (2005). Analysis of free or forced oscillations absorption by using of the snap-through truss is considered in Avramov and Mikhlin (2004, 2006).

The snap-through truss with three equilibrium positions is attached to the linear oscillator which is chosen as the simplest model of some elastic system. The system dynamics is studied by the NNMs approach. If the localized mode is stable, the system energy is concentrated in the nonlinear absorber. This situation is the most appropriate to absorb elastic vibrations. Figure 1 shows the system under consideration. The following notations are used: φ is the angle, which defines the equilibrium position; L is a length of the undistorted spring; c is a stiffness of the truss spring; c_1 is a stiffness of the elastic subsystem. Coordinates (u,w), which describe displacements of the systems, are transformed to dimensionless coordinates (U,W): $u = U/L; w = W/L$. One introduces too the dimensionless time, $t = (M/c_1)^{1/2}\tau$ and the new variable, $u_1 = u + \gamma\,(1-c)\,/\,(1+\gamma)$, where $\gamma = c/c_1; \mu = m/M$. By assumption, the mass and stiffness of the truss are significantly smaller than corresponding parameters of the elastic system. Therefore, the following relations are introduced: $\mu = \varepsilon\bar{\mu}; \gamma = \varepsilon\bar{\gamma}; \varepsilon << 1$. The Taylor-series expansions are performed. The truss is shallow, so, remaining the terms up to the third order, the following system of motion, is derived:

$$\ddot{u}_1 + (1+\varepsilon\bar{\gamma})\,u_1 - \frac{\varepsilon\bar{\gamma}}{\rho^3}u_1 w^2 - \frac{\varepsilon\bar{\gamma}}{2\rho^2}w^2 = 0;$$

$$\mu\ddot{w} - \bar{\gamma}\alpha^2 w - \frac{\bar{\gamma}}{\rho^2}wu_1 + \frac{\bar{\gamma}\beta^2}{2}w^3 = 0, \tag{12}$$

where $\rho = \frac{\gamma+c}{1+\gamma}; \alpha^2 = \frac{1}{\rho} + \frac{1}{c} - 2; \beta^2 = \frac{1}{\rho^3} + \frac{1}{c^3}$.

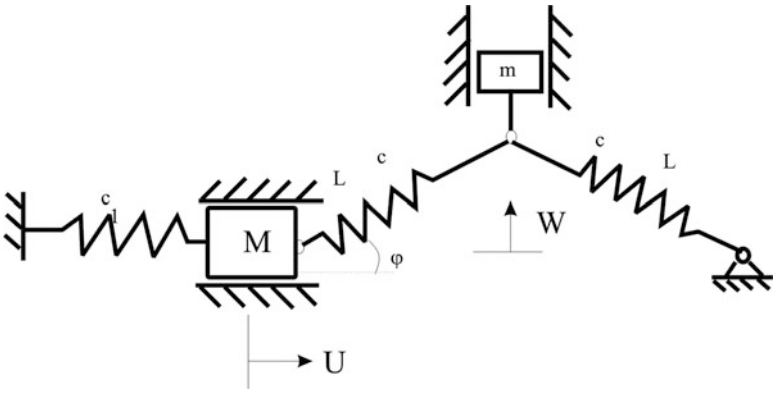

Fig. 1 The snap-through truss as an absorber of elastic vibrations

As the localized NNM, as well the non-localized NNM can be selected. The localized periodic motions near the equilibrium position are presented of the form $u_1 = \varepsilon\bar{u}_1(w_1)$, where: $w - \sin\varphi = \varepsilon w_1$, and then the following power series are used: $\bar{u}_1 = b_0 + b_1 w_1 + b_2 w_1^2 + \ldots$. The equations to obtain the NNM trajectory (3) and the corresponding boundary conditions (4) are used. The obtained modal line is a near-straight line close to y-axis. The non-localized NNM can be constructed in power series too. The checking numerical simulation of the system shows a good accuracy of the obtained analytical results.

Periodic motions of the system (12) with large amplitudes are studied by using the NNMs approach too. The NNM is presented in the following form:

$$u_1 = \varepsilon\bar{u}_1(w); \bar{u}_1(w) = a_0 + a_1 w + a_2 w^2 + \ldots \tag{13}$$

where a_0,a_1, ... are unknown coefficients. These coefficients are obtained from the equation for the NNM trajectories in configuration space of the form (3) and the corresponding boundary conditions (4). The checking numerical simulation confirms a good accuracy of the analytical results (Fig. 2). The snap- through truss has significant amplitudes of oscillations and the main elastic system has small amplitudes. If such motions are stable, it guarantees the vibration absorption.

In region of the non-localized NNM instability the transfer to the through-truss motion is taken place. Stability of the absorption mode (13) is analyzed in Avramov and Mikhlin (2004). The following conclusions can be made. If the angle φ is not large, the unstable oscillations regions have an order $O(\varepsilon)$. It can choose such values of φ, that the considered NNM is always stable. In this case the snap-through truss has large oscillation amplitudes, and the main linear subsystem has small amplitudes.

Forced oscillations of a system, containing the snap-through truss, close to its equilibrium position, are investigated too. In instability regions of non-localized forced oscillations the absorber is fallen into the snap-through motions. These vibrations, which are the most appropriate for absorption of the linear vibrations, are analyzed in Avramov and Mikhlin (2006). The absorption mode is constructed by using the NNMs method and the Rauscher approach. It is shown that the vibration absorption mode is stable for almost all values of the system parameters, excepting the very narrow resonance region. Therefore, the snap – through absorber is effective.

6 Nonlinear Oscillations of the Non-ideal Cylindrical Shells in a Supersonic Flow

A lot of studies were devoted to large amplitude vibrations of circular cylindrical shells. In some of them the nonlinear oscillations of the non-ideal cylindrical shells, that is cylindrical shells with initial imperfections, were considered. It can select some review-type publications on the subject, in particular, papers (Budiansky and Hutchinson 1966; Fung and Sechler 1974). There are too a great number of papers

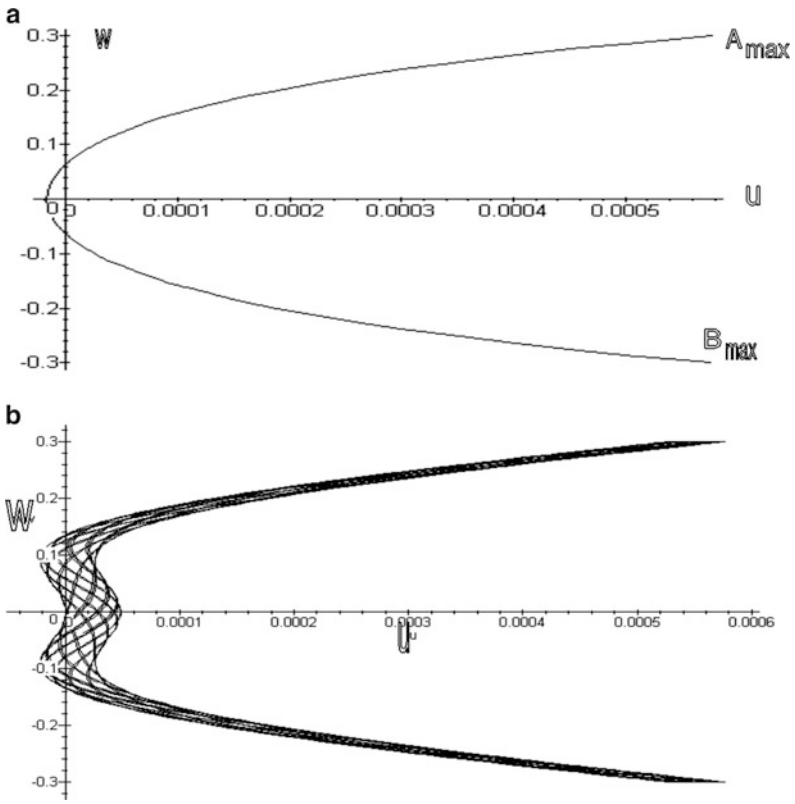

Fig. 2 Large amplitude periodic motions. (**a**) Analytical solution. (**b**) Numerical simulation with initial conditions corresponding to the analytical results

which are available to the dynamics of cylindrical shells in the supersonic flow (Fung and Sechler 1974; Bolotin 1963). The NNMs concept is used in Avramov et al. (2007) to investigate the non-ideal cylindrical shells dynamics.

Free nonlinear oscillations of the circular cylindrical shells with imperfections are described by the well-known Donnell equations, connecting the normal deflection w and the Airy stress function Φ, as a functions of the space coordinates x,y and of the time t (Fung and Sechler 1974; Kubenko et al. 1984). The shell normal deflection is represented of the form:

$$w = f_1(t)\sin rx\ \sin sy + f_2(t)\sin rx\ \cos sy + f_3(t)\sin^2 rx \tag{14}$$

Here $s = n/R, r = m\pi/L$; n is a number of waves in the circumference direction; m is a number of half-wave in the longitudinal direction; unknown functions $f_1(t)$, $f_2(t)$ describe two asymmetric modes; $f_3(t)$ is a general coordinate, which characterizes the axisymmetric mode. It is assumed that a length of the middle surface transverse section is constant during oscillations.

The imperfections are chosen of the following form, which corresponds to the first principal asymmetric mode:

$$w_0 = f_{10} \sin rx \ \sin sy + f_{20} \sin rx \ \cos sy \tag{15}$$

Using the Bubnov-Galerkin approach to the Donnell equations, two nonlinear ODEs having quadratic and cubic nonlinearities can be derived (Bolotin 1963; Avramov et al. 2007). If the initial imperfections are equal to zero, all NNM trajectories in the configuration space of the system are rectilinear, and a number of these NNMs are equal to infinity. So, it is advisable for a case of small initial imperfections to use the straight line to approximate the NNMs in the system:

$$f_2 = k f_1 \tag{16}$$

Both analytical and numerical analysis shows that in the wide range of the system parameters only a single stable nonlinear vibration mode exists. The system trajectory is close to (16), where $k = f_{20}/f_{10}$.

One considers the NNMs approach to analyze the nonlinear dynamics of cylindrical shells in a supersonic flow and a construction of periodic solutions with large amplitudes. The Donnell equations are used to study dynamics of ideal cylindrical shells in a supersonic flow. A first-order linear piston theory (Fung and Sechler 1974; Bolotin 1963) is used to approximate the pressure. The shell deflection is presented as

$$\begin{aligned} w = {} & f_1 \sin rx \ \sin sy + f_2 \sin rx \ \cos sy + f_3 \sin 2rx \ \sin sy \\ & + f_4 \sin 2rx \ \cos sy + f^*(x,t) \end{aligned} \tag{17}$$

The inextensibility condition of a middle surface is used. The initial continuous system is reduced, by using the Bubnov-Galerkin procedure, to the discrete one of the form of four nonlinear ODEs. The region of the flutter is considered. In the linear approximation the normal mode of vibration of the form $f_1 = f_2$, $f_3 = f_4$ exists (Fig. 3a). In the plane f_1, f_3 corresponding modal lines are of the closed oval-type ones (Fig. 3b). Accounting of the nonlinearity gives us some deformation of the linear system modal lines. So, the periodic limit circle of the form of the NNM in the flutter region is obtained. But on the large calculation interval the obtained limit circle is unstable. One can observe a transfer to regime of beating, which amplitudes are essentially more than ones of the unstable limit circle. This beating was obtained in experiments (Fung and Sechler 1974). Additional analysis by using the harmonic balance method and the numerical simulation confirm this result.

One considers now the combined influence of the initial imperfections and the supersonic flow to the shell nonlinear dynamics. The following approximation of the normal deflection is chosen:

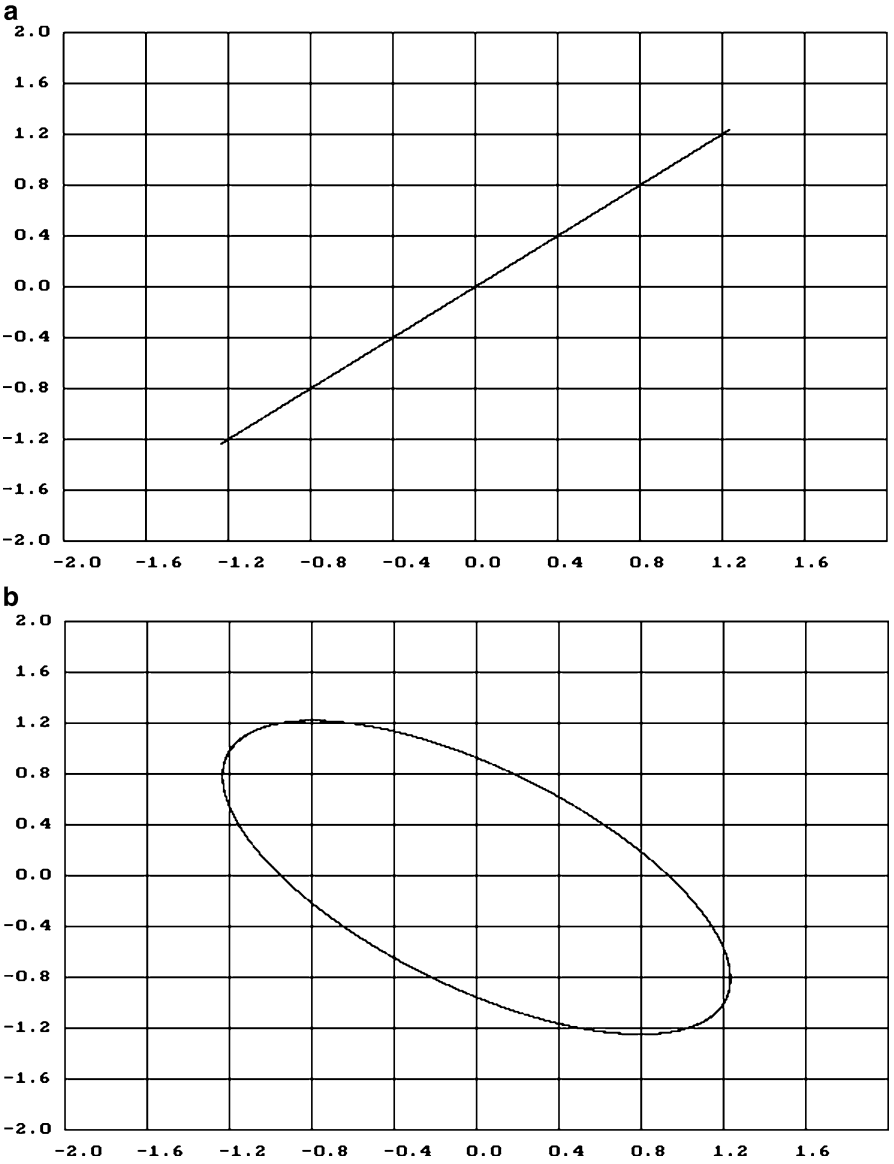

Fig. 3 Trajectories of the NNMs in the region of the flutter. (**a**) The NNM trajectory in the plane f_1, f_2. (**b**) The NNM trajectory in the plane f_1, f_3

$$w = (f_1 - f_{10}) \sin rx \sin sy + (f_2 - f_{20}) \sin rx \cos sy + f_3 \sin 2rx \sin sy$$
$$+ f_4 \sin 2rx \cos sy + \frac{n^2}{4R}\left[(f_1 \sin rx + f_3 \sin 2rx)^2 + (f_2 \sin rx + f_4 \sin 2rx)^2\right] \tag{18}$$

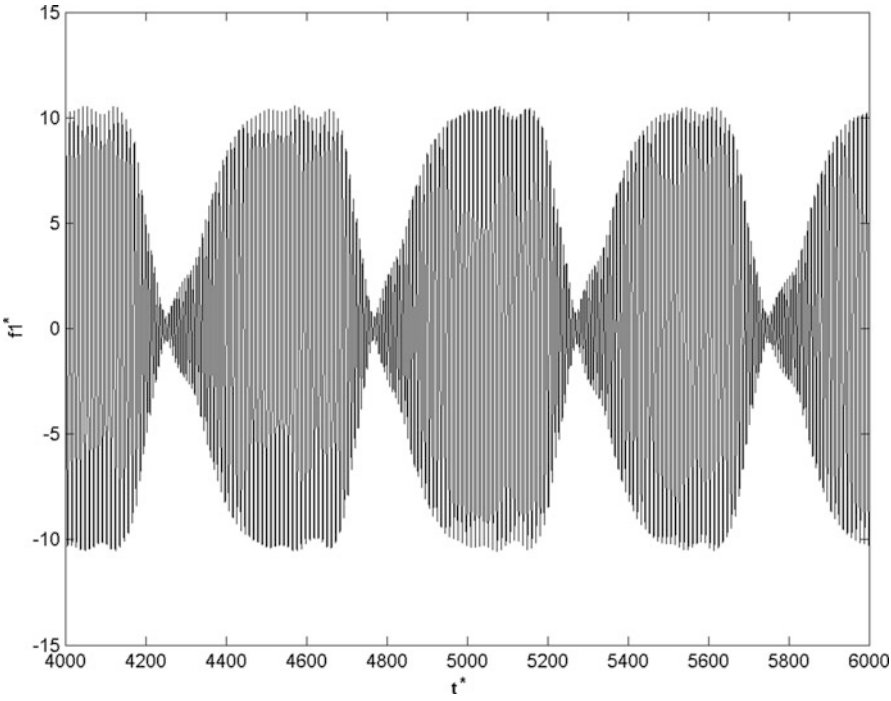

Fig. 4 Regime of beating for not large values of the initial imperfections

Initial imperfections are chosen of the form (15). Then after determination of the Airy stress function, and by using the Bubnov-Galerkin procedure, one has the system of four nonlinear ODEs, which contains the unknown functions, $f_i(t),\ i = 1, 2, 3, 4$. For the numerical calculations some physical parameters were fixed. In Fig. 4 it is shown vibration regimes for not large values of the initial imperfections. We can see regimes of beating. In the Fig. 4 $f_1^* = f_1/h, t^* = \omega_{11}t$, where ω_{11} is the first fundamental frequency of the system.

In the flutter region it can observe the NNMs modal lines, which are similar to ones in the non-ideal shell without the flow influence (Fig. 3). Simultaneously, a behavior in time is analogous to ones in the ideal shell in the flow. But these vibration regimes are not typical for large values of the initial imperfections. The chaotic dynamics of the shell is typical if the initial imperfections have an order more that the shell thickness.

7 NNMs in the Vehicle Dynamics

In fact the vehicle models are nonlinear because it contains elastic components with nonlinear characteristics. Nonlinear 7-DOF model of the vertical and axial vehicle dynamics of a double-tracked road vehicle is considered here for a case

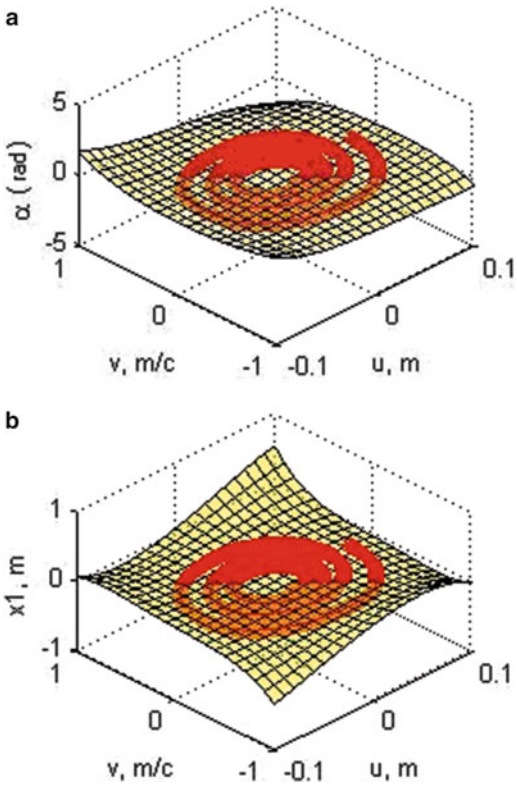

Fig. 5 The first vibration mode of the nonlinear system (independent coordinates are $u = z$ and $v = \dot{z}$; initial values: $z = 0,075$, and $\dot{z} = 0$). (**a**) Change of the angle α depending on variables u and v. (**b**) Change of displacement x_1 depending on variables u and v

of independent-solid axle suspension to predict the vehicle body and wheel states (Avramov et al. 2007; Kubenko et al. 1984). It is possible to study, by using this model, all principal vehicle motions. In some cases, for example, after impact, the NNMs are, may be, the dominant regimes in the vehicle dynamics, because a transient is very short-term due to a strong dissipation in the system.

In the 7-DOF model of the suspension dynamics the car body is represented as a rigid body. The corresponding generalized coordinates are the following: z is the vertical displacement, α is the pitch angle, β is the roll angle, x_i are the vertical displacement of i-th suspended mass which are equivalent to the wheel. In this model tires are presented as elastic elements with linear characteristics. The suspension is characterized by nonlinear elastic characteristics of the front and rear springs, and by linear damping characteristics.

The NNMs concept by Show and Pierre is used. Solutions are obtained as power series by new independent variables u and v, which are dominant coordinates of chosen mode. This procedure permits to obtain seven NNMs of the system under consideration. Two surfaces, which characterize the first NNM, and corresponding trajectories of motion on these surfaces for some concrete values of the system parameters are shown in the Fig. 5. Here the coordinate z, describing the vertical

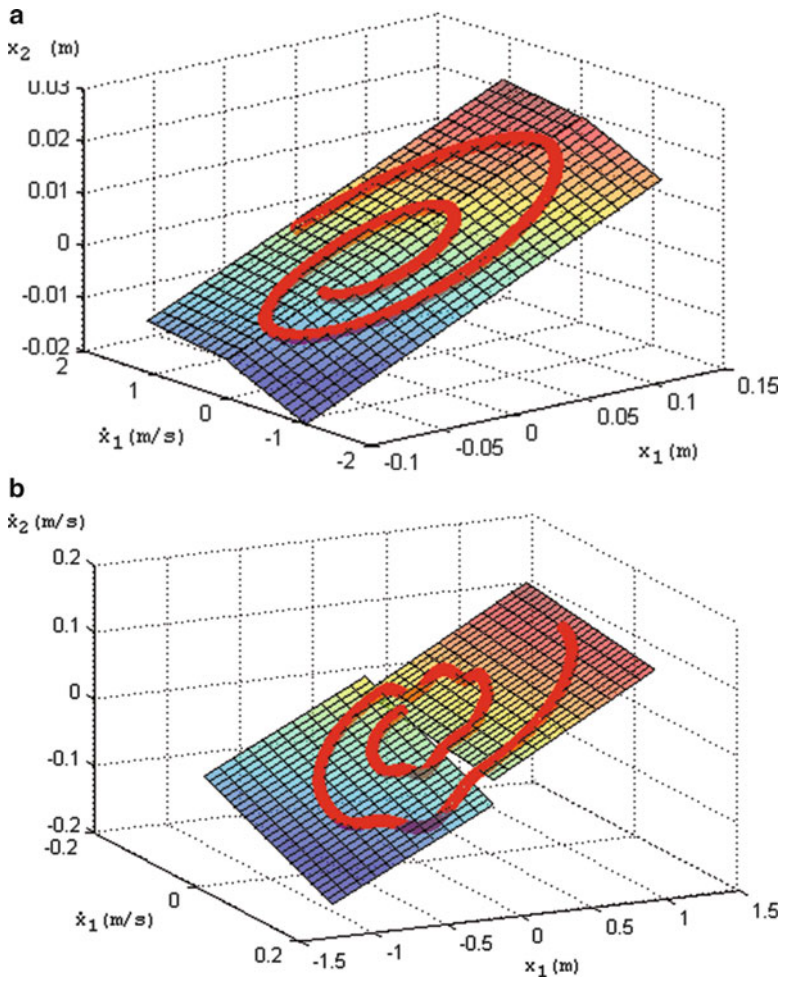

Fig. 6 The first vibration mode of the quarter car model (the piecewise linear damping characteristic of the shock absorber). Independent variables are $u = x_1$ and $v = \dot{x}_1$. (**a**) Change of displacement x_2. (**b**) Change of the $\dot{x}_2$ (depending on u and v)

displacement, is chosen as the independent variable u, and the corresponding velocity $\dot{z}$ is chosen as the independent coordinate v. Numerical calculations show a good exactness of the obtained analytical results.

To investigate the suspension dynamics taking into account a non-smooth characteristic of the shock absorber, the quarter-car model is considered. Characteristic of the damping functions is chosen as piecewise linear one. The first NNM obtained by using the method described below are shown for some concrete values of the system parameters in Fig. 6. It can be observed as motions on places corresponding to the NNMs, as well a transient from one place to another one after gap of the piecewise linear damping characteristic.

Piecewise linear damping is considered as an approximation of more exact characteristic. The stiffness characteristic in the suspension is chosen here as linear.

Similar results are obtained in a case of more realistic nonlinear elastic and damping characteristics (in particular, in a case of the piecewise cubic damping).

8 Conclusion

Nonlinear normal modes (NNMs) are typical regimes which exist in different classes of conservative or near-conservative finite-DOF systems. The Kauderer-Rosenberg conception, when all positional coordinates are single-valued functions of some of them, is associated with trajectories in configuration space. The Shaw-Pierre conception is based on the computation of invariant manifolds of motion. In this case the NNMs can be obtained as single-valued functions of two selected phase coordinates. An efficiency of the NNMs theory is shown in some applied problems.

Acknowledgments This work was supported in part by a grant M9403 0109U002426 from the Ministry of Science and Education of Ukraine and by a grant 28/257 from the National Academy of Science of Ukraine and Russian Foundation for Basic Research.

References

Avramov, K.V., Mikhlin, Y.V.: Snap- through truss as a vibration absorber. J. Vib. Control. **10**, 291–308 (2004)

Avramov, K.V., Mikhlin, Y.V.: Snap-through truss as an absorber of forced oscillations. J. Sound Vib. **29**, 705–722 (2006)

Avramov, K.V., Mikhlin, Y.V., Kurilov, E.: Asymptotic analysis of nonlinear dynamics of simply supported cylindrical shells. Nonlinear Dyn. **47**, 331–352 (2007)

Bolotin, V.V.: Non-Conservative Problems of the Theory of Elastic Stability. Macmillan, New York (1963)

Budiansky, B., Hutchinson, J.W.: Dynamic buckling of imperfect-sensitive structures. Appl. Mech., pp. 636–657. Springer, Berlin (1966)

Fung, Y.C., Sechler, E.E. (eds.): Thin- Shell Structures, Theory, Experiment and Design. Prentice-Hall, Englewood Cliff (1974)

Kauderer, H.: Nichtlineare Mechanik. Springer, Berlin (1958)

King, M.E., Vakakis, A.F.: An energy-based formulation for computing nonlinear normal modes in undamped continuous systems. J. Vib. Acoust. **116**(3), 332–340 (1993)

Kinney, W., Rosenberg, R.: On the steady state vibrations of nonlinear systems with many degrees of freedom. J. Appl. Mech. **33**, 406–412 (1966)

Kubenko, V.D., Koval'shuk, P.S., Krasnopolskaya, T.S.: Nonlinear Interaction of Modes of Bending Shell Oscillations. Naukova Dumka, Kiev (1984) (in Russian)

Manevich, L.I., Mikhlin, Y.V.: Periodic solutions close to rectilinear normal vibration modes. Prikl. Mat. i Mekhanica (PMM USSR) **36**, 1051–1058 (1972)

Manevich, L., Mikhlin, Y., Pilipchuk, V.: The Method of Normal Oscillation for Essentially Nonlinear Systems. Nauka, Moscow (1989) (in Russian)

Mikhlin, Y.: Resonance modes of near-conservative nonlinear systems. Prikl. Mat. I Mekhanica (PMM USSR) **38**, 425–429 (1974)
Mikhlin, Y.: Matching of local expansions in the theory of nonlinear vibrations. J. Sound Vib. **182**, 577–588 (1995)
Mikhlin, Y.: Normal vibrations of a general class of conservative oscillators. Nonlinear Dyn. **11**, 1–16 (1996)
Mikhlin, Y., Morgunov, B.: Normal vibrations in near-conservative self-exited and viscoelastic nonlinear systems. Nonlinear Dyn. **25**, 33–48 (2001)
Mikhlin, Y.V., Reshetnikova, S.N.: Dynamical interaction of an elastic system and essentially nonlinear absorber. J. Sound Vib. **283**, 91–120 (2005)
Mikhlin, Yu.V., Avramov, K.V.: Nonlinear normal modes of vibrating mechanical systems. Review of theoretical developments. Appl. Mech. Rev. (2011, in press)
Nayfeh, A., Nayfeh, S.: On nonlinear modes of continuous systems. J. Vib. Acoust. **116**, 129–136 (1994)
Pilipchuk, V.N.: Impact modes in discrete vibrating systems with rigid barriers. Int. J. Non-Linear Mech. **36**, 999–1012 (2001)
Pilipchuk, V.N.: Nonlinear Dynamics. Between Linear and Impact Limits. Springer, Berlin (2010)
Rauscher, M.: Steady oscillations of system with nonlinear and unsymmetrical elasticity. J. Appl. Mech. **5**, A-169 (1938)
Rosenberg, R.M.: The normal modes of nonlinear n-degrees-of-freedom systems. J. Appl. Mech. **30**, 7–14 (1962)
Rosenberg, R.M.: Nonlinear vibrations of systems with many degrees of freedom. In: Advances of Applied Mechanics 9, pp. 156–243. Academic Press, New York (1966)
Shaw, S., Pierre, C.: Nonlinear normal modes and invariant manifolds. J. Sound Vib. **150**, 170–173 (1991)
Shaw, S., Pierre, C.: Normal modes for nonlinear vibratory systems. J. Sound Vib. **164**, 85–124 (1993)
Shaw, S., Pierre, C.: Normal modes of vibration for non-linear continuous systems. J. Sound Vib. **169**(3), 319–347 (1994)
Vakakis, A.F., Cetinkaya, C.: Mode localization in a class of multi-degree-of-freedom systems with cyclic symmetry. SIAM J. Appl. Math. **53**, 265–282 (1993)
Vakakis, A.F., Rand, R.: Normal modes and global dynamics of a two-degree-of freedom nonlinear system. I. Low energies. II. High energies. Int. J. Non-Linear Mech. **27**, 861–888 (1992)
Vakakis, A., Manevitch, L., Mikhlin, Y., Pilipchuk, V., Zevin, A.: Normal Modes and Localization in Nonlinear Systems. Wiley, New York (1996)
Vakakis, A.F., Gendelman, O.V., Bergman, L.A., McFarland, D.M., Kerschen, G., Lee, Y.S.: Nonlinear Targeted Energy Transfer in Mechanical and Structural Systems. Springer, Berlin (2008)

Soliton-Mediated Electron Transfer and Electric Transport Arising from Coupling Electron Quantum Mechanics to Nonlinear Elasticity in Anharmonic Crystal Lattices

M.G. Velarde, W. Ebeling, and A.P. Chetverikov

Abstract After recalling features of solitons in the Toda (more precisely an adapted Morse-Toda) lattice a succint discussion is provided about the stability of such solitons when the lattice is heated up to physiological temperatures for values of parameters typical of bio-macro-molecules. Then the discussion is focused on the soliton trapping of an added *excess* (originally free) electron thus creating the solectron electric carrier. Results are presented for 1d- and 2d-anharmonic crystal lattices.

Keywords Cristal Lattices • Solitons • Electric transport • Heating

1 Background: Solitons

The study of anharmonic lattices owes much to the seminal work done by Fermi, Pasta and Ulam (1955). They tried numerically albeit with no success to explain equipartition of energy (of paramount importance in statistical mechanics) by using the first few non-Hookean corrections to linear elasticity as a mechanism to allow energy sharing and exchange between harmonic modes otherwise non-interacting. The difficulty was clarified by Zabusky and Kruskal (1965) and Zabusky (2005) who studied solitary waves, their overtaking collisions in such anharmonic lattices

M.G. Velarde (✉)
Instituto Pluridisciplinar, Paseo Juan XXIII, 1, Madrid-28040, Spain
e-mail: mgvelarde@pluri.ucm.es

W. Ebeling
Institut für Physik, Humboldt-Universität Berlin, Newtonstrasse, 15, Berlin-12489, Germany
e-mail: ebeling@physik.hu-berlin.de

A.P. Chetverikov
Department of Physics, Saratov State University, Astrakhanskaya, 83, Saratov-410012, Russia
e-mail: ChetverikovAP@info.sgu.ru

M. Wiercigroch and G. Rega (eds.), *IUTAM Symposium on Nonlinear Dynamics for Advanced Technologies and Engineering Design*, IUTAM Bookseries (closed) 32, DOI 10.1007/978-94-007-5742-4_4,

and their continuum counterpart. In view of their remarkable particle-like behavior, these waves reappearing unaltered following collisions, the hallmark of their dynamics, they denoted them by solitons (solit/solitary wave; on/like in electron, proton, etc.). In fact, before the discovery of the soliton, Visscher and collaborators numerical computations (Payton et al. 1967) had revealed "soliton-like" mediated behavior and enhanced heat transport. Solitary waves and solitons, found also in other realms of science, appear as potential "universal" carriers of almost anything (del Rio et al. 2007; Nayanov 1986) (like surf waves/non-topological solitons in the ocean or bores/topological solitons in rivers). Of particular interest to us here is the model-lattice invented by Toda (1989) for which analytical, exact solutions are known.

Let us recall how solitons appear in the anharmonic Toda lattice. Consider an one-dimensional (1d) lattice of units (equal masses, m and $m = 1$ for simplicity) interacting with their nearest-neighbors via a potential $U(x)$. Then, classically, for the displacement of the nth-lattice unit/particle from its equilibrium position, Newton's equations are

$$\ddot{x}_n = U'(x_{n+1} - x_n) - U'(x_n - x_{n-1}), \tag{1}$$

where x_n denotes displacement (depending on circumstances it is of interest to focus on local lattice deformations or on gradient of displacements) of the unit at site "n". A dash indicates a derivative with respect to the argument. No on-site dynamics or structure is considered. There are cases of, e.g., biological interest where an intra-unit dynamics is added. If rather than actual unit-displacements, relative displacements, $\xi_n = x_{n+1} - x_n$, are considered, then Eqs. (1) become

$$\ddot{\xi}_n = U'(\xi_{n+1}) - 2U'(\xi_n) + U'(\xi_{n-1}). \tag{2}$$

The paradigmatic interaction potential introduced by Toda is

$$U(\xi_n) = -\frac{a}{b}\left[e^{-b(\xi_n - \sigma)} + b(\xi_n - \sigma) - 1\right], \tag{3}$$

where σ is the mean equilibrium interparticle distance; $a > 0$ and $b > 0$ are parameters; b accounts for the non-Hookean stiffness of the "springs" in the lattice; the last term (-1) is added for computational convenience and need not to be included. Note that with ab finite for $b \to 0$, the function (3) becomes the harmonic potential (linear Hookean "springs" for a standard crystal lattice) and $\omega_0^2 \equiv ab/m$ defines the angular frequency of vibrations in the harmonic limit. In the extreme opposite case $b \to \infty$, the potential (3) approaches the hard-rod/sphere limit (fluid-like system). Note also that under an external force or for finite temperatures the lattice constant equilibrium distance may not correspond to the minimum of the potential. Figure 1 shows the Toda potential adequately compared with Morse and Lennard-Jones potentials of current use in Physics and Chemistry. In what follows consideration will be given only to strong interparticle

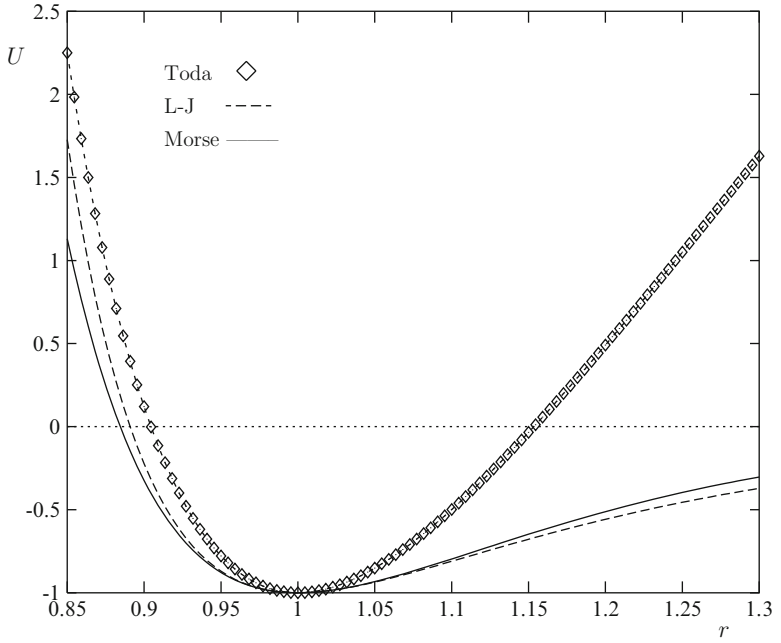

Fig. 1 Rescaled representation with a common minimum (using r rather them x) of the Toda potential $\left(U = U^T = \frac{a}{b}\left[e^{-b\sigma(r-1)} + b\sigma\,(r-1) - 1\right]\right)$, Morse potential $\left(U = U^M = \frac{a}{2b}\left[\left(e^{-b\sigma(r-1)} - 1\right)^2 - 1\right]\right)$ and Lennard-Jones potential $\left(U = U^{L-J} = U_0\left[\frac{1}{r^{12}} - \frac{1}{r^6} - 1\right]\right)$

compressions such that $\xi \leq \sigma/2$ (for simplicity $\sigma = 1$). Materials are usually stronger when compressed and weaker when stretched. In view of this, the fact that the attractive part of Toda's potential (3) is unphysical is of no concern to the study here.

For any finite value of b, in the infinite lattice, the equations of motion (2) possess a one-parameter family of soliton solutions

$$\xi_n = \sigma - 1\,(1/b)\,\ell n\left[1 + \sinh^2\kappa \mathrm{sech}^2\,(\kappa n \mp \sinh\kappa)\,\omega t\right]. \tag{4}$$

Inverting the logarithm it is just the sech^2 for $e^{-b(\xi_n - \sigma)}$. This exponential is related to the force (3) and characterizes the strength of the solitonic pulse. The parameter κ controls the wave velocity and by the same token the wave amplitude (higher solitons travel faster),

$$v_{soliton}(\kappa) = \pm\omega_0\,(\sinh\kappa)\,/\kappa, \tag{5}$$

which in dimensionless units shows its supersonic character as the linear sound velocity is here given by $v_{sound} = \omega_0$ (positive and negative signs merely give

direction of wave propagation). When a periodic hence finite lattice is considered the exact solution of the equations of motion is a periodic "cnoidal" wave formed with Jacobian elliptic functions and complete elliptic integrals of the first and second kind (Toda 1989). It can be shown that in the *continuum* limit the solution of the discrete lattice can be approximated by the *cnoidal* solution of the Boussinesq-Korteweg de Vries equation (Boussinesq 1877; Korteweg and Vries 1895; Nekorkin and Velarde 2002) and in another limit by the solitary wave solution in the form of sech^2. When the lattice has fixed constant length, as expansion is not permitted, experiences internal stress (pressure). If, however, the lattice length is free but no external force to it is applied (like compression or stretching at a free end), it can be shown that the lattice expands as it vibrates. The solitary wave is a *compression* pulse, and cnoidal waves cause expansion with, however, high compression at each periodic wave "peak" (or maximum). The exact wave dispersion relation of the Toda lattice is known explicitely.

Incidentally, the Toda lattice cannot sustain a thermal gradient although it permits a temperature difference, hence it is "transparent" to heat (solitons with exponential interaction like (3) run freely in the Toda lattice). This problem does not arise with Lennard-Jones interactions. In view of this, use is to be done of an *imperfect* Toda lattice and, recalling that interest here focused only on rather-strong lattice compressions, this can be achieved by substituting (3) with an *adapted* (non-integrable, hence imperfect) Toda-Morse lattice whose solutions and corresponding features should not differ significantly from the exact Toda solutions given above (Chetverikov et al. 2006; Dancz and Rice 1977; Rolfe et al. 1979). Thus rather than (3) we shall use:

$$U_M(\xi) = D\left[e^{-B(\xi-\sigma)} - 1\right]^2. \tag{6}$$

The specific heat at constant length/volume of the Toda lattice was obtained long ago (Toda 1989). The high-temperature limit $C_L = 0,5$ corresponds well with the fluid-like, hard-sphere phase. Then around $T = 1$, $C_L \approx 0,75$ it is the *soliton* range (T unit: 2D; see below for further scalings). Well below $T = 1 = T_{transition}$, phonons (Fourier modes) control the thermodynamics (and dynamics) of the system. Similar phenomena can be observed in the dynamical structure factor (DSF) (typical for *inelastic* thermal neutron scattering experiments, $4\,\text{Å} \sim 5\,\text{meV} \sim 60\,\text{K}$ even up to $0.3\,\text{Å} \sim 0.1\,\text{eV} \sim 10^3\,\text{K}$). The latter is the double Fourier transform of the density-density correlation. When T is well below $T = T_{transition}$ a single phonon peak appears that provides the linear sound velocity. As the transition temperature is approached from below the phonon spectrum gets multipeaked with many phonons or highly deformed phonons showing up (multiphonon range), until a much higher peak clearly emerges above a messy background. It corresponds to the soliton with supersonic velocity (5). Both the specific heat and DSF point to the significant role played by strong lattice compressions leading to solitons (Chetverikov et al. 2006).

2 Electron Capture and Electron Transfer

2.1 The Solectron Concept

If we now consider that lattice units are atoms with electrons and we add an *excess* electron we can consider two possibilities, one is electron transfer (ET) from a donor (D) to an acceptor (A) as schematized in Fig. 2 (Velarde et al. 2010a). The other possibility is electric transport or current in the presence of an external electric field. In both cases we have to follow the time evolution of the electron coupled to that of the lattice units, one affects the other. In the simplest form we can use the tight binding approximation (TBA) hence placing the electron at a lattice site and allowing electron hopping to nearby sites. In the TBA the time evolution of the electron follows the Schrödinger equation (for the lattice "space") augmented with the coupling with the anharmonic lattice, that reduces to

$$\mathrm{i}\hbar\dot{c}_n = E_n c_n - (V_{n,n-1}c_{n-1} + V_{n+1,n}c_{n+1})\,, \tag{7}$$

where the coupling of electron (normalized) probability density (amplitude, $|c_n|^2$) to lattice variables implicit in the $V_{n,m}$ appears. The choice

$$V_{n,\,n-1} = V_0 e^{-\alpha(\xi_n - \xi_{n-1})}, \tag{8}$$

is of current use dealing with, e.g., biomolecules. The parameter α is an inverse characteristic "length" scale.

To have a universal description suffices to make quantities dimensionless by introducing suitable scales/units: $\tau = V_0/\hbar\omega_M$, $\tilde{\alpha} = \alpha/B$, and $\tilde{V} = V_0/2D$ thus using the depth of the Morse potential as unit/scale; $\omega_M = \left(DB^2/M\right)^{1/2}$, M denotes lattice units mass (typical parameter values for some biomolecules (Gray and Winkler 2003, 2005) are: $B = 4.45\,\text{Å}^{-1}$, $\alpha = 1.75B$, $D = V_0 = 0.1\,\text{eV}$, $\omega_M = 3.10^{12}\,\text{s}^{-1}$, $V_0/\hbar = 0.6 \cdot 10^{14}\,\text{s}^{-1}$, $\tau = 10$). Then we can rewrite (7) as

$$\mathrm{i}\dot{c}_n = -\tau\left[e^{-\alpha(\xi_n - \xi_{n-1})}c_{n-1} + e^{-\alpha(\xi_{n+1} - \xi_n)}c_{n+1}\right]. \tag{9}$$

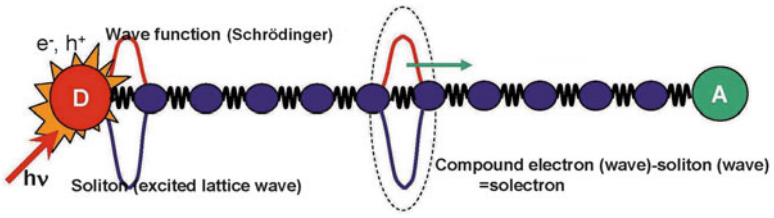

Fig. 2 ET along a biomolecule modeled by a lattice. The excess electron (wave function Ψ) is emitted from site **D** (donor) by appropriate energy supply and travels along the bridge or "backbone" lattice made of *anharmonic* elements down to the site **A** (acceptor)

The parameter τ shows explicitely the time scale of electron motions while the time t corresponds to the slower time scale of the lattice vibrations. The latter obey the Eq. (2) augmented with the coupling to electron *hopping* motions or better said, electron probability coefficients,

$$\ddot{\xi}_n = \left[1 - e^{(\xi_{n+1}-\xi_n)}\right] e^{-(\xi_{n+1}-\xi_n)} - \left[1 - e^{-(\xi_n-\xi_{n-1})}\right] e^{-(\xi_n-\xi_{n-1})} - \\ -\alpha V \left[\left(c^*_{n+1}c_n + c_{n+1}c^*_n\right) e^{-\alpha(\xi_{n+1}-\xi_n)} + \left(c^*_n c_{n-1} + c_n c^*_{n-1}\right) e^{-\alpha(\xi_n-\xi_{n-1})}\right]. \tag{10}$$

Clearly, the interplay between electron and lattice vibrations has now a genuinely new element, the soliton-mediated effect. This permits to consider the compound electron-soliton "quasiparticle", due to its "universal" carrier character, as a new physical entity which is the "solectron" one way of providing electron "surfing" on a subsonic/supersonic sound (longitudinal lattice soliton) wave (Cantu Ros et al. 2011; Velarde 2010).

2.2 Soliton Electron Trapping

Consider an electron placed at site "n" in a lattice. Then let alone the electron, its evolution is dictated by Eq. (9) with $\alpha = 0$. Figure 3 shows how from an initially peaked probability density as time proceeds the probability spreads down to a uniform distribution over all lattice sites and hence ends up by being *completely delocalized*.

Other evolution possibilities have been explored (Hennig et al. 2006, 2007). Taking now Eq. (2) and launching as an initial condition a soliton at a certain lattice site and then switching-on the electron-lattice interaction hence switching-on Eq. (10), for an initial condition of the electron completely *delocalized*, and then operating Eq. (9) in full, the striking result found is illustrated in Fig. 4. Subsequently, after trapping the electron, the compound or bound state soliton-electron, i.e., the *solectron* proceeds moving unaltered along the lattice.

When two solitons which are allowed to collide in their evolution along the lattice are launched and the electron starts being trapped and carried by one of the solitons, e.g. by the one moving left-to-right, then as the collision proceeds and "finishes", the electron may leave the first soliton and reappear trapped and carried by the second soliton. Accordingly, the electron may change both partner and direction of motion after the collision. Another striking result also observed numerically is the electron probability density splitting thus illustrating how quantum mechanically the electron (in probability sense) can move simultaneously! in both directions (Velarde et al. 2008a).

If an external electric field is acting there is current, it suffices to add to Eq. (9) the term $(-n\mathbf{E}c_n)$ and then to compute

$$j = \mathrm{i} \sum \left(c^*_{n+1}c_n - c^*_n c_{n-1}\right), \tag{11}$$

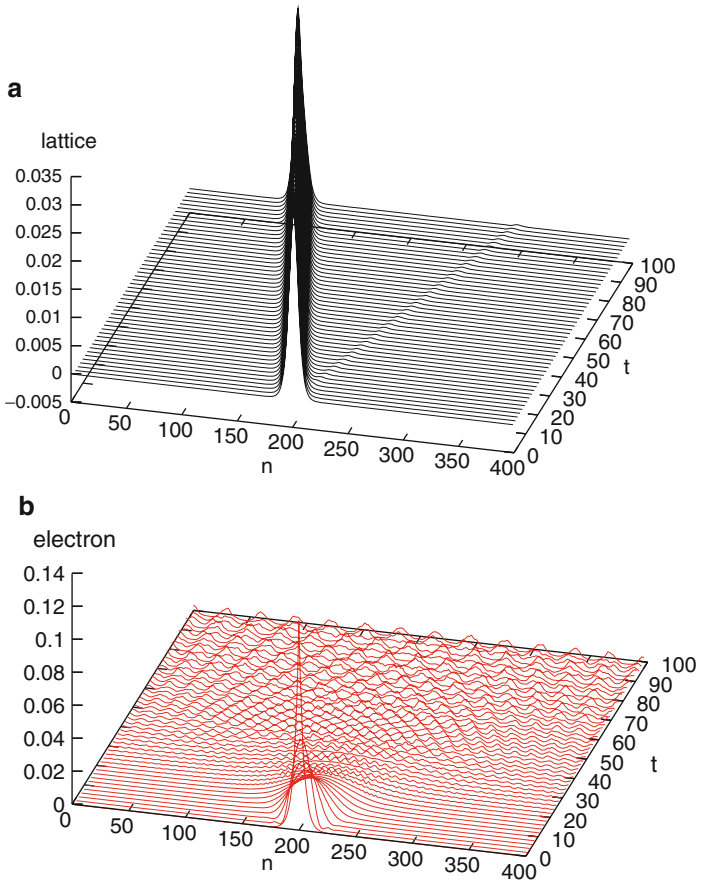

Fig. 3 Soliton and electron taken separately (no interaction). (**a**) lattice soliton time evolution starting at site $n = 200$. (**b**) Electron probability density time evolution. From initial "localization" at site $n = 200$ the electron ends up *completely delocalized*, i.e., the proability density is spread "uniformly" everywhere along the lattice

which then depends on the external field strength. This is apparently so but not always in reality. Indeed, for high enough field strength it can be seen that the latter forces the electron to follow Ohm's law. But as the field strength becomes low enough it is rather the soliton which commands the electric current which becomes field-independent thus remaining constant as the field strength tends to zero. This striking result is not unexpected if we recall what the "soliton" wave does to a surfer.

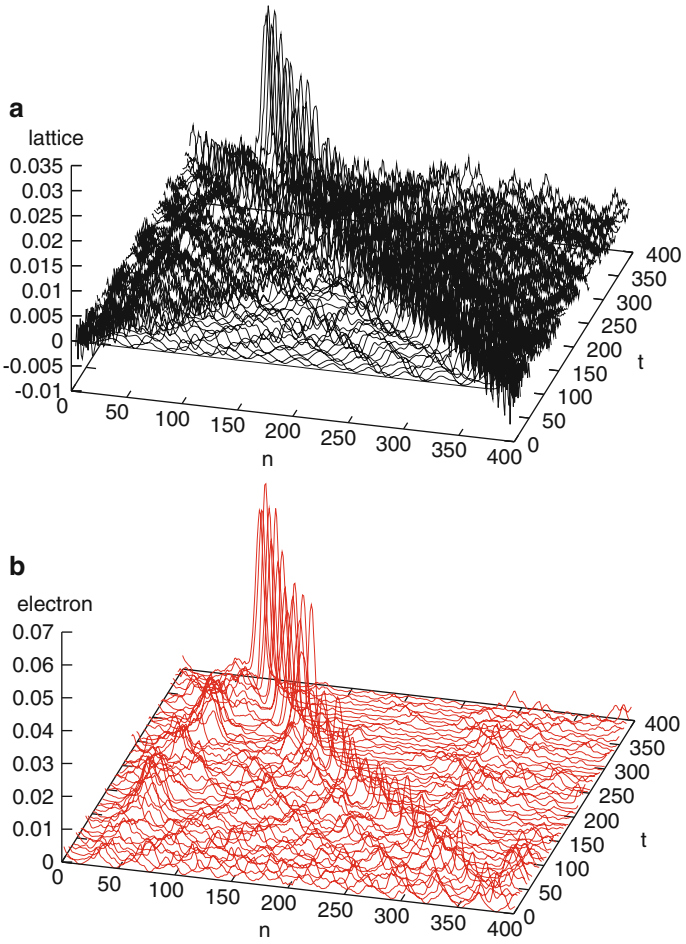

Fig. 4 Interaction of a *soliton* with a *completely delocalized* electron. *Right figure*: the electron after following evolution dictated by Schrödinger equation ends up *completely delocalized* with probability density spread like "dust" over the entire lattice. Then at such time instant the soliton is launched taking as initial condition for the electron the final state of the right picture in Fig. 3. *Left figure*: the soliton after gathering the electron dusty probability density eventually reconstructs the electron probability density in a kind of "vacuum cleaner" process

3 Heated Crystal Lattices

So far no mention was done of temperature other than when referring to the specific heat (Fig. 5). Strictly speaking the results described above hold at zero-K. Let us now consider that the system is heated-up from zero-K to the soliton range ($T \approx 0.1-1$) defined in Fig. 5. The heating can be done by a suitable thermal bath satisfying Einstein's relation between noise strength and equivalent temperature in K. As we

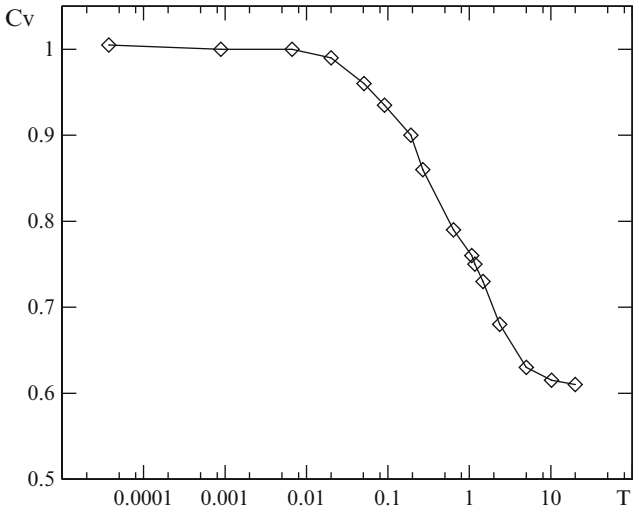

Fig. 5 Specific heat at constant length/volume in k_B units. $T_{transition} = 1$, for which here $C_L \equiv C_v = 0.75$. $C_v = 1$ is the Dulong-Petit (Einstein) value (solid phase; harmonic interaction) and $C_v = 0,5$ corresponds to the fluid-like phase (hard-rod interaction). Missing in the figure is the low temperature values arising from genuinely quantum mechanics (T^d Debye law with d denoting space dimension)

shall continue restricting consideration to 1d lattices let us recall the Hamiltonian, H_a, using x_n as lattice coordinates. Then we have

$$H_a = \frac{m}{2}\sum_{n=1}^{N} v_n^2 + \frac{1}{2}\sum_{n,i=1}^{N} U\,(x_n, x_i), \tag{12}$$

where v_n denote velocities, and U corresponds to the Morse potential (6) (Fig. 1). Then in the presence of random forces (hence nonzero temperature) and also external forces the evolution of lattice particles is given by the Langevin equations

$$\frac{d}{dt}v_n + \frac{1}{m}\frac{\partial H_a}{\partial x_n} = -\gamma_0 v_n + \sqrt{2D_v}\,\xi_n(t). \tag{13}$$

The stochastic forces $\sqrt{2D_v}\,\xi_n(t)$ define a time delta correlated Gaussian white noise. The parameter γ_0 describes the standard friction frequency acting from the bath. The Einstein relation is $D_v = k_B T\gamma_0/m$, where T denotes absolute temperature and k_B is Boltzmann's constant.

In order to visualize the solitons we can focus attention to the "atomic" density. We assume that each lattice unit is surrounded by a Gaussian electron density providing a screened ion core of width $s = 0.35\sigma$. Then the total atomic electron density, defining a lattice unit, is given by

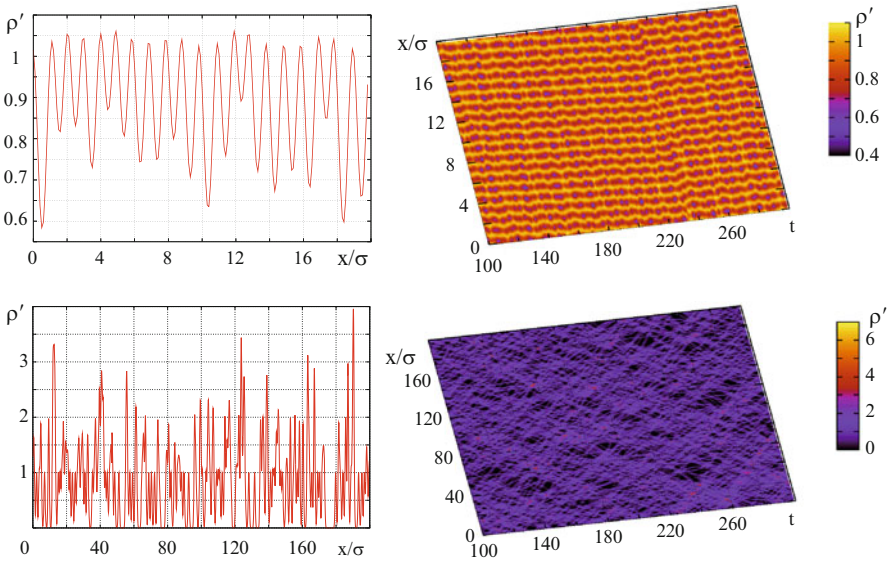

Fig. 6 Visualisation of soliton-like running excitations. Density $\rho' = \rho\sqrt{2\pi}s$ refers to electrons in lattice atoms (color coding in arbitrary units). $N = 200, B\sigma = 1, s = 0.35\sigma$. For two temperatures (given in units of $2D$) we have: *Upper set of figures*: (i) $T = 0.005$: Only harmonic lattice vibrations show up with no evidence of soliton-like excitations; and *bottom set of figures*: (ii) $T = 1$: Besides many excitations also a few strong solitons appear running with velocity around $1.3v_{sound}$. In both cases a snapshot of the distribution for a certain time instant and the actual time evolution of the distribution are displayed

$$\rho(x) = \sum_n \frac{1}{\sqrt{2\pi}s} \exp\left[-\frac{(x - x_n(t))^2}{2s^2}\right]. \tag{14}$$

Hence we assume that the atom is like a spherical object with continuous electron density concentrated around each lattice site. In regions where the atoms overlap, the electron density is enhanced. This permits easy visualization of soliton-like excitations based on the colors in a density plot. This is of course a rough approximation. Figure 6 shows the result of simulations for the temperatures $T = 0.005$ and $T = 1$. The diagonal stripes correspond to regions of enhanced density which are running along the lattice. This is a sign of solitonic excitations. Checking the slope we see excitations which over 10 time units move with *supersonic* velocity. We have solitonic excitations living about 10–50 time units corresponding to $1-3$ ps. Besides they survive even at $T = 1$ which is well above the physiological temperature (about 300 K which is above $T \approx 0.1$ with $D \simeq 0.1$ eV). Due to lack of space we shall not discuss here the solectron survival as we heat the lattice. The formation of solectron occurs as indicated above and does survive as a compound up to such temperatures. For details we refer the reader to the analyses presented in Chetverikov et al. (2009, 2010, 2012), Ebeling et al. (2009), and Velarde et al. (2008b).

4 Two-Dimensional Soliton-Like Excitations

Let us now extend the study to the case of a two-dimensional (2d) lattice still with Morse interactions. The lattice Hamiltonian (12) becomes now

$$H_a = \frac{m}{2}\sum_n v_n^2 + \frac{1}{2}\sum_{i,j} V(r_i,\, r_j). \tag{15}$$

The subscripts locate atoms at lattice sites n with coordinates (i, j) and the summations run from 1 to N. As before the characteristic distance determining the repulsion between the particles in the lattice is σ. We limit ourselves to nearest-neighbors only using the relative distance $r = |r_n - r_k|$. The Morse potential (Fig. 1) if for convenience, expressed as

$$U_M = D\left\{\exp[2B(r-\sigma)] - 2\exp[-B(r-\sigma)]\right\}. \tag{16}$$

In order to avoid unphysical cumulative interaction effects, a suitable cut-off rules out a stronger interaction than due arising from the influence of particles outside the first neighborhood of each particle. In fact, rather than a cut-off we consider the interaction with a smooth decay to zero as distance increases. Hence rather than (16) for the 2d lattice we take

$$\begin{aligned} U_M(r) = 2D\left\{\exp\left[-2b(r-\sigma)\right] - 2\exp\left[-b(r-\sigma)\right]\right\}\cdot \\ \cdot\left\{1+\exp[(r-d)/2\nu]\right\}^{-1}. \end{aligned} \tag{17}$$

As a rule the cut-off "interaction radius" is supposed to be equal to 1.5σ, together with parameter values $d = 1.35\sigma$ and $\nu = 0.025$. Beyond the cut-off radius the potential is set to zero. To study, at varying temperature, the nonlinear excitations of the lattice and the possible electron transport in a lattice it is sufficient to know the lattice (point) particles coordinates at each time and the potential interaction of lattice deformations with electrons. The former are obtained by solving the equations of motion of each particle (15) under the influence of all possible forces. The latter include forces between particles which are supposed to be of the Morse kind and the friction and random forces accounting for a Langevin model bath in the heated lattice. We use complex coordinates $Z = x + iy$, where x and y are Cartesian coordinates for each r. Then the Langevin equations (13) for the lattice units, n, become now

$$\frac{d^2 Z_n}{dt^2} = \sum_k F_{nk}(Z_{nk}) z_{nk} + \left[-\gamma\frac{Z_n}{dt} + \sqrt{2D_v}\left(\xi_{nx} + i\xi_{ny}\right)\right], \tag{18}$$

where γ, D_v and $\xi_{nx,y}$ have earlier defined roles. $Z_{nk} = Z_n - Z_k$, then $z_{nk} = (Z_n - Z_k)/|Z_n - Z_k|$ is a unit vector defining the direction of the interaction force F_{nk}.

To have dimensionless variables we consider the spatial coordinates normalized to the length σ. The energy is scaled with $2D$. The interaction force F_{nk} is given by

$$F_{nk} = F_{nk}(|Z_{nk}|) = -\frac{dV(r)}{dr}|_{r=|Z_{nk}|}. \tag{19}$$

In view of the above only those lattice units with coordinates Z_k, satisfying the condition $|Z_n - Z_k| < 1.5$, are taken into account in the sum in Eq. (18). In computer simulations the interaction of particles is considered to take place inside a rectangular cell $L_x \cdot L_y$ with periodic boundary conditions and $L_{x,y}$, depending on the symmetry of an initial distribution of units and their number N. For illustration we consider a distribution corresponding to the minimum of potential energy for an equilibrium state of a *triangular* lattice $10\sigma \cdot 10\sqrt{3/2}\sigma$ for $N = 100$ or $20\sigma \cdot 20\sqrt{3/2}\sigma$ for $N = 400$.

As in the preceding Section, we will assume that the atomic electrons may be represented by a Gaussian distribution centered on each lattice site:

$$\rho(Z,t) = \sum_{|Z-Z_i(t)|<1.5} \exp\left[-\frac{|Z - Z_i(t)|^2}{2\lambda^2}\right]. \tag{20}$$

In Fig. 7 we show the evolution of one localized soliton-like excitation in a triangular Morse lattice. The initial form of the excitation is a small piece of a plane soliton-like wave with a front oriented along one of symmetry axes of a triangular lattice and a velocity directed along an other axis (x-axis here). The density distribution (left column), and the cumulated during the time mentioned at each row amplitude-filtered density-distribution (right column) are presented for three time instants. We observe the transformation of the initial piece of a plane wave to a soliton-like horseshoe-shaped supersonic excitation. As the excitation travels a distance of about 16 units in the time internal $t = 8$, its supersonic velocity is $16/8 = 2$ in units of the sound velocity in 1D lattice. Note that $v_{sound} = 1$ for 1d-lattices. In a 2d-triangular lattice the sound velocity is $\sqrt{2} \simeq 1.4$ times higher than the sound velocity in a 1d-lattice.

In a subsequent set of simulations we studied two solitons excited initially, the left one propagating to the right, the right one – to the left. The parameter values are the same as in the one-soliton case above. We have observed first a transformation of the initial pieces of a plane wave to a 2d horseshoe-shaped soliton-like wave fronts and then both moving head-on against each other. Looking at Fig. 8 we observe that the two localized and supersonic excitations pass through each other without changing their form. This is a signature of solitons. They are not solitons in the rigorous mathematical sense because we do not prove that they are exact stationary waves (indeed our 2d excitations are "long lasting" transitory waves) but clearly their behavior is like that of surface solitons observed in fluids (Chetverikov et al. 2011b,c; Nepomnyashchy et al. 2002).

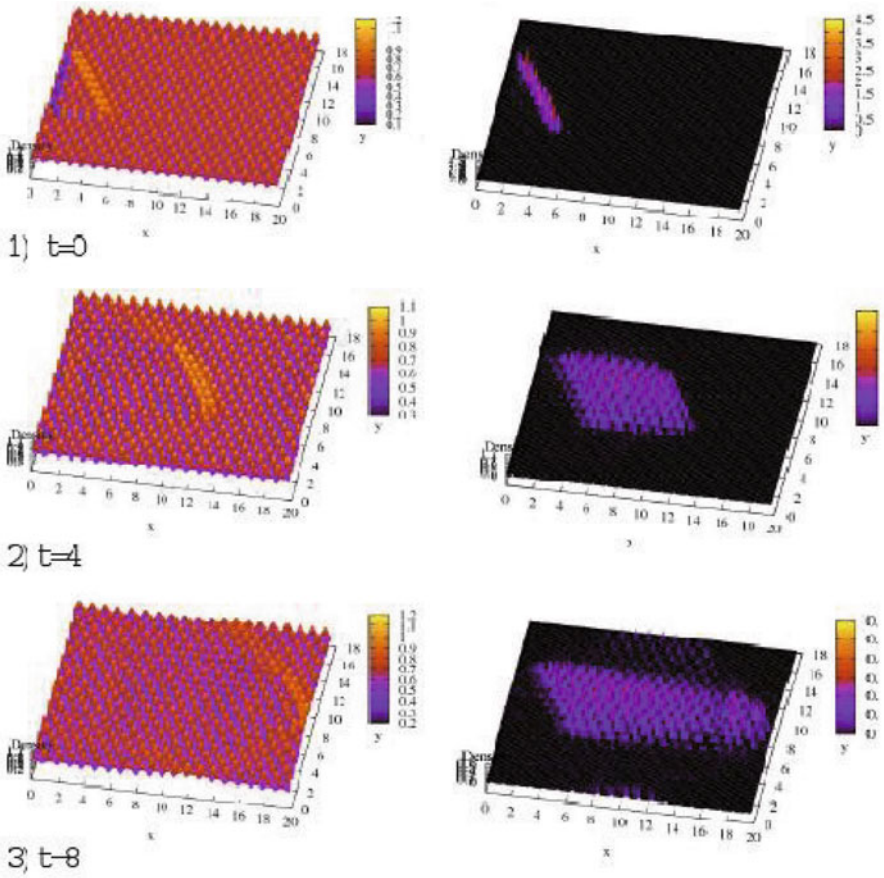

Fig. 7 Propagation of soliton-like excitation in a triangular lattice. *Left column*: density of the atom cores. *Right column*: a cumulated representation at final time. In order to study the evolution of perturbations we changed the initial positions of the atoms at $t = 0$ in a small region. Parameter values: $N = 400$, $b\sigma = 4$, $\lambda = 0.3$, $T = 0.01$

We have also studied the role of heating and hence observing excitations at finite temperatures. As we have no space to discuss this problem here we refer the reader to Chetverikov et al. (2011a).

5 Conclusion

We have succintly discussed features of solitons in 1d and 2d anharmonic crystal lattices and, in particular, some consequences of heating the system. We have also discussed features of coupling lattice solitons to added *excess* electrons leading to

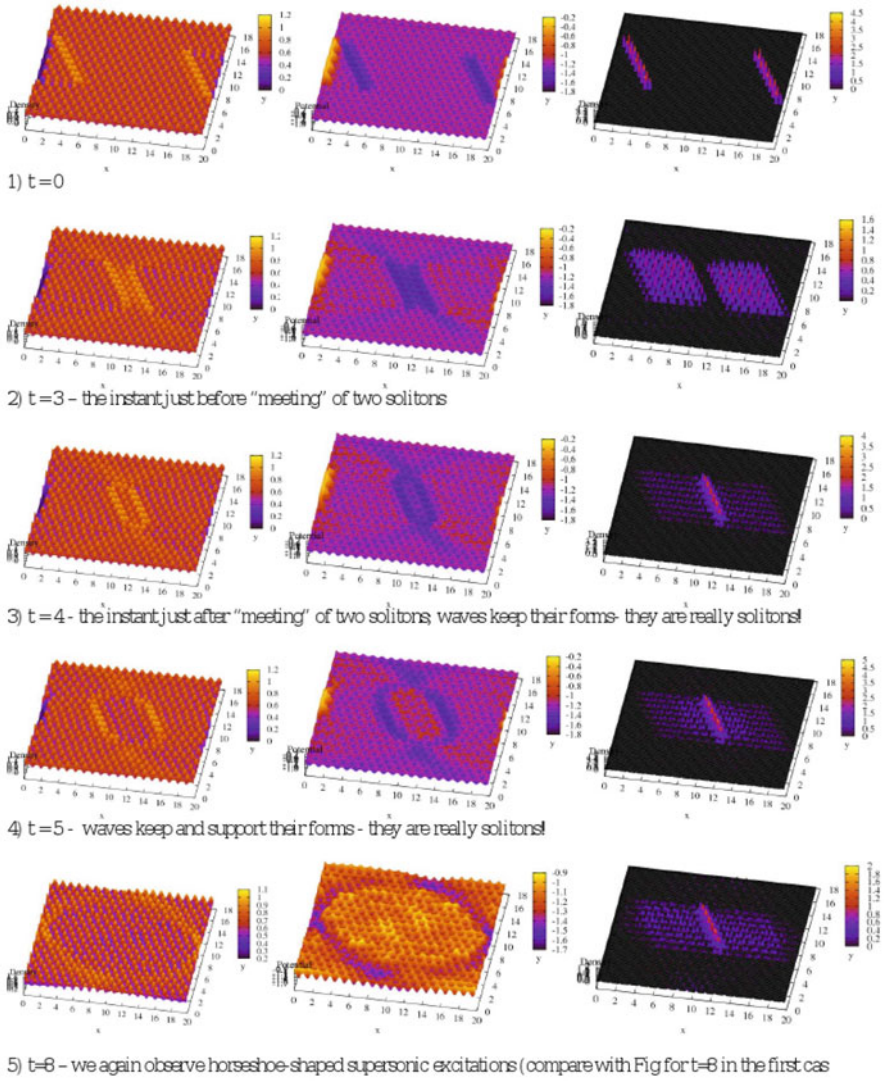

Fig. 8 Triangular lattice: Head-on collision of two oppositely moving solitons in the interval $t = 0 - 8$, both with the same parameters values: $N = 400$, $b\sigma = 4$, $\lambda = 0.3$, $T = 0.01$

the formation of bound states or compounds electron-soliton, denoted solectrons. Recently, we have also studied, albeit only in the 1d case, the formation of electron pairs (with opposite spins satisfying Pauli's exclusion principle and experiencing Coulomb repulsion using Hubbard's local approximation) (Hennig et al. 2008; Velarde and Neissner 2008; Velarde et al. 2010b, 2012). Finally, three recent experiments have provided collateral verification of the major predictions of the

theory here presented. One (Slinker et al. 2011) provides evidence of *ballistic* transport in synthetic DNA and the other two (Hermelin et al. 2011; McNeil et al. 2011) (see also Chetverikov et al. (2012) and Nayanov (1986)) provide evidence of electron "surfing" on sound waves in piezoelectric *GaAs*. Further details about comparison between theory and experiments would be provided elsewhere.

Acknowledgements The authors are grateful to A.S. Alexandrov, E. Brändäs, L. Brizhik, L. Cruzeiro, F. de Moura, J. Feder, D. Hennig, R. Lima, R. Miranda, R. McNeil, G. Röpke and G. Vinogradov for enlightening discussions. This research has been sponsored by the Spanish Ministerio de Ciencia e Innovacion, under Grants EXPLORA-FIS2009-06585-E and MAT2011-26221.

References

Boussinesq, J.V.: Mem. presentes par divers savants a l'Acad. Sci. Inst. France (Paris) **23**, 1 (1877); ibidem **24**, 1 (1878), Eq. (283 bis)
Cantu Ros, O.G., Cruzeiro, L., Velarde, M.G., Ebeling, W.: Eur. Phys. J. B **80**, 545 (2011)
Chetverikov, A.P., Ebeling, W., Velarde, M.G.: Int. J. Bifurc. Chaos **16**, 1613 (2006)
Chetverikov, A.P., Ebeling, W., Velarde, M.G.: Eur. Phys. J. B **70**, 217 (2009)
Chetverikov, A.P., Ebeling, W., Velarde, M.G.: Int. J. Quantum Chem. **110**, 46 (2010)
Chetverikov, A.P., Ebeling, W., Velarde, M.G.: Eur. Phys. J. B **80**, 137 (2011a)
Chetverikov, A.P., Ebeling, W., Velarde, M.G.: Phys. D **240**, 1954 (2011b)
Chetverikov, A.P., Ebeling, W., Velarde, M.G.: Wave Motion **48**, 753 (2011c)
Chetverikov, A.P., Ebeling, W., Velarde, M.G.: Eur. Phys. J. B **85**, 291 (2012)
Dancz, J., Rice, S.A.: J. Chem. Phys. **67**, 1418 (1977)
del Rio, E., Velarde, M.G., Ebeling, W.: Phys. A **377**, 435 (2007)
Ebeling, W., Velarde, M.G., Chetverikov, A.P.: Condens. Matter Phys. **12**, 633 (2009)
Fermi, E., Pasta, J.R., Ulam, S.: Los Alamos Nat. Lab. Report LA-1940 (1955); In: Collected Papers of Enrico Fermi, pp. 978–988. University of Chicago Press, Chicago (1965)
Gray, H.B., Winkler, J.R.: Q. Rev. Biophys. **36**, 341 (2003)
Gray, H.B., Winkler, J.R.: Proc. Natl. Acad. Sci. **102**, 3534 (2005)
Hennig, D., Neissner, C., Velarde, M.G., Ebeling, W.: Phys. Rev. B **73**, 024306 (2006)
Hennig, D., Chetverikov, A.P., Velarde, M.G., Ebeling, W.: Phys. Rev. E **76**, 046602 (2007)
Hennig, D., Velarde, M.G., Ebeling, W., Chetverikov, A.P.: Phys. Rev. E **78**, 066606 (2008)
Hermelin, S., Takada, S., Yamamoto, M.: Nature **477**, 435 (2011)
Korteweg, D.J., de Vries, G.: Philos. Mag. **39**, 442 (1895)
McNeil, R.P.G., Kataoka, M., Ford, C.J.B., Barnes, C.H.W., Anderson, D., Jones, G.A.C., Farrer, I., Ritchie, D.A.: Nature **477**, 439 (2011)
Nayanov, V.I.: JETP Lett. **44**, 314 (1986)
Nekorkin, V.I., Velarde, M.G.: Synergetic Phenomena in Active Lattices. Patterns, Waves, Solitons, Chaos. Springer, Berlin (2002). Chap. 1
Nepomnyashchy, A.A., Velarde, M.G., Colinet, P.: Interfacial Phenomena and Convection. Chapman & Hall/CRC, London (2002). Chap. 5.
Payton, D.N. III, Rich, M., Visscher, W.M.: Phys. Rev. **160**, 706 (1967). See also Proceedings International Conference on Localized Excitations in Solids, pp. 657–664. Plenum, New York (1968)
Rolfe, T.J., Rice, S.A., Dancz, J.: J. Chem. Phys. **70**, 26 (1979)
Slinker, J.D., Muren, M.B., Renfrew, S.E., Barton, J.K.: Nat. Chem. **3**, 228 (2011)
Toda, M.: Theory of Nonlinear Lattices, 2nd edn. Springer, Berlin (1989)

Velarde, M.G., J. Comput. Appl. Math. **233**, 1432 (2010)
Velarde, M.G., Neissner, C.: Int. J. Bifurc. Chaos **18**, 885 (2008)
Velarde, M.G., Ebeling, W., Chetverikov, A.P., Hennig, D.: Int. J. Bifurc. Chaos **18**, 521 (2008a)
Velarde, M.G., Ebeling, W., Chetverikov, A.P.: Int. J. Bifurc. Chaos **18**, 3815 (2008b)
Velarde, M.G., Chetverikov, A.P., Ebeling, W., Hennig, D., Kozak, J.J.: Int. J. Bifurc. Chaos **20**, 185 (2010a)
Velarde, M.G., Ebeling, W., Chetverikov, A.P.: Int. J. Bifurc. Chaos **21**, 1595 (2010b)
Velarde, M.G., Brizhik, L., Chetverikov, A.P., Cruzeiro, L., Ebeling, W., Röpke, G.: Int. J. Quantum Chem. **112**, 551 (2012); ibidem 112, 2591 (2012)
Zabusky, N.J.: Chaos **15**, 015102 (2005)
Zabusky, N.J., Kruskal, M.D.: Phys. Rev. Lett. **15**, 57 (1965)

Dynamics of a Large Ring of Unidirectionally Coupled Duffing Oscillators

P. Perlikowski, S. Yanchuk, M. Wolfrum, A. Stefanski, and Tomasz Kapitaniak

Abstract In this paper we study the dynamics of a large ring of unidirectionally coupled autonomous Duffing oscillators. We paid our attention to the role of unstable periodic solutions for the appearance of spatio-temporal structures and the Eckhaus effect. We provide an explanation for the fast transition to chaos showing that the parameter interval, where the transition from a stable periodic state to chaos occurs, scales like the inverse square of the number of oscillators in the ring.

Keywords Coupled oscillators • Duffing • Spatio-temporal structures • Transition to chaos

1 Introduction

In the last decade, one can observe a growing interest in the studies of the networks of coupled oscillators (Strogatz 2001). The knowledge of the dynamical behavior of such systems can lead to the understanding of fundamental dynamical features of physical, biological, engineering or economical coupled

P. Perlikowski • A. Stefanski • T. Kapitaniak (✉)
Division of Dynamics, Technical University of Lodz, Stefanowskiego 1/15, 90-924 Lodz, Poland
e-mail: przemyslaw.perlikowski@p.lodz.pl; steve@p.lodz.pl; tomaszka@p.lodz.pl

S. Yanchuk
Institute of Mathematics, Humboldt University of Berlin, Unter den Linden 6, 10099 Berlin, Germany
e-mail: yanchuk@math.hu-berlin.de

M. Wolfrum
Weierstrass Institute for Applied Analysis and Stochastics, Mohrenstrasse 39, 10117 Berlin, Germany
e-mail: Matthias.Wolfrum@wias-berlin.de

M. Wiercigroch and G. Rega (eds.), *IUTAM Symposium on Nonlinear Dynamics for Advanced Technologies and Engineering Design*, IUTAM Bookseries (closed) 32, DOI 10.1007/978-94-007-5742-4_5,

systems (Zillmer et al. 2006; Mosekilde et al. 2002). The most important question is how the specific properties of the individual behavior and the coupling architecture can give rise to different types of collective behavior (Pikovsky et al. 2001). The other problem, which is discussed here, is connected with the structure of the attractors in higher dimensional phase space and, in particular, with the occurrence of the hyperchaotic attractors. When a map is at least two-dimensional or a flow is at least four-dimensional, its evolution can take place on a hyperchaotic attractor. Such attractors are characterized by at least two positive Lyapunov exponents for typical trajectories on them. The first example of such a system with hyperchaotic attractor was presented by Rossler (1976) for a chemical reaction model. Later, hyperchaotic attractors have been found in electronic circuits and other chemical reactions (Baier and Klein 1991; Peinke et al. 1992). In the works Kapitaniak et al. (1994) it was shown that by a weakly coupling of N chaotic systems it is possible to obtain a hyperchaotic attractor with N positive Lyapunov exponents. The transition from chaos to hyperchaos has been studied in Kapitaniak and Steeb (1991), Kapitaniak (1993), and Harrison and Lai (1999). It was shown that at this transition the attractor's dimension and the second Lyapunov exponent grow continuously. The role of the unstable periodic solutions in this transition has been discussed in Lai (1999), Yanchuk and Kapitaniak (2001), and Kapitaniak et al. (2000).

In this paper we present a interesting phenomena which occur in a ring with large number of unidirectionally coupled autonomous Duffing oscillators. As a control parameter we take the coupling strength. We use numerical integration and path-following. We observe the coexistence of several periodic solution branches with a stability boundary that can be interpreted in terms of the classical Eckhaus scenario as a sideband instability within a family of solutions with different periods in space and time (Eckhaus 1965; Tsiveriotis and Brown 1989; Tuckerman and Barkley 1991; Mukolobwiez et al. 1998; Wolfrum and Yanchuk 2006; Yanchuk and Wolfrum 2008). We calculate the symmetric unstable periodic orbits (UPO), identify their role in the skeletons of the chaotic and hyperchaotic attractors, and point out their importance for the development of spatio-temporal structures. We point out that the transition from equilibrium to a chaos, that has been observed for certain choices of nonlinearities in considered system, can take place in a parameter interval that scales as $1/N^2$, i.e., for a large number of oscillators this interval tends to zero and a practically immediate transition to chaos is observed.

This paper is organized as follows: In Sect. 2 we introduce our system. In Sect. 3 we show the dynamics in the ring of 400 systems. Then, in Sect. 4 we present the creation of complex spatio-temporal patterns. In Sect. 5 we present the scaling law which is observed when the dynamics goes from a stable equilibrium to chaos and the number of systems in ring is growing. Finally, we give conclusions in Sect. 6.

2 The Model

We consider the ring of unidirectionally coupled oscillators shown in Fig. 1. As a node system we take the autonomous Duffing oscillator described by the following ODE:

$$\ddot{z} + d\dot{z} + az + z^3 = 0, \tag{1}$$

where a and d are positive constants. In all numerical examples we use the fixed the parameter values $a = 0.1$ and $d = 0.3$. The system (1) is a single-well Duffing oscillator which has a single equilibrium point at $z = \dot{z} = 0$. Due to the presence of damping ($d > 0$) in the oscillator this equilibrium is an attractor for all initial conditions.

Introducing the new coordinates $x = z$, $y = \dot{z}$ in Eq. (1) the dynamics of the ring of oscillators shown in Fig. 1 can be described by the following system:

$$\begin{aligned} \dot{x_j} &= y_j, \\ \dot{y}_j &= -dy_j - ax_j - x_j^3 + k\left(x_{j-1} - x_j\right), \end{aligned} \tag{2}$$

where k is a linear coupling coefficient and $j = 1, \ldots, N$ is considered modulo N. This type of unidirectional coupling appears in different applications, e.g. in reactive flows (Rovinsky and Menzinger 1992; Yakhnin et al. 1994), motions of active Brownian particles (Schimansky-Geier et al. 1995), etc. It should be mentioned here that typically the studies of the dynamics of the rings of coupled oscillators are concentrated on the possibility of the oscillators synchronization or the appearance of clusters of synchronized attractors (Kaneko 1990; Akopov et al. 2005; Belykh and Mosekilde 1996; Belykh et al. 2000, 2003; Verichev et al. 2007, 2009). Considered study differs in that way that all observed here phenomena appear in the case when all oscillators in the ring are unsynchronized. The synchronizations of oscillators in the ring (Eq. (2)) reduce its dynamics to the stable steady state.

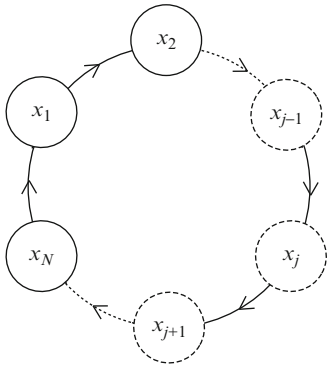

Fig. 1 Ring of unidirectionally coupled oscillators

3 The Dynamics in the Large Ring

The number of nodes is crucial for the development of complex behavior in the networks of coupled oscillators, see e.g. Strogatz et al. (2005). In this section, we investigate the dynamics of a large network of unidirectionally coupled Duffing oscillators (2) with $N = 400$. The choice of N is motivated from one side by numerical limitations (path-following of a large system) and from another side by the fact that this is about the value where some important spatio-temporal features like Eckhaus phenomenon become visible. In Fig. 2 we show the bifurcation diagram versus coupling coefficient k. The transition to chaotic behavior takes place for a much lower value of the coupling coefficient ($k = 0.1435$) than in the case of three coupled oscillators, but also one can observe the coexistence of several stable periodic solutions, and the coexistence of stable periodic solutions and chaos (see Fig. 3).

In a ring of $N = 400$ coupled systems one can observe $(N-1)/2$ Hopf bifurcations of the symmetric equilibrium. Each bifurcation leads to the appearance of a branch of *periodic solutions* (PS) and most of the branches are unstable. The increase of the number of unstable PS indicates already that one should expect here more complex dynamics as the coupling parameter increases. The Hopf curve, on which PS appear, can be obtained from the condition (for details see Perlikowski et al. (2010))

$$i\omega = -\frac{d}{2} + \sqrt{\left(\frac{d}{2}\right)^2 - a - k\left(1 - e^{i\varphi}\right)}, \tag{3}$$

where the real part of eigenvalues vanishes at Hopf bifurcation. Equation (3) can be solved with respect to the coupling parameter k and the Hopf frequency ω

$$k(\varphi) = \frac{\omega(\varphi) d}{\sin\varphi},$$

$$\omega(\varphi) = \frac{d\alpha(\varphi)}{2} + \sqrt{\left(\frac{d\alpha(\varphi)}{2}\right)^2 + a}, \tag{4}$$

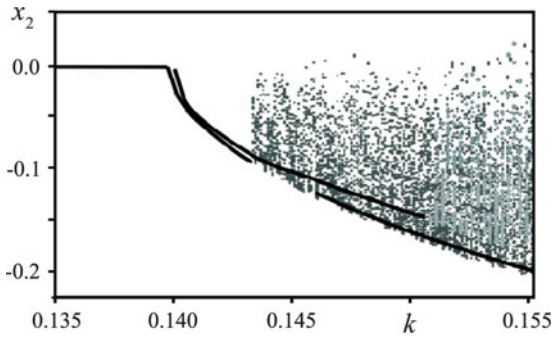

Fig. 2 Bifurcation diagram for 400 unidirectionally coupled Duffing oscillators versus coupling coefficient k. Parameters of the system: $a = 0.1$, $d = 0.3$

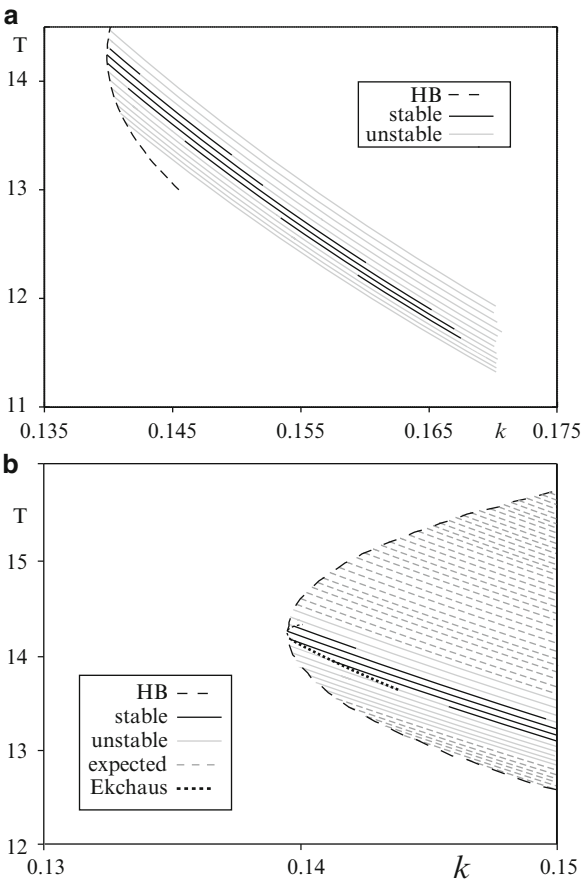

Fig. 3 Period T (**a**) and (**b**) along branches of periodic solutions for 400 unidirectionally coupled Duffing oscillators versus coupling coefficient k. The zoom and extension of (**a**) is shown in (**b**). Stable periodic solution – *black bold line*, unstable periodic solution – *gray lines*; Hopf curve – *bold black dashed line*, Eckhaus stability boundary – *bold black dotted line*. Parameters of the system are $d = 0.3$ and $a = 0.1$

where $\alpha(\varphi) = (1 - \cos\varphi)/\sin\varphi$ and $\varphi \in (0, 2\pi)$ is the parameter along the Hopf curve. We take into account only positive solutions with $k(\varphi) \geq 0$. The Hopf curve is shown in Fig. 3 as black dotted line, from which the branches of PS emerge. Note that the period of the emerging PS on the Hopf curve is $T(\varphi) = 2\pi/\omega(\varphi)$.

In Fig. 3a we plot the period T along the branches of PS versus coupling coefficient k. All shown solutions are rotating waves. The branches have been calculated numerically by path following method using the software package Auto (Doedel 2006). Due to numerical limitations we calculate only the 12 PS branches closest to the stable region. Stable and unstable PS along the branches are shown by black and gray lines respectively. In Fig. 3b we show an enlargement of the left part of Fig. 3a. In addition to the numerically computed branches of PS (grey lines), we show schematically also other branches, which appear from the Hopf bifurcation of the symmetric equilibrium (gray dashed lines). One can observe here the occurrence of the Eckhaus scenario (Wolfrum and Yanchuk 2006; Yanchuk and Wolfrum 2008;

Eckhaus 1965), i.e. the emergence of a region of stable PS that covers a certain range of frequencies and spatial wave numbers in the neighborhood of the primary stable branch, emerging from the primary Hopf bifurcation. Except for the primary branch, the PS branches emerge unstable at the Hopf bifurcation. Then the branches closest to the primary branch become stable in a cascade of Neimark-Sacker bifurcations. Note that here, the stability region is rather narrow and some branches are leaving the stability region after passing through a further Neimark-Saker bifurcation. The Eckhaus curve which encloses the stable region is shown in bold black dotted and does not depend on N.

An important property of the Eckhaus stability region is its independence of the number of oscillators (Yanchuk and Wolfrum 2008) in the network. With an increasing number of oscillators, the PS branches become more dense, thus filling more and more densely the Eckhaus stability region. In our example of Duffing oscillators this region is rather small and therefore multiple coexistence can be observed only for large N.

4 Spatio-Temporal Patterns

In Fig. 4 we show some spatio-temporal plots. The oscillator number is shown along the horizontal axis and the time along the horizontal axis. The amplitude of oscillators $x_j(t)$ is shown using a color gradient. For better visibility we restricted the space to $N = 200$ oscillators. In Fig. 4a one observes a pattern corresponding to a stable periodic rotating wave. The corresponding initial conditions are taken from the primary branch of PS with $k = 0.148$. With increasing k, the PS escapes the Eckhaus stability region and becomes unstable. The solution shows now the

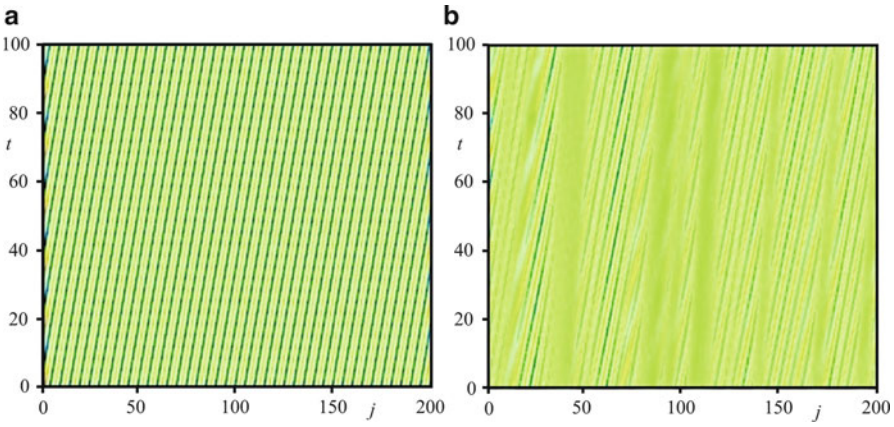

Fig. 4 Spatio-temporal plots for 400 coupled Duffing oscillators. Number of oscillators versus time. Oscillation amplitude is shown by a color gradient. Stable periodic pattern for $k = 0.148$ (**a**) and chaotic dynamics for $k = 0.171$ (**b**). The space is restricted to $1 \leq j \leq 200$

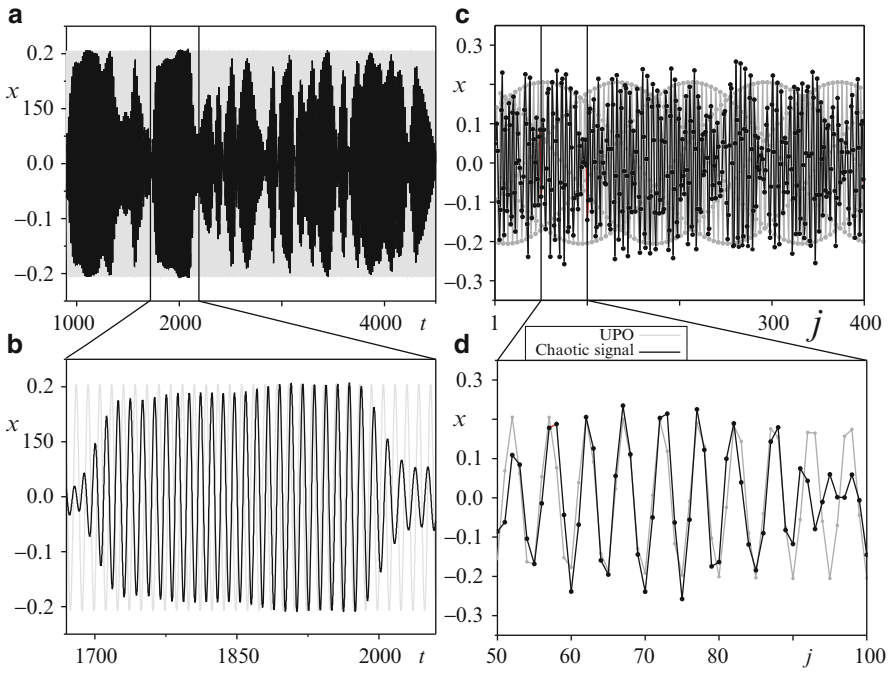

Fig. 5 Cross sections of spatio-temporal plot (Fig. 4) in time (**a**) and (**b**) and in space (**c**) and (**d**). Chaotic time evolution (*black line*) and irregular spatial pattern (*black dots*) follow locally the unstable PS on the primary branch (*grey*); $k = 0.171$

irregular pattern given in Fig. 4b for $k = 0.171$. Although all the rotating waves are already unstable, an intermittent periodic structure still exists locally in space and time. The existence of such structures indicates that the unstable rotating waves become a part of a new chaotic attractor after destabilization. As a result, the system visits intermittently and locally in space such unstable PS during its evolution along the chaotic attractor (Ott 2002). This phenomenon can be seen in more detail in Fig. 5 where we show two cross-sections of Fig. 4b. The first one shows the time evolution of one fixed oscillator (Fig. 5a, b). The second shows the amplitudes of all oscillators for some fixed time moment (Fig. 5c, d). We plot the hyperchaotic trajectory (black) and the unstable PS from the primary branch (grey). The black dots in Fig. 5c, d indicate the positions of single oscillators. Figure 5a shows that the chaotic trajectory frequently comes close to the unstable PS (see also enlargement in Fig. 5b), where the amplitude and the period of the chaotic trajectory and PS are close. The same scenario can be observed in the second cross-section in Fig. 5c, d. In Fig 5d it is easy to see the good local correlation between the spatial profile of the chaotic orbit and of the unstable PS.

5 Scaling Law of Fast Transition to Chaos

In this section we show the scaling law of transition to chaos. For this configuration it has been shown in Perlikowski et al. (2010) that already for $N = 3$ an increasing coupling strength k induces a destabilization of the equilibrium at zero and a rich dynamical behavior starting from periodic oscillations to hyperchaos. Here we focus our attention on the transition to chaos and study its dependence on the increasing number of oscillators. We calculate the maximum Lyapunov exponents for different number of oscillators N varying the coupling coefficient k. We detect two values: k_H, at which the primary Hopf bifurcation occurs and k_{Ch}, at which the transition to chaos takes place. A more or less reliable computation of the Lyapunov exponents was possible for sizes of the ring up to $N = 30$. For larger systems, we used the bifurcation diagrams for an appropriately chosen Poincare section to determine k_H and k_{Ch}. We plot these two values in Fig. 6a and observe that the distance between

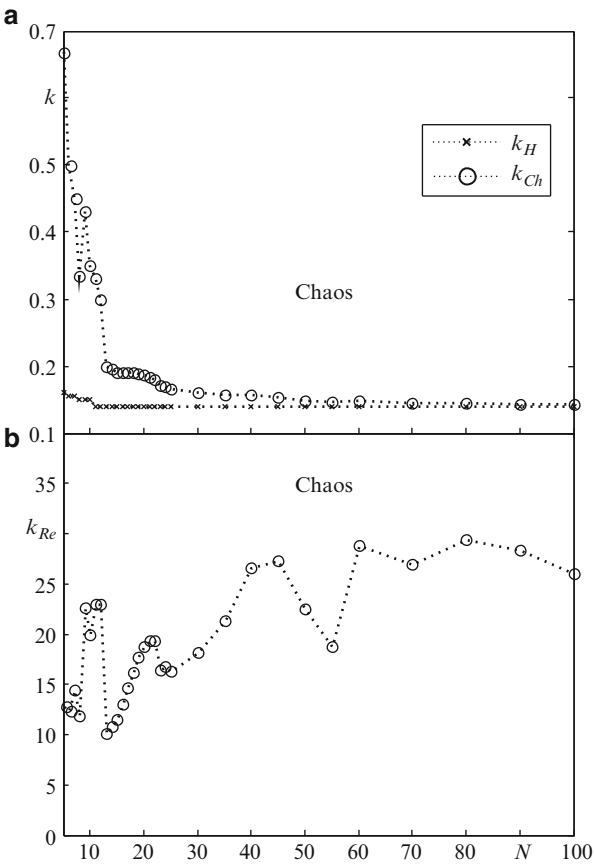

Fig. 6 (**a**) Coupling parameter for Hopf bifurcation (k_H, *crosses*) and transition to chaos (k_{Ch}, *circles*) versus number of oscillators N. (**b**) Rescaled transition interval k_{Re}(*circles*) versus N

k_H and k_{Ch} is decreasing when the number of oscillators N is growing. Finally, for a large enough number of oscillators, the transition to chaos appears practically immediately after the Hopf bifurcation. In order to verify the $1/N^2$ scaling law, we plot the scaled transition intervals

$$k_{Re} = (k_{Ch} - k_H)\, N^2$$

in Fig. 6b. The numerical results clearly indicate that the scaled transition interval neither tends to zero nor diverges to infinity, which supports the scaling result. More details as well as a supportive multiscale analysis can be found in Yanchuk et al. (2010).

6 Conclusion

We studied the appearance of complex dynamics in a ring of unidirectionally coupled autonomous Duffing oscillators. Although the individual uncoupled system has only trivial dynamics as a globally stable equilibrium, the coupled system shows (with increasing coupling strength) a transition to periodic and chaotic and hyperchaotic behavior. When the number of oscillators in the ring is large, the system shows interesting phenomena. After destabilization we observed the coexistence of multiple stable periodic solutions in a band of frequencies and wave numbers close to the primary branch of periodic solutions, that can be interpreted in terms of the well known Eckhaus scenario. We identified the symmetric unstable periodic orbits, which are in the skeletons of the chaotic attractor. We discuss their role in the development of spatio-temporal structures.

The next result is concerned with destabilization processes that can be observed in the ring of unidirectionally coupled Duffing oscillators and with its dependence on the system size. We have investigated the so-called fast transition to chaos. This fast transition manifests itself as a decreasing parameter interval, in which the transition takes place. More precisely, the distance between the parameter value k_H at which the primary Hopf bifurcation occurs and k_{Ch}, at which chaos appears, decreases with the size of the system N. As a result one observes for large N a practically immediate transition from a steady state to chaos. We show by numerical computations that for increasing N, the size of the transition interval scales as $1/N^2$.

Acknowledgements The authors acknowledge the support of DFG Research Center Matheon "Mathematics for key technologies" under the projects D8 (M.W.) and D21 (S.Y.). P.P. acknowledges the support from Foundation for Polish Science (the START fellowship).

References

Akopov, A., Astakhov, V., Vadivasova, T., Shabunin, A., Kapitaniak, T.: Phys. Lett. A **334**, 169 (2005)
Baier, G., Klein, M.: A Chaotic Hierarchy. World Scientific, Singapore (1991)
Belykh, V.N., Mosekilde, E.: Phys. Rev. E **54**, 3196 (1996)
Belykh, V.N., Belykh, I.V., Hasler, M.: Phys. Rev. E **62** (2000)
Belykh, V.N., Belykh, I., Hasler, M., Nevidin, K.V.: Int. J. Bifurc. Chaos **13**, 755 (2003)
Doedel, E.J.: AUTO-07P: Continuation and bifurcation software for ordinary differential equations. Concordia University, Montreal (2006). http://sourceforge.net/projects/auto2000
Eckhaus, W.: Studies in Non-Linear Stability Theory. Springer Tracts in Natural Philosophy. Springer, Berlin/New York (1965)
Harrison, M.A., Lai, Y.-C.: Phys. Rev. E **59**, R3799 (1999)
Kaneko, K.: Physica D **41**, 137 (1990)
Kapitaniak, T., Steeb, W.H.: Phys. Lett. A **152**, 33 (1991)
Kapitaniak, T.: Phys. Rev. E **47**, R2975 (1993)
Kapitaniak, T., Chua, L., Zhong, G.-Q.: IEEE Trans. Circ. Syst. I **41**, 499 (1994)
Kapitaniak, T., Maistrenko, Y., Popovich, S.: Phys. Rev. E **62**, 1972 (2000)
Lai, Y.-C.: Phys. Rev. E **59**, R3807 (1999)
Mosekilde, E., Maistrenko, Y., Postnov, D.: Chaotic Synchronization. Application to Living Systems. World Scientific, Singapore/River Edge (2002)
Mukolobwiez, N., Chiffaudel, A., Daviaud, F.: Phys. Rev. Lett. **80**, 4661 (1998)
Ott, E.: Chaos in Dynamical Systems, 2nd edn. Cambridge University press, Cambridge/New York (2002)
Peinke, J., Parisi, J., Rossler, O.E., Stoop, R.: Encounter with Chaos. Springer, Berlin (1992)
Perlikowski, P., Yanchuk, S., Wofrum, M., Stefanski, A., Mosiolek, P., Kapitaniak, T.: Chaos **20** (2010)
Pikovsky, A., Rosenblum, M., Kurths, J. Synchronization. A Universal Concept in Nonlinear Sciences. Cambridge University Press, Cambridge (2001)
Rossler, O.: Phys. Lett. A **57**, 397 (1976)
Rovinsky, A.B., Menzinger, M.: Phys. Rev. Lett. **69**, 1193 (1992)
Schimansky-Geier, L., Mieth, M., Rosé, H., Malchow, H.: Phys. Lett. A **207**, 140 (1995)
Strogatz, S.H.: Nature **410**, 268 (2001)
Strogatz, S.H., Abrams, D.M., McRobie, A., Eckhardt, B., Ott, E.: Nature **438**, 43 (2005)
Tsiveriotis, K., Brown, R.A.: Phys. Rev. Lett. **63**, 2048 (1989)
Tuckerman, L., Barkley, D.: Phys. Rev. Lett. **67**, 1051 (1991)
Wolfrum, M., Yanchuk, S.: Phys. Rev. Lett. **96**, 220201 (2006)
Verichev, N.N., Verichev, S.N., Wiercigroch, M.: Chaos Solitons Fract. **34** 1082 (2007)
Verichev, N.N., Verichev, S.N., Wiercigroch, M.: Chaos Solitons Fract. **42**, 686 (2009)
Yakhnin, V.Z., Rovinsky, A.B., Menzinger, M.: J. Phys. Chem. **98**, 2116 (1994)
Yanchuk, S., Kapitaniak, T.: Phys. Lett. A **290**, 139 (2001)
Yanchuk, S., Wolfrum, M. Phys. Rev. E **77** (2008)
Yanchuk, S., Perlikowski, P., Wofrum, M., Stefanski, A., Kapitaniak, T.: arXiv:1011.4786v1 (2011)
Zillmer, R., Livi, R., Politi, A., Torcini, A.: Phys. Rev. E **74** (2006)

Real-Time Subspace Tracking for Condition Monitoring Using Karhunen–Loève–Transform

Edwin Kreuzer and Michael Steidl

Abstract In order to monitor the dynamics of a distributed or high-dimensional dynamical system, an infinite- or high-dimensional Hilbert space is required as this class of systems may show various and complex dynamics. For example, different operational regimes can be observed depending on the current external loads. However, very often, the relevant dynamics of each of the observed operational regimes take place in a low-dimensional active subspace which is spanned by a low number of active modes. For changes in operational conditions, the active modes and therefore the low-dimensional subspace will be subjected to change as well. As Karhunen–Loève–Transform (KLT) is always applied to a history of measurements, good convergence and fast detection of changes in system dynamics conflict when choosing the length of the time interval. We present an algorithm based on KLT which uses an adaptive sliding time window. It can be employed for real-time tracking of the active subspace. The data from the real-time subspace tracking can be used to categorize different operational conditions and thus monitor the system in real time. We show that with currently available technology, an efficient implementation of the subspace tracking with sampling frequencies of 1,000 Hz is possible.

Keywords Karhunen–Loève–Transform • POD • Real–time subspace tracking

E. Kreuzer (✉) • M. Steidl
Institute of Mechanics and Ocean Engineering, Hamburg University of Technology, Eißendorfer Str. 42, D-21071 Hamburg, Germany
e-mail: kreuzer@tuhh.de; steidl@tuhh.de

M. Wiercigroch and G. Rega (eds.), *IUTAM Symposium on Nonlinear Dynamics for Advanced Technologies and Engineering Design*, IUTAM Bookseries (closed) 32, DOI 10.1007/978-94-007-5742-4_6,

1 Introduction

In order to completely describe the dynamics of a distributed or high-dimensional dynamical system, an infinite- or high-dimensional Hilbert space is required. When looking at the vibrations of mechanical structures, the system dimension is infinite-dimensional due to the distributed character of those structures, which implies that for a complete characterization of such systems, an infinite number of modes is necessary. However, various studies of high-dimensional structures indicated, that usually a low-dimensional subspace exists, in which the most relevant part of the dynamics takes place (Kerschen et al. 2005, 2006; Yan and Golinval 2006; He et al. 2007). Therefore, the spatio-temporal behavior of the considered structure can often be described with only few modes; i.e. the relevant dynamics can be described with a small number of active modes, which span the low-dimensional active subspace. The dimension of the low-dimensional active subspace determines the number of active modes. During operation, mechanical systems are frequently exposed to time-variant (environmental influences, different operating state) and nonlinear loads (friction, hardening nonlinearities, etc.). Forces and torques occurring during operation are therefore time-variant and nonlinear, hence the considered systems often show complex dynamical behavior, with both intensity and complexity of the observed vibrations depending strongly on current operating conditions. Accordingly, the number of active modes as well as the mode shapes depend on the current dynamical behavior or operational regime of the system. Often, and especially during the occurrence of unwanted vibrations, the considered system behaves stationary over a longer period of time. During these intervals of quasi-stationary behavior, the subspace spanned by the active modes is stationary as well. On the other hand, the subspace in which the system dynamics takes place will be time-variant when the system dynamics changes from one quasi-stationary operational state to another one. Via real-time measurements of the system dynamics at n discrete measurement points and real-time determination of the number and shape of the active modes based on those measurements, the relevant active subspace can be monitored continuously. The projection on the low-dimensional subspace reduces the high- or infinite-dimensional system dynamics and can be employed for condition monitoring or as a basis for adaptive, robust controllers to reduce unwanted vibrations.

2 Application of KLT on a Finite Number of Measurement Vectors

The Karhunen–Loève–Transform, Karhunen (1946) and Loève (1945), is a widely used tool for examination of statistical data, but also for identification of multi-dimensional processes (Kreuzer and Kust 1996) and model order reduction Holmes et al. (1996). Recently, KLT is also applied for condition monitoring (Gloesmann

and Kreuzer 2004, 2005; Tumer and Huff 2002). In Azeez and Vakakis (2001) it was already suggested to employ KLT for real-time identification of structural changes in mechanical systems. In the subsequent sections, vibrations of mechanical structures are considered, which are described by the process $u(x,t)$, defined on the domain Ω. Here, $u(x,t)$ is the spatial-temporal-distributed velocity field or displacement field of the considered mechanical structure. Aim of the Karhunen–Loève–Transform is the determination of a finite number of basis modes $\varphi_i(x)$ (Characteristic Functions), which, through a series of the form

$$u_m(x,t) = \sum_{i=1}^{m} a_i(t)\varphi_i(x), \tag{1}$$

approximate the process $u(x,t)$ better than any other basis of the same dimension. For condition monitoring of mechanical structures, the continuous process $u(x,t)$ is not available. Instead, only spatially and temporally discrete measurements are available. With n points of measurement, the dynamics of the continuous process $u(x,t)$ can be approximated. The n scalar measurements can be comprised in the measurement vector

$$\mathbf{y}(k) = \begin{pmatrix} y_1(k) \\ \vdots \\ y_n(k) \end{pmatrix}, \tag{2}$$

where k is the discrete time variable at which the measurements are sampled. In the literature, the process $\mathbf{y}(k)$ is often interpreted as the result of an ergodic stochastic process (e.g. Glösmann (2007)). Under this condition the expected value E exists, which is defined as

$$E\{\bullet\} = \lim_{N\to\infty} \frac{1}{N} \sum_{k=1}^{N} (\bullet). \tag{3}$$

Since the KLT is applied to a history of measurement vectors and is intended to detect changes in the system behavior in real time, the condition of stationarity and existence of an ergodic process are not fulfilled. Therefore, the existence of the expectation value can not be assumed. The assumptions on stationarity and ergodicity of the processes $\mathbf{y}(k)$ are, however, not a prerequisite for the derivation of the KLT (Bellizzi and Sampaio 2006). The KLT can be derived from the optimality condition given above according to Lumley (1970), Holmes et al. (1996), Kust (1998) and Kerschen (2002). In the following, an alternative derivation of the discrete KLT is presented for a finite number of N measurement vectors, $k = 1,\ldots,N$, using the properties and prerequisites of KLT, which are zero-mean of the process $\mathbf{y}(k)$, orthonormality of the Characteristic Functions $\varphi_i(x)$ and the pairwise uncorrelated weighting factors a_i. In case $\mathbf{y}(k)$ is not zero-mean in the interval $k = 1,\ldots,N$, zero-mean can be achieved by subtracting the mean value

$$M_{\text{discrete}}\{\bullet\} = \frac{1}{N}\sum_{k=1}^{N}(\bullet). \tag{4}$$

Sought-after is a linear decomposition of $\mathbf{y}(k)$ with the weighting factors $a_i(k)$ and the Characteristic Functions φ_i for $i = 1, \ldots, n$:

$$\mathbf{y}(k) = \sum_{i=1}^{n} a_i(k)\varphi_i. \tag{5}$$

Re-writing the weighting factors $a_i(k)$ as a vector $\mathbf{a}(k) = [a_1(k)\ a_2(k) \ldots\ a_n(k)]^{\mathrm{T}}$ and the Characteristic Functions φ_i as matrix $\Phi = [\varphi_1\ \varphi_2\ \ldots\ \varphi_n]$, (5) can be written as

$$\mathbf{y}(k) = \Phi\mathbf{a}(k). \tag{6}$$

As the Characteristic Functions φ_i form an orthonormal basis, the following holds:

$$\mathbf{a}(k) = \Phi^{\mathrm{T}}\mathbf{y}(k). \tag{7}$$

The weighting factors $a_i(t),\ i = 1, \ldots, n$, are pair-wise uncorrelated:

$$M_{\text{discrete}}\left\{a_i a_j\right\} = \lambda_i \delta_{ij}. \tag{8}$$

Plucking (7) in (8) yields:

$$M_{\text{discrete}}\left\{\varphi_i^{\mathrm{T}}\mathbf{y}\mathbf{y}^{\mathrm{T}}\varphi_j\right\} = \lambda_i \delta_{ij}. \tag{9}$$

The Characteristic Functions φ_i can now be excluded from the calculation of the mean value:

$$\varphi_i^{\mathrm{T}} M_{\text{discrete}}\left\{\mathbf{y}\mathbf{y}^{\mathrm{T}}\right\}\varphi_j = \lambda_i \delta_{ij}. \tag{10}$$

Due to the orthonormality of the Characteristic Functions

$$\varphi_i^{\mathrm{T}}\varphi_j = \delta_{ij} \tag{11}$$

it is obvious that the Characteristic Functions, $\varphi_i,\ i = 1, \ldots, n$, solve the eigenvalue problem

$$M_{\text{discrete}}\left\{\mathbf{y}\mathbf{y}^{\mathrm{T}}\right\}\varphi = \lambda\varphi. \tag{12}$$

The expression $M_{\text{diskret}}\left\{\mathbf{y}\mathbf{y}^{\mathrm{T}}\right\}$ in (12) corresponds to the covariance matrix $\mathbf{C}$ of the zero-mean process; thus the eigenvalue problem (12) can be simplified to

$$\mathbf{C}\varphi = \lambda\varphi. \tag{13}$$

Due to the discretization, the calculation of the covariance matrix simplifies to

$$C\{\bullet\} = \frac{1}{N}\sum_{k=1}^{N}(\bullet)(\bullet)^{\mathrm{T}}. \tag{14}$$

3 Application of KLT for Condition Monitoring

The application of KLT for Condition Monitoring and for spatio-temporal analysis of dynamic systems is described in Gloesmann and Kreuzer (2004) and Gloesmann and Kreuzer (2005). By applying KLT in the sense of a sliding window on a series of measurements originating from a mechanical system, qualitative and quantitative changes in the system dynamics can be detected. The KLT provides, as described in Sect. 2, a set of parameters, which can be utilized to characterize the system state:

Eigenvalues λ_i: The eigenvalues indicate the contribution of the respective Characteristic Function to the intensity of motion. The sum of eigenvalues is thus a measure for the entire intensity of motion. The number of $\lambda_i > 0$ is a measure for the number of active Characteristic Functions or active modes and therefore for the complexity of the system dynamics. It determines the necessary dimension of the subspace to embed the measurements.

Characteristic Functions $\varphi_i(x)$: The Characteristic Functions indicate the main directions of the signal space. The subspace spanned by the first m Characteristic Functions is optimal in the sense of Sect. 2. Since the measurement vectors for the calculation of the Characteristic Functions stem from scanning of a mechanical system, they can be interpreted as the main directions of motion of the system.

Weighting Factors $a_i(t)$: The weighting factors determine the course of the Characteristic Functions over time.

The intention of using KLT for condition monitoring is not to describe every possible system behavior or to identify the monitored system. Instead, it is intended to describe only the current system behavior. For this purpose, the KLT has to be applied to a sliding window, which, next to the current measurement vector, comprises a history of N measurement vector. In the following section, three different algorithms, based on a sliding window, are presented which can be utilized for real-time subspace tracking.

4 Algorithms for Real-Time Subspace-Tracking

For real-time subspace-tracking, KLT is always applied on a sequence of measurement vectors. In order to detect changes in the system behavior in real time, algorithms with a 'sliding window' calculate the KLT on a basis of a history of

measurement vectors. The measurement vector recorded at t_0 is denoted as $\mathbf{y}(0)$. In real-time applications, after each time interval $\Delta t = T$, a new measurement vector is added. The measurement vectors recorded at times $t_0 + k \cdot T$, $k = 1, 2, \ldots$, are denoted as $\mathbf{y}(k)$. The most recent measurement vector is given by $\mathbf{y}(l)$. At time $k = l$, the measurement vector $\mathbf{y}(0)$ is $l \cdot T$ in the past. When using a sliding window, slow changes in the system dynamics will always be detected, since older data will not be used for the calculation of the covariance matrix. When rapid changes in the system dynamics occur, KLT might not reflect the current system dynamics correctly, as measurement vectors from the former system dynamics will be used in the calculation of the covariance matrix. This is important especially with regard to potential control applications, as false assumptions about the system dynamics may lead to false controller settings and thus in the worst-case may result in instability. In order to detect changes in the system dynamics fast, a small window length is desirable. However, for the accurate and robust determination of KLT-parameters, a longer interval is advantageous. To combine these requirements, an algorithm with variable window length was developed, which is compared with an algorithm with fixed window length and an iterative algorithm with exponential forgetting.

4.1 Iterative Algorithm with Exponential Forgetting

In Hyvärinen et al. (2001) and Struck (2004), an algorithm is described which calculates the covariance matrix C iteratively for each new measurement vector:

$$\mathbf{C} = \frac{1}{N}\big((N-1)\mathbf{C} + \mathbf{C}(N)\big), \tag{15}$$

with $\mathbf{C}(l) = \mathbf{u}(l)\mathbf{u}(l)^T$. To weight newer measurement vectors stronger, a forgetting factor $\nu \in [0, 1]$ is introduced:

$$\mathbf{C}^N = \frac{1}{n_N}\left(\mathbf{C}(N) + \nu\mathbf{C}(N-1) + \nu^2\mathbf{C}(N-2) + \ldots + \nu^{N-1}\mathbf{C}^1\right). \tag{16}$$

The covariance matrix can now iteratively be calculated to

$$\mathbf{C}^N = \frac{1}{1 + \nu n_{N-1}}\left(\mathbf{C}(N) + \nu\mathbf{C}^{N-1}\right) \tag{17}$$

with $n_N = 1 + \nu n_{N-1}$. The advantage of the algorithm is the fast computation of the Characteristic Functions, as the covariance matrix is updated iteratively and only one computation step is necessary.

4.2 Sliding Window with Fixed Window Length

For a fixed window length N, the window is moved with each new measurement vector $\mathbf{y}(l)$, so the latest measurement vector will be taken into account, while the measurement vector $\mathbf{y}(l-N)$ is removed. The covariance matrix is given by

$$C = \frac{1}{N}\sum_{j=1}^{N}\mathbf{y}(l+1-j)\mathbf{y}^{\mathrm{T}}(l+1-j). \tag{18}$$

4.3 Sliding Window with Adaptive Window Length

Algorithms with fixed window length have the disadvantage that they cannot distinguish between stationary and non-stationary system behavior. Thus, measurement vectors may be used for the computation of the Characteristic Functions which do not describe the current system dynamics. As a result, these algorithms are not capable of fast detection of changes in the system dynamics (due to changes in external loads, bifurcations, etc.). Furthermore, these algorithms cannot distinguish between stationary and non-stationary system behavior. Aim of the following algorithm with variable window length is to find a meaningful interval of measurement vectors, which is suited to describe the current system dynamics. As the system dynamics and therefore the covariance matrix are not known a priori, a fixed reference does not exist. To solve this problem, the covariance matrices of overlapping time intervals are compared. When the covariance matrices in both intervals converge to the same values, this implies a similar system dynamics in both time intervals. By adapting the window length, the algorithm is capable of detecting fast changes in the system dynamics and thus can be applied for systems with sudden changes in external loads or nonlinear systems which show rapidly changing dynamics due to bifurcations. The following algorithm does not compare the whole covariance matrix, but only the auto-covariance sequences:

$$c_{ii} : N \in \mathbb{N} \rightarrow c_{ii}(N) = \frac{1}{N}\sum_{j=1}^{N} y_i(l+1-j)^2 \in \mathbb{R}. \tag{19}$$

For the comparison, we use the concept of convergence rates developed in Glösmann (2007). In order to facilitate a relative comparison, a second, shifted auto-covariance sequence, the so-called peer-covariance, is defined as:

$$c_{ii}^{\Delta} : N \in \mathbb{N} \rightarrow c_{ii}^{\Delta}(N) = \frac{1}{2\Delta}\sum_{j=N-\Delta}^{N+\Delta} y_i\left(l+1-\frac{N}{2}-j\right)^2 \in \mathbb{R}. \tag{20}$$

We chose $\Delta = \frac{1}{2} \cdot N$, so the peer-covariance sequence and the auto-covariance-sequence are of same length:

$$c_{ii}^{\Delta} : N \in \mathbb{N} \to c_{ii}^{\Delta} = \frac{1}{2N} \sum_{j=N-N/2}^{N+N/2} y_i \left(l + 1 - \frac{N}{2} - j \right)^2 \in \mathbb{R}. \tag{21}$$

This implies that the peer-covariance is computed on an interval of equal length, but the interval is shifted by $\frac{N}{2}$ time steps to the past. The convergence rate is now defined as the comparison of both covariance sequences:

$$\varsigma_{ii} : N \in \mathbb{N} \to \varsigma_{ii}(N) = \frac{|c_{ii}(N) - c_{ii}^{\Delta}(N)|}{c_{ii}^{\Delta}(N)} \in \mathbb{R}. \tag{22}$$

The convergence rates can now be combined in a single vector:

$$\varsigma = \begin{pmatrix} \varsigma_{11} \\ \vdots \\ \varsigma_{nn} \end{pmatrix}.$$

The window length is controlled by comparison of the largest element of the convergence rate vector with a predefined, fixed convergence threshold value Δ_{ς}. For stationary system behavior and $N \to \infty$ holds: $\Delta_{\varsigma} \to 0$. If the largest element of ς is smaller than Δ_{ς}, the system dynamics is assumed to be stationary in the considered time interval. In this case, the time interval is extended. In case the maximal element of ς is larger than Δ_{ς}, the auto-covariance sequel and the peer-covariance sequel do not converge to the same values. This implies that the system dynamics in the considered time interval is not stationary. The window length is now decreased until the largest element of ς is smaller than Δ_{ς} or until the minimal window length is reached. The choice of Δ_{ς} strongly influences the convergence of the algorithm. Depending on sensor noise, the desired sensitivity of the algorithm and the properties of the monitored system, Δ_{ς} has to be adjusted.

The choice of Sampling Rate influences the sensitivity of all algorithm. A lower sampling rate leads to lower sensitivity of the algorithm, as changes in the system dynamics influence the covariance matrix less rapidly. The choice of the sampling rate and the choice of Δ_{ς} are therefore not independent of each other and have to be tuned together.

5 Comparison of Algorithms

The capability of the three algorithms presented above in detecting changes in the system dynamics is compared using a simple generic spring-mass model (Fig. 1) with mass $m_i = 1$, damping $d = 0.1$ and stiffness $k = 1$. The change in system dynamics is caused by a change in the external force:

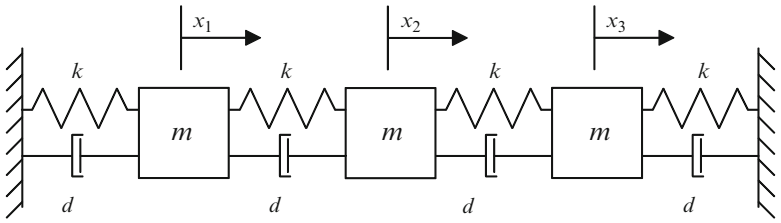

Fig. 1 Generic mass-spring system

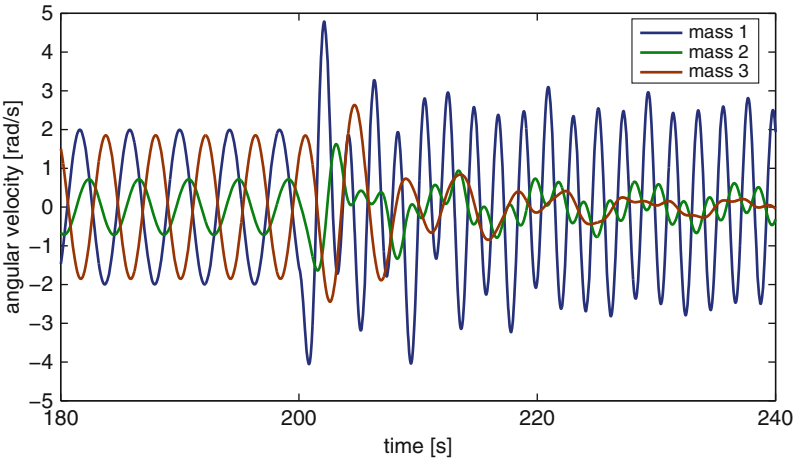

Fig. 2 Velocities of three masses

$$F(t) = \begin{pmatrix} \sin(1.5t) \\ 0 \\ 0 \end{pmatrix} 0 \leq t < 200, \qquad F(t) = \begin{pmatrix} 6 \cdot \sin(3t) \\ 0 \\ 0 \end{pmatrix} t \geq 200. \quad (23)$$

The velocities of the three masses are plotted in Fig. 2. Before and after the change in the external forcing, the active subspace is two-dimensional, but the two active Characteristic Functions spanning the active subspace differ.

The angle ϕ between the active subspaces can be calculated to:

$$\phi = \arccos(< (v1 \times v2), (w1 \times w2) >) = 38.5°. \quad (24)$$

The average kinetic energy and the corresponding sums of eigenvalues for the three algorithms are shown in Fig. 3. It is clearly visible that the adaptive algorithm (red line) follows the actual kinetic energy better than the algorithms with fixed window size. Especially the short period of higher kinetic energy is not detected by the algorithms with fixed window size. This is especially important for condition

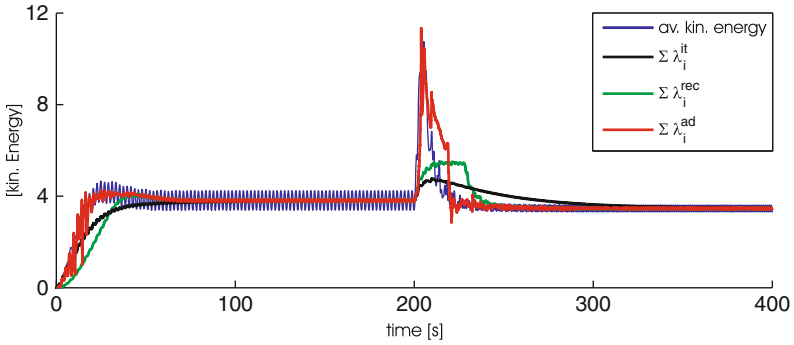

Fig. 3 Kinetic Energy and $\sum \lambda$ for twisting of subspace

monitoring, as one wishes to rapidly detect strong vibrations or instabilities. At the same time, the convergence for steady-state behavior of the adaptive algorithm is as good as the convergence of algorithms with fixed window size.

6 Application Examples: Vibrating Plate and Drill-String

The vibrations of a thin rectangular metal plate with side length of 1 m are monitored. The dynamics of the plate are calculated with 100 Finite Elements, the out-of-plane velocities of the plate are measured at nine discrete points. The measurements are used for the calculation of KLT. The quality of the approximation of the out-of-plane motion with the first two dominant KLT Characteristic Functions is considered here for different dynamics of the plate. The three algorithms are parameterized to converge to the same approximation error for quasi-stationary motion. In this example, several of the dominant eigenmodes of the shell are excited, however, the first eigenmode is explicitly not excited. Then, at time $t = 30$, the first eigenmode is excited, which leads to a significant change in the system dynamics, depicted in Fig. 4. The algorithm with adaptive window length is capable of detecting this change and, therefore, adapting its window size, while the other algorithms take longer to adapt to the new dynamics (Fig. 5). Due to the infinite response character of the iterative algorithm, this algorithm is not well-suited to detect immediate changes in system dynamics.

The algorithm with adaptive window length is applied for condition monitoring of an experimental setup of a scaled drill-string of 10 m length at the Institute of Mechanics and Ocean Engineering. While drilling, the real drill-strings are subjected to various unknown, time-variant and nonlinear external forces and disturbances at the drilling bit, but also along the string, which lead to several different operational regimes, e.g. stick-slip vibrations at the drilling bit. Many of these regimes can be reconstructed at the experimental setup, e.g. different friction characteristics between bit and rock can be simulated via an AC-Motor.

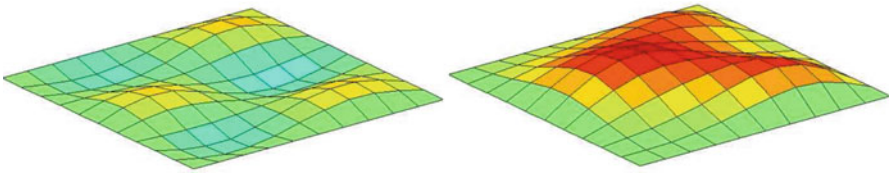

Fig. 4 Change in the dynamics of a vibrating plate

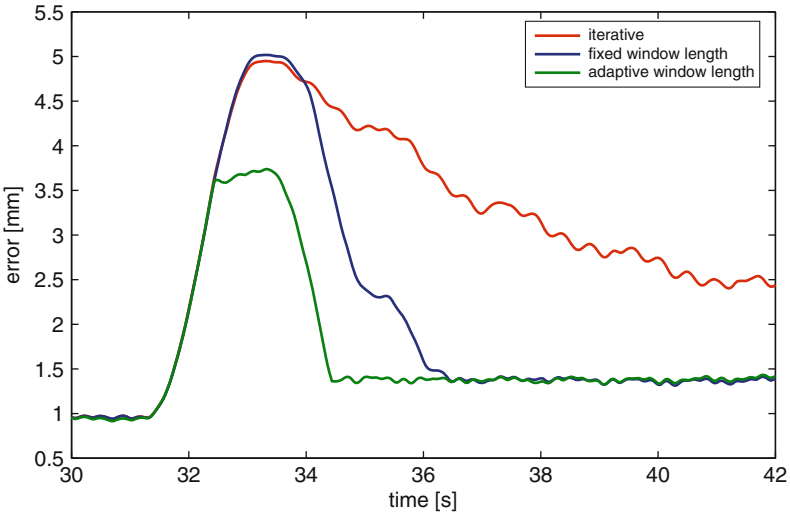

Fig. 5 Approximation error of different algorithms

Angular velocities of the drill-string are measured with angular encoders at the top, the bottom and at three equidistant points along the string. The real-time subspace tracking algorithm with variable window length is written in C and implemented as a dynamic link library which is called from a Lab-View Real-Time (RT) System used to obtain the measurements and to display the results of the algorithm. The LabView RT-System runs on a standard Quad-Core PC with 2,800 MHz, with one of the processors reserved for the calculation of the real-time KLT. For a measurement vector of five measurements and a total (overlapping) window length of 2,100 vectors, frequencies of up to 1,000 Hz for the RT-subspace tracking can be achieved easily. For the drill-string model, frequencies between 100 and 250 Hz are more than sufficient, as the dynamics itself is in the range below 10 Hz. The subspace-tracking performs very well in calculating the active modes in real time and in detecting changes in the dynamics and adapting the time window, e.g. for the change from normal operations to stick-slip vibrations caused by a strongly nonlinear friction characteristic at the bit.

7 Conclusions

The analysis performed shows that KLT can be applied for real-time system monitoring via subspace tracking. The problem is to find a meaningful time interval onto which KLT is applied. Although the optimality property of KLT is preserved in the way that any data used for KLT analysis is represented with a minimum number of Characteristic Functions, an interpretation of the active Characteristic Functions for condition monitoring is not possible when KLT is calculated with data from different operational regimes. As algorithms with fixed window size cannot distinguish between quasi-stationary and non-stationary system behavior, an algorithm with adaptive window size was developed which recognizes changes in the operational regime and adapts the window size to avoid using data for calculation of KLT that does not represent the current operational regime. Tests of the presented algorithm with numerical examples showed that the algorithm adapts the active Characteristic Functions faster when changes in system dynamics occur. The implementation for condition monitoring of an experimental setup of a drill-string showed that the numerical effort can be handled with currently available technology. Future work will be the analysis of adaptive control concepts based on the real-time subspace tracking.

References

Azeez, M.F.A., Vakakis, A.F.: Proper orthogonal decomposition (pod) of a class of vibroimpact oscillations. J. Sound Vib. **240**(5), 859–889 (2001)

Bellizzi, S., Sampaio, R.: Poms analysis of randomly vibrating systems obtained from Karhunen-Loève expansion. J. Sound Vib. **297**(3–5), 774–793 (2006)

Gloesmann, P., Kreuzer, E.: Nonlinear state monitoring with Karhunen–Loève transform. Proceedings of IMECE2004, 2004

Gloesmann, P., Kreuzer, E.: Nonlinear system analysis with Karhunen–Loève transform. Nonlinear Dyn. **41**, 111–128 (2005)

Glösmann, P.: Monitoring nichtlinearer rad/schiene–systeme mit der Karhunen–Loève–transformation, Ph.D. thesis, Hamburg–Harburg, Technische Universität, Institut für Mechanik und Meerestechnik (2007)

He, Q., Kong, F., Yan, R.: Subspace-based gearbox condition monitoring by kernel principal component analysis. Mech. Syst. Signal Process. **21**(4), 1755–1772 (2007)

Holmes, P., Lumley, J.L., Berkooz, G.: Turbulence, coherent structures, dynamical systems and symmetry. Cambridge University Press, Cambridge (1996)

Hyvärinen, A., Karhunen, J., Oja, E.: Independent component analysis. Wiley, New York/. . . (2001)

Karhunen, K.: Über lineare methoden in der wahrscheinlichkeitsrechnung. Ann. Acad. Sci. Fennicae A **37**, 3–79 (1946)

Kerschen, G.: On the model validation in non–linear structural dynamics, Ph.D. thesis, Liège, Université, Vibrations et Identification des Structures, Département d'Aérospatiale, Mécanique et Matériaux (2002)

Kerschen, G., Golinval, J.C., Vakakis, A.F., Bergman, L.A.: The method of proper orthogonal Decomposition for dynamical Characterizsation and order Reduction of mechanical systems: An overview. Nonlinear Dyn. **41**, 147–169 (2005)

Kerschen, G., Worden, K., Vakakis, A., Golinval, J.-C.: Past, present and future of nonlinear system identification in structural dynamics. Mech. Syst. Signal Process. **20**(3), 505–592 (2006)

Kreuzer, E., Kust, O.: Analysis of long torsional strings by proper orthogonal decomposition. Arch. Appl. Mech. **67**(1), 68–80 (1996)

Kust, O.: Selbsterregte drehschwingungen in schlanken torsionssträngen, Ph.D. thesis, Hamburg–Harburg, Technische Universität (1998)

Loève, M.: Functions aléatoire de second ordre. Comptes Rendus Acad. Sci. **220** (1945)

Lumley, J.L.: Stochastic Tools in Turbulence. Applied Mathematics and Mechanics, vol. 12. Academic, New York/. . . (1970)

Struck, H.: Modellierung, simulation und aktive dämpfung selbst-erregter schwingungen eines gekrümmten torsionsstranges, Ph.D. thesis, Technische Universität Hamburg–Harburg (2004)

Tumer, I., Huff, E.: Analysis of triaxial vibration data for health monitoring of helicopter gearboxes. J. Vib. Acoust. **125**(1), 120–128 (2003)

Yan, A., Golinval, J.-C.: Null subspace-based damage detection of structures using vibration measurements. Mech. Syst. Signal Process. **20**(3), 611–626 (2006)

Stability of the Elliptically Excited Pendulum Using the Homoclinic Melnikov Function

Richard A. Morrison and Marian Wiercigroch

Abstract In this paper we investigate the dynamics of a pendulum subject to an elliptical pattern of excitation. The physical model is motivated by the development of sea wave energy extraction systems which exploit the rotating solutions of pendulum systems to drive generation. We formulate the homoclinic Melnikov function for the system and then demonstrate bounds on the set of parameters which can support homoclinic bifurcation. As the homoclinic bifurcation is a precursor to escape and the formation of rotating solutions in the evolution of the system under increasing forcing, these estimates provide bounds on the parameter space outwith which stable rotating solutions are not observed.

Keywords Elliptically excited pendulum • Homoclinic Melnikov function • Rotating solutions

1 Introduction

The mathematical pendulum is an archetypal model in nonlinear dynamical systems – sits investigations date at least as far back as Galileo and it has been revisited continually since his time. Stephenson, for example, demonstrated the stabilisation of the upright solution of the pendulum using high frequency excitation in 1908 (Stephenson 1908). This particular phenomena continued to generate interest nearly a century later in the work of Acheson (1993) and Clifford and Bishop (1998).

R.A. Morrison (✉) • M. Wiercigroch
Centre for Applied Dynamics Research, School of Engineering, Kings College, Aberdeen AB24 3UE, Scotland, UK
e-mail: r02ram8@abdn.ac.uk; m.wiercigroch@abdn.ac.uk

M. Wiercigroch and G. Rega (eds.), *IUTAM Symposium on Nonlinear Dynamics for Advanced Technologies and Engineering Design*, IUTAM Bookseries (closed) 32, DOI 10.1007/978-94-007-5742-4_7,

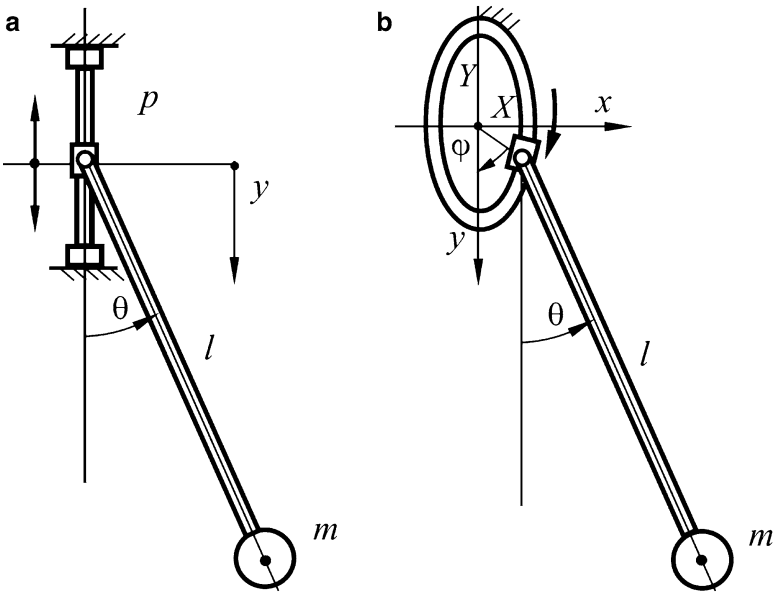

Fig. 1 Schematic for (**a**) parametrically excited pendulum system and (**b**) pendulum with mixed parametric (*vertical*) and *horizontal* excitation

The pendulum benefits from the ability to write down a relatively straightforward mathematical model which accurately describes the observed dynamics and is amenable to analysis and simulation, but which nevertheless captures the vast complexity of behavior that pendulums exhibit. It is possible to build experimental models which can be subjected to well controlled conditions and measured closely to verify and inform the theoretical investigations, see for example Xu et al. (2007).

The dynamically stable rotating solutions exhibited by pendulums under certain forcing conditions represent a mechanism that allows the generation of rotational motions from bounded excitation. Utilising these solutions to generate systems for energy extraction, for example from sea wave excitation, is an active area of research in the Centre for Applied Dynamics Research, at the University of Aberdeen, which has been ongoing for several years (M. Wiercigroch, 2003, Energy extraction from sea waves via a parametric pendulum, Private Communication; Xu 2005; Horton 2009). Specifically, we have focussed on harvesting the rotational motion as it is much more efficient in terms of the energy being captured.

The structure and stability of the rotational solutions and the bifurcation structure in the parameter space are of obvious importance when considering this application.

The transition from oscillating solutions to rotation in the pendulum can be characterized in terms of escape (Clifford and Bishop 1994). Such escape is often preceded by the emergence of chaotic behaviour (Thompson 1989) and in the parametrically excited pendulum, where the pivot is vertically excited, see Fig. 1a, the structure of the homoclinic bifurcation is important in understanding the transition to the escape region (Bishop and Clifford 1996). The Melnikov function provides an

analytical tool which can be used to develop bounds on the parameter space where these bifurcations can take place, see Guckenheimer and Holmes (1983). Koch and Leven (1985) use Melnikov analysis to study the parametric pendulum and provide expressions for both the subharmonic and homoclinic Melnikov functions.

In Xu et al. (2005) the authors explore the parameter space of the parametrically excited pendulum and illustrate the organising effect the structure of the resonances in the linearised equation have on the dynamics in the parameter space. The further development of this line of investigation is reported in Xu and Wiercigroch (2007), where perturbation arguments are used to provide analytical bounds in the parameter space delineating the different possible motion and approximate analytical solutions for the period one rotational orbits are computed. Most recently Lenci et al. (2008) reported an extensive analytical study of the rotating solutions of the pendulum. As well as developing the approach to provide approximate analytical solutions via perturbation arguments, their methods allow computation of stability of the rotating solutions.

2 System Specification

When analysing the potential of sea wave energy extraction, it is useful to consider a model with both horizontal and vertical components of forcing. A schematic of this mode of excitation, where planar excitation takes place on an ellipse, is in Fig. 1b. Assuming that the horizontal component of excitation x and the vertical (parametric) component y are both functions of time, the non-dimensional equation of motion for this pendulum system can be cast in the form

$$\ddot{\theta} + \gamma\dot{\theta} + (1 + y(t))\sin\theta + x(t)\cos\theta = 0. \tag{1}$$

If we further assume that both components of excitation are described by Fourier series, which we truncate to first order for initial analysis, i.e.

$$x(t) = ep\cos(\omega t - \alpha) \text{ and } y(t) = p\cos(\omega t), \tag{2}$$

we have a pendulum system with a parameter e which controls the extent to which excitation is elliptical. The effect of adding an element of ellipticity to the excitation of the parametrically excited pendulum is studied in some detail numerically in Horton et al. (2011). The two main effects discussed are the merging of the two 1:2 and 1:1 resonance tongues into a single region of instability of the oscillating solution and tendency of solutions of the system to prefer rotations with the same direction as the pivot excitation. In effect the parameter regime supporting rotating solutions is increased.

In this paper, we extend the analysis of Koch and Leven (1985) to calculate the homoclinic Melnikov function for the elliptically excited pendulum. This provides a straightforward proof that the system exhibits chaos and practical analytical bounds

on the parameter space where escape can occur and therefor in which rotating solutions can be stable. Analysis of this bound can then inform design of pendulum systems where escape is desirable in order to attain such solutions for energy harvest.

3 Calculation of Melnikov Function

A pendulum without forcing or damping such as (1) with $\gamma = x = y = 0$ has one stable fixed point corresponding to the hanging solution and a saddle point at the inverted position; $p = (0, \pi)$ in the $(\theta, \dot{\theta})$ phase plane. There are two orbits (one clock wise and one counterclockwise) which are homoclinic to the inverted rest point. These orbits represent the coincidence of the stable and unstable manifolds of the point. When ε small damping and forcing are applied the point p becomes a small periodic oscillation $p_0 + O(\varepsilon)$. The perturbation leads to a splitting of the stable and unstable manifolds, see Fig. 2. Developing a measure of their separation becomes important because, if they do intersect transversally, a homoclinic tangle will occur. The distance d between the two manifolds can be shown to take the form $d = \varepsilon M(t_0) + O(\varepsilon^2)$ where $M(t_0)$ is the Melnikov function and t_0 can be interpreted as a phase variable in the parameterisation of the unperturbed homoclinic orbit. The zeros of the Melnikov function under appropriate assumptions can therefor be taken as indicative of homoclinic tangling. A comprehensive development of the Melnikov function and its analysis is found in Guckenheimer and Holmes (1983).

To exploit Melnikov theory in this formulation we cast the system (1) in the form of a first order perturbation problem

$$\dot{x} = f(x) + \varepsilon g(x, t) \tag{3}$$

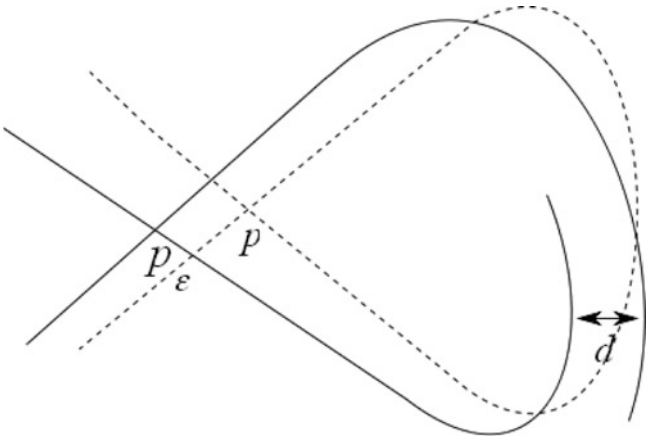

Fig. 2 Illustration of the splitting of the manifolds as ε small perturbation acts

by writing

$$\dot{x} = y,$$
$$\dot{y} = -\sin x - \gamma y - p\cos(\omega t)\sin x - ep\cos(\omega t - \alpha)\cos x.$$

This is (3) with

$$f(x) = \begin{pmatrix} y \\ -\sin x \end{pmatrix} \text{ and } g(x,t) = \begin{pmatrix} 0 \\ -\gamma y - p\cos(\omega t)\sin x - ep\cos(\omega t - \alpha)\cos x \end{pmatrix}. \tag{4}$$

The Melnikov function takes the form:

$$\begin{aligned} M(t_0) &= \int_{-\infty}^{\infty} f(x_h(t)) \wedge g(x_h(t), t_0)dt \\ &= \int_{-\infty}^{\infty} -\gamma y_h^2(t) - p\cos(\omega(t + t_0))\sin(x_h(t))y_h(t) + \\ &\quad -ep\cos(\omega(t + t_0) - \alpha)\cos(x_h(t))y_h(t)\,dt \end{aligned} \tag{5}$$

Here $x_h(t) = 2\arcsin(\tanh(t)) = 2\arctan(\sinh(t))$ and $y_h(t) = \pm\text{sech}(t)$ is a parameterisation of the orbit homoclinic to the saddle point which represents the pendulum balanced on the vertical. If we write the Eq. (5) as

$$M(t_0) = I_1 + I_2 + I_3, \tag{6}$$

the evaluation of three integrals provides us with an expression for the Melnikov function. We have

$$I_1 = -4\gamma \int_{-\infty}^{\infty} \text{sech}^2 t\,dt = -8\gamma, \tag{7}$$

$$\begin{aligned} I_2 &= -2p \int_{-\infty}^{\infty} \cos(\omega(t + t_0))\sin(2\arctan(\sinh(t)))\text{sech}(t)dt \\ &= -4p\sin\omega t_0 \frac{\pi\omega^2 \sinh\frac{\omega\pi}{2}}{1 - \cosh\pi\omega} \text{ and} \end{aligned} \tag{8}$$

$$\begin{aligned} I_3 &= -2ep \int_{-\infty}^{\infty} \cos(\omega(t + t_0) - \alpha)\cos(2\arcsin(\tanh t))\text{sech}(t)dt \\ &= -4ep\cos(\omega t_0 - \alpha)\frac{\pi\omega^2 \cosh\frac{\omega\pi}{2}}{1 + \cosh\pi\omega}. \end{aligned} \tag{9}$$

The integral (7) is standard and residue calculus provides the closed forms for (8) and (9). Substituting these expressions into (6) provides us with

$$M(t_0) = -2\gamma - p\pi\omega^2 \frac{\sin \omega t_0 \sinh \frac{\omega\pi}{2}}{1 - \cosh \pi\omega} - ep\pi\omega^2 \frac{\cos(\omega t_0 - \alpha) \cosh \frac{\omega\pi}{2}}{1 + \cosh \pi\omega} \tag{10}$$

This calculation adapts the Melnikov function for the parametrically excited pendulum found in Koch and Leven (1985) with an additional term which accounts for the addition of the extra excitation term.

4 Analysis

The system will exhibit homoclinic tangling when the Melnikov function (10) vanishes. It is common in the literature, see for example Szemplińska-Stupnicka (1995), to exploit this fact to find expressions for the minimal value of forcing which will provide a zero and therefor a homoclinic event in terms of the other parameters. In Koch and Leven (1985) the criteria for the parametrically excited pendulum is found as

$$p_M = \frac{4\gamma}{\pi\omega^2} \sinh \frac{\pi\omega}{2}, \tag{11}$$

in other words for $p > p_M$ one can expect homoclinic behavior.

To find the equivalent criteria for the elliptically excited pendulum we start by setting $M(t_0) = 0$ and solving for the forcing amplitude p, which gives

$$p = \frac{2\gamma}{\pi\omega^2} \frac{\cosh^2 \pi\omega - 1}{(\sin \omega t_0 \sinh \frac{\pi\omega}{2})(1 + \cosh \pi\omega) + e(\cos \omega t_0 \cosh \frac{\pi\omega}{2})(1 - \cosh \frac{\pi\omega}{2})}. \tag{12}$$

In this case the estimate is minimised by selecting a value of

$$t_0 = \frac{\pi}{\omega} - \frac{1}{\omega} \arctan\left(\frac{\sinh \frac{\pi\omega}{2}(\cosh \pi\omega + 1)}{\cosh \frac{\pi\omega}{2}(e \cosh \pi\omega - 1)} \right) \tag{13}$$

which reduces to $t_0 = \frac{\pi}{2\omega}$ when $e = 0$.

Evaluating (12) at the minimising value of t_0 specified in (13) provides the expression used in Fig. 3 to illustrate the boundaries in the p, ω parameter space. The area above each curve contains parameters for which homoclinic tangles are possible. The plots are show for $\gamma = 0.1$ and illustrate that increasing e from 0 tends to decrease the estimate of the amplitude parameter p. This finding is consistent with the numerical picture of the bifurcation structure of the system presented in Horton et al. (2011).

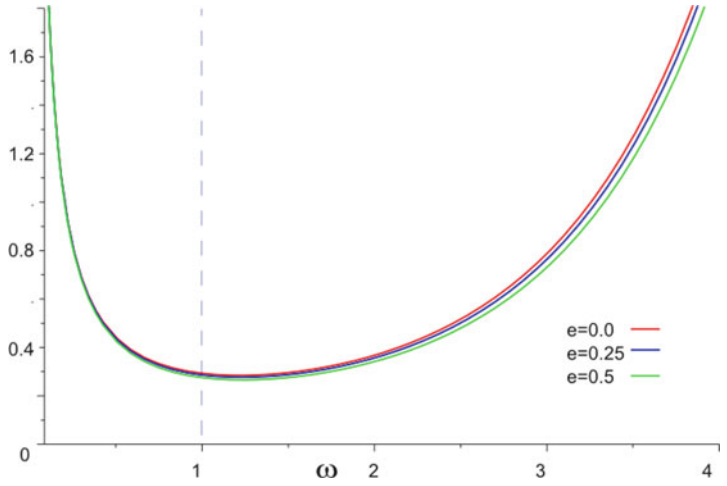

Fig. 3 Plot of minimal forcing amplitude for a given frequency and increasing values of the ellipticity parameter e. The *dashed line* indicates the position of the primary 1:1 resonance at $\omega = 1.0$ which occurs for the system with $e = 0.0$

In the general bifurcation sequence for the system the homoclinic event occurs before (with respect to increasing excitation amplitude) the regime under which rotational solutions become stable. In other words the Melnikov function not only provides the criteria for detecting the homoclinic tangle and the associated chaotic phenomena, it also provides a lower bound on the forcing amplitude required for stable rotation motions to take place.

5 Conclusion

In this paper we have studied stability of an elliptically excited pendulum analytically, which can be used for energy extraction. The elliptically excited pendulum can be considered a parametrically excited pendulum with an additional (horizontal) forcing term. We have formulated the homoclinic Melnikov function for a such pendulum and this approach is used to provide analytical conditions on the system parameters to determine a homoclinic bifurcation.

As can be seen from Fig. 3 the Melnikov conditions for the elliptically excited pendulum have the same character to those found with only parametric excitation. The increasing ellipticity has a small quantifiable effect in moving the Melnikov curves downwards, implying that for given excitation frequency a smaller amplitude parameter p is required for a homoclinic bifurcation to occur. It is clear however that the effect is not large. We can therefore add the elliptically excited pendulum to the catalogue of Melnikov criteria detailed in Szemplińska-Stupnicka (1995).

Acknowledgements The authors are grateful to acknowledge comments from the reviewer and for correspondence with David Pritchard at the University of Strathclyde for input received in finalising the results reported herein.

References

Acheson, D.: A pendulum theorem. Proc. R. Soc. Lond. A **443**(1917), 239–245 (1993)

Bishop, S., Clifford, M.: The use of manifold tangencies to predict orbits, bifurcations and estimate escape in driven systems. Chaos Solitons Fract. **7**(10), 1537–1553 (1996)

Clifford, M., Bishop, S.: Approximating the escape zone for the parametrically excited pendulum. J. Sound Vib. **172**(4), 572–576 (1994)

Clifford, M., Bishop, S.: Inverted oscillations of a driven pendulum. Proc. R. Soc. Lond. A **454**(1979), 2811 (1998)

Guckenheimer, J., Holmes, P.: Nonlinear Oscillations, Dynamical Systems, and Bifurcations of Vector Fields. Applied Mathematical Sciences, vol. 42. Springer, New York (1983)

Horton, B.: Rotational motion of pendula systems for wave energy extraction, Ph.D. thesis, University of Aberdeen (2009)

Horton, B., Sieber, J., Thompson, J., Wiercigroch, M.: Dynamics of the nearly parametric pendulum. Int. J. Nonlinear Mech. **46**, 436–442 (2011)

Koch, B., Leven, R.: Subharmonic and homoclinic bifurcations in a parametrically forced pendulum. Phys. D **16**(1), 1–13 (1985)

Lenci, S., Pavlovskaia, E., Rega, G., Wiercigroch, M.: Rotating solutions and stability of parametric pendulum by perturbation method. J. Sound Vib. **310**(1–2), 243–259 (2008)

Stephenson, A.: On a new type of dynamic stability. Mem. Lit. Philos. Soc. Manch. **52**(8), 1–10 (1908)

Szemplińska-Stupnicka, W.: The analytical predictive criteria for chaos and escape in nonlinear oscillators: a survey. Nonlinear Dyn. **7**(2), 129–147 (1995)

Thompson, J.: Chaotic phenomena triggering the escape from a potential well. Proc. R. Soc. Lond. A **421**(1861), 195–225 (1989)

Xu, X.: Nonlinear dynamics of parametric pendulum for wave energy extraction, Ph.D. thesis, University of Aberdeen (2005)

Xu, X., Wiercigroch, M.: Approximate analytical solutions for oscillatory and rotational motion of a parametric pendulum. Nonlinear Dyn. **47**(1), 311–320 (2007)

Xu, X., Pavlovskaia, E., Wiercigroch, M., Romeo, F., Lenci, S.: Dynamic interactions between parametric pendulum and electro-dynamical shaker. Z Angew. Math. Mech. **87**(2), 172–186 (2007)

Xu, X., Wiercigroch, M., Cartmell, M.: Rotating orbits of a parametrically-excited pendulum. Chaos Solitons Fract. **23**(5), 1537–1548 (2005)

Viscous Damping, Plasticity and Buckling on Large Amplitude Vibrations of Beams

Pedro Ribeiro

Abstract Curious dynamic behaviour that beams may experience is discussed in this article. In the model of the beams a simple type of viscous damping, an elasto-plastic stress–strain relation and Von Kármán type of non-linearity are assumed. The continuum system is discretized following a finite element, *p*-version approach, and the equations of motion are numerically solved in the time domain. The analyses focuses on the qualitative differences that appear in the oscillations of damped beams when plasticity is present and on a buckling like phenomenon that plasticity may induce, leading to a dynamic behaviour difficult to anticipate.

Keywords Large amplitude oscillations • Plasticity and damping • *p*-version FEM model

1 Introduction

Much effort has been put – since, at least, 1950 (Woinowski-Krieger 1950) – in the analysis of oscillations in one plane of straight beams with large displacements, but in the elastic regime. This geometrically non-linear problem is rather well understood, with many approximation methods proposed to derive more or less detailed models, a few studies on the evolution of the vibration modes with the vibration amplitude, investigations on forced oscillations under different forces and with diverse boundary conditions.

P. Ribeiro (✉)
DEMec/IDMEC, Faculdade de Engenharia, Universidade do Porto, rua Dr. Roberto Frias, s/n, 4200-465 Porto, Portugal
e-mail: pmleal@fe.up.pt

M. Wiercigroch and G. Rega (eds.), *IUTAM Symposium on Nonlinear Dynamics for Advanced Technologies and Engineering Design*, IUTAM Bookseries (closed) 32, DOI 10.1007/978-94-007-5742-4_8,

The analysis of oscillations with plasticity becomes necessary when the yield stress is passed in part of the beam. Whilst geometrically non-linearity is "smooth", expressed by polynomials in the equations of motion, plasticity depends on history, is non-reversible in the sense that it does not disappear with unloading, and may affect only parts of the beams, parts which eventually change with the evolving stresses. Hence, the analysis of geometrically non-linear and elasto-plastic oscillations is more complex than linear elastic analysis.

This work explores curious behaviour – markedly different from the one experienced by geometrically non-linear but elastic beams – that elasto-plastic and geometrically non-linear beams can experience. Two issues are addressed. First we focus on viscous damping and on the way it affects oscillations when concomitant with plasticity; after we examine the appearance of a buckling type phenomenon, which is induced by plasticity and can be avoided by increasing damping. The *p*-version FEM model of Ribeiro and van der Heijden (2009) is employed to achieve a detailed model of the beam. Pulse and harmonic loadings are considered.

2 Main Assumptions and Model

The next two sections describe the main points of the formulation and the method to solve the equations derived. These equations and the stress computation procedure were presented in Ribeiro and van der Heijden (2009).

2.1 Displacements Field and Stress-Strains Relations

Displacements are defined with respect to three fixed reference axes, labeled as x_1, x_2 and x_3. x_1 is the longitudinal axis that crosses the centroids of the cross sections of the undeformed beam; the other two are transverse axis. Subscripts 1, 2 and 3 in any variable indicate directions x_1, x_2 and x_3.

A first order shear deformation approach is adopted, being the displacement field written as

$$u_1(x_1, x_3, t) = u_1^0(x_1, t) + x_3\theta^0(x_1, t) \tag{1}$$

$$u_3(x_1, x_3, t) = u_3^0(x_1, t) \tag{2}$$

where $u_i(x_1, x_3, t)$ represents the displacement component along axis x_i and $\theta^0(x_1, t)$ is the rotation of the cross section about axis x_2. The superscript ^{0} indicates that the point is on axis x_1.

Keeping only the more important non-linear term $(\partial u_3/\partial x_1)^2$ in the longitudinal Green strain $\varepsilon_{11}(x_1, x_3, t)$ (a Von Kármán type of model; the definition of Green

strain can be found, for example, in Kojić and Bathe 2005), the longitudinal strain and the transverse shear engineering strain, $\gamma_{13}(x_1, t)$, are

$$\varepsilon_{11}(x_1, x_3, t) = \frac{\partial {u_1}^0(x_1, t)}{\partial x_1} + \frac{1}{2}\left(\frac{\partial {u_3}^0(x_1, t)}{\partial x_1}\right)^2 + x_3 \frac{\partial \theta^0(x_1, t)}{\partial x_1} \tag{3}$$

$$\gamma_{13}(x_1, t) = 2\varepsilon_{13}(x_1, t) = \frac{\partial {u_3}^0(x_1, t)}{\partial x_1} + \theta^0(x_1, t) \tag{4}$$

The relation between stresses σ_{11} and σ_{13} – other stresses are neglected – and the strains involves the total and the plastic strain:

$$\begin{Bmatrix} \sigma_{11}(x_1, x_3, t) \\ \sigma_{13}(x_1, x_3, t) \end{Bmatrix} = \begin{bmatrix} E & 0 \\ 0 & G \end{bmatrix} \begin{Bmatrix} \varepsilon_{11}(x_1, x_3, t) - \varepsilon_{11}^p(x_1, x_3, t) \\ \kappa\gamma_{13}(x_1, t) - \gamma_{13}^p(x_1, x_3, t) \end{Bmatrix} \tag{5}$$

In the former, E represents Young's modulus and G the shear modulus of elasticity $G = E/(2(1+\nu))$. Poisson's ratio is represented by ν and κ is a shear correction factor. Expression $\kappa = (5+5\,\nu)/(6+5\,\nu)$ is chosen, because it appears to be a proper choice for beams with rectangular cross section (Kaneko 1975). The longitudinal and shear plastic strains are respectively represented by $\varepsilon_{11}^p(x_1, x_3, t)$ and $\gamma_{13}^p(x_1, x_3, t)$.

2.2 Equations of Motion

The reference displacements are written as

$$\begin{Bmatrix} u_1^0(\xi,\ t) \\ u_3^0(\xi,\ t) \\ \theta^{\mathbf{0}}(\xi,\ t) \end{Bmatrix} = \begin{bmatrix} \mathrm{N}^{u_1}(\xi)^{\mathrm{T}} & \mathbf{0} & \mathbf{0} \\ \mathbf{0} & \mathrm{N}^{u_3}(\xi)^{\mathrm{T}} & \mathbf{0} \\ \mathbf{0} & \mathbf{0} & \mathrm{N}^{\theta}(\xi)^{\mathrm{T}} \end{bmatrix} \begin{Bmatrix} \mathrm{q}_{u_1}(t) \\ \mathrm{q}_{u_3}(t) \\ \mathrm{q}_{\theta}(t) \end{Bmatrix} \tag{6}$$

where $\mathbf{q}$ represents time dependent generalised displacement vectors. The vectors of longitudinal, transverse and rotational shape functions are, respectively, $\mathrm{N}^{u_1}(\xi)$, $\mathrm{N}^{u_3}(\xi)$ and $\mathrm{N}^{\theta}(\xi)$; they are formed by the displacement shape functions $g_i(\xi)$, $f_j(\xi)$ and $\Theta_k(\xi)$, which belong to a set of polynomials of arbitrary high order (Ribeiro 2004) (in practice almost arbitrary high order, since extremely high order polynomials may lead to ill-conditioning), with i, j and k taking values from 1 to a positive integer; ξ represents a non-dimensional coordinate. If one wishes to increase the accuracy of the model, one should increase the number of shape functions and generalized coordinates, i.e., increase the value of i, j or k.

The equations of motion can be obtained by the principle of virtual work and have the following form

$$\begin{bmatrix} \mathrm{M}_{u_1} & \mathbf{0} & \mathbf{0} \\ \mathbf{0} & \mathrm{M}_{u_3} & \mathbf{0} \\ \mathbf{0} & \mathbf{0} & \mathrm{M}_{\theta} \end{bmatrix} \begin{Bmatrix} \ddot{\mathrm{q}}_{u_1}(t) \\ \ddot{\mathrm{q}}_{u_3}(t) \\ \ddot{\mathrm{q}}_{\theta}(t) \end{Bmatrix} + \boldsymbol{\beta} \begin{bmatrix} \mathrm{M}_{u_1} & \mathbf{0} & \mathbf{0} \\ \mathbf{0} & \mathrm{M}_{u_3} & \mathbf{0} \\ \mathbf{0} & \mathbf{0} & \mathrm{M}_{\theta} \end{bmatrix} \begin{Bmatrix} \dot{\mathrm{q}}_{u_1}(t) \\ \dot{\mathrm{q}}_{u_3}(t) \\ \dot{\mathrm{q}}_{\theta}(t) \end{Bmatrix} +$$
$$+ \begin{bmatrix} \mathrm{K}_{\ell_{11}}{}^{p} & \mathbf{0} & \mathbf{0} \\ \mathbf{0} & \mathrm{K}_{\ell_{22}}{}^{\gamma} & \mathrm{K}_{\ell_{23}}{}^{\gamma} \\ \mathbf{0} & \mathrm{K}_{\ell_{32}}{}^{\gamma} & \mathrm{K}_{\ell_{33}}{}^{\gamma} + \mathrm{K}_{\ell_{33}}{}^{b} \end{bmatrix} \begin{Bmatrix} \mathrm{q}_{u_1}(t) \\ \mathrm{q}_{u_3}(t) \\ \mathrm{q}_{\theta}(t) \end{Bmatrix} + \begin{bmatrix} \mathbf{0} & \mathrm{K}_{n\ell_{12}} & \mathbf{0} \\ \mathrm{K}_{n\ell_{21}} & \mathrm{K}_{n\ell_{22}} - \mathrm{K}_{plast} & \mathbf{0} \\ \mathbf{0} & \mathbf{0} & \mathbf{0} \end{bmatrix} \times$$
$$\times \begin{Bmatrix} \mathrm{q}_{u_1}(t) \\ \mathrm{q}_{u_3}(t) \\ \mathrm{q}_{\theta}(t) \end{Bmatrix} = \begin{Bmatrix} \mathrm{F}_{u_1}(t) \\ \mathrm{F}_{u_3}(t) \\ \mathrm{F}_{\theta}(t) \end{Bmatrix} + \begin{Bmatrix} \mathrm{F}_{u_1}^{plast}\left(\varepsilon_{11}^{p}\right) \\ \mathrm{F}_{\gamma u_3}^{plast}\left(\gamma_{13}^{p}\right) \\ \mathrm{F}_{\theta}^{plast}\left(\varepsilon_{11}^{p}\right) + \mathrm{F}_{\gamma\theta}^{plast}\left(\gamma_{13}^{p}\right) \end{Bmatrix} \tag{7}$$

The mass matrices $\mathbf{M}_{u_1}$, $\mathbf{M}_{u_3}$ and $\mathbf{M}_{\theta}$; the so-called linear stiffness matrices, which are written as $\mathbf{K}_{\ell_{ij}}^{k}$, where i, j range from 1 to 3, and k can be p, γ or b (letters that here indicate longitudinal, shear and bending, respectively); the geometrically non-linear stiffness matrices $\mathbf{K}_{n\ell_{ij}}$, $i, j = 1{,}2$; and the vectors of generalized external forces $\mathbf{F}_{u_1}(t)$, $\mathbf{F}_{u_3}(t)$ and $\mathbf{F}_{\theta}(t)$ are given in Ribeiro (2004). The former matrices and vectors are computed using analytical integration. β is a proportionality damping parameter.

The forces and matrix that depend upon plastic strains are computed employing numerical integration based on a grid of Gauss points. The forces that depend upon plastic strains are $\mathbf{F}_{u_1}^{plast}$, $\mathbf{F}_{\theta}^{plast}$, $\mathbf{F}_{\gamma u_3}^{plast}\left(\gamma_{13}^{p}\right)$ and $\mathbf{F}_{\gamma\theta}^{plast}\left(\gamma_{13}^{p}\right)$; the matrix is $\mathbf{K}_{plast}$. These plasticity dependent terms are defined in Ribeiro and van der Heijden (2009).

The method of solution of the equations of motion is based on the implicit Newmark scheme with Newmark's parameters (Petyt 1990), and, in the presence of plasticity, involves two main cycles. In the first cycle, the plastic strains from the previous time step are assumed to be invariant and the generalized displacements are computed by solving Eq. (7) iteratively. Convergence in this cycle is achieved when the variation of the generalized displacements is below an accepted tolerance. It is additionally verified that equation of motion (7) is approximately satisfied.

After convergence in the above cycle has been achieved, the stresses are computed at the Gauss points using Eq. (5) and a yield criterion is employed to verify if yielding took place. Here, Von Mises criterion is adopted and the yield function f_y is defined by

$$f_y = \frac{1}{2}{}^{t+\Delta t}S_{ij}\,{}^{t+\Delta t}S_{ij} - \frac{1}{3}{}^{t+\Delta t}\sigma_y^2 \quad i, j = 1, 2, 3 \tag{8}$$

where the summation convention applies. ${}^{t+\Delta t}\sigma_y$ is the yield stress, which changes under hardening. In this particular work, a bilinear stress–strain relation, with isotropic strain hardening, is assumed, but a similar model can be employed with mixed hardening. S_{ij} are deviatoric stress components given by

$$S_{11} = 2\sigma_{11}/3\,, \quad S_{22} = S_{33} = -\sigma_{11}/3\,, \quad S_{13} = S_{31} = \sigma_{13} \tag{9}$$

The remaining deviatoric stresses are null ($S_{12} = S_{21} = S_{23} = S_{32} = 0$).

In the presence of yielding, plastic strains and the variables that depend upon those should be updated, a task that is carried out in the second main cycle. The plastic strains are computed via the governing parameter method, and the governing parameter used in this work is the increment of effective plastic strain, represented by Δe^P (Ribeiro and van der Heijden 2009; Kojić and Bathe 2005). The generalized displacements are re-calculated after.

Once the plastic-dependent terms have been re-calculated, the generalized displacements are corrected so that equations of motion (7) are respected. When convergence is achieved in this inner iterative procedure, the new generalized displacements are used to compute the strains and stresses, and one verifies if convergence has been as well achieved in the computation of the plastic strains and back stresses. If all convergence checks are passed, one progresses to the next time step, otherwise one returns to the computation of the plastic strains and repeats the steps above.

3 Numerical Tests

In this section numerical tests are presented and peculiarities of the dynamic behaviour of elasto-plastic beams are discussed. The first sub-section addresses an aspect related with damping that may become obvious when one considers it, but is nonetheless curious. The second sub-section presents examples of a phenomenon analogous to buckling and that is due to plastic strains under harmonic transverse forces. The two ends of the beams are clamped in all examples.

3.1 Damping and Plasticity

Consider a step force with amplitude F_0, as represented in Fig. 1, applied to a linear single degree of freedom system with stiffness k, natural frequency ω_n, so called damped natural frequency ω_d and non-dimensional damping ratio ξ.

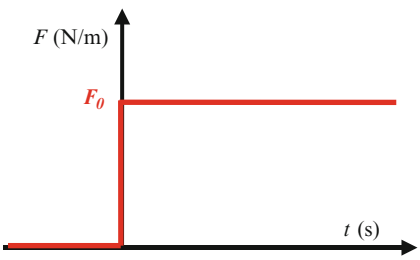

Fig. 1 Step excitation

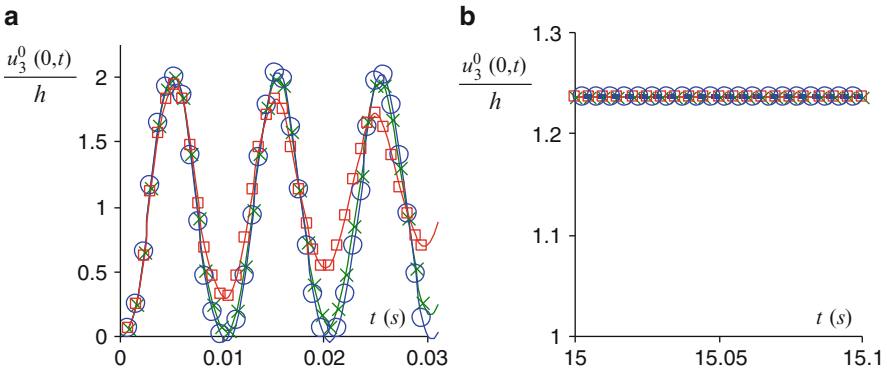

Fig. 2 Response of geometrically non-linear beam to step excitation (**a**) First cycles; (**b**) later cycles. The damping parameters are: β=1, β=10, β=50.

Using the established convolution or Duhamel integral (Meirovitch 1986) one obtains the following expression for the displacement $u(t)$:

$$u(t) = \frac{F_0}{k}\left[1 - e^{-\xi\omega_n t}\left(\cos(\omega_d t) + \frac{\xi}{\sqrt{1-\xi^2}}\sin(\omega_d t)\right)\right] \tag{10}$$

It results that the displacement tends to a value (the static solution) that solely depends upon the stiffness and the amplitude of the applied force:

$$\lim_{t\to\infty} u(t) = \frac{F_0}{k} \tag{11}$$

By modal analysis, one achieves the conclusion that also a multi-degree-of-freedom proportionally damped system will tend to a configuration (i.e., a set of displacements) that does not depend upon damping.

An analytical solution is not at hand for a geometrically non-linear multi-degree-of-freedom version of the former problem. Nevertheless, numerical tests indicate that also in the geometrically non-linear beam the steady state solution does not depend on damping. In the case study of Fig. 2, an elastic beam with width $b = 0.03$ m, thickness $h = 0.01$ m and length $L = 1.0$ m is analysed. Its Young modulus is $E = 2.00\ 10^{11}$ N m^{-2}, the ratio of Poisson is $\nu = 0.3$ and the density is $\rho = 7.8 \times 10^3$ kg m^{-3}. Damping differs as indicated in the figure caption. The variation in the damping coefficient is academic, and implemented to show how damping may affect the dynamic response. In practice, damping may be changed, for example, by adding a viscoelastic layer to part of the beam.

Now let us look at the same example, but in a beam with yield stress $\sigma_y = 3.50\ 10^8$ N m^{-2} and obeying a bilinear elasto-plastic law, with a tangent modulus $E_T = 10^9$ N m^{-2}, which is a value that may occur in steels (Kojić and Bathe 2005).

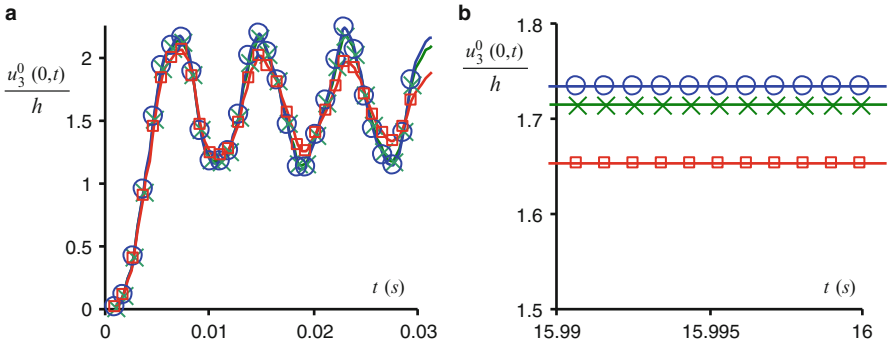

Fig. 3 Response of geometrically non-linear and elasto-plastic beam to step excitation: (**a**) first cycles; (**b**) later cycles. The damping parameters are: β=1, β=10, β=50.

Figure 3 shows that plasticity introduces important changes in the response. To start with, the peak displacement amplitude, which is attained in the beginning, is larger than without plasticity, due to the softening that the latter induces. Still regarding the initial cycles of the response, it is obvious that the difference between the amplitudes of successive peaks of oscillation decreases faster due to plasticity, a behaviour we can attribute to the plastic work. The vibration displacement amplitudes with respect to the undeformed configuration attained in the later cycles are larger than without plasticity. But possibly the more distinctive feature is that the final, steady-state, amplitude achieved under a step force now depends upon viscous damping.

The dependence of the final equilibrium position on viscous damping results from plasticity and is explained by the initial cycles. In fact, the diverse amounts of viscous damping lead to different oscillations in the first oscillation cycles. These different oscillations result in different plastic strain fields (see Figs. 4 and 5). Since plastic strains do not disappear, they lead to different "rest" configurations of the beam, unlike what occurred in the linear elastic structure with and without geometrical non-linearity.

Figures 4 and 5 provide an example of the different magnitude attained by longitudinal and shear strains with two damping factors. The shear plastic strains are rather small in this beam, where the length is 100 times the thickness.

3.2 Buckling Type Phenomenon

Another noticeable difference between the dynamic behaviour of elasto-plastic and elastic beams, geometrically non-linear in both cases, results from a buckling type phenomenon. This is shortly illustrated in this section, for a deeper study the reader is referred to Ribeiro (2011).

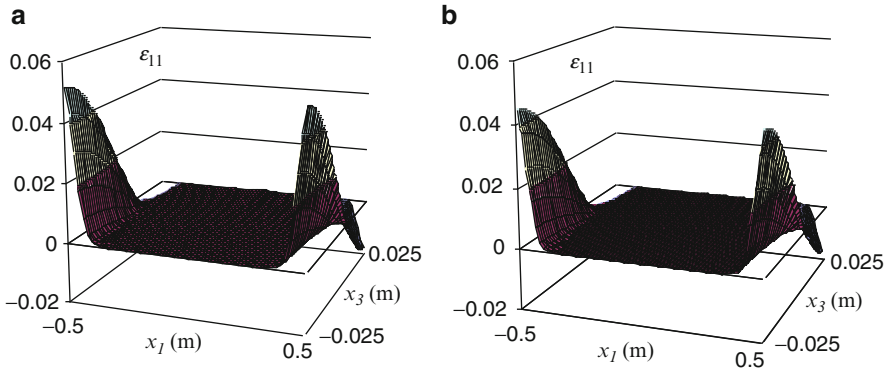

Fig. 4 Longitudinal plastic strains at later cycles when: (**a**) $\beta = 1$; (**b**) $\beta = 50$

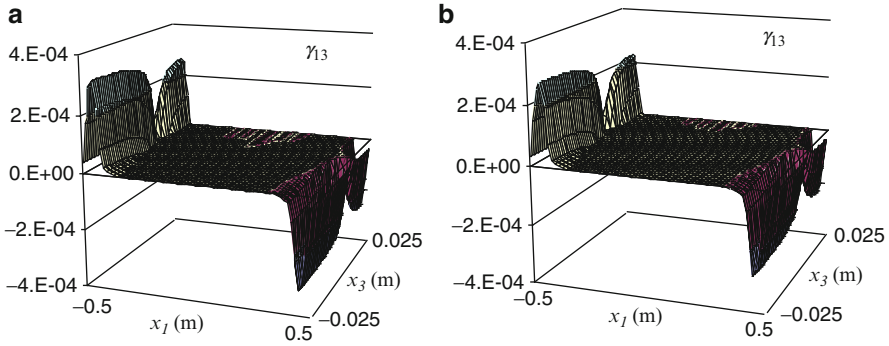

Fig. 5 Shear plastic strains at later cycles when: (**a**) $\beta = 1$; (**b**) $\beta = 50$

The beam now analysed has the width ($b = 0.03$ m), length ($L = 1.0$ m) and thickness ($h = 0.01\,L$) assumed in the previous section. Most material properties are also the same ($E = 2.00\ 10^{11}$ N m^{-2}, $\nu = 0.3$, $\rho = 7.8 \times 10^3$ kg m^{-3}) and so is the shear correction factor. The tangent modulus $E_T = 10^9$ N m^{-2} and the initial yield stress $\sigma_{yv} = 2.0 \times 10^8$ N m^{-2}, are from an example of reference Kojić and Bathe (2005).

Figure 6 shows the displacement in direction x_3 when an equally distributed force, sinusoidal in time, is applied. The results are computed with very similar models, but with different integration time steps, which are all small. One verifies that in the initial cycles all time integration steps provide the same results. Nevertheless, after a while, and when steady state appears to have been achieved, each time step leads to its own result. Furthermore, depending on the time step, the beam oscillates either about a negative or a positive reference position. Similar variations in the results were attained when "perturbations" were introduced in the number of Gauss points, in the thresholds defined for the errors, or in the number of shape functions.

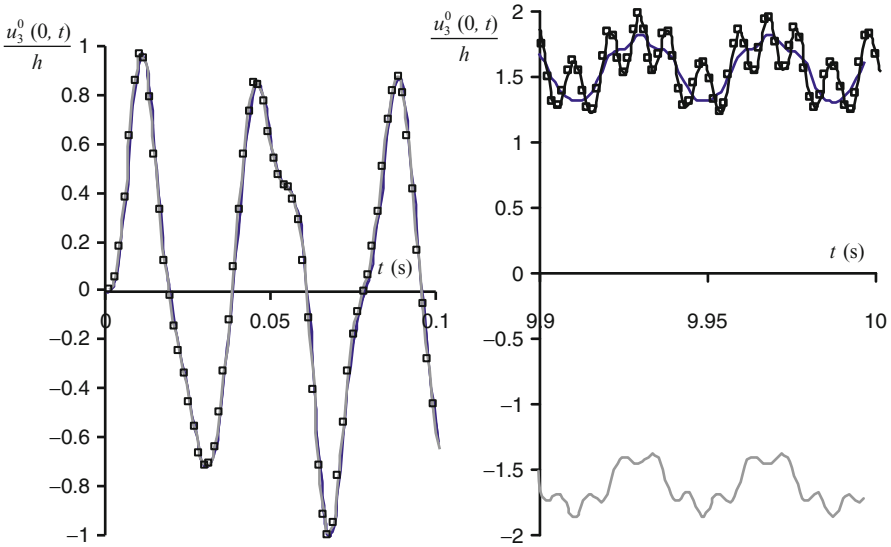

Fig. 6 Transverse displacement due to an equally distributed force, sinusoidal in time. Data was computed using a model with $p_o = 13$, $p_i = 15$, $p_\theta = 15$, and 64×64 Gauss points and the following time steps: — $\Delta t = 10^{-5}$ s, —⊟— $\Delta t = 5 \times 10^{-5}$ s, — $\Delta t = 7.5 \times 10^{-6}$ s

The variation in the predictions of the long term behaviour of this beam excited by a harmonic force is due to a buckling like phenomenon. The plastic strains accumulate under the excitation, imposing plastic forces and reducing the stiffness. As a result, at a certain stage "buckling" occurs – the word "buckling" is here used in the sense that the almost straight beam configuration suddenly is not the reference, stable equilibrium, configuration anymore, but two new equilibrium states appear. Curiously, although the oscillations found are – or in some cases approach – periodic oscillations the long term response to this harmonic excitation appears to be very difficult, or even impossible, to forecast.

Figures 7 and 8 show the plastic strains that are predicted after "buckling" using two time steps in the integration procedure. The strains are different and although not exactly symmetric, there is a certain inversion of the values. This inversion is to be related with the displacements with different signals that are computed employing the respective time steps.

Behaviour of a not very different nature from the one now discussed, has been – for example in Symonds and Yu (1985), Lee et al. (1992), Ma et al. (2005) – found to occur in vibrations of beams with fixed ends and with plasticity. The examples shown in these and other references differ from the ones shown in the present text not only in the models employed, but also in the fact that impulsive forces and/or external forces with a longitudinal component have been considered. Here we consider the case where the external applied force (apart from boundary forces) is harmonic and transverse.

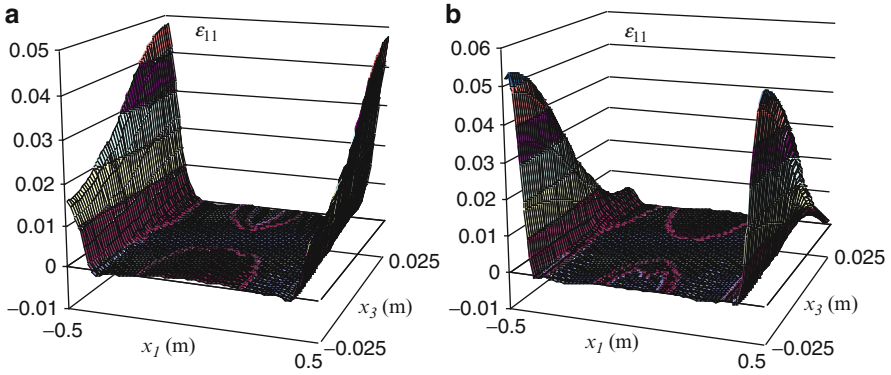

Fig. 7 Longitudinal plastic strains at $t = 1.5$ s computed using the following time steps: (**a**) $\Delta t = 10^{-5}$ s, (**b**) $\Delta t = 7.5 \times 10^{-6}$ s

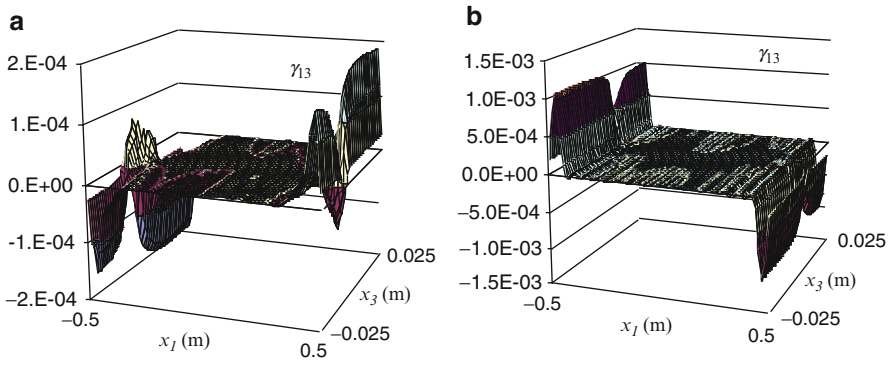

Fig. 8 Shear plastic strains at $t = 1.5$ s computed using the following time steps: (**a**) $\Delta t = 10^{-5}$ s, (**b**) $\Delta t = 7.5 \times 10^{-6}$ s

We must emphasize that diverse time steps were tried in the integration, and although rather small steps were experimented, convergence to a solution was not found. Recently, reference Ribeiro (2011), where this issue is discussed in detail, was accepted for publication.

Also, but not only, in order to connect with the previous section, a word on the effect of damping is now written. By increasing damping the displacement amplitude decreases; as a result, so do the stresses and eventually the plastic induced forces and the stiffness loss are not large enough to cause the buckling type of phenomenon just presented. The long term predictions are hence not so sensitive and do not qualitatively vary with small changes either in time or space discretizations, as occurs in the presence of buckling.

4 Conclusions

Oscillations of beams excited by transient and by harmonic forces were analysed taking into account two origins of non-linearity: (1) large displacements and (2) a non-linear constitutive relation, more specifically an elasto-plastic bilinear relation. It was verified that, although it is quite often neglected, plasticity can be important in the dynamic behaviour of beams. First, plasticity was found to be responsible for a variation of the rest configuration of damped beams excited by transient forces. This opposes to the fact that damping does not affect the asymptotic solution of linear elastic beams, even when the geometrical non-linearity is considered. In a second type of case studies, it was verified that the plastic strains that develop under harmonic transverse excitations can induce a buckling like phenomenon, and cause a rather unpredictable behaviour of the beam that suffers this buckling, because the plastic strains depend very significantly on the rapid buckling phase. Since plastic strains are history dependent, the characteristics predicted for the beam change with minor variations in the computational procedure, be it in the error thresholds, in the time step or in the model discretization.

References

Kaneko, T.: On Timoshenko's correction for shear in vibrating beams. J. Phys. D **8**, 1927–1936 (1975)

Kojić, M., Bathe, K.-J.: Inelastic Analysis of Solids and Structures. Springer, Berlin (2005)

Lee, J.-Y., Symonds, P.S., Borino, G.: Chaotic responses of a two-degree-of freedom elastic–plastic beam model to short pulse loading. Trans. ASME J. Appl. Mech. **59**, 711–721 (1992)

Ma, G.W., Liu, Y.M., Zhao, J., Li, Q.M.: Dynamic asymmetrical instability of elastic–plastic beams. Int. J. Mech. Sci. **47**, 43–62 (2005)

Meirovitch, L.: Elements of Vibration Analysis, 2nd edn. McGraw-Hill, New York (1986)

Petyt, M.: Introduction to Finite Element Vibration Analysis. Cambridge University Press, Cambridge (1990)

Ribeiro, P.: A *p*-version, first order shear deformation, finite element for geometrically non-linear vibration of curved beams. Int. J. Numer. Method. Eng. **61**, 2696–2715 (2004)

Ribeiro, P.: On the predictability of elasto-plastic and geometrically non-linear oscillations of beams under harmonic excitation. Nonlinear Dyn. (2011). doi:10.1007/s11071-011-0104-5

Ribeiro, P., van der Heijden, G.H.M.: Elasto-plastic and geometrically nonlinear vibrations of beams by the *p*-version finite element method. J. Sound Vib. **325**, 321–337 (2009)

Symonds, P.S., Yu, T.X.: Counter-intuitive behavior in a problem of elastic–plastic beam dynamics. Trans. ASME J. Appl. Mech. **52**, 517–522 (1985)

Woinowski-Krieger, S.: The effect of an axial force on the vibration of hinged bars. J. Appl. Mech. **17**, 35–36 (1950)

Part II
Smooth Engineering Systems

Motion of Oscillating Two-Link System in Fluid

Felix L. Chernousko

Abstract Locomotion of a mechanical system consisting of two rigid bodies, a main body and a tail, connected by a cylindrical joint, is considered. The system moves in a resistive fluid and is controlled by periodic angular oscillations of the tail relative to the main body. The resistance force acting upon each body is a quadratic function of its velocity. Under certain assumptions, a nonlinear equation of motion is derived and simplified. The average velocity of locomotion is estimated. This velocity is positive, if the deflection of the tail is performed slower that its retrieval. The optimal time history of oscillations is found that corresponds to the maximal locomotion velocity.

Keywords Oscillations • Quadratic resistance • Locomotion • Optimal control

1 Introduction

It is well–known that a multilink mechanical system, whose links perform specific oscillations relative to each other, can move progressively in a resistive medium. This locomotion principle is used by fish, snakes, insects, and some animals (Blake 1983; Gray 1968; Lighthill 1975). In robotics, the same principle is applied to locomotion of snake-like robots along a surface (Hirose 1993).

Dynamics and optimization of snake-like multilink mechanisms that move along a plane in the presence of Coulomb's dry friction forces acting between the mechanism and the plane, have been studied in Chernousko (2001, 2003, 2005).

F.L. Chernousko (✉)
Institute for Problems in Mechanics of Russian Academy of Sciences, pr. Vernadskogo 101-1, Moscow, 119526, Russia
e-mail: chern@ipmnet.ru

M. Wiercigroch and G. Rega (eds.), *IUTAM Symposium on Nonlinear Dynamics for Advanced Technologies and Engineering Design*, IUTAM Bookseries (closed) 32, DOI 10.1007/978-94-007-5742-4_9,

Various aspects of fish-like locomotion in a fluid have been studied in many papers, and a number of swimming robotic systems have been developed, see, e.g., Colgate and Lynch (2004), Mason and Burdick (2000), Terada and Yamamoto (1999), and http://en.wikipedia.org/wiki/RoboTuna # References.

In this paper, we consider a progressive motion of a two-link system in a fluid in the presence of resistance forces proportional to the squared velocity of the moving body. The mechanical model is described in Sect. 2. The equation of motion is analyzed in Sect. 2, where the asymptotic method of averaging is applied. The important case of a piecewise constant angular velocity of the tail is considered in Sect. 3. Certain generalizations are discussed in Sect. 4, where the case of two links attached to the main body is considered, and in Sect. 5, where, besides the drag force, the lift force acting upon the tail is also taken into account. The optimal control problem for the motion of the tail is formulated, and its exact solution is presented in Sect. 6, along with an example. It is shown that the optimal motion does not differ much from the case of the piecewise constant angular velocity of the tail. The conclusions are stated in Sect. 7.

2 Mechanical Model and Preliminary Analysis

Consider a mechanical system consisting of two rigid bodies, called the main body and the tail, connected by a cylindrical joint O, see Fig. 1. The length of the tail OA is denoted by a, and its mass is negligible compared to the mass m of the main body.

Let us introduce the Cartesian coordinate frame Cxy connected with the main body and denote by **i** and **j** the unit vectors directed along the axes Cx and Cy.

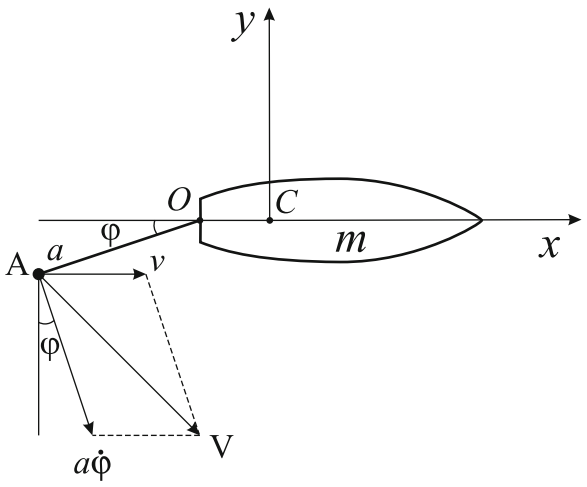

Fig. 1 Mechanical model: main body of mass m with a link OA attached to it

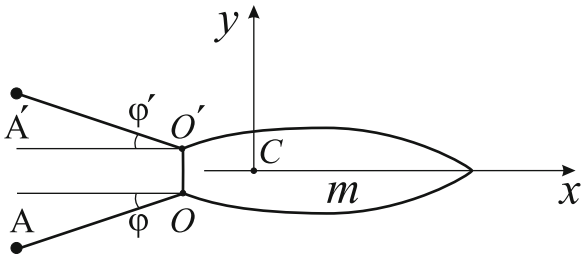

Fig. 2 Two symmetric links attached to the main body

The tail performs periodic oscillations of period T about the joint O that are symmetric relative to the axis Cx. Hence, the angle φ between the tail OA and the axis Cx satisfies the equations

$$\varphi(t+T) = \varphi(t), \quad \varphi(t+T/2) = -\varphi(t) \tag{1}$$

for each time instant t.

The two-body system moves in a resistive fluid that acts upon each moving element with a force directed against the velocity of the element and proportional to its squared velocity.

Under certain assumptions listed below, the motion of the main body can be regarded as a translational rectilinear motion, so that the axis Cx does not change its direction in the inertial space. These assumptions are:

1. The oscillations of the tail obey the periodicity and symmetry conditions (1).
2. The frequency of the oscillations is high enough.
3. The moment of inertia of the main body is large enough.
4. The main body is symmetric with respect to the axis Cx.
5. The resistance force of the main body in the lateral direction (along the axis Cy) is much higher than its resistance in the longitudinal direction (along the axis Cx).

Under the assumptions made, the change of the orientation of the main body, as well as its angular and lateral motions, can be neglected.

Note that the translational motion of the main body occurs also in the case of two equal and symmetric links OA and $O'A'$ attached to the main body by cylindrical joints O and O', see Fig. 2. Suppose that these two links perform synchronous and symmetric oscillations about the axes O and O', so that the link $O'A'$ is always symmetric to the link OA with respect to the axis Cx.

If the system of Fig. 1 can be considered as a model of a fish with a tail, the system of Fig. 2 models swimming of an animal with two legs (e.g. a frog) or flying of a bird. The case of two links attached to the main body is considered in Sect. 5.

Denote by v the velocity of the progressive motion of the main body along the axis Cx. We will consider only forward motions, so that $v \geq 0$. The value of the resistance force acting upon the body is denoted by $c_0 v^2$, where c_0 is a positive constant.

Suppose for simplicity that the resistance forces acting upon the tail OA can be reduced to a force applied at the point A. Denote by $\mathbf{V}$ the velocity of this point and by ω the angular velocity of the tail OA, We have (see Fig. 1):

$$\mathbf{V} = v\mathbf{i} + a\omega \sin\varphi \mathbf{i} - a\omega \cos\varphi \mathbf{j}, \quad \omega = \dot{\varphi}. \tag{2}$$

Here and below, dots denote derivatives with respect to time t.

The resistance force applied to the point A is given by

$$\mathbf{F} = -k_0 V \mathbf{V}, \tag{3}$$

where $k_0 > 0$ is a constant coefficient.

Under the assumptions made, the equation of the progressive motion of the main body can be written as follows:

$$m\dot{v} = -c_0 v^2 + F_x \ , \tag{4}$$

where F_x is the projection of the vector $\mathbf{F}$ from (3) onto the axis Cx. Note that the added mass of the main body can be included into m. Introducing the denotations

$$c_0/m = c, \qquad k_0/m = k$$

and using Eqs. (2) and (3) to determine F_x, we convert Eq. (4) to the form:

$$\dot{v} = -cv^2 - k(v + a\omega \sin\varphi)\sqrt{v^2 + a^2\omega^2 + 2va\omega \sin\varphi}. \tag{5}$$

Note that the coefficients c and k have the dimension inverse to length. To clarify their physical meaning, let us consider the linear motion of a unit mass in the presence of the quadratic resistance. The equations of motion of this system are

$$\dot{x} = v, \qquad \dot{v} = -cv^2,$$

where x is the coordinate of the mass and v is its velocity. Integrating these equations under the initial conditions $x(0) = 0$, $v(0) = v_0$, we obtain $v = v_0 \exp(-cx)$. Hence, the inverse c^{-1} of the coefficient c is the distance that the moving mass covers in the resistive fluid while its velocity decreases by factor $e = 2.718\ldots$.

We assume that the resistance of the point A is much less than the resistance of the main body: $k \ll c$. Let us introduce a small parameter

$$\mu = k/c \ll 1 \tag{6}$$

and suppose that the oscillations of the tail have a short period and small amplitude.

Let us introduce new variables:

$$\varphi = \mu\psi, \quad T = \mu T_0, \quad t = T\tau = \mu T_0 \tau, \quad v = \mu(a/T_0)u. \tag{7}$$

Here, the new variable ψ and constant T_0 are of order $O(1)$, τ is a new (fast) time, and u is the new non-dimensional velocity.

Let us transform the equation of motion (5) using the change of variables (7) and omitting terms of higher order of small parameter μ from (6). After simplifications, we obtain the equation

$$\frac{du}{d\tau} = -\varepsilon\left[u^2 + \left(u + \psi\frac{d\psi}{d\tau}\right)\left|\frac{d\psi}{d\tau}\right|\right], \quad \varepsilon = ca\mu^2. \tag{8}$$

Here, ε is a small parameter, and $\psi(\tau)$ is a periodic function of τ with a period equal to 1. By virtue of (1) and (7), we have

$$\psi(\tau + 1) = \psi(\tau), \quad \psi(\tau + 1/2) = -\psi(\tau). \tag{9}$$

Applying the asymptotic methods of averaging (Bogoliubov and Mitropolsky 1961) to Eq. (8), we obtain the equation of the first approximation as follows:

$$\frac{du}{d\tau} = -\varepsilon(u^2 + I_1 u + I_0)\ , \tag{10}$$

where the notation

$$I_1 = 2\int_0^{1/2}\left|\frac{d\psi}{d\tau}\right|d\tau, \quad I_0 = 2\int_0^{1/2}\psi\frac{d\psi}{d\tau}\left|\frac{d\psi}{d\tau}\right|d\tau \tag{11}$$

is used. Here, the properties (9) are taken into account. The solution $u(\tau)$ of the averaged Eq. (10) differs from the solution of Eq. (8), under the same initial conditions, by the terms of order ε for the large time interval of order ε^{-1}.

Note that, according to (11), $I_1 > 0$.

If $I_0 > 0$, then the right-hand side of Eq. (10) is positive for all $u > 0$. Hence, $du/d\tau < -\varepsilon I_0 < 0$, the velocity decreases and reaches zero in finite time. In this case, the forward motion of the system is impossible.

We will consider below a more interesting case, where $I_0 < 0$. Then Eq. (10) has a unique positive stationary solution

$$u^* = [-I_0 + (I_1^2/4)]^{1/2} - I_1/2 > 0 \tag{12}$$

which is globally asymptotically stable. Thus, for any initial condition $u(\tau_0) = -u_0 \geq 0$, we have $u(\tau) \to u^*$ as $\tau \to \infty$.

To check the inequality $I_0 < 0$ and evaluate the velocity u^*, we are to specify the periodic function $\psi(\tau)$ subject to conditions (9) and calculate the integrals I_1 and I_0 from (11).

3 Piecewise Constant Angular Velocity

Let us first consider a piecewise linear time history of the angle $\varphi(t)$. We assume that the normalized angle $\psi(\tau)$ from (7) is described by

$$\psi(\tau) = \begin{cases} b_1\tau, & \tau \in [0, \theta] \\ b_2(1/2 - \tau), & \tau \in [\theta, 1/2] \\ b_1(1/2 - \tau), & \tau \in [1/2, +\theta] \\ b_2(\tau - 1), & \tau \in [1/2 + \theta, 1]. \end{cases} \tag{13}$$

Here, b_1, b_2, and $\theta \in (0, 1/2)$ are positive constants. Since $\psi(\tau)$ should be a continuous function, its values for $\tau = \theta - 0$ and $\tau = \theta + 0$ must coincide.

Thus, we obtain the condition $b_1\theta = b_2(1/2 - \theta)$ imposed on parameters b_1, b_2, and θ. Hence, we can express θ through the dimensionless angular velocities of the deflection (b_1) and retrieval (b_2) as follows:

$$\theta = \frac{b_2}{2(b_1 + b_2)}. \tag{14}$$

The graph of function $\psi(\tau)$ is shown in Fig. 3.

Substituting (13) into integrals (11) and using also (14), we obtain

$$I_1 = \frac{2b_1b_2}{b_1 + b_2}, \quad I_0 = \frac{b_1^2b_2^2(b_1 - b_2)}{4(b_1 + b_2)^2}. \tag{15}$$

The condition $I_0 < 0$ is satisfied, if and only if $b_1 < b_2$. Inserting (15) into Eq. (12), we evaluate the stationary velocity:

$$u^* = \frac{b_1b_2}{b_1 + b_2}\left[\left(1 + \frac{b_2 - b_1}{4}\right)^{1/2} - 1\right] > 0, \quad b_2 > b_1. \tag{16}$$

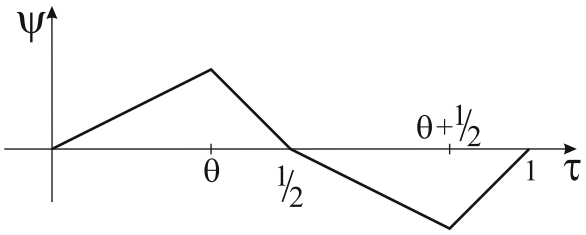

Fig. 3 Piecewise linear function $\psi(\tau)$

Denote by ω_1 and ω_2 constant dimensional angular velocities of the deflection and retrieval of the tail, respectively. By virtue of (7), they are expressed through b_1 and b_2 as follows:

$$\omega_i = \mu b_i / T = b_i / T_0, \quad i = 1, 2. \tag{17}$$

On the strength of Eqs. (7), (16), and (17), the dimensional stationary velocity v^* is given by

$$v^* = \frac{\mu a}{T_0} u^* = \frac{\mu a \omega_1 \omega_2}{\omega_1 + \omega_2} \left\{ \left[1 + \frac{(\omega_2 - \omega_1) T_0}{4} \right]^{1/2} - 1 \right\}, \quad T = \mu T_0, \quad \mu = \frac{k}{c}. \tag{18}$$

We see from Eq. (18) that our system will move forward ($v^* > 0$), if and only if the angular velocity of the retrieval of the tail is higher than the angular velocity of the deflection: $\omega_2 > \omega_1$.

4 Two Links Attached to a Body

Let us consider the case of the three-element system shown in Fig. 2. We assume that the symmetric links OA and $O'A'$ perform periodic oscillations about the respective joints O and O' so that the angles φ and φ' between these links and the axis Cx are always equal: $\varphi(t) = \varphi'(t)$.

The analysis of this case is quite similar to the case of one link attached to the main body. First, we should replace k in Eq. (5) by $2k$. By contrast to the case of one link, here the angle φ (and also φ') is always positive and changes within the interval $[0, \varphi_0]$, where $\varphi_0 > 0$. Introducing the dimensionless variables (7) with $\mu = 2k/c$, we again obtain Eq. (8) for $u(\tau)$ and the averaged Eq. (10), where, instead of (11), we have

$$I_1 = \int_0^1 \left| \frac{d\psi}{d\tau} \right| d\tau, \quad I_0 = \int_0^1 \psi \frac{d\psi}{d\tau} \left| \frac{d\psi}{d\tau} \right| d\tau. \tag{19}$$

For the average velocity u^*, we obtain Eq. (12) with I_1 and I_0 defined by (19).

Suppose that the normalized angle $\psi(\tau)$ is a piecewise linear function of time similar to (13):

$$\psi(\tau) = \begin{cases} b_1 \tau, & \tau \in [0, \theta_1], \\ b_2(1 - \tau), & \tau \in [\theta_1, 1], \end{cases} \tag{20}$$

where b_1, b_2, and θ_1 are positive constants. Since the function $\psi(\tau)$ is continuous at $\tau = \theta_1$, we have $b_1 \theta_1 = b_2(1 - \theta_1)$. This condition entails

$$\theta_1 = b_2/(b_1 + b_2). \tag{21}$$

Similarly to (15) and (16), we obtain from (19)–(21):

$$I_1 = \frac{4b_1b_2}{b_1+b_2}, \quad I_0 = \frac{b_1^2b_2^2(b_1-b_2)}{(b_1+b_2)^2},$$
$$u^* = \frac{2b_1b_2}{b_1+b_2}\left[\left(1+\frac{b_2-b_1}{4}\right)^{1/2}-1\right]. \tag{22}$$

To return to the dimensional variables in (22), we use Eqs. (7) and (17) to obtain:

$$v^* = \frac{2\mu a\omega_1\omega_2}{\omega_1+\omega_2}\left\{\left[1+\frac{(\omega_2-\omega_1)T_0}{4}\right]^{1/2}-1\right\},$$
$$T = \mu T_0, \quad \mu = 2k/c, \quad \omega_i = \mu b_i/T, \quad i = 1,2. \tag{23}$$

Thus, for the case of two links attached to the main body, we have obtained expression (23) for the average velocity similar to the respective expression (18) for the case of one link attached.

5 Lift Force

Let us return to the case of one link attached to the main body (Fig. 1). We assumed above that the fluid acts upon the tail OA with the resistance force called drag and applied at the endpoint A. Let us suppose now that the tail ends with a rectangular fin, its shorter side being oriented along OA whereas its longer side is perpendicular to the plane Cxy. In this case, besides the drag force applied to the tail, the lift should be also taken into account. It is shown that the lift force acting upon the tail always increases the average velocity of motion.

Certain results of computer simulation of the motion of our system in the presence of both drag and lift components of the hydrodynamical force are shown in Figs. 4 and 5. In these figures, the dependence of the average velocity v^* on the length of the tail a and angular velocity of deflection ω_1 is shown. The lower/upper curves in correspond to the absence/presence of the lift.

6 Optimal Control

Let us consider the optimal control problem for the angular motion of the tail. We will regard the dimensionless angular velocity Ω as the control subject to the constraints

$$-\Omega_- \le \Omega = d\psi/d\tau \le \Omega_+, \tag{24}$$

where Ω_- and Ω_+ are given positive constants.

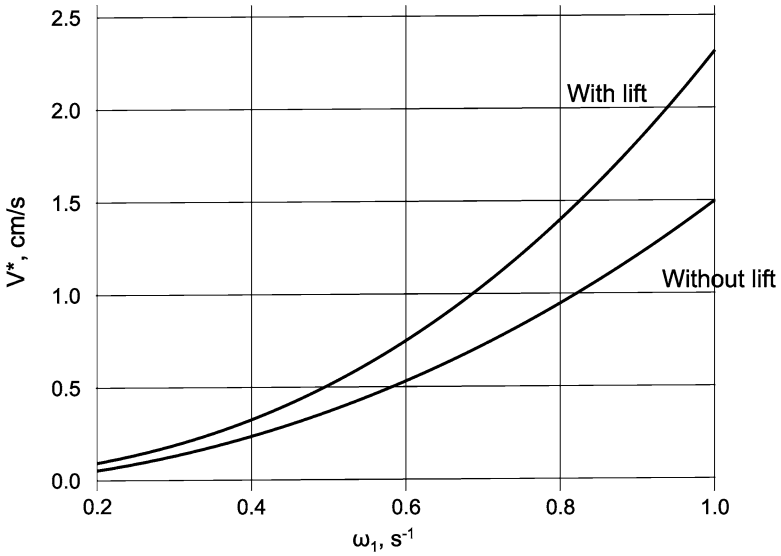

Fig. 4 Velocity vs. length of the tail for the cases with and without lift

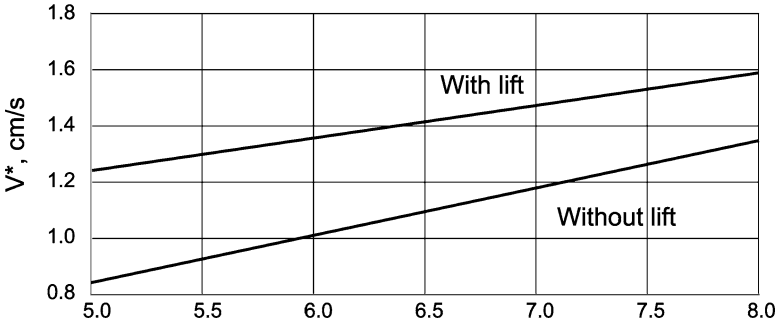

Fig. 5 Velocity vs. angular velocity of the tail for the cases with and without lift

Suppose that the normalized angle ψ changes over the interval $\tau \in (0, 1/2)$ as follows: it grows from $\psi(0) = 0$ to $\psi(\theta) = \psi_0 > 0$ and then decreases from ψ_0 do $\psi(1/2) = 0$. Here, $\theta \in (0, 1/2)$ and $\psi_0 > 0$ are constant parameters. The behavior of $\psi(\tau)$ for $\tau \in (1/2, 1)$ is defined by the second condition (9). The problem is to find functions $\Omega(\tau)$ and $\psi(\tau)$ that satisfy (24), the boundary conditions imposed above and maximize the average velocity u^* defined by (12).

The solution of this problem is obtained by means of Pontryagin's maximum principle (Pontryagin et al. 1986). After that, parameter $\theta \in (0, 1/2)$ is chosen in order to maximize u^*. Omitting this rather lengthy analysis, we present below the final results.

The optimal control $\Omega(\tau)$ and the corresponding optimal time history of the normalized angle $\psi(\tau)$ are given by equations

$$\Omega = \Omega_+, \quad \psi = \Omega_+ \tau \quad \text{for} \quad \tau \in (0, \tau_*),$$
$$\Omega = \Omega_+ \left[1 + \frac{3(\tau - \tau_*)}{2\tau_*}\right]^{-1/3},$$
$$\psi = \Omega_+ \tau_* \left[1 + \frac{3(\tau - \tau_*)}{2\tau_*}\right]^{2/3} \quad \text{for} \quad \tau \in (\tau_*, \theta),$$
$$\Omega = -\Omega_-, \quad \psi = \Omega_-(1/2 - \tau) \quad \text{for} \quad \tau \in (\theta, 1/2). \tag{25}$$

Here, parameters τ_* and θ are defined by equations

$$\tau_* = s\theta, \qquad \theta = 1/2 - \psi_0/\Omega_-, \tag{26}$$

where s is the only root of the cubic equation

$$s(3 - s)^2 = 4(\psi_0/\Omega_+)^3(1/2 - \psi_0/\Omega_-)^{-3} \tag{27}$$

lying in the interval $s \in (0, 1)$. Equations (25)–(27) define the functions $\Omega(\tau)$ and $\psi(\tau)$ for the interval $(0, 1/2)$; for the rest of the period $\tau \in (1/2, 1)$, these functions are defined according to Eq. (9).

The maximum value of the average stationary velocity u^* that corresponds to the solution presented above is given by

$$u^* = [\psi_0^2 \Omega_- - 4(\psi_0^3/\theta)(2 - s)(3 - s)^{-2} + 4\psi_0^2]^{1/2} - 2\psi_0, \tag{28}$$

where $s \in (0, 1)$ is the root of Eq. (27).

Thus, the optimal control is completely determined in terms of normalized variables. To return to the original dimensional ones, one is to use Eq. (7).

If the upper bound (24) on the angular velocity is absent ($\Omega_+ \to \infty$), we obtain from Eqs. (27) and (26): $s = 0, \tau_* = 0$. In this case, Eqs. (25), (26) and (28) are reduced to

$$\Omega = (2/3)\psi_0 \theta^{-2/3} \tau^{-1/3}, \quad \psi = \psi_0 (\tau/\theta)^{2/3} \quad \text{for} \quad \tau \in (0, \theta),$$

$$\Omega = -\Omega_-, \quad \psi = \Omega_-(1/2 - \tau) \quad \text{for} \quad \tau \in (\theta, 1/2), \quad \theta = 1/2 - \psi_0/\Omega_-,$$
$$u^* = [\psi_0^2 \Omega_- - (8/9)(\psi_0^3/\theta) + 4\psi_0^2]^{1/2} - 2\psi_0.$$

If the lower bound on Ω in (24) is absent ($\Omega_- \to \infty$), we have, by virtue of Eqs. (26) and (27), $\theta = 1/2, u^* \to \infty$. Here, the interval $(\theta, 1/2)$ in Eq. (25) vanishes, the retrieval becomes instantaneous, and the velocity u^* formally tends to infinity.

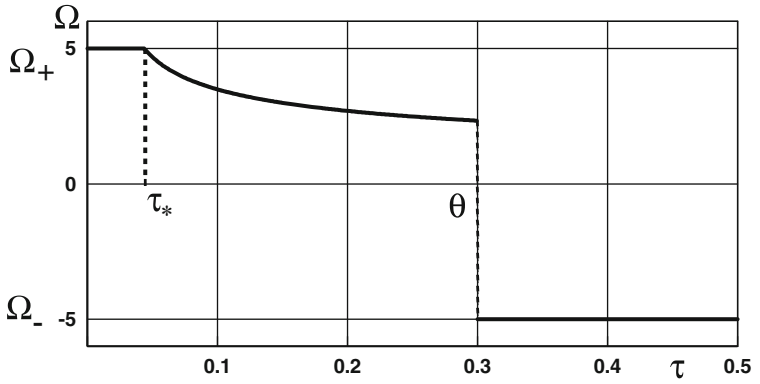

Fig. 6 Optimal control $\Omega(\tau)$

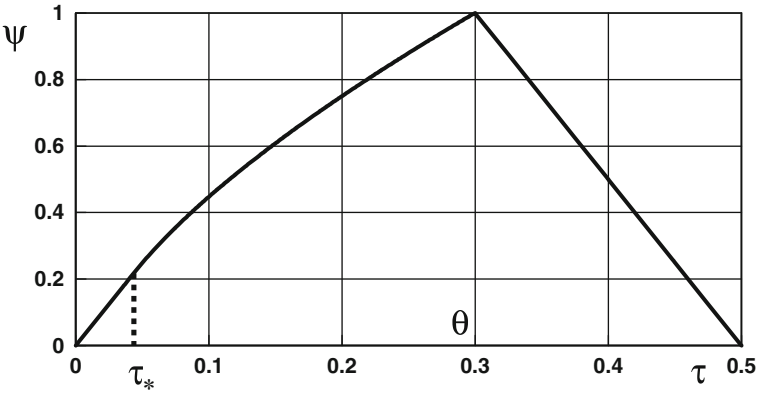

Fig. 7 Optimal trajectory $\psi(\tau)$

As an example, let us consider a numerical example. We assume that $\psi_0 = 1$, $\Omega_+ = \Omega_- = 5$ and obtain from the optimal solution (25)–(27):

$$\theta = 0.3, \quad s = 0.145, \quad \tau_* = 0.044, \quad u^* = 0.442. \tag{29}$$

The time histories of functions $\Omega(\tau)$ and $\psi(\tau)$ from Eq. (25) are shown in Figs. 6 and 7, respectively.

Let us compare this optimal solution with the case of a piecewise constant angular velocity from Sect. 4. We choose parameters b_1, b_2, and θ so that the piecewise linear function $\psi(\tau)$ from (13) coincides with the optimal one from (25) (see Fig. 7) at three time instants: $\tau = 0$, $\tau = \theta$, and $\tau = 1/2$. Thus we obtain $\theta = 0.3$, $b_1 = 10/3$, $b_2 = 5$.

The corresponding average velocity defined by (16) is $u^* = (17/3)^{1/2} - 2 = 0.380$. Comparing this result with the optimal value u^* from (29), we see that the difference is about 14%.

7 Conclusions

A mechanical system consisting of a main body and one or two links attached to it by cylindrical joints can move progressively in a medium that acts upon moving bodies with forces proportional to the squared velocities of the bodies. Under assumptions made, the equation of motion is simplified, and the average velocity of the progressive motion is evaluated.

The case of a piecewise constant angular velocity of the links is analyzed. It is shown that the progressive forward motion occurs, if the angular velocity of the deflection of the links attached is lower than the angular velocity of their retrieval.

The optimal time history of the angular oscillations of the links is obtained that corresponds to the maximal, under the conditions imposed, average speed of the progressive motion.

The obtained results correlate well with observations of the process of swimming.

Acknowledgements The work was supported by the Russian Foundation for Basic Research (Projects 11–01–00513 and 11-01-12110) and by the Program of Support for Leading Scientific Schools (NSh–64817.2010.1).

References

Blake, R.W.: Fish Locomotion. Cambridge University Press, Cambridge (1983)

Bogoliubov, N.N., Mitropolsky, Y.A.: Asymptotic Methods in the Theory of Nonlinear Oscillations. Gordon and Breach, New York (1961)

Chernousko, F.L.: Controllable motions of a two-link mechanism along a horizontal plane. J. Appl. Math. Mech. **65**, 565–577 (2001)

Chernousko, F.L.: Snake-like locomotions of multilink mechanisms. J. Vib. Control **9**, 237–256 (2003)

Chernousko, F.L.: Modelling of snake-like locomotion. J. Appl. Math. Comput. **164**, 415–434 (2005)

Colgate, J.E., Lynch, K.M.: Mechanics and control of swimming: a review. IEEE J. Ocean. Eng. **29**, 660–673 (2004)

Gray, J.: Animal Locomotion. Norton, New York (1968)

Hirose, S.: Biologically Inspired Robots: Snake-Like Locomotors and Manipulators. Oxford University Press, Oxford (1993)

http://en.wikipedia.org/wiki/RoboTuna#References

Lighthill, J.: Mathematical Biofluiddynamics. SIAM, Philadelphia (1975)

Mason, R., Burdick, J.: Construction and modelling of a carangiform robotic fish. In: Korcke, P., Trevelyan, J. (eds.) Experimental Robotics VI. Lecture Notes in Control and Information Sciences, vol. 250, pp. 235–242. Springer, London/New York (2000)

Pontryagin, L.S., Boltyanskii, V.G., Gamkrelidze, R.V., Mishchenko, E.F.: The Mathematical Theory of Optimal Processes. Gordon and Breach, New York (1986)

Terada, Y., Yamamoto, I.: Development of oscillating fin propulsion system and its application to ships and artificial fish. Mitsubishi Heavy Ind. Tech. Rev. **36**, 84–88 (1999)

Nonlinear Dynamics of Low-Prandtl Number Rayleigh-Bénard Convection

Pankaj Wahi, P.K. Mishra, S. Paul, and M.K. Verma

Abstract We present a detailed bifurcation structure and associated flow patterns for lowPrandtl-number (P = 0.005, 0.02) Rayleigh-Bénard convection near its onset. We use both direct numerical simulations and a 30-mode low-dimensional model for this study. The main flow patterns observed for this range are 2D straight rolls, stationary squares, asymmetric squares, oscillating asymmetric squares, relaxation oscillations, and chaos. At the onset of convection, low-P convective flows have stationary 2D rolls and associated stationary and oscillatory asymmetric squares. The range of Rayleigh numbers for which the stationary 2D rolls exist decreases rapidly with decreasing Prandtl numbers and vanishes in the zero-P limit giving rise to chaotic solutions at the onset itself. Our results are in qualitative agreement with results reported earlier on this topic.

Keywords Rayleigh-Bénard convention • Numerical simulation • Instability and bifurcation

1 Introduction

In this paper we study the nonlinear dynamics of low-Prandtl number Rayleigh-Bénard convection (RBC) using DNS and a low-dimensional model. Low-Prandtl number fluids, for example, mercury ($P \approx 0.02$), liquid sodium ($P \approx 0.01$), solar plasma in the convective zone ($P \sim 10^{-3}$), exhibit interesting convective

P. Wahi (✉)
Mechanical Engineering Department, Indian Institute of Technology-Kanpur, Kanpur, UP, 208016, India
e-mail: wahi@iitk.ac.in

P.K. Mishra • S. Paul • M.K. Verma
Department of Physics, Indian Institute of Technology-Kanpur, Kanpur, UP, India
e-mail: kumarpk@iitk.ac.in; supriyo@iitk.ac.in; mkv@iitk.ac.in

M. Wiercigroch and G. Rega (eds.), *IUTAM Symposium on Nonlinear Dynamics for Advanced Technologies and Engineering Design*, IUTAM Bookseries (closed) 32, DOI 10.1007/978-94-007-5742-4_10,

patterns and chaos (Chandrashekhar 1961; Croquette 1989a,b). For low-Prandtl number (low-P) convection, the inertial term $\mathbf{u} \cdot \nabla \mathbf{u}$ becomes quite important and generates vertical vorticity. As a result, the flow pattern becomes three-dimensional, and oscillatory waves along the horizontal axes are generated just near the onset of convection (Busse 1970).

The instabilities and patterns near the onset for low-P have been studied experimentally (Croquette 1989a,b), analytically (Newell et al. 1990; Segel 1969; Siggia and Zippelius 1981; Busse and Bolton 1985) and numerically (Bolton and Busse 1985; Thual 1992). Readers are referred to Mishra et al. (2010) for more details. Busse (1970) showed using perturbative analysis that for small Prandtl numbers, the 2D rolls become unstable beyond a critical value for the amplitude of the convective motion. Busse and Bolton (1985) argued that under free-slip boundary conditions, stable 2D rolls exists only for Prandtl numbers above a critical value P_c which is around 0.543. Clever and Busse (1974) extended the oscillatory instability analysis to no-slip boundary conditions and showed that the convective rolls are unstable for Prandtl numbers less than about 5. Thual (1992) performed detailed DNS to study the different types of instabilities that occur for low-P and zero-P convection and established that zero-P convection may be treated as a limiting approximation of low-P convection.

Several low-dimensional models have been proposed to study the patterns and instabilities near the onset for the limiting case of zero-P convection. Kumar et al. (1996) showed using a six-mode model of zero-P convection that the growth of the 2D rolls saturate through the generation of the vertical vorticity (wavy nature). Pal and Kumar (2002) explained the mechanism of selection of the square patterns using a 15-mode model of the zero-P RBC. Pal et al. (2009) constructed a 13-mode low-dimensional model for zero-P convection wherein they observed various convective patterns including squares, asymmetric squares, oscillating asymmetric squares, relaxation oscillations with an intermediate square pattern, and chaos. In this paper, we discuss some salient nonlinear dynamical features of a 30-mode model for low-P convection which was originally presented in Mishra et al. (2010).

The main motivation of our study is to understand the dynamics of different nonlinear instabilities that appear near the onset of convection for low-P convection through DNS and low-dimensional models. We present a detailed analysis of instabilities and bifurcations observed near the onset for low-P convection in a 3-d box with free-slip and conducting boundary conditions on top and bottom plates, and periodic conditions in the horizontal directions. The low-dimensional model has been constructed with the large scale modes of DNS that are most active in the regime near the onset of convection. Low-P convection exhibits static patterns, such as rolls, squares, asymmetric square, and time-dependent patterns, such as oscillating asymmetric squares, relaxation oscillations. We observe the presence of chaotic attractors both in DNS and low-dimensional model for low-Prandtl numbers ($P \preceq 0.005$). However, low-P convective flows always exhibit stationary 2D rolls and associated stationary and oscillatory asymmetric squares in contrast to zero-P convection where chaos appears at the onset itself (Pal et al. 2009). The generation of chaos at the onset itself for zero-P has been explained by considering the limiting case of $P \to 0$.

2 Governing Equations and Parameters of RBC

The governing hydrodynamical equations of RBC flow (Chandrashekhar 1961; Busse 1970) are

$$\frac{\partial \mathbf{u}}{\partial t} + (\mathbf{u}\cdot\nabla)\mathbf{u} = -\frac{1}{\rho_0}\nabla\sigma + \frac{1}{\rho_0}\rho(T)g\hat{z} + \nu\nabla^2\mathbf{u}, \tag{1}$$

$$\frac{\partial T}{\partial t} + (\mathbf{u}\cdot\nabla)T = \kappa\nabla^2 T, \tag{2}$$

$$\nabla\cdot\mathbf{u} = 0, \tag{3}$$

where $\mathbf{u} = (u_1, u_2, u_3)$ is the velocity field, T is the temperature field, σ is the pressure field, g is acceleration due to gravity and $\hat{z}$ is the buoyancy direction. ν is the kinematic viscous coefficient, κ is the thermal diffusivity coefficient, ρ_0 is the fluid density at a reference temperature, and $\rho(T)$ is the density of the fluid at temperature T. We assume Boussinesq approximation under which all the properties (e.g., ν, κ) of the fluid are considered to be independent of temperature, and the fluid is considered to be incompressible except for the buoyancy term where $\rho \propto -\rho_0(1-\alpha T)$ with α as the heat expansion coefficient.

We consider that the fluid is confined in a box with dimension $L_x \times L_y \times d$, where L_x and L_y are the lengths in x and y directions respectively, and d is the vertical height of the container. In experiments, top and bottom plates are kept at constant temperatures, i.e., $T|_{z=0} = T_L$, $T|_{z=d} = T_U$. The Boussinesq approximation is valid for small $\Delta T = T_L - T_U$. Considering $T(\mathbf{x}, t) = T_L - \frac{\Delta T}{d}z + \theta(\mathbf{x}, t)$, where $\theta(\mathbf{x}, t)$ is the fluctuation about the linear conduction profile, Eqs. (1)–(3) become

$$\frac{\partial \mathbf{u}}{\partial t} + (\mathbf{u}\cdot\nabla)\mathbf{u} = -\frac{1}{\rho_0}\nabla\sigma + \nu\nabla^2\mathbf{u} + \alpha g\theta\hat{z}, \tag{4}$$

$$\frac{\partial \theta}{\partial t} + (\mathbf{u}\cdot\nabla\theta) = \frac{\Delta T}{d}u_3 + \kappa\nabla^2 T, \tag{5}$$

$$\nabla\cdot\mathbf{u} = 0\,, \tag{6}$$

where an additional term $\alpha g\rho_0\left(\frac{\Delta T}{2d}z^2 - T_L z\right)$ has been absorbed into pressure. The boundary condition for the θ at the top and bottom plates would imply

$$\theta|_{z=0} = 0 = \theta|_{z=d}\,. \tag{7}$$

For the velocity field, typical boundary conditions used are no-slip

$$\mathbf{u}|_{z=0} = 0 = \mathbf{u}|_{z=d}\,, \tag{8}$$

and free-slip or stress-free conditions

$$u_3|_{z=0} = 0 = u_3|_{z=d},$$
$$\partial_z u_1|_{z=0} = 0 = \partial_z u_1|_{z=d}, \quad \partial_z u_2|_{z=0} = 0 = \partial_z u_2|_{z=d}, \tag{9}$$

at the thermal plates. We use the free-slip boundary condition in this study. For the lateral walls, we use periodicity for both the velocity and the temperature fields to ignore the effects of the side walls. Equations (4)–(6) with the boundary conditions (7), and (8) or (9) form the mathematical model of *Rayleigh-Bénard* convection.

Equations (4)–(6) contain various parameters such as α, g, κ, ν etc. whose number can be reduced by choosing relevant length, time, and temperature scales. Choosing d as a length scale, d^2/ν as a time scale (thus ν/d for velocity), $\nu\Delta T/\kappa$ as a scale for the temperature, the corresponding non-dimensional equations of RBC are

$$\frac{\partial \mathbf{u}}{\partial t} + (\mathbf{u}\cdot\nabla)\mathbf{u} = -\nabla\sigma + R\theta\hat{z} + \nabla^2\mathbf{u}, \tag{10}$$

$$P\left(\frac{\partial\theta}{\partial t} + \mathbf{u}\cdot\nabla\theta\right) = u_3 + \nabla^2\theta, \tag{11}$$

$$\nabla\cdot\mathbf{u} = 0, \tag{12}$$

where $R = \dfrac{\alpha g \Delta T d^3}{\nu\kappa}$ is the Rayleigh number, and $P = \dfrac{\nu}{\kappa}$ is the Prandtl number. These two dimensionless numbers, together with the boundary conditions, characterize the convection problem and hence they are the main control parameters. The Prandtl number (P) measures the relative importance of the advection of momentum with heat advection, thus affecting the non-linear properties of the convection accordingly. The Rayleigh number (R) is proportional to the temperature difference across the fluid layer, and relates the strength of the driving mechanism (buoyancy force) to the dissipative processes (viscous diffusion and thermal diffusion). For our analysis we will typically use the reduced Rayleigh number $r = R/R_c$, where R_c is the critical Rayleigh number at which convection begins as our control parameter.

The dynamical equations (10)–(12) are relevant to low Prandtl number fluids since the viscous diffusive time scale used for non-dimensionalization is the dominant scale in this regime. These equations can also be written in an alternate form using the vertical velocity (u_3) and the vertical vorticity (ω_3), where $\omega_3 = \hat{z}\cdot(\nabla\times\mathbf{v})$ as

$$\partial_t(\nabla^2 u_3) = \nabla^4 u_3 + R\nabla_H^2\theta - \hat{z}\cdot\nabla\times[(\boldsymbol{\omega}\cdot\nabla)\mathbf{u} - (\mathbf{u}\cdot\nabla)\omega], \tag{13}$$

$$\partial_t\omega_3 = \nabla^2\omega_3 + [(\boldsymbol{\omega}\cdot\nabla)u_3 - (\mathbf{u}\cdot\nabla)\omega_3], \tag{14}$$

$$P(\partial_t \theta + (\mathbf{u} \cdot \nabla)\theta) = u_3 + \nabla^2 \theta, \tag{15}$$

$$\nabla \cdot \mathbf{u} = 0 \tag{16}$$

where $\boldsymbol{\omega} = \nabla \times \mathbf{u}$, and $\nabla_H^2 = \partial_{xx} + \partial_{yy}$ is the horizontal Laplacian.

3 Various Patterns in Low-P RBC

We perform direct numerical simulations (DNS) of convective flows by solving equations (13)–(16) with the boundary conditions (7) and (9) for $P = 0.02, 0.005, 0.002$ and 0.0002. We use a pseudo-spectral scheme for the simulations with a 64^3 rectangular grid for r ranging from 1 to 1.25. We use the fourth-order Runge-Kutta scheme for time-stepping. The aspect ratio of our simulations is $\Gamma_x = L_x/d = 2\sqrt{2}, \Gamma_y = L_y/d = 2\sqrt{2}$. Equations (13) and (15) provide us an estimate of $dt \sim P\theta/v_3 \sim P/R$ for the DNS. For $P = 0.0002$, $dt \sim 10^{-7}$ that makes numerical simulations very demanding.

In DNS of low-Prandtl number convection, we observe various static patterns such as a 2-D roll, asymmetric square (ASQ), square (SQ), and time-dependent patterns such as oscillatory asymmetric square (OASQ), oscillatory rolls with square pattern in the intermediate regime and chaotic attractors near the onset of convection. Some of these patterns were first observed in the numerical observations of Thual (1992) and Meneguzzi et al. (1987) for low-P and/or zero-P convection. For $P = 0.02$, Fig. 1 shows the static convective flow patterns in the mid-plane ($z = 0.5$) at different values of Rayleigh numbers near the onset of convection. Figure 1a exhibits straight rolls along the x-axis observed at $r = 1.0005$. As the Rayleigh number is increased, roll starts appearing in the perpendicular direction and superposition of two perpendicular rolls gives rise to static asymmetric square (ASQ) and square (SQ) patterns. The two perpendicular rolls have unequal intensity for ASQ patterns while they have equal intensity for SQ patterns. Figure 1b, c show the "weak" and "strong" asymmetric square patterns respectively. Figure 2 shows a periodic transition from roll pattern in one direction to the roll pattern in the perpendicular direction with square patterns in the transition regime (SQOR) for $P = 0.02$ at $r = 1.031$. Figure 2a shows the roll along x-axis at $t = 0$; Fig. 2b shows the intermediate square at $t = T/4$ (T is the time period of the oscillation); and Fig. 2c shows the roll along y-axis at $t = T/2$.

Similar patterns were observed for other low-Prandtl numbers ($P = 0.002$, 0.005, 0.0002) considered for our study with the range of static patterns appearing near the onset decreasing with decreasing Prandtl number. For low-Prandtl numbers ($P = 0.005$ and $P = 0.0002$) we also observe chaotic behaviour of the flow close to onset. The origin of these different patterns for low-P convection cannot be explored through DNS since each simulation run takes significantly long time. Therefore, for a systematic study of the instabilities giving rise to these patterns we construct a low-dimensional model of low-P convection presented in the next section.

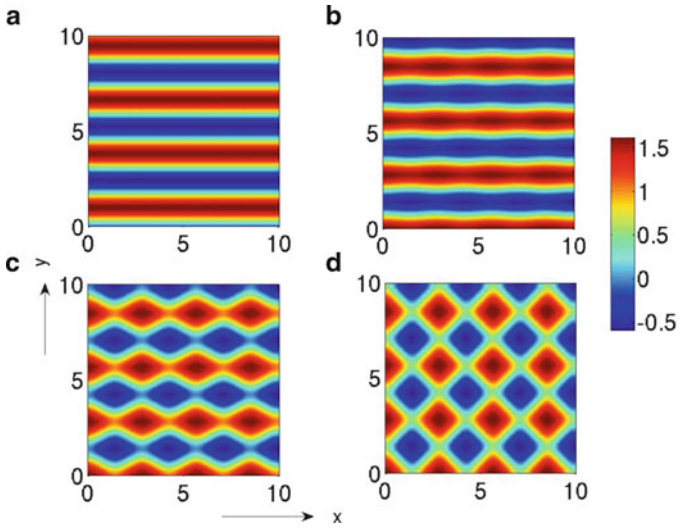

Fig. 1 Static patterns in the mid-plane of the convection 3-d box observed in DNS near the onset for $P = 0.2$ on 64^3 grid size. Temperature snapshots at: (**a**) $r = 1.0005$ exhibits roll pattern, (**b**) at $r = 1.007$ exhibits "weak" asymmetric square (ASQ) pattern, (**c**) $r = 1.186$ exhibits "strong" asymmetric square (ASQ) pattern, and (**d**) $r = 1.217$ exhibits square (SQ) pattern. *Blue* and *red* regions represent the upcoming and downgoing convective flow of the fluid respectively

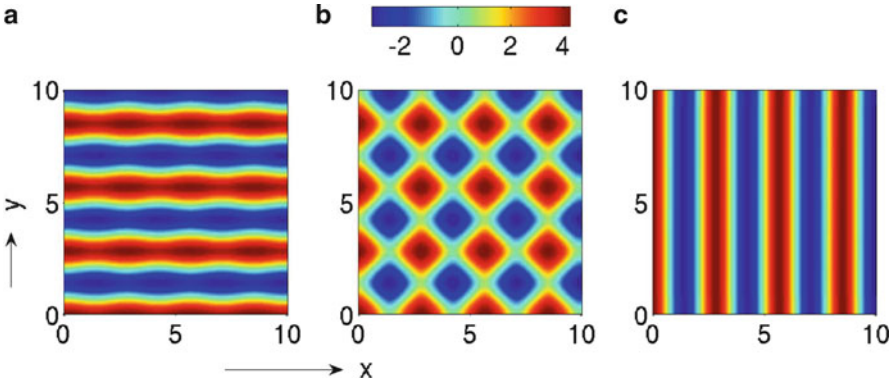

Fig. 2 Relaxation oscillation with an intermediate square regime (SQOR) pattern observed in DNS at $r = 1.031$ for $P = 0.02$. Snapshots of temperature at: (**a**) $t = 0$, (**b**) $t = T/4$, and (**c**) $t = T/2$, where T is the time period of oscillation

4 Low-Dimensional Model and Associated Bifurcation Diagrams

A careful analysis of the DNS data reveals that a few large scale modes are instrumental in the dynamics of convection near the onset and are dominant for all the observed flow patterns. Using these important modes we construct a 30-mode

low-dimensional model for low-Prandtl number convection. We run the model and DNS in the range of $r = 1 - 1.25$. Cumulative energy contained in these modes ranges from 85 to 98% of the total energy of DNS, and each of these modes has 1% or more of the total energy. We pick 11 large-scale vertical velocity modes: W_{101}, W_{011}, W_{112}, W_{211}, W_{121}, W_{301}, W_{103}, W_{013}, W_{031}, W_{202}, W_{022}; 12 large-scale θ modes: θ_{101}, θ_{011}, θ_{112}, θ_{211}, θ_{121}, θ_{301}, θ_{103}, θ_{013}, θ_{031}, θ_{202}, θ_{022}, θ_{002}; and 7 large-scale vertical vorticity modes: Z_{110}, Z_{112}, Z_{211}, Z_{121}, Z_{220}, Z_{310}, Z_{130}. The three subscripts here are the indices of the wavenumbers along the x, y, and z directions. All the Fourier modes, 30 in total, are taken to be real. We perform a Galerkin projection of the RBC equations (Eqs. (13)–(15)) on the above modes, and obtain a set of 30 equations for the amplitudes of the above Fourier modes. As a preliminary test, we numerically solve the 30-mode model by employing accurate implicit ODE solvers of MATLAB and observe the solutions corresponding to the patterns observed in DNS. The Fourier amplitudes of all the modes obtained from the low-dimensional model for SQ and ASQ patterns match with corresponding DNS values within 20%.

We investigate the origin of various convective flow patterns for low-Prandtl numbers ($P = 0.02, 0.005, 0.0002$) through the bifurcation diagrams generated using the low dimensional model. To generate the bifurcation diagram, we start first with the fixed points of the system. Branches of fixed points are obtained using a fixed arc-length based continuation scheme (Wahi and Chatterjee 2008) in conjunction with the Newton-Raphson method. An eigenvalue analysis of the Jacobian evaluated at a fixed point determines its stability and this process on the branch of fixed points determines the bifurcation points. New branches of fixed points and limit cycles born as a result of the bifurcation are obtained analogously. For aperiodic and chaotic solutions, we resort to numerical integration and report the extremum values of the important modes. We use our own MATLAB code as well as MATCONT (Dhooge et al. 2003) for the analysis.

Among all the 30 modes representing the phase space of our system, W_{101}, W_{011}, θ_{101}, and θ_{011} are the most important modes of our model, and they represent the rolls along the y and the x directions respectively. We will describe the fixed points and associated time-dependent patterns using a bifurcation diagram in the range of $0.95 \leq r \leq 1.25$. Figure 3 illustrates the bifurcation diagram for $P = 0.02$ where we plot the positive value of $(W_{101})_{extremum}$ as a function of r. A three-dimensional bifurcation diagram depicting variation of the fixed points with r is given in Mishra et al. (2010).

At $r = 1$ the conduction state bifurcates to stationary 2D rolls (purple curve) through a codimension-2 pitchfork bifurcation. Unstable stationary SQ (shown as dashed black curve) with $W_{101} = \pm W_{011}$ are also generated as a result of this bifurcation. As r is increased further, at $r \approx 1.0035$, these 2D rolls bifurcate to ASQ patterns (solid blue curves) through a pitchfork bifurcation. Subsequently, at $r \approx 1.0114$, ASQ patterns bifurcate to limit cycles (red curves) through a Hopf bifurcation. These limit cycles represent OASQ and their oscillatory flow patterns form standing waves along the roll axis that have been discussed earlier by Thual (1992). Figure 4a, b illustrate the projection of two of these stable limit cycles for

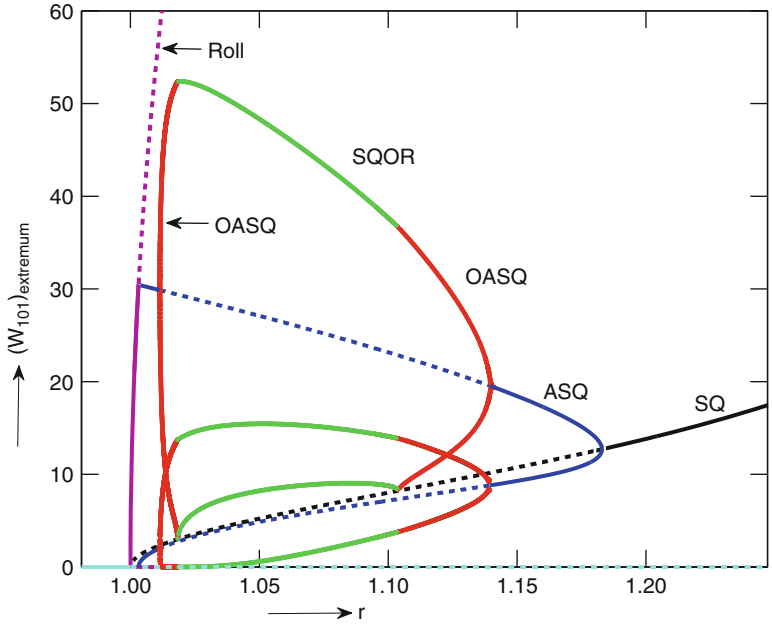

Fig. 3 Bifurcation diagram of the low-dimensional model for $P = 0.02$ in the range $0.95 \leq r \leq 1.25$. The stable branches corresponding to conduction state, 2D rolls, SQ, and ASQ are represented by *solid cyan*, *solid purple*, *solid black*, and *solid blue curves* respectively. The *red* and *green curves* depict the extrema of OASQ and SQOR respectively. The *dashed curves* represent unstable solutions

$r = 1.016$ on the $W_{101} - W_{011}$ plane. The time-period and amplitude of these limit cycles increase as r is increased. At $r \approx 1.0184$, these limit cycles collide with the unstable SQ fixed points (saddles) originating from $r = 1$ and form homoclinic orbits whose phase space projection on the $W_{101} - W_{011}$ is shown in Fig. 4c, d.

Beyond $r \approx 1.0184$, there is a smooth transition to regular limit cycles corresponding to SQOR, illustrated as green curves in the bifurcation diagram. The dynamical behaviour of the W_{101} and W_{011} modes in the SQOR regimes is similar to the homoclinic orbit shown in Fig. 4c, d. There is an alternate but periodic growth and decay of the W_{101} and W_{011} modes. The flow pattern corresponding to the SQOR pattern is shown in Fig. 2 and it changes in time from an approximate roll in one direction to a roll in the other direction. The limit cycles corresponding to SQOR form another set of homoclinic orbits at $r \approx 1.1034$ after which it bifurcates into two separate limit cycles. These limit cycles (OASQ shown as red curves) diminish in size as r is increased until they transform to stable fixed points (ASQ shown as blue curves) through an inverse Hopf bifurcation. As r is increased further, at $r \approx 1.183$, the stable ASQ branches meet the unstable SQ branch (the dashed black curve) resulting in stabilization of the SQ pattern (solid black curves). Thus, the low-dimensional model for $P = 0.02$ exhibits patterns that are consistent with the

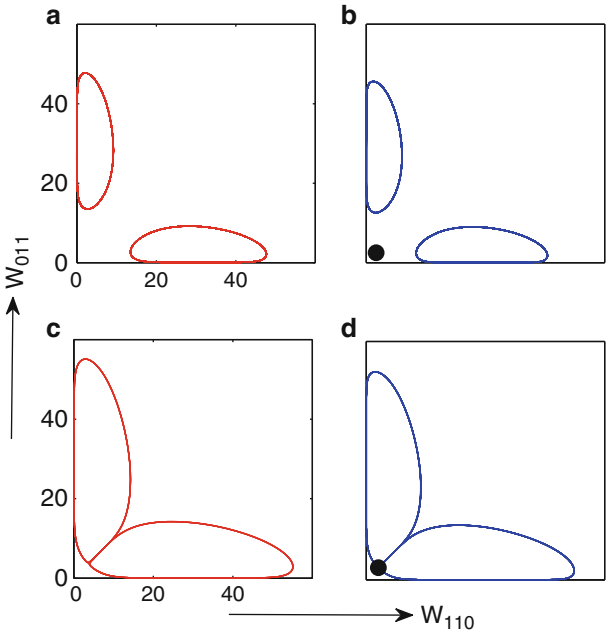

Fig. 4 Phase space projection on W_{101} and W_{011} plane is shown to compare between the DNS and the model results in OASQ and SQOR regimes of convection for $P = 0.02$. *Red* and *blue curves* show the results obtained from DNS and the model respectively. (**a**) shows the limit cycle obtained in DNS at $r = 1.016$, (**b**) shows the limit cycle obtained in the model for $r = 1.0129$, (**c**) shows the homoclinic orbit obtained in DNS at $r = 1.027$, and (**d**) shows the homoclinic orbit at $r = 1.0184$ for the model. The *black dots* shown in (**b**) and (**d**) indicate the symmetric square saddle point. Note that the two limit cycles corresponding to OASQ in the Homoclinic orbit are very close but they don't touch each other

earlier investigations of low-P convection (Thual 1992; Meneguzzi et al. 1987). The DNS and low-dimensional results for $P = 0.02$ are in good agreement with each other (also see Table 1).

In the following discussion we will consider the bifurcation diagrams for lower Prandtl numbers ($P = 0.005, 0.002, 0.0002$) for which we observe several chaotic attractors near the onset of convection. We start with $P = 0.005$ for which the bifurcation diagram shown in Fig. 5, is similar to Fig. 3 with a major difference that chaotic attractors appear near the onset in the band of $r = 1.000685 - 1.0068$. There are three qualitatively different chaotic attractors *Ch1, Ch2*, and *Ch3* shown in the inset of Fig. 5 as (i)–(iii), and with phase space projections depicted in Fig. 6b–d for $r = 1.0023$, $r = 1.0053$, and $r = 1.0064$ respectively. We explore the origin of these chaotic attractors in the following discussions.

As we increase r beyond 1, we observe 2D rolls, ASQ, and OASQ just like $P = 0.02$, however, at lower r values (see Table 2). The phase space projection on the $W_{101} - W_{011}$ plane of two of the limit cycles corresponding to OASQ are

Table 1 Range of reduced Rayleigh number r corresponding to various flow patterns observed in the 30-mode model and the DNS for $P = 0.02$. Here SQ, ASQ, OASQ, and SQOR represent stationary squares, stationary asymmetric squares, oscillatory asymmetric squares, and relaxation oscillation of squares respectively

Flow patterns	r (model)	r (DNS)
Roll	1 — 1.0032	1 — 1.0038
ASQ	1.0033 — 1.0122	1.0039 — 1.0114
OASQ	1.0123 — 1.0183	1.0115 — 1.0236
SQOR	1.0184 — 1.1027	1.0237 — 1.0874
OASQ	1.1028 — 1.1402	1.0875 — 1.1407
ASQ	1.1403 — 1.1830	1.1408 — 1.2015
SQ	1.1831 — 1.4859	1.2015 — 1.2528

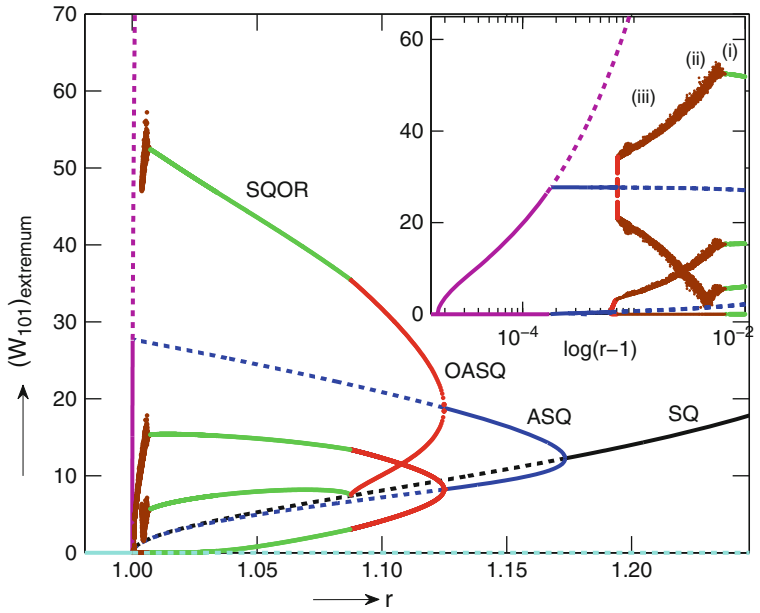

Fig. 5 Bifurcation diagram of the low-dimensional model for $P = 0.005$ in the range $0.95 \leq r \leq 1.25$. The color convention is same as that for $P = 0.02$ (Fig. 3). The chaotic attractors are shown in *brown* colour. A zoomed view of the bifurcation diagram for the chaotic regime is shown in the *inset* where the x axis is chosen as $\log(r - 1)$ to highlight the behaviour near $r = 1$. The three attractors *Ch1, Ch2* and *Ch3* are shown as (*i*), (*ii*), and (*iii*) respectively

shown in Fig. 6a. Subsequently these limit cycles appear to approach their basin boundary (the horizontal axis of the figure), and the system becomes chaotic due to a "gluing bifurcation" Meron and Procaccia (1987) related to the "attractor merging crisis" Ott (2002). These terminologies refer to the phenomena wherein two or more distinct attractors simultaneously hit their common basin boundaries to result in a

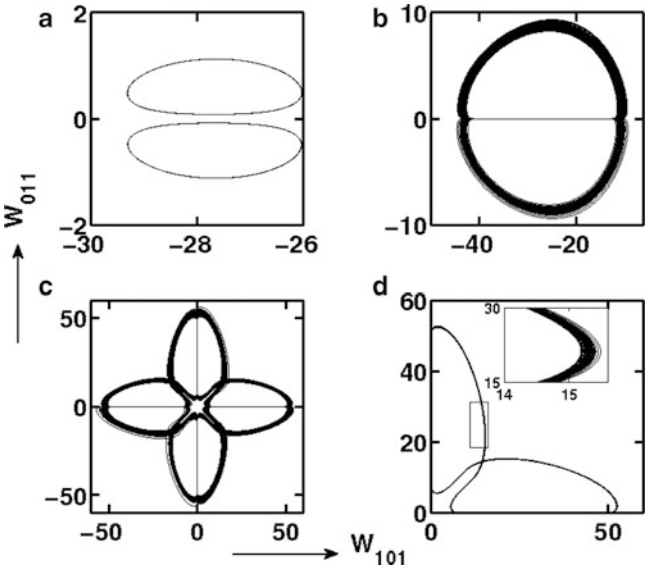

Fig. 6 Phase space projections of the attractors on the $W_{101} - W_{011}$ plane obtained from the low-dimensional model for $P = 0.005$ near $r = 1$: (**a**) two of the limit cycles at $r = 1.0006844$; (**b**) the chaotic attractor *Ch3* at $r = 1.0023$; (**c**) the chaotic attractor *Ch2* at $r = 1.0053$; (**d**) the chaotic attractor *Ch1* at $r = 1.0064$, with the inset depicting the chaotic nature of the attractor

Table 2 Table depicting the reduced Rayleigh number r_p at which the 2D rolls bifurcate to ASQ, r_t where ASQ patterns bifurcate to limit cycles, and the frequency ω of the limit cycle at the Hopf bifurcation point. These values are computed for Prandtl numbers $P = 0.02, 0.005, 0.002$ and 0.0002

P	r_p	r_t	ω
0.02	1.0035	1.01139	1.15×10^{-3}
0.005	1.000179	1.000683	2.9×10^{-5}
0.002	1.000042	1.00012	1.15×10^{-5}
0.0002	$1 + 2.5 \times 10^{-7}$	1.000018	1.15×10^{-7}

single large attractor. The former is used when the pre-bifurcation attractors are regular, e.g., limit cycles, while the latter involves chaotic attractors. The resulting chaotic attractor is *Ch3* whose phase space projection is shown in Fig. 6b. As r is increased further, the *Ch3* attractors merge together to yield a single large chaotic attractor *Ch2*. At a larger r value, the *Ch2* attractor breaks into four separate chaotic attractors *Ch1*. The *Ch1* chaotic attractors become regular for $r \geq 1.0068$ giving rise to the SQOR limit cycles. The subsequent patterns are same as those for $P = 0.02$. The *Ch1* chaotic attractors are generated as a result of "homoclinic chaos" where the stable and unstable manifolds of a saddle intersect each other. The chaotic attractors

observed in the low-dimensional model are also observed in DNS and their phase space projections are provided in Mishra et al. (2010).

A further lowering of the Prandtl number from $P = 0.005$ shifts the range of stationary 2D rolls and the associated ASQ patterns even nearer to $r = 1$ as evident from the entries of Table 2. The branch points corresponding to ASQ (r_p) and OASQ (r_t) asymptotically approach $r = 1$ as $P \to 0$ (Table 2). The 2D rolls and ASQ occur for $1 < r < 1 + 2.5 \times 10^{-7}$ and $1 + 2.5 \times 10^{-7} < r < 1 + 1.8 \times 10^{-7}$ respectively (a very small window) for $P = 0.0002$. Consequently it would be very difficult to observe them in experiments and DNS; a small noise is sufficient to push the system from the ordered region to chaos which is the feature of zero-P convection (Pal et al. 2009).

We observe from Table 2 that $r_p - 1$, $r_t - 1$, and ω (imaginary part of the eigenvalue at $r = r_t$) appear to vary approximately as P^2 with prefactors around 10, 30 and 3 respectively. The P^2 dependence is consistent with the theoretical predictions of Busse (1970) that $r_t - 1 \geq 0.310 P^2$ for free-slip boundary conditions. Our analysis indicates stable 2D rolls for any nonzero P, in contrast to the prediction of absence of these rolls for $P < P_c = 0.543$ by Busse and Bolton (1985). Our results are in agreement with the experiments on mercury ($P = 0.02$) by Krishnamurti (1970) where she found stable 2D rolls near the onset ($r \approx 1.3 \pm 0.1$) indicating that P_c predicted in Busse and Bolton (1985) is an overestimate. Comparing our results with those of Pal et al. (2010) when oscillatory modes like Z_{010} etc. are included in their model, we find that the bifurcation scenario for $P \to 0$ is exactly the same as $P = 0$ as noted by Thual (1992). Hence, zero-P convection is a valid limiting case of low-P convection.

5 Conclusion

In this paper, we presented a detailed bifurcation structure and associated flow patterns for low-Prandtl number ($P = 0.0002, 0.002, 0.005, 0.02$) Rayleigh-Bénard convection near its onset using a low-dimensional model. The results of the low-dimensional models are in good agreement with those of DNS. We observed that low-Prandtl number convection exhibits various patterns, namely squares, asymmetric squares, oscillating asymmetric squares, and relaxation oscillations. We observed that the bifurcation diagram for low-P convection is very similar to zero-P convection (Pal et al. 2009, 2010), except near the onset of convection where 2D stationary rolls, and stationary and oscillatory asymmetric squares are observed for finite P. Chaotic solutions have been observed for very low Prandtl numbers ($P \preceq 0.005$). The range of Rayleigh numbers for which 2D rolls and associated ASQ and OASQ are observed shrinks rapidly ($\sim P^2$) as P is decreased. For $P \leq 0.0002$, the range of reduced Rayleigh numbers for which the stationary 2D rolls could be observed is too narrow ($<1 + 10^{-7}$) to be observed in experiments or in DNS making it equivalent to zero-P for all practical purpose. This pushes the critical Prandtl number P_c below which stable rolls does not exist to $P \sim 0.0002$ which

is much lower than that predicted by Busse and Bolton (1985). Our comparative study of low-P convection with zero-P convection of Pal et al. (2009) shows how the limiting behavior of zero-P convection is obtained as P approaches zero. Our analysis provides useful insights into the origin of patterns and chaos for low-P and the limiting case of zero-P convection.

Acknowledgements We thank S. Fauve, M. Proctor, K. Kumar and P. Pal for useful discussions and comments, Computational Research Laboratory, India for providing access to the supercomputer EKA where some of the DNS runs were performed, and DST India for financial support.

References

Bolton, E.W., Busse, F.H.: Stability of convection rolls in a layer with stress-free boundaries. J. Fluid Mech. **150**, 487–498 (1985)

Busse, F.H.: The oscillatory instability of convection rolls in a low Prandtl number fluid. J. Fluid Mech. **52**, 97–112 (1970)

Busse, F.H., Bolton, E.W.: Instabilities of convection rolls with stress-free boundaries near threshold. J. Fluid Mech. **146**, 115–125 (1985)

Chandrashekhar, S,: Hydrodynamic and Hydromagnetic Stability. Cambridge University Press, Cambridge (1961)

Clever, R.M., Busse, F.H.: Transition to time-dependent convection. J. Fluid Mech. **65**, 625–645 (1974)

Croquette, V.: Convective pattern dynamics at low Prandtl number: Part I. Contemp Phys. **30**, 113–133 (1989a)

Croquette, V.: Convective pattern dynamics at low Prandtl number: Part II. Contemp. Phys. **30**, 153–171 (1989b)

Dhooge, A., Govaerts, W., Kuznetsov, Y.A.: Matcont: a MATLAB package for numerical bifurcation analysis of ODEs. ACM TOMS **29**, 202–214 (2003)

Krishnamurti, R.: On the transition to turbulent convection. Part2. The transition to timedependent flow. J. Fluid Mech. **42**, 309–320 (1970)

Kumar, K., Fauve, S., Thual, O.: Critical self-tuning: the example of zero Prandtl number convection. J. Phys. II (France) **6**, 945–951 (1996)

Meneguzzi, M., et al.: Three-dimensional numerical simulation of convection in low Prandtl number fluid. J. Fluid Mech. **182**, 169–191 (1987)

Meron, E., Procaccia, I.: Gluing bifurcations in critical flows: the route to chaos in parametrically excited surface waves. Phys. Rev. A **35**, 4008–4011 (1987)

Mishra, P.K., Wahi, P., Verma, M.K.: Patterns and bifurcations for low-P Rayleigh-Bénard convection. Europhys. Lett. **89**, 44003 (2010)

Newell, A.C., Passot, T., Soul, M.: The phase diffusion and mean drift equations for convection at finite Rayleigh numbers in large containers. J. Fluid Mech. **220**, 187–252 (1990)

Ott, E.: Chaos in Dynamical Systems. Cambridge University Press, Cambridge (2002)

Pal, P., Kumar, K.: Wavy strips and squares in zero-Prandtl number convection. Phys. Rev. E **65**, 047302 (2002)

Pal, P., et al.: Bifurcations and chaos in zero-Prandtl number convection. Europhys. Lett. **87**, 54003 (2009)

Pal, P., Paul, S., Wahi, P., Verma, M.K.: Dynamics of zero-Prandtl number convection near the onset (2010). arXiv:1008.0752v1.

Segel, L.A.: Distant side-walls cause slow amplitude modulation of cellular convection. J. Fluid Mech. **38**, 203–224 (1969)

Siggia, E.D., Zippelius, A.: Patterns selection in Rayleigh-Bénard convection near threshold. Phys. Rev. Lett. **47**, 835–838 (1981)
Thual, O.: Zero-Prandtl number convection. J. Fluid Mech. **240**, 229–258 (1992)
Wahi, P., Chatterjee, A.: Self interrupted metal cutting in turning. Int. J. Nonlin. Mech. **43**, 111–123 (2008)

Mixed-Modal Self-Excited Oscillation of Fluid-Conveying Cantilevered Pipe with End Mass

Kiyotaka Yamashita, Hiroshi Yabuno, Yuuki Hirose, and Masatsugu Yoshizawa

Abstract An experimental and theoretical investigation was conducted into the spatial motion of the self-excited oscillation of a pipe which is built-in at upper end and has an attached mass at the other. A certain characteristic mode of the pipe vibration is self-excited when the axial flow velocity in the pipe exceeds a certain value. For higher flow velocity, the two distinct eigen modes of the pipe can be simultaneously self-excited with two different natural frequencies, which called mixed-mode flutter. Equations governing amplitudes and the phases were derived and used to clarify nonlinear modal interactions numerically the above specific cases. It is theoretically clarified that the planes, on which second modal oscillation and the third modal oscillation are produced, are perpendicular. Furthermore experiments were conducted with the silicon rubber pipe conveying fluid. As a result, typical features of the mixed-mode flutter were confirmed qualitatively by experiments.

Keywords Fluid-conveying pipe • Self-excited oscillation • Linear and nonlinear stability

1 Introduction

The spatial behavior of pipe-conveying fluid is a subject of study attracting the interest of many researchers from the viewpoint of nonlinear dynamics. Recent

K. Yamashita (✉) • Y. Hirose
Department of Mechanical Engineering, Fukui University of Technology, 3-6-1 Gakuen, Fukuishi, Fukui 910-0028, Japan
e-mail: yamashita@fukui-ut.ac.jp

H. Yabuno • M. Yoshizawa
Department of Mechanical Engineering, Keio University, 3-14-1 Hiyoshi, Kouhoku-ku, Yokohama 223-8522, Japan
e-mail: yabuno@mech.keio.ac.jp

M. Wiercigroch and G. Rega (eds.), *IUTAM Symposium on Nonlinear Dynamics for Advanced Technologies and Engineering Design*, IUTAM Bookseries (closed) 32, DOI 10.1007/978-94-007-5742-4_11,

developments in the field of spatial pipe vibration started with the work of Bajaj and Sethna (1984) and Steindl and Troger (1992).

It is well known that the attached end mass enrich the spatial dynamical features of pipe conveying fluid. Copeland and Moon revealed some complex spatial behaviors following an increase of the fluid velocity by visual inspection (Copeland and Moon 1992). Païdousis and Semler clarified the chaotic motion of a fluid-conveying cantilevered pipe with an end mass (Païdousis and Semler 1998). A certain characteristic mode of the pipe vibration is self-excited when the axial flow velocity in the pipe exceeds a certain value (Païdousis 1998). As increasing the flow velocity, another higher mode can be also destabilized. Then, the two eigen modes of the pipe are simultaneously self-excited with two natural frequencies, which is called mixed-mode flutter (Chamara and Coller 2004). The phenomenon in the case of cantilevered pipe is essentially different from the coupled-mode flutter in case of the pined-pined or clamped-clamped pipe (Païdoussis 2005).

In the present study, the equations govern the nonlinear dynamics of amplitudes and phases of the self-excited vibration modes are derived from the basic equations of the spatial lateral vibrations of a vertical fluid-conveying pipe with an end mass. It is clarified theoretically that the behavior of the mixed-modal self-excited pipe vibration consists of the lower modal oscillation on a plane and the higher modal oscillation on the perpendicular plane. Furthermore, experiments were conducted with a silicon rubber pipe conveying water. The mixed-modal self-excited vibrations of the vertical fluid-conveying pipe with an end mass were observed using the image processing system with two CCD cameras.

2 Basic Equations

The system under consideration (Fig. 1), consists a flexible pipe, built-in at one end and with an end mass at the other. The pipe conveys an incompressible fluid which discharges to atmosphere from the free end. The pipe is flexible in bending yet

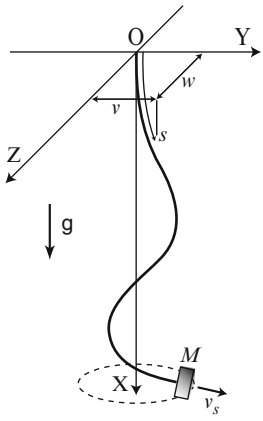

Fig. 1 Analytical model of a pipe conveying fluid with an end mass

inextensible. It also has uniform circular cross section and a length far in excess of its diameter. The pipe, of length ℓ, flexural rigidity EI, mass per unit length m and bore area S, is hung vertically under the influence of gravity g in its rest state.

Let $v(s,t)$ and $w(s,t)$ be the displacements along the pipe centerline in the Y and Z directions respectively. These are expressed as functions of coordinate s along the pipe axis and time t. Assuming that v and w are small but finite and the pipe is not subjected to torsion about centerline, the governing equations of the spatial pipe behavior may be derived (Yoshizawa et al. 1998).

First, some dimensionless variables are introduced (denoted with *): $s = \ell s^*$, $v = \ell v^*$, $w = \ell w^*$, $t = \sqrt{(m+\rho S)\ell^4/EI}t^*$. Retaining terms up to the third order of v^* and w^*, the dimensionless equation for pipe vibrations in the $X-Y$ plane can be expressed:

$$\ddot{v} + c\dot{v} + \delta\dot{v}'''' + 2\sqrt{\beta}V_s\dot{v}' + V_s^2 v'' - \gamma\left[(\alpha+1-s)v'\right]' + v'''' = n_v \qquad (1)$$

where $(\dot{\cdot})$ and $()'$ denote the derivatives with respect to t and s, respectively. The asterisks indicating the dimensionless variables are omitted in Eq. (1) and hence forward except for Sect. 4. The boundary conditions for both ends of the pipe in $X-Y$ plane are expressed as follows:

$$\begin{aligned} s &= 0: \quad v = v' = 0 \\ s &= 1: \quad v'' + \delta\dot{v}'' = 0,\ v''' - \alpha\gamma v' - \alpha\ddot{v} - c\dot{v} + \delta\dot{v}''' = b_v \end{aligned} \qquad (2)$$

From the governing Eqs. (1) and (2) and the similar equations associated with w, the lateral deflections v and w are uncoupled in the linear sense and coupled through nonlinear terms described n_j and b_j (j = v,w). The equation of the pipe motion in the $X-Z$ plane and its boundary conditions, are expressed by exchanging v for w and w for v.

As a result, the spatial behavior of the pipe is described by two equations and eight boundary conditions with respect to v and w. There are six dimensionless parameters involved in Eqs. (1) and (2) and their similar equations in $X-Z$ plane, i.e. the dimensionless velocity V_s, the ratio of the lumped mass to the total mass $\alpha = M/(m+\rho S)l$, the ratio of the fluid mass to the total mass $\beta = \rho S/(m+\rho S)$, the ratio of the gravity force to the elastic force to the pipe $\gamma = (m+\rho S)gl^3/EI$, the dimensionless external damping coefficient $c = Cl^2/\sqrt{EI(m+\rho S)}$, the dimensionless internal damping coefficient $\delta = E^*/[l^2E\sqrt{EI/(m+\rho S)}]$.

The governing equations (1) and (2) and similar equations associated w can be converted to the vector forms by defining $\boldsymbol{v}_v = {}^t(v\ \partial v/\partial t)$, $\boldsymbol{v}_w = {}^t(w\ \partial w/\partial t)$. The governing equations of $\boldsymbol{v}_j$ ($j = v$ and w) are expressed in the vector form as follow:

$$\frac{\partial \boldsymbol{v}_j}{\partial t} = \boldsymbol{L}\boldsymbol{v}_j + \boldsymbol{N}_j \qquad (3)$$

Boundary conditions associated with $\boldsymbol{v}_v$ are as follows:

$$s = 0 : \boldsymbol{B}_1 \boldsymbol{v}_j = 0, \quad s = 1 : \boldsymbol{B}_2 \dot{\boldsymbol{v}}_j = \boldsymbol{B}_3 \boldsymbol{v}_j - \boldsymbol{N}_{bj} \tag{4}$$

where $\boldsymbol{N}_j =^t (0 \quad n_j)$ and $\boldsymbol{N}_{bj} =^t (0 \quad b_j)$ $(j = v, w)$ in Eqs. (3) and (4) are expressed as the nonlinear polynomials with respect to v and w.

3 Method of Solution

In this section, the solution method of mixed modal self-excited pipe vibration is briefly described by using the method of Lyapnov-Schmidt reduction.

3.1 Linear Stability

Neglecting the nonlinear terms with respect to v and w in Eqs. (3) and (4), $\boldsymbol{v}_v$ and $\boldsymbol{v}_w$ become independent of each other and they have the identical linear eigenvalues and eigenfunctions. Letting $\boldsymbol{v}_j = \boldsymbol{q} e^{\lambda t}$, $\boldsymbol{q}(s) =^t (\Phi_1(s) \ \Phi_2(s))$ and substituting them into Eqs. (3) and (4), we can cast into the eigenvalue problem.

The eigenvalue, being the root of the complex characteristic equation, which is symbolically described by $f(\lambda : V_s, \alpha, \beta, \gamma, c, \delta) = 0$ can be found numerically. The jth eigenvalue is equal to $i(\omega_{jr} + i\omega_{ji})$, where ω_{jr} is the linear natural frequency and ω_{ji} corresponds to the damping ratio.

Figure 2 shows ω_{ji} as a function of V_s for the second and third modes of the system in the case of $\alpha = 0.36, \beta = 0.30, \gamma = 42.2, c = 0.025$ and $\delta = 0.8 \times 10^{-3}$. These parameter values used in the numerical examples henceforward are equal to the values of the experimental ones in Sect. 4. Second mode of the pipe vibration is self-excited when the axial flow velocity in the pipe exceeds $V_s = 5.98$. As increasing the flow velocity, third mode can be also destabilized. Then, the two eigen modes of the pipe are simultaneously self-excited with two natural frequencies.

From the condition: $\langle \boldsymbol{L}\boldsymbol{q}_i, \ \boldsymbol{q}_i^* \rangle = \langle \boldsymbol{q}_i, \boldsymbol{L}^* \boldsymbol{q}_i^* \rangle$, we can determine the adjoint vector $\boldsymbol{q}_i^*$ of $\boldsymbol{q}_i$, where brackets denote the inner product $< \boldsymbol{x}, \boldsymbol{y} >= \int_0^1 \boldsymbol{x}(s)\bar{\boldsymbol{y}}(s)ds$.

3.2 Nonlinear Stability

In this subsection, the equations governing the amplitudes and phases of v and w are derived for the case when the second and third modes of the pipe vibration can be simultaneously self-excited. The Banach space, which includes $\boldsymbol{v}_v$ and $\boldsymbol{v}_w$, is expressed as $Z = X \oplus M$ (Carr 1981). X is the eigenspace spanned by the

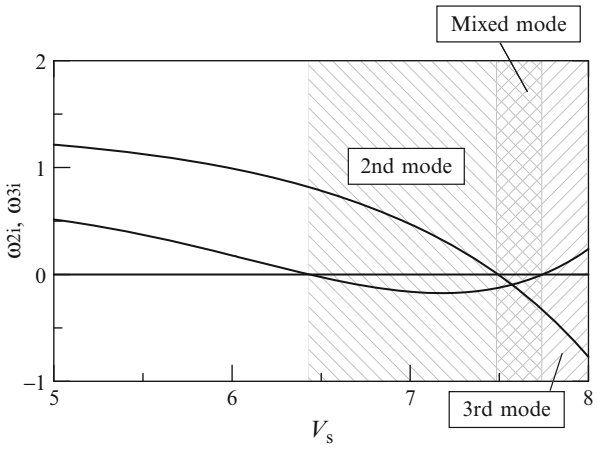

Fig. 2 The damping ratio ω_{2i} and ω_{3i} as functions of the flow velocity V_s ($\alpha = 0.36$, $\beta = 0.30$, $\gamma = 42.2$, $c = 0.025$ and $\delta = 0.8 \times 10^{-3}$)

eigenvectors $\boldsymbol{q}_2$ and $\boldsymbol{q}_3$, which correspond to the linear unstable vibration modes of $\boldsymbol{v}_v$ and $\boldsymbol{v}_w$. M is the subspace of X. Therefore $\boldsymbol{v}_j$ ($j = v, w$) are expressed as follows:

$$\begin{aligned} \boldsymbol{v}_v(s,t) &= C_2(t)\boldsymbol{q}_2(s) + C_3(t)\boldsymbol{q}_3(s) + \boldsymbol{y}_v + c.c., \\ \boldsymbol{v}_w(s,t) &= D_2(t)\boldsymbol{q}_2(s) + D_3(t)\boldsymbol{q}_3(s) + \boldsymbol{y}_w + c.c., \end{aligned} \tag{5}$$

where c.c. stands for the complex conjugate of the preceding terms and the C_2, C_3, D_2 and D_3 are complex valued functions, which will be determined by the Lyapunov-Shmidt reduction at the next level of approximation. C_i and D_i are the complex amplitudes of the ith mode vibration in the $X - Y$ plane and $X - Z$ plane respectively. $\boldsymbol{y}_v$ and $\boldsymbol{y}_w$ are the elements of M. So $\boldsymbol{y}_j$, which spanned by the linear stable vibration modes, become zero with time.

We use the following projection $\boldsymbol{P}_j$ which project $\boldsymbol{x}$ onto jth eigenspace $\boldsymbol{q}_j$.

$$\boldsymbol{P}_j \boldsymbol{x} = < \boldsymbol{x}, \boldsymbol{q}_j^* > \boldsymbol{q}_j. \tag{6}$$

Using the projection $\boldsymbol{P}_2$ onto the eigenspace spanned by second mode, the Eq. (3) with boundary conditions (4) and their associated equations about w are decomposed as follows:

$$\begin{aligned} \dot{A}_2 = {} & (-\omega_{2i} + \xi_{12}|A_2|^2 + \xi_{22}|A_3|^2 + \xi_{32}|B_2|^2 + \xi_{42}|B_3|^2)A_2 \\ & + \xi_{52}\overline{A_2}B_2^2 + (\xi_{62}A_3\overline{B_3} + \xi_{72}\overline{A_3}B_3)B_2, \end{aligned} \tag{7}$$

$$\begin{aligned} \dot{B}_2 = {} & (-\omega_{2i} + \xi_{12}|B_2|^2 + \xi_{22}|B_3|^2 + \xi_{32}|A_2|^2 + \xi_{42}|A_3|^2)B_2 \\ & + \xi_{52}\overline{B_2}A_2^2 + (\xi_{62}B_3\overline{A_3} + \xi_{72}\overline{B_3}A_3)A_2, \end{aligned} \tag{8}$$

where $C_2 = A_2 e^{i\omega_{2r}}$ and $D_2 = B_2 e^{i\omega_{2r}}$. In the same way, using the projection $\boldsymbol{P}_3$, the following amplitude equations are derived.

$$\begin{aligned}\dot{A}_3 = &(-\omega_{3i} + \xi_{13}|A_3|^2 + \xi_{23}|A_2|^2 + \xi_{33}|B_3|^2 + \xi_{43}|B_2|^2)A_3 \\ &+\xi_{53}\overline{A_3}B_3^2 + (\xi_{63}A_2\overline{B_2} + \xi_{73}\overline{A_2}B_2)B_3, \qquad (9)\\ \dot{B}_3 = &(-\omega_{3i} + \xi_{13}|B_3|^2 + \xi_{23}|B_2|^2 + \xi_{33}|A_3|^2 + \xi_{43}|A_2|^2)B_3 \\ &+\xi_{53}\overline{B_3}A_3^2 + (\xi_{63}B_2\overline{A_2} + \xi_{73}\overline{B_2}A_2)A_3, \qquad (10)\end{aligned}$$

where $C_3 = A_3 e^{i\omega_{3r}}$ and $D_3 = B_3 e^{i\omega_{3r}}$. The complex constant coefficients ξ_{12}, $\xi_{22}, \ldots, \xi_{73}$ in Eqs. (7) through (10) can be numerically determined as functions of α, β, γ, c, δ and V_s. Above equations govern the time variations of the complex amplitudes A_2, A_3, B_2 and B_3 for the second and third modes and are coupled through the cubic nonlinear terms. The interactions between the second and third vibration modes are examined by solving numerically Eqs. (7) through (10).

Letting $A_2 = a_2 e^{i\phi_2}/2, A_3 = a_3 e^{i\phi_3}/2, B_2 = b_2 e^{i\psi_2}/2, B_3 = b_3 e^{i\psi_3}/2$, separating the real and imaginary parts of Eqs. (7) through (10). We obtain the first-order ordinary differential equations, which govern the amplitudes and the phases of A_2, A_3, B_2 and B_3. Next we define the phase difference $\Omega_2 = \psi_2 - \phi_2$ and $\Omega_3 = \psi_3 - \phi_3$. Finally the autonomous equations governing a_2, a_3, b_2, b_3, Ω_2 and Ω_3 are obtained.

In the first place, we consider the effects of nonlinear interaction terms on A_2 using Eq. (7). These classifications can be performed as in the case of A_3, B_2 and B_3. The nonlinear interaction terms are divided into the following classes: $(a)|A_2|^2A_2$, $|A_3|^2A_2$, $|B_2|^2A_2$, $|B_3|^2A_2$, $(b)\bar{A}_2B_2^2$ and $(c)A_3\bar{B}_3B_2$, $\bar{A}_3B_3B_2$. The nonlinear interaction terms in class (a) can modify the linear damping ratio of A_2. Thus, theses terms act like self-excitation terms. The coefficient B_2^2 of $\bar{A}_2$ in class (b) originate in the nonlinear terms which shows a periodic change. This term is same form which appears in parametrically excited system. The terms in class (c) are inhomogeneous terms. These terms act like the external excitation terms. The nonlinear interaction terms between the second and the third modes are divided into (a) and (c).

Figure 3 shows the transient time histories for a_2, b_2, a_3, b_3, Ω_2 and Ω_3 and the steady state pipe motion in the horizontal plane ($s = 0.7$) for $V_s = 7.7$. In this case, the second and the third modes of the pipe are simultaneously self-excited with two distinct natural frequencies i.e. $\omega_{2i} < 0$, $\omega_{3i} < 0$. The initial conditions are $a_2(0) = 0.01$, $b_2(0) = 0.02$, $\Omega_2(0) = 0.3\pi$, $a_3(0) = 0.01$, $b_3(0) = 0.02$ and $\Omega_2(0) = 0.3\pi$. a_2, b_2, a_3 and b_3 converge to the steady state. Ω_2 and Ω_3 gradually approach zero and $-\pi$ respectively. So, both the second and third mode flutter is planar. It is also clarified that the planes, on which second modal oscillation and the third modal oscillation are produced, are perpendicular. These planes in which the second and the third mode flutter occur depend on the initial conditions a_2, b_2, a_3, b_3, Ω_2 and Ω_3.

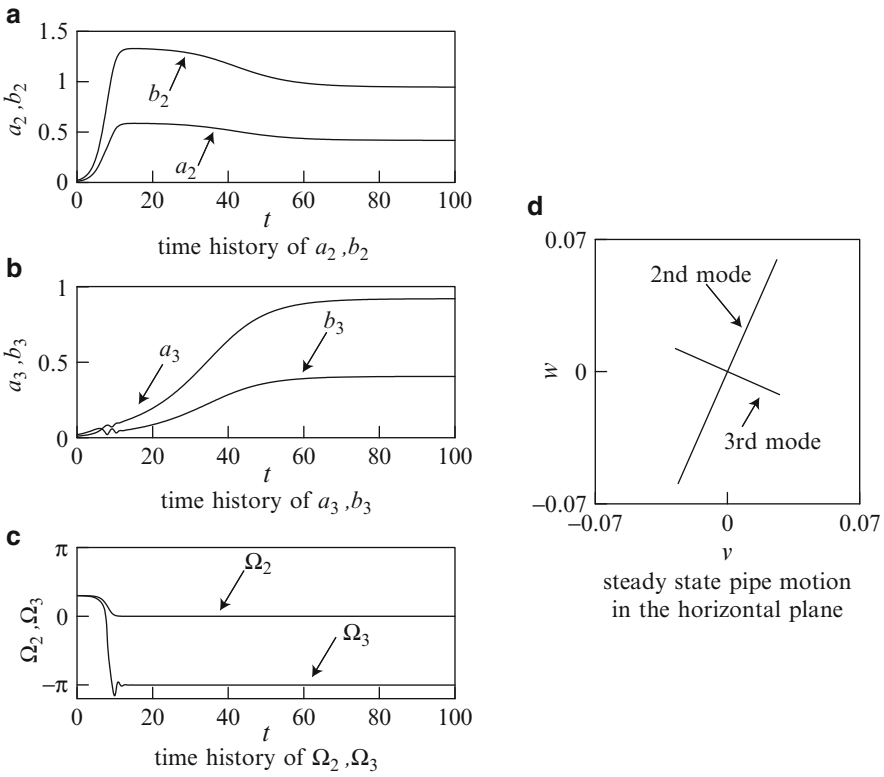

Fig. 3 Time histories of a_2, b_2, a_3, b_3, Ω_2 and Ω_3 for $V_s = 7.7$ and the steady state pipe motion in the horizontal plane. (**a**) Time history of a_2, b_2. (**b**) Time history of a_3, b_3. (**c**) Time history of Ω_2, Ω_3. (**d**) Steady state pipe motion in the horizontal plane

In the case of $B_3 \neq 0$, the third term of Eq. (7) $\xi_{22}|A_3|^2 A_2$ and the fifth term of Eq. (8) $\xi_{42}|A_3|^2 B_2$ serve as damping terms to reduce A_2 and B_2 respectively, since $\xi_{22} < \xi_{42} < 0$. Comparison of the size of these values reveals that the third mode flutter in $X - Z$ plane have more damping effects on B_2. The same idea applies well in A_2. As a result, the planes, on which second modal oscillation and the third modal oscillation are produced, become perpendicular.

4 Experiments

We conducted an experiment with a model that was based on the analytical model as described before and employs a 425 mm long silicon rubber pipe of 12 mm external diameter and 7 mm bore diameter. The equivalent bending rigidity EI, estimated

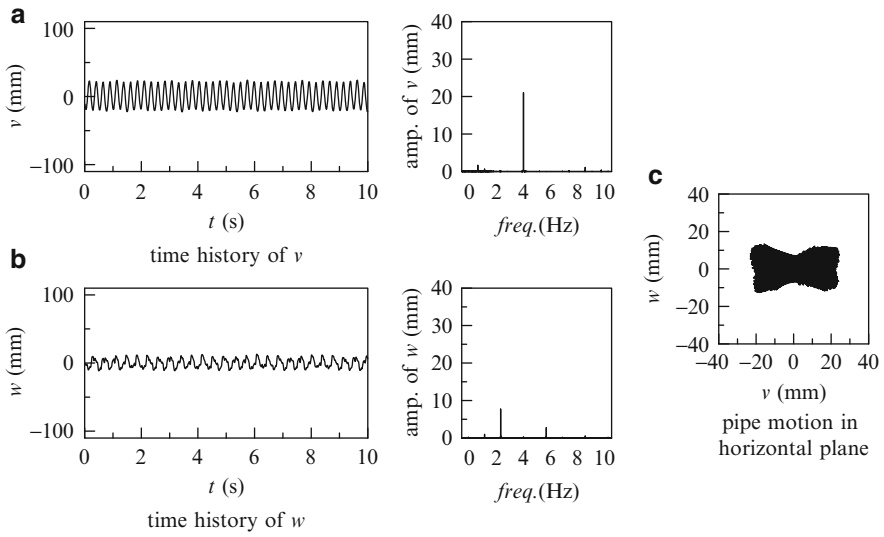

Fig. 4 Time histories and the pipe motion in rotated horizontal plane for $v_s = 3.7\,\mathrm{m/s}$. (**a**) Time history of v. (**b**) Time history of w. (**c**) Pipe motion in horizontal plane

using the first mode natural frequency $V_s = 0$, is $2.26 \times 10^{-3}\,\mathrm{Nm}^2$. The end mass is in the form of a brass ring fixed to the end of the pipe and the mass employed was $M = 19.6\,\mathrm{g}$. Water density $\rho = 1.0\,\mathrm{g/cm}^3$. The spatial motions of the flexible pipe were measured using an image processing system, based on the images from two CCD cameras, which is capable of performing measurements of a marker position in three dimensional space. The displacements v and w parallel to Y- and Z-axis respectively in a horizontal plane were then measures for a range of flow velocities. The mean flow velocity was measured by the electromagnetic flow-meter.

Over a certain value of mean flow velocity, non-planar pipe vibration was observed, shown in Fig. 4. This figure shows time histories of v and w at $v_s = 3.7\,\mathrm{m/s}$. This velocity is much higher than the critical velocity $v_{cr} = 2.2\,\mathrm{m/s}$, above which the second mode of the lateral pipe vibration is self-excited due to an internal flow. v has a dominant frequency, which corresponds to the natural frequency of the third mode. The frequency corresponds to the natural frequency of second mode is not observed. w has a dominant frequency, which corresponds to the natural frequency of the second mode. In short the plane in which planar vibration of third mode flutter occurred intersects at right angles with the plane planar second mode flutter occurred. Nonlinear interaction terms vw^2 and wv^2 produce the frequency components $\omega_3 - \omega_2$ and $2\omega_2 - \omega_3$ respectively.

At much higher velocity, the pipe oscillated in the third mode. The motions of the pipe vibration in its third mode were planar.

5 Conclusion

The mixed-mode vibration of the fluid-conveying cantilevered pipe with an end mass was experimentally observed under the condition that the flow velocity is much higher than the critical value for the second mode. Here the mixed-mode flutter includes both the second and third modes simultaneously. Complex amplitude equations of the second and third modes of the pipe vibration, which are coupled through the nonlinear terms caused by cubic nonlinear terms of the lateral pipe deflection, are derived with the use of the orthogonal condition between the linear eigenfunctions and their adjoint functions. It is clarified from the theoretical analysis that the planes, on which second modal oscillation and the third modal oscillation are produced, are perpendicular.

Acknowledgements The authors would like to thank Messrs. J. AJIRO, H. FURUYA, and Y. SHIMADA for their useful discussion and Mr. M. YAMAMOTO for his kind assistance.

References

Bajaj, A.K, Sethna, P.R.: Flow induced bifurcations to three-dimensional oscillatory motions in continuous tubes. SIAM J. Appl. Math. **44**(2), 270–286 (1984)

Carr, J.: Applications of Center Manifold Theory. Springer, New York (1981)

Chamara, P.A., Coller, B.D.: A study of double flutter. J. Fluid Struct. **19**, 863–879 (2004)

Copeland, G.S., Moon, F.C.: Chaostic flow-induced vibration of a flexible tube with end mass. J. Fluid Struct. **6**, 705–718 (1992)

Païdoussis M.P.: Fluid-Structure Interactions Slender Structures and Axial Flow, vol. 1. Academic, San Diego (1998)

Païdoussis, M.P.: Some unresolved issue in fluid-structure interactions. J. Fluid Struct. **20**, 871–891 (2005)

Païdousis, M.P., Semler, C.: Non-linear dynamics of a fluid-conveying cantilevered pipe with a small mass attached at the free end. Int. J. Non-linear Mech. **33**(1), 15–32 (1998)

Steindl, A., Troger, H.: Nonlinear three-dimensional oscillations of an elastically constrained fluid conveying viscoelastic tube with $\boldsymbol{O}(2)$-symmetry. Symp. Flow Indu. Vib. Noise **8**(152), 47–62 (1992)

Yoshizawa, M., Suzuki, T., Takayanagi, M., Hashimoto, K.: Nonlinear lateral vibration of a vertical fluid-conveying pipe with end mass. JSME Int. J. **41**(3), 652–661 (1998)

Parametric Study for Lock-In Detection in Vortex-Induced Vibration of Flexible Risers

Marko Keber, Marian Wiercigroch, and Jerzy Warminski

Abstract An observation that a parameter plot of a harmonically forced wake oscillator, which shows three distinct regions, in qualitative sense corresponds well with results of numerical and experimental investigations has prompted further investigations into dynamical behaviour of a flexible cylinder experiencing vortex-induced vibration. For this purpose, a reduced-order model representing a vertical pipe excited by surrounding fluid flow was built and certain aspects of its dynamics were studied. When resonance curves of a numerical and an analytical solution obtained with the method of multiple scales were compared, it became apparent that the former gives a much wider resonance region as the latter. This difference expectedly narrowed for lower values of the coupling strength parameter, indicating not only that the initial value might have been very large as defined in the method used, but also that because of this the overall dynamics were dominated by the linear part, the structure.

Keywords Flexible risers • Vortex-induced vibration • Wake oscillator • Lock-in dynamics

M. Keber (✉) • M. Wiercigroch
Centre for Applied Dynamics Research, School of Engineering, University of Aberdeen, Aberdeen AB24 3UE, Scotland, United Kingdom
e-mail: m.keber@abdn.ac.uk; m.wiercigroch@abdn.ac.uk

J. Warminski
Department of Applied Mechanics, Lublin University of Technology, Nadbystrzycka 36, 20-618 Lublin, Poland
e-mail: j.warminski@pollub.pl

M. Wiercigroch and G. Rega (eds.), *IUTAM Symposium on Nonlinear Dynamics for Advanced Technologies and Engineering Design*, IUTAM Bookseries (closed) 32, DOI 10.1007/978-94-007-5742-4_12,

1 Introduction

In the past three decades drilling for oil has moved into ever deeper waters and further from shore. Consequently, tools used in exploration and later in exploitation are subjected to harsher environments resulting in increased risk of fatigue and damage. This is true especially for structures such as risers, which are subjected to varying loading or excitation. Since future projections for offshore oil and gas exploration show that the trend of deepwater drilling will continue (Sasanow 2010) new demands will be imposed on designs of long, slender structures, fully or partially submerged, to guarantee their safe as well as cost effective operation.

From the perspective of dynamics, vortex-induced vibration (VIV) is commonly considered to be the most problematic phenomenon. This type of vibration, which is inherently nonlinear, is excited by the flow of the fluid surrounding the submerged structure, and in a certain speed range this causes vortices to shed behind the structure's bluff body. When the frequency of shedding approaches the natural frequency of the structure synchronisation of the two oscillations occurs. This synchronisation is manifested in large amplitudes of the structure and in a modified shedding pattern.

For practical purposes it is especially interesting to understand the onset of lock-in and how characteristics of the synchronisation region change under varying conditions. Such knowledge would lead to design solutions that would allow pipes and risers to avoid the critical regions of lock-in and thus prolong their operational life time.

Research presented in this paper is a step forward in an attempt to build a comprehensive model based on an approach using wake-oscillators for simulating the effect of vortex shedding. Wake oscillators have been used extensively in the past 30 years. Their popularity can be attributed especially to the fact that they can be easily adapted to different problems of VIV and, more importantly, to their efficiency with respect to computational time and complexity. However, because of their properties, they are capable of modelling only dynamics of cases where structural and fluid oscillations are synchronised. Therefore, the analysis is performed firstly in this region by employing methods of nonlinear dynamics to determine the system's parametric sensitivity and to give an indication of the effect of the forcing parameter on the amplitude as well as the shape of the resonance peak.

2 Model Description

Properties of a single wake oscillator forced by a harmonic function representing oscillations of a rigid riser were taken as the basis for this work. Its parametric analysis shows that there are three main regions, which can be very narrow when forcing from the structure is small and widen as excitation increases. With this increases also the transition area, in which a riser can experience a variety

of different oscillations before finally reaching the lock-in state (see Keber and Wiercigroch (2007) for more details). Since flexible risers experience the same excitation as the rigid ones, it can be expected that they will exhibit similar characteristics when speed of flow is varied. A simple phenomenological model of a vertical offshore riser has been built in order to verify how a flexible structure behaves during transition to lock-in.

Mathematical models in which geometrical complexity has been reduced to a minimum number of degrees of freedom have been used extensively for predicting the dynamic behaviour of submerged structures, especially for rigid cylinders (see for example a review by Gabbai and Benaroya (2005)). In many cases excellent correspondence with experimental data was obtained mainly because it could be assumed that properties of flow for at least the simplest, most basic examples didn't change much along the span of the structure. However, for a typical flexible riser a span-wise constant shedding pattern cannot be assumed even when the structure is submerged in fluid with perfectly uniform flow, as is the case here. For oscillations in the lock-in condition it can be predicted that no significant three-dimensional interactions between vortices will occur (Blevins 1990) but that the configuration of shedding will still be affected by the displacement of the structure as its parts can move in different directions with different amplitudes depending on their positions. Consequently, dynamics of both the structure as well as the fluid part of the coupled system need to be described with PDEs that include span-wise position z as a variable:

$$m^* \frac{\partial^2 v(z,t)}{\partial t^2} + EI \frac{\partial^4 v(z,t)}{\partial z^4} - T \frac{\partial^2 v(z,t)}{\partial z^2} = F_F \tag{1}$$

$$\frac{\partial^2 q(z,t)}{\partial t^2} + \lambda \Omega_R \left(q(z,t)^2 - 1\right) \frac{\partial q(z,t)}{\partial t} + \Omega_R^2 q(z,t) = F_S \tag{2}$$

The structural part is modelled as an Euler-Bernoulli beam with bending stiffness $E\,I$ and tension T, which is considered to be constant for simplicity. Effects of vortex shedding due to fluid flow are described with a separate, van der Pol-type equation (Eq. (2)) built by Facchinetti et al. (2004). Transfer of energy between the structural and fluid part is achieved through coupling terms, which for the latter is of the inertial type, as suggested in Facchinetti et al. (2004):

$$F_S = A \frac{\partial^2 v(z,t)}{\partial t^2} \tag{3}$$

For the structural part the input of energy is defined by the lift force, while the hydrodynamic damping acts as a limiting force:

$$F_F = \frac{1}{4} C_{L_0} \rho_F D U_0^2 q(t) - \frac{1}{2} C_D \rho_F D U_0 \frac{\partial v(z,t)}{\partial t} \tag{4}$$

2.1 Model Reduction

Configurations of forcing and flow condition as described above permit a reduction of the system to modal space of a single structural normal mode. By taking into account that lock-in occurs in the vicinity of the natural frequency, it can be assumed that the shape of the structure's response under uniform flow will closely resemble the shape of the normal mode that would be excited by the same natural frequency. In cases of linear systems, orthogonality of normal modes applies:

$$\int_0^1 \tilde{v}_n(z)\,\tilde{v}_i(z) \;=\; \begin{cases} 0; & n \neq i \\ \frac{L}{2}; & n = i \end{cases} \tag{5}$$

and the standard Galerkin procedure can be used to limit the dynamics of the distributed system only to its temporal part by expressing the solution in the following form:

$$v(z,t) \;=\; \sum_{n=1}^{\infty} v_n(t)\,\sin(\kappa\, z); \qquad q(z,t) \;=\; \sum_{n=1}^{\infty} q_n(t)\,sin(\kappa\, z) \tag{6}$$

where $sin\,(\kappa\, z)$ was chosen to describe modal shapes of a vertical offshore riser pinned at both ends. Such boundary conditions, although not always achievable, are most ideal from the point of view of curvatures and stresses since ends of the structure are not constrained. Therefore, the industry is developing and implementing solutions that resemble hinges to allow riser end rotations.

Because of the interaction, span-wise distribution of shedding (modelled by the variable $q(z,t)$) will follow the displacement of the structure $v(z,t)$. Therefore, its spatial component can be set to be the same as the spatial component of $v(z,t)$:

$$\tilde{q}_n(z) \;=\; \tilde{v}_n(z) \;=\; \sin\left(n\,\pi\,\frac{z}{L}\right) \;=\; \sin(\kappa z) \tag{7}$$

For the i-th structural mode the reduced-order model of the system described by Eqs. (1) and (2) becomes:

$$\frac{d^2 v_i(\tau)}{d\,\tau^2} + \omega_R^2\, v_i(\tau) \;=\; a\,\Omega_R\,\frac{d\,v_i(\tau)}{d\,\tau} \;+\; b\,\Omega_R^2\,q_i(\tau) \tag{8}$$

$$\frac{d^2 q_i(\tau)}{d\,\tau^2} + \lambda\,\Omega_R\,\left(\gamma\,q_i(\tau)^2 \;-\; 1\right)\frac{d q_i(\tau)}{d\,\tau} \;+\; \Omega_R^2\,q_i(\tau) \;=\; A\,\frac{d^2 v_i(\tau)}{d\,\tau^2} \tag{9}$$

where variables $v_i\,(\tau)$ and $q_i\,(\tau)$ have been nondimensionalised with respect to time:

$$\tau \;=\; t\,\omega_c \tag{10}$$

Reference frequencies ω_R and Ω_R are ratios of actual natural and shedding frequencies with the chosen arbitrary frequency ω_c:

$$\omega_R = \frac{\omega_{0_i}}{\omega_c}; \qquad \Omega_R = \frac{\Omega_{F_i}}{\omega_c} \tag{11}$$

In the analysis that follows the chosen frequency is that of the first mode, i.e. $\omega_c = \omega_{0_1}$, which gives for the perfect lock-in $\omega_R = \Omega_R = 1$, yielding a periodic and harmonic structural vibration and quasi-harmonic oscillation of the fluid variable, as would be expected. However, outside lock-in only amplitude and frequency change but there is no immediate indication of qualitative change in the response for the initial values of coupling strength $A = 12$ and the van der Pol parameter $\lambda = 0.3$ (Facchinetti et al. 2004). Consequently, it can be inferred that, although the model is very good for the lock-in region, more information is needed to understand how it behaves on its border, or even outside it. To this end, an analytical solution of Eqs. (8) and (9) was sought in the first step.

3 Analytical Solution of the Coupled Equations

Damping in Eq. (2) is the only nonlinear term in the coupled system. The advantage of including this term is that it allows the fluid equation to incorporate self-excited oscillations while limiting its maximum amplitude, which is precisely what occurs in VIV (Blevins 1990). On the other hand, this same term is responsible for the change in dynamical behaviour of the harmonically forced van der Pol. This can range from periodic, almost harmonically shaped oscillation, to quite complex transient behaviour, even chaotic response (Thompson and Stewart 2002), depending predominantly on numerical values of two main parameters—the coupling strength A and the van der Pol parameter λ. When coupled with a linear oscillator, as is done here, additional factors will most probably need to be considered. For this reason, all forces in both oscillators are multiplied by an arbitrary parameter ε:

$$\frac{d^2 v_i(\tau)}{d\tau^2} + \omega_R^2 v_i(\tau) = (\varepsilon\alpha)\,\Omega_R \frac{d v_i(\tau)}{d\tau} + (\varepsilon\beta)\,\Omega_R^2 q_i(\tau) \tag{12}$$

$$\frac{d^2 q_i(\tau)}{d\tau^2} + \Omega_R^2 q_i(\tau) = -(\varepsilon\lambda)\,\Omega_R \left(\gamma\, q_i(\tau)^2 - 1\right) \frac{d q_i(\tau)}{d\tau} + (\varepsilon\Delta) \frac{d^2 v_i(\tau)}{d\tau^2} \tag{13}$$

In the context of the analysis that follows, ε acts as a book-keeping device without prejudice about its size (Nayfeh 2000a). However, for better understanding of the procedure, terms on the right-hand side of Eqs. (12) and (13) can initially be presumed to be at least an order of magnitude smaller than the underlying linear autonomous systems. Forcing then acts as a small perturbation of the stable solution. Furthermore, by setting ε as small, the coupled system is at the beginning classified as weakly nonlinear and its analytical approximate solution is obtained with the help of the Method of Multiple Scales (see for example Nayfeh (2000b) for details).

A first-order expansion is carried out on nondimensional time:

$$\tau \;=\; T_0 \;+\; \varepsilon T_1 \tag{14}$$

Because the independent variable is now expressed with two time scales, T_0 and T_1, the displacement functions must also reflect this change:

$$v_i(\tau) \;=\; w_0(T_0, T_1) + \varepsilon w_1(T_0, T_1); \quad q_i(\tau) \;=\; q_0(T_0, T_1) + \varepsilon q_1(T_0, T_1) \tag{15}$$

For convenience, the structural nondimensionalised frequency ω_R is expressed with the shedding frequency Ω_R (representing frequency of external forcing) and a small perturbation $\varepsilon\,\sigma$ around it:

$$\omega_R^2 \;=\; \Omega_R^2 \;-\; \varepsilon\,\sigma \tag{16}$$

After substitution of Eqs. (15) and (16) into Eqs. (12) and (13), only terms related to ε^0 and ε^1 are collected. This way the system is expanded into four coupled equations, which are solved sequentially:

$$\begin{aligned} \varepsilon^0 : D_0^2\, w_0 + \Omega_R^2\, w_0 &= 0 \\ D_0^2\, q_0 + \Omega_R^2\, q_0 &= 0 \end{aligned} \tag{17}$$

$$\begin{aligned} \varepsilon^1 : D_0^2 w_1 + \Omega_R^2 w_1 &= -2D_0 D_1 w_0 \;+\; \alpha \Omega_R D_0 w_0 \;+\; \beta \Omega_R^2 q_0 \;+\; \sigma w_0 \\ D_0^2 q_1 + \Omega_R^2 q_1 &= -2D_0 D_1 q_0 + \Delta D_0^2 w_0 + \lambda \Omega_R D_0 q_0 - \lambda \Omega_R \gamma D_0 q_0 q_0^2 \end{aligned} \tag{18}$$

where D_0, D_1, and D_0^2 represent the first and second order derivatives, respectively:

$$D_0 \;=\; \frac{\partial}{\partial T_0}; \qquad D_1 \;=\; \frac{\partial}{\partial T_1}; \qquad D_0^2 \;=\; \frac{\partial^2}{\partial T_0^2} \tag{19}$$

Area 1 in Fig. 1 encloses the region where oscillation of the fluid variable $q(\tau)$ is synchronised with the forcing frequency for the single wake model (Keber and Wiercigroch 2007). In order to simulate the same kind of response for the wake coupled with a flexible linear structure, the first terms in variable expansions (Eq. (15)) are expressed in complex form as:

$$w_0 \;=\; X(T_1)\, e^{i\,\Omega_R\, T_0} \;+\; \overline{X}(T_1)\, e^{-i\,\Omega_R\, T_0} \tag{20}$$

for the structural part, and:

$$q_0 \;=\; Y(T_1)\, e^{i\,\Omega_R\, T_0} \;+\; \overline{Y}(T_1)\, e^{-i\,\Omega_R\, T_0} \tag{21}$$

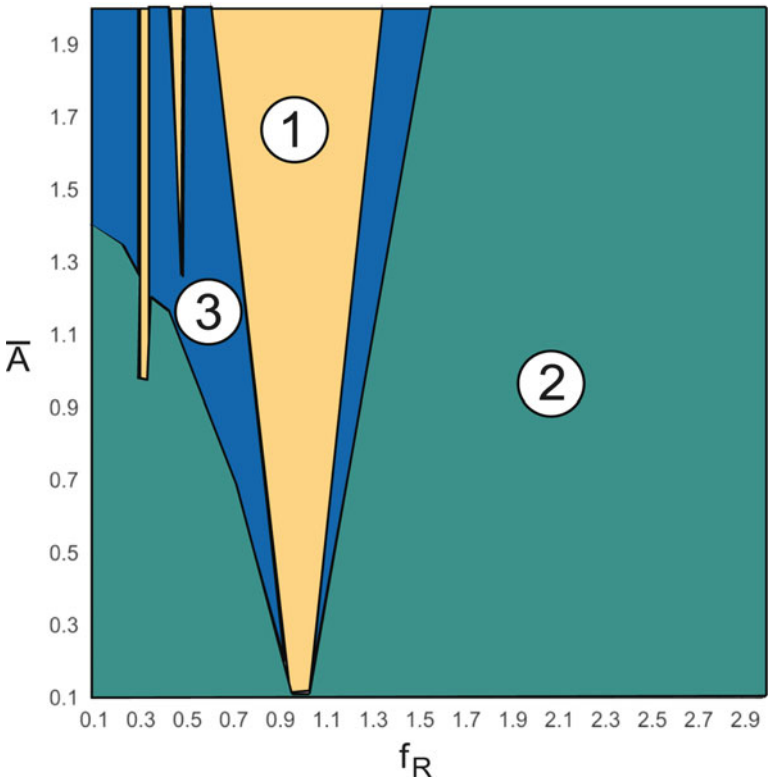

Fig. 1 Parameter plot showing qualitatively different responses of the forced single wake oscillator for varying frequency ratio f_R and forcing intensity $\overline{A}$ (Keber and Wiercigroch 2007): Area 1—lock-in region (periodic, harmonic oscillation), area 2—transition to lock-in (periodic and harmonic oscillation can occur after transient), area 3—out of lock-in (oscillation can resemble harmonic motion but generally it is not periodic, but quasiperiodic)

for the fluid part, which are also solutions of the zeroth-order equations (Eq. (17)). These are then substituted into Eq. (18) to get the correction of the first order. After reorganisation of terms the following system of equations is obtained:

$$\begin{aligned} &D_0^2 w_1(T_0,T_1) + \Omega_R^2 w_1(T_0,T_1) \\ &\quad = -e^{i\Omega_R T_0}\left(-\sigma X(T_1) - i\alpha\Omega_R^2 X(T_1) - \beta\Omega_R^2 Y(T_1) + i2\Omega_R D_1 X(T_1)\right) \\ &\qquad -e^{-i\Omega_R T_0}\left(-\sigma\overline{X}(T_1) + i\alpha\Omega_R^2\overline{X}(T_1) - \beta\Omega_R^2\overline{Y}(T_1) - i2\Omega_R\overline{X}(T_1)\right) \end{aligned} \quad (22)$$

$$\begin{aligned} &D_0^2 q_1(T_0,T_1) + \Omega_R^2 q_1(T_0,T_1) \\ &\quad = i e^{-i3\Omega_R T_0}\gamma\lambda\Omega_R^2\overline{Y}(T_1)^3 - , e^{i3\Omega_R T_0}\gamma\lambda\Omega_R^2 Y(T_1)^3 \\ &\qquad -e^{i\Omega_R T_0}\left(\Delta\Omega_R^2 X(T_1) - i\lambda\Omega_R^2\overline{Y}(T_1) + i\gamma\lambda\Omega_R^2\overline{Y}(T_1)Y(T_1)^2\right. \end{aligned}$$

$$+ i2\,\Omega_R\,D_1 Y(T_1)) - e^{-i\,\Omega_R\,T_0}\,\left(\Delta\,\Omega_R^2\,\overline{X}(T_1) - i\lambda\,\Omega_R^2\,\overline{Y}(T_1)\right.$$
$$\left. - i\gamma\,\lambda\,\Omega_R^2\,Y(T_1)\,\overline{Y}(T_1)^2 - i2\,\Omega_R\,D_1\overline{Y}(T_1)\right) \tag{23}$$

from where terms related to $e^{\pm i\,\Omega_R\,T_0}$ need to be equated to zero in order to eliminate secular properties of the final solution (Nayfeh 2000b), hence the correction to the response of the linear system will not include contributions at excitation frequency Ω_R. Complex amplitudes $X(T_1)$, $\overline{X}(T_1)$, $Y(T_1)$, and $\overline{Y}(T_1)$ in the remaining nonzero terms are at this stage converted to polar form for practical reasons:

$$X(T_1) = \frac{1}{2}\,x(T_1)\,e^{i\,\Phi_1(T_1)}; \quad \overline{X}(T_1) = \frac{1}{2}\,x(T_1)\,e^{-i\,\Phi_1(T_1)} \tag{24}$$

$$Y(T_1) = \frac{1}{2}\,y(T_1)\,e^{i\,\Phi_2(T_1)}; \quad \overline{Y}(T_1) = \frac{1}{2}\,y(T_1)\,e^{-i\,\Phi_2(T_1)} \tag{25}$$

Finally, corrections $w_1(T_0, T_1)$ and $q_1(T_0, T_1)$ can be calculated and by expressing them with trigonometric functions, the total solution in the time domain can be defined as:

$$v(\tau) = x(T_1)\cos\left(\Omega_R T_0 + \Phi_1(T_1)\right) \tag{26}$$

$$q(\tau) = y(T_1)\cos\left(\Omega_R T_0 + \Phi_2(T_1)\right) - \tfrac{\varepsilon}{32}\,y(T_1)^3\gamma\lambda\sin\left(3\Omega_R T_0 + 3\Phi_2(T_1)\right) \tag{27}$$

where $x(T_1)$ and $y(T_1)$ are amplitudes of structural and fluid responses, respectively, while $\Phi_1(T_1)$ and $\Phi_2(T_1)$ are the corresponding phases.

As expected, the response of the system has an underlying linear characteristic with a sinusoidal shape, which, depending on the strength of the nonlinearity, is more or less skewed at the peaks for the fluid part (Eq. (27)). However, the more important properties of the system's nature are given by the modulation equations, which define the amplitudes and phase angles in Eqs. (26) and (27). These are obtained by treating terms previously eliminated from Eq. (22). Expressed in trigonometric form, their real and imaginary parts can be easily separated and equated to zero to give further reduction for the coupled system:

$$\frac{dx(T_1)}{dT_1} = \frac{1}{2}\,\Omega_R\,\left(\alpha\,x(T_1) - \beta\,y(T_1)\,\sin\left(\Phi_1(T_1) - \Phi_2(T_1)\right)\right) \tag{28}$$

$$\frac{dy(T_1)}{dT_1} = \frac{1}{8}\Omega_R\left(4\lambda y(T_1) - \gamma\lambda y(T_1)^3 - 4\Delta x(T_1)\sin\left(\Phi_1(T_1) - \Phi_2(T_1)\right)\right) \tag{29}$$

$$\frac{d\Phi_1(T_1)}{dT_1} = \frac{\omega_R^2 - \Omega_R^2}{2\,\Omega_R} - \frac{\beta\,\Omega_R\,y(T_1)\,\cos\left(\Phi_1(T_1) - \Phi_2(T_1)\right)}{2\,x(T_1)} \tag{30}$$

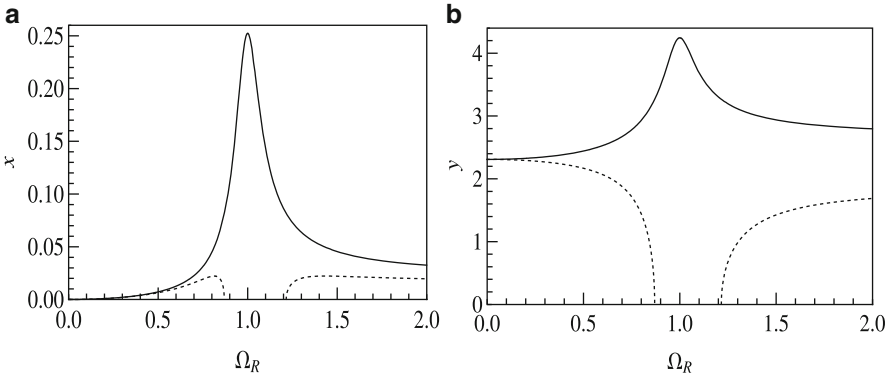

Fig. 2 Solutions of modulation equations for $A = 12$ and $\lambda = 0.3$: (**a**) amplitude of the structure's response $x(T_1)$, (**b**) amplitude of the shedding variable $y(T_1)$

$$\frac{d\Phi_2(T_1)}{dT_1} = \frac{\Delta\,\Omega_R\,x(T_1)\,\cos\left(\Phi_1(T_1) - \Phi_2(T_1)\right)}{2\,y(T_1)} \tag{31}$$

Again, periodic solutions are extracted from the above system of equations by setting the rates of change of all variables to zero:

$$\frac{dx(T_1)}{dT_1} = \frac{dy(T_1)}{dT_1} = \frac{d\Phi_1(T_1)}{dT_1} = \frac{d\Phi_2(T_1)}{dT_1} = 0 \tag{32}$$

Graphs in Fig. 2 show interesting solutions of variables $x(T_1)$ and $y(T_1)$. For both the structure and the fluid, two analytical solutions appear, one of which suddenly disappears as the frequency Ω_R approaches resonance. Stability of individual points of both solutions was determined next (see for example Thomsen (1997) for details of the method). Eigenvalues of the Jacobian matrix for points on the first curve (continuous line in Fig. 2) have either negative real values, or are complex numbers with negative real part, which implies that this solution may be stable for all Ω_R. Conversely, negative eigenvalues are observed for the second solution (dashed line in Fig. 2) only until it disappears (its real part becomes zero). Then the eigenvalues can be real or complex and negative or positive. Better understanding of what is happening in this region would be required before a definite statement could be made regarding the stability of the second solution.

4 Preliminary Parametric Study

Dynamical responses of any structure are determined by external forcing. Therefore, in systems like the one studied here, coupling, through which energy is exchanged, must be evaluated very carefully. Of particular interest in this study is the dominant

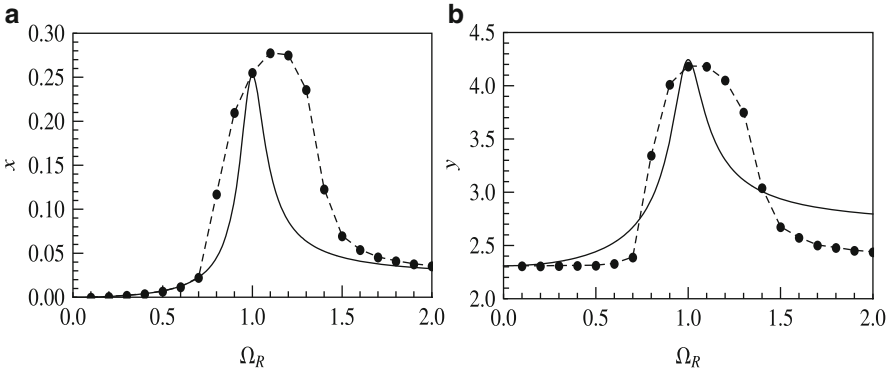

Fig. 3 Comparison of analytical (—) and numerical (− • −) solutions of Eqs. (8) and (9) with $A = 12$: (**a**) amplitude of the structure's response $x(T_1)$, (**b**) amplitude of the shedding variable $y(T_1)$

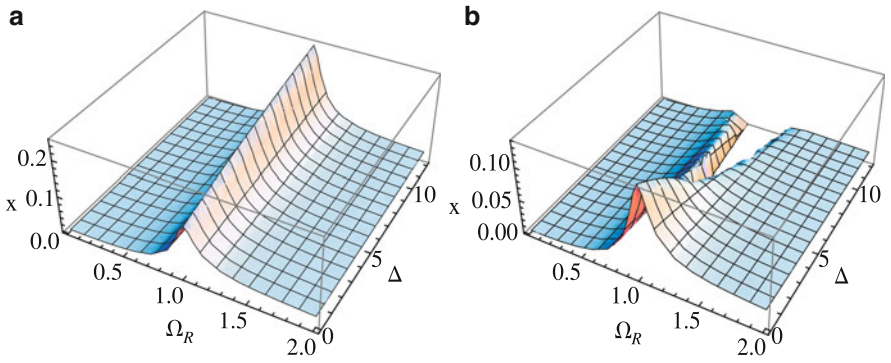

Fig. 4 Change of amplitude $x(T_1)$ as coupling strength A is varied from 0 to 12: (**a**) Solution 1, (**b**) solution 2

influence of the structure over the fluid. This becomes evident once the wake oscillator model is used outside the perfectly synchronised region, where effects of nonlinearity are not observed (at least for the typically small initial conditions used here—$v(0) = \dot{v}(0) = q(0) = 0, \dot{q}(0) = 0.01$). By varying the coupling strength A, evolutions of amplitudes and shapes of resonance curves could be plotted.

Comparisons of numerical and analytical solutions shown in Fig. 3 for the initial value $A = 12$ indicate that despite the almost perfect correspondence at $\Omega_R = 1$, the forcing of the wake oscillator is large and that its definition in terms of the method used should be re-evaluated. On the other hand, larger forcing of the wake gives a wider lock-in region for structural as well as shedding displacement, which is typical for vortex-induced vibration.

As the coupling strength is decreased, the width of the region decreases with it and soon becomes similar to the analytical solution. Interestingly, a relatively small difference can be seen along the A axis in Fig. 4a, indicating a smaller

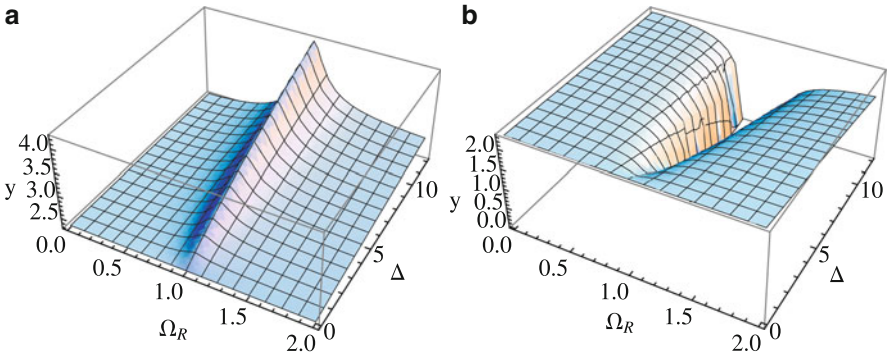

Fig. 5 Change of amplitude $y(T_1)$ as coupling strength A is varied from 0 to 12: (**a**) Solution 1, (**b**) solution 2

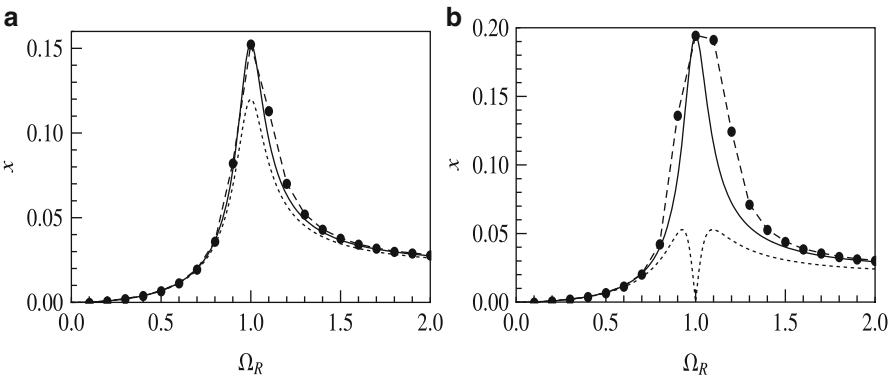

Fig. 6 Comparison of analytical (—— sol. 1, — — — sol. 2) and numerical solutions (— • —) for: (**a**) $A = 5.046067$, (**b**) $A = 1.2$

influence of the strength on the width of the analytical solution. However, it does have a much bigger effect on the second solution, which at smaller values of A becomes continuous for all Ω_R when plotted on a graph of real values (Figs. 4b and 5b). This inversion from complex to real numbers occurs at about $A = 5.05$. See Fig. 6 for comparisons of resonance curves obtained analytically (two solutions) and numerically at the point of inversion and with A ten times smaller than originally.

Future research should give more insight into what is happening around this particular value with respect to stability and how it varies when values of other parameters change. It should also evidence what role nonlinear damping in the fluid equation plays in the properties of the second solution.

5 Conclusions

Results presented here clearly show that many open questions remain unanswered and that much work will need to be invested in order to gain good understanding of even the simplest model of a flexible riser experiencing VIV. The method of multiple scales used in the analytical approach shows interesting results, namely two distinct resonance curves for the structural as well as for the fluid part. One of the curves experiences a jump from complex to real values as coupling strength is varied, which has implications also for the stability of the solution. Consequently, this will require a dedicated analysis.

Additional issues related to coupling strength have to do with the width of the lock-in region and, primarily, with the suitability of the current definition of forcing terms for the analytical method. Observations based on evolutions of VIV in the time domain (especially the response of the van der Pol equation) suggest that the system may have weakly nonlinear properties since time series do not appear to depart very much from perfectly linear oscillation. However, actual strength of the nonlinearity has yet to be determined. In future work, the analytical solution will be formulated in the second order approximation in order to try to get better agreement with direct numerical simulations.

Acknowledgements Marian Wiercigroch and Jerzy Warminski would like to acknowledge support from the European Union (FP7/2007-2013), FP7–REGPOT–2009–1, under grant agreement No. 245479.

References

Sasanow, S.: Deepwater developments. Pet. Rev. **64**(760), 14–15 (2010)

Keber, M., Wiercigroch, M.: A reduced order model for vortex-induced vibration of a vertical offshore riser in lock-in. In: Proceedings of the IUTAM Symposium on Fluid-Structure Interaction in Ocean Engineering, Hamburg, Germany (2007)

Gabbai. R.D., Benaroya, H.: An overview of modeling and experiments of vortex-induced vibration of circular cylinders. J. Sound Vib. **282**, 575–616 (2005)

Blevins, R.D.: Flow-Induced Vibration. Van Nostrand Reinhold, New York (1990)

Facchinetti, M.L., de Langre, E., Biolley, F.: Coupling of structure and wake oscillators in vortex-induced vibration. J. Fluids Struct. **19** 123–140 (2004)

Thompson, J.M.T., Stewart, H.B.: Nonlinear Dynamics and Chaos, 2nd edn. Wiley, New York (2002)

Nayfeh, A.H.: Nonlinear Interactions: Analytical, Computational, and Experimental Methods. Wiley, New York (2000)

Nayfeh, A.H.: Perturbation Methods. Wiley, New York (2000)

Thomsen, J.J.: Vibrations and Stability: Order and Chaos. McGraw Hill, London (1997)

Importance of Accurately Modeling Nonlinear Damping in Predicting Parametric Ship Rolling

Hisham Moideen and Jeffrey M. Falzarano

Abstract Parametric rolling has become an important design issue in the safe operation of large high-speed container ships. This interest is partly based upon the well-published large amplitude rolling incident of the APL China several years ago and numerous other incidents which have also since come to light. What we have found in our research is that a simple linear model of roll damping does not accurately predict the threshold nature of this phenomenon. However, when we accurately include nonlinear damping we are able to capture the qualitative nature of this phenomenon. Moreover the Mathieu Ince-Strutt stability diagram is limited to linear harmonic excitation. What we have done in this work is to extend the Mathieu Ince-Strutt stability diagram to include non-harmonic excitation and nonlinear damping.

Analysis of ship parametric rolling has generally been restricted to simple analytical models and sophisticated time domain simulations. However, simple analytical models do not capture all the critical dynamics while time-domain simulations are time consuming to implement. Our model captures the essential dynamics of the system without over simplification. This work incorporates important aspects of the system and assesses the significance of including or ignoring these aspects. Many of the previous works on parametric rolling make the assumption of linearized and harmonic behaviour of the time-varying restoring arm or metacentric height. This assumption enables modelling the roll as a Mathieu equation.

Keywords Ship parametric rolling • Nonlinear damping • Safe operation

H. Moideen • J.M. Falzarano (✉)
Texas A&M University, College Station, TX 77840, USA
e-mail: mhisham@neo.tamu.edu; jfalzarano@civil.tamu.edu

M. Wiercigroch and G. Rega (eds.), *IUTAM Symposium on Nonlinear Dynamics for Advanced Technologies and Engineering Design*, IUTAM Bookseries (closed) 32, DOI 10.1007/978-94-007-5742-4_13,

1 Introduction

Analysis of ship parametric roll has generally been restricted to simple analytical models and sophisticated time domain simulations. Simple analytical models do not capture the all the critical dynamics while time-domain simulations are often time consuming to implement. Our model captures the essential dynamics of the system without over simplification. This work incorporates various important aspects of the system and assesses the significance of including or ignoring these aspects. Many of the previous works on parametric roll make the assumption of linearized and harmonic behavior of the time-varying restoring arm or metacentric height. This assumption enables modeling the roll motion as a Mathieu equation.

It is well known that most hull forms especially container ships, Ro-Ro ships and fishing trawlers are found to be prone to parametric roll instability are asymmetric about the design water line. Hence the variation in the metacentric height will be asymmetric as well. This asymmetry invalidates the harmonic approximation. Studies by other researchers (Spyrou and Thompson 2000; ABS 2004) have shown that the harmonic assumption is very crude.

Many of the past research on ship parametric roll have been to predict the occurrence of parametric roll. Fewer analytical methods have been developed to predict the resulting roll amplitude. Some studies were done by Bulian et al. (2003). In his study a harmonic form was assumed for the response with a slowly varying amplitude and phase. However this required a complicated calculation and statistical linearization. Due to the large amplitude of motion resulting from the parametric instability the effects of non-linear damping also become important. Non-linear damping controls the bounded roll motion amplitude. So far there have been very few attempts to incorporate the effects of non-linear damping into analytical model to predict roll motion amplitude. Many researchers have attempted to evaluate the effects of non-linear damping using time simulations which is very time consuming and does not help in understanding the behavior of the non-linearity throughout the entire domain.

Ships typically have varying forward speeds and hence varying encounter or exciting frequency. This property of ships makes them susceptible to both sub and super harmonic parametric resonance and possible instability as compared to offshore structures. Perturbation methods and harmonic assumption greatly affect the domain under which boundaries between the stable and unstable regions are valid. Extending the model to higher harmonics will enable accurate prediction over the entire range of operation. Such simple yet more accurate models can be used as benchmarks to predict parametric instability as well as bounded roll motion amplitude which in-turn can be utilized in the preliminary design stage so as to avoid hull forms prone to parametric rolling.

2 Background

Ship rolling motions is perhaps the most studied of the ship motions considering the disastrous consequences of failure. Large amplitude ship rolling motions can lead to progressive flooding and may eventually lead to the capsizing or foundering of a ship. Roll motion for ships is more complicated as compared to the other ship motions due to the presence of a non-linear restoring moment and small linear radiation damping. The presence of light damping leads to large amplitude motion when forced at the resonant frequency. As a consequence of the large amplitude roll motion the non-linear viscous damping becomes important and this further adds to the complexity of the analysis. Hence many studies have been carried to out to predict ship roll motion in regular seas. The beam sea condition is believed to produce maximum rolling and hence has been extensively analyzed, see e.g. Nayfeh (1986). Falzarano et al. (1990) analyzed the complicated dynamics involved in roll motion leading to capsize using the Melnikov method. The beam seas rolling can be controlled with additional dampening such as that provided by bilge keels, roll tanks, stabilizing fins, etc.

Apart from the beam sea capsizing condition, capsizing in the astern or following seas has also been analyzed (Paulling 1961; Hamamoto et al. 1996; Umeda et al. 1995).

Parametric rolling is a form of parametric vibration due to time varying stiffness. Studies have shown that for some ships this phenomenon can lead to larger amplitude rolling motion in comparison to the beam seas condition. The change in the underwater hull form and hence the variation of the righting lever in waves leads to a time varying stiffness. If the variation in stiffness is large enough, it can result in large amplitude motion and eventual capsize. Numerical modeling of parametric rolling of ships in regular waves has been studied (Umeda et al. 2004; Bulian et al. 2004; Munif and Umeda 2006). The Mathieu instability criterion is the most common method used to determine the onset of parametric roll. Most of the studies have been done with stability charts that do not indicate the effects of damping. Damping dramatically affects the boundaries between the stable and unstable region. Among container ships the post-Panamax container ship (C11 class) is the most studied vessel as a result of the cargo damage it suffered in 1998. The effect of parametric roll on the failure of container lashing system was studied by the SNAME ad-hoc panel #13 on Parametric Rolling (France et al. 2001). Spyrou et al. (2008) also studied the prediction potential of the parametric rolling for the post Pana-max container ships. This current paper discusses the methods commonly used to study parametric roll. One of the most common methods is to use simple Ince-Strutt stability diagram for Mathieu's equation in predicting the onset of parametric roll. A major drawback of the method is that the Ince-Strutt diagram for Mathieu's equation is generic and does not depend on the ship characteristics. A stability chart which depends on the ship parameters would be a more accurate approach.

Since parametric excitation can lead to large amplitude roll motion, the effects of non-linear damping cannot be neglected. Nonlinear roll damping may lead to bounded motion. Hence incorporating the effects of non-linear damping into stability charts would give a more realistic prospect of predicting roll behavior Hence without getting into complicated analyses, we can analyze the occurrence of parametric roll and also predict the roll motion amplitude using these charts at an early design stage.

3 Parametric Roll Equation

The roll equation of motion in general for linear uncoupled motion is given by

$$(I + A(\omega_D))\ddot{\phi} + B(\omega_D)\dot{\phi} + C\phi = M\cos(\omega t) \tag{1}$$

Where,

Φ – Roll Amplitude
I – Moment of Inertia about Roll Axis
A(ω) – Added Interia
B(ω) – Roll radiation wave damping
C – Restoring moment in roll $= \Delta \bullet GM$
M – External roll moment
ω – Forcing Frequency

For the case of head/astern sea there would be no direct roll excitation. One would expect no motion considering (1). But as discussed, (1) only represents linear damping and stiffness. This is one of the assumptions in linear strip theory where the wave profile is approximated by a flat surface at the design draft. If one considers the actual wave profile then the underwater hull form of the vessel changes as the wave passes by the vessel. This leads to a time varying restoring moment and hence a time varying stiffness.

The parametric roll equation of motion in roll considering time varying hydrostatics is given by

$$(I + A(\omega_D))\ddot{\phi} + B(\omega_D)\dot{\phi} + C(t)\phi = 0 \tag{2}$$

Where,

$$\mathrm{C(t)} = \Delta g \bullet GZ(t)$$

GZ(t) – Time varying roll restoring arm
$\omega_D = \omega_n\sqrt{1-\zeta^2}$ – Damped natural frequency, ω_n -natural frequency
ζ – Damping ratio

Note that in (2) the nonlinear viscous damping is not yet explicitly considered in the roll equation of motion.

The righting arm of a vessel is generally approximated by a polynomial function of the roll angle.

$$GZ = C_1\phi + C_3\phi^3 + C_5\phi^5 \ldots \tag{3}$$

Here GM (metacentric height) of the vessel is given by slope of the GZ curve at origin, If we linearize and neglect higher order terms (since they are important only for large amplitudes of roll), then (2) becomes,

$$\left(I + A\left(\omega_D\right)\right)\ddot{\phi} + B\left(\omega_D\right)\dot{\phi} + \Delta GM(t)\phi = 0 \tag{4}$$

If the time varying GM is modeled as

$$GM(t) = GM_0 + \delta GM\cos\left(\omega t\right) \tag{5}$$

Where, GM_0-still water GM

Using the following transformation, Eq. (3) is converted into a non-dimensional form,

$$\begin{aligned} &\tau = \omega t, \quad \omega_D = \sqrt{\frac{g\Delta GM_0}{\left(I + A(\omega_D)\right)}}, \quad (\,)' = \frac{d}{d\tau} \\ &\alpha = \left(\frac{\omega_D}{\omega}\right)^2, \quad \gamma = \frac{\delta GM}{GM_0}\alpha, \quad \mu = \frac{B\left(\omega_D\right)}{\left(I + A\left(\omega_D\right)\right)\omega} \end{aligned} \tag{6}$$

$$\frac{d^2}{d\tau^2}\phi + \mu\frac{d}{d\tau}\phi + \left(\alpha + \gamma\cos\left(\tau\right)\right)\phi = 0 \tag{7}$$

With $\mu = 0$, Eq. (6) represents a typical Mathieu Type equation (undamped). The Ince-Strutt diagram/Mathieu stability charts help determine the occurrence of parametric vibration.

Hence by determining the GM variation in waves one can predict the occurrence of parametric roll using the Ince-Strutt diagram. The method for developing Mathieu Charts and effects of Damping are discussed in the next section.

4 Mathieu Equation and Stability Charts

Mathieu equation is extensively studied in the field of parametric vibration. Several approaches are used to develop the stability charts. The range of validity of these charts as expected is limited. Another method is called the Hill's infinite determinant

method can also be used to develop stability charts. These charts are very accurate in the region where they are defined.

The standard Mathieu Equation with damping is given by

$$x'' + \mu x' + (\alpha + \gamma \cos(\tau))\, x = 0 \tag{8}$$

In order to develop the Mathieu charts the solution (2π & 4π) of the equation is expressed as Fourier series,

$$x_{2\pi}(t) = a_0 + \sum_{n=1}^{\infty} (a_n \cos(n\tau) + b_n \sin(n\tau)) \tag{9}$$

$$x_{4\pi}(t) = a_0 + \sum_{n=1}^{\infty} \left(a_n \cos\left(\frac{n\tau}{2}\right) + b_n \sin\left(\frac{n\tau}{2}\right)\right) \tag{10}$$

Substituting Eqs. (8) and (9) into Eq. (7) and setting the secular terms to zero we get two matrices for each solution as given below.

$$\begin{bmatrix} \alpha & \frac{\gamma}{2} & 0 & 0 & 0 & .. & 0 \\ \gamma & \alpha - 1 & \mu & \frac{\gamma}{2} & 0 & .. & 0 \\ 0 & -\mu & \alpha - 1 & 0 & \frac{\gamma}{2} & .. & 0 \\ 0 & \frac{\gamma}{2} & 0 & \alpha - 4 & 2\mu & \frac{\gamma}{2} & 0 \\ .. & & & & & & \end{bmatrix} \cdot \begin{bmatrix} a_0 \\ b_0 \\ a_1 \\ b_1 \\ a_2 \\ b_2 \\ . \\ . \\ . \end{bmatrix} = 0 \tag{11}$$

$$\begin{bmatrix} \alpha - \frac{1}{4} + \frac{\gamma}{2} & \frac{\mu}{2} & \frac{\gamma}{2} & 0 & .. & 0 \\ -\frac{\mu}{2} & \alpha - \frac{1}{4} - \frac{\gamma}{2} & 0 & \frac{\gamma}{2} & .. & 0 \\ \frac{\gamma}{2} & 0 & \alpha - \frac{9}{4} & \frac{3\mu}{2} & \frac{\gamma}{2} & 0 \\ 0 & \frac{\gamma}{2} & -\frac{3\mu}{2} & \alpha - \frac{9}{4} & 0 & \frac{\gamma}{2} \\ .. & & & & & \end{bmatrix} \cdot \begin{bmatrix} a_1 \\ b_1 \\ a_2 \\ b_2 \\ a_3 \\ b_3 \\ . \\ . \\ . \end{bmatrix} = 0 \tag{12}$$

Neglecting the trivial case of $a_0 = a_1 = b_1 \ldots = 0$, the determinant of the parametric matrix (matrix containing α & γ) should be zero. This gives the relationship between the parameters α and γ. The instability boundaries for various damping ratios are shown in Fig. 1.

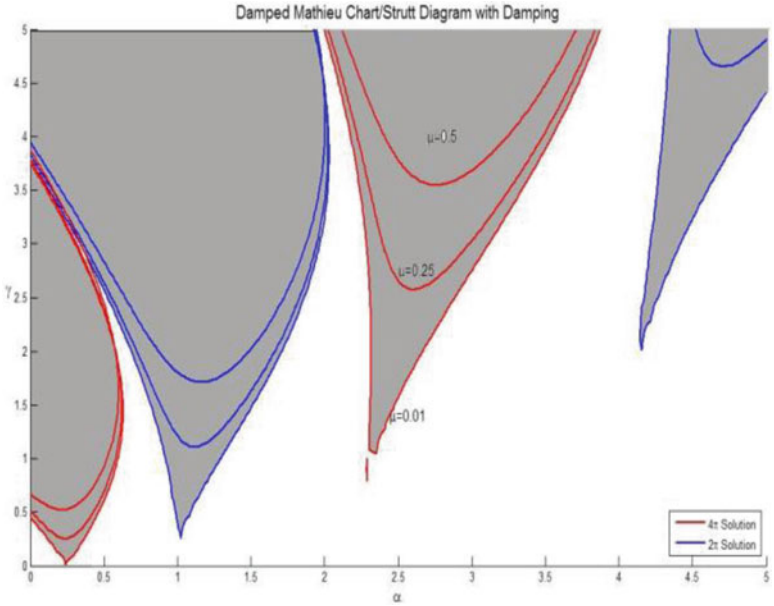

Fig. 1 Ince-Strutt diagram for Mathieu's equation with constant damping. The *shaded region* indicates the unstable zone

As evident from the charts, the effect of damping is to elevate the curves from the α axis, thereby reducing the unstable region. In terms of energy one can imagine damping tending to drain the energy from the excitation until the threshold energy is reached to instigate parametric vibration. Hence one method of avoiding parametric roll in ships would be to increase the damping.

The advantage of the chart above is that it can be used to study the parametric instability of any dynamical system whose equation of motion can be modeled as a Mathieu equation. This is so because the charts are not affected by the parameters of the system under study. Depending on where the (α, γ) pair falls in the chart, it becomes trivial to predict parametric instability.

If the stiffness variation is not single frequency harmonic and sinusoidal the system cannot be represented by a Mathieu equation. In such a case we can always represent the time varying coefficient (stiffness for ships) as a Fourier expansion. The resulting equation is called Hills Equation. Since the formulation of the Hills equation depends on ship parameters, these charts give a better prediction model. Our current and future work has concentrated on studying the details of Hills equation and developing the corresponding stability charts.

5 GM Variation in Waves

5.1 Ship Details

As discussed in the previous sections modern container ships seem to be more prone to parametric excitation. In order to develop realistic charts for prediction it is necessary to use a model which has parametric instability. It has been shown that post-Panamax C11 hull form exhibit parametric rolling (France et al. 2001). Here a modified C11 hull form is analyzed. The stern of the hull is modified to have fuller form, this model is named Pram aft body (MARIN Report No 17701-2-SMB, 2005). The main particulars of the vessel are shown in the Table 1.

The body plan of the modified C11 hull form is shown in Fig. 2. A 3D-wire mesh model of the vessel is shown in Fig. 2. The fine underwater hull form and wide flare above design draft is clearly evident from the wire mesh model. Such hull characteristics are one of the main reason for drastic variation of the submerged hull form and hence metacentric height. Hence ship stability in waves is a lot different from static stability.

Figure 3 shows the variation of the submerged hull with wave crest at midship and wave trough at midship.

Table 1 Main Particulars of C11 Hull form (pram aft body)

Parameter	Value
L_{PP} (m)	262.00
B (m)	40.00
D (m)	24.45
Mean Draught (m)	11.50
Displacement (tones)	69128.00
KG (m)	18.37
GM_t (m)	1.96
Natural Roll Period ,T_Φ (s)	25.14

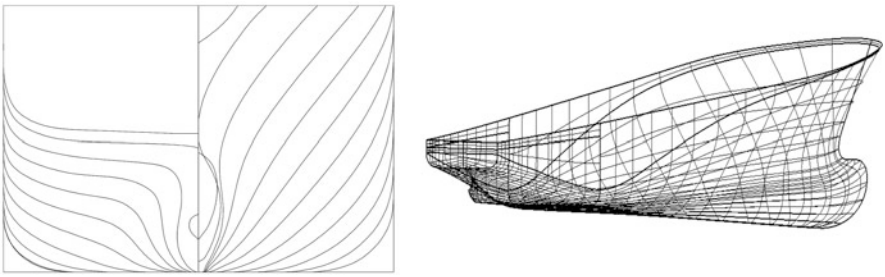

Fig. 2 *Left-Body Plan* of modified C11 Hull form (not to scale), *Right- Wire mesh* model of modified C11 Hull

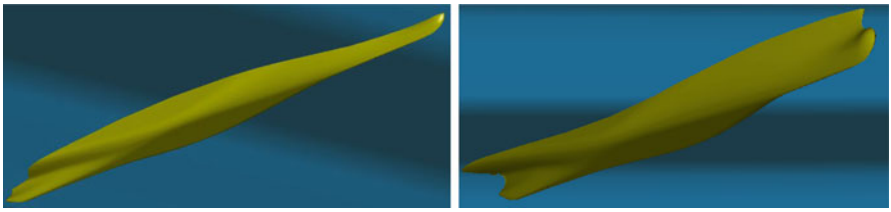

Fig. 3 Change in underwater Hull form in waves of modified C11 Hull form. *Left -Wave Crest* Midship, *Right -Wave Trough* Midship. Wave length = Ship LPP

5.2 GM in Regular Waves

In order to estimate the GM variation in regular waves, the roll restoring curve (GZ) for 10 different wave crest positions along the ship are calculated. The slope of the GZ curve at origin gives the GM. Standard hydrostatic software is used to obtain the GM for different wave crest position. Calculations are done for zero forward speed and free trim condition (hydrostatic balance). The details of the regular wave used for estimation is given below,

Wavelength $\lambda = \mathrm{L_{PP}} = 262\mathrm{m}$
Wave Number $= k = \frac{2\pi}{\lambda} = 0.024$
For deep water the wave frequency is given by

$$\omega^2 = gk, \omega = 0.485 \text{ rad/s}$$

The ship's natural frequency of roll is given by

$$\omega_n = \frac{2\pi}{T_\phi} = 0.25 \text{ rad/s}$$

The damping ratio $\zeta = \frac{B(\omega_n)}{2(I+A(\omega_n))\omega_n} \sim 0.003$
Hence $\omega_D \sim \omega_n$
Hence the parameter $\alpha = \left(\frac{\omega_n}{\omega}\right)^2 = 0.265$

Looking at the Mathieu Chart (Fig. 1) this value is very close to principal parametric resonance zone ($\alpha = 0.25$). The value of metacentric height (GM) for the wave crest at different position along the ship length is shown in Fig. 4.

A wave height equal to 1/40 of wave length is used to estimate GM, $H_W = 6.55$ m. The non-linear coupling effects of pitch and heave on the hydrostatics of the vessel is neglected. Figure 4 depicts a form for the GM variation and hence can be approximated into Mathieu's equation. The comparison between the Mathieu fit and actual GM is shown in Fig. 5. As shown by Spyrou et al. (2008) a case of cosine fit of GM with a phase shift (Fig. 5) has a better fit. The phase shift used here is $\pi/8$. The poor fit of the Mathieu approximation (even phase shifted) to the actual GM variation is clearly evident. Hence, there is a need to use a method with which we can approximate the GM variation more accurately. The Hill's equation and the corresponding stability charts could be a solution to this problem.

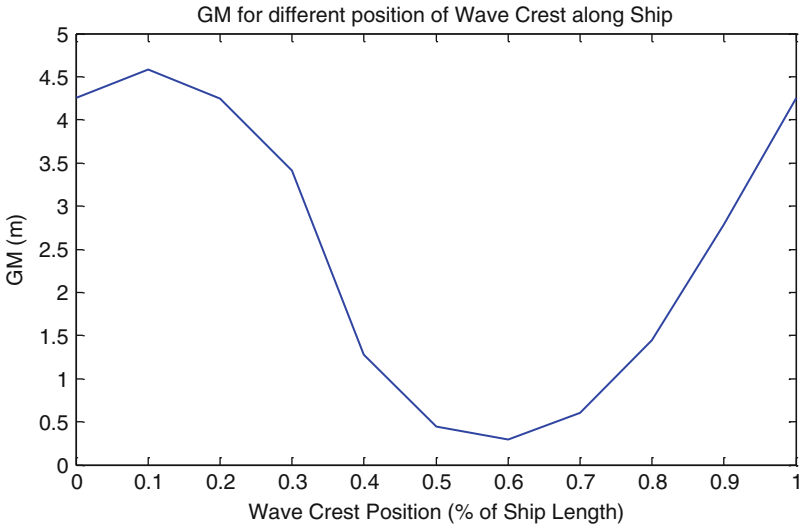

Fig. 4 GM for different position of wave crest

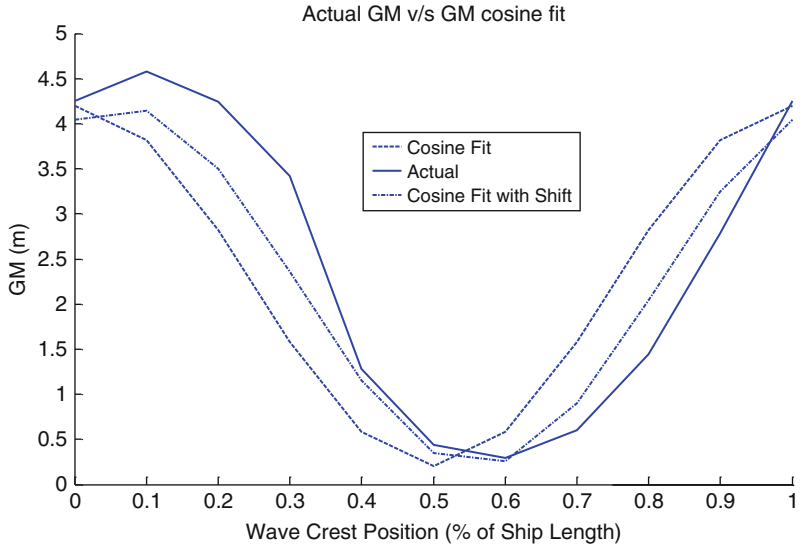

Fig. 5 Comparison of Cosine Fit of GM with Actual GM. (—— Cosine Fit and -.- Cosine Fit with Shift of $\pi/8$)

Considering Fig. 5, a more exact stability analysis of the equations of motion has been undertaken. This analysis considers both the non-harmonic nature of the variation in the roll restoring moment and the nonlinearity of the damping. The non-harmonic nature of the ship roll restoring moment curve has been taken into account

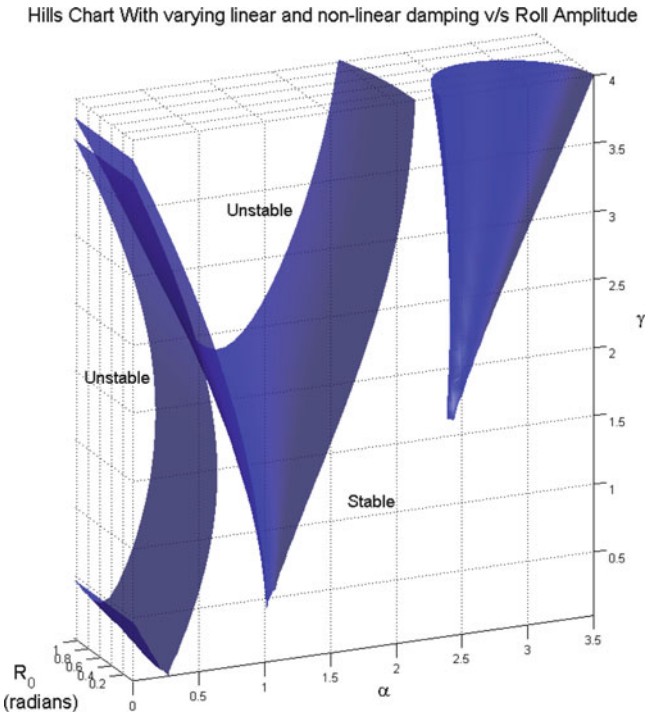

Fig. 6 Stability diagram for Hill's equation with linear and non-linear damping (R0 is bounded roll motion amplitude)

by considering the Hill's equation in lieu of the Mathieu equation. The nonlinear damping has been incorporated into the analysis by considering an equivalent linear damping term into the Hill's equation. Unfortunately the stability chart becomes three dimensional and depends not only on the particular vessel but also upon the amplitude of motion. An example of this more general stability chart is given in Fig. 6.

6 Conclusions

The abrupt changes in the underwater hull of the vessel are one of the primary reasons for the drastic change in stiffness of the vessel. The analysis carried out in the paper clearly exhibits the usefulness of simple Ince-Strutt diagrams or instability chart in predicting parametric roll of ships. The chart also demonstrates the implicit dependence of the phenomenon on damping.

The ability of the charts to predict the bounded roll motion amplitude is perhaps a feature so far not discussed. The effects of non-linear damping (which is important

due to large amplitude motion due to parametric roll) which is to bound the motion can be explained using these stability charts. Being able to estimate the bounded roll motion amplitude can be very helpful in the initial design stage to study the implications of parametric roll on the stability of the vessel.

The Hill equation tend to consider the time varying stiffness better in comparison to a Mathieu and hence the use of a stability diagram for Hill's equations would give a much more accurate prediction of the occurrence of parametric roll especially in higher instability zones. The charts can also be used to calculate the critical frequency and the threshold wavelength which would initiate large amplitude rolling motion.

The parametric stability of the vessel for different forward speeds can also be predicted using these charts. The charts also enable the study of parametric stabilization. For example by merely increasing or decreasing the speed of the vessel we might be able to avoid parametric roll or worsen the situation by moving into a more unstable region. These instability charts can act as a guide for crew onboard a ship experiencing large amplitude motion in head/following sea in deciding whether to increase or decrease the vessel speed and to what extent.

Hence apart from serving the purpose of a simple and practical tool for parametric roll study during the initial design stage the Mathieu or Hill stability charts can also be helpful during the operation of the vessel in a seaway.

Acknowledgements The authors would like to thank the Office and Naval Research and Texas A&M University for supporting the research.

References

ABS: ABS Guide for the Assessment of Parametric Roll Resonance in the Design of Container Carriers. American Bureau of Shipping, Houston (2004)

Bulian, G.: Development of analytical nonlinear models for parametric roll and hydrostatic restoring variations in regular and irregular waves. Ph.D. thesis, Department of Naval Architecture, Ocean and Environmental Engineering (DINMA), University of Trieste (2003)

Bulian, G., et al.: On the non linear modeling of parametric rolling in regular and irregular waves. Int. Shipbuild. Prog. **51**, 173–203 (2004)

Falzarano, J.M.: Predicting complicated dynamics leading to vessel capsizing. Ph.D. thesis, Naval Architecture and Marine Engineering, The University of Michigan, Michigan (1990)

France, W.N., et al.: An investigation of head-sea parametric rolling and its influence on container lashing systems. SNAME Annual Meeting (2001)

Hamamoto, M., et al.: Model experiment of ship capsize in astern seas-second report. J. Soc. Nav. Archit. Jpn. **179**, 77–87 (1996)

Munif, A., Umeda, N.: Numerical prediction on parametric roll resonance for a ship having no significant wave-induced change in hydrostatically-obtained metacentric height. Int. Shipbuild. Prog. **53**, 183–203 (2006)

Nayfeh, A.H.: Nonlinear rolling of ships in regular beam seas. Int. Shipbuild. Prog. **33**, 40–49 (1986)

Paulling, J.R.: The transverse stability of a ship in a longitudinal seaway. J. Sh. Res. **4**, 37–49 (1961)

Spyrou, K.J., Thompson, J.M.T.: The nonlinear dynamics of ship motions: a field overview and some recent developments. Philos. Trans. R. Soc. **358**, 1735–1760 (2000)

Spyrou, K.J., et al.: Prediction potential of the parametric rolling behaviour of a post-panamax containership. Ocean Eng. **35**, 1235–1244 (2008)

Umeda, N., et al.: Model experiments of ship vapsize in astern seas. J. Soc. Nav. Archit. Jpn. **177**, 207–217 (1995)

Umeda, N., et al.: Nonlinear dynamics on parametric roll resonance with realistic numerical modelling. Int. Shipbuild. Prog. **51**, 205–220 (2004)

Practical Stability of Rotating Solutions in a Parametrically Excited Experimental Pendulum via Dynamical Integrity Concepts

Stefano Lenci, William Luzi, Enrico Venturi, and Giuseppe Rega

Abstract This paper aims at showing how global safety can be used to interpret experimental results of a parametrically excited pendulum. The experimental investigation shows that rotations exist in a region smaller than the theoretical one, a discrepancy which has deeper motivations than the sole experimental approximations. By comparing the experimental results with the dynamical integrity profiles we understand that rotations exist only where a measure of dynamical integrity, accounting for both attractor robustness and basin compactness, is enough large to support experimental imperfections leading to changes in initial conditions.

Keywords Parametric pendulum • Rotating solutions • Experiments vs. theory • Robustness • Dynamical integrity • Practical stability

1 Introduction

The extraction of energy from sea waves by means of a parametrically excited pendulum is a potentially useful technological application of nonlinear dynamics, which has been proposed at the beginning of this millennium (Wiercigroch et al. 2010). The basic idea consists of exploiting the rotations of a pendulum on a pontoon undergoing a vertical motion induced by sea waves at a given (average)

S. Lenci (✉) • W. Luzi • E. Venturi
Department of Civil and Building Engineering, and Architecture, Polytechnic University of Marche, 60131 Ancona, Italy
e-mail: lenci@univpm.it

G. Rega
Department of Structural and Geotechnical Engineering, Sapienza University of Rome, 00197 Rome, Italy
e-mail: Giuseppe.Rega@uniroma1.it

M. Wiercigroch and G. Rega (eds.), *IUTAM Symposium on Nonlinear Dynamics for Advanced Technologies and Engineering Design*, IUTAM Bookseries (closed) 32, DOI 10.1007/978-94-007-5742-4_14,

frequency. In addition to the rest position, the excitation produces oscillations and rotations, which compete with each other. If one succeeds in getting *robust* rotations, a generator applied to the pendulum pivot may provide electrical energy. While being conceptually simple, this smart idea is quite difficult to be realized in practice, so that to date it is still at an early stage. The aim of this work is to make a step forward towards its practical implementation.

The investigations were first directed to obtain a fuller understanding of the parametric pendulum nonlinear dynamics, by adding to generic studies (Koch and Leven 1985; Szemplinska-Stupnicka et al. 2000; Garira and Bishop 2003) researches with the energy extraction hidden in the background (Xu et al. 2005; Xu and Wiercigroch 2007; Lenci et al. 2008; Horton et al. 2008; Lenci and Rega 2008). Both numerical (Szemplinska-Stupnicka et al. 2000; Garira and Bishop 2003; Xu et al. 2005; Horton et al. 2008; Lenci and Rega 2008) and analytical (Xu and Wiercigroch 2007; Lenci et al. 2008) studies were carried out. For a detailed literature review we refer to the introduction of Lenci et al. (2008).

To complement the theoretical investigations, the experimental approach has been developed in de Souza Paula et al. (2006), Blackburn et al. (1987). Focussing attention to the experiments developed within the energy generation framework, a shaker has been first used to provide vertical motion of the pivot (Xu et al. 2007). Successively, a pendulum-buoy prototype was put in a water channel at the Centre for Applied Dynamics Research at Aberdeen University, and wave-induced rotations and tumbling chaos were observed (Wiercigroch, M, private communication, 2007). Then, a systematic experimental campaign has been performed at the Polytechnic University of Marche, Ancona, with the specific goal of detecting rotations. The goal was challenging, since rotations have a small basin of attraction with respect to competing attractors, so that they are very difficult to be realized and maintained. Eventually we were successful with it, as discussed in the report (Lenci et al. in preparation) on the experimental investigation which is referred to for further details.

In the excitation frequency-amplitude parameters plane, rotations have been found within a strip strictly contained within the region of theoretical existence. Yet, in spite of many efforts, we were unable to enlarge this strip up to the whole theoretical region. This paper aims at finding a theoretical justification of this experimental evidence, and at enlightening on the *apparent* drawback, by using dynamical integrity arguments.

Dynamical integrity consists of studying the robustness of attractors and the safety of their basins in phase space. The basic idea, introduced earlier in Thompson (1989), Soliman and Thompson (1989) and recently reconsidered in Lenci and Rega (2008), Rega and Lenci (2005, 2008), is that stability is not enough for observing attractors in real cases. In fact, if the basin of attraction is "small," there is no hope to observe experimentally the associated attractor, since even small (and unavoidable) experimental uncertainties will certainly lead out of the basin of attraction.

In this paper, after presenting the mechanical model (Sect. 2) and summarizing the experimental results (Sect. 3), the dynamical integrity issue is discussed in Sect. 4 via integrity profiles which are used to interpret and justify the experimental observations.

2 The Mechanical Model

The dimensionless equation governing the planar motion of a pendulum (Fig. 1) subjected to a vertical displacement $y_0(t) = -(A/l)\cos[(2\pi f/\omega_0)t]$ of its axis of rotations is

$$\ddot{\theta} + h\dot{\theta} + [1 + p\cos(\omega t)]\sin\theta = 0, \tag{1}$$

where A and f are the physical amplitude and frequency, respectively, of the harmonic pivot motion, $\omega_0 = \sqrt{(g/l)}$ is the natural pulsation (the natural frequency is $f_0 = \omega_0/2\pi$), l is the *nominal* length of the pendulum, h is the damping coefficient, $\omega = 2\pi f/\omega_0 = f/f_0$ and $p = A\omega^2/l$.

3 Experimental Investigations

The experiments were conducted in the water channel of the Hydraulic Laboratory of the Polytechnic University of Marche, Ancona (Fig. 2). A detailed description of the setup and the experimental results is reported in Lenci et al. (in preparation). Herein the main relevant aspects are summarized.

The pendulum consists of a PVC bar with an added steel mass at the end (Fig. 3). It has $l = 586$ [mm], $\omega_0 = 4.090$, $f_0 = 0.651$ [Hz], it stands on a buoy made of polyurethane (Fig. 3) and is inserted in an aluminium frame built over the water

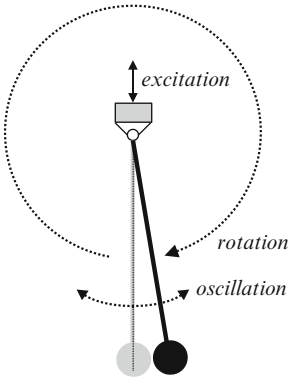

Fig. 1 A parametric pendulum exhibiting oscillation and rotation

Fig. 2 Photograph showing the Ancona experimental setup where the pendulum system shown in Fig. 3 below is excited by waves generated in a water tank

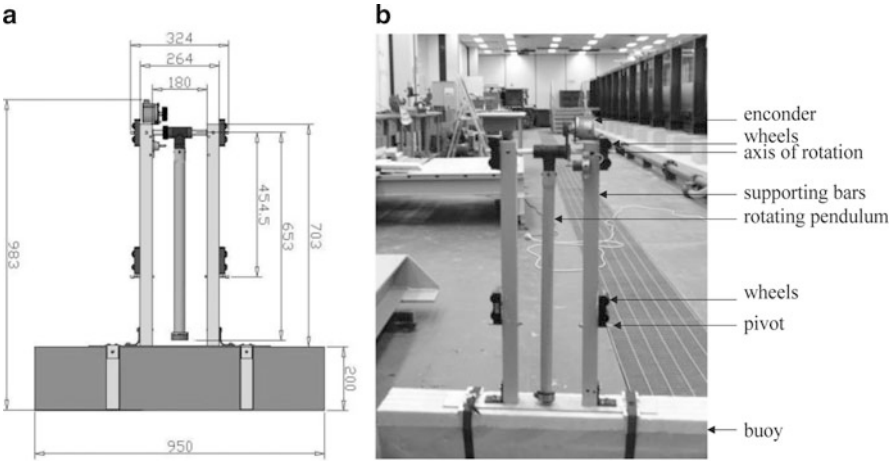

Fig. 3 (**a**) Design drawing and (**b**) photograph of the pendulum system

channel (Fig. 2). Attention was paid to the whole rig to guarantee that the pendulum axis can move only vertically. The damping coefficient $h = 0.015$ was determined experimentally.

The experimental campaign was based on the construction of several time histories, obtained by measuring the pivot displacement and the pendulum rotation.

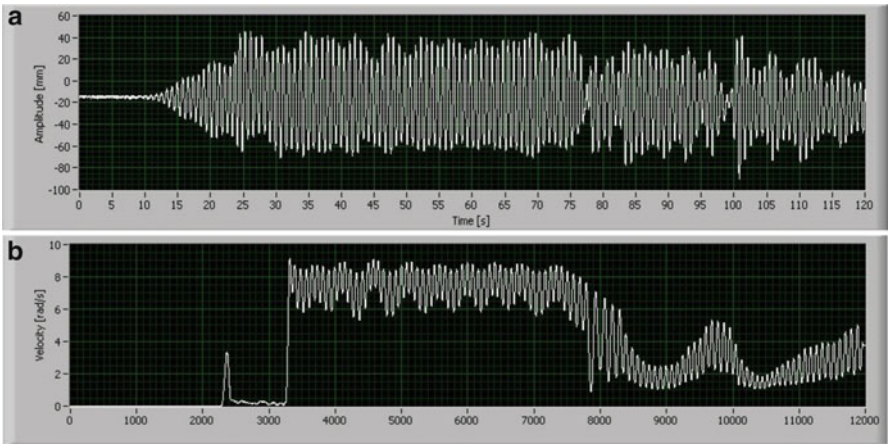

Fig. 4 Time histories (**a**) of the pendulum pivot and (**b**) of the angular velocity for $f = 1.2$ [Hz] (or $\omega = 1.84$) and a nominal amplitude of the waves imposed at the generator of 60 [mm]

A representative example is reported in Fig. 4. We can clearly distinguish the following different phases.

1. At $T \cong 12$ [s] the first travelling wave produced by the generator arrives at the buoy.
2. From $T \cong 12$ [s] to $T \cong 25$ [s] the transient behaviour develops, with an increasing amplitude, until, at $T \cong 25$ [s], a steady state wave supports the buoy.
3. During the transient the operator manually brings the pendulum from the rest position to the chosen initial position (first isolated peak in the time history of Fig. 4b).
4. At $T \cong 33$ [s], after the steady state waves have been set, the operator launches the pendulum.
5. From $T \cong 33$ [s] to $T \cong 75$ [s] we have 'regular' pivot motion (Fig. 4a) and pendulum rotation (Fig. 4b). This is the good part of the time histories, and it is actually the sole one used for interpreting the pendulum dynamics.
6. At $T \cong 75$ [s] the reflected wave arrives at the buoy, and suddenly destroys the harmonicity of the pivot motion.

We aimed at detecting in the (ω, p) parameters space the region where rotations can be found experimentally, irrespective of their robustness, i.e. even if they exist for just one single initial condition. With this objective, we spanned the frequency range $\omega \in [1.15;\ 2.30]$, and for each considered frequency we applied different increasing amplitudes, paying a special attention to determine the lowest and highest amplitude values where rotations can be found experimentally. The 34 considered couples of parameters are reported in Fig. 5, where the region of existence of experimental rotations is clearly seen to be a strip of finite magnitude, which shrinks for low frequencies.

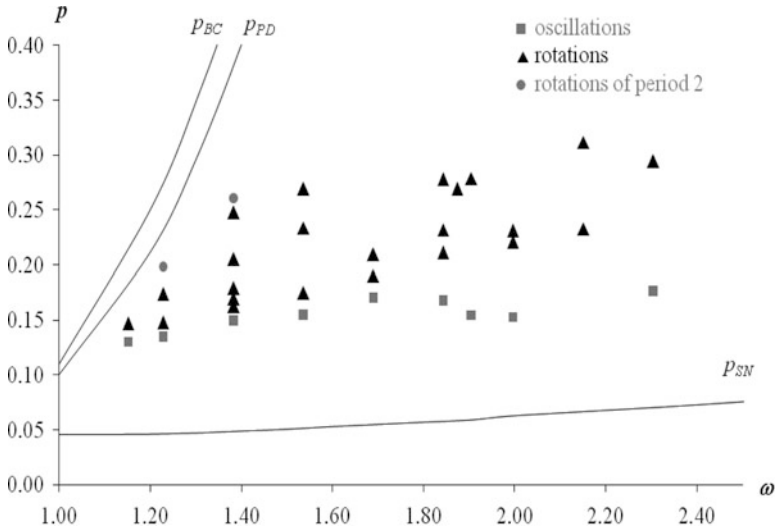

Fig. 5 The behaviour chart, i.e. the map where rotations can be found experimentally

Each rotation point was repeated at least twice to assess its reliability. Furthermore, as regards the oscillation points, we tried several initial conditions before deciding that rotations do not exist. Thus, strictly speaking, we cannot say that in the oscillation points rotations do not exist, but only that we were not able to find them, in spite of repeated attempts.

To better understand the experimental scenario it is necessary to compare it with the theoretical behavior. For each excitation frequency, rotations appear by a saddle-node (*SN*) bifurcation at a certain amplitude threshold p_{SN} (Lenci and Rega 2008). Then, they have an interval of existence and stability, which ends up with a period-doubling (*PD*) bifurcation at p_{PD}. This event triggers a period doubling cascade ending with a boundary crisis at p_{BC}, where rotations definitely disappear (Lenci and Rega 2008). The curves $p_{SN}(\omega)$, $p_{PD}(\omega)$ and $p_{BC}(\omega)$ are also reported in Fig. 5.

The theoretical ${p_{SN}}^{\text{theor}}$ and experimental ${p_{SN}}^{\text{exp}}$ thresholds in Fig. 5 are seen to share the same qualitative behavior, but the latter is significantly higher than the former. This has various motivations. In fact, as previously said, the real ${p_{SN}}^{\text{exp}}$ would be certainly lower, and closer to ${p_{SN}}^{\text{theor}}$, if we would be able to test many more initial conditions. Furthermore, the actual damping could be (slightly) larger than that measured experimentally. This is likely to be a consequence of aerodynamic dissipation during rotations which could rise to ${p_{SN}}^{\text{theor}}$. Then, of course, there are always experimental uncertainties which play some role. But these are not the main motivations. In fact, in Sect. 4 it will be shown by global dynamics arguments (Lenci and Rega 2008) that the theoretical threshold will never be obtained even in extremely careful experiments, since it is not robust enough.

Concerning the upper threshold of stability p_{PD}, we see that theoretically it is an increasing function of ω. We were able to experimentally detect this threshold for

low excitation frequencies. As the wave frequency ω increased, we reached the limit due to the water channel characteristics, which is thus an experimental constraint. But, as in the case of the lower bound, this is not enough to completely justify the experimental results. In fact, we were not able to find rotations even for amplitudes admitted in the water channel. Once more, this fact will be theoretically justified in Sect. 4 in terms of dynamical integrity.

The main conclusions which can be drawn from Fig. 5 is that, above a certain frequency threshold, experimental rotations have a well defined region of existence in the parameters plane. This is smaller than the theoretical one but in any case large and robust enough since it spreads over a 'large' frequency range, thus being possibly able to account, up to a certain extent, also for wave frequency modifications as they occur, e.g., in transients or sea waves.

4 Interpretation of Experimental Results via Dynamical Integrity

Referring to Eq. (1), the key tool for understanding why the rotating solutions can be practically observed only in a subset of the stability domain is the integrity profile, i.e. a curve which reports how the integrity measure varies for increasing excitation amplitude p. In this paper the safe basin (Rega and Lenci 2005, 2008) is the basin of attraction of the clockwise rotating solution, and the considered measure of attractor robustness and basin integrity is the Integrity Factor (*IF*), which is the normalized radius of the largest circle entirely belonging to the safe basin (Lenci and Rega 2008; Rega and Lenci 2005, 2008).

A representative integrity profile for $\omega = 1.3$ is reported in Fig. 6, where *IF* has been normalized with respect to its maximum value (accordingly, the maximum value of the curve is $IF = 1$).

For increasing amplitude p, we can clearly identify the following succession of events and properties.

- At $p = p_{SN} \cong 0.0476$ the rotation appears through a *SN* bifurcation. This is the starting point of the integrity profile of period 1 rotation.
- Just after the attractor is born, its basin of attraction enlarges around it; accordingly, the integrity profile increases.
- At $p = p_6 \cong 0.080$ a rotation of period 6 (the velocity has a period which is 6 times that of the excitation) appears, by means of a *SN* bifurcation, inside the basin of attraction of the main rotation. This entails an instantaneous decrement of the compact part of the safe basin, and the associated sudden reduction of its *IF*.
- Soon after being born, the period 6 rotation undergoes a classical *PD* cascade, and disappears at about $p \cong 0.090$, likely by a boundary crisis. The former basin of attraction of the disappearing solution is (re)captured by the main rotation, which in fact increases its robustness and recovers (and slightly increases) the former *IF*.

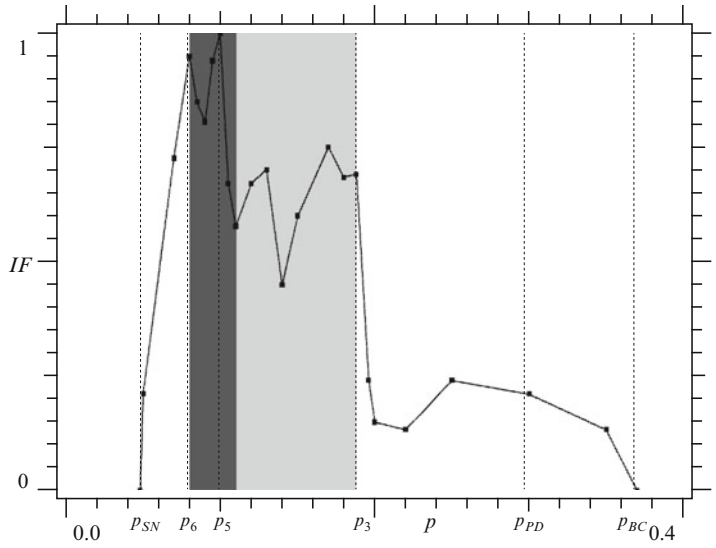

Fig. 6 The integrity profile of period 1 rotation for $h = 0.015$ and $\omega = 1.3$

- At $p = p_5 \cong 0.100$ a period 5 rotation appears, again by a *SN* bifurcation and again inside the basin of attraction of the main rotation. Since the period 5 rotation is more robust than the previous period 6 rotation, there is a larger fall down of the integrity profile.
- Like the period 6 rotation, also the period 5 rotation undergoes a classical period doubling cascade and disappears at about $p \cong 0.110$ by a boundary crisis. The former basin of attraction of the disappearing solution is partially recaptured by the main rotation, which slightly increases its *IF* up to a value which is however well below the value before the sudden fall. This is due to the fractalization occurring for increasing p, which erodes from outside the compact part of the basin of the main rotation, thus smoothly decreasing its *IF*.
- In the p-range $0.130 \div 0.140$ there is another phenomenon like the two just described, which entails a sudden reduction of *IF* and a subsequent recovery.
- At $p = p_3 \cong 0.190$ a period 3 rotation appears by a *SN* bifurcation inside the basin of attraction of the main rotation. It is more robust than the previous period 6 and 5 rotations, and accordingly there is a large decrement of *IF*. The sudden decrease due to the period 3 rotation was also observed in Lenci and Rega (2008) for $h = 0.1$, while the other minor attractors were not present in that case.
- The period 3 rotation has an interval of existence and stability which is larger than that of the period 6 and 5 rotations, but it is in any case small. Thus, it suddenly disappears and leaves the main rotation, which has however a merely residual *IF*, since the disappeared attractor had previously tangled with the surrounding fractal part, so that integrity is definitely lost.

- After $p \cong 0.200$ the dynamical integrity is residual. The basin of attraction is definitely small and almost completely eroded.
- At $p =_{pBC} \cong 0.369$ the path ensuing from the rotation solution, which previously underwent a period doubling cascade, disappears by a boundary crisis. This is the last point of the integrity profile.

For the purpose of interpreting Fig. 5, the main property of Fig. 6 is that the *IF* of the period 1 rotation is high only in the central part, where the attractor is relatively robust and its basin is substantially uneroded. It is clear that out of this central part the dynamical integrity is marginal (a small and eroded basin), and thus the attractor cannot be observed in practice. This provides the theoretical justification for experimentally observing rotations only in the central strip of the excitation amplitude range.

This justification is not limited to the case $\omega = 1.3$, since (not reported) integrity profiles built for different values of the excitation frequency share the same qualitative properties.

It is worth to remark that, looking at the dynamical integrity, not only we understand why we have not observed rotations for large excitation amplitudes, which is somehow expected, but also why we have not observed rotations for excitation amplitudes just above the *SN* bifurcation, which is much less intuitive.

It is useful to stress out the importance of secondary attractors, which variously affect the reduction of robustness of the main attractor and/or of integrity of its basin. They are completely lost by a *local* analysis, also of path-following or brute force bifurcation type, and this further stresses the importance of a *global* analysis for a modern and reliable approach to system dynamics.

The previous considerations provide a qualitative justification of the experimental results. To proceed with a quantitative comparison, we report in Fig. 7 the contour plot of $IF(p, \omega)$ together with the experimental points of Fig. 5. The contour curves are partially smoothed for graphical reasons.

Figure 7 shows that for 'low' excitation frequencies, say $\omega < 1.6$, the experimental points are on the 'plateau' of high *IF* (see the light gray region of Fig. 6). It is particularly remarkable that the *PD* points are just after the sudden fall of *IF*, which therefore can be considered, up to the experimental approximation, as the upper practical threshold for the existence of rotation. Note that it corresponds to the onset of period 3 rotations, p_3, and only global safety arguments show why it constitutes an upper limit for main rotations: above, the dynamical integrity is marginal, and there is no hope for the relevant region to be observed experimentally.

In this range, the bottom curve $p_{SN}{}^{\exp}$ seems to follow the minor fall after the first peak of the integrity profile, i.e. it approximately follows the boundary between the dark and the light gray of Fig. 6. The fact that it is not below, at least in correspondence of the principal peak, is likely due to experimental approximations.

For 'large' values of excitation frequencies, say $\omega > 1.6$, the experimental points are clearly around the main ridge of *IF*, which is a definitive confirmation that only rotations with large dynamical integrity can be practically observed. The fact that for

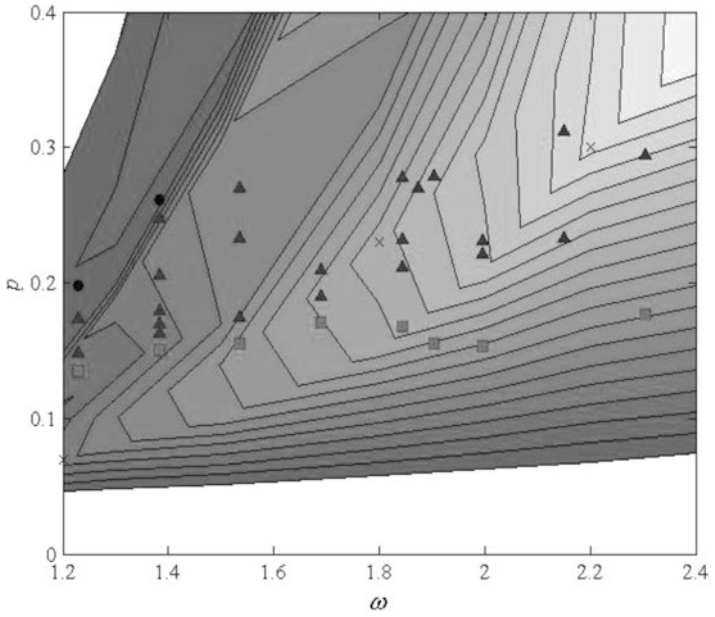

Fig. 7 The contour plot of $IF(p, \omega)$ and the experimental data. *Square* = oscillations, *triangles* = rotations and *circles* = rotations of period 2. The value increases from *dark to light gray*

'very large' ω, say $\omega > 2.2$, the points no longer follow the ridge is a consequence of the fact that in he experiment the amplitudes have a technical upper bound which cannot be overcome.

The bottom curve $p_{SN}^{\exp}$ now approximately stands on a contour level of *IF*, showing the minimal dynamical integrity necessary for the onset of experimental rotations.

5 Conclusions

An experimental apparatus to simulate the production of energy from sea waves has been built at the Polytechnic University of Marche, Ancona, Italy. An extensive experimental programme has been undertaken, showing that main rotations of the pendulum are possible only in a strict subset of their theoretical region of existence and stability.

With the aim of justifying this experimental evidence, the dynamical integrity of the pendulum has been systematically investigated, showing that the generic integrity profile suddenly increases after appearance of the associated attractor. The successive onset of a number of secondary, highly periodic rotations suddenly reduces the basin of attraction of the main rotation, so that the integrity

profile suddenly falls down. Although the main attractor may sometimes regain its robustness, the fractalization induced by the secondary attractors with increasing excitation amplitude generally entails a non-recoverable loss of basin compactness, which corresponds to a decrease of the *IF* measure down to a marginal value.

Comparing the numerical integrity profiles with experimental data we have found that the latter occur in ranges of solely high integrity, thus permitting to understand why rotations are not observed elsewhere, namely where the dynamical integrity is not enough to sustain experimental imperfections and guarantee practical stability of rotations.

The main conclusion is that the experimental results are theoretically fully justified, up to the experimental uncertainties. Furthermore, this paper constitutes an experimental proof of the Thompson's (1989; Soliman and Thompson 1989) and authors' (Rega and Lenci 2005, 2008) idea that local stability is not enough for practical use, and must be complemented with the analysis of global safety.

Acknowledgments The experiments were done at the Hydraulic Laboratory of the Polytechnic University of Marche, Ancona, Italy. We thank Prof. A. Mancinelli, Prof. M. Brocchini and Prof. C. Lorenzoni for the permission of using this facility. Thanks are also due to the PhD student M. Postacchini for the help with the water channel. Finally, we thank Prof. P. Castellini, of the Department of Mechanics, for the help with the measurements set-up and tools.

References

Blackburn, J.A., Zhou-jing, Y., Vik, S., Smith, H.J.T., Nerenberg, M.A.H.: Experimental study of chaos in a driven pendulum. Phys. D **26**, 385–395 (1987)

de Souza Paula, A., Savi, M.A., Pereira-Pinto, F.H.I.: Chaos and transient chaos in an experimental nonlinear pendulum. J. Sound Vib. **294**, 585–595 (2006)

Garira, W., Bishop, S.R.: Rotating solutions of the parametrically excited pendulum. J. Sound Vib. **263**, 233–239 (2003)

Horton, B., Wiercigroch, M., Xu, X.: Transient tumbling chaos and damping identification for parametric pendulum. Philos. Trans. R. Soc. A: Math. Phys. Eng. Sci. **366**, 767–784 (2008)

Koch, B.P., Leven, R.W.: Subharmonic and homoclinic bifurcations in a parametrically forced pendulum. Phys. D **16**, 1–13 (1985)

Lenci, S., Rega, G.: Competing dynamic solutions in a parametrically excited pendulum: attractor robustness and basin integrity. ASME J. Comput. Nonlinear Dyn. **3**, 041010-1-9 (2008)

Lenci, S., Pavlovskaia, E., Rega, G., Wiercigroch, M.: Rotating solutions and stability of parametric pendulum by perturbation method. J. Sound Vib. **310**, 243–259 (2008)

Lenci, S., Brocchini, M., Lorenzoni, C.: Experimental rotations of a pendulum on water. ASME J. Comput. Nonlinear Dyn. **7**, 11007-1-9 (2012)

Rega, G., Lenci, S.: Identifying, evaluating, and controlling dynamical integrity measures in nonlinear mechanical oscillators. Nonlinear Anal. **63**, 902–914 (2005)

Rega, G., Lenci, S.: Dynamical integrity and control of nonlinear mechanical oscillators. J. Vib. Control **14**, 159–179 (2008)

Soliman, M.S., Thompson, J.M.T.: Integrity measures quantifying the erosion of smooth and fractal basins of attraction. J. Sound Vib. **135**, 453–475 (1989)

Szemplinska-Stupnicka, W., Tyrkiel, E., Zubrzycki, A.: The global bifurcations that lead to transient tumbling chaos in a parametrically driven pendulum. Int. J. Bifurc. Chaos **10**, 2161–2175 (2000)

Thompson, J.M.T.: Chaotic behavior triggering the escape from a potential well. Proc. R. Soc. Lond. A **421**, 195–225 (1989)

Wiercigroch, M.: A new concept of energy extraction from waves via parametric pendulor, UK patent application (Pending) (2010)

Xu, X., Wiercigroch, M.: Approximate analytical solutions for oscillatory and rotational motion of a parametric pendulum. Nonlinear Dyn. **47**, 311–320 (2007)

Xu, X., Wiercigroch, M., Cartmell, M.P.: Rotating orbits of a parametrically-excited pendulum. Chaos Solitons Fract. **23**, 1537–1548 (2005)

Xu, X., Pavlovskaia, E., Wiercigroch, M., Romeo, F., Lenci, S.: Dynamic interactions between parametric pendulum and electro-dynamical shaker. ZAMM Zeit. Ang. Math. Mech. **87**, 172–186 (2007)

Dynamics, Synchronization and Control of Parametric Pendulums

Anna Najdecka, Vahid Vaziri, and Marian Wiercigroch

Abstract In this work the dynamics and synchronization of the coupled parametric pendulums system is examined with a view to its application for wave energy extraction. The system consisting of two parametric pendulums on a common support has been modeled and its response studied numerically, with a main focus on synchronized rotation. Different methods of controlling the response the pendulums have been introduced and compared. Numerical results have been verified in experimental studies.

Keywords Parametric pendulum • Synchronization of pendulums • Delayed feedback control

1 Introduction

The concept of parametric pendulum application for wave energy extraction has been proposed by Wiercigroch, where a vertical wave motion of the parametric pendulum is transformed to a rotation of a shaft. The dynamics of the pendulum regarding this application has been extensively studied by Xu et al. (2005) and by Horton et al. (2008). A floating structure containing the pendulum, would be subjected not only to the excitation originating from the sea waves but also reaction forces related to the rotating pendulum acting on the pontoon. Therefore the real system for energy extraction would consist of multiple pendulums, so that the forces associated with single pendulums acting on the pontoon compensate each other, resulting in a stable structure. The dynamical behavior of a system consisting

A. Najdecka (✉) • V. Vaziri • M. Wiercigroch
Centre for Applied Dynamics Research, School of Engineering, University of Aberdeen, AB24 3UE, Aberdeen, UK
e-mail: a.najdecka@abdn.ac.uk; vahid.vaziri@abdn.ac.uk; m.wiercigroch@abdn.ac.uk

M. Wiercigroch and G. Rega (eds.), *IUTAM Symposium on Nonlinear Dynamics for Advanced Technologies and Engineering Design*, IUTAM Bookseries (closed) 32, DOI 10.1007/978-94-007-5742-4_15,

of at least two coupled oscillators under common excitation needs to be studied. The main interest of this study lies in examining the synchronization phenomena, as the target state for energy extraction is to achieve synchronized counter rotating motion of pendulums.

2 Physical and Mathematical Modeling

The system considered in the first stage of the study consists of the two pendulums mounted on the commonly excited flexible supporting structure. It has been modeled as a four-degree of freedom system illustrated at the Fig. 1, where x and y denote the displacement of the structure in horizontal and vertical direction, θ_1 and θ_2 describe the angular displacement from the downward zero position. Synchronized state can be achieved due to coupling effect of the elastic base, capable of transmitting vibrations between the pendulums. The forcing of the harmonic nature has been applied in the horizontal and vertical direction (approximating the movement of the sea waves). For such an arrangement of the pendulum the whole problem can be treated on the x, y plane. After nondimensionalisation with respect to the natural frequency the equations of motion for the two pendulums are given by:

$$\begin{aligned} \theta_1'' + x'' \cos\theta_1 + \left(1 + y''\right) \sin\theta_1 + \gamma_\theta \theta_1' + e_1 = 0 \\ \theta_2'' + x'' \cos\theta_2 + \left(1 + y''\right) \sin\theta_2 + \gamma_\theta \theta_2' + e_2 = 0 \end{aligned} \tag{1}$$

where γ_θ denotes the damping on the pendulum shaft and e_1, e_2 are the nondimensionalised energy extraction terms, corresponding to the loading torque, which can be applied on the rotating shaft. The external forcing is applied at the base. Initially purely vertical forcing has been considered, i.e. $p_x = 0$. The parametric excitation terms x″, y″ included in the above equations are described by the equation of motion of the flexible supporting structure:

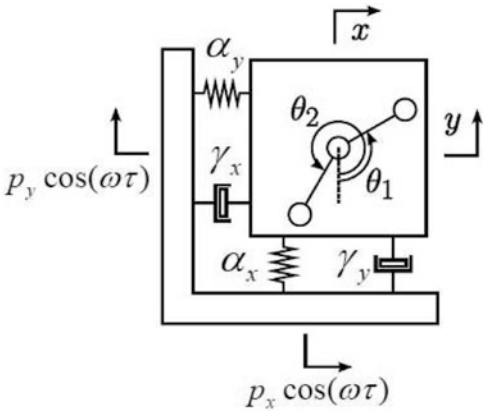

Fig. 1 Model of the two pendulums system under parametric excitation (Adopted from Yokoi et al. (2009))

$$x'' + \gamma_x x' + \alpha_x x + a\left(\theta_1'' \cos\theta_1 - \theta_1'^2 \sin\theta_1 + \theta_2'' \cos\theta_2 - \theta_2'^2 \sin\theta_2\right) = 0$$
$$y'' + \gamma_y \left(y' + p_y \omega \sin(\omega\tau)\right) + \alpha_y \left(y - p_y \cos(\omega\tau)\right)$$
$$+ a\left(\theta_1'' \sin\theta_1 + \theta_1'^2 \cos\theta_1 + \theta_2'' \sin\theta_2 + \theta_2'^2 \cos\theta_2\right) = 0 \quad (2)$$

where all the system parameters are nondimesional. γ_x and γ_y are the damping coefficients in horizontal and vertical direction respectively, α_x and α_y are the stiffness coefficients, p_y the forcing amplitude, ω is the forcing frequency, τ is the time, a is a mass ratio. The relation between the pendulums equations is not given explicitly. It exists through x″ and y″ terms, which depend on both θ_1 and θ_2. In this case, all of the above equations are mutually coupled.

3 Numerical Results

The response of the aforementioned system has been simulated with MatLab, using the set of parameters corresponding to the experimental rig, used for the further studies. The non-dimensional values of the system parameters are given by: $\alpha_x = 7.8808, \alpha_y y = 23.4398, \gamma_\theta = 0.0121, \alpha_x = 118, 1.3961, \alpha_y = 463, 292.5726$, and $a = 0.0540$. The forcing parameters have been chosen according to the limitations of the experimental rig, with p_y ranging from 0.0127 to 0.0929 and ω from 1.0360 to 3.1250. The pendulums systems can experience a variety of responses. For small forcing level it is equilibrium point in zero position, when increasing the forcing, oscillations, rotations and finally chaotic motion appear. Several types of synchronized motion have been observed, including oscillations, rotations, and rotations of one pendulum synchronized in phase with the oscillations of the second one. The some of the responses have been show at the Fig. 2. The pendulums have a natural tendency to synchronize with each other through the external force. However,

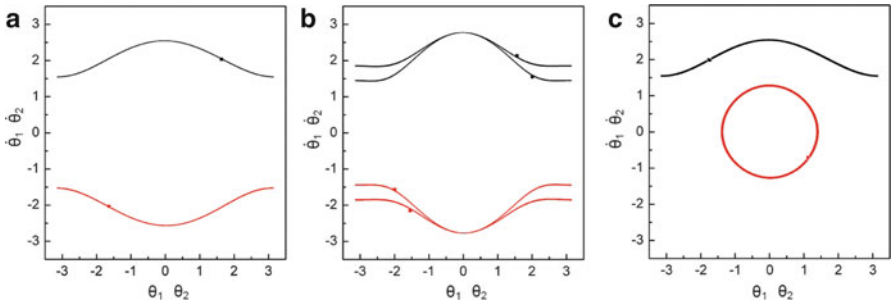

Fig. 2 Numerical phase diagrams showing different types of synchronized motion of the two pendulums. (**a**) Synchronized period one rotation, (**b**) synchronized period two rotation, (**c**) rotation of pendulum 1 synchronized with the oscillation of pendulum 2

only very specific initial conditions result in synchronized rotational response. For the majority of initial conditions the steady state responses will be oscillations. Therefore to achieve the target state of synchronized rotation controlling algorithm is necessary with the primary function of initiating rotational responses.

4 Experiments

The experimental studies have been carried out in the Centre for Applied Dynamics Research at the University of Aberdeen. In the experimental studies the harmonic excitation of the system has been provided by the electromagnetic shaker, model 806 LS by Ling Dynamical Systems Ltd. In the first step the system forced with only vertical excitation has been considered. The two pendulums system has been fixed on the shaker and using LabView the response of the system has been observed for different initial conditions and varying frequency and amplitude. The experimental setup is shown at the Fig. 3.

5 Control Methods

A robust control algorithm is necessary to both start up the rotational motion and then to maintain the synchronized rotation state irrespective of changes in the excitation. Therefore the control function can be divided into two steps, initialization

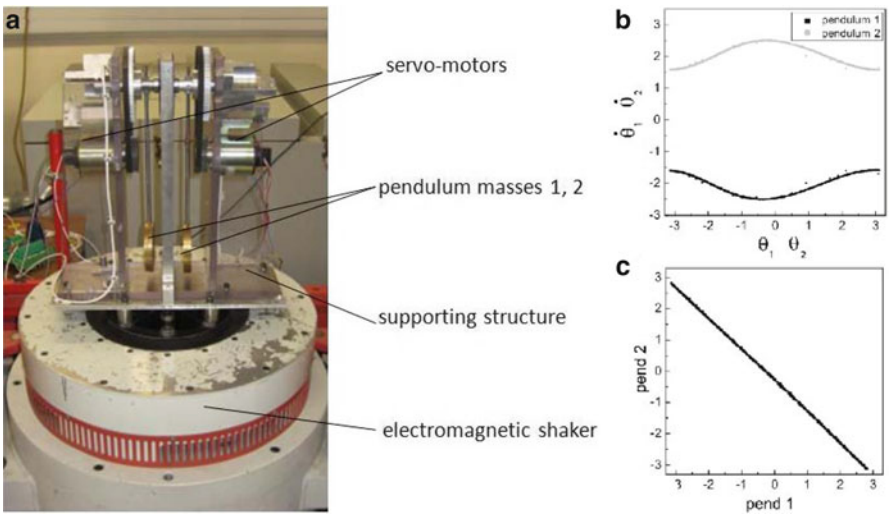

Fig. 3 (**a**) Experimental rig. Experimentally observed synchronized counter-rotation of pendulum 1 (*black*) and 2 (*gray*), for $\omega = 2$, $p_y = 0.07$; (**b**) phase diagram, (**c**) angular displacement of pendulum 2 as a function of the displacement of pendulum 1

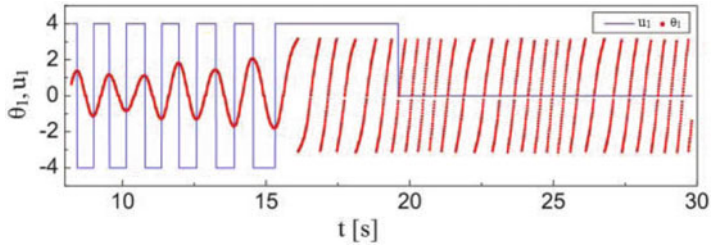

Fig. 4 Initialization of the rotation of a single pendulum using the bang-bang method (multi-switch). Control signal and angular displacement plotted against time (experimental results)

of the desired motion and its maintenance. Different methods of control have been discussed and applied numerically and experimentally. In the experimental study the controlling action is performed by two servo-motors attached to the pendulums shafts, working alternating as a motor, to provide the torque necessary to initiate rotational motion or to synchronize the two pendulums. Once the motion is stabilized it can act as a generator extracting energy form the rotating shaft. In the experimental conditions the limitations of the driving motor need to be taken into account while choosing the control method.

5.1 Bang-Bang Method

The simplest method for initiating the rotational motion of the pendulum is bang-bang control. In this method the constant magnitude signal is used to initiate the rotation. If the maximum power of the motor is not sufficient for achieving rotational motion directly, multi-switching control needs to be applied to swing up the pendulum, where the control signal is given by:

$$u_i = k_i sgn(\theta_i); \tag{3}$$

where u_i is a control signal k_i is the signal gain and is the control variable representing angular velocity of i-th pendulum. The motor is providing the torque in two directions: clockwise and anticlockwise, so that irrespective of the direction of pendulum swing, the action of the motor amplifies the amplitude of the oscillation until the pendulum rotates. In this method the critical point is the switch off time for the motor. Immediate setting the control signal to zero once the first rotation is achieved does not guarantee stabilization of this motion. The position and velocity of pendulum at the switch off time need to belong to the rotational attractor, so that the stable rotation can be maintained (Fig. 4). Therefore the knowledge of the structure of the basins of attraction for particular forcing parameters is required so that the switch off point can be determined accurately in each case. This makes the method difficult to implement.

5.2 Velocity Comparison

To solve the problem of the bang-bang method, a second method has been proposed. In this method, the velocities of the two reference points have been compared with the known velocities of the corresponding point on the desired orbit. $-\pi$ and 0 has been chosen as the reference points and the velocities there compared with the period one rotational orbit. For an angular displacement of the pendulum between $-\pi$ and 0, the difference between the previous velocity of pendulum at the zero point and the velocity expected there was applied as a control signal, between 0 and π the difference between the previous velocity of the pendulum at $\theta = \pi$ and the velocity expected there was applied:

$$\begin{aligned} u_i &= k_i(\dot{\theta}_{i(\theta=0)} - \theta'_{i(\theta=0)}) \text{ if } -\pi < \theta_i < 0 \\ u_i &= k_i(\dot{\theta}_{i(\theta=\pi)} - \theta'_{i(\theta=\pi)}) \text{ if } 0 < \theta_i < \pi \end{aligned} \tag{4}$$

where $\dot{\theta}_{i(\theta=0)}$ and $\dot{\theta}_{i(\theta=\pi)}$ are the velocities of the particular pendulums at the zero point and at π, while $\theta'_{i(\theta=0)}$ and $\theta'_{i(\theta=\pi)}$ are the velocities for period one rotation at the zero point and at π. In the experiments due to the limitations of the motor the control method has been modified. The multiswitch approach has been applied to use more efficiency the power of the motor. The modified control signal is given by:

$$\begin{aligned} u_i &= k_i sgn(\dot{\theta}_i)(\dot{\theta}_{i(\theta=0)} - \theta'_{i(\theta=0)}) \text{ if } -\pi < \theta_i < 0 \\ u_i &= k_i sgn(\dot{\theta}_i)(\dot{\theta}_{i(\theta=\pi)} - \theta'_{i(\theta=\pi)}) \text{ if } 0 < \theta_i < \pi \end{aligned} \tag{5}$$

5.3 Delayed Feedback Control

The continuous method, so-called delayed feedback control, has been proposed by Pyragas (1992). In this method the system can be stabilized by a feedback perturbation proportional to the difference between the present and a delayed state of the system. The delay time can be determined from the period of the forcing. The period of stable period n-rotation of the parametric pendulum needs be a n-multiple of the period of excitation, where n is a natural number. As period one rotations are of most interest for this study $n = 1$ and therefore the delay time equals to the period of excitation $t = \tau$. The angular displacement for period one rotation increased 2π for each forcing cycle, therefore the control signal is given by:

$$u_i = k_i(\theta_i(t - \tau) - \theta_i(t) + 2\pi). \tag{6}$$

Once the pendulum stabilizes on the period one rotational orbit the control signal automatically goes to zero. This method is capable of initiating period one rotation

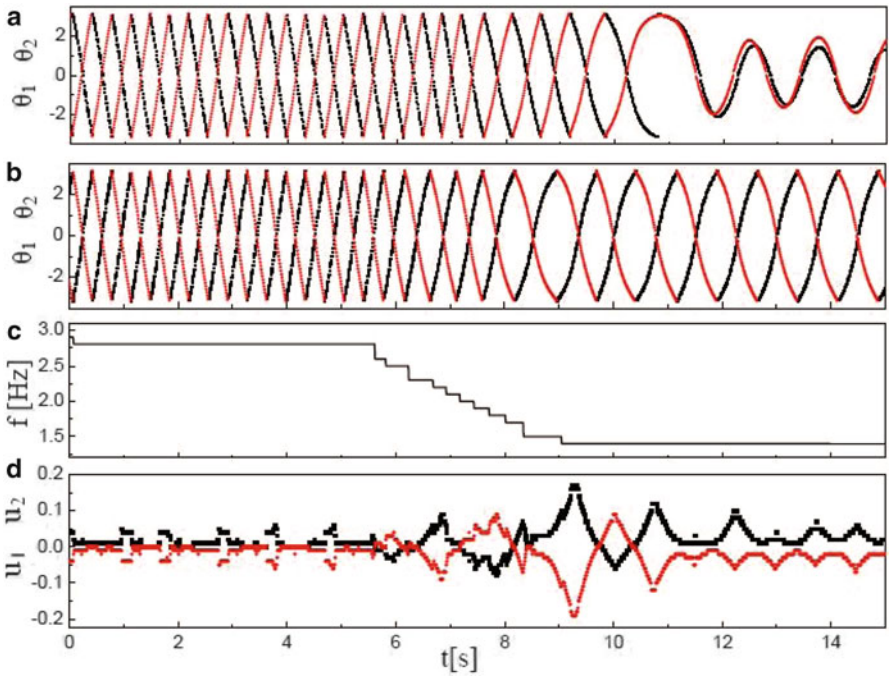

Fig. 5 Experimental results showing angular displacements of the two pendulums without (**a**) and with delayed feedback control (**b**) while changing the excitation frequency form 2.9 to 1.3 Hz (**c**) and control function over time (**d**)

from all initial conditions, if only such an orbit exists for the system parameters. Additionally, the delayed feedback method can be applied to maintain the rotational motion while parameters of the forcing are varied. Figure 5 shows the difference in the responses of the system with and without control, while the forcing frequency was rapidly decreased. In Fig. 6 the response with the control has been simulated numerically. Both numerical and experimental results show that the pendulums with the delayed feedback control applied remain completely synchronized in antiphase irrespectively of the parameter change. A jump in the control signal value for the frequency around 1.5–1.3 was observed both numerically and experimentally.

5.4 Synchronization

One of the methods to synchronize the two pendulums is an application of the two independent delayed feedback controllers of rotational motion. Once the pendulums rotate, their phases lock as the transient time elapses and remain locked as long as the rotational motion is maintained (Fig. 5). Another approach to synchronizing and

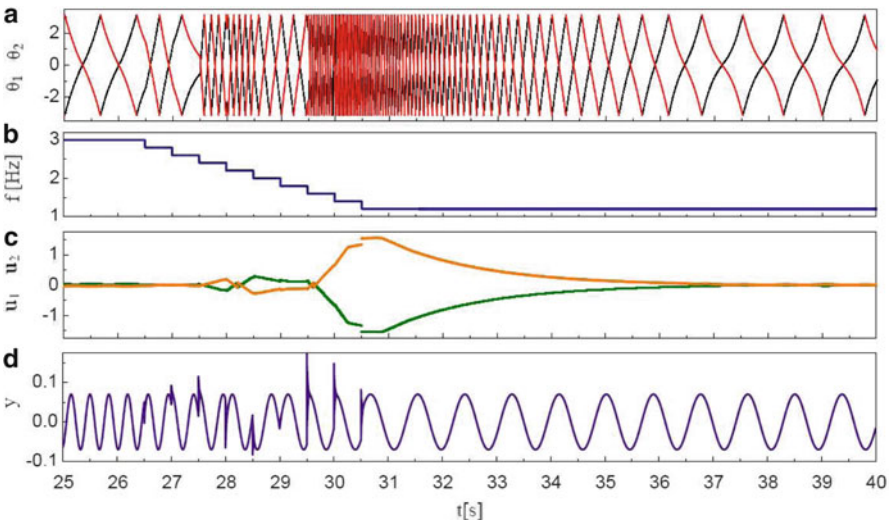

Fig. 6 Numerical results showing the response of the system with the delayed feedback control applied for the frequency changing in the range 2.9–1.3 Hz. (**a**) Synchronized response of two pendulums in terms of their angular displacements, (**b**) the forcing frequency, (**c**) control signals, (**d**) response of the base (vertical oscillation)

controlling the system is to make use of the interactions between the two pendulums and use the information about the state of one of them as a control input for the second one. The idea is to apply a delayed-feedback control to maintain the rotation of one of the pendulums and synchronize the second pendulum with the first one. The velocity difference between the driving and driven pendulum has been used as a second control input. By this control algorithm the pendulums are coupled according to the master-slave scheme, where the 'slave' pendulum is forced to synchronize with the 'master' and supplied with following control signal:

$$u_i = k_i(\dot{\theta}_1(t) - \dot{\theta}_2(t)). \tag{7}$$

The numerical results showing initialization of the synchronized rotation with this method are shown in the Fig. 7.

6 Conclusions

In this study it has been found that the most dominant response of the system consisting of two pendulums coupled by a common base is a synchronized motion. The synchronisation in anti-phase rotation of the two pendulums can be relatively easy to control and several control methods have been proposed. It has been shown that the synchronized rotation can be maintained with both with two dependent and

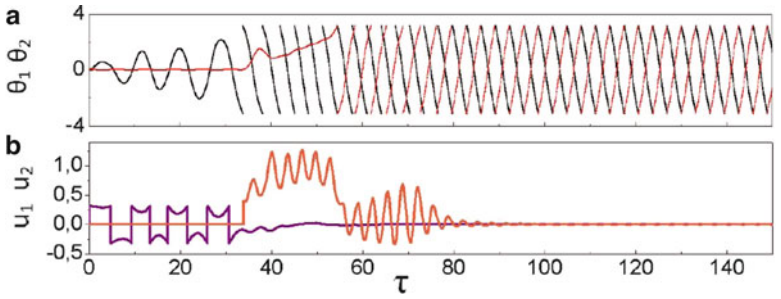

Fig. 7 Numerical results showing the initialization of synchronized rotation for $p_y = 0.07$, $\omega = 2$. (**a**) Angular displacements of pendulum 1 (*black*) and pendulum 2 (*red*), (**b**) control signals $u1$ (*violet*) and $u2$ (*orange*)

independent controllers. Investigating their efficiency is a scope of further study, where the optimal control strategy minimizing the energy input is to be developed.

References

Horton, B., Wiercigroch, M., Xu, X.: Transient tumbling chaos and damping identification for parametric pendulum. Philos. Trans. R. Soc. A, **366**, 767–784 (2008)

Pyragas, K.: Continuous control of chaos by self-controlling feedback. Phys. Lett. A, **170**(6), 421–428 (1992)

Xu, X., Wiercigroch, M., Cartmell, M.P.: Rotating orbits of a parametrically excited pendulum. Chaos Solitons Fractals **23**, 1537–1548 (2005)

Yokoi, Y., Morrison, R., Wiercigroch, M., Hokihara, T.: modelling synchronisation of parametrically excited pendulums. Book of Abstracts, International Conference on Recent Advanced in Nonlinear Mechanics, 24–27 August 2009, Kuala Lumpur, Malaysia (2009)

A Combined Semi-analytical and Experimental Approach for Multiphysical Nonlinear MEMS Resonators

R.M.C. Mestrom, Rob H.B. Fey, K.L. Phan, and H. Nijmeijer

Abstract A combined semi-analytical and experimental approach is proposed for predictive modelling of the nonlinear dynamic behaviour of microelectromechanical resonators. The approach is demonstrated for a clamped-clamped beam resonator, for which the mechanical, electrical, and thermal domains are relevant. Multiphysics modelling is applied, based on first principles, to derive a reduced-order model of the resonator. A qualitative correspondence between numerical and experimental steady-state responses has been obtained. Depending on the excitation values, both simulations and experiments show hardening and softening nonlinear dynamic behaviour. Since the model captures the observed experimental behaviour, it can be used to optimize the resonator behaviour with respect to nonlinear dynamic effects.

Keywords Nonlinear MEMS resonators • Multiphysics modelling • Simulation vs experiments

R.M.C. Mestrom
Electromagnetics and Wireless Group, Department of Electrical Engineering, Eindhoven University of Technology, P.O. Box 513, 5600 MB Eindhoven, The Netherlands
e-mail: r.m.c.mestrom@tue.nl

R.H.B. Fey (✉) • H. Nijmeijer
Dynamics and Control Group, Department of Mechanical Engineering, Eindhoven University of Technology, P.O. Box 513, 5600 MB Eindhoven, The Netherlands
e-mail: r.h.b.fey@tue.nl; h.nijmeijer@tue.nl

K.L. Phan
NXP-TSMC Research Center, NXP Semiconductors, P.O. Box WAG 02, 5656 AE Eindhoven, The Netherlands
e-mail: kim.le.phan@nxp.com

M. Wiercigroch and G. Rega (eds.), *IUTAM Symposium on Nonlinear Dynamics for Advanced Technologies and Engineering Design*, IUTAM Bookseries (closed) 32, DOI 10.1007/978-94-007-5742-4_16,

1 Introduction

During the past two decades, there has been strongly increasing attention for development of microelectromechanical systems (MEMS), because they can be easily integrated in electronic circuits due to their small size and their fabrication process, which is compatible with IC technology. Moreover, in general they offer much lower dissipation levels than their fully electronic component counterparts, resulting in lower noise sensitivity and lower power needs. An important class of MEMS components are MEMS resonators. These find wide application, e.g. in oscillator circuits for timing devices (Nguyen 2007), in sensors, in switches, in filters, and in micro-mirrors.

In order to avoid costly trial-and-error prototyping of MEMS devices, it is desired to have accurate predictive modelling and analysis tools available for the devices in the design and optimisation stage. Scaling effects in MEMS cause the models to be intrinsically multiphysical of nature. Often, the mechanical, electrical, thermal, and fluidic domains are intertwined. Additionally, due to their limited energy storage capability, MEMS devices are often driven into nonlinear regimes to obtain signals with good signal to noise ratios. Therefore, it is essential to take nonlinear behaviour into account, which may be caused by various effects from the involved domains (Kaajakari et al. 2004; Mestrom et al. 2008). Multiphysics finite element modelling may be used, but in general, this is less appropriate for carrying out extensive parameter studies, due to high model dimensions.

In this paper, a combined semi-analytical and experimental approach will be proposed for fast and accurate predictive modelling of MEMS devices. The approach will be demonstrated on a specific MEMS device, namely a clamped-clamped beam MEMS resonator. The approach extends lumped modelling efforts (Kaajakari et al.2004; Shao et al. 2008) to a first-principles based approach. Such an approach has been described in, for instance, Younis et al. (2003) (simulations only). The main benefit of this modelling approach is that the derived model is much more suitable for parameter studies and optimisation, since physical and geometrical parameters will appear in the model explicitly.

The outline of the paper is as follows. First, the MEMS resonator that is used for the case study will be introduced in Sect. 2. Next, the modelling approach will be explained in Sect. 3. Numerical and experimental results will be presented in Sect. 4 and the paper will be concluded in Sect. 5.

2 MEMS Resonator

In this work, an electrostatically actuated clamped-clamped beam MEMS resonator is under investigation. A schematic representation of the resonator is depicted in Fig. 1. The resonator beam has a length of $l = 47.75\,\mu\text{m}$, a width of $h = 4\,\mu\text{m}$ and a of $b = 1.4\,\mu\text{m}$ (out-of-plane). The electrode gaps (of electrodes 1 and 2) are

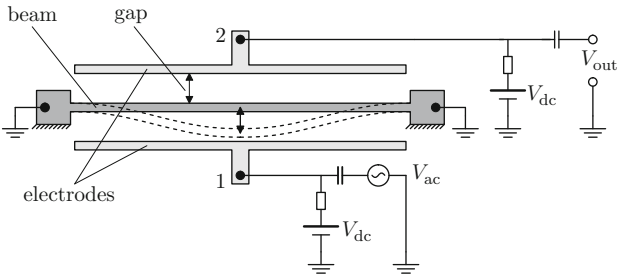

Fig. 1 Schematic layout of the clamped-clamped beam resonator

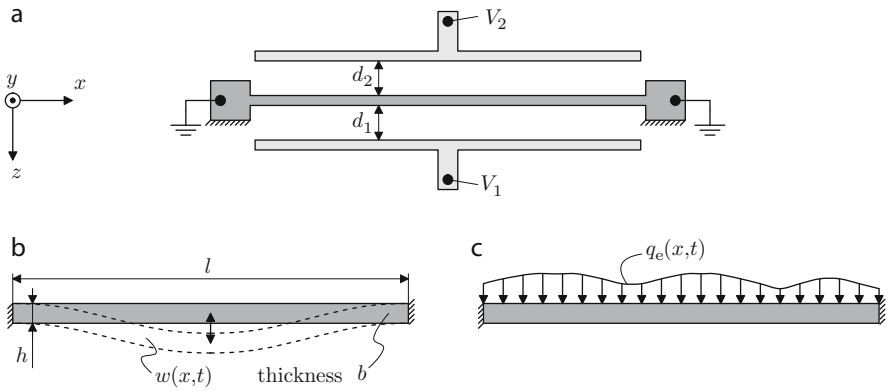

Fig. 2 Schematic model of the clamped-clamped beam resonator. (**a**) Schematic layout. (**b**) Beam dimensions and deflection. (**c**) Distributed electrostatic load.

$d_1 = d_2 = 342\,\text{nm}$. A more detailed schematic of the model will be given in Fig. 2 in Fig. 2 in Sect. 3. The characteristic flexural vibration shape of the beam is depicted by the dashed lines. The resonator is actuated by a dc (V_{dc}) and an ac (V_{ac}) voltage component, which are applied to the electrodes of the resonator by means of bias tees. During measurements, the resonator is located in a vacuum chamber (pressure $p = 4.6 \times 10^{-4}\,\text{mbar}$). The steady-state dynamic behaviour of the resonator is investigated by measuring the resonator output voltage V_{out} as a function of the ac excitation frequency f. From the peak-to-peak values of V_{out} during a (stepped) sweep-up and sweep-down in frequency, an amplitude-frequency curve can be constructed. Voltage V_{out} results from capacitive detection of the resonator motion and is related to the clamped-clamped beam flexural displacement and velocity, as will become clear from Sect. 3. The resonators are fabricated using Silicon-On-Insulator (SOI) wafers. For more details on the fabrication process, see Mestrom et al. (2008).

3 Modelling

The semi-analytical modelling approach for the MEMS resonator is based on first-principles descriptions (partial differential equations (PDEs) and functional relations) of relevant effects in three physical domains. Since the resonator is operated in vacuum, the fluidic domain will not be included. The model will contain effects from the mechanical, thermal, and electrical domain. In the next two sections, the model of the MEMS resonator and its implementation as a reduced-order model will be described, respectively.

3.1 Model of the MEMS Resonator

A detailed representation of the clamped-clamped beam resonator is depicted in Fig. 2. The schematic layout of the resonator depicted in Fig. 2a is the same as given in Fig. 1. Dimensions and the transverse displacement of the beam are depicted in Fig. 2b and the distributed electrostatic force q_e, acting on the beam, is shown in Fig. 2c. For the MEMS resonator considered in this work, the width-to-length ration h/l (see Sect. 2) is such that shear deformation may play a role. Therefore, Timoshenko beam theory will be used (Timoshenko 1921), which includes both shear deformation and rotary inertia. By using this theory, the transverse displacement $w(x,t)$ and shear deformation $\varphi(x,t)$ can be described by two coupled PDEs:

$$\rho A\frac{\partial^2 w}{\partial t^2} - k_s GA\left(\frac{\partial \varphi}{\partial x} + \frac{\partial^2 w}{\partial x^2}\right) - \left[\frac{EA}{2l}\int_0^l \left(\frac{\partial w}{\partial x}\right)^2 \mathrm{d}x - \frac{1}{l}\int_0^l N_T\,\mathrm{d}x\right]\frac{\partial^2 w}{\partial x^2} = q_e, \tag{1a}$$

$$\rho I\frac{\partial^2 \varphi}{\partial t^2} - EI\frac{\partial^2 \varphi}{\partial x^2} + \frac{\partial M_T}{\partial x} + k_s GA\left(\varphi + \frac{\partial w}{\partial x}\right) = 0, \tag{1b}$$

where x denotes the coordinate along the beam length, see also Fig. 2a. Furthermore, ρ is the mass density, $A = bh$ and $I = bh^3/12$ denote the area and the area moment of inertia, respectively, E is Young's modulus, G is the shear modulus, $k_s = (5+5\nu)/(6+5\nu)$ is the shear correction factor (Kaneko 1975), where ν is Poisson's ratio. The term with $\int(\frac{\partial w}{\partial x})^2\mathrm{d}x$ in (1a) denotes midplane stretching of the beam, resulting in cubic stiffness terms. This will yield a hardening nonlinear effect, see for instance (Kaajakari et al. 2004). Furthermore, the terms M_T and N_T are related to thermoelastic damping and couple (1) to the temperature distribution (or thermal field) $\theta(x,z,t)$ through:

$$M_T = E\alpha b\int_{-\frac{h}{2}}^{\frac{h}{2}} z\theta\,\mathrm{d}z, \qquad N_T = E\alpha b\int_{-\frac{h}{2}}^{\frac{h}{2}} \theta\,\mathrm{d}z, \tag{2}$$

where α is the thermal expansion coefficient and z is the coordinate across the beam width. The heat equation, which describes the thermal field of the beam, is derived from general thermoelasticity theory (Boley and Weiner 1960). The resulting heat equation is in line with results from Lifshitz and Roukes (2000) and Zener (1937) and reads:

$$\rho c_{\mathrm{p}} \frac{\partial \theta}{\partial t} = k \frac{\partial^2 \theta}{\partial z^2} - T_0 \alpha E \frac{\partial}{\partial t}\left[\frac{1}{2}\left(\frac{\partial w}{\partial x}\right)^2 + z\frac{\partial \varphi}{\partial x}\right], \tag{3}$$

where c_{p} denotes the heat capacity per unit volume, k is the thermal conductivity, and where T_0 is the equilibrium temperature. Thermal variable θ denotes the temperature difference with respect to T_0.

For the distributed electrostatic load, q_{e} in (1a), first-order fringing field correction (Osterberg and Senturia 1997) is included. The load is given by:

$$q_{\mathrm{e}} = \frac{\varepsilon_0 b V_1^2(t)}{2(d_1 - w)^2}\left(1 + 0.65\frac{d_1 - w}{b}\right) - \frac{\varepsilon_0 b V_2^2}{2(d_2 + w)^2}\left(1 + 0.65\frac{d_2 + w}{b}\right), \tag{4}$$

where ε_0 denotes the permittivity of vacuum and where the voltages on the electrodes (see Figs. 1 and 2a) are given by:

$$V_1(t) = V_{\mathrm{dc}} + V_{\mathrm{ac}} \sin(2\pi f t) \quad \text{and} \quad V_2 = V_{\mathrm{dc}}. \tag{5}$$

Equation (4) corresponds with recently reported work on an electrostatically actuated microbeam (Krylov 2007). It is known from literature (Kaajakari et al. 2004; Mestrom et al. 2008) that electrostatic actuation causes softening nonlinear behavior.

Finally, boundary conditions for the mechanical PDEs (1) and the thermal PDE (3) correspond to clamped edges and insulated boundaries, respectively, and are given by:

$$w = 0, \quad \varphi = 0 \quad \text{at} \quad x = 0, l\,, \qquad \text{and} \qquad \frac{\partial \theta}{\partial z} = 0 \quad \text{at} \quad z = \pm\frac{h}{2}\,. \tag{6}$$

Several dissipation mechanisms can be present in MEMS resonators. Fluidic loss mechanisms (such as squeeze film damping or viscous drag) are considered to have negligible influence, since the resonators are operated in vacuum. Next to thermoelastic damping, anchor loss is included in the resonator model, since the MEMS resonator is clamped at two edges. In the current model, anchor loss will be accounted for by means of an effective Q-factor. The amount of dissipation in a structure can be expressed by means of a total mechanical quality factor Q_{tot} (Tilmans et al. 1992):

$$Q_{\mathrm{tot}} = 2\pi \frac{\mathscr{W}}{\Delta \mathscr{W}}, \tag{7}$$

where $\mathscr{W}$ equals the total energy stored in the resonator and $\Delta\mathscr{W}$ is the total energy dissipated per cycle of vibration. All loss mechanisms contribute to the total energy dissipated. Under the assumption of linear dissipation effects, the principle

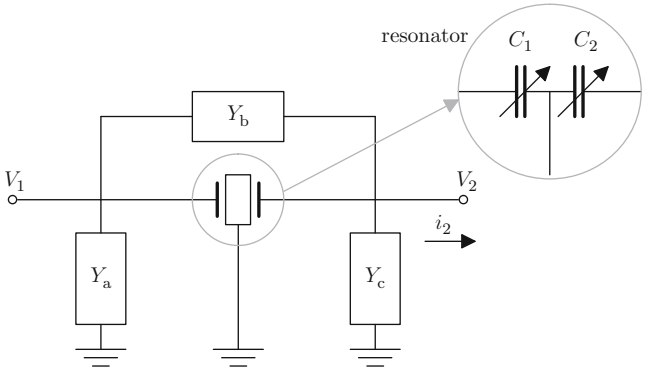

Fig. 3 Measurement circuit for the MEMS resonator containing parasitic effects

of superposition holds for individual Q-factors. By introducing quality factors Q_i, attributed to each loss mechanism, Q_{tot} then becomes:

$$\frac{1}{Q_{\text{tot}}} = \frac{1}{Q_{\text{a}}} + \frac{1}{Q_{\text{th}}}, \tag{8}$$

where Q_{a} and Q_{th} denote the quality factors related to anchor loss and thermoelastic damping, respectively. In Hao and Xu (2009), 2D elastic wave theory has been applied in order to derive an analytical estimate of the anchor loss. In the theory, elastic waves are assumed to radiate into an infinite substrate. By applying this theory, an estimate of $Q_{\text{a}} = 120$ is found. From experiments, see Sect. 4, this value is found to be much too low. This is believed to be caused by the fact that the current resonator layout does not correspond well with the one analysed in Hao and Xu (2009) and by wave reflections in the anchors. For this reason, tuning freedom will be allowed for Q_{a} in the model.

Furthermore, the effect of thermal noise is taken into account. In every electrical system, thermal agitation of the electrons inside electrical conductors forms a source of noise. This noise is called Johnson-Nyquist or thermal noise (Nyquist 1928). The expression for the root mean square (rms) of the noise voltage v_{n} generated in a resistor is given as Nyquist (1928):

$$v_{\text{n}} = \sqrt{4k_{\text{B}}TR\Delta f}, \tag{9}$$

where k_{B} denotes Boltzmann's constant, T denotes absolute temperature, R is the resistor value, and Δf is the bandwidth, in which the noise is measured. An estimate for the thermal noise can be found by using the resonator motional resistance R_{m} for the resistor value R in (9). This will become clear in Sect. 4.

As indicated in Sect. 2, the motion of the resonator is sensed capacitively and transformed to an output voltage V_{out}. This is done using the measurement circuit around the resonator as depicted in Fig. 3. The resonator is depicted in the gray

circle. From an electrical point of view, it can be considered as a pair of varying capacitors C_1 and C_2, denoting electrode gaps 1 and 2, respectively, see also (4). Voltages V_1 and V_2 are given in (5). Admittances Y_a, Y_b, and Y_c have been included in a Π-network around the resonator, in order to describe the response of the parasitics in the circuit. In general, each of these admittances can be written as a parallel combination of a resistor and a capacitor. Therefore, the admittances become:

$$Y_i = \frac{1}{R_i} + j\omega C_i, \quad i = \mathrm{a}, \mathrm{b}, \mathrm{c}. \tag{10}$$

Note that this is a mathematical description, based on a resistor and capacitor in parallel, which may result in negative resistance or capacitance values. If this happens, a representation using a series combination of a resistor and a capacitor would be physically more appropriate.

Only parasitics Y_b of the circuit in Fig. 3 contribute to the measured response V_{out}. Parasitics in Y_a do not influence the output at port 2 and only a single electrode of the resonator—variable capacitor C_2—is used for output measurements. In addition, at port 2, a bias tee is present to decouple the dc component from the output current i_2 (hence, Y_c does not influence V_{out}). As a result, the ac part of the output current i_2 can be found using Kirchoff's current law and equals:

$$i_2 = \frac{V_1 - V_2}{R_b} + C_b \frac{\mathrm{d}(V_1 - V_2)}{\mathrm{d}t} - \frac{\mathrm{d}(C_2 V_2)}{\mathrm{d}t}. \tag{11}$$

Using (5) gives:

$$i_2 = \frac{V_{ac}}{R_b} \sin(2\pi f t) + 2\pi f V_{ac} C_b \cos(2\pi f t) - V_{dc} \frac{\mathrm{d}C_2}{\mathrm{d}t}. \tag{12}$$

The capacitance C_2 depends on the resonator deformation w. Similar as in the electrostatic distributed force q_e (4), first-order fringing field effects are included, giving:

$$C_2 = \int_0^l \frac{\varepsilon_0 b}{d_2 + w} \left[1 + \frac{2(d_2 + w)}{\pi b} + \frac{2(d_2 + w)}{\pi b} \ln\left(\frac{\pi b}{d_2 + w} \right) \right] \mathrm{d}x. \tag{13}$$

By elaborating the time derivative of C_2, the output current ($i_{out} = i_2$) of the resonator becomes:

$$\begin{aligned} i_{out} = {} & \frac{V_{ac}}{R_b} \sin(2\pi f t) + 2\pi f V_{ac} C_b \cos(2\pi f t) \\ & + V_{dc} \int_0^l \frac{\varepsilon_0 b}{(d_2 + w)^2} \left(1 + 0.65 \frac{d_2 + w}{b} \right) \frac{\partial w}{\partial t} \, \mathrm{d}x, \end{aligned} \tag{14}$$

which is measured on a 50 Ω resistor R_{50}. Therefore the measured output voltage equals:

$$V_{\text{out}} = R_{50}\, i_{\text{out}}. \tag{15}$$

3.2 Reduced-Order Model

The total model of the MEMS resonator under consideration is formed by the PDEs describing the transverse deflection and the heat equation (1)–(5), together with the associated boundary conditions (6) and the anchor loss dissipation mechanism. Galerkin discretisation (Meirovitch 2001) will be applied to arrive at a reduced-order model for the PDEs. In this weighted residual technique, the solution to the PDEs is assumed to be in the form of a linear combination of trial functions that satisfy the boundary conditions a priori. The method can also be applied to nonlinear systems, both conservative and non-conservative.

For the reduced-order model, the transverse deflection $w(x,t)$, the shear deformation $\varphi(x,t)$, and thermal variable $\theta(x,z,t)$ can be written as summations of n basis functions (modes):

$$w(x,t) = \sum_{i=1}^{n} q_i(t) W_i(x), \tag{16}$$

$$\varphi(x,t) = \sum_{i=1}^{n} p_i(t) \Phi_i(x), \tag{17}$$

$$\theta(x,z,t) = \sum_{i=1}^{n} r_i(t) \Theta_i(x,z), \tag{18}$$

where $q_i(t)$, $p_i(t)$, and $r_i(t)$ denote time-dependent generalised coordinates and $W_i(x)$, $\Phi_i(x)$, and $\Theta_i(x,z)$ are spatial basis functions. Undamped eigenmodes are used as spatial basis functions for the mechanical part (1), see also (Han et al. 1999). For the thermal field, basis functions $\Theta_i(x,z)$ have been derived from the linearized version of (3) in a similar way as presented in Lifshitz and Roukes (2000). An overview of the expressions for the basis functions is presented in Table 1. Furthermore, only symmetric modes will be used for Galerkin discretisation, since the electrodes of the resonator span the whole beam length. This translates to $i = 1, 3, 5, \ldots$ in Table 1.

After the application of Galerkin discretisation, a set of nonlinear coupled ordinary differential equations (ODEs) in the time-dependent generalised coordinates p_i, q_i, and r_i is obtained. This set of ODEs is solved using dedicated numerical techniques, available in the package AUTO97 (Doedel et al. 1998). This package can be used to calculate branches of steady-state periodic solutions for varying excitation frequency f. In addition, it calculates the local stability of these solutions and detects local bifurcation points on these branches. In this way, numerical amplitude-frequency curves can be determined for the MEMS resonator.

As explained before, two dissipation mechanisms are included in the model. Thermoelastic damping is included intrinsically, through the mutual coupling between the structural and heat PDEs. Quality factor Q_{th} can be obtained from the

Table 1 Spatial basis functions for the fields w, φ, and θ

Function	Expression
$\Phi_i(x)$	$\alpha_i \sin\frac{a_i x}{l} + \beta_i \sinh\frac{b_i x}{l} + \alpha_i \sigma_i \left(\cos\frac{a_i x}{l} - \cosh\frac{b_i x}{l}\right)$
$W_i(x)$	$\cos\frac{a_i x}{l} - \cosh\frac{b_i x}{l} - \sigma_i \left(\sin\frac{a_i x}{l} - \frac{\alpha_i}{\beta_i}\sinh\frac{b_i x}{l}\right)$
	$\sigma_i = \dfrac{\cos a_i - \cosh b_i}{\sin a_i - \frac{\alpha_i}{\beta_i}\sinh b_i}$
	$a_i = l\sqrt{\left(\frac{1}{E} + \frac{1}{k_s G}\right)\frac{\rho\omega_i^2}{2} + \frac{1}{2}\sqrt{\left(\frac{1}{E} + \frac{1}{k_s G}\right)^2 \rho^2\omega_i^4 + 4\left(\frac{A\rho}{EI}\omega_i^2 - \frac{\rho^2}{k_s GE}\omega_i^4\right)}}$
	$b_i = l\sqrt{-\left(\frac{1}{E} + \frac{1}{k_s G}\right)\frac{\rho\omega_i^2}{2} + \frac{1}{2}\sqrt{\left(\frac{1}{E} + \frac{1}{k_s G}\right)^2 \rho^2\omega_i^4 + 4\left(\frac{A\rho}{EI}\omega_i^2 - \frac{\rho^2}{k_s GE}\omega_i^4\right)}}$
	$\alpha_i = \dfrac{k_s GAa_i^2 - \rho Al^2\omega_i^2}{k_s GAla_i} \qquad \beta_i = \dfrac{k_s GAb_i^2 + \rho Al^2\omega_i^2}{k_s GAlb_i}$
	where ω_i are the roots of the frequency equation, using $a_i, b_i, \alpha_i, \beta_i$:
	$\alpha^2 \sin a \sinh b + 2\alpha\beta \cos a \cosh b - \beta^2 \sin a \sinh b - 2\alpha\beta = 0$
$\Theta_i(x,z)$	$-\dfrac{E\alpha T_0}{\rho c_p}\dfrac{\mathrm{d}\Phi_i(x)}{\mathrm{d}x}\left(z + \dfrac{h}{2\pi}\sin\frac{2\pi z}{h}\right)$

physical and geometrical parameters of the system. Secondly, an effective Q-factor Q_a accounts for anchor loss in the reduced-order model. Its value will be determined from experiments, since a theoretical derivation of Q_a was too low. Subsequently, using (8), the total Q-factor Q_{tot} can be determined.

Preliminary simulations have been performed to determine the number of basis functions needed to describe the dynamic response of the system accurately. For the MEMS resonator considered, a single-mode discretisation for each field has been found to be sufficient to accurately describe the dynamic response in the frequency range of operation, i.e. near the first harmonic resonance peak.

4 Results

A series of experiments has been performed in order to validate the simulation model derived in the previous section. Physical parameter values for the model have been obtained from literature (evaluated at a temperature of $T_0 = 300\,\mathrm{K}$). These are listed in Table 2. Geometrical and other parameter values are also listed in Table 2. With respect to the beam geometry, the width h and thickness b are assumed to be fixed (see Sect. 2). The length of the beam is adjusted such that the first natural frequency in the simulations is the same as in the experiment. The length may differ from the nominal design value due to under-etching of the clamped ends. Additionally, this may compensate for non-ideal clamping. The first natural frequency of the resonator equals $f_0 = 13.0724\,\mathrm{MHz}$. Values of the

Table 2 Physical and geometrical parameter values used in the simulations

Parameter	Value	Unit	Parameter	Value	Unit
ρ	2,329	$\mathrm{kg\,m^{-3}}$	l	47.75	μm
E	130.02	GPa	d_1, d_2	342	nm
G	79.51	GPa	h	4	μm
ν	0.2785	(–)	b	1.4	μm
k	156	$\mathrm{W\,m^{-1}\,K^{-1}}$	f_0	13.0724	MHz
c_p	716	$\mathrm{J\,kg^{-1}\,K^{-1}}$	C_b	7.156	fF
α	$2.616 \cdot 10^{-6}$	$\mathrm{K^{-1}}$	R_b	−2.9886	GΩ
T_0	300	K	Q_th	14,250	–

parasitic electrical parameters C_b and R_b have been determined from electrical characterization of the resonator (using S-parameter measurements, see Pozar (2005)). It can be seen that the resistance value R_b is negative, indicating that the parasitic admittance Y_b is more appropriately modelled as a series combination of a capacitor and a resistor. The Q-factor related to thermoelastic damping can be determined from a damped eigenvalue analysis of the model. Its value is also listed in Table 2.

For various V_ac and V_dc excitation settings, measurements and simulations will be compared. For a range of values corresponding approximately to a constant $V_\mathrm{dc}V_\mathrm{ac}$ product, the influence of V_dc is investigated, by varying it between 10 and 40 V. The product $V_\mathrm{ac}V_\mathrm{dc}$ is a measure for the harmonic excitation amplitude (due to V^2-terms in the excitation).

Figure 4 shows amplitude-frequency curves in terms of the peak-to-peak values of V_out versus ac excitation frequency f. Excitation settings as listed in Table 3 have been used. The four measurement results are shown in Fig. 4a and the four corresponding simulation results are depicted in Fig. 4b. The measured response is observed to jump between high-amplitude and low-amplitude solutions, indicated by the arrows in Fig. 4a. It can be seen from Fig. 4 that for higher V_dc-values, the resonance frequency is lower. Furthermore, jumps in the measured amplitude-frequency curves indicate that for $V_\mathrm{dc} = 10\,\mathrm{V}$, hardening nonlinear behavior is present, whereas the curves at $V_\mathrm{dc} = 30$ and $40\,\mathrm{V}$ show softening nonlinear behavior. The response at $V_\mathrm{dc} = 20\,\mathrm{V}$, for $V_\mathrm{ac} = 500\,\mathrm{mV}$ shows a resonance without frequency hysteresis.

In the simulated steady-state responses, the occurrence of cyclic fold (CF) bifurcation points (Thomsen 2003) coincides with experimentally observed jumps in amplitude. In the simulations, CF bifurcations mark turning points, where transitions from stable to unstable periodic solutions (and vice versa) occur. Simulation results show the same transition from hardening to softening nonlinear behaviour for increasing V_dc as the experimental results. For the hardening responses, the mid-plane stretching effect is dominant, whereas for the softening responses, the electrostatic nonlinear effect is dominant. This has also been observed in simulations in Younis and Nayfeh (2003). By comparing numerical and experimental results, it can be seen that a good qualitative match has been obtained. Simulated and

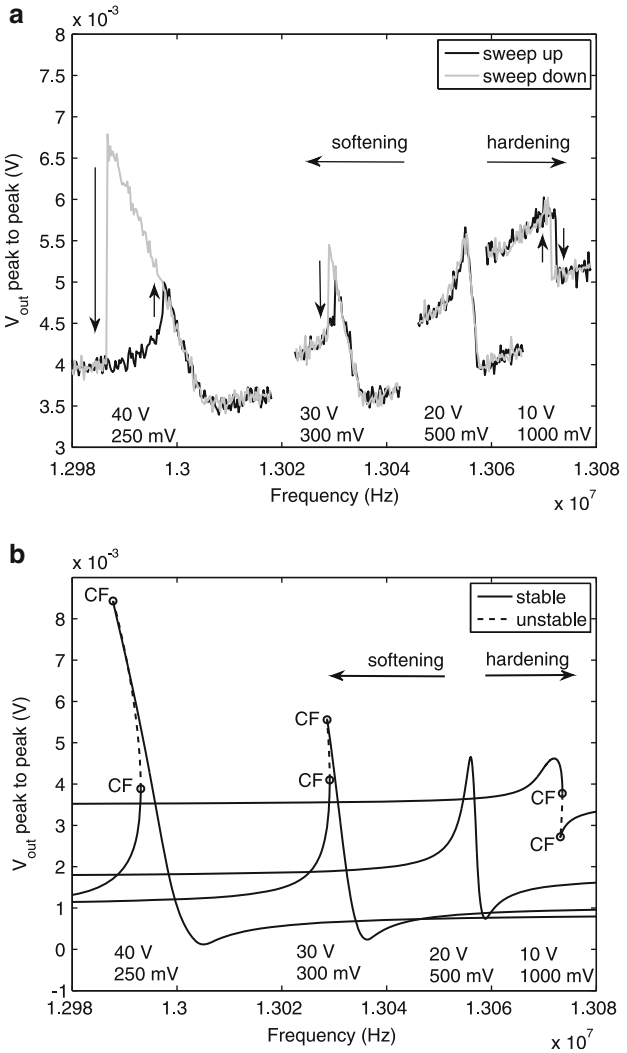

Fig. 4 Transition from hardening to softening nonlinear behavior for varying excitation values. **(a)** Experimental results. **(b)** Simulation results

Table 3 Excitation settings corresponding approximately to $V_{dc}V_{ac} = \text{constant}$

V_{dc} (V)	V_{ac} (mV)
10	1,000
20	500
30	300
40	250

measured resonance peaks are located at the same frequencies and they also have similar shapes. However, a mismatch in amplitudes is present, which is likely to be caused by thermal noise (9) and by cabling impedance (impedance mismatch). The explanation is as follows. Firstly, the effect of thermal noise can be included as a postprocessing step (see Mestrom et al. 2008), resulting in a vertical shift of the curve. The motional impedance R_m of the resonator ranges from 396 kΩ up to 1.63 mΩ. Using (9), this translates to rms noise voltages of $v_n = 1.3{-}2.6$ mV. The effect of noise can most clearly be observed as the mismatch away from resonance. Secondly, the mismatch in impedance varies with the resonator response, since, from an electrical point of view, the impedance is a function of frequency and vibration amplitude. For a nonlinear resonator, this relation cannot be determined in a straightforward way. This effect is most pronounced as a mismatch in amplitude of the resonance peak. The total observed mismatch pattern results from a combination of these two effects, which makes it difficult to distinguish between these two error sources. The dip in the amplitude-frequency curves, both in experiments and simulations, at a frequency slightly above the resonance frequency, is caused by the presence of parasitic effects Y_b (mainly by C_b) in the measurement circuit.

As described in Sect. 3.2, anchor loss has been implemented by means of a Q-factor Q_a. Using relation (8), Q_a is tuned such that the shapes of the simulated resonance peaks match the experimental ones and such that the downward jump frequency in experiments corresponds with the upper cyclic fold (CF) bifurcation points in simulations. In this way, a value of $Q_a = 11{,}000$ is found, to obtain an overall Q-factor of $Q_{tot} = 6{,}210$, see (8).

5 Conclusions

In this paper, a combined semi-analytical and experimental approach has been proposed for fast and accurate predictive modelling and analysis of a nonlinear MEMS resonator. A good qualitative correspondence between simulations and experiments has been obtained, thereby validating the multiphysical model. Characteristic hardening and softening nonlinear dynamic behaviour is captured well. A main advantage of the followed approach is that the obtained model is in parameterised form, containing physical parameters, instead of a more heuristic (or lumped) description. The approach is not restricted to the specific MEMS resonator considered in this paper. It can also be applied to other MEMS devices. In addition to characterization of the dynamic response, the efficient semi-analytical modelling and analysis approach also enables optimisation of pre-designs of MEMS devices. Finite element modelling and analysis may be seen as a complementary approach, which can be used in the final design stage.

References

Boley, B.A., Weiner, J.H.: Theory of Thermal Stresses. Wiley, New York (1960)

Doedel, E., Champneys, A.R., Fairgrieve, T.F., Kuznetsov, Y.A., Sandstede, B., Wang, X.: AUTO97: Continuation and Bifurcation Software for Ordinary Differential Equations (with HomCont), Technical Report, Concordia University (1998)

Han, S.M., Benaroya, H., Wei, T.: Dynamics of transversely vibrating beams using four engineering theories. J. Sound Vib. **225**(5), 935–988 (1999)

Hao, Z., Xu, Y.: Vibration displacement on substrate due to time-harmonic stress sources from a micromechanical resonator. J. Sound Vib. **322**(1–2), 196–215 (2009)

Kaajakari, V., Mattila, T., Oja, A., Seppä, H.: Nonlinear limits for single-crystal silicon microresonators. J. Microelectromech. Syst. **13**(5), 715–724 (2004)

Kaneko, T.: On Timoshenko's correction for shear in vibrating beams. J. Phys. D **8**, 1927–1936 (1975)

Krylov, S.: Lyapunov exponents as a criterion for the dynamic pull-in instability of electrostatically actuated microstructures. Int. J. Non-Linear Mech. **42**(4), 626–642 (2007)

Lifshitz, R., Roukes, M.L.: Thermoelastic damping in micro- and nanomechanical systems. Phys. Rev. B **61**(8), 5600–5609 (2000)

Meirovitch, L.: Fundamentals of Vibrations. McGraw-Hill, London (2001)

Mestrom, R.M.C., Fey, R.H.B., Beek, J.T.M.v., Phan, K.L., Nijmeijer, H.: Modelling the dynamics of a MEMS resonator: simulations and experiments. Sens. Actuators A **142**(1), 306–315 (2008)

Nguyen, C.T.C.: MEMS technology for timing and frequency control. IEEE Trans. Ultrason. Ferroelectr. Freq. Control **54**(2), 251–270 (2007)

Nyquist, H.: Thermal agitation of electric charge in conductors. Phys. Rev. **32**(1), 97–109 (1928)

Osterberg, P.M., Senturia, S.D.: M-TEST: a test chip for MEMS material property measurement using electrostatically actuated test structures. J. Microelectromech. Syst. **6**(2), 107–118 (1997)

Pozar, D.M.: Microwave Engineering, 3rd edn. Wiley, Hoboken (2005)

Shao, L.C., Wong, C.L., Palaniapan, M.: Study of the nonlinearities in micromechanical clamped-clamped beam resonators using stroboscopis SEM. J. Micromech. Microeng. **18**(8), 085019 (11pp) (2008)

Thomsen, J.J.: Vibrations and Stability; Advanced Theory, Analysis and Tools, 2nd edn. Springer, Berlin (2003)

Tilmans, H.A.C., Elwenspoek, M., Fluitman, J.H.J.: Micro resonant force gauges. Sens. Actuators A **30**(1), 35–53 (1992)

Timoshenko, S.P.: On the correction for shear of the differential equation for the transverse vibrations of prismatic bars. Philos. Mag. **41**, 744–746 (1921)

Younis, M.I., Nayfeh, A.H.: A study of the nonlinear response of a resonant microbeam to an electric actuation. Nonlinear Dyn. **31**(1), 91–117 (2003)

Younis, M.I., Abdel-Rahman, E.M., Nayfeh, A.H.: A reduced-order model for electrically actuated microbeam-based MEMS. J. Microelectromech. Syst. **12**(5), 672–680 (2003)

Zener, C.: Internal friction in solids; I. theory of internal friction in reeds. Phys. Rev. **52**(3), 230–235 (1937)

Vibration Reduction Using Shape Memory Alloys

Marcelo A. Savi, R.A.A. Aguiar, and P.M.C.L. Pacheco

Abstract Smart materials have a growing technological importance due to their unique thermomechanical characteristics. Shape memory alloys (SMAs) belong to this class of materials being easy to manufacture, relatively lightweight, and able of producing high forces or displacements with low power consumption. These aspects could be explored in different applications including vibration control. Nevertheless, there is a lack in literature concerning the experimental analysis of SMA dynamical systems. This contribution deals with the experimental analysis of SMA dynamical systems by considering an experimental apparatus composed of low-fiction cars free to move in a rail. A shaker that provides harmonic forcing excites the system. Vibration analysis reveals that SMA elements introduce complex dynamical responses to the system and different thermomechanical loadings are of concern showing the main aspects of SMA dynamical response. Special attention is dedicated to the analysis of vibration reduction that can be achieved by considering different approaches exploiting either temperature changes or vibration absorber techniques.

Keywords Smart material • Shape memory alloy • Vibration reduction

M.A. Savi (✉)
Department of Mechanical Engineering, Universidade Federal do Rio de Janeiro,
P.O. Box 68.503, 21 941 972 Rio de Janeiro, RJ, Brazil
e-mail: savi@mecanica.ufrj.br

R.A.A. Aguiar • P.M.C.L. Pacheco
Department of Mechanical Engineering, CEFET/RJ, 20271-110 Rio de Janeiro, RJ, Brazil
e-mail: raaguiar@cefet-rj.br; calas@cefet-rj.br

M. Wiercigroch and G. Rega (eds.), *IUTAM Symposium on Nonlinear Dynamics for Advanced Technologies and Engineering Design*, IUTAM Bookseries (closed) 32, DOI 10.1007/978-94-007-5742-4_17,

1 Introduction

The remarkable properties of SMAs are attracting much technological interest, motivating different applications in several fields of sciences and engineering. Robotics, aerospace and biomedical applications are some areas where SMAs have been applied (Lagoudas 2008; Paiva and Savi 2006; Machado and Savi 2002, 2003). Due to their high dissipation capacity related to hysteretic behaviour, SMA elements are being used in vibrating systems (Williams et al. 2005; Rustighi et al. 2005a, b; Elahinia et al. 2005; Tiseo et al. 2010). Moreover, the temperature induced phase transformation can be used in order to promote stiffness variations and, as a consequence, altering system dynamical characteristics. Dynamical behaviour of SMA systems is investigated in different research efforts, presenting complex behaviours. For details, see some of the references: (Savi et al. 2002, 2008; Machado et al. 2003, 2009; Savi and Pacheco 2002). Recently, SMAs are being used in impact systems where the dissipative characteristics of SMA can produce very different behaviours when compared with elastic systems: (Sitnikova et al. 2010; Santos and Savi 2009). This paper deals with an experimental analysis of the dynamical behaviour of oscillators with SMA elements. An experimental apparatus composed of low-fiction cars free to move in a rail is attached to an SMA helical spring. This apparatus is used to investigate two different systems: one- and two degrees-of-freedom. A shaker that provides harmonic forcing excites the system. Vibration analysis reveals that SMA elements introduce complex dynamical responses to the system and different thermomechanical loadings are of concern showing the main aspects of SMA dynamical response. Vibration reduction can be achieved by considering different approaches exploiting either temperature changes or vibration absorber techniques.

2 Experimental Apparatus

The dynamical behaviour of SMA oscillators is studied with the use of the apparatus shown in Fig. 1, composed of low-fiction cars free to move in a rail. Basically, two different configurations are of concern: one- and two degrees-of-freedom. The one-degree of freedom (1DOF) system is composed of a car connected to two springs: elastic and SMA spring. The elastic spring is connected to an excitation system composed of an electrodynamic shaker (LabWorks ET-126 with 58 N peak force capacity) connected to the system with the aid of an extra car. The SMA spring is fixed to the load-cell (Alfa SV-20 with 196 N capacity). Figure 1 presents the schematic draw together with a picture of the 1DOF system.

The two-degree of freedom (2DOF) system considers a new car connected to the system. This system is employed to represent a vibration absorber composed of a primary system with linear elastic characteristics, and a secondary system composed

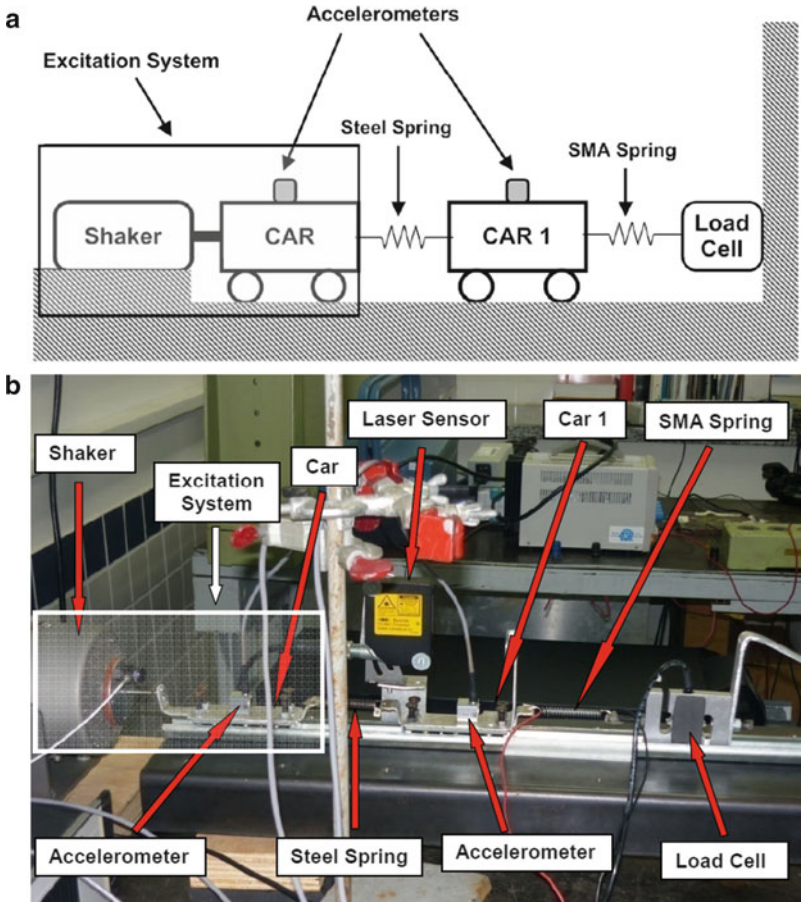

Fig. 1 Experimental apparatus to study the dynamical behaviour of one-degree of freedom SMA oscillator – (**a**) schematic draw and (**b**) picture of the system

of a linear elastic spring together with an SMA spring. Therefore, this system is composed of two elastic springs. On one side, there is a spring connected to the excitation system. On the other side, there is a spring connected to the car of the secondary system. This new car is connected to an SMA spring that is connected to a load cell. Figure 2 presents the details of the 2DOF system.

The vibration system is mounted in a close-loop configuration controlled by a vibration controller system (LabWorks VibeLab VL-145s Digital Sine Controller) with sine-sweep controller capability. Cars are monitored by accelerometers transducers (Kyowa AS-10GB with 10 g capacity) connected to a data acquisition system (HBM Spider 8) with 400 Hz acquisition rate. A laser sensor is also employed to monitor displacements (Baumer OADM 20I4460/S14C). Temperature variations

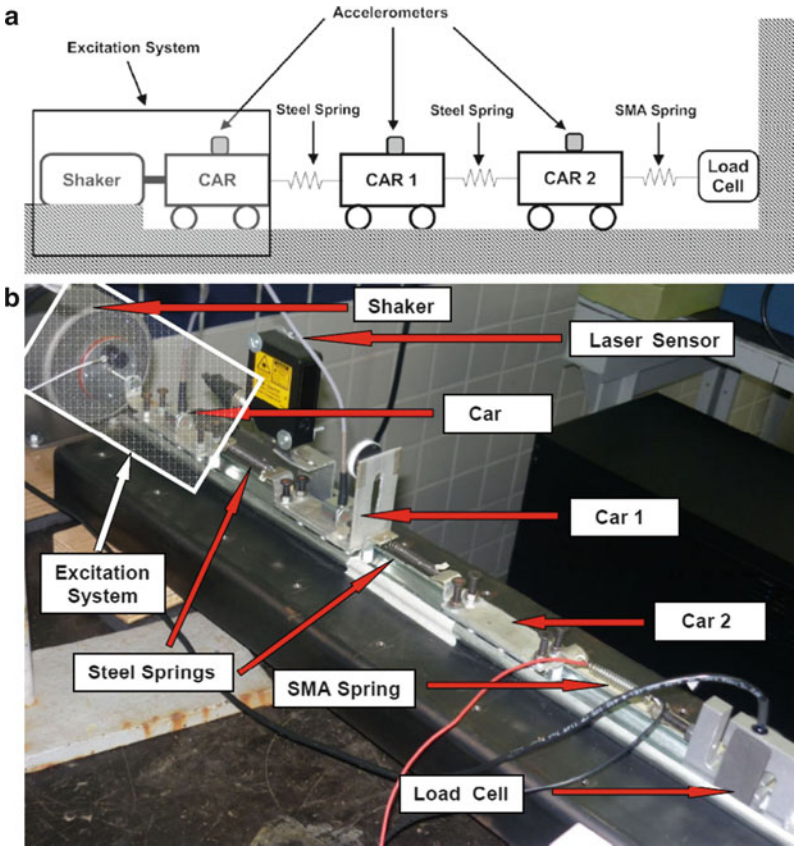

Fig. 2 Experimental apparatus to study the dynamical behaviour of two degrees-of-freedom SMA oscillator – (**a**) schematic draw and (**b**) picture of the system

Table 1 Transducer and accelerometer technical specifications

	Laser transducer	Accelerometers
Resolution	<0.06 mm	–
Linearity error	±0.2 mm	± 1.0% RO
Response time / release time	<10 ms	–
Max. switching frequency	1,000 Hz	350 Hz
Hysteresis	–	±1.0% RO

are induced through joule effect by the application of an electrical current using a stabilized current source (Minipa MPL-1303). Temperature is monitored by an infrared camera FLIR A-320. Table 1 presents the technical specifications of laser transducer and accelerometers.

3 Spring Characterization

Elastic and SMA springs are employed in experimental apparatus. Tension helical springs made of steel with an external diameter of 7.3 mm, a wire diameter of 0.85 mm and 40 active coils are used. Moreover, the system uses an SMA helical spring built with NiTi that is in martensitic phase at room temperature. This SMA spring has an external diameter of 6 mm, a wire diameter of 0.75 mm, 20 active coils, and an activation temperature in the range of 45–55°C. Table 2 shows the stiffness of the elastic springs used in experiments.

The thermomechanical analysis of the SMA spring is presented in (Aguiar et al. 2010). The characterization is obtained through force-displacement and displacement-current tests. The tensile test device shown in Fig. 3 is employed in both situations. Basically, this device is composed of a rigid frame that has a load-cell (Alfa SV-20 with 196 N capacity) fixed at the top. SMA spring is connected to the load-cell and the other end is attached to the rod of a resistive displacement transducer (Gefran PY-1-F-100 with 100 mm span). Both transducers

Table 2 Stiffness of the springs

Spring	Type	k [N/mm]
1 (steel)	Linear elastic	0.573
1 (steel)	Linear elastic	0.528
SMA	Nonlinear	Nonlinear

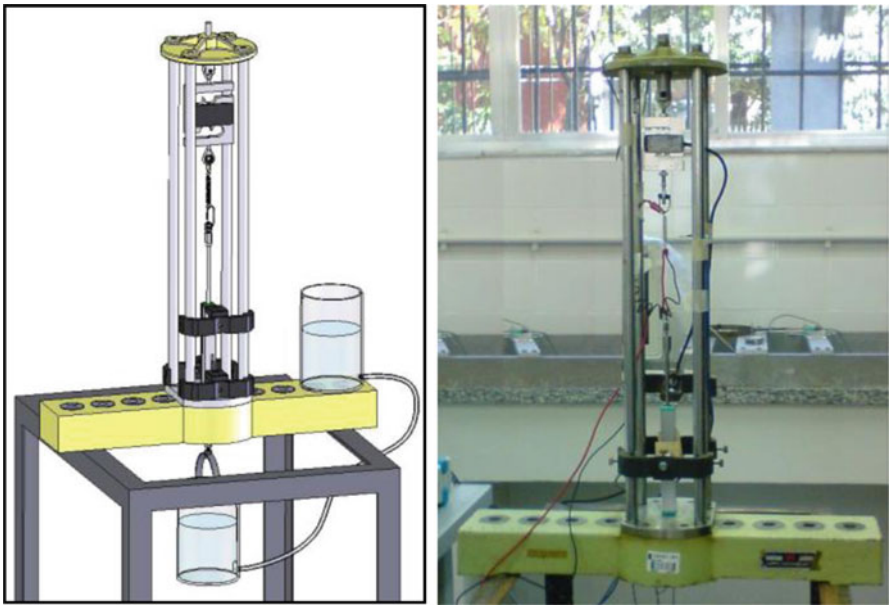

Fig. 3 Tensile test device for thermomechanical characterization of SMA helical springs

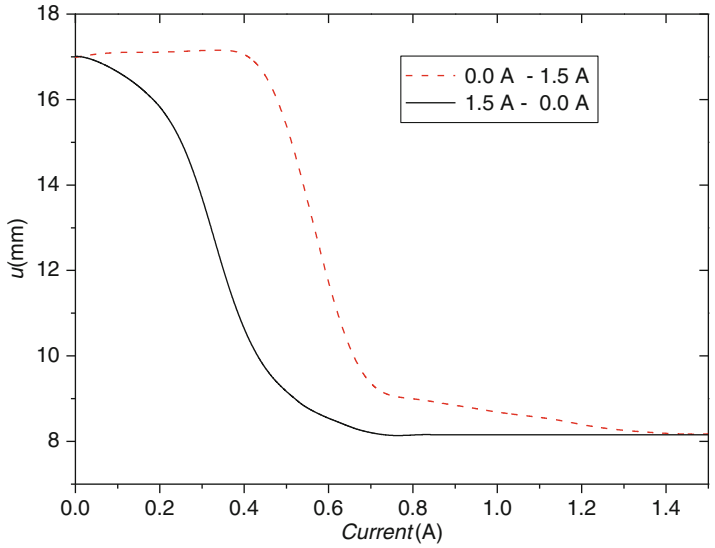

Fig. 4 Experimental data related to displacement-electric current curves

are connected to a data acquisition system (HBM Spider 8). A fluid reservoir is attached to the other end of the transducer rod in order to produce mechanical loadings. The SMA spring is subjected to mechanical loading controlled by the fluid level of the reservoir that is done by changing the vertical position of a second fluid reservoir that is connected to the first by a tube. This procedure allows one to apply smooth loading-unloading conditions to the spring element. Temperature variations are induced through Joule effect by the application of an electrical current using a stabilized current source (Minipa MPL-1303). The SMA spring is subjected to different thermomechanical loading-unloading processes in order to reproduce shape memory and pseudoleastic effects.

The shape memory effect is imposed by considering a two-stage thermomechanical test: (1) a mechanical loading-unloading followed by (2) a thermal heating-cooling. The first stage promotes a residual strain that is eliminated during the second stage. Three different maximum load levels are considered: 3, 3.5 and 4 N. The heating of the SMA helical spring to a temperature where austenitic formation is completed is performed by applying an electric current of 1.2 A. All tests are performed at room temperature (22°C). The pseudoelastic test is performed by assuming a constant temperature loading together with a mechanical loading-unloading test. Two different mechanical loading-unloading procedures are performed being related to maximum load levels (7 and 8 N) together with a constant temperature induced by applying an electrical current of 0.8 A. Initially, SMA spring is characterized by considering a temperature variation with a constant stress level. This test has the objective to establish a relation between electric current and phase transformation. Figure 4 presents

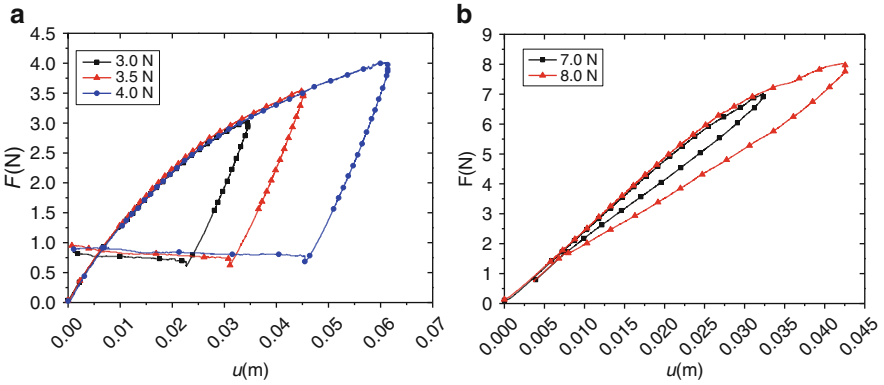

Fig. 5 Experimental data related to the spring force-displacement. Shape memory effect (*left panel*); pseudoelasticity (*right panel*)

the displacement-electric current curve showing the hysteresis loop that allows one to identify the phase transformation current related to phase transformation temperatures.

SMA spring force-displacement curves are now in focus trying to represent shape memory effect (SME) and pseudoelasticity. Figure 5 presents experimental curves for both situations. At the beginning of each test, the SMA helical spring is at room temperature (22°C), a situation where martensitic phase is stable. In order to assure that each test is done with a spring where its wire section has a homogeneous twinned martensitic phase distribution, the following process is applied. Initially, all mechanical loads are removed and then, an electric current of 1.2 A is applied to the spring. Finally, the spring is subjected to cooling prescribed in order to allow a thermal equilibrium with the medium. SME test is performed after this initial stage by imposing a mechanical loading that promotes the formation of detwinned martensite. This phase remains present after the mechanical loading removal, causing a residual displacement. At this point, an electric current of 1.2 A is applied and the SMA helical spring recovers part of the residual displacement developed during the loading stage. A residual load with a magnitude of approximately 1 N is still present at the end of the unloading as a consequence of the devices attached to the spring (for example, resistive displacement transducer and fluid reservoir). A loading rate of approximately 2.7×10^{-2} N/s is used in the developed tests. Pseudoelastic test is performed by considering an applied electric current of 0.8 A that increases the SMA temperature promoting a phase transformation from twinned martensite to austenite. Afterwards, mechanical loading–unloading process is imposed to the spring by considering two different maximum values: 7 and 8 N. As expected, pseudoelastic test shows a complete reverse phase transformation after the loading is removed and, as a consequence, there is no residual displacement. Figure 5 presents force-displacement curves related to shape memory and pseudoeleastic experimental tests.

4 One Degrees-of-Freedom System (1DOF) Dynamical Analysis

Experimental tests are conducted to investigate the possibility of vibration attenuation using the temperature variation of the SMA systems. Temperature variation promotes phase transformation that changes the system characteristics as the equilibrium points and the SMA helical spring stiffness. Several situations involving the influence of temperature on the system dynamics are explored.

At the beginning of each test, a standard procedure is considered. The SMA helical spring in load-free condition is heated, by applying an electric current of 0.8 A in order to recover its original length. Afterwards, SMA helical spring is attached to the device in a high temperature condition and the shaker provides an excitation with amplitude of 0.25 g. Before the signal acquisition a stabilization period of 1960s is adopted. The system is subjected to sinusoidal excitation with a constant frequency. SMA helical spring temperature variation is obtained by changing the applied electric current.

Figure 6 shows experimental results involving SMA one-degree of freedom oscillator. Basically, the system is subjected to a sinusoidal excitation with 10 Hz that coincides with the resonant frequency for 0.8 A. The test starts with an electric current of 0.8 A and after 2.5 s this value is increased and stabilized on three new electric current values: 2, 2.5 and 3 A. Two different signals are presented: acceleration measured by accelerometer (left panel) and displacement measured by the laser sensor (right panel). Note that vibration reduction is achieved by the variation of SMA temperature. Figure 7 presents a comparison between both cars accelerations for an applied electric current of 3A. It should be highlighted the sinusoidal excitation and the amplitude decrease associated with the car when the electric current is increased.

An infrared camera monitors temperature variation imposed by the electrical current. Figure 8 shows an infrared thermal image of the SMA spring during the

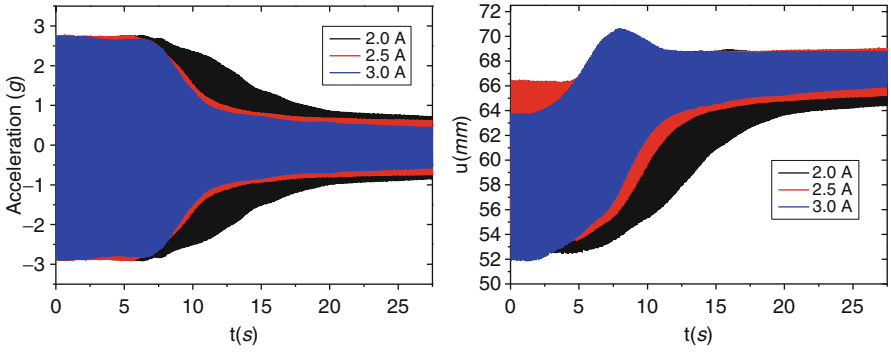

Fig. 6 Vibration reduction promoted by SMA oscillator temperature variation

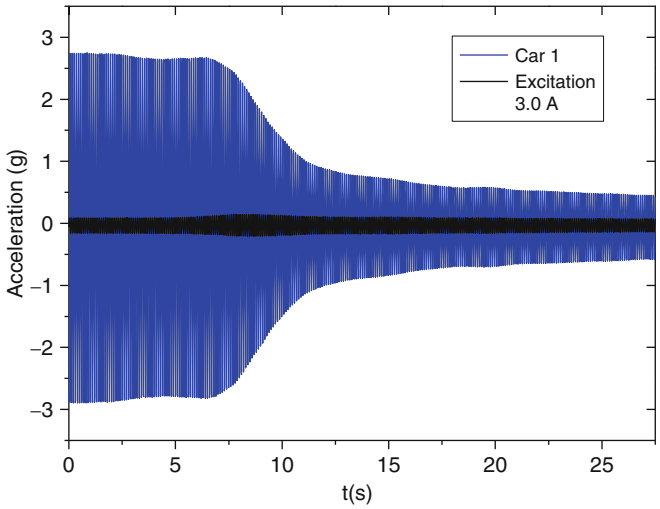

Fig. 7 Vibration reduction promoted by SMA oscillator temperature variation

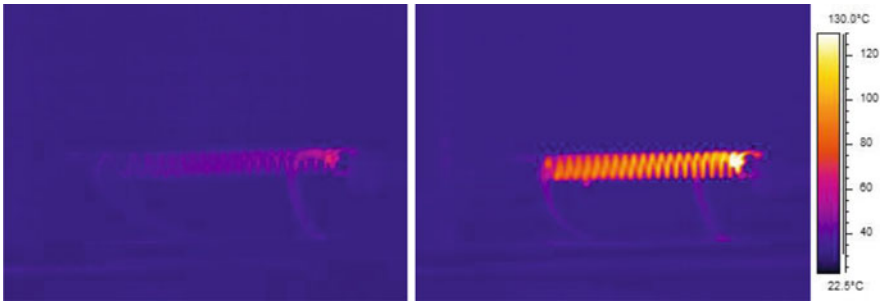

Fig. 8 Thermal infrared image of the SMA spring submitted to a current of 0.8 A (*left panel*) and 3.0 A (*right panel*)

experimental procedure where temperature variation promotes vibration reduction. Left panel of Fig. 8 is related to a current of 0.8 A while the right panel is associated with a current of 3.0 A.

5 Two Degrees-of-Freedom System (2DOF) Dynamical Analysis

At this point, a two degrees-of-freedom system (2DOF) is of concern. The basic idea is to represent a vibration absorber with an SMA element. The tuned vibration absorber (TVA) is a well established passive vibration control device for achieving

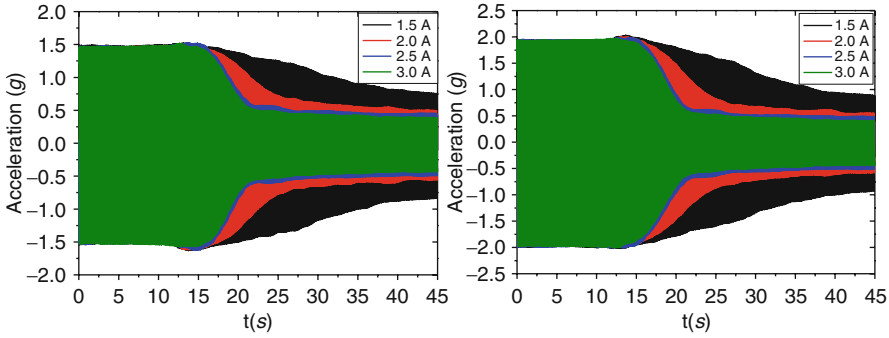

Fig. 9 Vibration reduction of the 2DOF system. Primary (*left*) and secondary (*right*) systems

reduction in the vibration of a primary system subject to external excitation. The TVA consists of a secondary oscillatory system that once attached to the primary system is capable of absorbing vibration energy from the primary system. By tuning the natural frequency of the TVA to a chosen excitation frequency, one produces an attenuation of the primary system vibration amplitude for this specific forcing frequency. An alternative for systems where the forcing frequency varies or has a kind of uncertainty is the concept of an adaptive tuned vibration absorber (ATVA). This device is an adaptive–passive vibration control similar to a TVA but with adaptive elements that can be used to change the tuned condition. SMA represents an alternative to be used in ATVA where temperature variations can be used to promote system adaptability. In the experimental set up, an extra car is connected to the primary system, introducing a secondary system.

Initially, we present a test where the primary system is subjected to a harmonic excitation with a 0.25 g amplitude and frequency of 6.9 Hz. SMA spring is subjected to 0.8A of electric current. The SMA spring is then subjected to different electric current after 10 s reaching the following values: 1.5, 2.0, 2.5, and 3.0 A. Figure 9 presents acceleration of primary and secondary systems for different electric current. It is noticeable the amplitude reduction. Figure 10 presents a comparison of acceleration of the three cars. The left panel presents acceleration response that shows that the constant amplitude excitation is reduced in both primary and secondary systems after the electric current increases. The right panel presents the displacement of the primary system.

Sweep tests are now performed trying to verify the influence of frequency on the vibration reduction. Basically, the system is harmonically excited with a 0.25 g sinusoidal acceleration with constant amplitude. The excitation frequency signal changes linearly during the test from 6 to 18 Hz with 0.02 Hz/s. Different temperatures are also considered by assuming variation of the electrical current: 0.8 and 1.4 A. Figure 11 shows the acceleration time history of the primary system (left panel). Once again, it should be highlighted the vibration reduction promoted by the temperature increase. A frequency analysis is presented in the right panel of

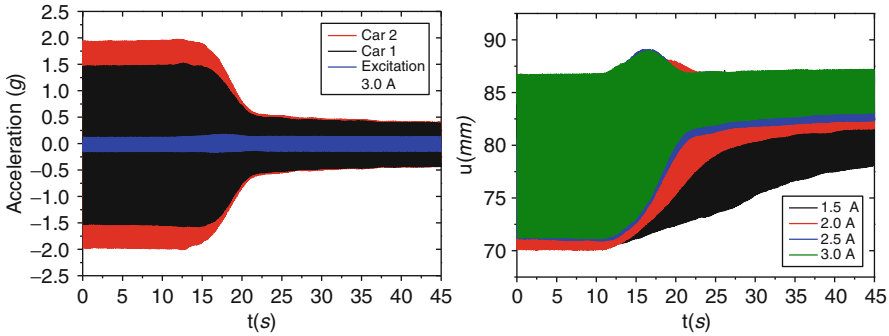

Fig. 10 Vibration reduction of the 2DOF system: acceleration (*left panel*) and displacement of the primary system (*right panel*)

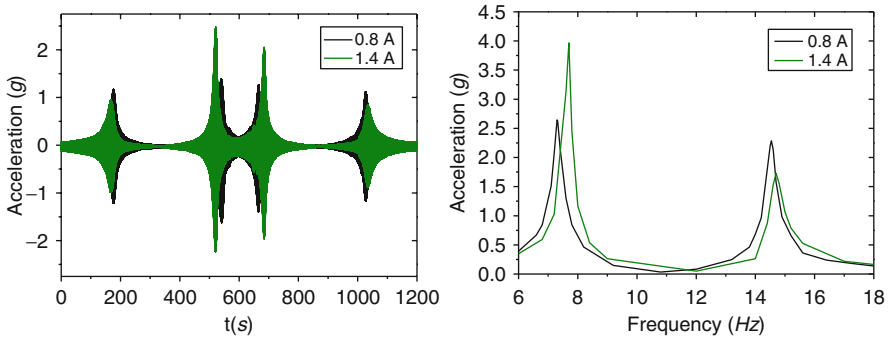

Fig. 11 Sine-sweep tests of the 2DOF system: primary system

Fig. 11 by considering the maximum amplitudes of the acceleration. Note that the peaks can change the position with temperature variation. This behaviour defines an important characteristic of this system since it is possible to change the tuned frequency related to vibration reduction. It is important to highlight that there is a competition between stiffness and hysteresis in order to define the system response. Hence, the temperature change can reduce the stiffness changing the position of the resonant peaks, but this change is also related to different hysteretic behaviour that cause an amplitude change. Figure 12 presents the same curves for the secondary system, showing the same qualitative behaviour.

6 Conclusions

This paper deals with an experimental investigation of the nonlinear dynamics of shape memory alloys systems. The system is composed of low-fiction cars free to move in a rail. Two different systems are treated: one- and two-degree of freedom.

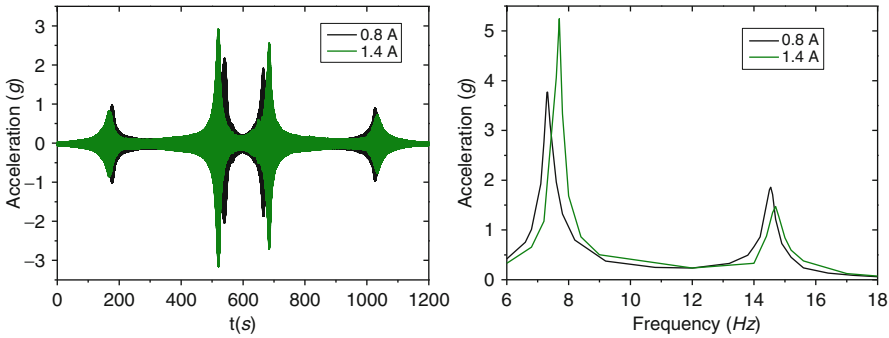

Fig. 12 Sine-sweep tests of the 2DOF system: secondary system

The main objective is the investigation of the vibration reduction exploring the SMA behaviour due to temperature variations imposed by electric current. Sensors are employed to monitor the main system variables. Concerning the 1DOF system, it is shown the vibration reduction due to temperature variations. The 2DOF system represents an adaptive vibration absorber with SMA element. Therefore, there is a primary system connected to a secondary system with SMA spring. Once again, vibration reduction is achieved and it is important to highlight the capacity of the SMA system to change the tuned frequency.

Acknowledgments The authors would like to thank the Brazilian Research Agencies CNPq and FAPERJ and through the INCT-EIE (National Institute of Science and Technology – Smart Structures in Engineering) the CNPq and FAPEMIG for their support. The Air Force Office of Scientific Research (AFOSR) is also acknowledged.

References

Aguiar, R.A.A., Savi, M.A., Pacheco, P.M.C.L.: Experimental and numerical investigations of shape memory alloy helical springs. Smart Mater. Struct. **19**, 1–9 (2010)

Elahinia, M.H., Koo, J.H., Tan, H.: Improving robustness of tuned vibration absorbers using shape memory alloys. Shock Vib. **12**, 349–361 (2005)

Lagoudas, D.C.: Shape Memory Alloys: Modeling and Engineering Applications. Springer, New York (2008)

Machado, L.G., Savi, M.A.: Odontological applications of shape memory alloys. Rev. Bras. Odontol. **59**, 302–306 (2002)

Machado, L.G., Savi, M.A.: Medical applications of shape memory alloys. Braz. J. Med. Biol. Res. **36**, 683–691 (2003)

Machado, L.G., Savi, M.A., Pacheco, P.M.C.L.: Nonlinear dynamics and chaos in coupled shape memory oscillators. Int. J. Sol. Struct. **40**, 5139–5156 (2003)

Machado, L.G., Lagoudas, D.C., Savi, M.A.: Lyapunov exponents estimation for hysteretic systems. Int. J. Sol. Struct. **46**, 1269–1286 (2009)

Paiva, A., Savi, M.A.: An overview of constitutive models for shape memory alloys. Math. Probl. Eng. **2006**, 1–30 (2006)

Rustighi, E., Brennan, M.J., Mace, B.R.: A shape memory alloy adaptive tuned vibration absorber: design and implementation. Smart Mater. Struct. **14**, 19–28 (2005a)
Rustighi, E., Brennan, M.J., Mace, B.R.: Real-time control of a shape memory alloy adaptive tuned vibration absorber. Smart Mater. Struct. **14**, 1184–1195 (2005b)
Santos, B.C., Savi, M.A.: Nonlinear dynamics of a nonsmooth shape memory alloy oscillator. Chaos Solitons Fractals **40**, 197–209 (2009)
Savi, M.A., Pacheco, P.M.C.L.: Chaos and hyperchaos in shape memory systems. Int. J. Bifurc. Chaos **12**, 645–657 (2002)
Savi, M.A., Pacheco, P.M.C.L., Braga, A.M.B.: Chaos in a shape memory two-bar truss. Int. J. Nonlinear Mech. **37**, 1387–1395 (2002)
Savi, M.A., Sa, M.A.N., Paiva, A., Pacheco, P.M.C.L.: Tensile-compressive asymmetry influence on the shape memory alloy system dynamics. Chaos Solitons Fractals **36**, 828–842 (2008)
Sitnikova, E., Pavlovskaia, E., Wiercigroch, M., Savi, M.A.: Vibration reduction of the impact system by an SMA restraint: numerical studies. Int. J. Nonlinear Mech. **45**(9), 837–849 (2010)
Tiseo, B., Concilio, A., Amerudi, S., Gianvito, A.: A shape memory alloy based tuneable dynamic vibration absorber for vibration tonal control. J. Theor. Appl. Mech. **48**, 135–153 (2010)
Williams, K.A., Chiu, G.C.C., Bernhard, R.J.: Dynamic modelling of a shape memory alloy adaptive tuned vibration absorber. J. Sound Vib. **280**, 211–234 (2005)

Nonlinear Dynamics and Instability as Important Design Concerns for a Guyed Mast

Diego Orlando, Paulo B. Gonçalves, Giuseppe Rega, and Stefano Lenci

Abstract This paper analyses the static and dynamic buckling behavior of a simplified 2-DOF model of a cable stayed tower with emphasis on the safety of the pre-buckling solutions whose stability must be preserved for a safe design. First, the influence of the inherent symmetries of the model on the buckling loads and the post-buckling paths emerging from the bifurcation point is investigated. Then, a global dynamic analysis is conducted to investigate the degree of safety of the static pre-buckling solution. To understand the behavior of the guyed mast in a dynamic environment, a base excitation is considered and the influence of its direction on the escape stability boundary in the force control space is studied. Finally, the erosion and integrity of the basins of attraction of the stable solutions are investigated.

D. Orlando
Tecgraf – Computer Graphics Technology Group, Catholic University, PUC-Rio,
22453-900 Rio de Janeiro, Brazil
e-mail: dorlando@tecgraf.puc-rio.br

P.B. Gonçalves (✉)
Department of Civil Engineering, Catholic University, PUC-Rio,
22453-900 Rio de Janeiro, Brazil
e-mail: paulo@puc-rio.br

G. Rega
Department of Structural and Geotechnical Engineering, Sapienza University of Rome,
00197 Rome, Italy
e-mail: giuseppe.rega@uniroma1.it

S. Lenci
Department of Civil and Building Engineering, and Architecture, Polytechnic University
of Marche, 60131 Ancona, Italy
e-mail: lenci@univpm.it

M. Wiercigroch and G. Rega (eds.), *IUTAM Symposium on Nonlinear Dynamics for Advanced Technologies and Engineering Design*, IUTAM Bookseries (closed) 32, DOI 10.1007/978-94-007-5742-4_18,

The paper shows how the tools of nonlinear dynamics can help in the understanding of the global safety and integrity of the model, thus leading to a safe structural design.

Keywords Guyed mast • Static and dynamic buckling • Nonlinear dynamics • Basin erosion • Dynamic integrity • Safe design

1 Introduction

Cable stayed masts are used in several engineering areas including off shore, mechanical, telecommunications and aero space engineering. The efficiency of these structures in supporting axial loads is due to the cables and their behavior is characterized by large displacements associated with high load bearing ratios. As cable stayed structures show large displacements, high nonlinearities are associated to their static and dynamic behavior. Therefore, the knowledge of their nonlinear behavior is of great interest to engineers and scientists. The analysis of cable stayed structures has been object of several investigations in the last decades. Among the most important studies we can mention the works by Xu et al. (1997), Wahba et al. (1998), Kahla (1997), Chan et al. (2002) and Yan-Li et al. (2003).

In the present paper the stability and integrity of a simplified 2-DOF model of a guyed tower is studied. The static stability analysis of the model was performed by Thompson and co-workers (Thompson and Gaspar 1977; Thompson and Hunt 1984). They showed that this model displays a complex post-buckling behavior with a strong modal coupling leading to several unstable post-buckling paths. In such cases, the load-carrying capacity of the structure is governed by the unstable branches of the post-buckling response. Also, in these structures the imperfections may substantially decrease the load capacity of the structure and the choice of a safe load level for design becomes usually a complex and difficult task for the engineer. However, most of the studies in this area rely on the local stability analysis of an equilibrium configuration and no additional information is given on the safety of a given equilibrium state. In such case a global stability analysis using the mathematical methods of classical mechanics, in particular Lagrangian or Hamiltonian mechanics, can help the engineer in the understanding of the problem and in evaluating the degree of safety of the ~~safe~~ pre-buckling configuration (Gonçalves et al. 2007, 2010). To understand the behavior of the guyed mast in a dynamic environment, a base excitation is considered and the influence of its direction on the escape stability boundary in the force control space is studied. Finally, the erosion and integrity of the basins of attraction of the stable solutions are investigated. The paper shows how the tools of non-linear dynamics can help in the understanding of the safety and integrity of the model, thus leading to a safe structural design.

2 Problem Formulation

Figure 1 illustrates a simplified model of a cable stayed tower. It is an inverted spatial pendulum composed of a slender, rigid (but massless) bar of length l, pinned at the base and with a tip-mass m. The lateral displacements are restricted by three linear springs, initially inclined at 45°. The first spring of stiffness k_1, is located in the $y \times z$ plane, while the others, k_2 and k_3, are located symmetrically about the y axis, with their positions defined by the angle β. The two degrees of freedom are $u_1 = \sin\theta_1$ and $u_2 = \sin\theta_2$, where θ_1 and θ_2 are the pendulum rotations in the vertical planes $x \times z$ and $y \times z$, respectively (Orlando 2010).

The potential energy of the system is given by

$$
\begin{aligned}
V = & \frac{1}{2}k_1\left(l\sqrt{2} - l\sqrt{2-2u_2}\right)^2 + \\
& \frac{1}{2}k_2\left(l\sqrt{2} - l\sqrt{(\sin\beta - u_1)^2 + (\cos\beta - u_2)^2 + 1 - {u_1}^2 - {u_2}^2}\right)^2 + \\
& \frac{1}{2}k_3\left(l\sqrt{2} - l\sqrt{(-\sin\beta - u_1)^2 + (\cos\beta - u_2)^2 + 1 - {u_1}^2 - {u_2}^2}\right)^2 - \\
& Pl\left(1 - \sqrt{1 - {u_1}^2 - {u_2}^2}\right)
\end{aligned}
\tag{1}
$$

where $P = mg$.

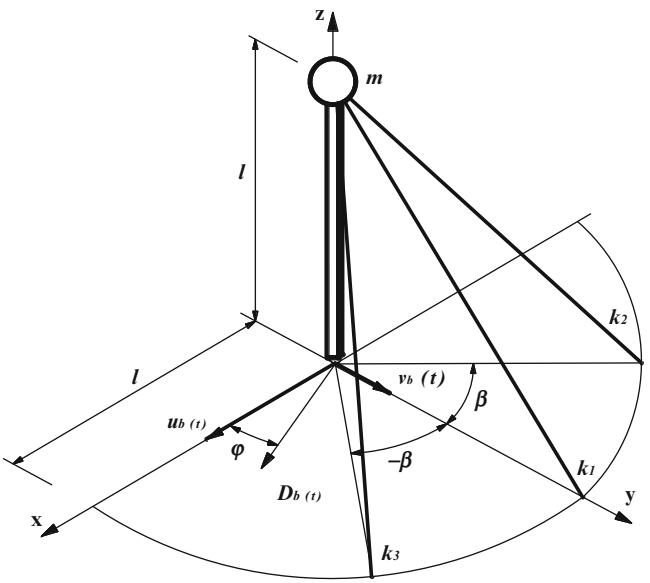

Fig. 1 Model of a guyed mast

Following Thompson and Gaspar (1977), it is assumed that the stiffness of the second and third springs are equal, i.e., $k_2 = k_3 = \upsilon K$, where $\upsilon = 1 \big/ \left(4 \sin^2 \beta\right)$, a positive constant, the stiffness of the first spring is given by $k_1 = (1 - 2\upsilon)\, K$ and $\beta = 120°$. The latter value corresponds to the usual configuration of stay cables in practical applications. Thus, Eq. (1) can be rewritten as:

$$V = \frac{1}{2}k_1\left(l\sqrt{2} - l\sqrt{2 - 2u_2}\right)^2 + \frac{1}{2}k_2\left(\left(l\sqrt{2} - l\sqrt{2 - \sqrt{3}u_1 + u_2}\right)^2 + \left(l\sqrt{2} - l\sqrt{2 + \sqrt{3}u_1 + u_2}\right)^2\right) - Pl\left(1 - \sqrt{1 - {u_1}^2 - {u_2}^2}\right) \tag{2}$$

The kinetic energy is given by

$$T = \frac{1}{2}m\left(l^2\dot{u}_1^2 + l^2\dot{u}_2^2 - \frac{\left(l\dot{u}_1u_1 + l\dot{u}_2u_2\right)^2}{{u_1}^2 + {u_2}^2 - 1}\right) \tag{3}$$

The equations of motion of the system are obtained using Lagrange equations by considering an harmonic base excitation $D_b(t)$, Fig. 1, acting at an angle φ with respect to the x axis. The excitation $D_b(t)$ is decomposed into two components, $u_b(t)$ in the x direction and $v_b(t)$ in the y direction. These components are given by $u_b = F_b \cos\varphi \sin\left(\omega_e t\right)$ and $v_b = F_b \sin\varphi \sin\left(\omega_e t\right)$, where is the base displacement magnitude and ω_e is the excitation frequency.

The dynamics of the system is described by the following equations of damped forced motion in non-dimensional form, containing both geometric and inertial non-linearities (Orlando 2010),

$$\ddot{u}_1\left(1 - {u_1}^2 - 2{u_2}^2 + {u_1}^2{u_2}^2 + {u_2}^4\right) + \ddot{u}_2\left(u_1u_2 - {u_1}^3u_2 - u_1{u_2}^3\right) + \dot{u}_1^2\left(u_1 - u_1{u_2}^2\right) + \dot{u}_2^2\left(u_1 - {u_1}^3\right) + 2{u_1}^2u_2\dot{u}_1\dot{u}_2 + \left[\frac{2}{\sqrt{3}\lambda\Omega^2}\left\{\left(\left(\sqrt{2} - \sqrt{2 - \sqrt{3}u_1 + u_2}\right) \Big/ \sqrt{2 - \sqrt{3}u_1 + u_2}\right) - \left(\left(\sqrt{2} - \sqrt{2 + \sqrt{3}u_1 + u_2}\right) \Big/ \sqrt{2 + \sqrt{3}u_1 + u_2}\right)\right\} - \frac{1}{\Omega^2}\frac{u_1}{\sqrt{1 - {u_1}^2 - {u_2}^2}} + \frac{2\xi_1}{\Omega}\dot{u}_1\right]\left(-1 + {u_1}^2 + {u_2}^2\right)^2 = F\cos\varphi \sin\tau\left(-1 + {u_1}^2 + {u_2}^2\right)^2 \tag{4}$$

$$\ddot{u}_2\left(1-{u_2}^2-2{u_1}^2+{u_1}^2{u_2}^2+{u_1}^4\right)+\ddot{u}_1\left(u_1u_2-{u_1}^3u_2-u_1{u_2}^3\right)+$$

$$\dot{u}_2^2\left(u_2-{u_1}^2u_2\right)+\dot{u}_1^2\left(u_2-{u_2}^3\right)+2u_1{u_2}^2\dot{u}_1\dot{u}_2+\left[-\frac{2}{3\lambda\Omega^2}\left\{\right.\right.$$

$$\left(\left(\sqrt{2}-\sqrt{2-\sqrt{3}u_1+u_2}\right)\Big/\sqrt{2-\sqrt{3}u_1+u_2}\right)-$$

$$\left.\left(\left(\sqrt{2}-\sqrt{2+\sqrt{3}u_1+u_2}\right)\Big/\sqrt{2+\sqrt{3}u_1+u_2}\right)\right\}+$$

$$\frac{4}{3\lambda\Omega^2}\frac{\left(\sqrt{2}-\sqrt{2-2u_2}\right)}{\sqrt{2-2u_2}}-\frac{1}{\Omega^2}\frac{u_2}{\sqrt{1-{u_1}^2-{u_2}^2}}+\frac{2\xi_2}{\Omega}\dot{u}_2\Bigg]\left(-1+{u_1}^2+{u_2}^2\right)^2=$$

$$F\sin\varphi\sin\tau\left(-1+{u_1}^2+{u_2}^2\right)^2 \tag{5}$$

where the dot means $d/d\tau$ and $\Omega=\omega_e/\omega_p$, being $\omega_p^2=g/l$, $\tau=\omega_e t$, $F=F_b/l$, $K/ml^2=\omega_p^2/\lambda$, $\lambda=P/Pcr$ and ξ_i are the damping factors.

3 Stability Analysis and Safe Pre-buckling Region

The behavior of the model for different values of the angle β was studied by Thompson and co-workers (Thompson and Gaspar 1977; Thompson and Hunt 1984). They found that the value of β has a significant influence on the stability of the model. For the case herein considered, $\beta=120°$, $k_2=k_3=\upsilon K$, $k_1=(1-2\upsilon)\,K$, with $\upsilon=1/3$, namely equal stiffnesses of all springs, the cable stayed tower displays two coincident buckling loads, $Pcr_1=Pcr_2=Pcr=Kl/4$. Due to symmetry, the model also displays two coincident natural frequencies, leading to possible internal resonances.

Figure 2 shows the fundamental path ($u_1=u_2=0$), which is stable up to the static critical load ($\lambda=P/Pcr=1.0$) and the three post-buckling paths: two coupled unstable solutions, and one uncoupled unstable solution with $u_1=0$. The interaction of the buckling modes leads to increased imperfection sensitivity. Three different projections of the equilibrium paths are shown in Fig. 3.

The analysis of post-buckling paths is not actually sufficient to reliably evaluate the global safety of the system, which depends on the robustness of the equilibrium solution, namely on the extent of its safe basin.

Safe basins are objects of the same dimension as the phase space, four-dimensional in our case. From Fig. 2 one can conclude that, for load levels lower then the critical load, the safe basin, defined here as the set of initial conditions that lead to safe motions around the static pre-buckling configuration, is bounded

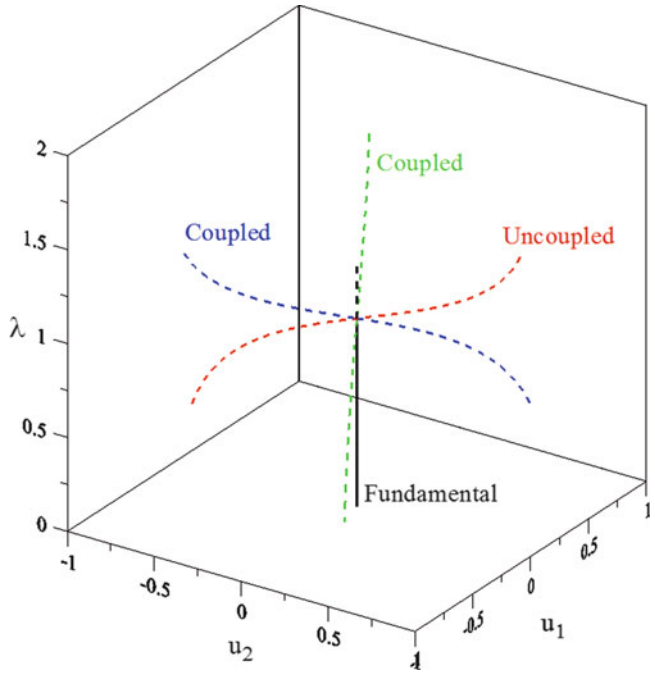

Fig. 2 Equilibrium paths of the system

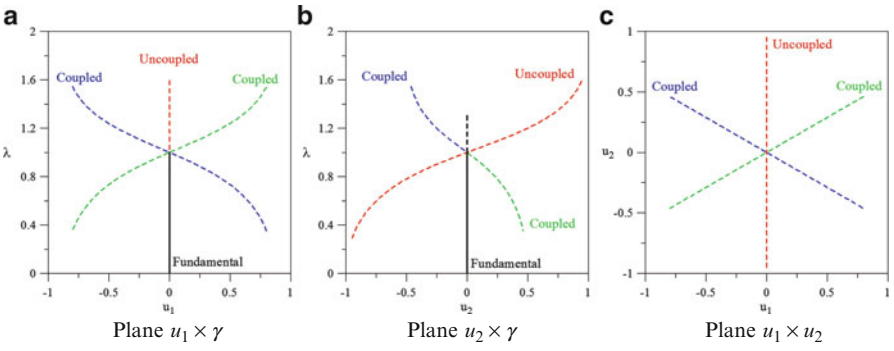

Fig. 3 Projections of the equilibrium paths onto three different planes

by the invariant manifolds of the three saddles associated with the three unstable post-buckling paths. Figure 4a shows the curves of equal energy for $\lambda = 0.7$. Each saddle has an independent homoclinic orbit which encompasses the minimum point at the origin and lays in an equally spaced plane, see the two projections in Fig. 4b. They separate the initial conditions that lead to bounded solutions surrounding the

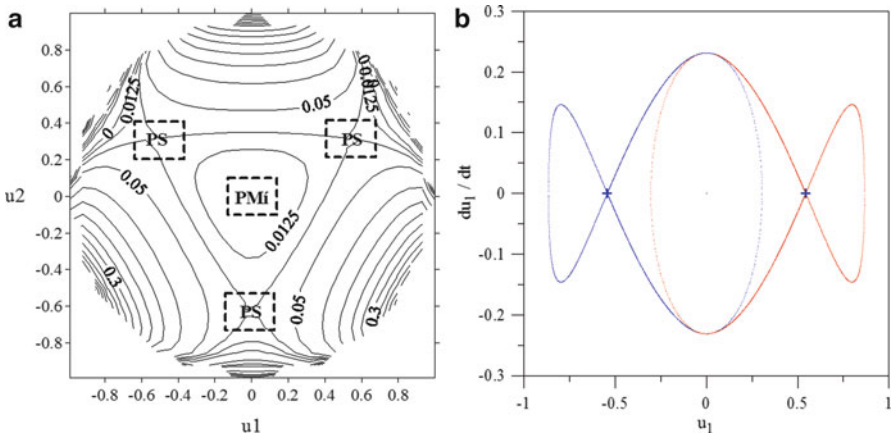

Fig. 4 (**a**) Curves of equal energy for $\lambda = 0.7$. PS: Saddles. PMi: Stable position corresponding to a local minimum. (**b**) Projection of the homoclinic orbits of the upper two saddles on the plane $u_1 \times \dot{u}_1$, for $\lambda = 0.7$

pre-buckling configuration from those leading to unbounded escape solutions. The knowledge of these frontiers helps the designer to separate the phase space into safe and unsafe domains.

Useful insight of the four-dimensional safe region can be obtained from observation of its two- and three-dimensional cross-sections. The geometry of the hypersurface that bounds the initial conditions leading to bounded solutions around the trivial pre-buckling solution can be obtained by the conservation of the total energy principle, equating the sum of expressions (2) and (3) to the value of the total energy at one of the saddles, that is

$$T\left(u_i, \dot{u}_i\right) + V\left(u_i\right) = C_{saddle} \tag{6}$$

Two three-dimensional projections of the safe region are shown in Fig. 5.

This 4D region is defined as the conservative safe basin of the pre-buckling configuration. This safe hyper-volume decreases swiftly as the static load increases and vanishes at the critical point. So, the choice of a suitable safe region, based on some design constraints (e.g. maximum stresses or displacements), enables to determine a safe design load.

4 Nonlinear Dynamic Analysis

In order to understand the behavior of the structure in a dynamical environment, a parametric analysis of the tower under a base excitation is now conducted.

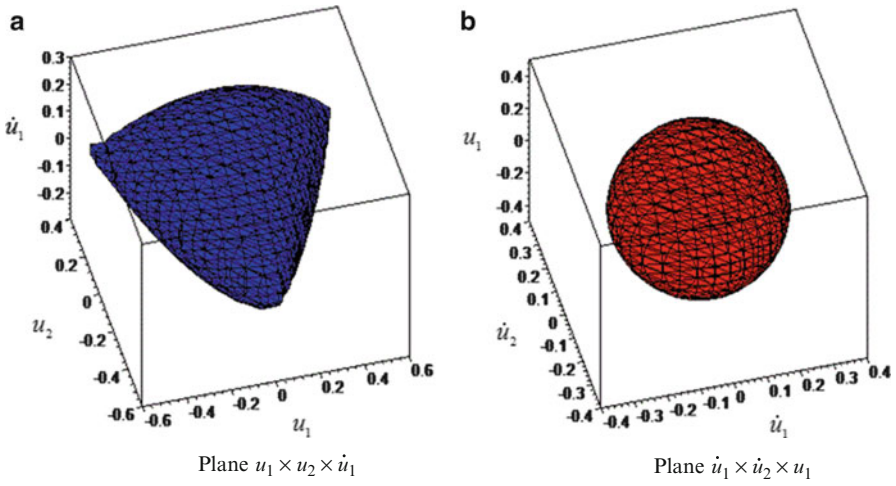

Fig. 5 Two three-dimensional sections of safe pre-buckling region for $\lambda = 0.7$

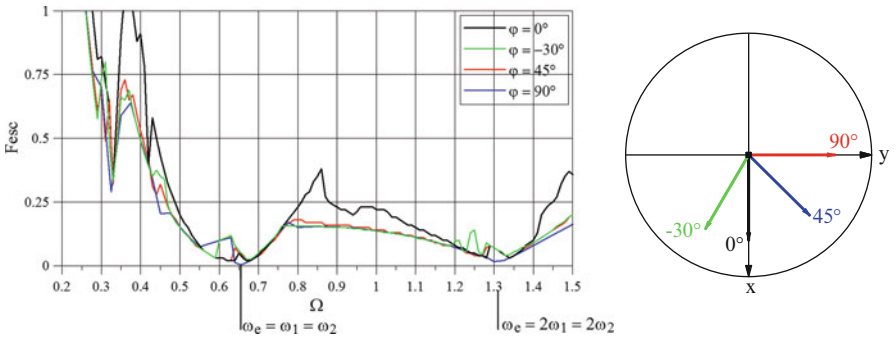

Fig. 6 Escape stability boundaries vs. excitation frequency for different values of the excitation direction φ with $\lambda = 0.7$ and $\xi_1 = \xi_2 = 0.01$. F_{esc}: escape load

4.1 Escape Boundaries

Figure 6 shows the escape stability boundaries in force control space for different values of the excitation direction ϕ (Orlando 2010). The escape load, F_{esc}, corresponds to escape from the pre-buckling potential well in a slowly evolving system (dynamic buckling). For any value of ϕ the lowest escape loads occur in the neighborhood of the fundamental resonance $\omega_e = \omega_1 = \omega_2$. A second important instability region occurs in the neighborhood of twice the natural frequencies of the structure.

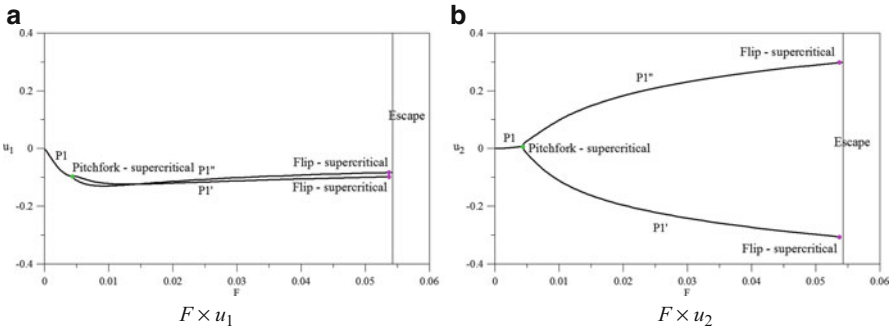

Fig. 7 Bifurcation diagrams for $\phi = 0°$, $\Omega = 0.6546$, $\lambda = 0.7$ and $\xi_1 = \xi_2 = 0.01$

4.2 Bifurcation Diagrams, Basin Erosion and System Dynamic Integrity

In practical terms, information on the stability boundaries as obtained here are not enough to assess the safety of the structure. These data are based on the assumption that the bifurcation parameter varies slowly. In order to evaluate the safety of a structure (in particular structures liable to catastrophic bifurcations) one should analyze the behavior of the basins of attraction of competing solutions (here, the in-well and the unbounded escape solutions). The safety of the structure under dynamic excitation depends not only on the local stability of its solutions, but also on the continuous and uncorrupted basin surrounding each one of them, the total erosion of a given basin corresponding to the system failure.

Figure 7 shows the bifurcation diagram for $\Omega = 0.6546$ and $\phi = 0°$. As F increases from zero the system exhibits a period one solution. At $F = 0.0043$ the response undergoes a pitchfork bifurcation, leading to two period one solutions, P1′ and P1″. The two solutions experience a supercritical flip bifurcation just prior to escape. Figure 8 shows the cross-sections of the 4D basin of attraction by the $u_2 \times \dot{u}_2$ plane for $\phi = 0°$ and $\Omega = 0.6546$ (main resonance region, $\omega_e = \omega_1 = \omega_2$) for increasing values of the excitation magnitude. The two colors identify in this case two period one solutions arising from a pitchfork bifurcation. For $F = 0.01$, an uncorrupted basin is observed. As F increases to 0.02 most of the reference region becomes fractal and when the load level reaches 0.03, most of the initial conditions lead to unbounded solutions and the compact region surrounding each fixed point of the Poincaré map becomes almost zero.

Figure 9 shows the variation of the local integrity measure (LIM) proposed by Soliman and Thompson (1989), which is defined for a multidimensional system as the maximum radius of the hyper-sphere entirely belonging to the safe basin and centered at the attractor, as a function of the excitation amplitude. The resulting integrity profile clarifies the evolution of the robustness of the in-well solutions

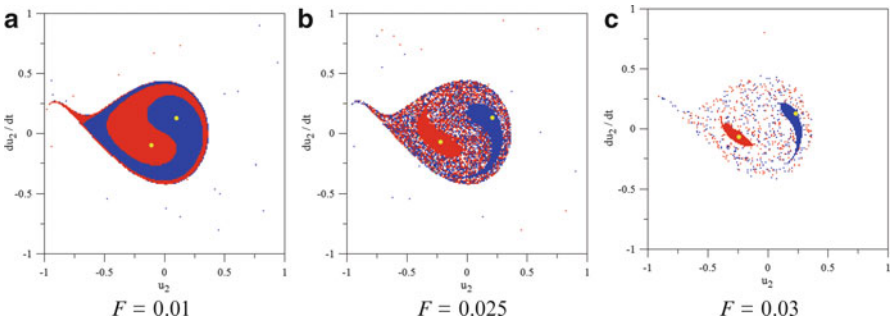

Fig. 8 Erosion of the basins of attraction of P1′ and P1″ with increasing forcing magnitude F for $\phi = 0°$, $\Omega = 0.6546$, $\lambda = 0.7$ and $\xi_1 = \xi_2 = 0.01$

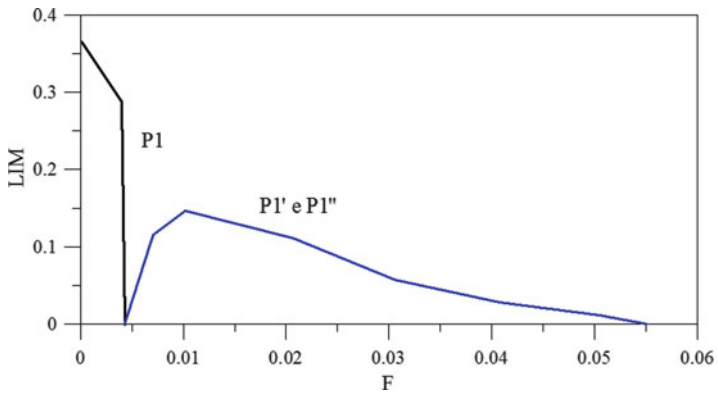

Fig. 9 Variation of the integrity factor LIM as a function of the forcing magnitude F for $\phi = 0°$, $\Omega = 0.6546$, $\lambda = 0.7$ and $\xi_1 = \xi_2 = 0.01$

along with the overall erosion of the in-well safe basin from the escape solution, thus showing to be a good measure of the safety of the structure in an evolving environment.

5 Conclusions

This paper analyses the buckling and nonlinear dynamic behavior of a simplified 2DOF model of a cable stayed tower with emphasis on the safety of the static pre-buckling configuration, whose stability must be preserved for a safe design, and of the ensuing dynamic solutions. Due to inherent symmetries of the model, it displays two coincident buckling loads. This leads to a strong modal coupling and the existence of several unstable post-buckling paths emerging from the static

bifurcation point. These unstable branches limit the safe region surrounding the equilibrium configuration. This region decreases as the load increases and becomes zero at the critical load. So, as the applied load increases the magnitude of the allowable perturbations decreases. The safe region is defined by the saddles associated with the unstable post-buckling paths. The same overall behavior is observed in the forced case. As the force approaches the critical value (escape), the safe basin decreases steadily and, as shown here, may become fractal, due to a global bifurcation (homoclinic or heteroclinic intersection), for load levels well below the escape value. Due to symmetry, the model also displays two coincident natural frequencies leading to 1:1 internal resonances. The lowest escape load occurs in the vicinity of this region. These features are characteristic of structural and mechanical systems exhibiting unstable post-buckling response (Gonçalves and Santee 2008), in particular those exhibiting modal interaction (Orlando et al. 2011). The system safety may be increased by enlarging the manifolds distance and thus postponing the homoclinic (or heteroclinic) intersection as much as possible (Lenci and Rega 2009, 2011).

The paper shows that the tools of analytical dynamics can give the engineer a satisfactory understanding of the safety and integrity of the model, essential for a safe design of the structure.

Acknowledgments The authors acknowledge the financial support of the Brazilian research agencies CAPES, CNPq and FAPERJ.

References

Chan, S.L., Shu, G.P., Lü, Z.T.: Stability analysis and parametric study of pre-stressed stayed columns. Eng. Struct. **24**, 115–124 (2002)

Gonçalves, P.B., Santee, D.: Influence of uncertainties on the dynamic buckling loads of structures liable to asymmetric post-buckling behavior, mathematical problems in engineering, p. 24. Article ID 490137 (2008)

Gonçalves, P.B., Silva, F.M.A., Del Prado, Z.J.G.N.: Global stability analysis of parametrically excited cylindrical shells through the evolution of basin boundaries. Nonlinear Dyn. **50**, 121–145 (2007)

Gonçalves, P.B., Silva, F.M.A., Rega, G., Lenci, S.: Global dynamics and integrity of a two-dof model of a parametrically excited cylindrical shell. Nonlinear Dyn. **63**, 61–82 (2010)

Kahla, N.B.: Nonlinear dynamic response of a guyed tower to a sudden guy rupture. Eng. Struct. **19**, 879–890 (1997)

Lenci, S., Rega, G.: Recent advances in control of complex dynamics in mechanical and structural systems. In: Sanjuan, M.A.F., Grebogi, C. (eds.) Recent Progress in Controlling Chaos, Series on Stability Vibration and Control of Systems, vol. 16, pp. 189–237. World Scientific, ISBN 978-981-4291-69-9 (2009)

Lenci, S., Rega, G.: Load carrying capacity of systems within a global safety perspective. Part II. Attractor/basin integrity under dynamic excitations. Int. J. Nonlinear Mech. **46**(9), 1240–1251 (2011)

Orlando, D.: Nonlinear dynamics, instability and control of structural systems with modal interaction, PhD dissertation, Pontifícia Universidade Católica do Rio de Janeiro, Brazil (in Portuguese) (2010)

Orlando, D., Gonçalves, P.B., Rega, G., Lenci, S.: Influence of modal coupling on the nonlinear dynamics of Augusti's model. J. Comput. Nonlinear Dyn. ASME **6**(4), 041014-1–041014-11 (2011). doi:10.1115/1.4003880

Soliman, M.S., Thompson, J.M.T.: Integrity measures quantifying the erosion of smooth and fractal basins of attraction. J. Sound Vib. **135**, 453–475 (1989)

Thompson, J.M.T., Gaspar, Z.: A buckling model for the set of umbilic catastrophes. Math. Proc. Camb. Philos. Soc. **82**, 497 (1977)

Thompson, J.M.T., Hunt, G.W.: Elastic Instability Phenomena. Wiley, London (1984)

Wahba, Y.M.F., Madugula, M.K.S., Monforton, G.R.: Evaluation of non-linear analysis of guyed antenna towers. Comput. Struct. **68**, 207–212 (1998)

Xu, Y.L., Ko, J.M., Yu, Z.: Modal analysis of tower-cable system of Tsing Ma long suspension bridge. Eng. Struct. **19**, 857–867 (1997)

Yan-Li, H., Xing, M., Zhao-Min, W.: Nonlinear discrete analysis method for random vibration of guyed masts under wind load. J. Wind Eng. Ind. Aerodyn. **91**, 513–525 (2003)

A Problem of Stability in Milling Process of Materials Used in Aviation Industry

Rafal Rusinek, Krzysztof Kecik, and Jerzy Warminski

Abstract The paper presents results of stability analysis of milling process. Machining of nickel superalloys Inconel 713C, titanium alloy Ti6Al4V and epoxide-polymer matrix composite reinforced carbon fibers (EPMC) is studied here, classically using stability lobe diagrams (SLD) received by modal analysis and next verified by recurrence quantification analysis (RQA). Finally some measures of recurrence quantification analysis are proposed as a tool for stability examination.

Keywords Superalloys • Milling • Recurrence quantification analysis • Aviation industry

1 Machining of Superalloys

Nowadays, superalloys, such as titanium or nickel alloys, are more and more popular mainly because of its low mass and high strength combined with high heat resistance and corrosion as well. Therefore they are applied for extremely loaded components e.g. in civil and military aviation where rotor blades of jet engines are made of nickel (Inconel) or titanium alloys. Composite materials are also willingly used for parts of modern aircrafts such as fuselages, wing skins, flaperons and rudders. Initially, the percentage of structural weight of composites used in manufacturing was very small, at around 2% in the fighter aircraft F15. However, the percentage has grown considerably, through 19% in the F18 up to 24% in the F22 and 50% in the Boeing 878 (Deo et al. 2001), where mainly carbon-fiber composite are used for most of its construction. Therefore the problem of composite materials cutting is important and difficult because of its high strength, tendency to delamination and very fast cutting tool wear.

R. Rusinek (✉) • K. Kecik • J. Warminski
Lublin University of Technology, Nadbystrzycka 36, 20-880 Lublin, Poland
e-mail: r.rusinek@pollub.pl; k.kecik@pollub.pl; j.warminski@pollub.pl

M. Wiercigroch and G. Rega (eds.), *IUTAM Symposium on Nonlinear Dynamics for Advanced Technologies and Engineering Design*, IUTAM Bookseries (closed) 32, DOI 10.1007/978-94-007-5742-4_19,

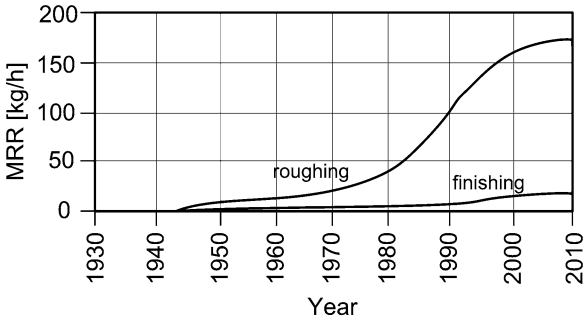

Fig. 1 Development of titanium alloy machining as material removal rate (*MMR*)

Demand for a steadily growing productivity and product quality lead to increasing of cutting parameters and this, in combination with particular mechanical and physical properties of superalloys and composites can also make difficult machining. High productivity can be ensured by high speed machining (HSM) process but chatter vibrations which are generated during cutting can deteriorate a final surface quality of workpiece, shorten tool life time or even destroy the tool or product. Thus, stability analysis of cutting process is so important to avoid chatter vibrations. Usually, stability conditions of machining process are visualized by stability charts (called stability lobe diagram SLD*)* which plot the maximum chatter-free chip width or depth of cut as a function of spindle speed. Theoretical stability analysis is done by many researches, who use a theoretical model (Fofana 2002a, b; Insperger et al. 2003) but verification of their results is still an open question and should be taken into thorough consideration. Therefore, this chapter presents outcomes of cutting forces measurements during milling titanium alloy (Ti6Al4V), nickel alloy (Inconel 713C) and epoxide-polymer matrix composite reinforced carbon fibers (EPMC). Next, the time series of cutting force is analysed with the help of newer methods like recurrence plots (RP), recurrence quantification analysis (RQA), reconstructed phase portraits (RPP), Hurst (H) and Lyapunov (λ) exponents. The methods are applied in order to compare cutting process dynamics and choose a proper index to recognize stable and unstable behaviour.

1.1 Titanium Alloys

Machining of titanium alloys has started since 1940s last century but the fastest development, measured by material removal rate (MMR), is observed in the 1980s and 1990s (Fig. 1).

Nowadays, a tendency of high increase is slowed down (plateau in Fig. 1) mainly due to very strength modern materials which are as hard as cutting tools. Therefore, researchers look for suitable tool materials and tool coat. Some of them believe that alloyed cemented carbide (W–Ti/Ta)C–Co is not suitable for machining of titanium alloys. However, the result of study reported in Haron et al. (2007) shows

that this tool and also alloyed CVD-coated carbide have good possibility to use in end milling of titanium alloy Ti-6242S even under extreme dry cutting condition but in the range of cutting speed between 60 and 150 m/min which are not accepted as HSM. Faster cutting speed, up to 300 m/min, is applied in the study (Sun et al. 2009), where the most common titanium alloy Ti6Al4V is cut on a lathe with a tool CNMX1204A2-SMH13A (Sandvik). Classical dependence between the cutting forces and feed rate is noticed. Cutting forces increase with feed, however, a drop in cutting forces is observed in the feed range 0.122–0.149 mm. On the other hand, the variation of average cutting force with the cutting speed is more complicated. It increases initially with cutting speed up to 21 m/min due to strain hardening and then decreases dramatically with cutting speed from 21 to 57 m/min, which is attributed to thermal softening due to the increase of cutting temperature and next from about 120 to 250 m/min. What is more, the authors prove that the cyclic frequency of cutting force is directly proportional to the cutting speed and indirectly proportional to the feed rate. General tendency of the cutting forces decrease with increasing cutting speeds (up to 700 m/min) is also reported in Abele and Frochlich (2008).

The problem of chatter specially during finish machining of titanium alloy is described in Ezugwu and Wang (1997). According to authors, the low modulus of elasticity of titanium alloys is a principal cause of the chatter. The appearance of chatter may also be partially ascribed to the high dynamic cutting forces in machining. This can be up to 30% of the value of static forces.

Despite the fact that static and dynamic cutting forces are analysed and also their cyclic frequency, there is a lack of stability analysis on the basis of measurements. There are only stability diagrams made for mathematical model.

1.2 Nickel Alloy

Generally it is known that nickel-base super alloys are one of the most difficult materials to machine. Poor selection of machining parameters causes fast cutting tools wear and even tool break and also economical losses produced by damaged workpiece and poor surface quality. One of the most popular nickel based superalloy – Inconel 718 is machined by using cemented carbide inserts at lower speeds while it is machined by using ceramic cutting tools at higher speeds (Nalbant et al. 2007a). The investigation performed on a lathe in the paper concerns the effects of cutting tool coating material and cutting speed on cutting forces and surface roughness. The lowest main cutting force is found at cutting speed of 75 m/min with multicoated cemented carbide insert whose top layer is coated by Al2O3. Lowest average surface roughness is obtained at the cutting speed of 15 m/min with single coated (TiN) cemented carbide inserts. Moreover, relationship between main cutting force and cutting speed indicates that there is a linear relationship between main cutting force and cutting speed that is unexpected because the others study demonstrate weak or even strong nonlinear dependence (Arunachalam et al. 2004a – axial cutting force, Devillez et al. 2007; Liao et al. 2008; Nalbant et al. 2007b).

As it is demonstrated in the previous literature, the cutting force decreases with cutting speed in certain speed regions whereas an increase of feed rate always increases the cutting forces (Kose et al. 2008).

The cutting speed is very important factor that influences the tool wear and tool life when cutting nickel based alloys. Therefore a number a publications present the influence of cutting speed on tool wear and tool life. In the paper (Altin et al. 2007) authors use round and square silicon nitrite based and whisker reinforced aluminum oxide (Al2O3 + SiCw) ceramic inserts for Inconel 718 turning. Based on experimental results, the optimum cutting speed can be deduced as 250 m/min and the tool life is affected negatively above this speed. Generally, square type inserts show good performance compared to round type inserts at low cutting speeds whilst round type insert was recommended at high cutting speeds.

For optimizing the cutting speed in the turning of Inconel 718 a series of experiments using various coated carbides and ceramics are presented in Li et al. (2002). The experiment results show that PVD-coated carbides are more suitable for cutting than CVD-coated carbides, and ceramic inserts with negative rake angle of round type are the best choice for high speed turning up to 300 m/min. General conclusion can be drawn that the magnitude of all the forces is lower at higher than at lower cutting speed (Pawde et al. 2007).

Other studies show effect of cutting edge preparation and geometric modification when turning Inconel 718 at high speed cutting (HSM) conditions (Coelho et al. 2004) or residual stress and surface roughness during turning with cubic boron nitride (CBN) and ceramic tools (Arunachalam et al. 2004a). Sometimes coated carbide cutting tools are used (Arunachalam et al. 2004b).

Most of the available machinability data on nickel-based superalloys is based on orthogonal turning operations where a continuous engagement of tool – work material exists. Despite many publications on tool wear in turning, reports of tool wear with respect to milling are still lacking. The paper (Jawaid et al. 2001) compares milling performance of PVD TiN coated and uncoated tungsten carbide with identical geometry. The uncoated tool performs better at the lowest cutting speed of 25 m/min while PVD TiN coated tool gives better performance at cutting speed of 50 m/min. according to authors, this can be attributed to the high wear resistance and low thermal conductivity of TiN coating layer.

Cutting force variation in the dry end milling of Inconel 718 with coated carbide inserts is shown in Li et al. (2006), while with cemented carbide tools is presented in Liao et al. (2008). Only the peak value of the forces is analysed without deeper investigations of vibrations.

1.3 Composite Materials

The problem of metal cutting stability based on regenerative model is quite well known but the stability lobes of composite material cutting is still being developed. It arises from the lack of detailed specification of composite materials,

their mechanical properties which are necessary to obtain the proper stability lobe diagram (SLD). Nowadays, publications which are concerned with composite material machining, frequently focus on tool wear (Conceicao and Davim 2002; Davim and Conceicao 2001) or methods of avoiding delamination (Davim and Reis 2005). The investigations of composite material machinability refers both to carbon-fiber or glass-fiber reinforced materials (Davim et al. 2004; Langella et al. 2005; Ramulu et al. 2003) and metal matrix composites (Zhu and Kishawy 2005). As far as tool wear is concerned, diamond tools are the most suitable for use in finishing turning of carbon-carbon composite. In rough turning, the carbide tools can be used but with some restrictions parameters. Tool flank wear is the least for high speed cutting, in the range from 500 to 800 m/min (Ferreira et al. 2001).

Generally, there is a lack of experimental methods which can tell us about process dynamics and their stability. One of the most interesting approaches is presented in Ramulu et al. (2003) where the effect of fiber orientation on the normalized frequency spectrum in orthogonal cutting glass fiber reinforced polyester (GFRP) is analysed. Thus, taking into account achievements in this field, a stability analysis should be also done. Therefore, this study proposes to engage recurrence plot technique to estimate cutting process stability.

2 Experimental Methodology

The experimental investigations are conducted on three material, used in aviation industry, namely nickel alloy – Inconel 713C, titanium alloy – Ti6Al4V and epoxide-polymer matrix composite reinforced carbon fibers (EPMC). For nickel and titanium alloy stability lobs diagrams (SLD) are determined with the help of CutPro software which bases on the tool modal analysis. SLD for EPMC cannot be done because of difficulties coming from the software limitations. Therefore, the experimental setup, presented schematically in Fig. 2, is used in order to measure all components of the total cutting forces (F_x, F_y and F_z) and torque (M_z). The experimental system is composed of the numerical controlled milling machine DMU 80P duoBlock Deckel Maho, the piezoelectric rotating four component dynamometer Kistler 9123C, piezoelectric conditioner Kistler 5134 and the analog-digital converter NI 6062E by National Instruments.

For the purpose of modal analysis, the hammer PCB model 086C03 which has 8 kHz frequency range and 10 mV/lbf sensitivity is used and, the 2-axes piezoelectric accelerometers 352C43 as well. The gauging point of modal hammer is the tool tip. The modal hammer is used for delivering impulse forces into the tested structure. Hammer model selection involves determining the size and mass of the hammer, which provide the force amplitude and frequency content required for proper excitation of the structure under the test. In the experiment, three end milling cutters specially designed for finishing milling of hard materials are used. The first made of solid carbide with diameter of 16 mm and four cutting edges (Kasuka DM600 WND16) to cut Ti6Al4V alloy. Second, Al-Tec ECH060B16-6C06 made

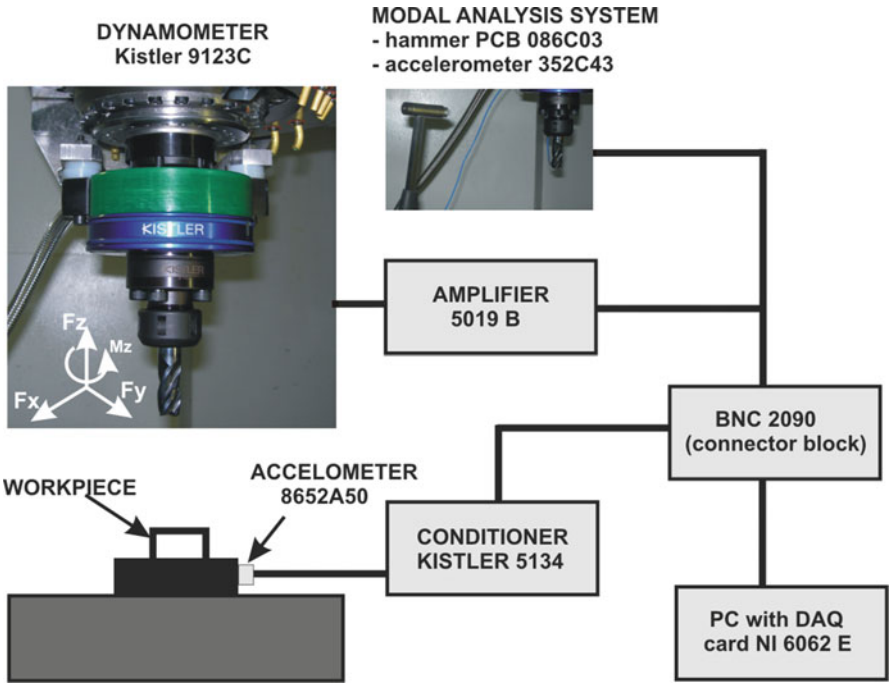

Fig. 2 Experimental setup scheme

also of solid carbide with diameter of 6 mm and four cutting edges. The third, made of PCD with diameter of 12 mm (CutTech). The sampling rate of data reordered during the test equals 3 kHz.

Next, the signal of cutting force is put to further analysis which is based on recurrence plots (RP) technique, recurrence qualification analysis (RQA) and also Hurst and Lyapunov exponents.

3 Cutting Process Stability

Most often milling process is modeled as single or two degree of freedom system with regenerative effect. Then the process is described by delay differential equations. Stability of the process is determined by stability lobes diagram (SLD). In this study, SLD is plotted by commercial CutPro9 module using modal analysis. This software identifies the structural dynamic parameters of a tool-machine from Frequency Response Function (FRF). Accurately prediction of natural frequency, damping ratio and modal stiffness from FRF let us identify parameters which are crucial in predicting chatter vibration and stable lobs. The stability lobe diagram for Ti6Al4V and Inconel 713C are presented in Figs. 3 and 4, respectively. The cutting

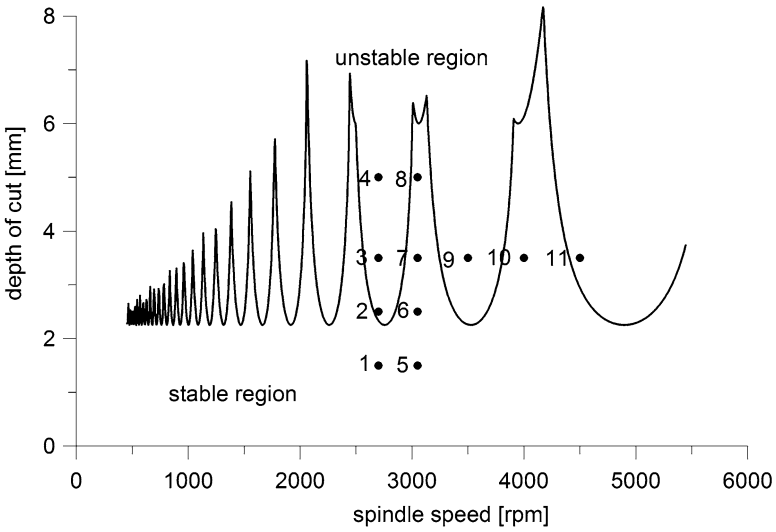

Fig. 3 Stability lobe diagrams for milling Ti6Al4V

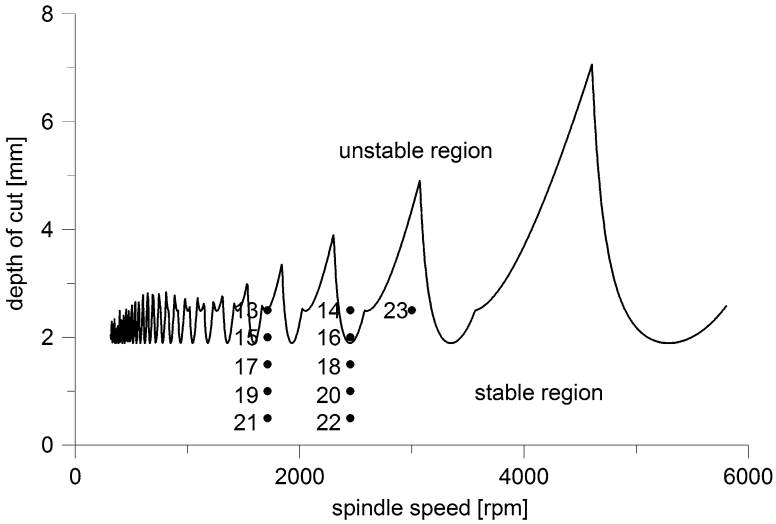

Fig. 4 Stability lob diagrams for milling Inconel 713C

conditions – spindle speed and depth of cut are shown in Table 1. Above black line areas the process produces chatter vibrations, while machining with parameters below stability lobs should be free from harmful chatter vibrations.

Milling Ti6Al4V at cutting depth below 2.25 mm should be stable all time regardless of spindle speed (Fig. 3). While, in case of Inconel 713C, the stable

Table 1 Cutting conditions – spindle speed and depth of cut for Ti6Al4V and Inconel 713C

Point for Ti6Al4V	Speed [rpm]	Depth of cut [mm]	Point for Inconel 713C	Speed [rpm]	Depth of cut [mm]
1	2,700	1.5	13	1,714	2.5
2	2,700	2.5	14	2,450	2.5
3	2,700	3.5	15	1,714	2.0
4	2,700	5.0	16	2,450	2.0
5	3,050	1.5	17	1,714	1.5
6	3,050	2.5	18	2,450	1.5
7	3,050	3.5	19	1,714	1.0
8	3,050	5.0	20	2,450	1.0
9	3,500	3.5	21	1,714	0.5
10	4,000	3.5	22	2,450	0.5
11	4,500	3.5	23	3,000	2.5

limit is lower, about 1.9 mm (Fig. 4). The black points marked at SDL represent parameters where the cutting forces *Fx, Fy* and *Fz* are measured for the purpose of further analysis. As far as titanium alloy is concerned, stable points 1 and 10 are chosen and unstable 4, 9 (Fig. 3).

Points 1, 4 are obtained under the same spindle speed of 2,700 rpm. The forces in points 9 and 10 are recorded at cut depth of 3.5 mm for 3,500 and 4,000 rpm, respectively. This let us compare an influence of cutting depth and spindle speed on process stability. Similarly, in case of Inconel 713C milling, the points 14 and 22 are selected from Fig. 4. Unstable points 14 and stable 22 is received at 2,450 rpm.

4 Recurrence Qualification Analysis

For chosen points from Figs. 3 and 4, cutting force signals (F_x) is analysed with the help of recurrence plot (RP) technique originally introduced by Eckmann et al. in (1987). RP graphically presents the system state when recurrence between points exists. More detailed description of RP technique and the delay coordinates method which is used to obtain embedding parameters required for RP construction can be found in Abarbanel (1996), Kantz and Schreiber (1997). Analysis of RPs sometimes may be labour consuming and equivocal, therefore later the recurrence quantification analysis (RQA) is developed mainly by authors of the following papers (Marwan 2003; Webber and Zbilut 1994; Zbilut and Webber 1992). RQA quantifies the number and duration of recurrences of a dynamical system presented by its state space trajectory. The main advantage of RQA is that it can provide useful information as a index number even for short and non-stationary data, where other methods fail. According to Marwan et al. (2007), there are 14 measures of RQA. All of them have been tested in this study and next recurrence rate (RR)

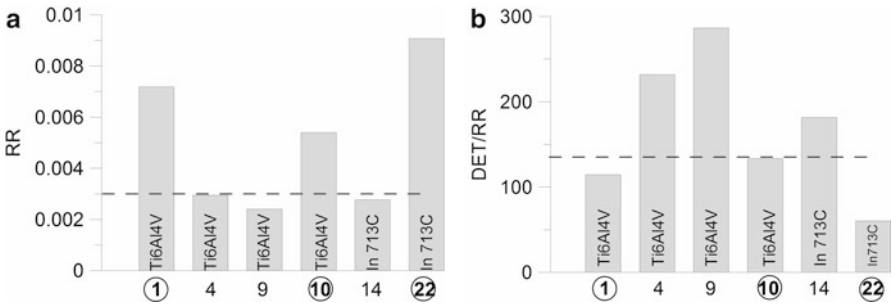

Fig. 5 Recurrence qualification analyses for Inconel 713C and Ti6Al4V; Recurrence Rat (*RR*) (**a**); ratio DET/RR (**b**)

and ratio (DET/RR) between determinism (DET) and RR are selected for cutting process analysis. Recurrence Rate (RR) is the density of recurrence points in a recurrence plot. Determinism or predictability (DET) is the fraction of recurrence points forming diagonal lines. The results of calculations RR and DET/RR for TI6Al4V and Inconel 713C is shown in Fig. 5, where the circled numbers represent stable points while unstable ones are marked just by number. Recurrence rate of stable points is distinctly higher than the points considered as unstable. The stability limit of milling TI6Al4V and Inconel 713C can be put at 0.003 (dashed line in Fig. 5a). High RR means that there are many points in recurrence.

On the other hand, the ratio DET/RR of stable points is small (below dashed line in Fig. 5b) that means the number of points which create diagonal lines (DET) is not big compared to the all recurrence points. This is because the cutting force signal (Fx) obtained for stable points (1, 10, 22) is less regular than time series of cutting force of unstable cutting.

Next, series of measurements of composite (EPMC) milling are performed with feed rate of 520 mm/min and cutting depth and speed depicted graphically as black points in Fig. 6. Some of the measurements have been analysed in the paper (Rusinek 2010) where a simple stability criterion based on ratio between dynamic and static force is introduced. Furthermore, recurrence plots and reconstructed Poincaré maps are used to check the criterion. Now, RR and DET/RR (Fig. 7) is applied to investigate where the process is stable. Finding a critical value of RR_{cr} and $(DET/RR)_{cr}$ is a main problem. Point can be recognized as stable when both $RR > RR_{cr}$ and $(DET/RR) < (DET/RR)_{cr}$. Such points have circled number in Figs. 6 and 7. Looking at Fig. 6 it can be noticed that stable points appear periodically versus spindle speed. This proves that SLD for composite material, or others whose mechanical properties are not clearly defined, can be found without solving dynamic equations of motion but just by analyzing cutting forces. We should remember that the procedure is time consuming because needs to calculate RQA for every or almost every points in stability diagram. The proposal how SLD looks like for EPMC is presented in Fig. 6.

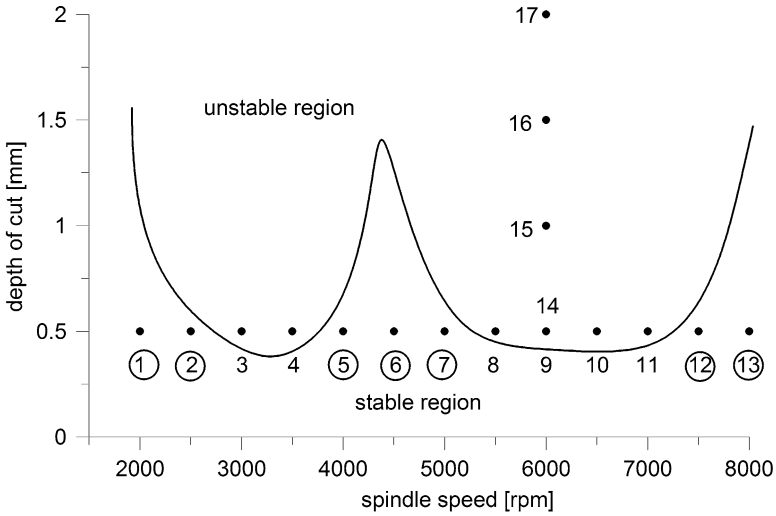

Fig. 6 Measured points during EPMC milling

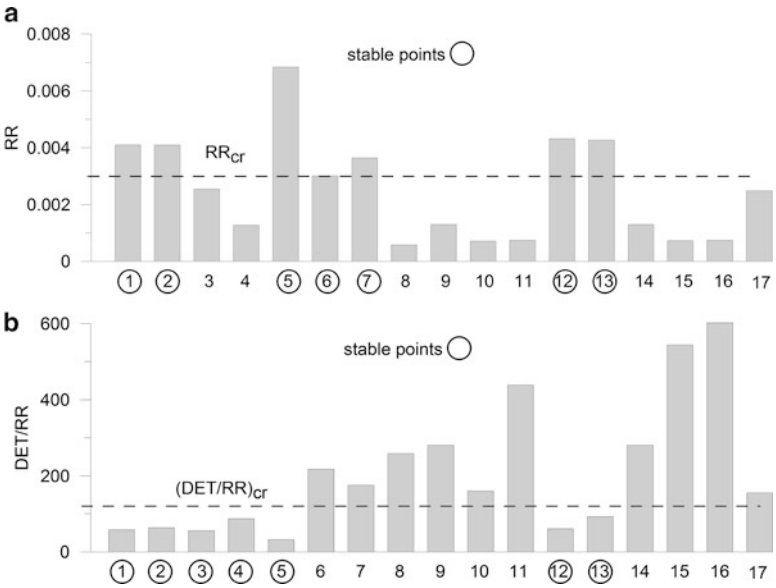

Fig. 7 Recurrence rate (*RR*) and ratio DET/RR for milling EPMC

5 Conclusions

This study focuses on verification of milling process stability in case of superalloys and composite materials machining used in aviation industry. Stability of cutting process of typical, common used materials is quite well done. The problem arises when workpiece is made of material which has heterogeneous properties e.g. composite (EPMC). In this case recurrence quantifications analysis looks promising. Among all recurrence quantification measures recurrence rate (RR) and ratio DET to RR are chosen because their efficiency is satisfactory. In case of stable cutting, RR of cutting force signal is higher than some critical value RR_{cr} on the other hand DET/RR ratio is less than critical indicator $(DET/RR)_{cr}$. The proper choice of RR_{cr} and $(DET/RR)_{cr}$ is the main problem which is solved here. The critical value should be about half of maximum value of the measures obtained both for stable and unstable cutting parameters. The new method of stability analysis has been verified in case of Ti6AlV4 and Inconel 713C milling and applied for finding unstable, unwanted cutting parameters of epoxide-polymer matrix composite reinforced carbon fibers. The results demonstrate that RQA method can be used for short time series analysis that can be taken full advantage in damage detecting of cutting tool, dull of tool or instability control.

Acknowledgments Financial support of Structural Funds in the Operational Programme – Innovative Economy (IE OP) financed from the European Regional Development Fund – Project No POIG.0101.02-00-015/08 is gratefully acknowledge.

The research leading to these results has received funding from the European Union Seventh Framework Programme (FP7/2007–2013), FP7-REGPOT-2009-1, under grant agreement No:245479.

References

Abarbanel, H.D.I.: Analysis of Observed Chaotic Data. Springer, New York (1996)

Abele, E., Frochlich, B.: High speed milling of titanium alloys. Adv. Prod. Eng. Manag. **3**, 131–140 (2008)

Altin, A., Nalbant, M., Taskesen, A.: The effects of cutting speed on tool wear and tool life when machining Inconel 718 with ceramic tools. Mater. Des. **28**, 2518–2522 (2007)

Arunachalam, R.M., Mannan, M.A., Spowage, A.C.: Residual stress and surface roughness when facing age hardened Inconel 718 with CBN and ceramic cutting tools. Int. J. Mach. Tool Manuf. **44**, 879–887 (2004a)

Arunachalam, R.M., Mannan, M.A., Spowage, A.C.: Surface integrity when machining age hardened Inconel 718 with coated carbide cutting tools. Int. J. Mach. Tool Manuf. **44**, 1481–1491 (2004b)

Coelho, R.T., Silva, L.R., Braghini Jr., A., Bezerra, A.A.: Some effects of cutting edge preparation and geometric modifications when turning INCONEL 718 at high cutting speeds. J. Mater. Process. Technol. **148**, 147–153 (2004)

Conceicao, C.A., Davim, J.P.: Optimal cutting conditions in turning of particulate metal matrix composites based on experiment and genetic search model. Compos. Part A **33**, 213–219 (2002)

Davim, J.P., Conceicao, C.A.: Optimisation of cutting conditions in machining of aluminum matrix composites using a numerical and experimental model. J. Mater. Process. Technol. **112**, 78–82 (2001)

Davim, J.P., Reis, P.: Damage and dimensional precision on milling carbon fiber-reinforced plastics using design experiments. J. Mater. Process. Technol. **160**, 160–167 (2005)

Davim, J.P., Reis, P., Conceicao, C.A.: Experimental study of drilling glass fiber reinforced plastics (GFRP) manufactured by hand lay-up. Compos. Sci. Technol. **64**, 289–297 (2004)

Deo, R.B., Starnes, J.H., Holzwarth, R.C.: Low-cost composite materials and structures for aircraft applications. Presented at NATO Research and Technology Agency Applied Vehicle Technical Panel Specialists' Meeting on Low Cost Composite Structures, pp. 444–447 (2001)

Devillez, A., Schneider, F., Dominiak, S., Dudzinski, D., Larrouquere, D.: Cutting forces and wear in dry machining of Inconel 718 with coated carbide tools. Wear **262**, 931–942 (2007)

Eckmann, J.-P., Kamphorst, S.O., Ruelle, D.: Recurrence plots of dynamical systems. Europhys. Lett. **5**, 973–977 (1987)

Ezugwu, E.O., Wang, Z.M.: Titanium alloys and their machinability – a review. J. Mater. Process. Technol. **68**, 262–274 (1997)

Ferreira, J.R., Coppini, N.L., Levy Neto, F.: Characteristics of carbon ± carbon composite turning. J. Mater. Process. Technol. **109**, 65–71 (2001)

Fofana, M.S.: Effect of regenerative process on the sample stability of a multiple delay differential equation. Chaos Solitons Fractals **14**, 301–309 (2002a)

Fofana, M.S.: Sufficient conditions for the stability of single and multiple regenerative chatter. Chaos Solitons Fractals **14**, 335–347 (2002b)

Haron, C.H.C., Ginting, A., Arshad, H.: Performance of alloyed uncoated and CVD-coated carbide tools in dry milling of titanium alloy Ti-6242S. J. Mater. Process. Technol. **185**, 77–82 (2007)

Insperger, T., Stepan, G., Bayly, P.V., Mann, B.P.: Multiple chatter frequency in milling processes. J. Sound Vib. **262**, 333–345 (2003)

Jawaid, A., Koksal, S., Sharif, S.: Cutting performance and wear characteristics of PVD coated and uncoated carbide tools in face milling Inconel 718 aerospace alloy. J. Mater. Process. Technol. **116**, 2–9 (2001)

Kantz, H., Schreiber, T.: Nonlinear Time Series Analysis. Cambridge University Press, Cambridge (1997)

Kose, E., Kurt, A., Seker, U.: The effects of the feed rate on the cutting tool stresses in machining of Inconel 718. J. Mater. Process. Technol. **196**, 165–173 (2008)

Langella, A., Nele, L., Maio, A.: A torque and thrust prediction model for drilling of composite materials. Compos. Part A **36**, 83–93 (2005)

Li, L., He, N., Wang, M., Wang, Z.G.: High speed cutting of Inconel 718 with coated carbide and ceramic inserts. J. Mater. Process. Technol. **129**, 127–130 (2002)

Li, H.Z., Zeng, H., Chen, X.Q.: An experimental study of tool wear and cutting force variation in the end milling of Inconel 718 with coated carbide inserts. J. Mater. Process. Technol. **180**, 296–304 (2006)

Liao, Y.S., Lin, H.M., Wang, J.H.: Behaviors of end milling Inconel 718 superalloy by cemented carbide tools. J. Mater. Process. Technol. **201**, 460–465 (2008)

Marwan, N.: Encounters with neighbours current developments of concepts based on recurrence plots and their applications. Dissertation, University of Potsdam (2003)

Marwan, N., Romano, M.C., Thiel, M., Kurths, J.: Recurrence plots for the analysis of complex systems. Phys. Rep. **438**, 237–329 (2007)

Nalbant, M., Altin, A., Gokkaya, H.: The effect of coating material and geometry of cutting tool and cutting speed on machinability properties of Inconel 718 super alloys. Mater. Des. **28**, 1719–1724 (2007a)

Nalbant, M., Altin, A., Gokkaya, H.: The effect of cutting speed and cutting tool geometry on machinability properties of nickel-base Inconel 718 super alloys. Mater. Des. **28**, 1334–1338 (2007b)

Pawde, R.S., Joshi, S.S., Brakmankar, P.K., Rahman, M.: An investigation of cutting forces and surface damage in high-speed turning of Inconel 718. J. Mater. Process. Technol. **192–193**, 139–146 (2007)

Ramulu, M., Kim, D., Choi, G.: Frequency analysis and characterization in orthogonal cutting of glass fiber reinforced composites. Compos. Part A **34**, 949–962 (2003)

Rusinek, R.: Cutting process of composite materials: an experimental study. Int. J. Non-Linear Mech. **45**, 458–462 (2010)

Sun, S., Brandt, M., Dargusch, M.S.: Characteristics of cutting forces and chip formation in machining of titanium alloys. Int. J. Mach. Tool Manuf. **49**, 561–568 (2009)

Webber Jr., C.L., Zbilut, J.P.: Dynamical assessment of physiological systems and states using recurrence plot strategies. J. Appl. Phys. **76**, 965–973 (1994)

Zbilut, J.P., Webber Jr., C.L.: Embeddings and delays as derived from quantification of recurrence plots. Phys. Lett. A **171**, 199–203 (1992)

Zhu, Y., Kishawy, H.A.: Influence of alumina particles on the mechanics of machining metal matrix composites. Mach. Tool. Manuf. **45**, 389–398 (2005)

Dynamical Integrity for Interpreting Experimental Data and Ensuring Safety in Electrostatic MEMS

Laura Ruzziconi, Mohammad I. Younis, and Stefano Lenci

Abstract A dynamical integrity analysis is performed for an electrostatic micro-electro-mechanical system (MEMS) device. The analysis starts from the experimental data of dynamic pull-in due to a frequency-sweeping process in a capacitive accelerometer. The loss of dynamical integrity is investigated by curves of constant percentage of integrity factor. We found that these curves follow exactly the experimental data and succeed in interpreting the existence of disturbances. On the other hand, instead, the theoretical curves of disappearance of the attractors represent the limit when disturbances are absent, which never occurs in practice. Also, the obtained behavior chart can serve as a design guideline in order to ensure safety of the device.

Keywords Dynamical integrity • Integrity factor • MEMS • Dynamic pull-in

L. Ruzziconi (✉)
Department of Civil and Building Engineering, and Architecture, Polytechnic University of Marche, Ancona, Italy

Department of Mechanical Engineering, State University of New York, Binghamton, USA
e-mail: l.ruzziconi@univpm.it

S. Lenci
Department of Civil and Building Engineering, and Architecture, Polytechnic University of Marche, Ancona, Italy
e-mail: lenci@univpm.it

M.I. Younis
Department of Mechanical Engineering, State University of New York, Binghamton, USA
e-mail: myounis@binghamton.edu

M. Wiercigroch and G. Rega (eds.), *IUTAM Symposium on Nonlinear Dynamics for Advanced Technologies and Engineering Design*, IUTAM Bookseries (closed) 32, DOI 10.1007/978-94-007-5742-4_20,

1 Introduction

As remarked by Thompson (1989) and realized by others since then (Rega and Lenci 2005), the existence of an attractor in a dynamical system does not guarantee its safety from a practical point of view. This is because in experiments and practice, disturbances exist, giving uncertainty to the operating initial conditions. If the safe basin is not sufficiently robust, the dynamical outcome can be totally different from what is theoretically predicted.

The shrinkage and erosion of the safe basin particularly concerns systems of softening-type behavior, such as those with asymmetric potential wells. The consequence of this out-of-well phenomenon is the escape, which is dangerous from a practical point of view because it leads to failure. This phenomenon arises in several applications in MEMS (Senturia 2001). For example, in the so-called electrostatic MEMS, which is the class of MEMS we are referring to in this paper, a device can be operated with high level of electrodynamic excitations. For growing excitation amplitude the energy of the system increases up to exceeding the barrier of its potential well (Nayfeh et al. 2007; Alsaleem et al. 2009; Krylov and Dick 2010). The resulting escape manifests itself through the dynamic pull-in instability, i.e. the resonating microstructure collapses on the substrate leading to its failure through stiction or short circuiting.

The present work starts from the experimental data of dynamic pull-in of a particular MEMS device, a capacitive accelerometer. They are obtained by a frequency-sweeping process, where the voltage is kept fixed and the frequency is increased or decreased slowly, i.e. quasi-statically. Performing a classical dynamical analysis, we note that identifying the inevitable escape zones does not succeed in predicting the experimental pull-in bands. This calls for a more detailed analysis, where also dynamical integrity concepts are considered. This is the aim of the present paper.

The response of the device is simulated by a nonlinear single degree of freedom (d.o.f.) model (Sect. 2). It shares the same main qualitative features of other softening systems investigated in depth (Gottlieb and Champneys 2005; Lenci and Rega 2006) (Sect. 3). After these traditional simulations, we focus on the range where tongues of the out-of-well attractor enter the potential well, and the erosion proceeds up to the complete destruction of the safe basin for sufficiently high dynamic voltage (Sect. 4).

Our main theoretical motivation is to highlight the effectiveness of the dynamical integrity for interpreting the experimental data. To guarantee the accuracy of the analysis, a continuous parallelism between theory and experiments is established. All the chosen theoretical tools, as the definition of the safe basin and the integrity factor measure, are constantly justified by the experimental conditions of the sweeping process. Finally, the curves of constant percentage of integrity factor are constructed. They follow exactly the experimental data, succeeding in the interpretation of the presence of disturbances.

In addition to the theoretical motivation, there is also a practical benefit. In fact, the chart serves as a guideline for the design. Depending on the expected disturbances, it allows to identify the most dangerous ranges in order that the safety of the device is ensured.

2 Experimental Data and Mechanical Model

The considered capacitive accelerometer (Fig. 1a) consists of a proof mass suspended by two cantilever beams. The upper electrode is formed by the proof mass, with length 9 mm, width 5.32 mm, and thickness 150 μm. The lower electrode is placed directly underneath it on a silicon substrate; it is of the same length of the proof mass and slightly smaller width, 4.4 mm. The separation gap is 42 μm. When electrically excited, the proof mass oscillates in the out-of-plane direction, i.e. out of the plane of the substrate. Although the mass is not in a micro-range, the system has the same main characteristics of a MEMS device: gap and thickness are in the micro-range and it is actuated electrostatically. Differently from other devices, it has the advantage of surviving the repetitive failures due to pull-in, which allows a deep experimental investigation.

The capacitive accelerometer is simulated using a spring-mass model (Fig. 1b) with a single d.o.f. Its governing equation of motion is

$$m\ddot{x} + c\dot{x} + kx = \frac{\varepsilon A[V_{DC} + V_{AC}\cos(\Omega t)]^2}{2(d-x)^2} \tag{1}$$

In Eq. (1) x is the deflection of the proof mass, m is its mass, c is the viscous damping coefficient due to the squeeze film effect, k is the linear effective stiffness of the cantilever beams, ε is the dielectric constant of the gap medium (air, $\varepsilon = 8.854 \cdot 10^{-12}$ C^2/(N m^2)), A is the lower electrode area, d is the capacitor gap

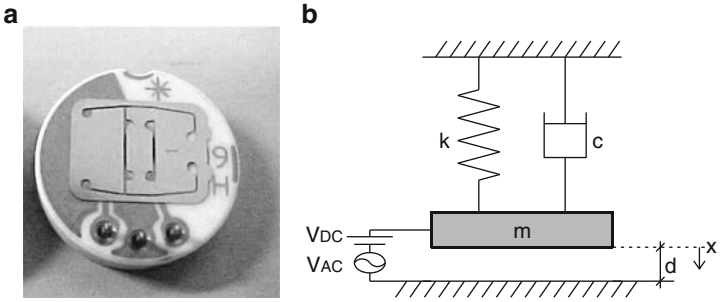

Fig. 1 (**a**) A picture of the considered capacitive accelerometer and (**b**) the spring-mass model

width, V_{DC} and V_{AC} are respectively the electrostatic and electrodynamic voltage, Ω is the electrodynamic voltage frequency, t is the physical time, and the superscript dot denotes the time derivative.

The device has been experimentally tested in (Alsaleem et al. 2009, 2010), which are referred for the experimental data. From these data, the coefficients in Eq. (1) have been derived as explained in (Alsaleem et al. 2009).

The experimental static response of the proof mass is analyzed for different increasing V_{DC} inputs, and the static pull-in voltage is determined, $V_{pull\text{-}in} = 115.3$ V. This value is used to obtain the stiffness coefficient k by drawing, in the static case, the bifurcation diagrams of the governing Eq. (1) for increasing V_{DC}, and by tuning the stiffness in order to produce in the model a saddle-node just at $V_{pull\text{-}in}$. This yields $k = 215$ Nm^{-1}. The experimentally measured natural frequency is 192.5 Hz. From this information, the effective mass of the proof mass is evaluated, $m = 0.14697$ g.

The dynamical pull-in data come from a frequency-sweeping process, where the dynamic voltage is kept fixed and the frequency is increased or decreased slowly, i.e. quasi-statically. They refer to the case of primary resonance, with electrostatic voltage $V_{DC} = 40.1$ V, and pressure very close to an ultra-high vacuum environment, 153 mtorr. We consider only the viscous squeeze-film damping contribution, since it is the most significant source of energy loss in the analyzed MEMS device. The damping coefficient due to the squeeze-film effect is computed by means of an elaborate procedure, largely used in the MEMS literature, which is well explained for example in (Senturia 2001).

From the previous considerations, Eq. (1) becomes:

$$\ddot{x} + 10.1\dot{x} + 1.4629 \cdot 10^6 x = 1.2 \cdot 10^{-12} \cdot \frac{[40.1 + V_{AC} \cos(\Omega t)]^2}{(42 \cdot 10^{-6} - x)^2} \tag{2}$$

The frequency step is 0.5 Hz, and the time step is 1 s, which guarantees the steady-state condition at the end of each step. As an example, an experimental frequency sweeping is reported in Fig. 2 for $V_{AC} = 18.4$ V (almost half of the static voltage). Similar frequency sweepings are used to extract the data points of the experimental pull-in bands, shown with dots in the forthcoming Fig. 5.

3 Hamiltonian System and Homoclinic Bifurcation

Before analyzing the overall dynamics, we focus on the unforced, undamped system derived from Eq. (2). This system is Hamiltonian. It has a single asymmetric well, with the escape direction at right, showing the softening type behavior. Accordingly, there are only two physical equilibrium points: the elliptic center $x_c = 0.776$ μm, and the hill-top saddle $x_s = 35.942$ μm (Fig. 3).

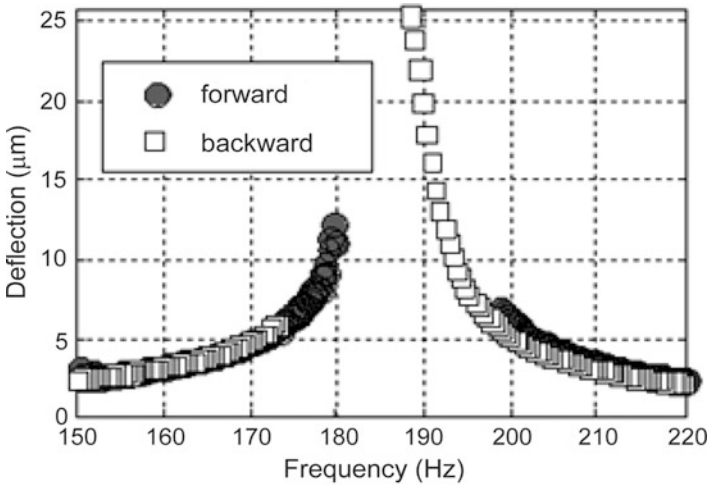

Fig. 2 An experimental frequency response curve obtained in Alsaleem et al. (2009) by the frequency-sweeping process (*forward sweep and backward sweep*) at $V_{AC} = 18.4$ V

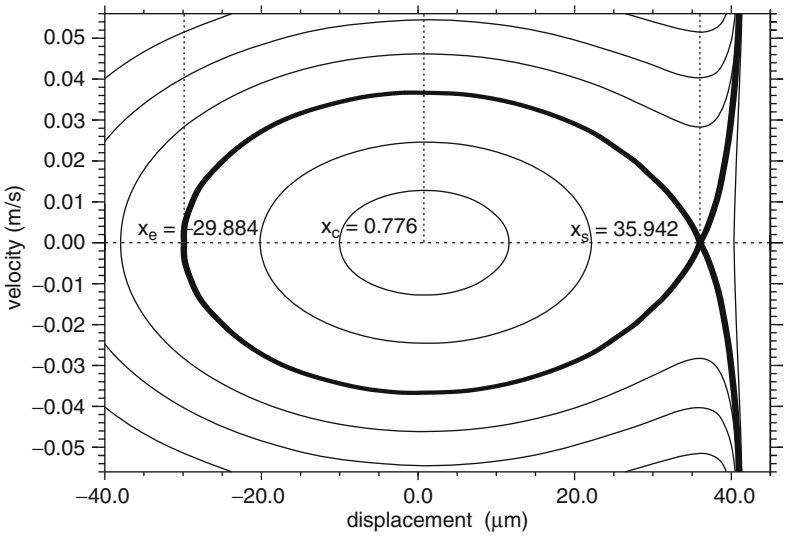

Fig. 3 The unperturbed phase space

The homoclinic orbit separating the in-well from the out-of-well oscillations is implicitly defined by:

$$t = \pm \int_{x_e}^{x} \frac{dr}{\sqrt{2\left[V\left(x_s\right) - V(r)\right]}} \tag{3}$$

where $x_e = -29.884$ μm is the intersection of the orbit with the horizontal axis and

$$V(x) = \frac{1}{m}\left(k\frac{x^2}{2} - \frac{\varepsilon A V_{DC}^2}{2\,(d-x)}\right) \tag{4}$$

is the potential function. Note that Eq. (3) is an even function of the time t and it can be computed only numerically.

Adding perturbations to the unforced undamped Hamiltonian system, the stable and unstable manifolds of the saddle x_s split. For some parameter values they may intersect, producing the erosion of the safe basin. The threshold that triggers this mechanism is represented by the homoclinic bifurcation, where the stable and unstable manifolds become tangent. It is detected using the Melnikov method. A similar analysis has been carried out in (Gottlieb and Champneys 2005; Lenci and Rega 2006) for the case of a thermoelastic electrostatically actuated MEMS device. We refer to them for more details.

The perturbed system is deduced considering both the damping and the electrodynamic force as small perturbations to the unforced undamped Hamiltonian case. The first order measure of the distance between the manifolds is proportional to the classical Melinkov function $M(t_0)$, which has the standard form (Guckenheimer and Holmes 1983):

$$M\,(t_0) = I_1 + I_2 \sin\left(\Omega t_0\right), \tag{5}$$

where I_1 depends on the damping and I_2 depends on the excitation frequency and amplitude. The values of damping, frequency, and amplitude where $M(t_0)$ has a quadratic zero are the homoclinic bifurcation values, which satisfy the equation $|I_1| = |I_2|$. Below this threshold, which is reported by a dotted line in the forthcoming Fig. 5, the erosion is prevented. The dynamic pull-in data are considerably far from it, i.e., the device continues being in safe conditions well above it. To analyze the safety of the mechanical system in this range, a dynamical integrity analysis is required since the triggered erosion makes the jump not so obvious.

4 Dynamical Integrity Analysis

Above the homoclinic bifurcation of the manifolds of the hill-top saddle, the escape area penetrates with fractal tongues into the in-well basins. Numerical simulations are performed by the combined use of frequency response diagrams and attractor-basins phase portraits. Next to the classical behavior chart, the loss of integrity of the safe basins is discussed. In particular, we focus on the interpretation of the experimental data of dynamical pull-in using curves of constant percentage of integrity factor.

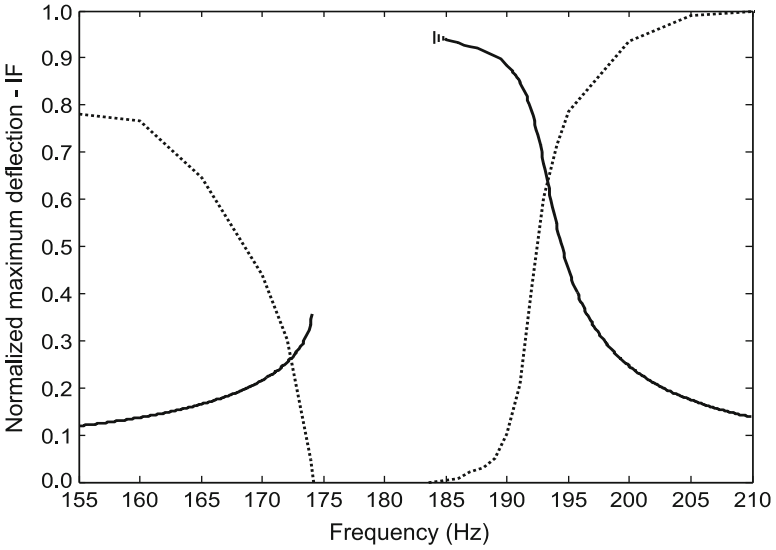

Fig. 4 Frequency response diagram (*solid lines*) and erosion profile (*dotted lines*) near primary resonance, at $V_{AC} = 30$ V

4.1 Behavior Chart and Basin Erosion

In a neighborhood of the primary resonance, the device behaves as a softening oscillator. To illustrate this, an example of frequency response diagram is reported in Fig. 4, where the solid lines represent the normalized maximum deflection for $V_{AC} = 30$ V. The attractors show the characteristic bending toward the left. Note that, in the range $\Omega = [174.1, 184]$ Hz the inevitable escape from the potential well, i.e. the dynamical pull-in, is the only possible outcome.

One can note from Fig. 4 that there are two kinds of bifurcations through which the stable steady-state frequency-response curve loses stability. The non-resonant attractor (left frequency curve of Fig. 4) disappears by a saddle-node bifurcation (SN). The resonant attractor, on the other hand (right frequency curve of Fig. 4), experiences the classical period-doubling cascade (PD) followed by chaotic motion and boundary crisis (BC). The frequency corresponding to these main dynamical phenomena have been reported in the behavior chart of Fig. 5 by solid lines. Repeating this process for different values of V_{AC}, the curves of appearance/disappearance and the curve of first period-doubling have been obtained. They summarize the overall scenario, which has the same main qualitative features of other softening oscillators (Lenci and Rega 2006; Szemplinska-Stupnicka 1992): the degenerate cusp bifurcation at $\Omega \cong 187.5$ Hz, where the saddle-nodes of the non-resonant and resonant branches collapse; the Δ-shaped region where the two attractors coexist; and the V-shaped region of inevitable escape, with vertex at $\Omega \cong 178.3$ Hz. Note that the experimental data do not follow these classical curves.

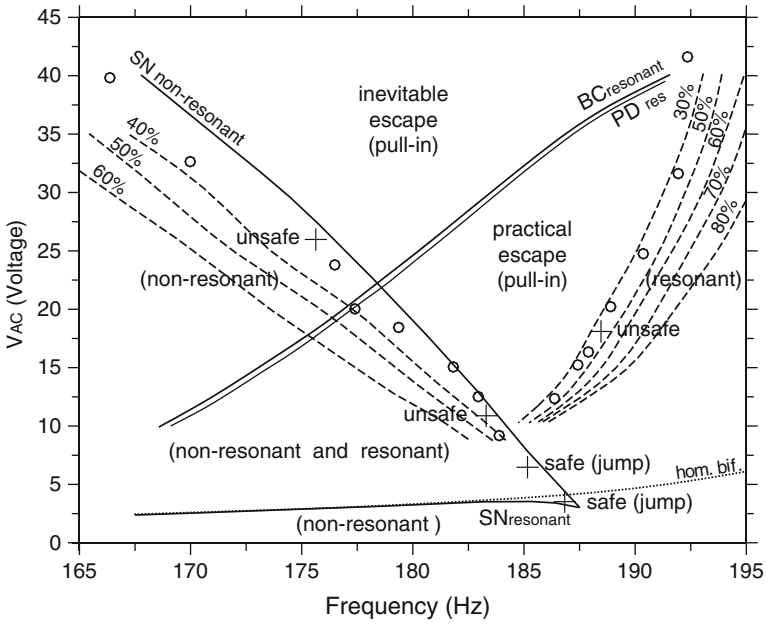

Fig. 5 Frequency-dynamic voltage behavior chart of the capacitive accelerometer with harmonic excitation close to the primary resonance $\Omega_{res} = 192.5$ Hz. The *solid lines* correspond to the main dynamical phenomena in the attractors (curves of appearance/disappearance, first period-doubling); the *dotted line* to the homoclinic bifurcation; the *dashed lines* to the curves of constant percentage of IF; the dots to the experimental data obtained in Alsaleem et al. (2010)

A similar behavior has been highlighted also in (Virgin 2000) for a different case-study. Interpreting the discrepancy between the experimental data and the theoretical inevitable escape requires other numerical simulations and the introduction of dynamical integrity concepts.

For low values of V_{AC} when an attractor disappears by the SN bifurcations, there is safe jump to the other (resonant or non-resonant, respectively) attractor, as can be noticed by the absence of dynamical pull-in in the experimental data.

The homoclinic bifurcation represents the threshold that triggers the erosion. Above it, we build attractor-basins phase portraits to analyze the shrinkage of the basins due to the penetration of fractal tongues of the out-of-well attractor into the safe well. Since the system is of the softening type, the development of the erosion is particularly dangerous because the out-of-well phenomenon is the escape, which leads to the failure of the device.

Two examples of this mechanism are reported in Fig. 6 at fixed dynamic voltages, $V_{AC} = 8$ V and $V_{AC} = 15$ V, and increasing frequency values. The fractal tongues of escape (white) enter the well though the resonant basin (dark gray). The non-resonant one (light gray), instead, is not involved because it is protected by the stable manifolds of its saddle.

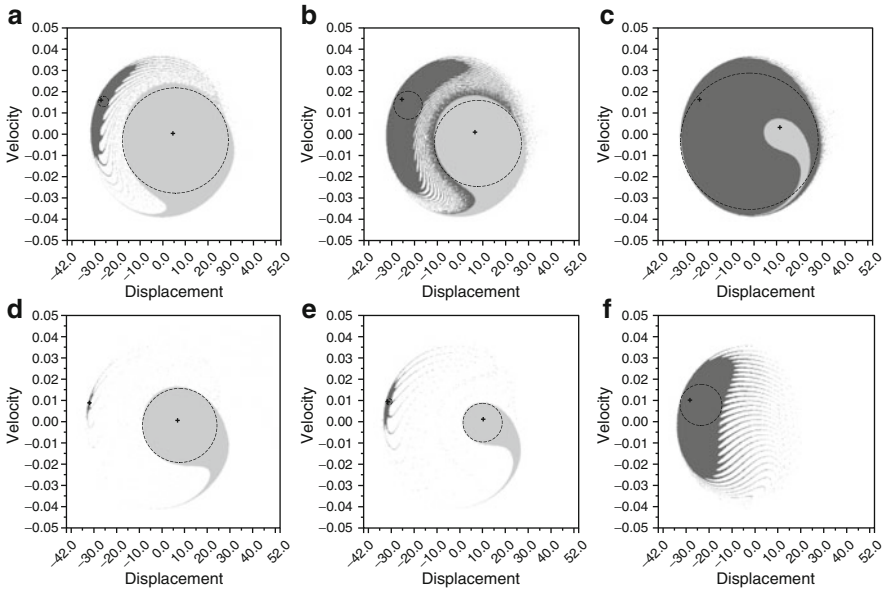

Fig. 6 Attractor-basins phase portraits for $V_{AC} = 8$ V and (**a**) $\Omega = 180$ Hz, (**b**) $\Omega = 183$ Hz, (**c**) $\Omega = 185$ Hz; $V_{AC} = 15$ V and (**d**) $\Omega = 178$ Hz, (**e**) $\Omega = 181$ Hz, (**f**) $\Omega = 187$ Hz. The circles used in the definition of the IF are in *dashed lines*

For lower values of V_{AC} the erosion concerns only a small part of the resonant basin boundary (not reported in pictures). At about $V_{AC} = 8$ V (Fig. 6a–c), instead, the fractal escape area starts developing more rapidly and, remarkably, it enters into the potential well and separates the two basins. For a small range of parameters, a part of the resonant basin continues surrounding the non-resonant one (Fig. 6b), even if with fractal tongues. Then, it quickly vanishes and the separation settles exactly along the boundary between the two basins, preventing any safe jump between the attractors (Figs. 6d–f). Although they coexist, when an attractor is disappearing (Fig. 6d–e), its basin is replaced by the escape area and not by the basin of the other attractor, even if this one exists and it is still robust.

4.2 Curves of Constant Percentage of Integrity Factor

Since disturbances commonly encountered in practice produce uncertainty to the operating initial conditions, the existence and stability (in the classical sense) of an attractor does not mean ‘safety’ from pull-in. Hence a dynamical integrity analysis is required to illustrate whether the attractors are paralleled with a sufficiently robust safe basin.

As we are interested in the vibrations of the device at steady state, following previous studies (Rega and Lenci 2005; Lenci and Rega 2006), we can consider the safe basin as the union of the classical basins of attraction of all the attractors inside the potential well, i.e. the union of the non-resonant and resonant basins. Note that the safe basin is then a property of the well. This is because the unwanted phenomenon is the out-of-well escape and not the in-well jump between the attractors: the escape leads to the failure of the device; the jump, instead, although undesirable in some applications, changes the response of the system without destroying it.

We choose the integrity factor (IF), introduced in (Lenci and Rega 2003), as a measure of the dynamical integrity of the safe basin. It is the normalized radius of the largest circle entirely belonging to the safe basin. It is an appropriate measure for the considered case-study. In fact, the IF is a property of the safe basin and not of the attractor. It succeeds in describing when the system is in safe or unsafe conditions, since it focuses on the compact 'core' of the safe basin, ruling out the fractality that induces unpredictability of motion. Therefore it is a rather conservative measure, more reliable for an engineering application. Finally, we compute IF in the steady dynamics, neglecting the transient. This is suitable for the experimental data we are analyzing because they come from a sweeping process, where at the end of each step the system is in steady state conditions.

Examples of the circles used in the definition of the IF are depicted in Fig. 6a–f in dashed line. Note that, when the escape enters into the potential well separating the basins, the resulting safe basin presents two distinct compact areas: one around the resonant, the other around the non-resonant attractor. Accordingly, in this range the IF of the well coincides with the IF of the most robust attractor.

From the previous considerations, the device remains in safe conditions up to $V_{AC} \cong 8$ V, which is beyond the homoclinic bifurcation threshold triggering the erosion. When the non-resonant basin is next to disappearance, the safe jump between the attractors is ensured by a large compact area including both the basins (Fig. 6c): at about the non-resonant saddle-node bifurcation, the resonant catches the trajectories, tolerating the experimental disturbances coming from the sweeping process. These theoretical predictions are well verified in practice, as can be seen in Fig. 5 by the absence of pull-in data in the experiment.

After this scenario, the increased fractality settles exactly near the saddle-node, separating the safe basin into two compact regions (similar to Fig. 6b, but with the non-resonant basin next to disappear). Nevertheless, in a very small range (not reported in the figures) the area around the non-resonant attractor includes a part of the resonant basin which succeeds in ensuring the safe jump.

Over this safe threshold, each compact region includes only one attractor. In the following, we focus on this range. We draw erosion profiles to investigate the loss of structural safety when the parameters are varying. They are obtained by plotting the IF, i.e. the chosen measure for the dynamical integrity, as a function of the increasing frequency amplitude. Therefore, they describe the changes in the IF, which depend both on the increased fractality in the resonant basin and on the shrinkage next to disappearance in the non-resonant one. An example of erosion profile is shown in

Fig. 4 with dotted line. It is overlapped to the frequency response curve, in order to compare the amplitude of the safe basins to the amplitude of the oscillations. Each radius used in the analysis is normalized with the analogous radius at $\Omega = 80$ Hz and $\Omega = 215$ Hz, respectively for the non-resonant and the resonant compact area. These choices for the normalization frequencies are justified by the fact that, far from resonance, the basins are not affected by the erosion and their amplitude is nearly constant.

We consider the resonant attractor when the frequency is decreasing (right side of Fig. 4). Far from resonance, the erosion of the safe basin is slightly sketched, producing only a slight decrement in the dynamical integrity. After this safe part, the erosion is very quick and it occurs together with the increasing in amplitude of the oscillations; experimental pull-in appears precisely in this range (30–50% of IF). Finally the wide range where the amplitude of oscillations is very high, ending with PD and possibly chaotic motion (difficult to be detected since it occurs in a very small range), is associated with a very small safe basin. From a practical point of view, under realistic conditions, it cannot be caught by the sweeping process. Similarly, the non-resonant attractor has an analogous behavior.

Several erosion profiles have been made for different values of V_{AC} and the curves of constant percentage of IF have been obtained and reported in the behavior chart in Fig. 5. They summarize the overall scenario of the loss of structural integrity in the analyzed device.

The experimental data follow "exactly" these curves. In particular, near primary resonance, safe conditions are ensured when the IF of the compact 'core' is at least above the 40% near the non-resonant attractor, and above the 50% near the resonant attractor. Below this percentage, the device becomes practically vulnerable to dynamical pull-in, since the safe basin is not sufficiently robust to tolerate the disturbances and the discontinuous steps coming from the sweeping process. Therefore, not only the classical area of inevitable escape, but also the practical pull-in area has to be avoided.

It is worth observing that, for the considered experimental conditions, the safe curves for the resonant case are considerably far from the curve of disappearance. The loss of structural safety in the analyzed mechanical system is summarized in Fig. 7 with a schematic behavior chart, where the three main different regions are identified: the safe no-escape area (white); the practical escape area whose wideness depends on the magnitude of disturbances (light grey); the theoretical inevitable escape (dark grey).

We conclude that the curves of constant percentage of IF succeed in interpreting the existence of disturbances existing in the experiments and under realistic conditions; the curves of disappearance, instead, represent the limit case when disturbances are absent.

Finally, the charts in Figs. 5 and 7 are guidelines for the design. Depending on the expected disturbances, they can be used to establish factors of safety in order to operate the system reliably far from the out-of-well escape phenomenon, i.e. from the pull-in bands and from the danger of pull-in.

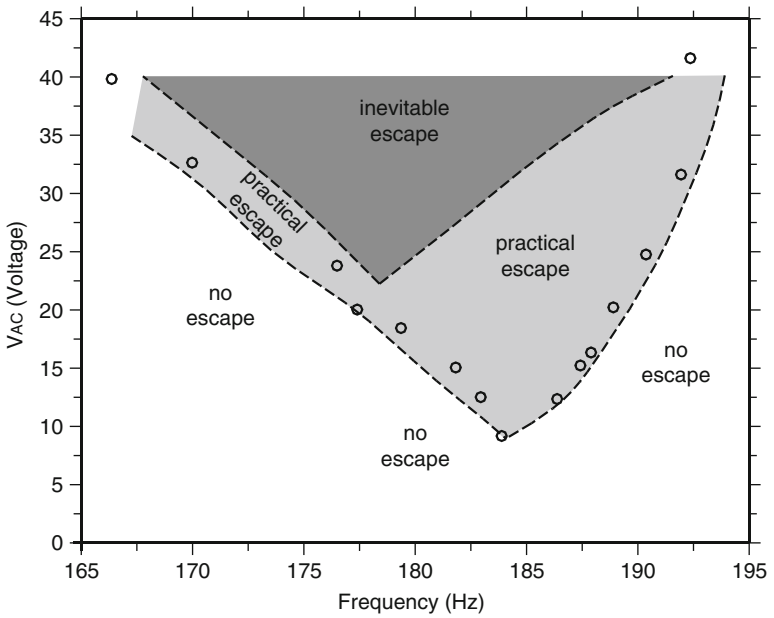

Fig. 7 Schematic behavior chart. The *white region* corresponds to the no-escape area; the *light grey region* to the practical escape; the *dark grey region* to the theoretical inevitable escape

5 Conclusion

Investigating the response of a capacitive accelerometer at primary resonance, the issue of the dynamical integrity in a mechanical system has been addressed. Its qualitative evaluation has been performed, choosing the most suitable tools according to the considered experimental conditions. The effectiveness of this analysis has been highlighted, showing the accuracy of the curves of constant percentage of IF in interpreting the existence of disturbances in experiments and practice. Also, their use in a design has been proposed.

Acknowledgments This work has been developed during Laura Ruzziconi stay at the State University of New York in Binghamton. The kind hospitality is gratefully acknowledged. The authors would like to thank Dr. F.M. Alsaleem for the experimental part and the National Science Foundation NSF for supporting in part this work through grant #0846775.

References

Alsaleem, F.M., Younis, M.I., Ouakad, H.M.: On the nonlinear resonances and dynamic pull-in of electrostatically actuated resonators. J. Micromech. Microeng. **19**, 45013–45026 (2009)

Alsaleem, F.M., Younis, M.I., Ruzziconi, L.: An experimental and theoretical investigation of dynamic pull-in in MEMS resonators actuated electrostatically. J. Microelectromech. Syst. **19**, 794–806 (2010)

Gottlieb, O., Champneys, A.R.: Global bifurcations of nonlinear thermoelastic microbeams subject to electrodynamic actuation. In: Rega, G., Vestroni, F. (eds.) IUTAM Symposium On Chaotic Dynamics and Control of System and Processes in Mechanics Solid Mechanics and Its Applications, vol. 122, pp. 47–57. Springer, Berlin (2005)

Guckenheimer, J., Holmes, P.J.: Nonlinear Oscillations, Dynamical Systems and Bifurcations of Vector Fields. Springer, New York (1983)

Krylov, S., Dick, N.: Dynamic stability of electrostatically actuated initially curved shallow micro beams. Continuum Mech. Therm. (2010). doi:10.1007/s00161-010-0149-6

Lenci, S., Rega, G.: Optimal control of nonregular dynamics in a duffing oscillator. Nonlinear Dyn. **33**, 71–86 (2003)

Lenci, S., Rega, G.: Control of pull-in dynamics in a nonlinear thermoelastic electrically actuated microbeam. J. Micromech. Microeng. **16**, 390–401 (2006)

Nayfeh, A.H., Younis, M.I., Abdel-Rahman, E.M.: Dynamic pull-in phenomenon in MEMS resonators. Nonlinear Dyn. **48**, 153–163 (2007)

Rega, G., Lenci, S.: Identifying, evaluating, and controlling dynamical integrity measures in nonlinear mechanical oscillators. Nonlinear Anal. Theory Methods Appl. **63**, 902–914 (2005)

Senturia, S.D.: Microsystem Design. Kluwer Academic, Dordrecht (2001)

Szemplinska-Stupnicka, W.: Cross-well chaos and escape phenomena in driven oscillators. Nonlinear Dyn. **3**, 225–243 (1992)

Thompson, J.M.T.: Chaotic behaviour triggering the escape from a potential well. Proc. R. Soc. Lond. A **421**, 195–225 (1989)

Virgin, L.N.: Introduction to Experimental Nonlinear Dynamics: A Case Study in Mechanical Vibration. Cambridge University Press, Cambridge (2000)

Suppressing Aeroelastic Instability in a Suspension Bridge Using a Nonlinear Absorber

B. Vaurigaud, L.I. Manevitch, and C.-H. Lamarque

Abstract We study a problem of passive nonlinear targeted energy transfer between a two degrees-of-freedom suspension bridge model and a single degrees-of-freedom nonlinear energy sink (NES). The system is studied under 1:1:1 nonlinear resonance involved in targeted energy transfer mechanisms. Analytical expansions are performed by mean of complexification methods, multiple scales expansions and exploits also the concept of limiting phase trajectories (LPTs). Several control mechanisms for aeroelastic instability are identified, and analytical calculations bring to efficient parameters for the absorber design. Numerical simulations are performed and good agreement with analytical predictions is observed. It results that the concept of Limiting Phase Trajectories (LPT) allows formulating adequately the problem of intensive energy transfer from a bridge to a nonlinear energy sink.

Keywords Aeroelastic instability • Nonlinear targeted energy transfer • Limiting phase trajectories

1 Introduction

Suspension bridges under wind of constant velocity are subjected to oscillating vertical external force due to vortex shedding by the separation of the wind along the deck of the bridge. In the case of suspension bridges with thin decks aeroelastic

B. Vaurigaud • C.-H. Lamarque (✉)
Université de Lyon, École Nationale des Travaux Publics de l'État, DGCB,
FRE CNRS 3237, Rue Maurice Audin, 69120, Vaulx-en-Velin Cedex, France
e-mail: bastien.vaurigaud@developpement-durable.gouv.fr; Lamarque@entpe.fr

L.I. Manevitch
N.N. Semenov Institute of Chemical Physics, Russian Academy of Sciences,
4, Kosygina street, 119991 Moscow, Russia
e-mail: lmanev@chph.ras.ru

M. Wiercigroch and G. Rega (eds.), *IUTAM Symposium on Nonlinear Dynamics for Advanced Technologies and Engineering Design*, IUTAM Bookseries (closed) 32, DOI 10.1007/978-94-007-5742-4_21,

instability can appear above a critical wind velocity and dangerously damage the structure. The use of control devices, by means of passive nonlinear absorbers and targeted energy transfer, to prevent from these instabilities, could be a powerful solution. These range of absorber have been studied theoretically/numerically by Gendelman and Manevitch (2001) and Vakakis and Gendelman (2001) and experimentally to control linear modes of a building reduce model by Gourdon et al. (2007) and Gourdon and Lamarque (2007, 2005). Their application have been also studied by Lee et al. to suppress linear instability of system: the instability suppression in the Van Der Pol oscillator (Lee et al. 2005), and in an aircraft wing (Lee et al. 2006, 2007) have been considered. This study focuses on the aeroelastic instability of a suspension bridge and investigates the efficiency of a single degree of freedom passive nonlinear absorber introduced in the bridge deck. We study the suppression mechanisms of the bridge aeroelastic instability by mean of this nonlinear absorber. This study introduces an original analytical approach based on the concept of Limiting Phase Trajectories (LPT) to predict the asymptotic behavior of the controlled system. The Limiting Phase Trajectories have been introduced by Manevitch et al., that showed in Manevitch (2007), Manevitch et al. (2007), Manevitch and Musienko (2009), Manevitch and Musienko (2008), Manevitch et al. (2009), Manevitch and Manevitch (2009a,b) and Manevitch (2009) that the energy exchange in systems of weakly coupled oscillators or oscillatory chains can be efficiently described introducing the concept of Limiting Phase Trajectories (LPT). Contrary to normal modes (NM), LPT corresponds to complete energy exchange between weakly coupled elements of the system. In appropriates coordinates LPT can be simply described in terms of non-smooth basic functions introduced in Pilipchuk (1985), Vakakis et al. (1996) and Manevitch et al. (1989) for solution of problems close to vibro-impact ones. It turns out, however, that the most adequate area for using these techniques is the problem of intensive energy transfer in linear and nonlinear oscillatory chains. The analytical approach of the aeroelastic instability problem throughout the LPTs concept gives a better understanding of energy pumping triggering mechanisms and how the system variables such as initial conditions or absorber nonlinearity interact during the control.

In Sect. 2 we introduce a two degrees of freedom model of a suspension bridge coupled with a purely cubic nonlinear absorber. In Sect. 3 this three degrees of freedom system is reduced to a single nonlinear oscillator. The more relevant resonance case is considered and the concept of LPT is used to predict analytically the asymptotic behavior of the whole system in Sect. 4. Finally Sect. 5 exhibits numerical simulations with good agreement with the analytical prediction, and show that the absorber is able to control the aeroelastic instability of the bridge.

2 Dynamics of the System

We investigate the response of a two DOF suspension bridge model from Blevins (1977). This model takes into account the coupling between aerodynamical actions

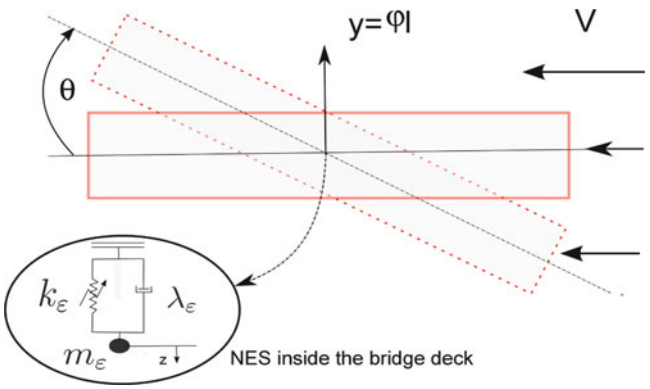

Fig. 1 Two DOF bridge deck coupled with a SDOF NES on the elastic axis

on the structure and its elastic response. Considering only the torsional and flexional natural modes the equations of motion representing the wind induced aeroelastic instability can be written as follows:

$$\begin{aligned} \ddot{\varphi} + \frac{m_0}{m}\omega_0\dot{\varphi} + \omega_1^2\varphi - \frac{m_0}{m}\omega_0^2\theta = 0 \\ \ddot{\theta} + \frac{m_1 l^2}{2mr^2}\omega_0\dot{\theta} + \left(\omega_2^2 - \frac{m_0 l^2}{2mr^2}\omega_0^2\right)\theta + \frac{m_0 l^2}{2mr^2}\omega_0\dot{\varphi} = 0 \end{aligned} \tag{1}$$

with the following variables:

k_ε : NES nonlinear stiffness
K : flexional rigidity
$2l$: width of the bridge deck
L : length of the bridge deck
m : mass per unit of length of the bridge
m_ε : NES mass
$m_0 \approx 4.5\rho l^2$
$m_1 \approx 6.3\rho l^2$
mr^2 : moment of inertia along longitudinal axis

λ_ε : NES damping
θ : torsional displacement
ρ : mass per unit of volume of air
φ : bending displacement
$\omega_1^2 = \mathrm{K/m}$
$\omega_0 = \mathrm{V/l}$
$\omega_2^2 = \mathrm{Kl^2/mr^2}$
V: wind velocity

These equations illustrate the aeroelastic instability of the bridge, this linear system exhibits linear instability for a critical value of wind velocity V.

We consider in this paper the solution of adding a SDOF NES, coupled along the bending direction on the elastic axis. This coupling is represented in Fig. 1.

The NES characteristics are in the previous nomenclature. Taking into account this nonlinear coupling equation (1) can be rewritten as a three DOF system:

$$\ddot{\varphi} + \frac{m_0}{m}\omega_0\dot{\varphi} + \omega_1^2\varphi - \frac{m_0}{m}\omega_0^2\theta + \frac{\lambda_\varepsilon}{m}(\dot{\varphi} - \dot{z}) + \frac{k_\varepsilon}{m}(\varphi - z)^3 = 0$$

$$\ddot{\theta} + \frac{m_1 l^2}{2mr^2}\omega_0\dot{\theta} + \left(\omega_2^2 - \frac{m_0 l^2}{2mr^2}\omega_0^2\right)\theta + \frac{m_0 l^2}{2mr^2}\omega_0\dot{\varphi} = 0$$

$$m_\varepsilon\ddot{z} + \lambda_\varepsilon(\dot{z} - \dot{\varphi}) + k_\varepsilon(z - \varphi)^3 = 0 \tag{2}$$

The terms involving $\omega_0\dot{\varphi}$ and $\omega_0\dot{\theta}$ cannot be ignored, as they are produced by wind loading ω_0. For simplicity, these terms are assumed small compared to all other terms of order 1. Considering the smallness of parameters it is reasonable to rewrite (2) as:

$$\ddot{\varphi} + \varepsilon^2\gamma_1\dot{\varphi} + \Omega_1^2\varphi - \varepsilon k\theta - \varepsilon^2\lambda\dot{\Psi} - \varepsilon^2 K\Psi^3 = 0$$

$$\ddot{\theta} + \varepsilon^2\gamma_2\dot{\theta} + \Omega_2^2\theta + \varepsilon^2\gamma_3\dot{\varphi} = 0$$

$$\ddot{\varphi} + \ddot{\Psi} + \lambda\dot{\Psi} + K\Psi^3 = 0 \tag{3}$$

where $\Psi = z - \varphi$ is the internal displacement between the NES and the bridge deck.

$$\Omega_1^2 = \omega_1^2, \qquad \varepsilon^2\gamma_2 = \frac{m_1 l^2}{2mr^2}\omega_0, \qquad \varepsilon k_2 = \frac{m_0 l^2}{2mr^2}\omega_0^2, \qquad \varepsilon k = \frac{m_0}{m}\omega_0^2,$$

$$\Omega_2^2 = \omega_2^2 - \varepsilon k_2, \qquad \varepsilon^2\gamma_1 = \frac{m_0}{m}\omega_0, \qquad \frac{m_\varepsilon}{m} = \varepsilon^2, \qquad \varepsilon^2\gamma_3 = \frac{m_0 l^2}{2mr^2}\omega_0,$$

$$\frac{\lambda_\varepsilon}{m} = \varepsilon^2\lambda, \qquad \frac{k_\varepsilon}{m} = \varepsilon^2 K.$$

3 Reduction of the System to a Single Oscillator and Resonance Oscillations

In this Section we study the system under 1:1 resonance using complexification, multiple scales methods and limit phase trajectory approach (Manevitch and Musienko 2009; Manevitch et al.). First we will reduce the three DOF system to a single oscillator considering the bridge behavior as an external forcing applied to the NES.

We solve the bridge equations without damping terms to reduce the bridge motion to an external forcing. We have to solve the following system:

$$\ddot{\varphi} + \Omega_1^2\varphi - \varepsilon k\theta = \varepsilon^2 K\Psi^3,$$

$$\ddot{\theta} + \Omega_2^2\theta = 0, \tag{4}$$

with initial conditions:

$$\varphi(0) = \varepsilon q_{10}, \quad \dot{\varphi}(0) = \varepsilon \Omega_1 v_{10}, \theta(0) = q_{20},$$
$$\dot{\theta}(0) = \Omega_2 v_{20}, z(0) = 0, \qquad \dot{z}(0) = 0.$$

Solution $\theta(t)$,$\varphi(t)$ is:

$$\begin{aligned} \theta(t) &= Y_2 \sin(\Omega_2 t + \phi_2) \\ \varphi(t) &= \varepsilon \Phi_1 \sin(\Omega_1 t + \phi_1) + \varepsilon k \Phi_2 \sin(\Omega_2 t + \phi_2) + \varepsilon^2 K_1 I(t) \end{aligned} \tag{5}$$

with the following parameters:

$$\Phi_2 = \frac{Y_2}{\Omega_1^2 - \Omega_2^2}, \qquad Y_2 = (q_{20}^2 + v_{20}^2)^{1/2}, \qquad \tan\phi_2 = \frac{v_{20}}{q_{20}},$$

$$\Phi_1 = (Z_1^2 + Z_2^2)^{1/2}, \qquad \tan\phi_1 = \frac{Z_2}{Z_1},$$

$$Z_1 = q_{10} - k\frac{q_{20}}{\Omega_1^2 - \Omega_2^2}, \qquad Z_2 = v_{10} - k\frac{v_{20}}{\Omega_1^2 - \Omega_2^2},$$

$$\text{for } i = 1, 2 \; Q_i = \Omega_i^2 \Phi_i, \qquad K_1 = \frac{K}{\Omega_1},$$

$$I(t) = \int_0^t \sin(\Omega_1(t-s))\Psi^3(s)\,\mathrm{d}s.$$

Finally we obtain the external forcing applied on the NES:

$$\ddot{\varphi}(t) = -\varepsilon Q_1 \sin(\Omega_1 t + \phi_1) - \varepsilon k Q_2 \sin(\Omega_2 t + \phi_2) + \varepsilon^2 K \Psi^3(t) - \varepsilon^2 K \Omega_1 I(t)$$

According to Eq. (3) we have:

$$\begin{aligned} &\ddot{\Psi} + \lambda\dot{\Psi} + K\Psi^3 = -\ddot{\varphi} \\ &\text{with} \quad -\ddot{\varphi} = \varepsilon F(t) - \varepsilon K_1 I(t) \\ &\text{and} \quad F(t) = Q_1 \sin(\Omega_1 t + \phi_1) + k Q_2 \sin(\Omega_2 t + \phi_2), \qquad K_\varepsilon = \varepsilon K \Omega_1 \end{aligned} \tag{6}$$

We investigate the 1:1 resonance of the system. For this reason we introduce parameter ω corresponding to the resonant pulsation of the system under 1:1 resonance assumption. We will determine later the vicinity of this parameter according to the bridge modal parameters. As a result Eq. (6) can be rewritten as follows:

$$\ddot{\Psi} + \omega^2\Psi + \varepsilon\mu[\lambda\dot{\Psi} + K\Psi^3 - \omega^2\Psi] = \varepsilon F(t) - \varepsilon K_\varepsilon I(t) \tag{7}$$

with $\mu = \dfrac{1}{\varepsilon}$. For parameter μ to be considered as independent from variable ε the sum in the square brackets must be small compared to the other terms of order 1. This means that we have to verify the following relation:

$$[\lambda\dot{\Psi} + K\Psi^3 - \omega^2\Psi] = o(1) \tag{8}$$

In Eq. (7) the term in Ψ^3 appears at first of higher order but we must consider that the integral term $I(t)$, under some special resonant cases can be of order ε^{-1} and must be taken into account for the asymptotic analysis. We will expand Eq. (6) using complexification and multiple scale expansions with ω near Ω_1 and ω near Ω_2 considering primary resonance only.

In order to describe the system evolution we introduce a complex valued transformation, with variables Φ and Φ^*, such that:

$$\begin{aligned} \Phi &= \dot{\Psi} + i\omega\Psi, & \Phi^* &= \dot{\Psi} - i\omega\Psi, \\ \dot{\Psi} &= \frac{\Phi + \Phi^*}{2}, & \Psi &= \frac{\Phi - \Phi^*}{2i\omega}. \end{aligned} \tag{9}$$

where $i = \sqrt{-1}$ and the asterisk denotes complex conjugate. Introducing these new variables in (6) we obtain:

$$\dot{\Phi} - i\omega\Phi + \varepsilon\frac{\mu\lambda}{2}(\Phi - \Phi^*) - \varepsilon\frac{3i\mu K}{8\omega}(\Phi - \Phi^*)^3 + \varepsilon\mu\frac{i\omega}{2}(\Phi - \Phi^*) = \varepsilon F(t) - \varepsilon K_\varepsilon I(t) \tag{10}$$

Then we apply a multiple scale method to construct an approximate solution of (10) as an ε expansion:

$$\begin{aligned} \Phi(t,\varepsilon) &= \Phi_{10}(T_0, T_1) + \varepsilon\Phi_{11}(T_0, T_1) + \ldots \\ \frac{d}{dt} &= \frac{\partial}{\partial T_0} + \varepsilon\frac{\partial}{\partial T_1} + \varepsilon^2\frac{\partial}{\partial T_2} + .. \end{aligned} \tag{11}$$

with $T_j = \varepsilon^j t,\ j = 0, 1, 2, \ldots$. We can substitute expression (11) in (10). Equating the different power of ε we obtain:

$$\varepsilon^0 : \frac{\partial\Phi_{10}}{\partial T_0} - i\omega\Phi_{10} = 0 \Rightarrow \Phi_{10}(T_0, T_1) = \varphi_{10}(T_1)e^{i\omega T_0} \tag{12}$$

$$\begin{aligned} \varepsilon^1 : &\frac{\partial\Phi_{10}}{\partial T_1} + \frac{\partial\Phi_{11}}{\partial T_0} - i\omega\Phi_{11} + \frac{\mu\lambda}{2}(\Phi_{10} - \Phi_{10}^*) \\ &- \frac{3i\mu K}{8\omega^3}(\Phi_{10} - \Phi_{10}^*)^3 + \frac{i\mu\omega}{2}(\Phi_{10} - \Phi_{10}^*) = F(t) - K_\varepsilon I(t) \end{aligned} \tag{13}$$

Suppressing secular terms from (13) we obtain:

$$\frac{\partial \varphi_{10}}{\partial T_1} + \frac{\mu\lambda}{2}\varphi_{10} - \frac{3i\mu K}{8\omega^3}\varphi_{10}^2\varphi_{10}^* + \frac{i\omega\mu}{2}\varphi_{10} = \frac{Q_1}{2i}(e^{i(\Omega_1-\omega)T_0+i\phi_1} - e^{-i(\Omega_1+\omega)T_0+i\phi_1}) + k\frac{Q_2}{2i}(e^{i(\Omega_2-\omega)T_0+i\phi_2} - e^{-i(\Omega_2+\omega)T_0+i\phi_2}) - C_\varepsilon(t) \tag{14}$$

$$C_\varepsilon(T_0) = \varepsilon K \frac{i}{8\omega^3} e^{-i\omega T_0} \int_0^{T_0} \sin(\Omega_1(T_0-s))(\varphi_{10}(s)e^{i\omega s} - \varphi_{10}^*(s)e^{-i\omega s})^3 \, \mathrm{d}s \tag{15}$$

In order to calculate C_ε it is convenient to introduce function:

$$G(\omega, \Omega_1) = \varepsilon K \frac{1}{16\omega^3} e^{-i\omega T_0} \int_0^{T_0} e^{i\Omega_1 T_0} e^{i(\omega-\Omega_1)s} \mathrm{d}s \tag{16}$$

The integral C_ε can be expressed in function of G:

$$\begin{aligned} C_\varepsilon(T_0) = {} & \varphi_{10}G(3\omega, \Omega_1) - \varphi_{10}G(3\omega, -\Omega_1) + \varphi_{10}^*G(-3\omega, \Omega_1) - \varphi_{10}^*G(-3\omega, -\Omega_1) \\ & + 3|\varphi_{10}|^2\varphi_{10}G(\omega, \Omega_1) - 3|\varphi_{10}|^2\varphi_{10}G(\omega, -\Omega_1) \\ & + 3|\varphi_{10}|^2\varphi_{10}^*G(-\omega, \Omega_1) - 3|\varphi_{10}|^2\varphi_{10}^*G(-\omega, -\Omega_1) \end{aligned} \tag{17}$$

These equations should be studied in the vicinity of different system pulsation ω. For the sake of simplicity and considering numerical evidence of Sect. 4 we will focus on the resonant case $\omega \approx \Omega_2$, which involves that Ω_1 does not generate resonant terms.

3.1 Case $\omega \approx \Omega_2$, Ω_1 Does Not Generate Resonance Terms

Let us consider $\omega \approx \Omega_2$, in this particular case Ω_1 does not generate resonance terms which involves that $C_\varepsilon(T_0)$ is not a resonance term. Secular terms give:

$$\frac{\partial \varphi_{11}}{\partial T_0} + \frac{\partial \varphi_{10}}{\partial T_1} + \frac{\mu\lambda}{2}\varphi_{10} - \frac{3i\mu K}{8\omega^3}\varphi_{10}^2\varphi_{10}^* + \frac{i\omega\mu}{2}\varphi_{10} = \tilde{f}(T_0)$$

$$\tilde{f}(T_0) = k\frac{Q_2}{2i}(e^{i(\Omega_2-\omega)T_0+i\phi_2} - e^{-i(\Omega_2+\omega)T_0+i\phi_2}) + \text{non-secular terms} \tag{18}$$

Considering $\Omega_2 = \omega - \varepsilon\sigma_2$ secular terms permit to write $\tilde{f}(T_0)$ as:

$$\tilde{f}(T_0) = -kQ_2\frac{i}{2}e^{-i(\sigma_2 T_1 - \phi 2)} + \text{non-secular terms} = \tilde{f}_2(T_0) + \text{non-secular terms} \tag{19}$$

We finally get the reduction to a single oscillator for $\Omega_2 = \omega - \varepsilon\sigma_2$:

$$\frac{\partial\varphi_{10}}{\partial T_1} + \frac{\mu\lambda}{2}\varphi_{10} - \frac{3i\mu K}{8\omega^3}\varphi_{10}^2\varphi_{10}^* + \frac{i\omega\mu}{2}\varphi_{10} = -kQ_2\frac{i}{2}e^{-i(\sigma_2 T_1 - \phi 2)} \tag{20}$$

3.2 Single Oscillator Differential System

We consider the ε-order equations of Sect. 3.1 and introduce the polar representation of complex variable $\varphi_{10} = ae^{i\gamma}$ into Eq. (20) and separate real and imaginary parts to get an amplitude-phase differential system. We obtain the following differential system for variables a and Δ:

$$\begin{cases} \dfrac{\partial a}{\partial T_1} &= \dfrac{-\mu\lambda}{2}a - F\sin\Delta \\ a\dfrac{\partial\gamma}{\partial T_1} &= \dfrac{-\mu\omega}{2}a + \dfrac{3\mu K}{8\omega^3}a^3 - F\cos\Delta \end{cases} \tag{21}$$

$$\Delta = \gamma + \sigma_2 T_1 - \phi_2 \qquad\qquad F = \frac{1}{2}kQ_2$$

$$\begin{cases} \dfrac{\partial a}{\partial T_1} = \dfrac{-\mu\lambda}{2}a - F\sin\Delta \\ a\dfrac{\partial\Delta}{\partial T_1} = \mu a(-s + \alpha a^2) - F\cos\Delta \end{cases} \tag{22}$$

$$\alpha = \frac{3K}{8\omega^3} \qquad\qquad s = \frac{\omega}{2} - \frac{\sigma_2}{\mu}$$

In the next section differential system (22) is studied. The fixed points of the system are first investigated and then the Hamiltonian of the undamped (22) system, corresponding to $\lambda = 0$ is considered.

4 Analytical Study of the Nonlinear SDOF Oscillator

In this part we will consider the differential system (22) in the damped ($\lambda \neq 0$) and undamped case ($\lambda = 0$). This analysis is mainly based on the analysis of Manevitch and Manevitch (2009b).

4.1 Fixed Points

Stationary points of the phase portraits correspond to periodic vibrations and can be found from conditions:

$$F^2 = \mu^2 a^2 \left(\frac{\lambda^2}{4} + (\alpha a^2 - s)^2 \right) \tag{23}$$

This equation is a cubic equation in the variable $X = a^2$, and (25) can be rewritten as:

$$X^3 - \frac{2s}{\alpha} X^2 + \frac{\lambda^2 + 4s^2}{4\alpha^2} X - \frac{F^2}{\mu^2 \alpha^2} = 0 \tag{24}$$

Equation (24) gives the fixed points of system (22), taking the bridge damping into account. To understand the general behavior of the system it is easier to get rid of damping. Let us consider system (22) without damping, which means for $\lambda = 0$.

Equating the system to zero we obtain:

$$\begin{cases} \sin \Delta = 0 \\ \mu a(\alpha a^2 - s) = F \cos \Delta \end{cases} \tag{25}$$

Let us consider a range $-\pi \leq \Delta \leq \pi$, then $\Delta = \pm\pi \ [2\pi]$ and amplitudes a for stationary vibrations satisfy the equation:

$$\mu a(\alpha a^2 - s) = \pm F \tag{26}$$

where $+F$ and $-F$ correspond to $\Delta = 0$ and $\Delta = \pi$ respectively. Discriminant of Eq. (26) is R:

$$R = \frac{1}{\alpha^2} \left[\frac{F^2}{\mu^2} - \frac{4}{27} \frac{s^3}{\alpha} \right] \tag{27}$$

If $R < 0$ system (22) has three real roots: a nonsensical negative one and two positive roots corresponding to saddle point and quasilinear center of the system.

If $R > 0$ system (22) has one single real root that corresponds to the nonlinear resonance center.

4.2 Analytical Study of the LPT

Equation (22), for the undamped oscillator, has the following Hamiltonian:

$$H = \mu \left(\frac{\alpha a^4}{4} - \frac{s a^2}{2} \right) - a F \cos \Delta \tag{28}$$

Let us consider Eq. (22) for the LPT ($H = 0$), $\Delta = 0$ or $\Delta = \pi$.

$$\frac{\mu\alpha}{2}a^3 - \mu s a \pm 2F = 0 \qquad a = 0 \tag{29}$$

This is a cubic equation of discriminant Q:

$$Q = \frac{16}{\alpha^2}\left(\frac{F^2}{\mu^2} - \frac{2s^3}{27\alpha}\right) \tag{30}$$

We will observe qualitative transformation of the phase plane for:

$$\alpha = \alpha_c = \frac{2\mu^2 s^3}{27F^2} \tag{31}$$

While $\alpha < \alpha_c$ the LPT encircles the non-resonance quasilinear center at $\Delta = -\pi$.

If $\alpha > \alpha_c$ the LPT does not encircle the quasilinear center, but the LPT encircles the resonance center at $\Delta = 0$.

If $\alpha > 2\alpha_c$ then quasilinear center and saddle point coincide and 'annihilate'. That can be explained studying the discriminant R of Eq. (26).

There are no other important transformations of the phase plane, for $\alpha > 2\alpha_c$ we get one single stationary point that decreases with the rise of parameter α.

5 Numerical Simulations in the Case $\omega \approx \Omega_2$

For the numerical simulations we fix the bridge parameters as :

$$\begin{array}{lll} V = 27.5\,\mathrm{m.s^{-1}} & \dfrac{m_0}{m} = \dfrac{m_1}{m} = \dfrac{1}{50} & \omega_1^2 \approx 0.72 \\ l = 6\,\mathrm{m} & \sigma = 0.5 & \omega_2^2 \approx 2\omega_1^2 \\ \dfrac{l^2}{2r^2} = 1 & \varepsilon^2 = 0.1 & \lambda = 0.1 \end{array} \tag{32}$$

And initial conditions to:

$$\begin{array}{llll} \varphi(0) = 0 & \dot{\varphi}(0) = 0.3 & \theta(0) = 0 & \\ \dot{\theta}(0) = 0.3 & z(0) = 0 & \dot{z}(0) = 0 & \end{array} \tag{33}$$

Under these initial conditions and choosing nonlinear parameter $K = 2.5\,\mathrm{N.m^{-3}}$ we observe that the NES is able to control the bridge instability. Figure 2 shows that both variables θ and φ are controlled. The dashed line represents the linear

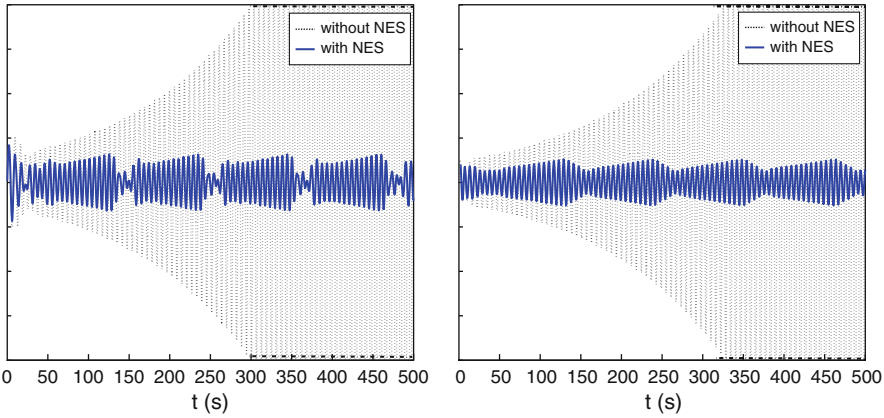

Fig. 2 Displacements of bridge variables φ and θ with and without nonlinear coupling with $K = 2.5\,\text{N.m}^{-3}$ and initial conditions (33) (— with coupling, ... without coupling)

unstable system whereas the solid line represents the system under the NES control (to display correctly the control the plot has been cut, and only the part $|\varphi(t)| < 2$ and $|\theta(t)| < 2$ is presented).

We now observe the different types of behavior that can occur for different values of K.

We choose to work under the assumption of a $\omega \approx \Omega_2$ resonance. This assumption is numerically verified as shown in Fig. 3a, the main harmonic of the signal correspond to frequency Ω_2, nevertheless the other resonance approximations give only small shift in the results, mainly because frequencies Ω_2 and Ω_1 are very close to each other.

We focus on parameter K to study the influence of the NES design, and specially the NES nonlinear stiffness, on the quality of the control. Investigating numerically the behavior of the bridge we can determinate three very different kind of behavior depending on the nonlinearity of the NES. These curves presented Fig. 3 show the displacements in time of variables φ and z. We can separate three very different types of behavior. Nevertheless they are linked together by the nonlinear beating that characterizes the nonlinear control that asymptotically occurs. When the stiffness is too low system displacements grow up until a critical value for the nonlinear beating and the control to start (see Fig. 3b), this is the first case: a long time before nonlinear control starts, and a control that occurs at very high displacements. On the contrary when the stiffness is too strong system displacements decrease until a critical value for the nonlinear control to start (see Fig. 3d), the bigger the stiffness is, the longer is the decrease. The control resulting from this case is very efficient (the displacement reduction is huge), but takes a long time to start.

If we choose a good balance between the two previous cases the nonlinear beating starts quickly enough, and reduces significantly the system vibrations (see Fig. 3c). These different cases underline a range of efficiency for the NES system.

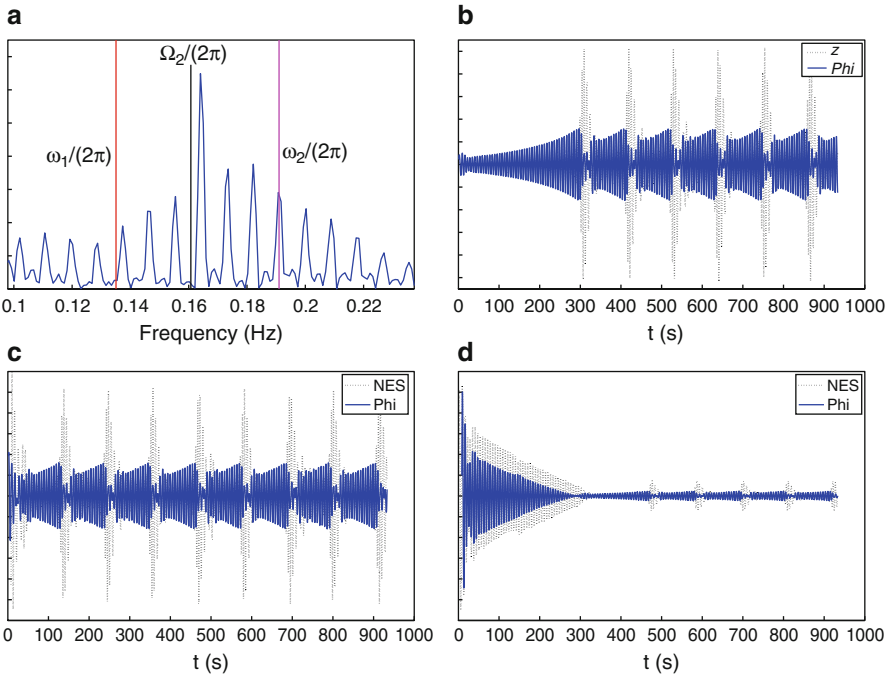

Fig. 3 (**a**) $K = 2.5\,\mathrm{N.m^{-3}}$ Frequency analysis of variable Ψ; (**b**) $K = 0.01\,\mathrm{N.m^{-3}}$, (**c**) $K = 2.5\,\mathrm{N.m^{-3}}$, (**d**) $K = 500\,\mathrm{N.m^{-3}}$ Displacements of variables φ and z for different value of K,φ in *solid line* and z in *dotted line*

5.1 Behavior of the Hamiltonian

Let us consider the case of initial conditions (33) and $K = 2.5\,\mathrm{N.m^{-3}}$, under the assumption of an $\omega \approx \Omega_2$ resonance. We perform numerical simulation on the general system (2) and on the reduce system (22), checking that assumption (8) is numerically confirmed.

In Fig. 4a the numerical integration of variable $a(t)$ from general system (2) is presented. This Figure shows a good agreement with Fig. 4b which represents the Hamiltonian of the associated single oscillator of system (22) with the numerical integration of variable a from this system. The LPT is highlighted with a large black line. It results that the concept of LPT allows predicting the asymptotic behavior of the controlled system. These numerical integrations show good agreement with the prediction made using the single oscillator approximation and its Hamiltonian.

It is also interesting to study the evolution of the Hamiltonian with the nonlinearity parameter α. According to Eq. (31) we obtain $\alpha_c \approx 0.147\,\mathrm{N.m^{-3}}$. The evolution of the Hamiltonian (28) around the critical value α_c is plotted in Fig. 5a–d.

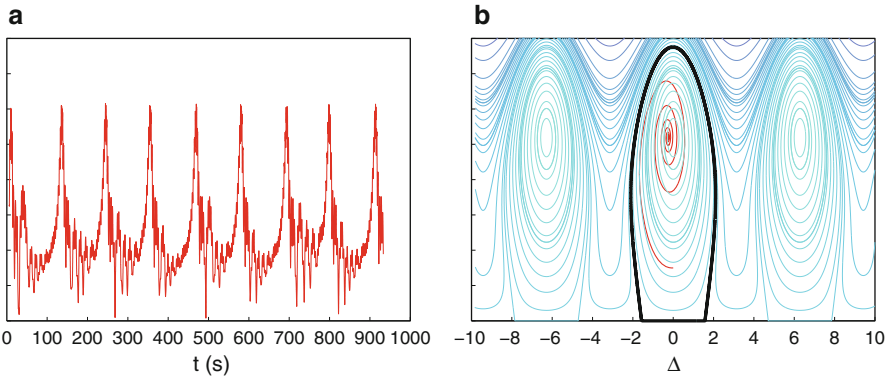

Fig. 4 $K = 2.5\,\mathrm{N.m}^{-3}$, (**a**) Numerical integration of variable a from (2), (**b**) Hamiltonian of Eq. (22) with LPT in *large line*

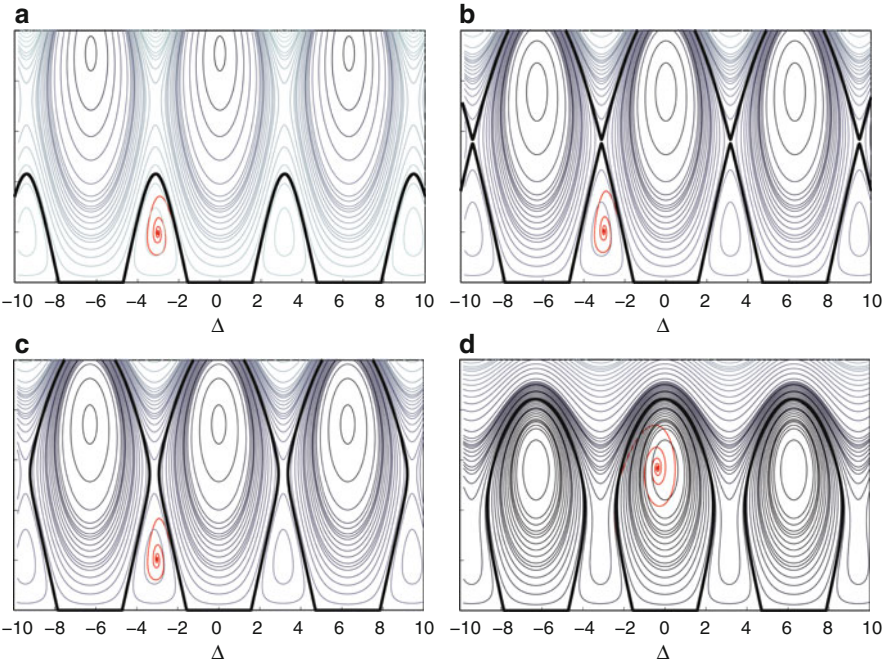

Fig. 5 Evolution of the Hamiltonian with the stiffness of the NES, the LPT is underlined in *large line*. (**a**) $\alpha < \alpha_c$, (**b**) $\alpha \approx \alpha_c$, (**c**) $\alpha > \alpha_c$, (**d**) $\alpha > 2\alpha_c$

The numerical simulations of Fig. 5a–d are in good agreement with the analytical predictions of Sect. 4.2. These figures correspond to the different cases $\alpha < \alpha_c$, $\alpha \approx \alpha_c$, and $\alpha > \alpha_c$. They are similar to the results obtained in Manevitch et al.,Manevitch and Musienko (2009), and Manevitch and Musienko (2008).

6 Conclusion

This study demonstrates that a NES (Nonlinear Energy Sink) can control the aeroelastic instability of a structure using targeted energy transfer. The example chosen was a two degree of freedom bridge under a constant wind excitation. Numerical and analytical calculations underline two different behaviors for the system, around a critical constant depending on the nonlinear stiffness and system initial conditions. The energy exchange in the system gives a good understanding of these behaviors.

The analytical approach gives approximate solutions under the assumption of 1:1:1 resonance using the concept of LPT (Limiting Phase Trajectories). The procedure applied in our study permits to reduce the Bridge/NES three degrees of freedom model to a single forced oscillator, and then allows us to construct the limiting phase trajectories and approximate the steady state of the resulting system. We have shown that LPT-concept provides efficient solution to the aeroelastic instability control problem. This method shows good agreement with numerical integration and gives elements to understand how the nonlinear stiffness and the initial conditions govern the system.

Acknowledgements This work has been supported by French National Research Agency under the contract ANR-07-BLAN-0193.

References

Blevins, R.: Flow-Induced Vibration. Van Nostrand Reinhold Co., New York (1977), 377p

Gendelman, O., Manevitch, L.: Energy pumping in nonlinear mechanical oscillators: part 1 dynamics of the underlying hamiltonian systems. J. Appl. Mech. **68**, 42–48 (2001)

Gourdon, E., Lamarque, C.-H.: Energy pumping for a larger span of energy. J. Sound Vib. **285**, 711–720 (2005)

Gourdon, E., Lamarque, C.-H.: Contribution to efficiency of irreversible passive energy pumping with a strong nonlinear attachment. Nonlinear Dyn. **50**, 793–808 (2007)

Gourdon, E., Alexander, N.A., Taylor, C.A., Lamarque, C.-H., Pernot, S.: Nonlinear energy pumping under transient forcing with strongly nonlinear coupling: theoretical and experimental results. J. Sound Vib. **300**, 522–551 (2007)

Lee, Y., Vakakis, A., Bergman, L., McFarland, D.: Suppression of limit cycle oscillation in the van der pol oscillator by means of passive nonlinear energy sinks (nes). Struct. Control Health Monit. **21**, 485–529 (2005)

Lee, Y., Vakakis, A., Bergman, L., McFarland, D., Kerschen, G.: Triggering mechanisms of limit cycle oscillations in a two-degree-of-freedom wing flutter model. J. Fluids Struct. **13**, 41–75 (2006)

Lee, Y., Vakakis, A., Bergman, L., McFarland, D., Kerschen, G.: Suppressing aeroelastic instability using broadband passive targeted energy transfers, part 1: theory. Am. Inst. Aeronaut. Astronaut. J. **45**, 693–711 (2007)

Manevitch, L.: New approach to beating phenomenon in coupled nonlinear oscillatory chains. Arch. Appl. Mech. **77**(5), 301–312 (2007)

Manevitch, L.: Limiting phase trajectories (lpt) and resonances in a strongly asymmetric 2dof system. In: Proceedings of 10th Conference on Dynamical Systems – Theory and Applications, December 7–10, 2009, Lodz, Poland (in print) (2009)

Manevitch, E., Manevitch, L.: Limiting phase trajectories and secondary resonances in the nonlinear periodically oscillator. In: Proceeding of XXXVII Summer School "Advanced Problems in Mechanics (APM 2009)", Repino, Saint-Petersburg, Russia (2009a).

Manevitch, E., Manevitch, L.: Limiting phase trajectories (lpt) in 1 dof asymmetric system with damping and 1:1 resonance. In: Proceedings of 10th Conference on Dynamical Systems – Theory and Applications, December 7–10, 2009, Lodz, Poland (in print) (2009b)

Manevitch, L., Musienko, A.: Transient forced vibrations of duffing oscillator. In: International Conference "Nonlinear Phenomena in Polymer Solids and Low-dimensional Systems", NPPS-2008, Moscow, Russia (2008)

Manevitch, L., Musienko, A.: Limiting phase trajectories and energy exchange between an harmonic oscillator and external force. Nonlinear Dyn. **58**, 633–642 (2009)

Manevitch, L., Mikhlin, Y., Pilipchuk, V.: The Method of Normal Oscillation for Essentially Nonlinear Systems. Moscow, Nauka (1989)

Manevitch, L., Gourdon, E., Lamarque, C.-H.: Toward the design of an optimal energetic sink in a strongly inhomogeneous two-degree-of-freedom system. J. Appl. Mech. **74**, 1078–1086 (2007)

Manevitch, L., Shepelev, D., Kovaleva, A.: Non-stationary vibrations of a nonlinear oscillator under random excitation. In: Proceeding of XXXVII Summer School "Advanced Problems in Mechanics (APM 2009)", Repino, Saint-Petersburg, Russia (2009)

Manevitch, L., Kovaleva, A., Manevitch, E.: Limiting phase trajectories and resonance energy transfer in a system of two coupled oscillators. Math. Probl. Eng. (accepted for publication)

Pilipchuk, V.: The calculation of strongly non-linear systems close to vibration impact systems. J. Appl. Math. Mech. **49**, 744–751 (1985)

Vakakis, A., Gendelman, O.: Energy pumping in nonlinear mechanical oscillators: part 2 resonance capture. J. Appl. Mech. **68**, 34–41 (2001)

Vakakis, A., Manevitch, L., Mikhlin, Y., Pilipchuk, V., Zevin, A.: Normal Modes and Localization in Nonlinear Systems. Wiley Interscience, New York (1996)

Part III
Non-smooth Engineering Systems

Near-Grazing Dynamics of Macro-scale and Micro-scale Cantilevers with Nonlinear Tip Interaction Forces

Ishita Chakraborty and Balakumar Balachandran

Abstract In this article, the dynamics of base-excited elastic cantilevers with non-linear attractive and repulsive forces in macro-scale and micro-scale systems are studied through experimental and numerical means. The macro-scale set-up consists of a base-excited elastic cantilever with a long-range attractive force and a short-range repulsive force. The attractive force is generated by a combination of two magnets, one located at the cantilever structure's tip and another on a movable translatory base. The repulsive force is generated through impacts between the cantilever tip and a compliant material that covers the magnet on the translatory stage. This macro-scale experimental system is motivated by micro-scale cantilevers used in tapping mode or dynamic mode atomic force microscopy (AFM). In tapping mode AFM, the micro-cantilever undergoes a long-range van der Waals attractive force and a short-range repulsive force as the cantilever tip approaches the sample. The authors study the macro-scale system and the micro-scale system, when the excitation frequency is away from the first natural frequency. For off-resonance excitations, period-doubling events are observed in these impacting systems. A reduced-order model is developed to numerically study these systems on the basis of a single mode assumption. In the numerical studies, similar nonlinear tip-sample forces are used to model the interaction forces on the cantilever's tip in both macro-scale and micro-scale systems. In an effort to understand the effects of noise on the dynamics, the responses of the systems are studied when Gaussian white noise is introduced into the base excitation, along with a harmonic component. It is observed that the addition of Gaussian white noise facilitates contact between the tip and the sample, for low levels of a harmonic base excitation.

I. Chakraborty • B. Balachandran (✉)
Department of Mechanical Engineering, University of Maryland, College Park, MD 20742, USA
e-mail: balab@umd.edu

M. Wiercigroch and G. Rega (eds.), *IUTAM Symposium on Nonlinear Dynamics for Advanced Technologies and Engineering Design*, IUTAM Bookseries (closed) 32, DOI 10.1007/978-94-007-5742-4_22,

Keywords Macro-scale and micro-scale systems • Tapping mode AFM • Near-grazing dynamics

1 Introduction

In this article, the dynamics of macro-scale and micro-scale base-excited elastic cantilevers are studied in the presence of attractive and repulsive interaction forces. The macro-scale system is constructed as a vehicle for understanding the dynamics of the micro-scale AFM micro-cantilevers operated in tapping mode. The focus of this study is to observe qualitative changes for off-resonance excitations. It is observed that when the impacts are of "grazing" type (i.e., "zero-speed" impacts between the tip and the sample), the period of response of the beam tip becomes twice the period of excitation for certain excitation frequencies between the first and the second natural frequencies of the system. This type of qualitative change is further analyzed by using a reduced-order numerical model developed with a single mode approximation. In addition to studying the bifurcations for near-grazing impacts, the authors explore the effects of additive Gaussian white noise into the inputs of these systems. Noise effects, which can be prominent in micro-scale system dynamics, can arise due to fabrication irregularities and thermal fluctuations. In what follows, to contextualize the current work, a brief discussion on prior work on impact dynamics, AFM cantilever dynamics, and stochastic dynamics of AFM cantilevers is provided.

Impact oscillators have been extensively studied over the past several decades (Shaw and Balachandran 2008). A special situation arises at zero-speed incidence or grazing impacts. Nordmark (1991) studied bifurcations caused by grazing impacts and studied the phenomenon by using a map construction. Dankowicz and Nordmark (2000) studied grazing impacts by constructing a discontinuity map around the bifurcation point. di Bernardo et al. (2001) derived a normal form map to study grazing incidence. Ing et al. (2010) studied impact induced bifurcations for near-grazing impacts for a linear oscillator. Long et al. (2008) studied corner-collision bifurcations for soft impacts, while Dick et al. (2009) reported period-doubling bifurcations for near-grazing impacts for excitation frequencies between the first and the second natural frequencies of the system. For off-resonance excitation frequencies, period-doubling bifurcations were reported for the current macro-scale experimental system and micro-cantilevers in the prior work of the authors Chakraborty and Balachandran (2011a,b, 2012).

For an AFM micro-cantilever operating in a tapping mode, the tip-sample interaction forces are inherently nonlinear and related nonlinear phenomena have been extensively studied (Hu and Raman 2006; Lee et al. 2002; Basak and Raman 2007). However, the focus of most of this literature is on cantilever dynamics, when the excitation frequency is at the first natural frequency of the cantilever. The tip-sample interaction forces between the tip and the sample have been modeled as Lennard-Jones potential forces, piece-wise linear forces, and a combination of van der Waals attractive and DMT contact forces. In the literature, the reported

nonlinear behaviors include bistability, period-adding bifurcations due to grazing contact, and chaos. The work carried out on addressing the effects of noise on micro-scale cantilever dynamics has been limited.

The presence of noise can have a significant effect on both micro-scale and macro-scale systems. For example, it was shown by Ramakrishnan and Balachandran (2010) that the addition of noise influences the formation of intrinsic localized modes in a micro-scale resonator array. In the studies of Butt and Jaschke (1995) and Stark et al. (2001), the thermal noise levels in AFM cantilevers was quantified by using numerical means. It is noted that the presence of a double-well potential can make the vibrating micro-cantilever system amenable to the phenomenon of stochastic resonance. The addition of noise may move the system from one potential well to another.

For micro-scale and macro-scale systems excited by off-resonance excitations, period-doubling bifurcations related to grazing contact have been examined in the present work. The effects of adding Gaussian white noise to the input signal is also studied for the considered systems. The rest of the article is organized as follows: The experimental arrangement and results for the macro-scale system are presented in Sect. 2. The reduced-order model and the numerical results generated by using it are presented in Sect. 3. The experimental and numerical results obtained for a micro-scale cantilever are presented in Sect. 4. The effects of Gaussian white noise on the system dynamics are explored in Sect. 5. Concluding remarks are provided at the end.

2 Experimental Arrangement and Results

The macro-scale experimental arrangement consists of a base-excited Aluminum cantilever structure, which has a small magnet attached to its tip. This magnet is attracted by another magnet that is fixed to a high-resolution translatory stage. The magnet on this stage is covered by a compliant material. The tip of the cantilever structure experiences a repulsive contact force, when this tip makes contact with the compliant material. The schematic of the experimental arrangement is shown in Fig. 1. The distance between the tip and the compliant material can be controlled by using the translatory stage. The experimental arrangement is oriented in the horizontal plane, so that the gravity effects on the bending mode of vibration can be neglected. The material properties related to the cantilever structure and the tip-interaction forces are provided in Table 1, and the associated material property and geometry values have been used to conduct the numerical simulations of Sect. 3. The first and the second natural frequencies of the cantilever structure are experimentally determined as 7.1 and 46.8 Hz, respectively. The authors use a single mode approximation to model the system, since the first and the second natural frequencies are well separated. The response of the system is studied for off-resonance excitation frequencies while maintaining near-grazing contact between the tip and the compliant material. The experimentally obtained

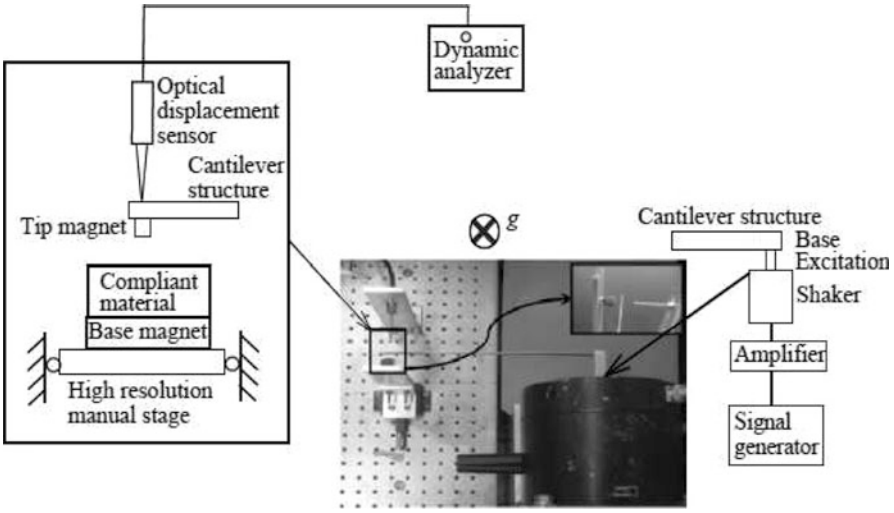

Fig. 1 Schematic of experimental arrangement at macro-scale

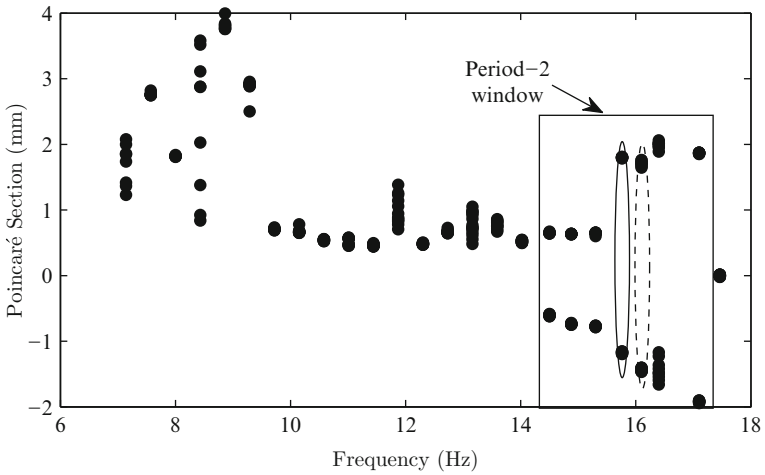

Fig. 2 Experimentally obtained diagram of qualitative changes on Poincaré section for excitation frequencies higher than the system's first natural frequency. Here, the scalar control parameter is the excitation frequency. The Poincaré sections are constructed by using the excitation frequency as the clock frequency

Poincaré section results are plotted in Fig. 2, where the excitation frequency is the quasi-statically varied scalar parameter. A period-doubling window is observed between the excitation frequencies of 14.5 Hz (2.03 times the first natural frequency) and 17.1 Hz (2.39 times the first natural frequency).

3 Numerical Results

The response of the impacting cantilever structure is studied by using a reduced-order model developed through a Galerkin projection of the governing equations of motion. The derivation of the open domain equation of motion and the corresponding boundary conditions are discussed in detail in the authors' previous work Chakraborty and Balachandran (2011b, 2012). The model of the base-excited cantilever with the tip-sample arrangement is shown in Fig. 3. The transverse displacement field is denoted by $w(s,t)$, where t is the time and s is the spatial coordinate along the length of the cantilever. After neglecting the nonlinear terms, the equation of motion of the base excited cantilever in the open domain can be written as

$$\rho A\ddot{w} + EIw^{iv} = \omega^2 \rho A X_0 \cos(\omega t), \tag{1}$$

where ρ is the density of the beam material, EI is the flexural rigidity, A is the cross section of the beam, ω is the excitation frequency, and X_0 is the amplitude of the base excitation. The boundary conditions for this system read as

$$\begin{aligned} &w(0,t) = 0, \qquad w'(0,t) = 0 \\ &w''(L,t) = 0, \qquad EIw'''(L,t) = m\ddot{w} + F_c. \end{aligned} \tag{2}$$

In Eq. (2), m is the mass of the beam tip and F_c is the net force experienced by the cantilever tip, due to the tip-sample interactions. The contact force along with the magnetic attractive force is taken into account in the boundary conditions. The tip-sample force is given by

$$F_{ts}(z) = \begin{cases} -\frac{K_M}{(z+d+A_0)^2} & \text{for } d+z > 0 \\ -\frac{K_M}{(A_0)^2} + K_E(-d-z)^{1.5} & \text{for } d+z \le 0 \end{cases} \tag{3}$$

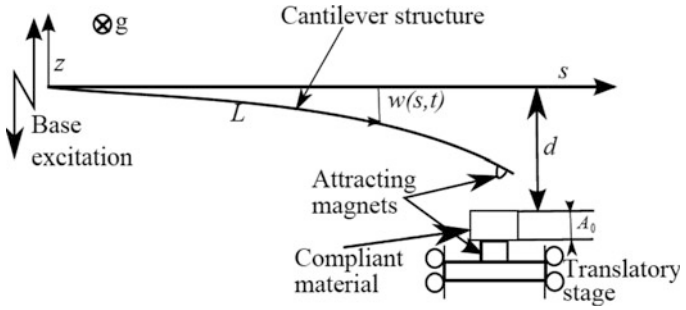

Fig. 3 Schematic of the elastic structure and the tip sample arrangement

Table 1 Simulation parameter values

Property	Value
Beam length (L)	295 mm
Cross-sectional area (A)	20 mm × 0.9 mm
Material density (ρ)	2,700 Kg/m^3
Cantilever Young's Modulus (E)	70 GPa
Tip mass (m)	0.094 gm
Thickness of compliant material (A_0)	5 mm
Quality factor (Q)	10
Constant related to magnetic force (K_M)	4.3×10^{-10}
Constant related to elastic force (K_E)	2.3×10^3

where z is the absolute displacement of the cantilever's tip, A_0 is the compliant material thickness, d is the initial separation between the cantilever tip and the sample (see Fig. 3 for details of the tip arrangement), and K_M and K_E are constants related to the attractive and repulsive forces, respectively. This force interaction is qualitatively similar to attractive-repulsive force interactions (modeled by van der Waals force and Derjaguin-Muller-Toporov forces) in tapping mode AFM (Chakraborty and Balachandran 2011b). In further development, all of the parameters used in the above equations are nondimensionalized, the displacement field is described by using a single mode assumption, and a reduced-order model is obtained in terms of the nondimensional parameters as

$$m_1\ddot{q}_1 + k_1 q_1 + c_1\dot{q}_1 = f_b + f_c. \tag{4}$$

Details of the different coefficients in Eq. (4) are given in the Appendix. The simulation parameter values used for the numerical simulations are listed in Table 1, which pertains to the experimental conditions described in Sect. 2. The numerical studies are performed at two selected frequencies, and the experimentally obtained Poincaré sections for the selected frequencies are marked by the solid and dotted ellipses in Fig. 2. The selected frequencies are 15.4 and 16.1 Hz as pointed out in Fig. 2. The comparisons between the numerically and experimentally obtained phase portraits are plotted in Fig. 4 for unconstrained and constrained motions.

4 Application to Micro-scale Cantilever

Following the observation of the period-doubling phenomenon close to grazing for off-resonance excitation frequencies in the macro-scale system, the authors studied qualitative changes for grazing impacts in the micro-scale system, for excitation frequencies in between the first and the second natural frequencies of the system. The micro-scale experiments were carried out by using an Asylum Research MFP 3D AFM equipment and a soft Si cantilever and a Si(100) sample.

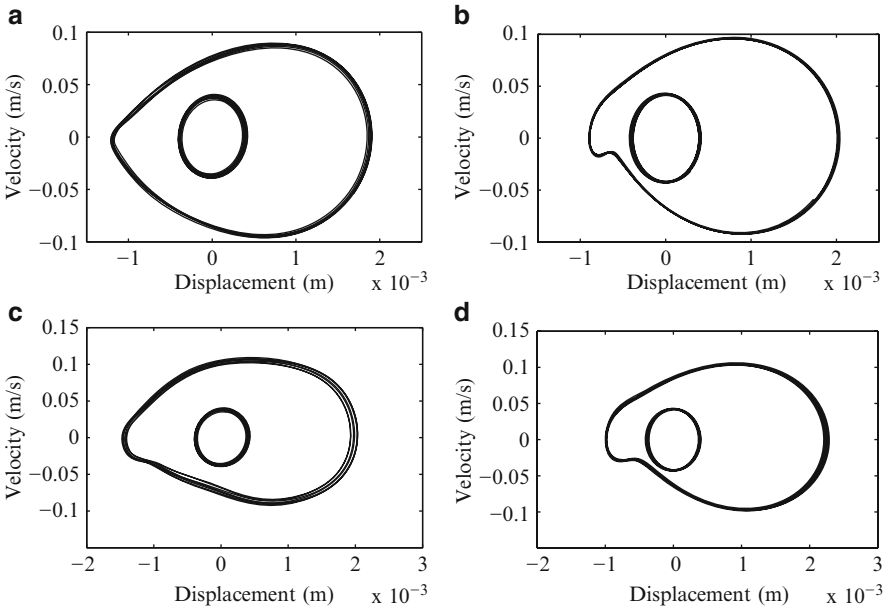

Fig. 4 (**a**) Experimentally obtained phase portraits for excitation frequency of 15.4 Hz, (**b**) numerically obtained phase portraits for excitation frequency of 15.4 Hz, (**c**) experimentally obtained phase portraits for excitation frequency of 16.1 Hz, and (**d**) numerically obtained phase portraits for excitation frequency of 16.1 Hz. The phase portrait that occupies a smaller area is obtained for the unconstrained motion and the other phase portrait is obtained for the constrained motion

The corresponding experimental arrangement is shown in Fig. 5. The length, width, and the thickness of the cantilever are 450, 50, and 2 μm, respectively. The first natural frequency of the system is at 12.72 kHz. The response signals are monitored by using a real time signal analyzer to identify qualitative changes associated with grazing contact, when the excitation frequency is in between the first and the second natural frequencies of the system.

The phase portraits shown in Fig. 6 are illustrative of the period-doubling phenomenon associated with near-grazing contact, when the excitation frequency is 2.34 times the first natural frequency; this phenomenon is similar to what was observed in the macro-scale system wherein the frequency location is different. The numerical model used for simulations of the micro-scale cantilever dynamics is similar to that reported in Sect. 3. However, the tip-sample forces are modeled as a combination of van der Waals attractive force and DMT contact force (see Chakraborty and Balachandran 2011b; Lee et al. 2002) and the tip mass of the cantilever is neglected in the micro-scale case.

For AFM cantilevers, a near-grazing contact can be identified by a period-doubling response for the chosen off-resonance excitation. This method of operation can ensure grazing contact between the AFM tip and sample which would

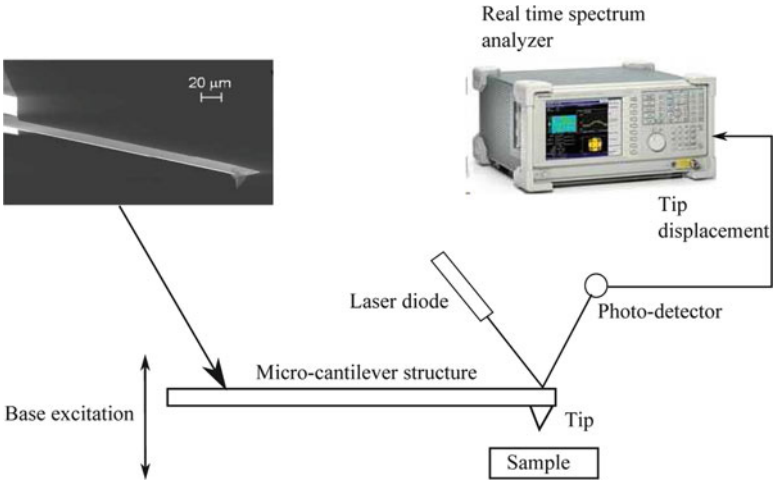

Fig. 5 Experimental arrangement with micro-scale cantilever

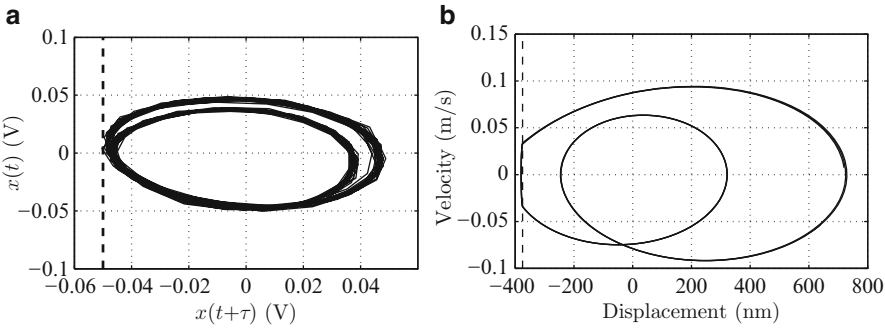

Fig. 6 (**a**) Experimentally obtained phase portrait for Si cantilever and Si(100) sample combination. (**b**) Numerically obtained phase portrait. The *dotted lines* correspond to the location of the sample

effectively reduce the repulsive tip-sample forces. High repulsive forces tend to destroy the tip of the cantilever or damage the soft samples.

5 Effects of Noise

In order to form a basis to study the effects of white noise on the tapping mode AFM operations, first, noise effects are studied in a macro-scale test apparatus. It is observed that grazing contact and associated period-doubling take place for low levels of harmonic excitation than previously observed, when white noise is added

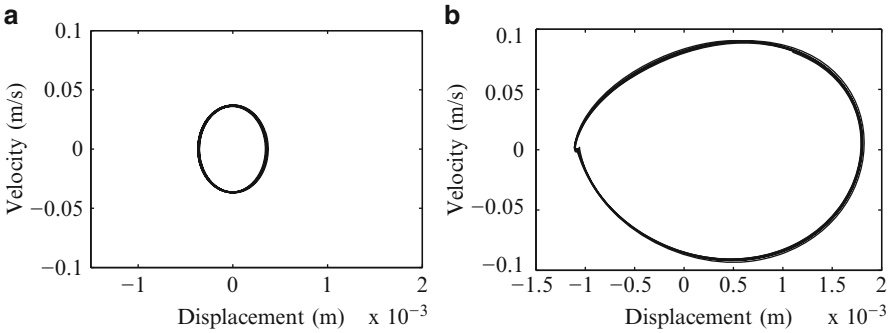

Fig. 7 (**a**) Phase portrait of the cantilever tip response for a harmonic base excitation. (**b**) Phase portrait of the cantilever tip response when noise is added to the harmonic base excitation and SNR is 402.88

along with the harmonic excitation. The experimental data obtained for the macro-scale system is presented in Fig. 7. For a harmonic excitation, the phase portrait for the cantilever tip response is plotted in Fig. 7a. It is seen that the fundamental response frequency is at the excitation frequency and that the cantilever's tip does not make contact with the sample. The excitation frequency is chosen as 16 Hz (which is within the period-doubling window), so that contact can be identified by a period-doubled response that occurs for near-grazing impacts. From Fig. 7b, it is noted that the orbit becomes nominally close to the period-doubled orbit when the signal to noise ratio (SNR) in the base excitation reaches a value of 402.88. This phenomenon is explored at length in the related work of the authors Chakraborty and Balachandran (2011a).

The potential function associated with tip-sample interactions and the elastic micro-cantilever has a double-well characteristic. This means that there is a possibility of "stochastic resonance" in such cases when the addition of noise pushes the system from one potential well to another. The authors have observed similar effects of noise in the micro-scale cantilever system, as in the macro-scale system.

Numerical simulations were carried out for a Si cantilever and HOPG sample combination. The selected forcing frequency is 2.24 times the first natural frequency of the system. The excitation amplitude and initial tip sample distance are selected as 56 and 100 nm, respectively. The potential function for this case is plotted in Fig. 8. The potential function is obtained from the van der Waals and DMT forces used to model the tip-sample forces in AFM. For the case without noise, the response phase portrait is shown in Fig. 9a. The associated harmonic oscillation corresponds to the dotted line in the potential function plot shown in Fig. 8. The motions are symmetric in the phase portrait and they occur around the lower potential well. Furthermore, it is observed that the fundamental response frequency is at the same frequency as the excitation frequency, and that the cantilever tip does not make contact with the sample. Next, Gaussian white noise is added to the harmonic input signal by using the MATLAB function 'awgn'. The harmonic excitation term is

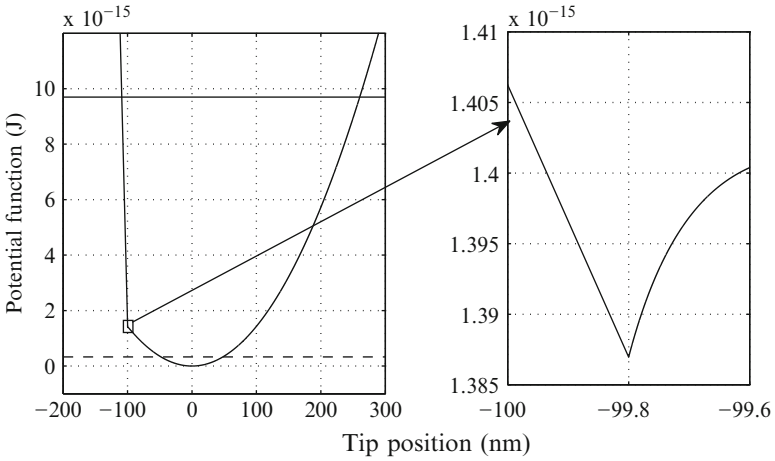

Fig. 8 Potential function for AFM cantilever. A magnified view of the second potential well is shown on the *right*

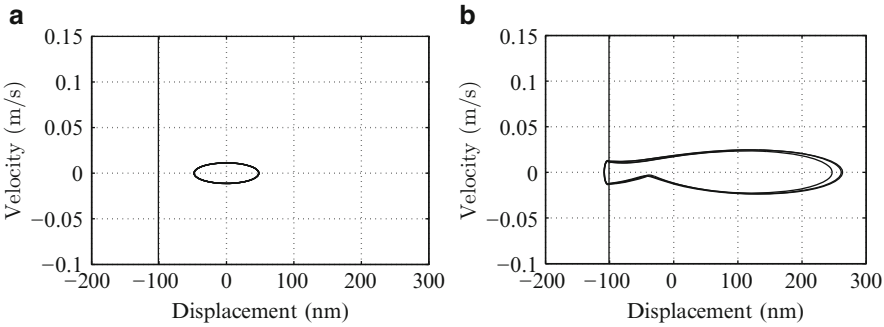

Fig. 9 (**a**) Phase portrait of the cantilever tip response when there is no noise addition in the base input. (**b**) Phase portrait of the cantilever tip response when there is noise added to the base input. The signal to noise ratio is 100. The *vertical lines* correspond to the location of the sample

passed through this additive noise channel, which adds noise of a prescribed SNR to the harmonic signal. For the case with noise and a signal to noise ratio of 100, the obtained response phase portrait is presented in Fig. 9b. The associated oscillation corresponds to the solid line in the potential function shown in Fig. 8. A "stochastic resonance" like phenomenon is observed, wherein the inclusion of noise in the base excitation pushes the solution to a higher energy level where the motions encounter a double-well potential. It is observed that the cantilever tip makes contact with the sample, due to the addition of white noise in the base excitation, with all of the other conditions remaining the same as in the previous case without noise and no contact. The fundamental response frequency of the cantilever is at half the excitation frequency. The contact induced through the addition of white noise

in the excitation signal and the corresponding period-doubled response is seen to be realizable in the micro-scale AFM cantilever system as previously noted in the macro-scale system.

6 Concluding Remarks

A macro-scale experiment with a base-excited cantilever structure with long-range attractive force and short-range repulsive force has been constructed and studied. This system is inspired by micro-cantilevers used in tapping mode AFM operations. During off-resonance excitations, period-doubling bifurcations are studied in macro-scale and micro-scale systems through experimental and numerical efforts, when the impacts between the tip and the sample have a zero speed. The period-doubling phenomenon is seen to be scalable, and furthermore, it takes place in a similar frequency ratio ranges for the two systems. The nonlinear phenomenon is numerically explored through a reduced-order model developed by using a single mode approximation. Effects of Gaussian white noise on such systems have also been studied through experimental and numerical means. It is observed that addition of Gaussian white noise to a harmonic base excitation input facilitates contact and period doubling, when previously no contact was observed for a harmonic base excitation. The present efforts provide a glimpse into the scalability of nonlinear phenomena and the application of it to atomic force microscopy.

Acknowledgements The authors gratefully acknowledge the support received for this work through NSF Grant No. CMMI-0800471. The authors thank Mr. G. Chawla and Prof. S. Solares of Mechanical Engineering, University of Maryland for their help with the AFM experiments.

Appendix

The terms in Eq. (4) can be expressed as:

$$
\begin{aligned}
m_1 &= \int_0^1 \phi_1(\bar{s})\phi_1(\bar{s})d\bar{s} + \gamma\,\{\phi_1(\bar{s}=1)\}^2 \\
k_1 &= \int_0^1 \phi_1(\bar{s})\phi_1(\bar{s})d\bar{s} \\
c_1 &= 2m_1\zeta \\
f_b &= \left(\int_0^1 \phi_1(\bar{s})d\bar{s}\right)\Omega^2\nu\cos(\Omega\tau) \\
f_c &= (\phi_1(\bar{s}=1))\; f_{ts}(\bar{z}).
\end{aligned}
$$

Here, ζ is the damping ratio, $\phi_1(\bar{s})$ is the spatial function related to the nondimensional displacement, γ is the ratio of the tip mass to the mass of the cantilever, ν is the nondimensional excitation amplitude, Ω is the nondimensional forcing frequency, τ is the nondimensional time, $\bar{z}$ is the nondimensional displacement, and f_{ts} is the nondimensional tip-sample force.

The nondimensional quantities are listed as:

$$\bar{w} = \frac{w}{L}, \bar{s} = \frac{s}{L}, \tau = \omega_n t, \nu = \frac{X_0}{L}, \eta = \frac{d}{L}, \xi = \frac{A_0}{L},$$

$$\gamma = \frac{m}{\rho A L}, \kappa = \frac{K_E}{\rho A \sqrt{L} \omega_n^2}, \lambda = \frac{K_M}{\rho A L^4 \omega_n^2}, \Omega = \frac{\omega}{\omega_n}.$$

For a single mode assumption, the response of the system is given by:

$$\bar{w}(\bar{s}, \tau) = q_1(\tau)\phi_1(\bar{s}),$$

where ϕ_1 is given by:

$$\phi_1(\bar{s}) = C_1 \left[\sin(\beta_1 \bar{s}) - \sinh(\beta_1 \bar{s})\right] + C_2 \left[\cos(\beta_1 \bar{s}) - \cosh(\beta_1 \bar{s})\right].$$

References

Basak, S., Raman, A.: Dynamics of tapping mode atomic force microscopy in liquids: theory and experiments. Appl. Phys. Lett. **91**, 064107 (2007)

Butt, H., Jaschke, M.: Calculation of thermal noise in atomic force microscopy. Nanotechnology **6**, 1–7 (1995)

Chakraborty, I., Balachandran, B.: Noise influenced elastic cantilever dynamics with nonlinear tip interaction forces. Nonlinear Dyn. **66**(3), 427–439 (2011a)

Chakraborty, I., Balachandran, B.: Off-resonance cantilever dynamics in the presence of attractive and repulsive tip-interaction forces. Int. J. Struct. Stab. Dyn. **11**(4), 603–620 (2011b)

Chakraborty, I., Balachandran, B.: Near-grazing dynamics of base-excited cantilevers with nonlinear interaction forces. Nonlinear Dyn. (In revision, 2012)

Dankowicz, H., Nordmark, A.B.: On the origin and bifurcations of stick-slip oscillations. Phys. D **136**, 280–302 (2000)

di Bernardo, M., Budd, C.J., Champneys, A.R.: Normal form maps for grazing bifurcations in n-dimensional piecewise-smooth dynamical systems. Phys. D **160**, 222–254 (2001)

Dick, A.J., Balachandran, B., Yabuno, H., Numatsu, M., Hayashi, K., Kuroda, M., Ashida, K.: Utilizing nonlinear phenomena to locate grazing in the constrained motion of a cantilever beam. Nonlinear Dyn. **57**(3), 335–349 (2009)

Hu, S., Raman, A.: Chaos in atomic force microscopy. Phys. Rev. Lett. **96**, 036107 (2006)

Ing, J., Pavlovskaia, E., Wiercigroch, M., Banerjee, S.: Bifurcation analysis of an impact oscillator with a one-sided elastic constraint near grazing. Phys. D **239**, 312–321 (2010)

Lee, S.I, Howell, S.W., Raman, A., Reifenberger, R.: Nonlinear dynamics of microcantilever in tapping mode atomic force microscopy: a comparison between theory and experiment. Phys. Rev. B **66**, 115409 (2002)

Long, X.H., Lin, G., Balachandran, B.: Grazing bifurcations in elastic structures excited by harmonic impactor motions. Phys. D **237**(8), 1129–1138 (2008)

Nordmark, A.B.: Non-periodic motion caused by grazing incidence in an impact oscillator. J. Sound Vib. **145**(2), 279–297 (1991)

Ramakrishnan, S., Balachandran, B.: Energy localization and white noise induced enhancement of response in a micro-scale oscillator array. Nonlinear Dyn. **62**, 1–16 (2010)

Shaw, S.W., Balachandran, B.: A review of nonlinear dynamics of mechanical systems in year 2008. J. Syst. Des. Dyn. **2**(3), 611–640 (2008)

Stark, R.W., Drobek, T., Heckl, W.M.: Thermomechanical noise of a free v-shaped cantilever for atomic-force microscopy. Ultramicroscopy **86**, 207–215 (2001)

Reduced Inductance in DC-DC Converter Circuits via the Application of Filippov's Method

O. Imrayed, B. Zahawi, Damian Giaouris, and V. Pickert

Abstract A method for reducing the size of filter inductance in DC-DC converter circuits based on Filippov's theory is presented in this paper. In this method, the state transitional matrix of the system over one complete switching cycle, including the state transitional matrices across the converter switching events, is used to stabilize converter operation with a substantially reduced inductor size while maintaining circuit average currents and voltages. An analysis of circuit conduction losses shows that losses are not significantly affected by higher inductor current ripple resulting from the use of the smaller inductor. The switching frequency of the converter will not vary or change compared to a conventionally designed DC-DC converter. The new control/design method is demonstrated using an experimental voltage-mode-controlled buck converter.

Keywords DC-DC converter circuits • Nonlinear design/control method • Reduced inductance

1 Introduction

DC-DC converters are some of the simplest and most widely used power electronics circuits and can be found in almost any power supply equipment in use today for anything from mobile phones and laptop computers to hybrid electric vehicles and aircraft power supplies. The main components of a DC-DC converter are the power electronic switches, an LC filter used to smooth the circuit voltage and current

O. Imrayed • B. Zahawi • D. Giaouris (✉) • V. Pickert
School of Electrical, Electronic and Computer Engineering, Merz Court, Newcastle University, Newcastle upon Tyne, NE1 7RU England, UK
e-mail: damian.giaouris@ncl.ac.uk

M. Wiercigroch and G. Rega (eds.), *IUTAM Symposium on Nonlinear Dynamics for Advanced Technologies and Engineering Design*, IUTAM Bookseries (closed) 32, DOI 10.1007/978-94-007-5742-4_23,

waveforms and the electronic controller needed to generate the switch firing pulses necessary to ensure the desired operation of the circuit.

Due to the inherent switching action of the circuit, the steady-state operating point of any DC-DC converter is a periodic oscillation around a predefined value determined by the application. Conventionally, these discontinuities introduced by the switching action of the circuit are ignored by converter designers who simply assume that the converter behaves like a 2nd order low pass filter implying that the system is always stable (Middlebrook and Ćuk 1977; Krein et al. 1990). Converter components are then chosen to guarantee the stable behaviour of the system and avoid any operating regions in which the converter is likely to exhibit any one of a number of unstable, nonlinear behaviours. As a result, converter components are significantly oversized giving a larger, more expensive, heavier and less efficient product than could be achieved by the application of appropriate nonlinear control methods (Di Bernardo et al. 1998; Di Bernardo and Vasca 2000; Hiskens and Pai 2000; Dranga et al. 2005; Giaouris et al. 2008).

A new control method based on the analysis of the behaviour of the system during the switching instants is presented in this paper to maintain the stable period-1 operation of the converter. Compared with conventional linear design methods, the analysis allows for substantially smaller circuit component sizes to be used thus increasing power-to-weight and power-to-size ratios and reducing cost without jeopardising the overall operation of the system. The proposed technique can be applied to any DC-DC converter topology (bi-directional power flow, uni-directional power flow, isolated or non-isolated designs) and does not require new materials or special magnetic components. What's more, the new design/control method can run on a simple microcontroller and does not require an expensive high speed DSP.

In this paper, the new design/control method is applied to a simple voltage controlled buck converter as a typical example of a simple DC-DC converter circuit. The new design method guarantees a substantially wider stable operating range and a reduction in the size of circuit components by incorporating the switching action of the converter switches into the design process. Results demonstrate the possibility of achieving a substantial reduction in the size of the converter inductance. The basic operation of the voltage mode controlled buck converter is presented in Sect. 2 of this paper. Section 3 gives an overview of the nonlinear dynamical phenomena observed in the buck converter circuit and a review of the Saltation matrix method of analysis (Leine et al. 2004) employed as the basis for the new design/control methodology proposed in this paper. Using this matrix, it is possible to add small perturbations to the control signal that will influence the stability of the periodic motion, without greatly influencing the steady-state performance and other transient properties of the converter, to guarantee a stable periodic motion with a substantially smaller inductor size as demonstrated in Sects. 4 and 5. The analysis is experimentally verified using a 24 V laboratory voltage-mode-controlled buck converter circuit.

2 Basic Operation of the Voltage-Mode-Controlled Buck Converter

The buck converter, also known as a step-down DC-DC converter, is a circuit used to convert an input DC voltage to a lower DC output voltage. Figure 1 shows a schematic diagram of the voltage mode controlled buck converter. The circuit comprises a diode *D* and a switch *S* controlled by a pulse-width modulated signal. The required output voltage is achieved by setting the switch's duty cycle *d*. The capacitor *C* and the inductor *L* work as a low pass filter to smooth the current and voltage waveforms seen by the load resistor *R*.

The most common control technique applied to power DC-DC converters is pulse width modulation (PWM). In voltage mode PWM control, the output voltage is compared with a reference voltage to generate an error signal which is amplified to provide the control signal. The switch firing pulses are generated by comparing the control signal with a saw-tooth signal as shown in Fig. 1. The switch will be closed if the ramp signal is greater than the control signal and open otherwise. During the interval when the switch is ON, the diode is reverse biased and the input voltage provides energy to the load and the inductor. During the interval when the switch is OFF, the inductor current flywheels through the diode transferring some of the stored energy to the load.

Assuming that the converter is designed to operate in continuous conduction mode (i.e. the inductor is sized to ensure that the converter current does not fall

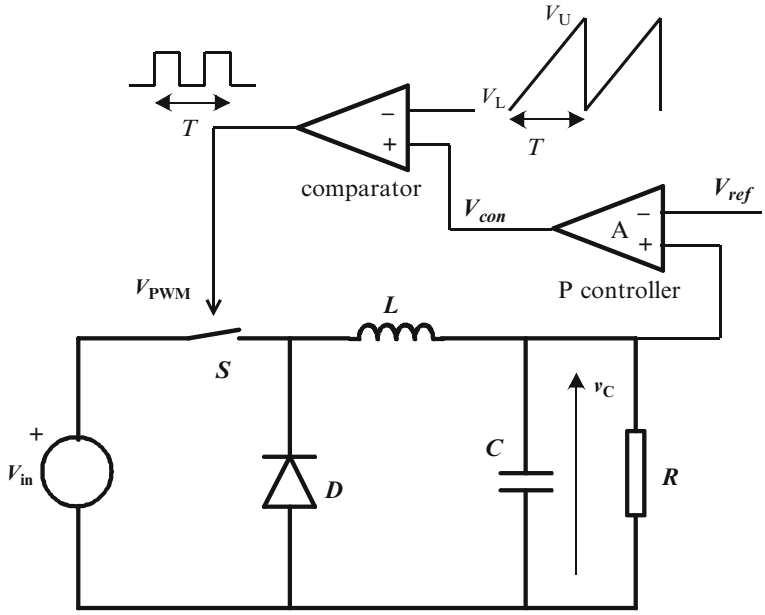

Fig. 1 The voltage mode controlled DC-DC buck converter

to zero at any time during its operation), the operation of the circuit during the OFF interval t_{off} (when the switch is open) can be described by the following equations:

$$\frac{dV_C}{dt} = \frac{1}{C}\left(i_L - \frac{v_C}{R}\right) \tag{1}$$

$$\frac{di_L}{dt} = -\frac{v_C}{L} \tag{2}$$

These equations can be written in state space form as:

$$\dot{\mathbf{X}} = \mathbf{A}_{\text{OFF}}\,\mathbf{X} + \mathbf{B}_{\text{OFF}}\,V_{in} \tag{3}$$

Where $\mathbf{X} = \begin{bmatrix} v_C & i_L \end{bmatrix}^T$, $\mathbf{A}_{\text{OFF}} = \begin{bmatrix} -\frac{1}{RC} & \frac{1}{C} \\ -\frac{1}{L} & 0 \end{bmatrix}$, $\mathbf{B}_{\text{OFF}} = \begin{bmatrix} 0 \\ 0 \end{bmatrix}$, V_{in} is the input voltage, v_C is the capacitor voltage and i_L is the inductor current.

During the ON interval t_{on} (when the switch is closed) the equations are:

$$\frac{dv_C}{dt} = \frac{1}{C}\left(i_L - \frac{v_C}{R}\right) \tag{4}$$

$$\frac{di_L}{dt} = \frac{V_{in} - v_C}{L} \tag{5}$$

These can be described in state space form as:

$$\dot{\mathbf{X}} = \mathbf{A}_{\text{ON}}\,\mathbf{X} + \mathbf{B}_{\text{ON}}\,V_{in} \tag{6}$$

where, $\mathbf{A}_{\text{ON}} = \begin{bmatrix} -\frac{1}{RC} & \frac{1}{C} \\ -\frac{1}{L} & 0 \end{bmatrix}$ and $\mathbf{B}_{\text{ON}} = \begin{bmatrix} 0 \\ \frac{1}{L} \end{bmatrix}$

The duty cycle d is defined as $t_{on}T$, where T is the switching period of the PWM waveform.

In the steady-state, the buck converter produces a lower output voltage than the input voltage. The mean output voltage can be expressed in terms of the input voltage and the duty ratio:

$$V_{out} = d\,V_{in} \tag{7}$$

Figure 2 shows the bifurcation diagram of a standard buck converter circuit design to accept an input voltage of 24 V and produce a regulated output voltage of about 12 V (Fossas and Olivar 1996), plotted for L as the bifurcation parameter. The diagram shows that the circuit is stable for larger values of L. However, as the value of the L is reduced, a period-doubling bifurcation occurs at $L = 19.5$ mH and the stability of the period-1 orbit is lost to another periodic orbit of double the period (period-2). This periodic solution continues until the value of L is further reduced to about 13.2 mH when it loses its period-2 stability and bifurcates to a period-4 response. As the value of L decreases further, a cascade of period-doubling

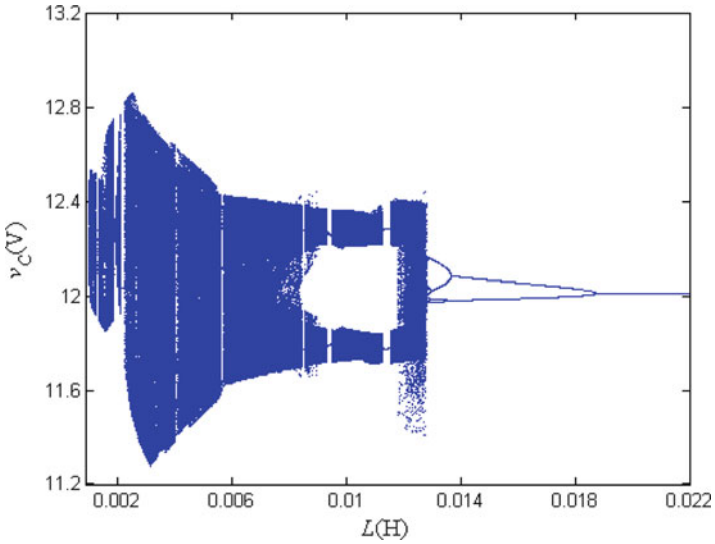

Fig. 2 Bifurcation diagram of the voltage mode controlled buck converter; $f_s = 2.5$ kHz, $V_u = 8.2$ V, $V_l = 3.8$ V, $V_{ref} = 11.3$ V, $C = 47$ μH and $R = 22$ Ω

bifurcations is interrupted by a border collision at $L = 13$ mH, which causes the system to behave chaotically. Parasitic circuit elements and are not included in this analysis. It has been shown (Di Bernardo et al. 1998; Di Bernardo and Vasca 2000) that these components move the bifurcation points slightly but do not change the bifurcation sequences and therefore have no significant or qualitative influence on the overall dynamics of the system.

Figure 3 shows the stable period-1 experimental output voltage and inductor current waveforms obtained with an inductor value of 20 mH. The period-1 stability of the system broken down and period-2 stability was born when the 20 mH inductor was replaced with a smaller 15 mH inductor as shown in Fig. 4. Finally Fig. 5 shows the system operating chaotically when a 7.8 mH inductor is used, completely in agreement with the bifurcation diagram of Fig. 2.

3 Analysis of Switching Converter Circuits

The theory developed by Filippov (1988) gives a generalised definition of a solution for systems involving a switching, including systems with a discontinuous right-hand side such as power electronics circuits. Such systems can be described as follows:

$$\dot{\mathbf{X}}(t) = \mathbf{f}(\mathbf{X}(t), t) = \begin{cases} \mathbf{f}_-(\mathbf{X}(t), t) & \mathbf{X} \in V_- \\ \mathbf{f}_+(\mathbf{X}(t), t) & \mathbf{X} \in V_+ \end{cases} \tag{8}$$

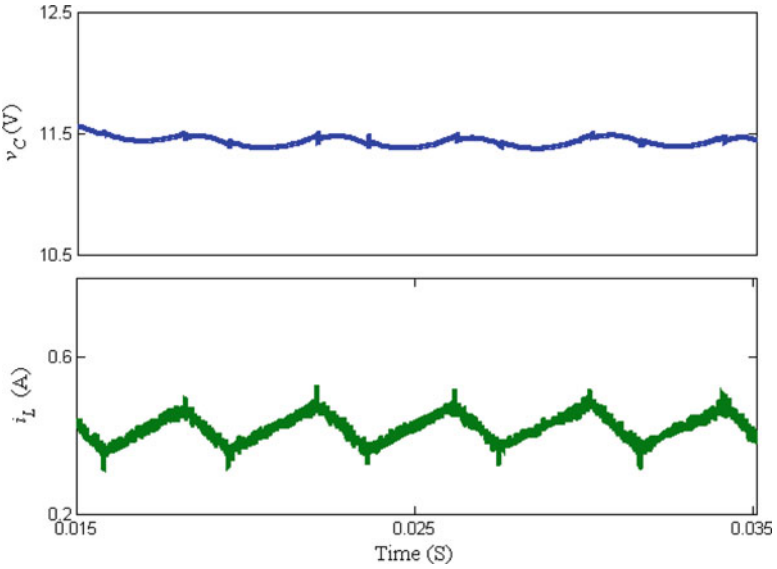

Fig. 3 Experimental output voltage and inductor current waveforms; stable period-1 operation, $L = 20$ mH

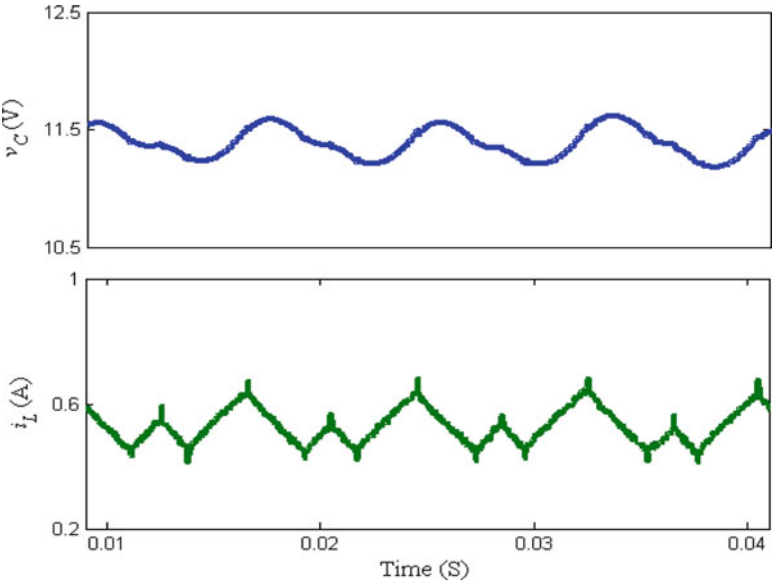

Fig. 4 Experimental output voltage and inductor current waveforms; period-2 operation, $L = 15$ mH

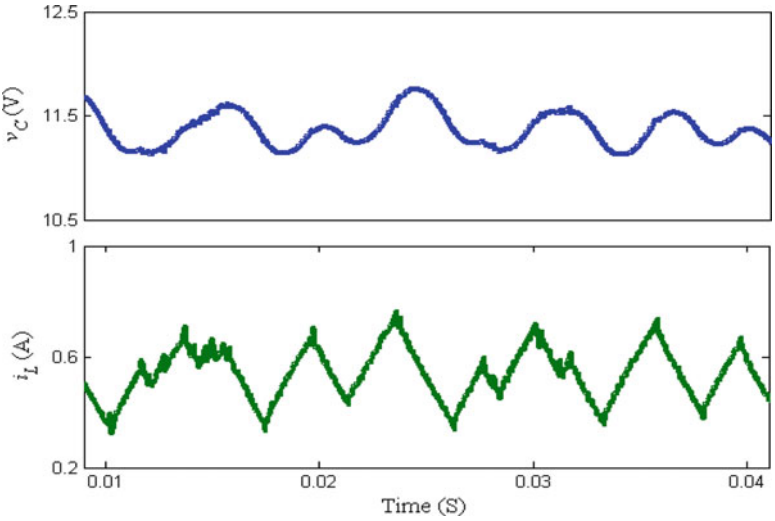

Fig. 5 Experimental output voltage and inductor current waveforms; chaotic operation, $L = 7.8$ mH

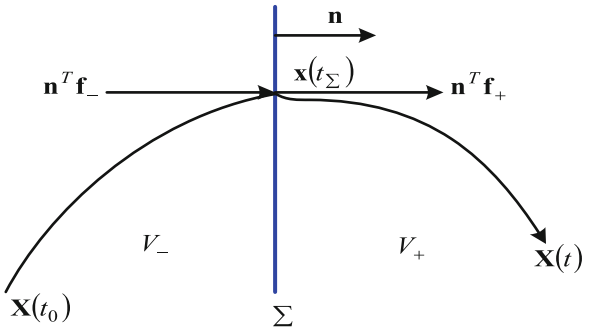

Fig. 6 Evaluation of a solution of a nonsmooth system

where $\mathbf{f}_-(\mathbf{X}(t), t)$ and $\mathbf{f}_+(\mathbf{X}(t), t)$ are the two smooth vector fields before and after the switching, respectively. V_- and V_+ are two different regions in state space separated by the switching hyper-surface Σ, as shown in Fig. 6 (in the case of a simple DC-DC converter these regions will correspond to the ON and OFF switch states).

The switching hypersurface is defined by an algebraic equation:

$$h\left(\mathbf{X}\left(t_\Sigma\right), t_\Sigma\right) = 0 \tag{9}$$

The vector field is piecewise continuous. It is smooth in V_- and V_+, and discontinuous on Σ. However, the vector field is not defined on the hypersurface given by Eq. (9). To avoid this problem, Filippov suggested that the vector field at the switching instance should not be a single valued function but a set valued

function whose limits are the values of the vector fields before and after the switching:

$$\dot{\mathbf{X}}(t) \in \mathbf{F}\left(\mathbf{X}(t), t\right) = \begin{cases} \mathbf{f}_{-}\left(\mathbf{X}(t), t\right) & \mathbf{X} \in V_{-} \\ \overline{co}\left\{\mathbf{f}_{-}\left(\mathbf{X}(t), t\right), \mathbf{f}_{+}\left(\mathbf{X}(t), t\right)\right\} & \mathbf{X} \in \Sigma \\ \mathbf{f}_{+}\left(\mathbf{X}(t), t\right) & \mathbf{X} \in V_{+} \end{cases} \tag{10}$$

Where $\overline{co}\left\{\mathbf{f}_{-}(\mathbf{X}(t), t), \mathbf{f}_{+}(\mathbf{X}(t), t)\right\}$ denotes the smallest closed convex set containing $\mathbf{f}_{-}(\mathbf{X}(t), t)$ and $\mathbf{f}_{+}(\mathbf{X}(t), t)$, and it can be defined as follows:

$$\overline{co}\left\{\mathbf{f}_{-}, \mathbf{f}_{+}\right\} = \left\{(1-q)\,\mathbf{f}_{-} + q\mathbf{f}_{+} \quad \forall q \in [0, 1]\right\} \tag{11}$$

The extension of a discontinuous system (8) to a convex differential inclusion (10) is known as Filippov's convex method (Leine et al. 2004; Filippov 1988). The existence of a Filippov solution can be guaranteed if $\mathbf{F}(\mathbf{X}(t), t)$ is upper semi-continuous. The solution is unique for every initial condition, if it crosses the hypersurface transversally and spends almost zero time on the switching manifold.

In smooth systems, the fundamental matrix $\mathbf{\Phi}$ will map the perturbation at the initial condition $\Delta\mathbf{X}(t_0)$ to the perturbations at the end of the period $\Delta\mathbf{X}(t)$ by $\Delta\mathbf{X}(t)=\Phi(t;\ \mathbf{X}_{\mathrm{p}}(t_0),t_0)\ \Delta\mathbf{X}(t_0)$. In nonsmooth systems, however, the vector field will be discontinuous at the switching instance. As a result, the fundamental matrix breaks down as the perturbed solution reaches the switching instance after or before the original trajectory, as shown in Fig. 7. A map is needed that will relate the perturbation vectors before the switching $\Delta\mathbf{X}(t_{\Sigma-})$ to the vectors after the switching $\Delta\mathbf{X}(t_{\Sigma+})$:

$$\Delta\mathbf{X}\left(t_{\sum+}\right) = \mathbf{S}\ \Delta\mathbf{X}\left(t_{\sum-}\right) \tag{12}$$

This map $\mathbf{S}$ is referred to as the *saltation matrix* (Leine et al. 2004) or the *jump matrix* (Baushev et al. 1992). The saltation matrix, when the solution transversally intersects the hypersurface, is derived in the following manner:Referring to Fig. 7, the perturbation vectors before and after the switching are given by:

$$\Delta\mathbf{X}\left(t_{\sum-}\right) = \mathbf{X}_{\tilde{p}}\left(t_{\sum}\right) - \mathbf{X}_{p}\left(t_{\sum}\right) \tag{13}$$

$$\Delta\mathbf{X}\left(t_{\sum+}\right) = \mathbf{X}_{\tilde{p}}\left(\tilde{t}_{\sum}\right) - \mathbf{X}_{p}\left(\tilde{t}_{\sum}\right) \tag{14}$$

Using Taylor's expansion theorem, it can be shown (Leine et al. 2004) that these two vectors are related by the saltation matrix $\mathbf{S}$ as $\Delta\mathbf{X}(t_{\Sigma+}) = \mathbf{S}\ \Delta\mathbf{X}(t_{\Sigma-})$, where

$$\mathbf{S} = \mathbf{I} + \frac{\left[\mathbf{f}_{+}\left(\mathbf{X}_{p}\left(t_{\Sigma}\right)\right) - \mathbf{f}_{-}\left(\mathbf{X}_{p}\left(t_{\Sigma}\right)\right)\right]\mathbf{n}^{T}}{\mathbf{n}^{T}\mathbf{f}_{-}\left(\mathbf{X}_{p}\left(t_{\Sigma}\right)\right) + h_{t}\left(\mathbf{X}_{p}\left(t_{\Sigma}\right), t_{\Sigma}\right)} \tag{15}$$

The saltation matrix is the state transition matrix across the switching hypersurface. Figure 8 shows a periodic solution of a nonsmooth system in which the

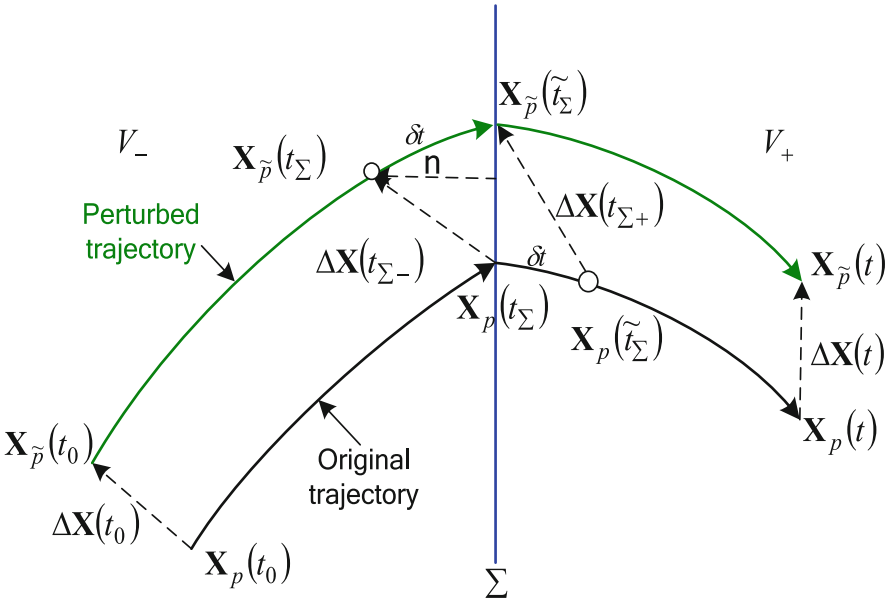

Fig. 7 Evaluation of a solution of a nonsmooth system and its perturbation

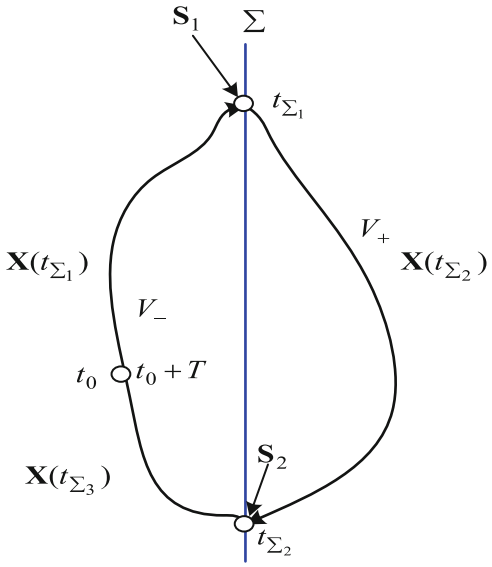

Fig. 8 The periodic solution of a non-smooth system

trajectory crosses the switching manifold Σ twice at $t_{\Sigma 1}$ and $t_{\Sigma 2}$. The fundamental solution matrix for one complete cycle (the Monodromy matrix) is given by:

$$\mathbf{M}(T) = \mathbf{X}\left(t_{\sum_3}\right)\mathbf{S}_2\,\mathbf{X}\left(t_{\sum_2}\right)\mathbf{S}_1\,\mathbf{X}\left(t_{\sum_1}\right) \tag{16}$$

Where $\mathbf{X}(t_{\Sigma 1}) = \mathbf{\Phi}_1(t_{\Sigma 1};\ \mathbf{X}(t_0),\ t_0)$ is the state transition matrix when $\mathbf{X} \in \boldsymbol{V}_-$; $\mathbf{X}(t_{\Sigma 2}) = \mathbf{\Phi}_2(t_{\Sigma 2};\ \mathbf{X}(t_{\Sigma 1}),\ t_{\Sigma 1})$ is the state transition matrix when $\mathbf{X} \in \boldsymbol{V}_+$; $\mathbf{X}(T) = \mathbf{\Phi}_3(t_0 + T;\ \mathbf{X}(t_{\Sigma 2}),\ t_{\Sigma 2})$ is the state transition matrix when $\mathbf{X} \in \boldsymbol{V}_-$; and $\mathbf{S}_1$ and $\mathbf{S}_2$ represent the state transition matrices at $\mathbf{X} \in \Sigma$.

4 Derivation of the Buck Converter Monodromy Matrix

With reference to Fig. 9 showing the steady-state waveforms of the buck converter, the operation of the circuit can be described by two sets of equations which, by defining $x_1(t) = v_{\mathrm{C}}(t)$ and $x_2(t) = i_{\mathrm{L}}(t)$, may be written as:

$$\frac{dx_2}{dt} = \begin{cases} \frac{V_{in} - x_1(t)}{L}, & A\left(x_1(t) - V_{ref}\right) < V_{ramp}, \quad \text{at} \quad \mathbf{\Phi_{ON}} \\ -\frac{x_1(t)}{L}, & A\left(x_1(t) - V_{ref}\right) > V_{ramp}, \quad \text{at} \quad \mathbf{\Phi_{OFF}} \end{cases}$$

$\frac{dx_1}{dt} = \frac{x_2(t) - x_1(t)/R}{C}$ at both $\mathbf{\Phi_{ON}}$ and $\mathbf{\Phi_{OFF}}$.

The switching hypersurface (h) at switching time $(d'T)$ is given by:

$$h\left(X(t), t\right) = x_1(t) - V_{ref} - \frac{V_{ramp}}{A} = 0$$

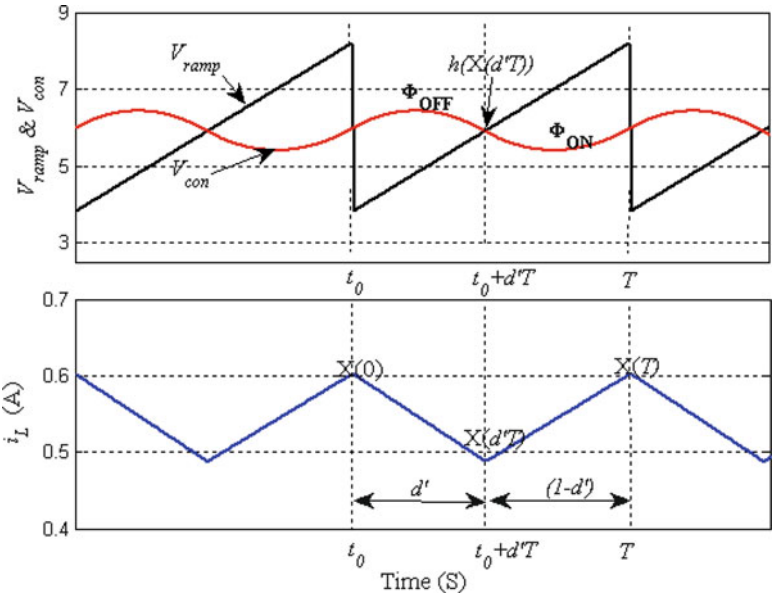

Fig. 9 Buck converter waveforms; the switch is OFF when $V_{con} > V_{ramp}$ and ON when $V_{con} < V_{ramp}$

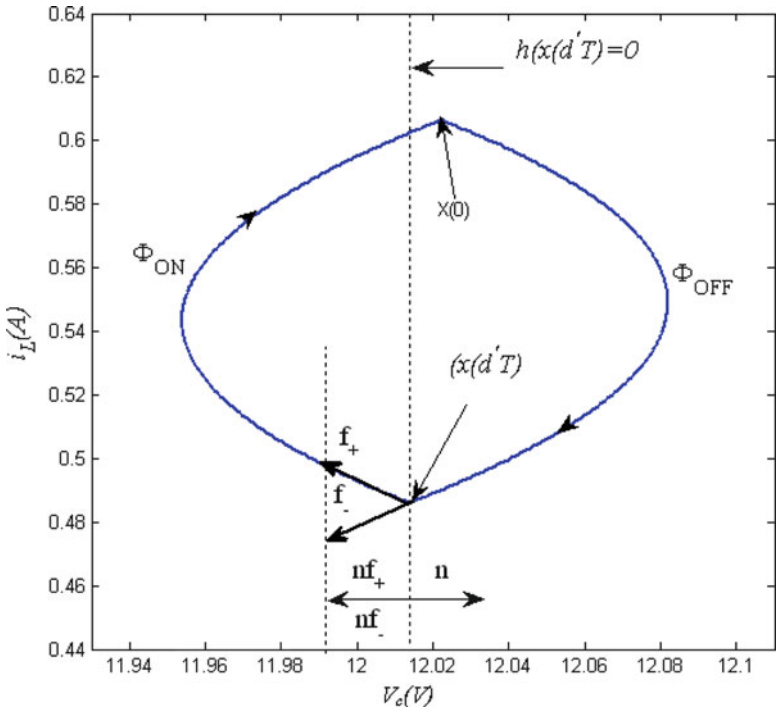

Fig. 10 Transversal intersections in the orbit of the buck converter

where $t = d'T$, $\mathbf{f}_{-}(\mathbf{x}(t), t)$ and $\mathbf{f}_{+}(\mathbf{x}(t), t)$ are the two smooth vector fields before and after the switching, defined as:

$$\mathbf{f}_{-}(\mathbf{x}(t), t) = \begin{bmatrix} x_2(t)/C - x_1(t)/RC \\ (V_{in} - x_1(t))/L \end{bmatrix} \tag{17}$$

$$\mathbf{f}_{+}(\mathbf{x}(t), t) = \begin{bmatrix} x_2(t)/C - x_1(t)/RC \\ -x_1(t)/L \end{bmatrix} \tag{18}$$

It is obvious from (17) and (18) that there is a discontinuity when the main switching element passes from the ON state to the OFF state, since $\mathbf{f}_{-}(\mathbf{x}(t), t) \neq \mathbf{f}_{+}(\mathbf{x}(t), t)$.

The normal to the switching manifold $\mathbf{n}$ is given by:

$$\mathbf{n} = \nabla h(x(t)) = \begin{vmatrix} \dfrac{\partial h(\mathbf{X}(t), t)}{\partial x_1(t)} \\ \dfrac{\partial h(\mathbf{X}(t), t)}{\partial x_2(t)} \end{vmatrix} = \begin{bmatrix} 1 \\ 0 \end{bmatrix} \tag{19}$$

As shown in Fig. 10, the solution intersects the switching manifold transversally and the orbit spends an infinitely small time on the switching manifold. Therefore,

Filippov's method for obtaining the saltation matrix and the Monodromy matrix of the system can be applied. This is true for all DC-DC converter circuits operating in continuous conduction mode (CCM) where the inductor current never falls to zero. In the case of discontinuous conduction, the orbits slide along the switching surface (Di Bernardo et al. 1998).

The components of the saltation matrix (Giaouris et al. 2007, 2008, 2009) are obtained as:

$$\lim_{t\to d'T} \mathrm{f}_{-}\left(x(t)\right) = \begin{bmatrix} x_2\left(d'T\right)/C - x_1\left(d'T\right)/RC \\ \left(V_{in} - x_1\left(d'T\right)\right)/L \end{bmatrix},$$

$$\lim_{t\to d'T} \mathrm{f}_{+}\left(x(t)\right) = \begin{bmatrix} x_2\left(d'T\right)/C - x_1\left(d'T\right)/RC \\ -x_1\left(d'T\right)/L \end{bmatrix}$$

$$n^T \lim_{t\to d'T} \mathrm{f}_{-}\left(x(t)\right) = \frac{x_2\left(d'T\right) - x_1\left(d'T\right)/R}{C}$$

The switching manifold is defined by a scalar indicator function $h(\mathbf{x},t) = 0$, thus the derivative of $h(\mathbf{x},t)$ with respect to t for period-1 operation $\mathrm{t} \in (0,T)$ is:

$$\frac{\partial h(\mathbf{x},t)}{\partial t} = -\frac{V_U - V_L}{AT},$$

giving the saltation matrix:

$$S = \begin{bmatrix} 1 & 0 \\ \dfrac{V_{in}/L}{\dfrac{x_2\left(d'T\right) - x_1\left(d'T\right)}{C} - \dfrac{V_U - V_L}{AT}} & 1 \end{bmatrix} \tag{20}$$

The state transition matrix during the first interval (when the switch is OFF) is given by $\Phi_{\mathrm{OFF}}\left(d'T, 0\right) = e^{A_1 d'T}$ and the state transition matrix for the second interval (when switch is ON) is given by $\Phi_{\mathrm{ON}}\left(T, d'T\right) = e^{A_2(T-d'T)}$, where

$$A_1 = A_2 = \begin{bmatrix} -1/RC & 1/C \\ -1/L & 0 \end{bmatrix}$$

It is now possible to calculate the Monodromy matrix $\mathbf{M}(T,0)$ of the system:

$$\mathbf{M}\left(T,0\right) = \mathbf{\Phi}_{\mathrm{ON}}(T, d'T) \times \mathbf{S}\left(d'T\right) \times \mathbf{\Phi}_{\mathrm{OFF}}(d'T, 0) \tag{21}$$

The stability of the periodic orbit can be determined by obtaining the Floquet multipliers of the system, i.e. the eigenvalues of the Monodromy matrix. Figure 11 shows that the computed eigenvalues of $\mathbf{M}$ leave the unit circle (and the system losses its stability via a period-doubling bifurcation) when the value of the inductance is reduced to 19.55 mH, completely in agreement with previous simulation and experimental results.

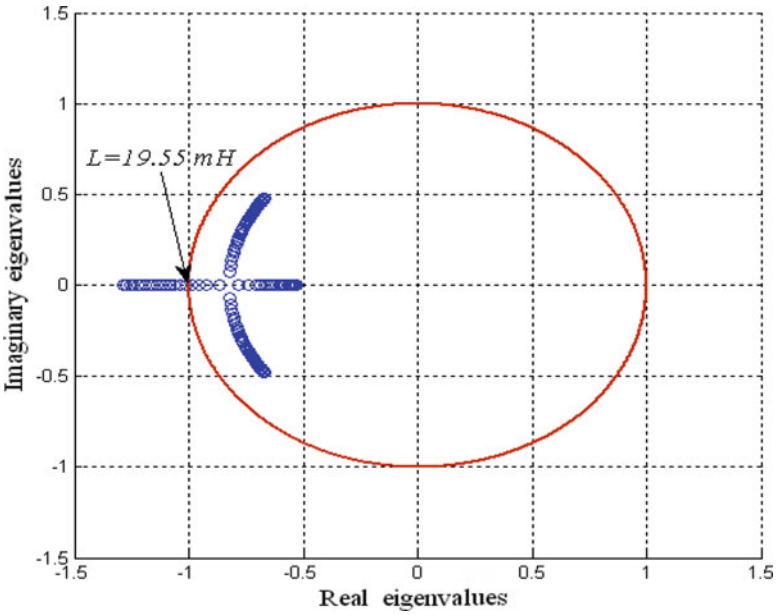

Fig. 11 Loci of the eigenvalues of the Monodromy matrix

5 Supervisory Control Based on the Saltation Matrix

In this section, two supervisory controllers based on the above analysis are applied to stabilise the operation of the buck converter and avoid the onset of the period doubling bifurcation as the value of the inductor is reduced. Computer simulations, as well as analytical and experimental results are used to support the theoretical analysis. The new controller has no impact on the switching frequency of the converter compared to a conventionally controlled DC-DC converter circuit.

5.1 Control Method-1 (Changing the Slope of the Ramp Signal)

The upper value of the ramp signal V_U is multiplied by factor $(1 + a)$, allowing us to manipulate the location of the Floquet multipliers by varying the value of a.

$$S = \begin{bmatrix} 1 & 0 \\ \dfrac{V_{in}/L}{\dfrac{x_2(d'T) - x_1(d'T)}{C} - \dfrac{aV_U - V_L}{AT}} & 1 \end{bmatrix},$$

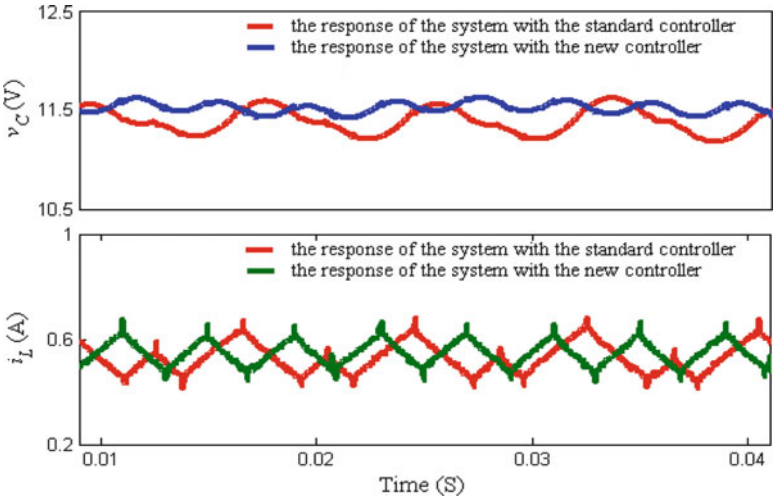

Fig. 12 Experimental waveforms for i_L and v_C with standard PWM control and the proposed supervisory controller; $L = 15$ mH, stable period-1 operation

It is now possible to calculate a value of a required to keep the Floquet multipliers within the unit circle and thus maintain system stability over a wider range of inductor values by solving a nonlinear equation such as $|\, eig\,(\mathbf{M}\,(T, 0))\,| - 0.8241 = 0$.

Figure 12 shows the experimental waveforms of the system with an inductor value of $L = 15$ mH. The figure shows a comparison between the responses of the standard voltage mode controlled buck converter and that of the new supervisory controller. Clearly, the new control strategy is able to alter the previous period-2 orbit and achieve the desired stable period-1 response despite the lower value of L.

5.2 Control Method-2 (Altering the Time Derivative of h)

The time derivative of $h(\mathbf{x}(t))$ can be altered by adding the function $(1 + b \sin(\omega t))$ to the reference signal V_{ref} result in the following expression for the saltation matrix:

$$S = \begin{bmatrix} 1 & 0 \\ \dfrac{V_{in}/L}{\dfrac{x_2\,(d'T) - x_1\,(d'T)}{C} - \left(\omega V_{ref}\, b \cos\omega + \dfrac{V_U - V_L}{AT}\right)} & 1 \end{bmatrix}$$

Altering the value of b will now have an effect on the eigenvalues of the Monodromy matrix allowing these to be placed at any chosen location within the unit cycle. In a similar approach to that adopted in the previous section, the

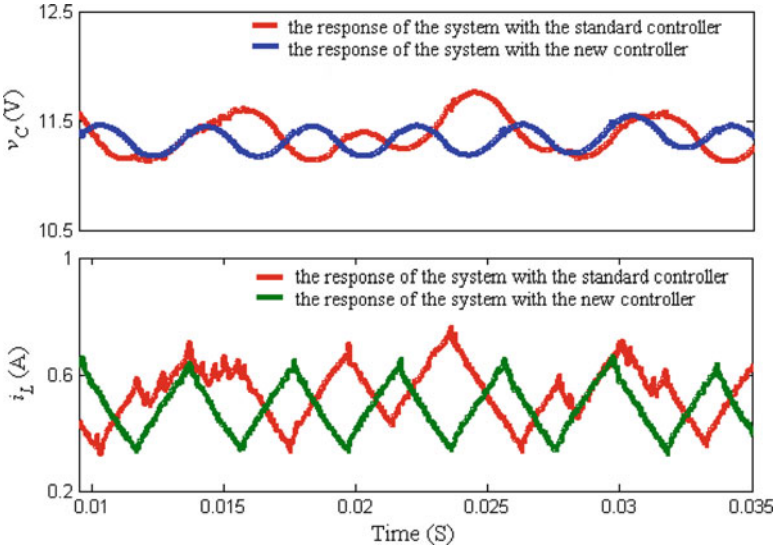

Fig. 13 Experimental waveforms for i_L and v_C with standard PWM control and the proposed supervisory controller; $L = 7.8$ mH, stable period-1 operation

eigenvalues can be maintained at a value corresponding to a stable period-1 orbit obtained for a higher value of L (for instance 0.8241 when $L = 20$ mH) by solving the nonlinear transcendental equation $|\, eig\, (\mathbf{M}\,(T, 0))\,| - 0.8241 = 0$.

Figure 13 shows the experimental waveforms of the system with an inductor value of $L = 7.8$ mH. The figure shows a comparison between the response of the system with a standard PWM controller and that of the new supervisory controller. The new controller is able to alter the previous chaotic orbit to achieve the desired stable period-1 response at the lower value of L.

6 Circuit Losses

The above results have clearly shown that it is possible to reduce the size of the circuit inductance substantially while maintaining stable period-1 operation of a buck converter with continuous current conduction by the application of advanced nonlinear control methods based on Filippov's method. However, a smaller inductor inevitably means a higher current ripple content as evident from Fig. 4. This issue needs further examination since it could imply higher total losses in the circuit because of the higher rms inductor current values. In this section, total conduction losses in the inductor, diode and MOSFET switch employed in the converter circuit are calculated with different inductor values to assess the impact of the higher

Table 1 Calculated circuit conduction losses; $R_{\text{on}} = 0.8\ \Omega$, $V_{\text{F}} = 0.75$ V, $R_{\text{F}} = 0.25\ \Omega$

		Conduction loss			
L (mH)	R_L	Mosfet	Diode	Inductor loss	Total
20	80 mΩ	0.139 W	0.210 W	0.024 W	0.373 W
7.8	50 mΩ	0.142 W	0.212 W	0.015 W	0.369 W

current ripple content. It was assumed that switching losses and other high frequency effects would not be affected by inductor size since the new control strategy has no impact on the switching frequency of the converter.

Table 1 gives the calculated conduction losses for operation with a 20 mH inductor and a 7.8 mH inductor at an average inductor current of 0.56 A and an average output voltage of 12.0 V, showing no significant change in the calculated total conduction loss when using the smaller inductor. The average inductor loss was calculated as the integral of $(i^2 R_L)$ over one switching cycle, where R_{L} is the measured inductor DC resistance. Average MOSFET loss was calculated as the integral of $(i^2 R_{on})$ over one switching cycle, where R_{on} is the on-resistance of the MOSFET. The forward voltage drop across the diode was modelled as a constant DC source V_F in series with a resistor R_F giving an average power loss calculated as the integral of $(i^2 R_F + iV_F)$ over one switching cycle.

7 Conclusions

Using the voltage-mode-controlled buck converter circuit as an example, we have demonstrated in this paper that the size of the filter inductance in a DC-DC converter can be substantially reduced by the application of Filippov's method of studying switching systems, reducing the size, weight and cost of the circuit. The method has been used as the basis for designing supervisory controllers to place the eigenvalues of the state transition matrix of the system over one complete switching cycle (the Floquet multipliers of the system) within the unit cycle to insure system stability for operation with the smaller inductor sizes without effecting the switching frequency of the circuit or converter average current and voltage values. The new design/control method has been demonstrated using a 24 V laboratory voltage-mode-controlled buck converter circuit. An analysis of the conduction losses in the main switching device, the diode and the inductor, have shown no significant change in losses as a result of the higher current ripple content when using the smaller inductor values.

Acknowledgments The authors wish to acknowledge the valuable advice received from Professor S. Banerjee during the development of the analysis presented in this paper.

References

Baushev, V.S., Zhusubaliev, Z.T., Kolokolov, Y.V., Terekhin, A.: Local stability of periodic solutions in sampled data control systems. Autom. Remote Control **53**(6, issue 2), 865–871 (1992)

Di Bernardo, M., Vasca, F.: Discrete time maps for the analysis of bifurcations and chaos in DC/DC converters. IEEE Trans. Circuits Syst. I **47**(2), 130–143 (2000)

Di Bernardo, M., Garofalo, F., Glielmo, L., Vasca, F.: Switchings, bifurcations, and chaos in DC/DC converters. IEEE Trans. Circuits Syst. I **45**(2), 133–141 (1998)

Dranga, O., Buti, B., Nagy, I., Funato, H.: Stability analysis of nonlinear power electronic systems utilizing periodicity and introducing auxiliary state vector. IEEE Trans. Circuits Syst. I **52**(1), 168–178 (2005)

Filippov, A.F.: Differential Equations with Discontinuous Right Hand Sides. Kluwer Academic Publishers, Dordrecht (1988)

Fossas, E., Olivar, G.: Study of chaos in the buck converter. IEEE Trans. Circuits Syst. I: Fundam. Theory Appl. **43**(1), 13–25 (1996)

Giaouris, D., Banerjee, S., Zahawi, B., Pickert, V.: Control of fast scale bifurcations in power-factor correction converters. IEEE Trans. Circuits Syst. II **54**(9), 805–809 (2007)

Giaouris, D., Banerjee, S., Zahawi, B., Pickert, V.: Stability analysis of the continuous-conduction-mode buck converter via Filippov's method. IEEE Trans. Circuits Syst. I **55**(4), 1084–1096 (2008)

Giaouris, D., Maity, S., Banerjee, S., Pickert, V., Zahawi, B.: Application of Filippov method for the analysis of subharmonic instability in dc-dc converters. Int. J. Circuit Theory Appl. **37**, 899–919 (2009)

Hiskens, I.A., Pai, M.A.: Trajectory sensitivity analysis of hybrid systems. IEEE Trans. Circuits Syst. I **47**(2), 204–220 (2000)

Krein, P., Bentsman, J., Bass, R.M., Lesieutre, B.C.: On the use of averaging for the analysis of power electronic systems. IEEE Trans. Power Electron. **5**(2), 182–190 (1990)

Leine, R.I., Nijmeijer, H.: Dynamics and Bifurcations of Non-Smooth Mechanical Systems. Springer, Berlin (2004)

Middlebrook, R.D., Ćuk, S.: A general unified approach to modelling switching-converter power stages. Int. J. Electron. **42**(6), 521–550 (1977)

Dynamics of a Drifting Impact Oscillator with a Conical Profile

Olusegun Ajibose, Marian Wiercigroch, Ekaterina Pavlovskaia, Alfred Akisanya, and Gyory Kaŕoyli

Abstract A new model of the progression phase of a drifting oscillator is proposed to account more accurately for the penetration of a conical impactor through elasto-plastic solids under a combination of a static and a harmonic excitation. The dynamic response of the semi-infinite elasto-plastic medium subjected to repeated impacts by a rigid impactor with conical contacting surface is considered and a power law force–penetration relationship is adopted to describe the loading and unloading phases of contact. These relationships are then used to develop a physical and mathematical model of this drifting oscillator, where the time histories of the progression through the medium include both the loading and unloading phases. A limited nonlinear dynamic analysis of the system was performed and it confirms that the maximum progressive motion of the oscillator occurs when the system exhibits periodic motion.

Keywords Drilling • Drifting impact oscillator • Progression dynamics

O. Ajibose (✉) • M. Wiercigroch • E. Pavlovskaia • A. Akisanya
Centre for Applied Dynamics Research, School of Engineering, King's College, University of Aberdeen, Aberdeen, AB24 3QB, Scotland, UK
e-mail: o.k.@ajibose.abdn.ac.uk; m.wiercigroch@abdn.ac.uk; e.pavlovskaia@abdn.ac.uk; a.akisanya@abdn.ac.uk

G. Károyli
Department of Structural Mechanics, Budapest University of Technology and Economics, Műegyetem rkp. 3, 1111 Budapest, Hungary
e-mail: karolyi@tas.me.bme.hu

M. Wiercigroch and G. Rega (eds.), *IUTAM Symposium on Nonlinear Dynamics for Advanced Technologies and Engineering Design*, IUTAM Bookseries (closed) 32, DOI 10.1007/978-94-007-5742-4_24,

1 Introduction

Some industrial applications such as ground moling, percussive drilling and ultrasonic machining involve the repeated impacts of machine elements upon different types of media aiming to induce a permanent deformation or damage to the medium and to drive the machine elements. These systems have been effectively modelled by various drifting oscillators, but very few attempts have been made to adequately describe the influence of contact geometries and the governing force–displacement relationship during the crashing stages of the interactions. For example, studies in Pavlovskaia et al. (2001), Pavlovskaia and Wiercigroch (2004, 2007), and Franca and Weber (2004) have described these systems by representing the impacted medium by so–called sliders. A slider consists of a pair of massless plates with a spring and damper between them.

However, all these previous models inadequately represented the force–penetration dependence for the medium impacted by inserts of conical surface geometry. Conical indenters are commonly found on drill-bits used in borehole drilling, and moling tools used in cable laying and mining. The optimisation of the loading, geometric and material parameters to enhance the penetration rate is of major importance to these industries. This work aims to incorporate the dependence of the penetration on the applied force in a new drifting oscillator model to assess the dynamic behaviour of the system.

Some authors Lee (1940), Shivakumar (1985), and Wu and Yu (2001) have proposed low–dimensional models that represent observed experimental force–penetration response of elasto-plastic structures under impact. The present work goes further and applies similar principles to modelling impacts upon an elasto-plastic semi-infinite medium. In Sect. 2, the force–penetration relationship are presented for the loading and unloading phases of contact and then built into a physical and mathematical model that describes the dynamics of a drifting oscillator. The corresponding equations of motion for the different phases of the system operation are derived. A nonlinear dynamic analysis of the system is presented in Sect. 3 for the conical impactor.

2 Modelling of a Drifting Oscillator

First, we note that the force–penetration relationship $F(\delta)$, during the loading phase of the impact of a cone on the elasto–plastic medium has been shown to be of the form (Ajibose 2009; Ajibose et al. 2010)

$$F_l(\delta) = K_{lc}\delta^{n_{lc}}, \quad n_{lc} = 2, \tag{1}$$

where K_{lc} is the contact stiffness during the loading. In the case of the unloading the phase the relationship becomes,

$$F_{ul} = K_{uc}(\delta - \delta_f)^{n_{uc}}. \tag{2}$$

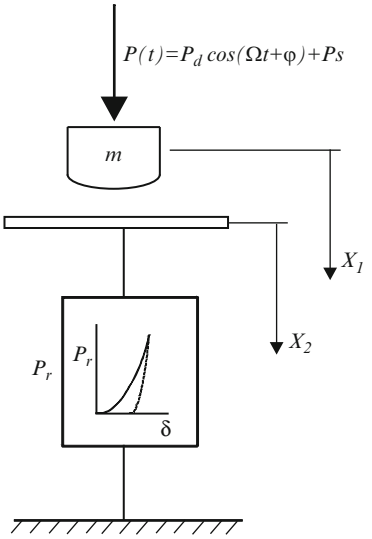

Fig. 1 Physical model of an impactor colliding with an elasto-plastic medium

Here, where $n_{uc} < 2$ and K_{uc} are material constants determined from experiments and δ_f is the final deformation of the elasto-plastic medium given as

$$\delta_f = \delta_m - \left[\frac{K_l(\delta_m)^{n_l}}{K_u}\right]^{1/n_u}. \tag{3}$$

It was noted earlier that some low dimensional models (Lee 1940; Shivakumar 1985) have already been put forward to describe the response of elasto-plastic structures to a single impact. Although these models were used for structures of finite size, they can afford us an insight for developing a physical and mathematical model for the considered problem of impacting an elasto-plastic semi-infinite medium. Hence, a system consisting of an oscillating mass colliding with a slider of nonlinear properties, see Fig. 1, is adopted in this paper to model the dynamic response of an impactor upon the elasto-plastic semi-infinite medium during repeated impacts. Here, the slider models the semi-infinite medium during the loading and unloading phases of the contact: its response is described by Eq. (1) during the loading phase, and by Eq. (2) during unloading. It is assumed that the dynamic response during subsequent impacts is not influenced by any material damage due to the preceding impacts. This is typically the situation in machining or drilling where the cuttings are carried away by the drilling fluid.

Here, the mass M is subjected to an external force $P(t) = P_s + P_d \cos(\Omega t + \varphi)$ consisting of a harmonic component of amplitude P_d, forcing frequency Ω and phase shift φ, and a static component P_s. The mass impacts intermittently with the slider which has nonlinear characteristics. The slider is used to represent the elasto–plastic half space. The absolute displacement of the mass is denoted by X_1, while the absolute displacement of the slider by X_2. All the displacements are referenced to the position at time $t = 0$.

At the beginning, the mass and the slider plate are not in contact and there exists a gap $G|_{t=0} = G_0$ between them. The size $G(t)$ of the gap changes as the mass is in motion. The mass and the slider are in contact at $G = 0$. The motion is characterised by three different phases namely: no contact, loading and unloading phases. In the no contact phase, there is no interaction between the mass and the slider. During the loading phase, the mass and the slider are in contact and move forward at the same velocity. This phase ends when the velocity of the mass becomes zero. The unloading phase then begins with the mass moving in the opposite direction, while still in contact with the slider, until the displacement of the mass is less than X_f. The whole process is then re-initiated with the no contact phase, which ends when the mass impacts the slider at its previously attained displacement. The mass then continues in contact with the slider till it reaches zero velocity. The unloading phase is then repeated.

The final progression X_f of the slider at the end of the actual contact phase is calculated using Eq. (3):

$$X_f = (X_1^* - X_p) - \left[\frac{K_l(X_1^* - X_p)^{n_l}}{K_u}\right]^{1/n_u}, \tag{4}$$

where X_1^* is the maximum displacement of the mass during the current loading phase, X_p is the original position of the slider at the beginning of the current contact phase.

The displacement X_2 of the slider during the loading and unloading phases of the contact is in phase with the displacement X_1 of the mass. The magnitude of X_1 is greater than X_2 by the gap G between the initial position of the slider and the mass, $X_1 = X_2 + G_0$.

The equations of motion of the system can be written in terms of dimensionless variables and parameters defined as

$$\tau = \Omega_0 t, \quad x = \tfrac{X_1}{\mu}, \quad y = \tfrac{dx}{d\tau}, \quad z = \tfrac{X_2}{\mu}, \quad x_p = \tfrac{X_p}{\mu}, \quad x_f = \tfrac{X_f}{\mu}, \; x_1^* = \tfrac{X_1^*}{\mu},$$

$$\omega = \tfrac{\Omega}{\Omega_0}, \; a = \tfrac{P_d}{M\mu\Omega_0^2}, \; b = \tfrac{P_s}{M\mu\Omega_0^2}, \; g = \tfrac{G}{\mu}, \; \kappa = \left[\tfrac{K_u}{K_l}\right]\mu^{n_u - n_l},$$

where $\Omega_0^2 = \mu^{n_l - 1} K_l / M$ and μ is a characteristic length defined as

$$\mu = \left[\frac{F_y}{K_l}\right]^{\frac{1}{n_l}}. \tag{5}$$

This implies that the equations of motion can now be written as follows:

No Contact $(x < z + g_0)$

$$\begin{aligned} x' &= y \\ y' &= a\cos(\omega\tau + \varphi) + b \\ z' &= 0 \end{aligned} \tag{6}$$

Loading ($x = z + g$ and $y \geq 0$)

$$\begin{aligned} x' &= y \\ y' &= a\cos(\omega\tau + \varphi) + b - (x - x_p)^{n_l} \\ z' &= y \end{aligned} \tag{7}$$

Unloading ($x = z + g_0,\ y < 0$ and $x - x_p \geq x_f$)

$$\begin{aligned} x' &= y \\ y' &= a\cos(\omega\tau + \varphi) + b - \kappa(x - x_p - x_f)^{n_u} \\ z' &= y \end{aligned} \tag{8}$$

where $'$ denotes differentiation with respect to non-dimensional time τ.

The dimensionless final deformation x_f is given by

$$x_f = (x_1^* - x_p) - \left[\frac{(x_1^* - x_p)^{n_l}}{\kappa}\right]^{1/n_u}. \tag{9}$$

3 Nonlinear Dynamic Analysis

In this section, the dynamic response of the impacting oscillator with a conical surface profile is investigated. In accordance with the discussion in Sect. 2, we assume $n_l = 2.0$ and $n_u = 1.7$. The time histories, bifurcation diagrams and phase space trajectories with superimposed Poincaré maps are calculated and the resulting dynamic behaviour is discussed in this section. In the presented numerical results, a number of parameters are kept constant: $a = 0.4$, $g = 0.02$, $\omega = 1.0$, $\varphi = 0$ and $\kappa = 1,000$.

The dynamic responses of the system described above are calculated for values $b = 0.10,\ 0.15,\ 0.2$ as shown in Fig. 2. The solid lines represent the motion of the impacting mass while the dashed lines represent the motion of the slider. It can be observed that the system exhibits a similar dynamics as that observed in Pavlovskaia et al. (2001), Pavlovskaia and Wiercigroch (2004, 2007), and Franca and Weber (2004). However, the slider shows motion in the opposite direction during the unloading phase (see Fig. 2b) which was not possible for the slider used in Pavlovskaia et al. (2001), Pavlovskaia and Wiercigroch (2004, 2007), and Franca and Weber (2004). This is because previous studies did not capture the unloading phase of the force–displacement relationships for the medium. Hence, this new dynamic model captures both the loading and unloading response of the elasto-plastic half space due to the conical impactor.

In Fig. 2b, the no contact phase is represented by the segment $\overline{ab}$ on the time history of the displacement of the mass. This is followed by loading phase

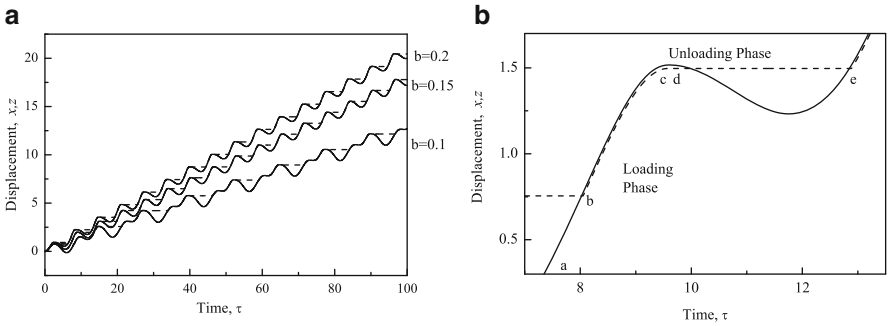

Fig. 2 Time histories of the conical impactor for various values b of the static load. Displacement x of the mass is shown by *solid lines*, displacement z of the slider by *dashed lines*. (**b**) Is a blow-up of a small part of (**a**)

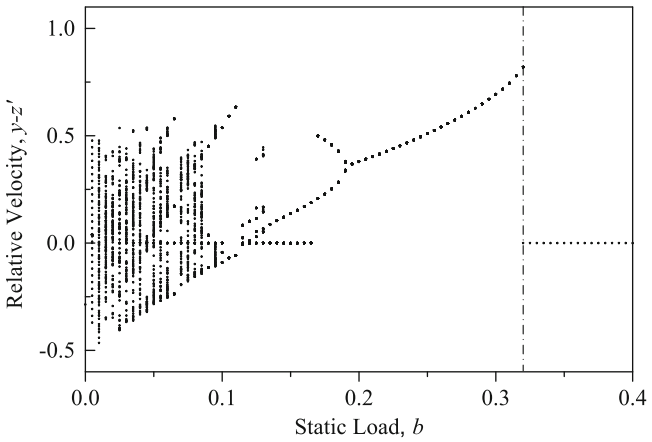

Fig. 3 Bifurcation diagram of the relative velocity $y - z'$ as a function of the static load b in case of the conical impactor

represented by segment $\overline{bc}$, while $\overline{cd}$ is the unloading phase. Notice here that the displacement curve of the slider and the mass have a similar shape in the segment $\overline{bd}$. Afterwards, the subsequent no contact phase is depicted by $\overline{de}$ where the displacement of the slider maintains a contact value, indicating the permanent deformation of the elasto–plastic solid at that stage.

The bifurcation diagram for the normalised relative velocity $y - z'$ (Fig. 3) shows how the behaviour of the system changes as a function of the normalised static load b. The figure is constructed using for 150 cycles of harmonic forcing while skipping the first 50 cycles. This diagram reveals that for $b < 0.1$ the response of the system is mainly chaotic with a few short ranges of the static force b where periodic motion occurs, while for $b \geq 0.1$, the system response is mainly periodic.

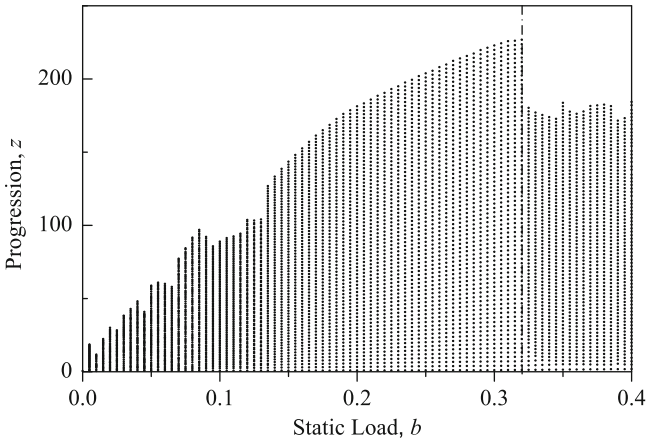

Fig. 4 Progression z during 150 cycles of forcing as a function of the static force b for the conical impactor

The relative velocity reaches the maximum value at $b = 0.32$, then drops to zero for values $b > 0.32$.

The time histories presented in Fig. 2 suggest that an increase in the static force tends to improve the progression of the impactor. If we measure the progression of the impactor as a function of the static load as shown in Fig. 4 using 150 cycles of harmonic forcing, it can be observed that an increase in the static force tends to improve the progression if the static load is less than 75% of the amplitude of the dynamic force. Note that the result shown were for a normalised force amplitude $a = 0.4$. Beyond this point, a further increase in the static load does not give greater progression. A comparison of Fig. 3 with Fig. 4 reveals that the maximum progression occurs at $b = 0.32$. This suggests that beyond the optimal static load the influence of the harmonic forcing is reduced and the oscillating mass tends to stay in contact with the medium for longer periods of time.

In Fig. 5a, the trajectory of the system is plotted in the phase plane $(x - z, y - z')$ for $b = 0.1$. Here $x - z$ is the normalised relative displacement and $y - z'$ is the normalised relative velocities between the impactor and the slider. This trajectory forms two distinct loops in the phase plane and also has a straight segment. The relative displacement $x - z$ along the straight segment is 0.02, which is the magnitude of the initial gap between the mass and the slider. This implies that the straight portion of the trajectory corresponds to the loading and unloading phases of the motion of the mass, while the loops correspond to the no contact phases of the motion. The three black diamonds are snapshots of the trajectory at each time periods of the dynamic forcing. The black diamond snapshot shown in Fig. 5b are the corresponding positions on the time histories where the Poincaré map were taken. As it can be seen from Fig. 5b the motion of the system is period–4 (i.e the motion repeats itself after every four time periods). However, this could not be

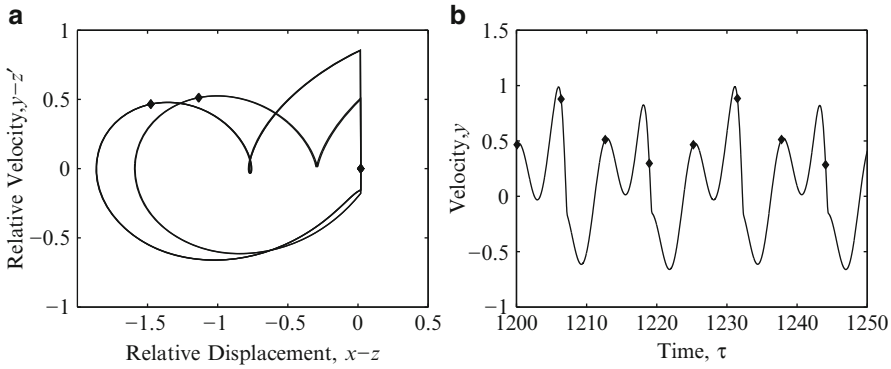

Fig. 5 (**a**) Trajectory of the conical impactor in the $(x - z, y - z')$ phase plane, and the Poincaré map. (**b**) Velocity y of the impactor as a function of time τ for $b = 0.1$

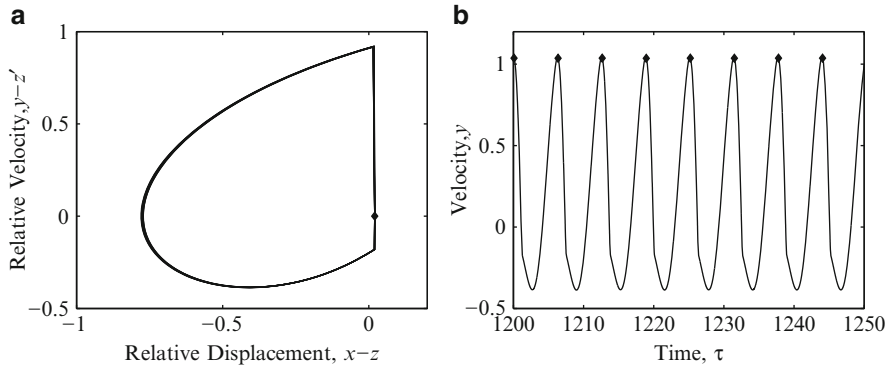

Fig. 6 (**a**) Trajectory of the conical impactor in the $(x - z, y - z')$ phase plane, and the Poincaré map. (**b**) Velocity y of the impactor as a function of time τ for $b = 0.2$

obtained on the phase plane trajectory shown in Fig. 5a because the relative velocity was plotted rather than the actual velocity, and there two snap shots appear as one when the relative velocity is zero. Figures 6a, b show the phase portraits and time dependence of the velocity of the mass, respectively, for $b = 0.2$. Here, the phase portrait, the velocity time history and the superimposed Poincaré map confirms a period–1 motion of the system.

4 Conclusions

In this work, the penetration of a conical impactor into an elasto-plastic solid has been investigated using a new model for the progression phase of a drifting impact oscillator. In our model, we assume a power–law relationship between the force

and penetration, with a power–law exponent which depends on the contact phase (loading or unloading).

These relationships were then used to develop a physical and mathematical model of a new drifting oscillator where the time histories of the progression through the medium include both the loading and unloading phases of the contact. The motion of the system was shown to consist of three phases: no contact, loading and unloading phases. The dynamic response of the system was calculated for a mass with a conical contacting surface.

The nonlinear dynamic analysis of the system was carried out, and it was found that the maximum progression occurs when the system exhibits periodic motion and the static load value is approximately 75% of the harmonic force amplitude. Past this critical value, the system tends to experience decreased progression because the mass is almost always in contact with the slider.

From the discussions on the results obtained from the nonlinear analysis of the new model presented here, it is expected that the design of vibro-impact systems could be optimised for enhanced performance. In addition, the model could also serve as a means of assessing the influence of the geometry of the impactor on the efficiency of the system.

References

Ajibose, O.K.: Nonlinear dyanmics and contact fracture mechanics of high frequency percussive drilling. PhD Thesis, University of Aberdeen, Aberdeen (2009)

Ajibose, O.K., Wiercigroch, M., Pavlovskaia, E., Akisanya, A.R.: Global and local dynamics of drifting oscillator for different contact force models. Int. J. Nonlinear Mech. **45**, 850–858 (2010)

Franca, L.F.P., Weber, H.I.: Experimental and numerical study of resonanance hammer drilling model with drift. Chaos Solitons Fractals **21**, 789–801 (2004)

Lee, E.H.: The impact of a mass striking a beam. J. Appl. Mech. **42**(E), 129–128 (1940)

Pavlovskaia, E., Wiercigroch, M.: Analytical drift reconstruction for visco-elastic impact oscillators operating in periodic and chaotic regimes. Chaos Solitons Fractals **19**, 151–161 (2004)

Pavlovskaia, E., Wiercigroch, M.: Low dimensional maps for piecewise smooth oscillators. J. Sound Vib. **305**, 750–771 (2007)

Pavlovskaia, E., Wiercigroch, M., Grebogi, C.: Modeling of an impact system with a drift. Phys. Rev. E **64**, 0562244 (2001)

Shivakumar, K.N.: Prediction of impact force due to low-velocity impact on circular composite laminates. J. Appl. Mech. **52**, 674–680 (1985)

Wu, K.Q., Yu, T.X.: Simple dynamic models of elastic-plastic structures under impact. Int. J. Impact Eng. **25**, 735–754 (2001)

Bit-Bounce and Stick-Slip in Drill-String Dynamics

K. Nandakumar, Marian Wiercigroch, and Chris Pearson

Abstract A recently proposed two degrees-of-freedom model for axial and torsional vibrations of drill-string elsewhere is here revisited. The model involves state-dependent time delay, with discontinuous cutting and friction force nonlinearities. The original model is, here, enhanced by introducing axial and torsional damping, and axial stiffness. Stability analysis, which is relatively recent for systems with state-dependent delays, is conducted on the enhanced model. For representative parameter values, it is concluded from the analysis that the original model (with no damping) had no stable operating regime, while the enhanced model possesses some practically relevant stable operating regime. The steady drilling state corresponding to the enhanced model is, however, still unstable for a major portion of the operating regime leading to stick-slip and bit-bounce situations.

Keywords Drill-string dynamics • Stick-slip • Axial and torsional damping • Delay differential equations

1 Introduction

Drill-string constitutes an important component in the rotary drilling equipment employed in oil and gas exploration (Spanos et al. 2003). Drill-strings primarily vibrate in axial, torsional and lateral modes, leading to axial – bit-bounce (Spanos et al. 1995), lateral – forward and backward whirl motions (Jansen 1991; Théron

K. Nandakumar (✉) • M. Wiercigroch
Centre for Applied Dynamics Research, University of Aberdeen, Aberdeen, Scotland, UK
e-mail: k.nandakumar@abdn.ac.uk; m.wiercigroch@abdn.ac.uk

C. Pearson
BG Energy Holdings Limited, Reading, Berkshire, UK
e-mail: Chris.Pearson@bg-group.com

M. Wiercigroch and G. Rega (eds.), *IUTAM Symposium on Nonlinear Dynamics for Advanced Technologies and Engineering Design*, IUTAM Bookseries (closed) 32, DOI 10.1007/978-94-007-5742-4_25,

et al. 1995), and torsional – stick-slip motions (Jansen and van den Steen 1995). The literature on drill-string vibrations is vast. In this paper, we restrict attention to the study of axial-torsional vibrations of the drill-string.

Stick-slip instabilities of the drill-string have been traditionally attributed to the drooping nature of the speed-dependent dry friction (Stribeck effect) at the bit-rock interface (Kyllingstad and Halsey 1987; Brett 1991; Challamel et al. 2000).

In contrast to these speed-dependent friction models, Richard et al. (2007) demonstrates stick-slip instabilities in a model with a constant friction coefficient, and traces the origin of stick-slip motion to the coupling between the axial and torsional motions at the bit-rock interface. In Richard et al. (2007) a two degree of freedom model for axial-torsional vibrations of drill-strings with drag bits is proposed. The model involves state-dependent delays arising due to the dependence of the instantaneous cutting forces on the history of the motion of the tool. It was shown in Richard et al. (2007), that the model exhibits stick-slip motions due to a combination of time-delay, and the coupling between the cutting and contact forces. The model of Richard et al. (2007) also exhibits bit-bounce for a vast operating regime. Indeed, the steady drilling solution is unstable, as will be shown here, for any operating weight on bit and rotary speed. It is important to note that this model neglected damping in axial and torsional motions. Also, the axial elasticity of the drill pipes is ignored in their model.

In this paper, we enhance the model of Richard et al. (2007) by incorporating axial and torsional damping. The axial compliance of the drillpipes is also accounted. In this context, we mention that in a recent work Besselink et al. (2011) a modification of the model presented in Richard et al. (2007) is proposed wherein axial stiffness of the drillpipes and axial damping are included. However, Besselink et al. (2011) still does not account for damping in the torsional direction. Also, the stability analysis decouples the axial and torsional dynamics by analysing a single delay differential equation.

Our model formulation leads to a system of state-dependent delay differential equations with discontinuous cutting and friction force nonlinearities. Subsequently, a detailed stability analysis, which was not attempted in Richard et al. (2007), of the ensuing state-dependent delay differential equations is conducted. Such stability analysis for state-dependent delay systems are relatively rare (Insperger et al. 2007). Linear stability analysis reveals the stable and unstable operating regimes in the weight on bit-rotary speed parameter plane. It is found that the addition of damping enhances stability for larger rotary table speeds.

2 Axial-Torsional Two Degrees-of-Freedom Model

A schematic of the model of Richard et al. (2007) is presented in Fig. 1 (left). In Richard et al. (2007), a two degree of freedom model (one-axial, and one-torsional) is proposed for the axial and torsional vibrations of drill-strings mounted with drag bits.

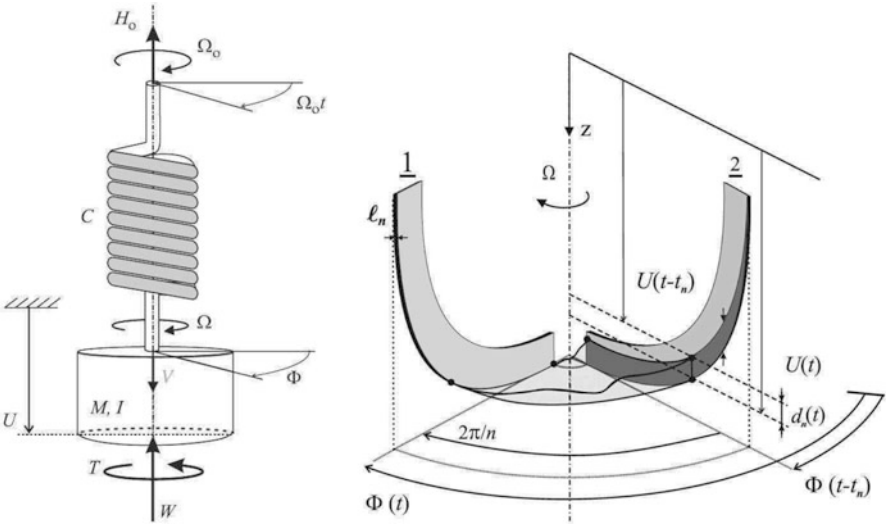

Fig. 1 A schematic of the axial torsional model (Adopted from Richard et al. (2007))

We present a brief description of the model here and refer the reader to Richard et al. (2007) for details. The torsional portion of the model idealizes the drill-string as a torsion pendulum. The combined rotational inertia of the BHA and drill-pipes, denoted by I, is lumped at the end of a torsion spring, of spring constant C, which represents the torsional rigidity of the drill-pipes. The top end of the torsion spring is assumed to rotate at a constant spin speed Ω_0. The rotation of the bottom end, connected to the rotational inertia, is measured by the angle Φ from a fixed reference. The torque-on-bit T arising due to the bit-rock interaction is applied to the rotational inertia.

The axial portion of the model idealizes the BHA and the drillstring as a single lumped mass M. The axial compliance of the drill-pipes is ignored in the model. A constant vertical hook load H_0 (which is directly related to the applied weight on bit W_0) is applied at the top of the mass M and the weight-on-bit W arising from the bit-rock interaction is applied on the mass as shown in Fig. 1.

Consider an idealized drag bit composed of n blades. Two blades are shown for clarity in Fig. 1 (right). Let U denote the axial position of the bit along the z direction as measured from a fixed reference. The total depth of cut per revolution for n blades is

$$d = n\,(U(t) - U(t - t_n)). \tag{1}$$

In the presence of torsional oscillations, the time delay t_n is state-dependent and is governed by

$$\Phi(t) - \Phi(t - t_n) = \frac{2\,\pi}{n}. \tag{2}$$

Thus the governing differential equations of the axial-torsional model of Richard et al. (2007) are

$$M\,\ddot{U} = W_0 - \left[\xi\, a\, \varepsilon\, d\;\; H(\dot{\Phi})\;\; H(d) + W_f\;\; H(d)\, H(\dot{U})\right], \tag{3}$$

$$I\,\ddot{\Phi} + C\,(\Phi - \Omega_0\, t) = -\left[\frac{a^2\,\varepsilon\, d}{2}\; H(d)\, H(\dot{\Phi}) + \frac{\mu\,\gamma\, a\, W_f}{2}\; H(d)\, sign(\dot{\Phi})\, H(\dot{U})\right], \tag{4}$$

where $H(.)$ is the Heaviside function and $sign(.)$ is the sign function. The applied weight on bit W_0 is a controlled parameter. The expressions for cutting and friction forces at bit involves: normal-contact force $W_f = \sigma\, a\, l$; bit parameters – a, γ, l; rock parameters: σ, ε; bit-rock interaction parameters: μ.

3 Modified Model

In this paper we enhance the model of Richard et al. (2007) by adding dissipation in the axial and torsional motions, and also add a spring in the axial direction to account for the compliance of the drill-pipes. The torsional portion of the model, with added viscous damping C_t, is shown in Fig. 2 (right). The axial portion, with added axial

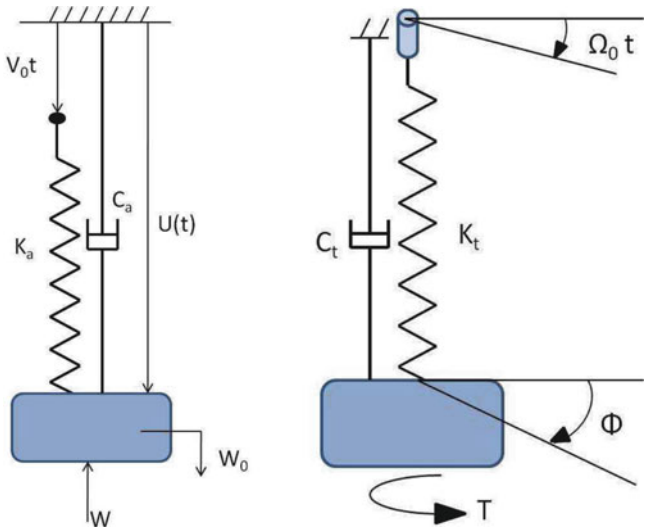

Fig. 2 *Left*: A schematic of the axial portion of the drillstring model with a lumped mass approximation for the BHA and a spring modeling the drill-pipes. *Right*: A schematic of the torsional portion of the model with a lumped inertia representing the BHA and a torsion spring modeling the drill-pipes. A constant rotary speed is assumed for the top end of the drill-pipe

stiffness K_a, is shown in Fig. 2 (left). The top end of the axial spring, of free length l_0, is assumed to descend at a constant velocity V_0. Axial viscous dissipation is accounted by C_a. We mention here that a constant hook load is used as the boundary condition at the top of the drill-pipes in Richard et al. (2007). However, a constant rate of hook could be a more appropriate boundary condition if the axial compliance effects of the drill pipes are to be accounted for. During steady drilling, however, the axial spring develops a constant deflection and in this situation, the constant hookload case (Richard et al. 2007) and the constant rate of penetration boundary condition are equivalent. In our model, when axial oscillations develop around steady drilling, the spring forces start fluctuating around the steady value thus leading to fluctuating hook loads. Such fluctuating hook loads are often observed in field situations whenever the drill-string undergoes axial vibrations. Thus the presence of an axial spring with a constant rate of descent of the top (as adopted in this paper) seems more closer to reality as opposed to the case of a constant hook load.

With these modifications, the equations of motion of the drilling system are:

$$\begin{aligned} &M\,\ddot{U} + C_a\,\dot{U} + K_a(U - V_0\,t - l_0) \\ &\quad = W_0 - \left[\xi\,a\,\varepsilon\,d\;\; H(\dot{\Phi})\;\; H(d) + W_f\;\; H(d)\,H(\dot{U})\right], \end{aligned} \tag{5}$$

$$I\,\ddot{\Phi} + C_t\,\dot{\Phi} + K_t\,(\Phi - \Omega_0\,t) = -\left[\frac{a^2\,\varepsilon\,d}{2}H(\dot{\Phi}) + \frac{\mu\,\gamma\,a\,W_f}{2}sign(\dot{\Phi})\,H(\dot{U})\right]H(d), \tag{6}$$

$$d = n\,(U(t) - U(t - t_n)), \tag{7}$$

$$\Phi(t) - \Phi(t - t_n) = \frac{2\,\pi}{n}. \tag{8}$$

3.1 Steady Drilling

Steady drilling state, whose stability we are interested in, corresponds to rotation of the drill bit at a constant rate Ω_0, and a constant axial penetration rate given by V_0. The depth of cut and, hence, the cutting forces and torques attain constant values. Denoting the steady state solutions with an overhat, we have:

$$V_0 = \frac{\Omega_0 \quad d_0}{2\,\pi}, d_0 = \frac{W_0 - \sigma\,a\,l}{\xi\,a\,\varepsilon + \frac{C_a\,\Omega_0}{2\,\pi}}, \quad \hat{U}(t) = V_0\,t + l_0\,. \tag{9}$$

Also,

$$\Phi_0 = -\left(\frac{a^2\,\varepsilon\,d_0 + \mu\,\gamma\,a^2\,\sigma\,l + 2\,C_t\,\Omega_0}{2\,K_t}\right), \quad \hat{\Phi} = \Omega_0\,t + \Phi_0, \quad \hat{t}_n = \frac{2\,\pi}{n\,\Omega_0}\,. \tag{10}$$

3.2 Perturbation, Non-dimensionalization, and Linearization

We introduce perturbations, which are small compared to the steady quantities, to the steady drilling solution as follows

$$U(t) = \hat{U}(t) + X(t), \tag{11}$$

$$\Phi(t) = \hat{\Phi}(t) + \phi(t), \tag{12}$$

$$t_n(t) = \hat{t}_n + S(t)\,. \tag{13}$$

The governing equations for small perturbations (ignoring the discontinuities) are

$$\begin{aligned} M\,\ddot{X} + C_a\,\dot{X} + K_a\,X \;&= -n\,\xi\,a\,\varepsilon\left[-\tfrac{V_0}{\Omega_0}\left\{\phi - \phi\left(t - \hat{t}_n - S\right)\right\}\right. \\ &\quad \left. +\ \left\{X - X\left(t - \hat{t}_n - S\right)\right\}\right], \end{aligned} \tag{14}$$

$$\begin{aligned} I\,\ddot{\phi} + C_t\,\dot{\phi} + K_t\,\phi \;&= -\frac{n\,a^2\,\varepsilon}{2}\left[-\tfrac{V_0}{\Omega_0}\left\{\phi - \phi\left(t - \hat{t}_n - S\right)\right\}\right. \\ &\quad \left. +\ \left\{X - X\left(t - \hat{t}_n - S\right)\right\}\right], \end{aligned} \tag{15}$$

The above equations are nonlinear due to the state-dependent nature of the delay.

In the lines of Richard et al. (2007), we introduce the following dimensionless variables and parameters:

$$\tilde{L} = \frac{2\,K_t}{\varepsilon\,a^2}, \qquad \psi = \frac{\xi\,a\,\varepsilon\,I}{M\,K_t}, \qquad x = \frac{X}{\tilde{L}}, \qquad \tau = \sqrt{\frac{K_t}{I}}\,t, \tag{16}$$

$$\delta_0 = \frac{d_0}{\tilde{L}}, \qquad \omega_0 = \frac{\Omega_0}{\sqrt{\frac{K_t}{I}}}, \qquad \nu_0 = \frac{\delta_0\,\omega_0}{2\,\pi}\,. \tag{17}$$

$$\zeta = \frac{C_a}{2\,\sqrt{K_a\,M}}, \qquad \kappa = \frac{C_t}{2\,\sqrt{K_t\,I}}, \qquad \beta = \frac{\sqrt{\frac{K_a}{M}}}{\sqrt{\frac{K_t}{I}}}, \tag{18}$$

$$s = \frac{S}{\sqrt{\frac{I}{K_t}}}, \qquad \hat{\tau} = \frac{\hat{t}_n}{\sqrt{\frac{I}{K_t}}} = \frac{2\,\pi}{n\,\omega_0}\,. \tag{19}$$

Note that ω_0 and ν_0, or equivalently, ω_0 and δ_0 are the non-dimensional operating control parameters.

Denoting τ-derivatives with overdots, the linearized, dimensionless equations are

$$\ddot{x} + 2\,\zeta\,\beta\,\dot{x} + \beta^2\,x = -n\,\psi\left[-\frac{\nu_0}{\omega_0}\left\{\phi - \phi\left(\tau - \hat{\tau}\right)\right\} + \left\{x - x\left(\tau - \hat{\tau}\right)\right\}\right], \tag{20}$$

$$\ddot{\phi} + 2\,\kappa\,\dot{\phi} + \phi = -n\left[-\frac{v_0}{\omega_0}\left\{\phi - \phi\left(\tau - \hat{\tau}\right)\right\} + \left\{x - x\left(\tau - \hat{\tau}\right)\right\}\right]. \quad (21)$$

Note that the linearization has resulted in equations with a *constant* delay as opposed to the state-dependent nature of the delay in the original system. The state-dependent nature of the delay in the original system, nevertheless, manifests in the above two equations through the first term in the right hand sides, which couples the axial and torsional degrees-of-freedom.

4 Linear Stability Analysis

We set $x = x_0\,e^{\lambda\,t}$ and $\phi = \phi_0\,e^{\lambda\,t}$ into Eqs. 20 through 21, and obtain the characteristic equation

$$\begin{aligned}(\lambda^2 + 2\,\zeta\,\beta\,\lambda + \beta^2)(\lambda^2 + 2\,\kappa\,\lambda + 1) - n\,v\left(1 - e^{-\frac{2\,\pi\,\lambda}{n\,\omega_0}}\right)(\lambda^2 + 2\,\zeta\,\beta\,\lambda + \beta^2)\\ + n\,\psi\left(1 - e^{-\frac{2\,\pi\,\lambda}{n\,\omega_0}}\right)(\lambda^2 + 2\,\kappa\,\lambda + 1) = 0, \end{aligned} \quad (22)$$

where we have $v = \frac{v_0}{\omega_0}$. On the stability boundaries we have $\lambda = i\,\omega$ with $\omega > 0$. After some routine manipulations, we get parametric equations for v and ω_0 governing the stability boundaries.

$$v = \frac{\left(\omega^4 - 2\,\omega^2 + 4\,\omega^2\kappa^2 + 1\right)\left(-\beta^4 - 2\,\beta^2 n\,\psi + 2\,n\,\psi\,\omega^2 + 2\,\beta^2\omega^2 - 4\,\zeta^2\beta^2\omega^2 - \omega^4\right)}{2\,n\,(\omega - 1)\,(\omega + 1)\left(\omega^4 - 2\,\beta^2\omega^2 + 4\,\zeta^2\beta^2\omega^2 + \beta^4\right)}, \quad (23)$$

$$\omega_0 = \frac{2\,\omega\,\pi}{n\,(2\,k\,\pi + \text{atan2}\,\{A(\omega), B(\omega)\})}, \qquad k = 0, 1, \cdots, \quad (24)$$

where $A(\omega)$ and $B(\omega)$ are lengthy expressions for sine and cosine functions, not provided here for brevity.

Since $v > 0$ and $\omega > 0$, we have the following range of ω to be considered for generating the stability charts

$$\omega \in (0, \min(\omega_1, 1)) \cup (\max(\omega_1, 1), \omega_2)\,,$$

where

$$\omega_1 = \sqrt{n\,\psi + \beta^2 - 2\,\zeta^2\beta^2 - \sqrt{n^2\psi^2 - 4\,\zeta^2\beta^2 n\,\psi - 4\,\zeta^2\beta^4 + 4\,\zeta^4\beta^4}} \quad (25)$$

$$\omega_2 = \sqrt{n\,\psi + \beta^2 - 2\,\zeta^2\beta^2 + \sqrt{n^2\psi^2 - 4\,\zeta^2\beta^2 n\,\psi - 4\,\zeta^2\beta^4 + 4\,\zeta^4\beta^4}}\,. \quad (26)$$

Table 1 List of parameter values for stability chart

Parameter	Symbol	Value	Units
Drillpipe axial stiffness	K_a	$7e5$	N/m
Drillpipe torsional stiffness	K_t	940	N m/rad
Vibrational mass	M	34,333	Kg
Vibrational mass moment of inertia	I	115.3	Kg m^2
Radius of bit	a	0.108	m
Wear flat length	l	0.0012	m
Rock specific strength	ε	60	MPa
Rock contact stress	σ	60	MPa
Coefficient of friction	μ	0.6	–
–	ξ	0.6	–
–	γ	1	–
Axial damping coefficient	ζ	0.01	–
Torsional damping coefficient	κ	0.01	–
Number of blades	n	4	–

4.1 Stability Chart

We provide stability charts for the set of parameters provided in Table 1. We vary ω over the permissible range of values and obtain v and ω_0. We finally convert the so-obtained v and ω_0 into dimensional forms (for practical utility) and plot the results.

For the case in hand, $\omega_1 = 1.5816$ and $\omega_2 = 10.6609$; thus we choose the limits of ω according to the previous section and plot the results. Two curves, one for each interval of ω, result for each value of k. A sample set of curves for various values of k and for each separate range of ω are plotted in Fig. 3. We have chosen to plot the effective weight on bit, which is the applied weight on bit less the wear flat reaction, along the Y axis. It is clear that negative Y values do not result in any penetration. The stable and unstable regions for the various lobes is determined by numerical study of the roots on either side of the lobes. The final stability chart, based on the lobes for all values of k, demarcating the stable and unstable regions is plotted in Fig. 4.

4.2 Some Numerical Results

To verify the conclusions of the stability analysis, we choose three representative parameters labelled 1–3 in Fig. 4. These parameters are

1. (200 rpm, 50 kN), 2. (250 rpm, 100 kN), 3. (80 rpm, 80 kN) .

For these parameters, Eqs. 5 through 8 are integrated numerically using a constant time-step Forward Euler scheme. The initial conditions are

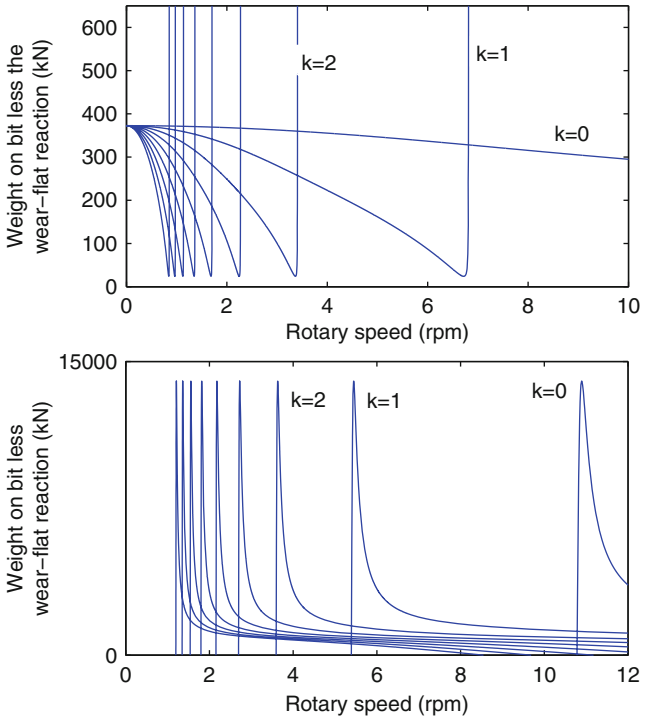

Fig. 3 Stability boundary curves for Eqs. 20 through 21. *Top*: $\omega \in (0, 1)$; *Bottom*: $\omega \in (\omega_1, \omega_2)$

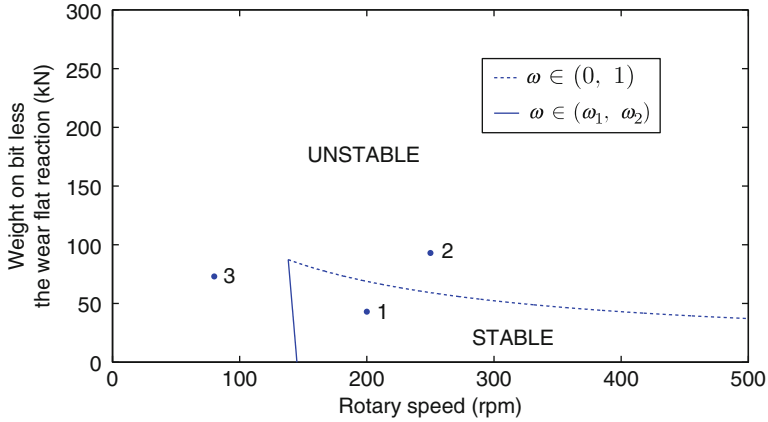

Fig. 4 Final stability boundaries for Eqs. 20 through 21 for the parameters of Table 1. Points labelled 1–3 are used for simulations (see text for details)

$$U = V_0\, t, \qquad \dot{U} = V_0, \qquad \Phi = \Phi_0 + \Omega_0\, t, \qquad \dot{\Phi} = \Omega_0, \qquad \forall t < 0, \tag{27}$$

$$U(0^+) = 0, \qquad \dot{U}(0^+) = V_0, \qquad \Phi(0^+) = \Phi_0, \qquad \dot{\Phi}(0^+) = 1.1\,\Omega_0\,. \tag{28}$$

From Fig. 5 it is clear that the stability of the steady drilling state as predicted by the stability chart is in accordance with direct numerical solutions, thus giving confidence on the stability analysis procedure. For example, the operating point 1 in Fig. 4 is predicted to be stable by our analysis, and the numerical integration results of Fig. 5a confirms that the steady drilling state is indeed stable for the perturbation introduced. The long term evolution of the solutions is out of the scope of the stability analysis, and may depend on the particular parameter values, initial conditions, and the nature of the nonlinearities. Thus although parameters labelled 2 and 3 in Fig. 4 represent unstable drilling, 2 corresponds stick-slip while 3 represents bit bouncing.

4.3 *Stability Chart for the Model of Richard et al. (2007)*

The model of Richard et al. (2007) is deduced as a special case of our model for $\kappa = \zeta = \beta = 0$. We plot in Fig. 6 the stability charts for three sets of parameters with progressively damping and axial stiffness (i.e., κ, ζ and β). It is seen from Fig. 6, that as the damping and stiffness are reduced, the extent of stable operating regime gets reduced. In the limiting case, the stability region degenerates to a straight line which starts at a point on the X axis and extends to ∞. To obtain this limit, we note that for the limiting case, from Eqs. 25 and 26, $\omega_1 = 0$ and $\omega_2 = \sqrt{2\,n\,\psi}$. Thus the range of variation of ω becomes $\omega \in (1, \sqrt{2\,n\,\psi})$. Also in the limiting situation $\kappa = \zeta = \beta = 0$ we have (from the characteristic equation: details omitted)

$$\cos\left(2\,\frac{\omega\,\pi}{n\,\omega_0}\right) = -1, \qquad \sin\left(2\,\frac{\omega\,\pi}{n\,\omega_0}\right) = 0\,.$$

Thus

$$\omega_0 = \frac{2\,\omega}{n},$$

which at $\omega = \omega_2$ yields

$$\omega_{0c} = 2\,\sqrt{\frac{2\,\psi}{n}}\,. \tag{29}$$

The stability chart in the limiting case to a portion of X axis starting at a speed, ω_{0c}, indicated by Eq. 29 and extending all the way upto ∞. The time-delay corresponding to this speed ω_{0c} is given by

$$\hat{\tau}_c = \frac{2\,\pi}{\omega_{0c}} = \frac{\pi}{\sqrt{2\,n\,\psi}}\,. \tag{30}$$

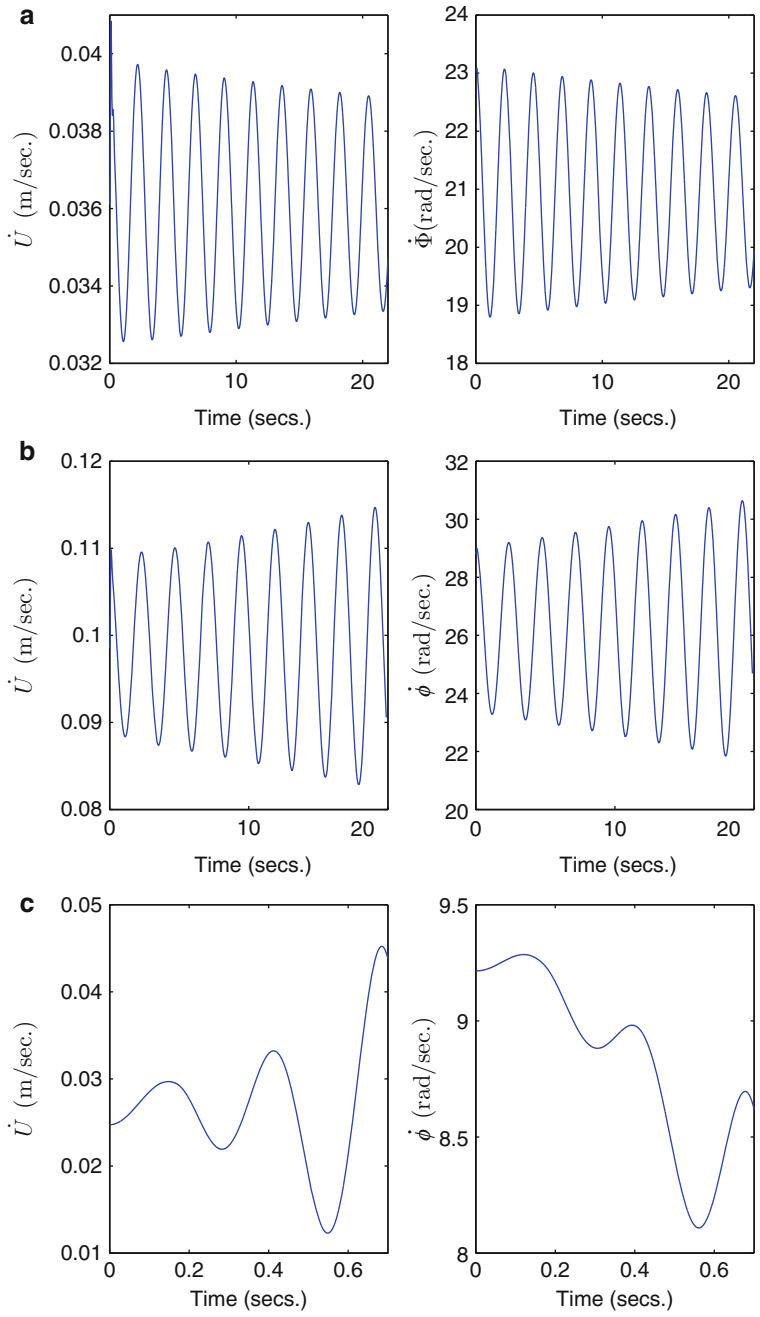

Fig. 5 Simulation results of Eqs. 5 through 8 with parameters from Table 1 with initial conditions as explained in text. The operating parameters are: (**a**) Stable operating point 1 (200 rpm, 50 kN) in Fig. 4. (**b**) Untable operating point 2 (250 rpm, 100 kN) in Fig. 4. (**c**) Stable operating point 1 (80 rpm, 80 kN) in Fig. 4

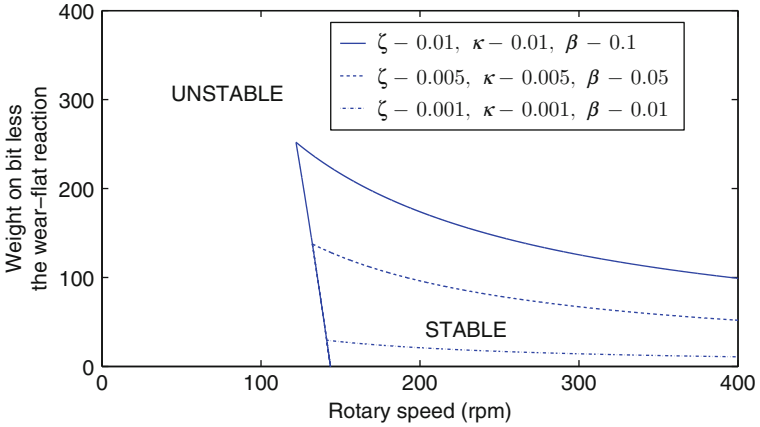

Fig. 6 Stability boundaries for Eqs. 20 through 21 for progressively decreasing axial damping (ζ), torsional damping (κ) damping and axial stiffness (β); The stability region is shrinking progressively and reaches the completely unstable limit for the model of Richard et al. (2007) for $\zeta = \kappa = \beta = 0$

For the parameters considered in Table 1, the critical speed (after converting to dimensional form) yields 143.7 rpm. This is also seen from Fig. 6 as the point corresponding to the point of intersection of the stability boundary with the X axis. It is interesting to note that the critical time-delay of Eq. 30 coincides with that of the analysis presented in Richard et al. (2007).

From the present analysis, it is clear that the stability in the limiting case is unrealistic as it requires no applied weight on bit and thus represents no penetration. For any non-zero weight on bit, and thus penetration, the steady drilling is unstable in the limiting case as the entire parameter plane represents unstable drilling regime.

5 Conclusions

We conclude our stability analysis of an enhanced two degree of freedom model for the axial and torsional vibrations of oilwell drillstrings. The model involves two coupled delay differential equations, with a state-dependent delay. The stability of the steady state drilling solution to infinitesimal perturbations is analyzed considering the coupled axial and torsional motions, unlike the uncoupled analysis of Richard et al. (2007). The predictions of stability charts are confirmed through direct numerical treatment of the original equations. The stability charts reveal that the addition of damping and axial stiffness renders the steady drilling stable for certain rotary speeds and weight on bit, while the model of Richard et al. (2007) predicts unstable drilling for the operating speed-weight on bit parameter regime.

Acknowledgements We thank the BG Group for financial assistance to carry out a research project on the modeling of drill-string dynamics of which this work forms a part. KN thanks Pankaj Wahi for technical discussions that gave initial directions to this work.

References

Besselink, B., van de Wouw, N., Nijmeijer, H.: A semi-analytical of stick-slip oscillations in drilling systems. ASME J. Comput. Nonlinear Dyn. **6**, 021006-1–021006-9 (2011)

Brett, J.F.: The genesis of torsional drillstring vibrations. Presented at the SPE/IADC Conference, Amsterdam SPE 21943 (1991)

Challamel, N., Sellami, H., Chenevez, E.: A stick-slip analysis based on rock/bit interaction: theoretical and experimental contribution. Presented at the SPE/IADC Conference, New Orleans, Louisiana IADC/SPE 59230 (2000)

Insperger, T., Stépán, G., Turi, J.: State-dependent delay in regenerative turning process. Nonlinear Dyn. **47**, 275–283 (2007)

Jansen, J.D.: Non-linear rotordynamics as applied to oilwell drillstring vibrations. J. Sound Vib. **147**(1), 115–135 (1991)

Jansen, J.D., van den Steen, L.: Active damping of self-excited torsional vibrations in oil well drillstrings. J. Sound Vib. **179**(4), 647–668 (1995)

Kyllingstad, Å., Halsey, G.W.: A study of slip/stick motion of the bit. Presented at the SPE Annual Technical Conference and Exhibition, Dallas SPE 16659 (1987)

Richard, T., Germay, C., Detournay, E.: A simplified model to explain the root cause of stick-slip vibrations in drilling systems with drag bits. J. Sound Vib. **305**, 432–456 (2007)

Spanos, P.D., Sengupta, A.K., Cunningham, R.A., et al.: Modeling of roller cone bit lift-off dynamics in rotary drilling. ASME J. Energy Resour. Technol. **117**, 197–207 (1995)

Spanos, P.D., Chevallier, A.M., Politis, N.P., et al.: Oil well drilling: a vibrations perspective. Shock Vib. Dig. **35**(2), 81–99 (2003)

Théron, A., de Langre, E., Putot, C.: The effect of dynamical parameters on precession in rotary drilling. ASME J. Energy Resour. Technol. **123**, 181–186 (1995)

Analysis of Stick-Slip Oscillations of Drill-String via Cosserat Rod Model

Marcos Silveira, Charles Wang, and Marian Wiercigroch

Abstract An integrated model for the study of the complex dynamical and geometrical behaviour of a drill-string is developed based on the modified Cosserat rod element method. The model includes general deformation of the rod with flexure, extension, torsion and shear, and allows analysis of the main vibration modes, torsional, axial and lateral, and also their couplings. Shape functions are obtained from the solution of nonlinear partial differential equations of motion in quasi-static sense, containing up to third order nonlinear terms, and the final ordinary differential equations of motion for the elements are derived from Lagrange's approach. Boundary conditions are taken as applied to a drill-string to account for the motor and the drill-bit. The model offers significant performance advantage over a standard Finite Element approach, which facilitates numerical analysis. Such model is capable of simulating stick-slip oscillations in the drill-bit–rock interface and contact of the drill-string with borehole wall along its length.

Keywords Drill-string • Stick-slip oscillations • Cosserat rod model

1 Introduction

Drilling a borehole for oil and gas extraction is done by means of rotary motion of a drill-bit against the rock. The rotary motion is transmitted to the bit from a motor, usually at the surface of the well, by the use of a drill-string. This drill-string is made of tube sections with threaded connections. It can reach lengths of various kilometers, making it a very slender structure. The lower part of the drill-string,

M. Silveira (✉) • C. Wang • M. Wiercigroch
Centre for Applied Dynamics Research, University of Aberdeen, Aberdeen, AB24 3UE, Scotland, UK
e-mail: m.silveira@abdn.ac.uk

M. Wiercigroch and G. Rega (eds.), *IUTAM Symposium on Nonlinear Dynamics for Advanced Technologies and Engineering Design*, IUTAM Bookseries (closed) 32, DOI 10.1007/978-94-007-5742-4_26,

comprised of drill-collars, stabilizers, vibration absorbers, MWD tools and the drill-bit is called the bottom-hole assembly (BHA). The drill-string vibrations can either be induced by drill-bit–formation and drill-string–bore-hole interactions, or be self induced (Spanos et al. 2003). The complexity of the drill-string dynamics comes in part from the coupling mechanisms. The drill-bit, which relates the axial force to torque, and the borehole are important players in these mechanisms. Low-dimensional models are useful tools to study separate modes and related phenomena, but in order to capture the full dynamics of the system a fully coupled nonlinear model needs to be employed. The model adopted in this study is based on the Cosserat theory of rods, from which a 3D rod element with general deformation including shear is developed (Cao et al. 2006; Wang et al. 2004; Liu et al. 2007).

2 Cosserat Rod

A slender structure in three dimensions is a body with high ratio of length to cross-sectional area. Such structures undergoing large displacements and rotations are often encountered in various engineering systems such as space structures, robotics, aircrafts, micro-electro-mechanical systems and even DNA strands. Nonlinear finite element method is suitable to model these structures, but its practical application is hampered by the large amount of elements needed because of the high frequency modes present, making such method computationally expensive. A new finite element method based on the Cosserat approach has been introduced in Cao et al. (2006), Wang et al. (2004) and Liu et al. (2007) giving an element (modified Cosserat rod element – MCRE) with general deformation, including shear.

By using the Cosserat theory, the equations of motion are nonlinear partial differential equations, which are functions of time and one space variable. For static problems, however, the equations become nonlinear ordinary differential equations, which can be solved approximately using standard techniques, like the perturbation method to satisfy boundary conditions. In contrast, for dynamical problems, it is necessary to introduce a numerical procedure which discretizes the equations.

The shear deformation may be of considerable importance and can not be negligible for studying the vibration of high frequencies when a dynamic rod is subdivided into comparatively short elements. In this study, the modelling strategy of a 3-D rod element with general deformation including shear, a modified Cosserat rod element (MCRE) is developed using the Cosserat theory. In this approach, the fundamental problem of any finite element formulation is the choice of the shape functions. The approximate solutions of the nonlinear equations of motion in a quasi-static sense are chosen as the shape functions with up to third order nonlinear terms of generic nodal displacements. In three dimensions, the nonlinear differential equations cannot be integrated in a close form even in the static sense, therefore the Frobeniu's method is employed here to solve the system approximately. This way the dynamics of the element is reliably defined through an action principle that guarantees basic conservation laws. Based on the Lagrangian constructed by

the Cosserat kinetic energy and strain energy expressions, the principle of virtual work is used to derive the ordinary differential equations of motion with third order nonlinear generic nodal displacements.

3 The Cosserat Rod and Its Directors

The motion of a nonlinear rod segment can be modelled as a Cosserat rod whose configuration is described by its neutral axis $r(s,t)$ (Cosserat curve) and three orthogonal unit vectors $d_i(s,t)$, $(i = 1,2,3)$ (Cosserat directors) where s, t denote a length parameter and time, respectively (see Fig. 1). At any time, r describes the axis of the rod whose cross-section orientations are determined by d_i such that $v_3 = \partial_s r \cdot d_3 > 0$. This condition implies that (I) the local ratio of deformed length to reference length of the axis cannot be reduced to zero since $|r_i| > 0$, and (II) a typical cross-section ($s = s_0$) cannot undergo a total shear in which the plane determined by d_1 and d_2 is tangent to the curve r at $r(s_0,t)$ (Antman 1995). In an inertial Cartesian basis e_1, e_2, e_3 and Newtonian time t, the Cosserat curve is defined as:

$$r(s,t) = r_i(s,t)e_i = x(s,t)e_1 + y(s,t)e_2 + z(s,t)e_3. \tag{1}$$

Let $d_i(s,t) = d_{ij}(s,t)e_j$ satisfying the orthogonality condition $d_{ik}d_{jk} = \delta_{ij}$. The motion involves both the velocity of the curve, $\partial_t r$, and angular velocity of the cross-sections, $w = w_i d_i$ so that $\partial_t d_i = w \times d_i$. The strains of the Cosserat rod

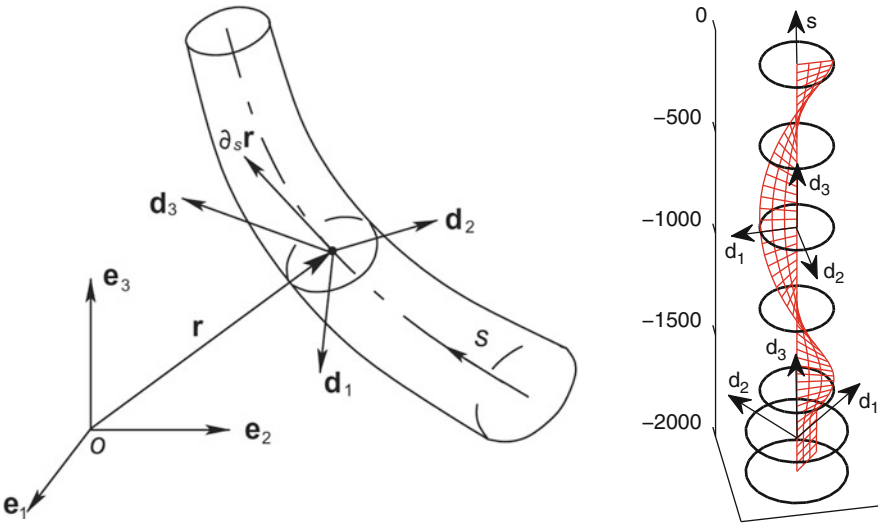

Fig. 1 A simple Cosserat rod described by its neutral axis $r(s,t)$ and three orthogonal unit vectors $d_i(s,t)$, $(i = 1,2,3)$ in an inertial Cartesian basis e_1, e_2, e_3 (**a**) and the model applied to a drill-string as shown from a snapshot of a stick-slip simulation (**b**)

are classified into 'linear strain' vector $v = \partial_s r = v_i d_i$ and 'angular strain' vector $u = u_i d_i$ so that $\partial_s d_i = u \times d_i$. The kinetic and strain energy expressions are used to construct the Lagrangian density that, through the variational principle with the action functional $S = \int L ds dt$, generates the dynamics of the Cosserat rod as follows (Wang et al. 2004; Liu et al. 2007):

$$\begin{cases} \rho A \partial_{tt} r = \partial_s n \\ \partial_t h = \partial_s m + \partial_s r \times n \end{cases} \tag{2}$$

where $h = I(w)$ is the angular momentum per unit length and $n = K(v - v_0)$ and $m = J(u - u_0)$ are contact force and moment densities, respectively.

The rotation matrix is chosen to be parameterised by the rotation vector, that is free of both singularities and constraints (Cao et al. 2006; Wang et al. 2004; Liu et al. 2007). Following this, the three directors $d_1(s,t)$, $d_2(s,t)$, $d_3(s,t)$ can be obtained by rotating Cartesian frame e_1, e_2, e_3 with rotation vector

$$\phi = \phi_x(s,t)e_1 + \phi_y(s,t)e_2 + \phi_z(s,t)e_3. \tag{3}$$

Assume the rod deformations are restricted in amplitude so that all nonlinearities can be expanded in Maclaurin's series. The directors $d_i(s,t)$ can be expanded up to third order in terms of ϕ_x, ϕ_y, ϕ_z.

4 Shape Functions for Modified Cosserat Rod Elements

For convenience, consider a uniform and initially straight rod element of constant length L, supported in an arbitrary manner at $s = a = 0$ and $s = b = L$. Assume that the static equilibrium of the rod corresponds to the situation where d_1, d_2 and d_3 are parallel to e_1, e_2 and e_3, respectively. The principal axes are chosen to parallel e_1, e_2 and e_3. For the sake of simplicity, it will be assumed that the axes along the directors d_1, d_2 and d_3 are chosen to be the principal axes of inertia of the cross section at s, and centered at the cross section's center of mass. Then, for a uniform rod with cross-section area $A(s)$, we have $J_{ij} = 0$, $I_{ij} = 0$ for $i \neq j$ Assume that the shape functions for a MCRE satisfy the corresponding static equations (2), i.e.

$$\begin{cases} \partial_s n(s) = 0 \\ \partial_s m(s) + v(s) \times n(s) = 0. \end{cases} \tag{4}$$

As a prelude to expanding the nonlinear shape functions to a form suitable for a perturbation analysis of the motion, it is useful to introduce some natural scales to obtain a dimensionless equation of motion. Introduce the dimensionless variables

$$\sigma = \tfrac{s}{L_0},\ \bar{r} = \tfrac{r}{L_0},\ \bar{x} = \tfrac{x}{L_0},\ \bar{y} = \tfrac{y}{L_0},\ \bar{z} = \tfrac{z}{L_0},\ \tau = \omega_0 t, \tag{5}$$

where L_0 and w_0 are the reference length and natural frequency yet to be determined later, respectively.

Assume that the dimensionless generic nodal displacements (boundary displacements and rotations) at $\sigma = 0$ and $\sigma = L/L_0$ are

$$q_a = \left[\varepsilon X_a \ \varepsilon Y_a \ \varepsilon Z_a \ \varepsilon \Phi_{xa} \ \varepsilon \Phi_{ya} \ \varepsilon \Phi_{za}\right]^T,$$
$$q_b = \left[\varepsilon X_b \ \varepsilon Y_b \ \varepsilon Z_b \ \varepsilon \Phi_{xb} \ \varepsilon \Phi_{yb} \ \varepsilon \Phi_{zb}\right]^T. \tag{6}$$

Substituting (6) into (1), we obtain the boundary conditions for $\bar{x}$, $\bar{y}$, $\bar{z}$, ϕ_x, ϕ_y and ϕ_z at $\sigma = 0$ and $\sigma = l$, where $l = L/L_0$ is the dimensionless length of the rod element. Treating ε as a perturbation parameter which is the order of the amplitude of the displacement, the shape functions can be obtained by solving the static equations (4) with the corresponding boundary conditions. To do this, we seek a straightforward expansion in x, y, z, ϕ_x, ϕ_y and ϕ_z of the form

$$\bar{x}(\sigma) = \varepsilon \hat{x}_1(\sigma) + \varepsilon^2 \hat{x}_2(\sigma) + \varepsilon^3 \hat{x}_3(\sigma) + \ldots, \tag{7}$$

Substituting (7) into (4) and, because $\hat{x}_i$, $\hat{y}_i$, $\hat{z}_i$ and $\hat{\phi}_{xi}$, $\hat{\phi}_{yi}$, $\hat{\phi}_{zi}$ are independent of ε, set the coefficient of each power of ε equal to zero. This leads to a set of linear ordinary differential equations which can be solved using the Frobeniu's method (Arfken 1985) under the corresponding boundary conditions. By solving (4), the approximate series solutions are obtained. All first orders terms are explicited in Liu et al. (2007). To investigate deflections up to third order nonlinearity in ε it is adequate to adopt the truncated (7) to ε^3 order terms.

5 Equations of Motion for Modified Cosserat Rod Elements

In this section, the Lagrangian approach is employed to formulate the ordinary differential equations of motion of the Cosserat rod elements. The generalized Hamilton's principle which, in its most general form, is given by the variational statement

$$\int_{t_1}^{t_2} \delta(T - V)\mathrm{d}t + \int_{t_1}^{t_2} \delta W \mathrm{d}t = 0, \tag{8}$$

where T is the total kinetic energy of the system, V is the potential energy of the system (including the strain energy and the potential energy of conservative external forces), δ represents the virtual displacement (or variational) operator, and δW is the virtual work done by nonconservative forces (including damping forces) and external forces not accounted for in V. The generalized displacement vector for the element can be described by

$$q^e(\tau) = \left[\, q_a^T(\tau) \ q_b^T(\tau) \,\right]^T. \tag{9}$$

Consistent with the kinematic and constitutive assumptions described in Cao et al. (2006), Wang et al. (2004) and Liu et al. (2007) and the shape functions derived previously, the kinetic energy per unit length is

$$T = \frac{1}{2}\rho A \partial_t r \cdot \partial_t r + I(w, w) = \frac{1}{2}\rho A \omega_0^2 L_0 \dot{\bar{r}} \cdot \dot{\bar{r}} + \omega_0^2 I(\bar{w}, \bar{w}) \tag{10}$$

where ρ and A are the density and the area of cross-section of the rod, respectively. Under small strain conditions the strain energy per unit length of rod can be expressed in terms of the strain vectors u and v as:

$$U = \frac{1}{2}J(u, u) + K(v - d_3, v - d_3) = \frac{1}{2}\frac{1}{L_0^2}J(\bar{u}, \bar{u}) + K(\bar{v} - \bar{d}_3, \bar{v} - \bar{d}_3) \tag{11}$$

Utilizing the time varying generic nodal displacements introduced in (9) instead of the static generic nodal displacements introduced in (6), the time varying generic displacements at any point within the element can be expressed as nonlinear functions of the length parameter σ and the nodal displacement vector $q^e(\tau)$.

To define the type of loading, let us assume that a load acting on the element is composed from three additive parts. The first one is the interaction of the neighbored elements f^{ie}. The second one is the external point (concentrated) loadings acting on the nodes f^{ce}. The last one represents a distributed load with fixed direction and prescribed intensity.

Same as done in Cao et al. (2006) and Liu et al. (2007), the generalized Lagrange equations of motion for the Cosserat rod element are:

$$\frac{\mathrm{d}}{\mathrm{d}\tau}\left(\frac{\partial L}{\partial \dot{q}_j}\right) - \frac{\partial L}{\partial q_j} = f_j^{ie}(\tau) + f_j^{ce}(\tau) + f_j^{de}(\tau, q^e). \tag{12}$$

For a general configuration with nonzero generic nodal displacements q^e, the ordinary differential equations of motion with up to third order nonlinearities of displacements and first order kinetic terms can be obtained as

$$M^e \ddot{q}^e + K^e q^e + g^e(q^e) = f^{ie}(\tau) + f^{ce}(\tau) + f^{de}(\tau, q^e), \tag{13}$$

where M^e and K^e are mass and (linear) stiffness matrices of the element model, $g^e(q^e)$ is a nonlinear vector with quadratic and cubic terms of q^e.

6 Boundary Conditions as Applied to a Drill-String

Boundary conditions for a drill-string are applied at the first node (top), where the motor and rotary table are, in this case, simulated with the imposition of a constant angular velocity Ω_1. This is achieved by eliminating the lines corresponding to lateral and axial degrees-of-freedom of the first node from the matrices in (13),

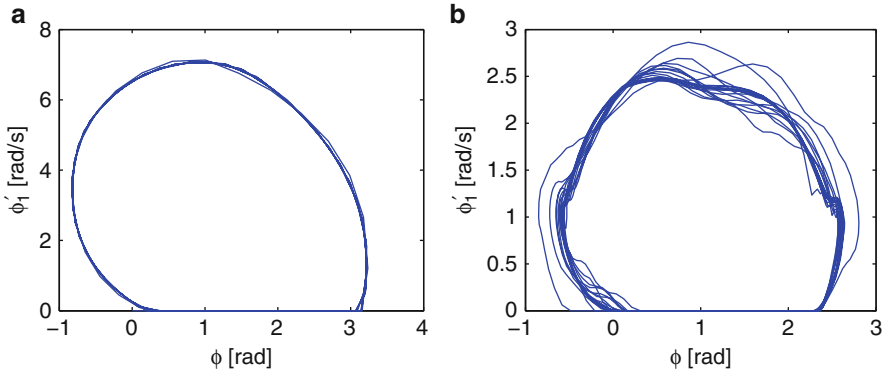

Fig. 2 Phase-plane of stick-slip vibrations of drill-string with length of 1,000 m (**a**) and 4,000 m (**b**), showing the deformations of the limit-cycle caused by higher order modes in the structure

leaving only possibility of rotational motion at this node. It is also possible to model the top drive as an electric motor coupled at the first node. The effect of damping of the drilling mud is included with a damping matrix D on the left hand side of (13).

Additionally, at the last node (bottom), a resisting torque is present following the friction torque characteristic as in Wang et al. (2004), in order to model the conditions experienced by the drill-bit. The torque-on-bit (T_b) is a friction law, a function that defines the resistive torque on the bit and models the interaction between the drill-bit and the rock. The simplest model for T_b is a piecewise Coulomb-like friction law (see Wiercigroch (1994); Galvanetto (2001)), with a value for static friction (T_{st}) and another, lower, value for sliding (or dynamic) friction (T_{sl}), which in this case is independent of the velocity. This effect is achieved by adding the sliding or sticking torque in the last element of f^{ce} in (13). The simulations have to tackle the problem in a piecewise manner, by separating the discontinuous phase space into a series of adjacent continuous regions. In the present case, two regions are necessary, one for the stick mode and one for the slip mode, with the stick region being a straight line. A switch function is used to perform the transitions from stick to slip modes, which is done by monitoring the velocity of the last node and the torque built in the drill-string to determine in which mode the system is. The simulations performed using the methodology described show the expected stick-slip oscillations of the bit. As is well known, the existence of stick-slip depends on a combination of torsional stiffness, angular velocity and damping effects. However, the simulations show that these oscillations excite higher torsional modes of the structure, causing deformations on the stick-slip limit-cycle and interfere in its stability, which can be seen in Fig. 2.

As is observed for lower order models aimed at studying stick-slip limit-cycles, this model also shows the limit cycle as it goes through a non-smooth fold bifurcation, ceasing to exist. This bifurcation is well known to occur in systems with the presence of stick-slip oscillations, when increasing the driving

velocity of the system. A point attractor co-exists at the centre of the stick-slip limit cycle, and its basin of attraction expands until it touches the limit cycle at the slip-to-stick transition point. When this occurs, the limit cycle is destroyed, meaning that there is no stick-slip oscillations. Apart from this wellknow destruction mechanism, the higher frequencies observed during the simulations could also cause the disappearence of the limit-cycle. Through a series of deformations, it can be observed that at some point the trajectory does not reach the sliding surface between the stick and slip motions, and therefore there is no stick-slip motion.

7 Conclusions

The modelling strategy with Cosserat rod element employs the exact nonlinear kinematic relationships in the sense of the Cosserat theory. The model accounts for finite displacements and rotations as well as finite extensional, torsional, bending strains, and shear deformation. The shape functions for MCREs are derived from the differential equations governing the non-planar flexural-torsional motion of extensional rods. Consequently, the higher accuracy of the dynamic responses can be achieved by dividing the rod into few elements, which is much less than the traditional finite element methods in which the interpolation functions are usually simple functions such as low order polynomials.

As an application of this model, a drill-string has been presented to illustrate the formulation procedure of the MCRE model. The comparison of MCRE model with classical beam theory has been carried out through the natural frequency analysis of the linearized equations and the numerical simulation of the nonlinear dynamic equations. Using appropriate boundary conditions and a piecewise approach, the model is able to simulate stick-slip oscillations.

References

Antman, S.S.: Nonlinear Problems of Elasticity. Applied Mathematical Sciences, vol. 107. Springer, New York (1995)

Arfken, G.: Mathematical Methods for Physicists. Academic, San Diego (1985)

Cao, D.Q., Liu, D., Wang, C.: Three dimensional nonlinear dynamics of slender structures: cosserat rod element approach. Int. J. Solid Struct. **43**, 760–783 (2006)

Galvanetto, U.: Some discontinuous bifurcations in a two-block stick-slip system. J. Sound Vib. **248**(4), 653–669 (2001)

Liu, D., Cao, D.Q., Rosing, R., Wang, C., Richardson, A.: Finite element formulation of slender structures with shear deformation based on the Cosserat theory. Int. J. Solid Struct. **44**, 7785–7802 (2007)

Silveira, M., Wiercigroch, M.: Low dimensional models for stick-slip vibrations of drill-strings. J. Phys. Conf. Ser. **181**, 012056 (2009)

Spanos, P.D., Chevallier, A.M., Politis, N.P., Payne, M.L.: Oil well drilling: a vibrations perspective. Shock Vib. Dig. **35**(2), 81–99 (2003)

Wang, C., Liu, D., Rosing, R., Richardson, A., Masi, B.D.: Construction of nonlinear dynamic MEMS component models using Cosserat theory. Analog Integr. Circuit Signal Process. **40**, 117–130 (2004)

Wiercigroch, M.: A note on the switch function for the stick-slip phenomenon. J. Sound Vib. **175**(5), 700–704 (1994)

Mechanical Oscillator in a Magnetic Field

J.-H. Ho, Ko-Choong Woo, V.C.-C. Lee, and Y.A. Abakr

Abstract An analytical solution for a system exhibiting oscillations of a conductor in magnetic field which is controlled by a discrete waveform is developed by means of multiple scales. The solution provides a guideline to design an effective control strategy so as to guide the system to a desirable attractor. Initial tests were also conducted to investigate the effect of hydrodynamic forces on an inertia excited by this mechanism.

Keywords Mechanical oscillator • Electromagnetic • Impact • Hydrodynamic

1 Introduction

A new electro-vibro-impact system (Nguyen et al. 2008), as shown in Fig. 1, has been studied experimentally (Nguyen and Woo 2008) and through numerical analysis (Ho et al. 2011). The system involves the use of a solenoid driven by a RLC circuit, coupled with a solid state relay (SSRL), to generate large electro-magnetic forces acting on a conductor, which oscillates within the solenoid. Impacts are generated by means of a stop in the path of bar oscillations. The forward progression of the device can then be generated. Experimental studies (Nguyen and Woo 2008) have shown that the performance of the device is closely related to the control frequency of the SSRL. This piece of work describes the approximate analysis of the electro-vibro-impact system without impacts by means of multiple scales.

The steady state response of the metal bar, in terms of oscillations is described. This solution is expressed in terms of system and circuit parameters. In this way, a large amplitude and high frequency of oscillations may be prescribed by an

J.-H. Ho • K.-C. Woo (✉) • V.C.-C. Lee • Y.A. Abakr
Department of Mechanical, Materials and Manufacturing Engineering, University of Nottingham Malaysia Campus, 43500 Semenyih, Selangor Darul Ehsan, Malaysia

M. Wiercigroch and G. Rega (eds.), *IUTAM Symposium on Nonlinear Dynamics for Advanced Technologies and Engineering Design*, IUTAM Bookseries (closed) 32, DOI 10.1007/978-94-007-5742-4_27,

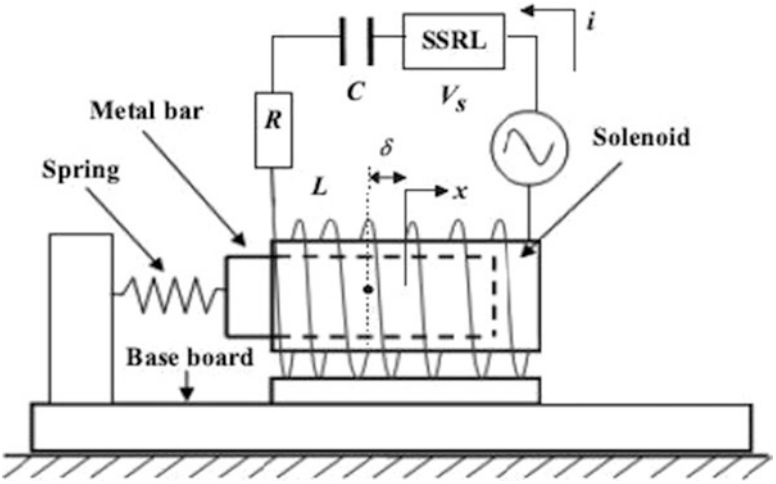

Fig. 1 New electro-vibro-impact system (Nguyen et al. 2008)

appropriate selection of mass, spring stiffness and electrical parameters, the latter of which may be varied in real time to maintain a certain dynamical response. While it would have been ideal to obtain a solution to a system with impacts, the strong system nonlinearity associated with hard impacts requires an analytical method alternative to that of multiple scales. With the present solution, the dependence of oscillatory amplitude and frequency on system characteristics is explicitly described. It would then be possible, in future work, to deduce this relationship for the case of impacts and forward progression. A detailed understanding of the system dynamics is required in order to design a feedback control system to achieve better progression rate. For investigate the effect of hydrodynamic forces, optimization of vibro-impact mechanism requires a mathematical model, which incorporates effects of excess water for cooling purposes. Mathematical description of hydrodynamics forces is possible, as demonstrated by the analysis of ship heave and roll by Thompson and De Souza (1996). The investigation of heave can be traced to the work of Ursell (1949) from a fundamental point of view. An application to marine engineering, Ellermann et al. (2003) had been approached with continuation methods and multiple scale analysis. A two-dimensional boundary-integral approach to ship hulls had been reported by Kral et al. (2003). This nonlinear function needs to describe characteristics in a vertical downward direction, and yet at the same time, should represent adequately the nature of hydrodynamic forces. A parameter identification procedure based on the approach of Jaksic et al. (2008) computes unknown coefficients of nonlinear restoring forces. An experimental rig has been constructed to mimic vibro-impact oscillator operating in a borehole filled

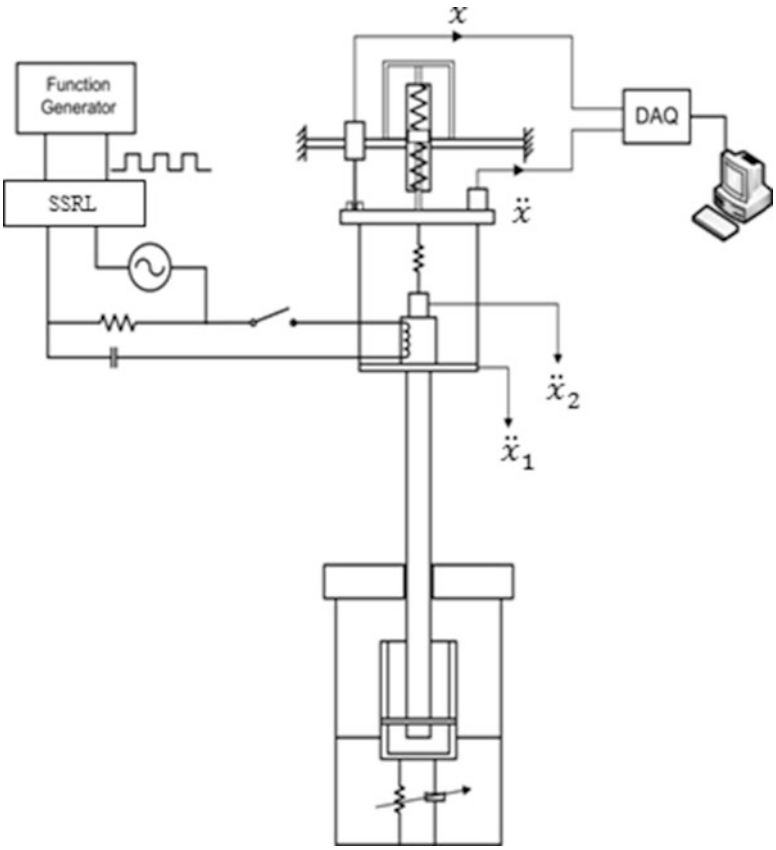

Fig. 2 Schematic of the experimental setup

with water. Of particular interest is the possibility of chaotic motion, which had previously been observed in ships by Lin and Yim (1995). It is also known that control of chaos is possible, as reported by Chacon (1846) and Kapitaniak (1994). The physical system is depicted in Fig. 1 and a schematic of the experimental setup is shown in Fig. 2.

The rig consists of two parts which is the oscillatory component and the acrylic cylinder containing water. The oscillatory component consists of three parts namely; electromechanical device mounted on a frame, and linked to the cylinder partially submerged in water by means of a connecting rod. The upper connection between the support and connecting rod is attached by means of force fit connection with tolerance of 1 μm. The lower connection between the connecting rod and the cylinder is secured by means of bolts and nuts.

2 Mathematical Model

In consideration of Newtonian mechanics, which, in an electromechanical system, is dependent on current fluctuation and resulting magnetic electromotive force, an equation of motion and current equation may be written as follows:

$$\ddot{x} + 2\xi\omega_n\dot{x} + {\omega_n}^2 (x - \delta) = \frac{1}{2}\frac{1}{m}\frac{\partial L}{\partial x} i^2 \tag{1}$$

$$L\frac{d^2 i}{dt^2} + \left[R + 2\frac{\partial L}{\partial x}\dot{x}\right]\frac{di}{dt} + \left[\frac{1}{C} + \frac{\partial^2 L}{\partial x^2}\dot{x}^2 + \frac{\partial L}{\partial x}\ddot{x}\right] i = \Omega V_s P_{ctr} \cos(\Omega t) \tag{2}$$

where dot denotes differentiation with respect to time t, x is the displacement of the metal bar, ξ is the damping ratio, ω_n is the natural frequency of the metal bar and the spring, δ is the initial displacement of the metal bar, m is the mass of the metal bar, L is the inductance function in the RLC circuit, I is the current flow through the circuit, R and C are the resistance and the capacitance in the RLC circuit respectively, V_s is the externally supplied time dependent voltage and Ω is the frequency of the power supply. The control waveform sent to a solid state relay is a square wave of frequency ω_c., $P_{c\tau\gamma}$ is the factor of control frequency which is given by the following expression

$$P_{ctr} = \begin{cases} 1, \; if \; \tau \left(\mathrm{mod}\frac{2\pi}{\omega_c}\right) < \frac{\pi}{\omega_c} \\ 0, \qquad otherwise \end{cases}.$$

To obtain an approximate analytical solution to the system equations, further information pertaining to inductance and discontinuous function is required. Experimental measurement of the inductance and subsequent approximation by a polynomial function is necessary for the multiple scales perturbation method to be made possible. Being a discontinuous function, $P_{c\tau\gamma}$ may be expanded in a Fourier series. Defining a parameter, ε, to describe small terms, it is then possible to state the range of oscillatory displacement, less than which system characteristics are weakly nonlinear. Since the electromagnetic forces increase with displacement, larger oscillations experience greater electromagnetic restoring forces. In the domain of weak nonlinearity, it is important to specify that the obtained analytical solution describes small oscillations where the metal bar is placed close to the centre of the solenoid. The obtained solution expresses the bar displacement retaining the first two terms in descending magnitude.

$$x(t, \varepsilon) = x_0(T_0, T_1) + \varepsilon x_1(T_0, T_1) + \ldots \tag{3}$$

Two cases were studied here, namely non-resonant and superharmonic resonance. In the non-resonant case, whereby ω_c and Ω are away from ω_n, the solution

to x_0 was found to decay exponentially, which an oscillatory description to x_1 had an amplitude expressed as a function of supplied voltage, solenoid inductance, circuit capacitance and resistance, as well as power supply frequency. This steady state solution $(x_1(T_0, T_1))$ is a periodic function consisting of frequencies of 2Ω, ω_c, $2\omega_c$, $3\omega_c$, $4\omega_c$, $6\omega_c$, $2\Omega \pm \omega_c$, $2\Omega \pm \omega_c$, $2\Omega \pm 3\omega_c$, $2\Omega \pm 4\omega_c$ and $2\Omega \pm 6\omega_c$.

In the second case, a superharmonic resonance was considered, whereby ω_c is close to $\frac{1}{2}\omega_n$ and Ω is away from ω_n, the solution x_0 was found to oscillate with the natural frequency, ω_n. To express the closeness of ω_c to $\frac{1}{2}\omega_n$, a detuning parameter, η, was introduced, whereby $2\omega_c = \omega_n + \varepsilon\eta$. Setting up the condition for secular terms, two differential equations containing the amplitude, a, and phase, β, of x_0 can be obtained. Steady state solution to x_0 can be solved by setting α' and β' to zero. Solution to x_1 contain 45 other combination frequencies, all amplitudes are small except for the terms involving ω_c. As a result, period 2 motion was observed with dominant frequencies of ω_c and ω_n.

To understand the effect of hydrodynamic forces, the nonlinear restoring forces are described in a cubic way.

$$m\ddot{x} + c_d\dot{x} + kx + \mu x^3 = 0 \tag{4}$$

where m denotes mass of experimental rig, c_d is a combined damping of both mechanical spring and water, and μ is an unknown coefficient which needs to be determined. Its value determines the strength of the nonlinearity from hydrodynamic forces.

For the case of a weak nonlinearity, an analytical solution can be found using the strained coordinates (Nayfeh 2000) by means of a series. Based on principles of perturbation methods, this approach yields convergent solutions for slight nonlinearities. However, the convergence may be elusive due to the large nonlinearity of water.

Hence, a numerical iteration solution is necessary so that parameters are computed by means of a least squares fit of chi-squared merit function. The chi-squared merit function written as:

$$\chi^2 = \left(\sum_{i=1}^{n} \ddot{x}_i + C_1\dot{x}_i + K_1 x_i + K_2 {x_i}^3\right)^2 \tag{5}$$

where $C_1 = \frac{c_d}{m}$, $K_1 = \frac{k}{m}$ and $K_2 = \frac{\mu}{m}$.

Curve fitting is performed in Matlab software and the predicted values are verified by generating system response to check with experimental observation. For purposes of comparison, the nonlinearity μ is estimated by numerical algorithm based on k and c_d values from analytical solution.

3 Approximate Analytical Solution

A non-dimensionalised form of the equations was derived.

$$\begin{aligned}\bar{x}'' + 2\xi\bar{x}' + \bar{x} - 1 = {} & \left(\bar{L}_a + \bar{L}_b\bar{x}\right)\bar{i}^2 \\ & \left(1 + \bar{L}_a\bar{x} + \frac{\bar{L}_b}{2}\bar{x}^2\right)\bar{i}'' + \left(\bar{R} + 2\bar{L}_a\bar{x}' + 2\bar{L}_b\bar{x}\bar{x}'\right)\bar{i}' \\ & + \left(\bar{C} + \bar{L}_b\bar{x}'^2 + \left(\bar{L}_a + \bar{L}_b\right)\bar{x}''\right)\bar{i} = \bar{V}_s\bar{P}_{ctr}\cos\left(\bar{\Omega}\tau\right)\end{aligned} \tag{6}$$

where

$$\bar{P}_{ctr} = \begin{cases} 1, \; if \; \tau \left(\mathrm{mod}\frac{2\pi}{\bar{\omega}_c}\right) < \frac{\pi}{\bar{\omega}_c} \\ 0, \qquad otherwise \end{cases}.$$

This discontinuous function was expanded in a Taylor series and two terms were retained.

$$\bar{P}_{ctr} = \frac{1}{2}\left[\frac{4}{\pi}\left(\sin\left(\bar{\omega}_c\tau\right) + \frac{\sin\left(3\bar{\omega}_c\tau\right)}{3}\right) + 1\right].$$

For small oscillations, a smallness of the inductance and damping were described by a minute parameter, ε.

$$\varepsilon\bar{l}_a = \bar{L}_a; \quad \varepsilon\bar{l}_b = \bar{L}_b; \quad \varepsilon\bar{\xi} = 2\xi\omega_n$$

Different time scales are introduced by

$$T_n = \varepsilon_n\tau \quad \text{for} \quad n = 0,\ 1,\ 2\cdots$$

For example, a first term of solutions for bar displacement and current flow are written as

$$\bar{x}_0\left(T_0, T_1\right) = A_0\left(T_1\right)e^{iT_0} + \bar{A}_0\left(T_1\right)e^{-iT_0} + 1 \tag{7}$$

by comparison of like terms of ε. A_0 and B_0 are complex functions and $\bar{A}_0$ is the complex conjugate of A_0.

4 Results and Discussion

To verify the approximate solution obtained from multiple scale analysis, a linear variable displacement transducer (LVDT, RS model 646-460) was used to measure the displacement of the metal bar oscillations. The following parameters were used

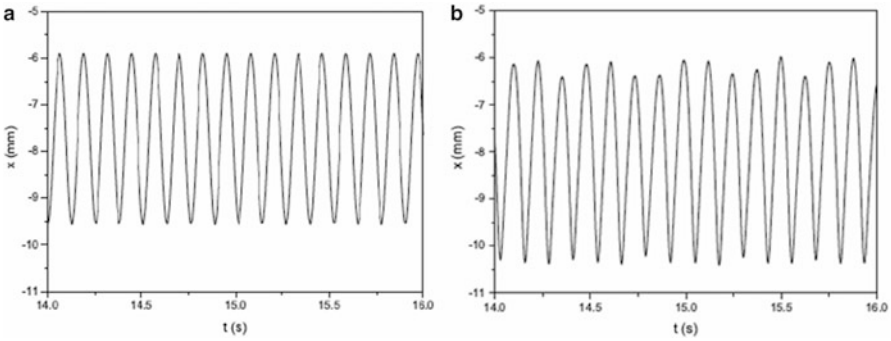

Fig. 3 (**a**) The experimental result of the metal bar displacement and (**b**) the approximate displacement function obtained from multiple scales analysis. The SSRL control frequency was set at 49.51 rad/s (7.88 Hz)

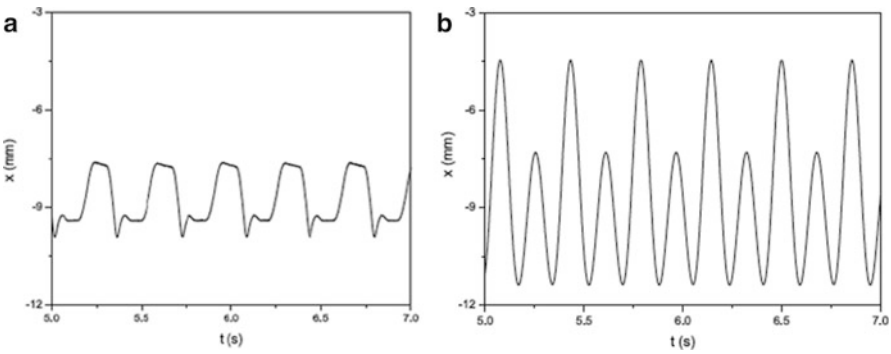

Fig. 4 (**a**) The experimental result of the metal bar displacement and (**b**) the approximate displacement function obtained from multiple scales analysis. The SSRL control frequency was set at 17.66 rad/s (2.81 Hz)

in the experiment: $V_s = 56.57$ V, $m = 0.975$ kg, $k = 1{,}243$ N/m, $\Omega = 314.16$ rad/s (50 Hz), $C = 30\ \mu$ F, $R = 22\ \Omega$ and $\omega_n = 35.71$ rad/s (5.68 Hz). In this first case, period 1 motion was observed with $\omega_c = 49.51$ rad/s (7.88 Hz) and $\delta = -0.0094$ m. The experimental result and the approximate solution were showed in Fig. 3a, b respectively. Results showed close co-relationship in both amplitude and frequency with some offset value. In the second case, experimental results showed that there are some discrepancies in amplitude, but period 2 motion can be observed with $\omega_c = 17.66$ rad/s (2.81 Hz) and $\delta = -0.0094$ m. This is shown in Figs. 3 and 4.

A numerical computation was performed with Fluent software (ANSYS, Inc 2006) to gain insight to the behaviour of water under the influence of a descending inertia, so that pressure and velocity profiles may be predicted with a variation of depth and time. Computation of the fluid dynamics allows for visualisation of water movement at different instants in time (Figs. 5 and 6).

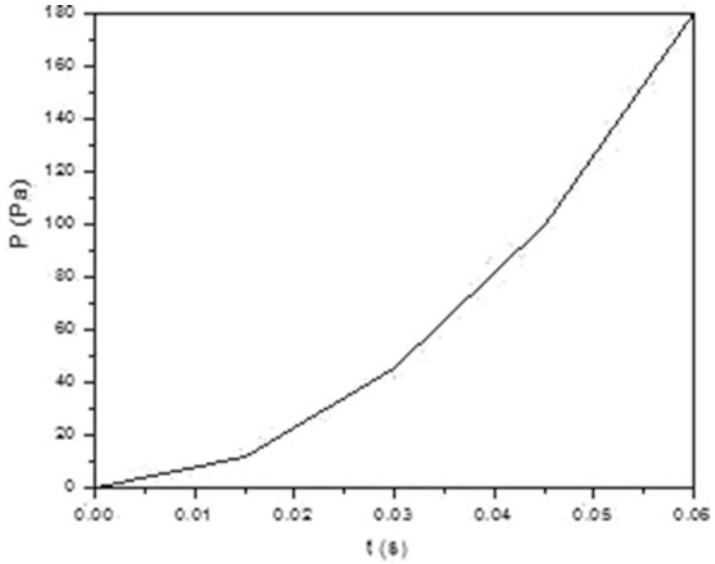

Fig. 5 Plot of dynamic pressure of water plotted against time

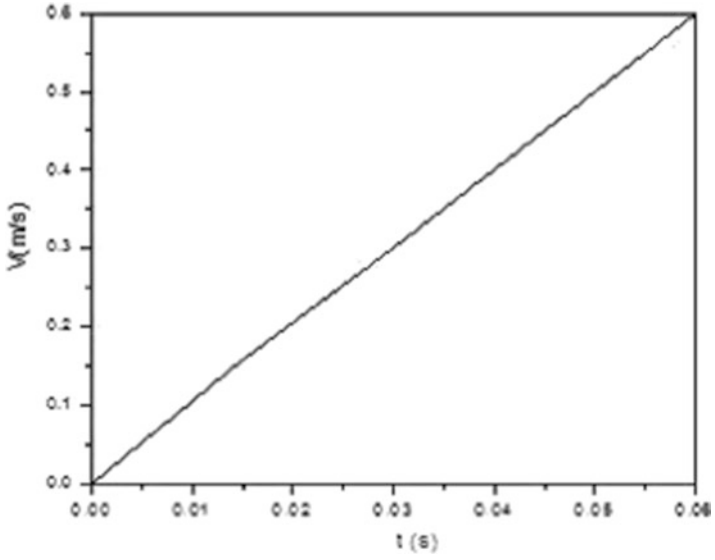

Fig. 6 Plot of velocity magnitude of water plotted against time

The analytical solution for the system with no water returns c_d and k of 4.893 Ns/m and 1,680.288 N/m. By applying a numerical method, μ is estimated numerically program to be 0.163 N/m^3 with chi-squared merit function error of 2.187×10^{-7}. From the numerical iteration, c_d is found to be 4.902 Ns/m, $k = 1{,}673.828$ N/m and $\mu = 0.0863$ N/m^3. The chi-merit function error is $9, 476 \times 10^{-9}$.

Table 1 Parameters of system with no water

Parameter	Analytical solution	Numerical solution	Combination
Damping c_d (Ns/m)	4.893	4.902	4.893
Stiffness k (N/m)	1,680.288	1,673.828	1,680.288
Nonlinear stiffness μ (N/m^3)	Not available	0.0863	0.1626
Chi-squared merit function error (N)	Not available	9.476×10^{-9}	2.187×10^{-7}

Table 2 Parameters of water damped system

Parameter	Analytical solution	Numerical solution	Combination
Damping c_d (Ns/m)	13.267	12.988	13.267
Stiffness k (N/m)	1,318.273	1,259.766	1,318.273
Nonlinear Stiffness μ (N/m^3)	Not available	0.163	4.893
Chi-squared merit function error (N)	Not available	1.7456×10^{-10}	1.496×10^{-6}

Displacement and velocity responses of the estimated parameter are plotted by 4th order Runge Kutta method using Matlab, using an adaptive step size and a tolerance of 1e-6 in both absolute and relative terms (Tables 1 and 2).

Based on a computation of fluid dynamics, an approximate tendency of hydrodynamic resistance to vary with respect to downward displacement in the manner of a polynomial has been observed, and a cubic form of nonlinearity has been a subject of parameter identification. Convergence of numerical algorithm has been achieved by implementing a bisection method to avoid divergence as reported by Martinez (1994). Selection of algorithm formulation had been based on a recommendation by Hirsch et al. (2009). The unknown damping, linear stiffness and nonlinear coefficients have been calculated to a high precision. Comparison of numerically integrated time history without forcing based on identified parameter values compares favourably with transient responses observed in a laboratory.

5 Results and Discussion

An approximate analytical solution to a system exhibiting oscillations of a conductor in magnetic field which is controlled by a discrete waveform is sought by means of multiple scales. The solution provides a guideline to design an effective control strategy so as to guide the system to a desirable attractor. Initial tests were also conducted to investigate the effect of hydrodynamic forces on an inertia excited by this mechanism. Results from the studies show that nonlinearity of a vibro-impact oscillator is mainly contributed by nonlinear restoring forces in water instead of other factors such as springs and stiffness of air. Similar situation applies to the real moling machine where the borehole created accumulates water. By using the

procedure developed, nonlinearity in actual system can be quantified. The estimated values of damping and nonlinearity in a water-damped system are significantly larger than in the case of no water.

Acknowledgments The funding from the University of Nottingham Malaysia Campus for Jee-Hou Ho, as well as that from the National Science Foundation of Malaysia for Vincent Lee, are gratefully acknowledged. Thanks are due to Wen-Jia Khoo for his contributions in programming numerical procedures.

References

ANSYS, Inc.: Fluent 6.3. Canonsburg, PA (2006)

Chacón, R.: Melnikov method approach to control of homoclinic/heteroclinic chaos by weak harmonic excitations. Phil. Trans. R. Soc. A **364**(1846), 2335–2351 (2006)

Ellermann, K., Kreuzer, E., Markiewicz, M.: Nonlinear primary resonances of a floating cranes. Mecc. Int. J. Theor. Appl. Mech. **38**, 5–19 (2003)

Hirsch, M.J., Pardalos, P.M., Resende, M.G.C.: Solving systems of nonlinear equations with continuous GRASP. Nonlinear Anal. Real World Appl. **10**(4), 2000–2006 (2009)

Ho, J.H., Nguyen, V.D., Woo, K.C.: Nonlinear dynamics and chaos of new electro-vibro-impact system. Nonlinear Dyn. **63**, 35–49 (2011)

Jaksic, N., Foong, C.-H., Wiercigroch, M., Boltezar, M.: Parameter identification of the fatigue-testing rig. J. Mech. Sci. **50**(7), 1142–1152 (2008)

Kapitaniak, T.: Synchronisation of chaos using continuous control. Phys. Rev. E. **50**, 1642–1644 (1994)

Kral, R., Kreuzer, E., Schlegel, V.: Elasto-dynamics of multihulls in nonlinear beam seas – a multibody – BEM approach. J. Fluids Struct. **17**(6), 875–885 (2003)

Lin, H., Yim, S.C.S.: Chaotic roll motion and capsize of ships under periodic excitation with random noise. Appl. Ocean Res. **17**(3), 185–204 (1995)

Martinez, J.M.: Algorithms for solving nonlinear systems of equations. In: Continuous Optimization: State of Arts, pp. 81–108 (1994)

Nayfeh, A.H.: Perturbation Methods. Wiley, New York (2000)

Nguyen, V.-D., Woo, K.-C.: New electro-vibro-impact system. Proc. Inst. Mech. Eng. Part C J. Mech. Eng. Sci. **222**(C4), 629–642 (2008)

Nguyen, V.-D., Woo, K.-C., Pavlovskaiia, E.: Experiment study and mathematical modelling of a new of vibro-impact moling device. Int. J. Non-Linear Mech. **43**, 542–550 (2008)

Thompson, J.M.T., De Souza, J.R.: Suppression of escape by resonant modal interactions: in shell vibration and heave-roll capsize. Proc. R. Soc. Lond. Part A Math. Phys. Eng. Sci. **452**, 2527–2550 (1996)

Ursell, F.: On a heaving motion of a circular cylinder on the surface of a fluid. Q. J. Mech. Appl. Math. **2**(2), 218–231 (1949)

Part IV
Nonlinear Control of Engineering Systems

Control of Intrinsic Localized Mode in Coupled Cantilever Array

Masayuki Kimura and Takashi Hikihara

Abstract Intrinsic localized mode (ILM) in coupled oscillators is one of nonlinear modes, which show the temporally periodic and spatially localized characteristics. Since the theoretical discovery of the mode, the existence of ILM has been confirmed in many system including biological molecular chains, 1D material structure, and MEMS. In the paper, we are going to discuss control of ILM in a coupled cantilever array.

Keywords Coupled cantilever array • Intrinsic localized mode • Global dynamics and control

1 Introduction

1.1 Background

Coupled vibrators or resonators are considered as a simple model to describe mechanical structure and material science. The spatio-temporal phenomena of the distributed system are also analyzed by coupled lattice of oscillators. Those are the thermal propagation, acoustic waves, electromagnetic field, and so on. In 1988, Takeno and Sievers theoretically found an intrinsic localized mode (ILM) in the discrete lattice structures through the analysis for the anharmonic resonant

M. Kimura
The University of Shiga Prefecture, 2500 Hassaka-cho, Hikone, Shiga 522-8533, Japan
e-mail: kimura.m@e.usp.ac.jp

T. Hikihara (✉)
Kyoto University, Katsura, Nishikyo-ku, Kyoto 615-8510, Japan
e-mail: hikihara@kuee.kyoto-u.ac.jp

M. Wiercigroch and G. Rega (eds.), *IUTAM Symposium on Nonlinear Dynamics for Advanced Technologies and Engineering Design*, IUTAM Bookseries (closed) 32, DOI 10.1007/978-94-007-5742-4_28,

modes in perfect crystal (Sievers and Takeno 1988; Takeno and Sievers 1988). The localized mode is a typical nonlinear mode in the discrete system related to breather in continuous systems. The mode is temporally periodic and spatially localized waves. Since the discovery, the localized mode has attracted many researchers. General features such as the existence, the stability, and the movability have been investigated both theoretically and numerically (Flach and Willis 1998). In addition, the number of experimental studies increases in this decade. The localized mode is experimentally generated or observed in various systems, for instance, Josephson-junction array (Trías et al. 2000; Binder et al. 2000; Ustinov 2003), optic wave guides (Eisenberg et al. 1998; Morandotti et al. 1999), micro-mechanical oscillators (Sato et al. 2003a), and electronic circuits (Sato et al. 2007). These experiments directly suggest us the phenomenological universality of ILM and the possible application phase. In fact, there appear the studies toward future applications both in fundamental science and in practical engineering (Campbell et al. 2004).

Observation of ILM in micro-cantilever arrays is first reported by Sato et al. (2003a,b). They used a well-designed micro-cantilever array which is fabricated by micro-electromechanical system (MEMS) technology. In the tiny cantilever array, ILM not only stands at a certain site but also wanders in the array. This implies that ILM can be manipulated without decaying of the energy concentration. In fact, it has been reported that ILM can be manipulated by a locally added impurity (Sato et al. 2004, 2006). Since cantilever structure is widely used in MEMS devices (Waggoner and Craighead 2007), these experimental results in micro-meter scale suggest the possibility of a micro-/nano-device using energy localization phenomena. Obviously, establishing control method for ILM is imperative to realize such applications. Therefore, the global dynamics of traveling ILMs should be investigated as well as the local dynamics of standing ILMs.

The global dynamics of traveling wave was investigated with the phase structure around standing waves in a coupled magneto-elastic beam system which is qualitatively similar to the micro-cantilever array (Hikihara et al. 1997, 2001a,b). It is revealed that there coexists several standing waves and the phase structure around them governs the onset behavior of traveling waves. Since ILM can be thought of as a standing wave, the global dynamics for ILM can be investigated with the same manner. In this paper, we will first discuss the relationship between the phase structure and the global behavior of traveling ILM. Then a method for manipulating ILM is proposed based on structure of phase space. In addition, another method is shown in experiments.

1.2 Intrinsic Localized Mode

Intrinsic localized modes are roughly classified into two kinds, “Sievers-Takeno mode (ST-mode)” and “Page mode (P-mode)” (Flach and Gorbach 2005) when the energy is concentrated at only a few sites. ST-mode has an odd-symmetry in its amplitude distribution as shown in Fig. 1a. On the other hand, two neighboring

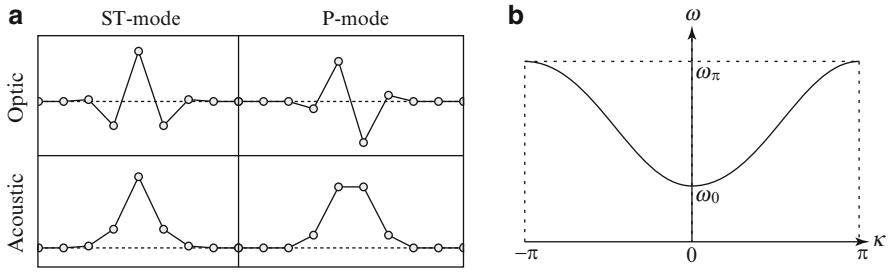

Fig. 1 Sievers-Takeno (*ST*) mode and Page (*P*) mode for both optic and acoustic ILMs (Flach and Gorbach 2008) and dispersion relation for $\ddot{u}_n = -\omega_0^2 u_n + C(2u_n - u_{n+1} - u_{n-1})$. ω_0 and $\omega_\pi = \sqrt{\omega_0^2 + 4C}$ represent the *lower* and the *upper* bound of frequency, respectively. (**a**) Spatial symmetry. (**b**) Dispersion curve

oscillators have the same amplitude for P-mode. That is, ST-mode stands on a site whereas P-mode is centered between sites. In addition, ILM is called *optic/acoustic* ILM when oscillators move in *anti-*/ *in*-phase (Campbell et al. 2004). For coupled cantilever arrays, all cantilevers obey the linear ordinary differential equation, $\ddot{u}_n = -\omega_0^2 u_n + C(2u_n - u_{n+1} - u_{n-1})$ while the amplitude is sufficiently small. The linear ODE leads a dispersion relationship, namely, a band shown in Fig. 1b. If a nonlinear lattice allows ILM to exist, optic/acoustic one appears above/below the band.

2 Coexistence and Stability

2.1 Coupled Cantilever Array

Intrinsic localized modes were observed in the micro-cantilever array which is fabricated by using photolithography technology (Sato et al. 2003a). The micro-cantilever array consists of a thin SiN_x film, which forms cantilevers and overhang, and a thick Si support. Here we assume that each cantilever has the same length to one another for simplicity. The overhang provides the coupling between neighboring cantilevers by bending itself. The size of the array is determined as followed in Sato et al. (2003b).

The vibration of cantilever is described by a partial differential equation. Since the cantilever is thin, Euler-Bernoulli beam theory can be applied to obtain the resonant frequencies and shape functions of the cantilever. The lowest resonant frequency corresponds to the first mode oscillation of cantilever. Because the micro-cantilever array is excited near the lowest frequency (Sato et al. 2003b), we only focus on the first mode oscillation. The shape function of the first mode shows the maximum amplitude at the free end of cantilever. Here we describe the motion of the tip of cantilever by a simple spring-mass model which has the same resonant frequency as the original cantilever.

The nonlinearity of cantilever is arisen by more precise analysis. On the basis of the theoretical analyses (Crespo da Silva and Glynn 1978; Crespo da Silva 1988; Malatkar and Nayfeh 2003), the cantilever tends to be hard as the deformation increases. This hardening nonlinearity is arisen from geometric nonlinearity. The hardening nonlinearity, which appears as a cubic term in the restoring force, has already been confirmed by experimental analyses (Sato et al. 2006; Malatkar and Nayfeh 2003). Therefore the cantilever is depicted by a spring-mass system with cubic nonlinearity in the spring. The coupling force caused by the overhang is modeled by the same way (Sato et al. 2006). The difference in displacements of neighboring cantilevers causes the deformation of the overhang region. The restoring force also has a cubic nonlinearity (Sato et al. 2006). Consequently, the motion of the micro-cantilever array is depicted by

$$\begin{aligned}\ddot{u}_n = &-\alpha_1 u_n - \alpha_2 \Big\{ (u_n - u_{n-1}) + (u_n - u_{n+1}) \Big\} \\ &-\beta_1 u_n^3 - \beta_2 \Big\{ (u_n - u_{n-1})^3 + (u_n - u_{n+1})^3 \Big\}, \end{aligned} \tag{1}$$

where u_n represents the displacement at the free end of nth cantilever. The first and third terms represent the restoring force caused by bending each cantilever with coefficients, α_1 and β_1. The second and fourth terms with α_2 and β_2 describe the nonlinear coupling force. Since the equation of motion has no term of $\dot{u}_n$ in the right-hand side, the total energy

$$H = \sum_{n=1}^{N} \left\{ \frac{1}{2}\dot{u}_n^2 + \frac{\alpha_1}{2}u_n^2 + \frac{\beta_1}{4}u_n^4 + \frac{\alpha_2}{2}(u_n - u_{n-1})^2 + \frac{\beta_2}{4}(u_n - u_{n-1})^4 \right\} \tag{2}$$

is conserved.

The equation of motion is nondimensionalized by scaling with appropriate unit time and length. The unit time is chosen so that α_1 is 1. The unit length is set to let β_1 be 0.01. Consequently, α_2 and β_2 are determined to respectively be 0.1 and 0.001 by using values regarding the micro-cantilever array (e.g. material constants, size of the array) in Sato et al. (2003b). This means that the linear and nonlinear coupling coefficients are uniquely determined by the design of cantilever array. This paper thus investigates ILMs for various value of the coupling coefficients, especially β_2.

2.2 Coexistence

Intrinsic localized modes what we focused on are temporally periodic solutions in Eq. (1). The periodic solutions can be treated as fixed points on a hyper surface in the phase space. Let Σ_p be a hyper surface defined by

$$\Sigma_p = \left\{ (\mathbf{u}, \dot{\mathbf{u}}) \in \mathbb{R}^{16} \mid u_p > 0, \dot{u}_p = 0 \right\}, \tag{3}$$

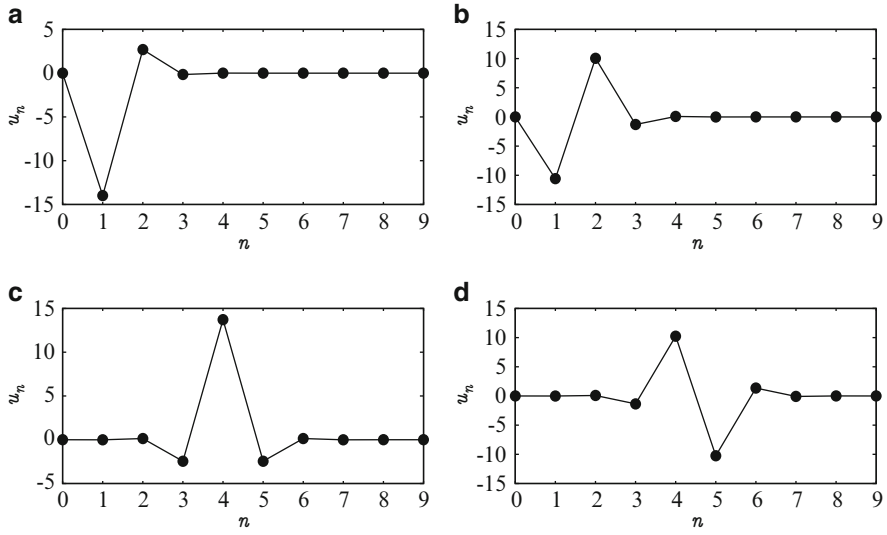

Fig. 2 Coexisting ILMs at $\alpha_1 = 1$, $\alpha_2 = 0.1$, $\beta_1 = 0.01$, and $\beta_2 = 0.001$. (**a**) ST1. (**b**) P1-2. (**c**) ST4. (**d**) P4-5

where p is the index of cantilever and is set at 4. An ILM corresponds to a fixed point $\mathbf{x}^* \in \Sigma_p$ for the Poincaré map $P : \Sigma_p \to \Sigma_p$. According to the Floquet theory, the stability of the ILM is equivalent to that of the corresponding fixed point. The stability of $\mathbf{x}^*$ can be investigated with eigenvalues of the matrix DP which is obtained by linearizing P around $\mathbf{x}^*$. If one of the eigenvalues is located outside unit circle on complex plane, the ILM is *unstable* solution in Eq. (1). Since Eq. (1) is a Hamiltonian system, the ILM is determined not to be unstable if and only if all the eigenvalues are on unit circle. It is called *marginally stable* or simply *stable* (Flach and Gorbach 2005).

By using the anticontinuous limit (Marín and Aubry 1996), several ILMs are obtained in the coupled cantilever array at which the boundaries are fixed and parameters are set at $N = 8$, $\alpha_2 = 0.1$, $\beta_2 = 0.001$, and $H = 250$. Some of the obtained ILMs are shown in Fig. 2. ILMs shown in Fig. 2a, c correspond to ST-mode. They are obtained by initial guesses that only one cantilever is excited. P-modes are shown in Fig. 2b, d. The initial guesses for P-modes are that two neighboring cantilevers are excited in anti-phase.

Coexisting ILMs in the cantilever array can be distinguished by the index number of cantilevers which have large amplitude. In this paper, the ST-mode standing at m-th site is called STm. For example, ST4 corresponds to the ST-mode centered on the 4th cantilever as shown in Fig. 2c. The P-mode is depicted Pm-m' with $m' = m + 1$, because the P-mode has even symmetry in amplitude distribution. The locus of the P-mode is found at $m + 1/2$.

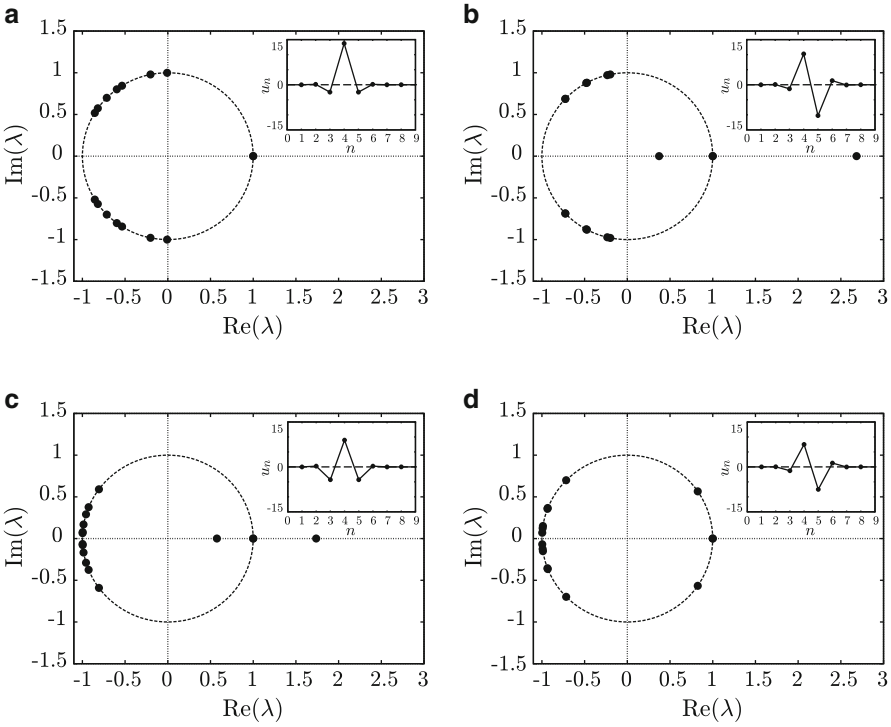

Fig. 3 Floquet multipliers of ST4 and P4-5 for $\beta_2 = 0.001$ and 0.01. The *circle* drawn by *dashed curve* indicates unit circle in complex plane. Insets show the corresponding ILMs. (**a**) ST4 at $\beta_2 = 0.001$. (**b**) P4-5 at $\beta_2 = 0.001$. (**c**) ST4 at $\beta_2 = 0.01$. (**d**) P4-5 at $\beta_2 = 0.01$

2.3 Stability

The stability of ILM generally depends on the symmetry of amplitude distribution in space (Flach and Willis 1998). As mentioned in the previous section, coexisting ILMs in the coupled cantilever array are classified into two kinds. Generally, one is stable if the other is unstable and *vise versa*. Floquet multipliers of ST4 and P4-5 at $\beta_2 = 0.001$ are shown in Fig. 3a, b, respectively. All the multipliers for ST4 are on unit circle. ST4 is thus stable. On the other hand, P4-5 is unstable because one of the multipliers is outside unit circle as shown in Fig. 3b. For the other coexisting ILMs, P-modes are unstable while ST-modes are stable. The relationship between the stability and the spatial symmetry is the same as that of nonlinear Klein-Gordon lattices (Flach and Willis 1998). Therefore, in terms of the stability of ILM, the coupled cantilever array at $\beta_2 = 0.001$ is similar to the nonlinear KG lattices.

However the relationship between the stability and the spatial symmetry is changed for $\beta_2 = 0.01$. Figure 3c shows the Floquet multipliers of ST4. One of

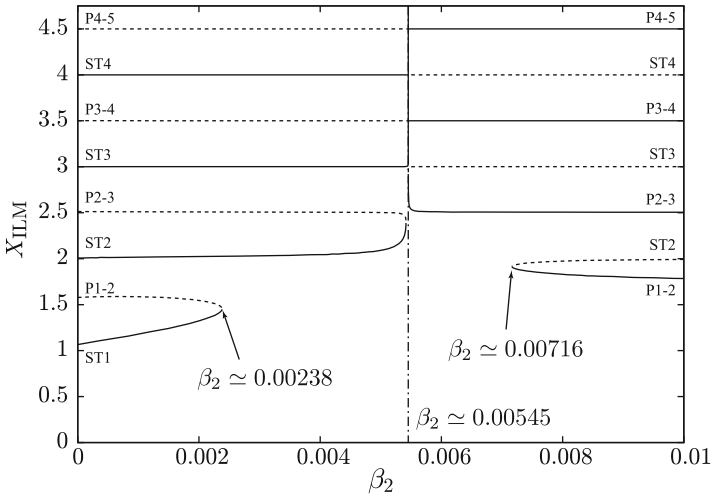

Fig. 4 Locus and stability of coexisting ILMs. *Solid curve* corresponds to stable ILMs. Unstable ILMs are represented by *dashed curve*

the multipliers is clearly located outside unit circle. In the case of $\beta_2 = 0.01$ all coexisting ST-modes are unstable. The stability of P-modes is also flipped. All the Floquet multipliers of P4-5 are on unit circle as shown in Fig. 3d. Such stable P-modes are also observed in Fermi-Pasta-Ulam (FPU) lattices (Sandusky et al. 1992), while ST-modes are unstable. Thus, the cantilever array at $\beta_2 = 0.01$ is similar to the FPU lattices in terms of the stability of ILM.

In the coupled cantilever array, the ratio between on-site and inter-site nonlinearity depends on the design of the array. The ratio determines whether the cantilever array is similar the nonlinear KG lattice or the FPU lattice. Since the stability of ILM is different between nonlinear KG and FPU lattice, the stability of ST- and P-modes is exchanged between $\beta_2 = 0.001$ and 0.01. It implies that local bifurcations are caused by varying the nonlinear inter-site coefficient β_2 with fixing the nonlinear on-site coefficient β_1.

The locus and the stability of coexisting ILMs are shown with respect to β_2 in Fig. 4, where the total energy H is kept at 250 and the locus is obtained by $X_{\mathrm{ILM}} = \sum_{n=1}^{8} n|u_n| / \sum_{n=1}^{8} |u_n|$ (Zueco et al. 2005). The figure clearly shows how the stability of coexisting ILMs is flipped with the change of the nonlinear inter-site coefficient. ILMs standing around the center of array almost simultaneously gain or lose stability at $\beta_2 \simeq 0.00545$.

On the other hand, ST1 coincides with P1-2 at $\beta_2 \simeq 0.00238$ and disappears with increment of β_2. The disappeared P1-2 appears again with ST2 at $\beta_2 \simeq 0.00716$. That is, a wide parameter gap exists near the end of array. The wide parameter gap is caused with the fixed end because it vanishes in the ringed array (Kimura and Hikihara 2008).

The almost simultaneous stability change implies that a drastic change of global phase structure is also caused. If the traveling ILM is governed by the global phase structure, it can be controlled by varying β_2. In the next section, a manipulation using the stability change is discussed after the relationship between the global phase structure and traveling ILMs is investigated.

3 Control for ILM

3.1 Invariant Manifolds of Standing ILMs

Invariant manifolds are globally extended in the phase space. Then the phase space and the configuration space are not suitable for discussing the global structure of coupled cantilever array. Hence a projection $G : \Sigma_p \to \mathbb{C}$ is introduced to extract the position of ILM in the array. The projection G is the inner product of the energy distribution of ILM and the sinusoidal wave whose wave number is unity in the array (Houle 1997). Therefore, the phase of $G(\mathbf{x}_k)$, namely $\theta_k = \arg G(\mathbf{x}_k)$, in complex plane reveals the locus of the energy distribution, where $\mathbf{x}_k$ and k are an ILM solution and the number of the Poincaré map iterations, respectively. For the case of coexisting ILMs, the phase corresponds to the center of ILM. In addition, the velocity of an traveling ILM can be estimate from the differences between θ_k and θ_{k+1}, namely, $\Delta\theta_k = \theta_{k+1} - \theta_k$ (Houle 1997).

In the previous section, it was revealed that the stability of coexisting ILMs is flipped by the nonlinear inter-site coefficient β_2. Structures of unstable manifolds in phase space also depend on β_2. Figure 5a, b show structures of unstable manifolds at $\beta_2 = 0.005$ and 0.006. As mentioned in the previous section, the stability change occurs between $\beta_2 = 0.005$ and 0.006.

For $\beta_2 = 0.005$, the structure connecting the vicinities of unstable P-modes are observed. The right branch of W^u(P3-4) reaches the vicinity of P4-5 as shown in Fig. 5a. The unstable manifold returns to the vicinity of P3-4 again (see the inset

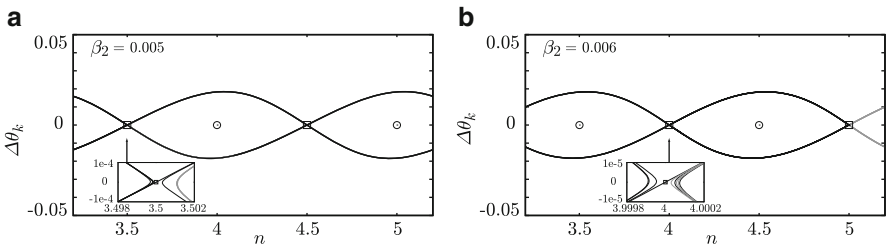

Fig. 5 Coexisting ILMs and unstable manifolds at $\beta_2 = 0.005$ and 0.006. Structure of the vicinity of an unstable ILM is shown in the insets. Although unstable manifolds are located very close to each unstable ILM, any homo- or heteroclinic connection cannot be observed for $\beta_2 = 0.005$ and 0.006. (**a**) $\beta_2 = 0.005$. (**b**) $\beta_2 = 0.006$

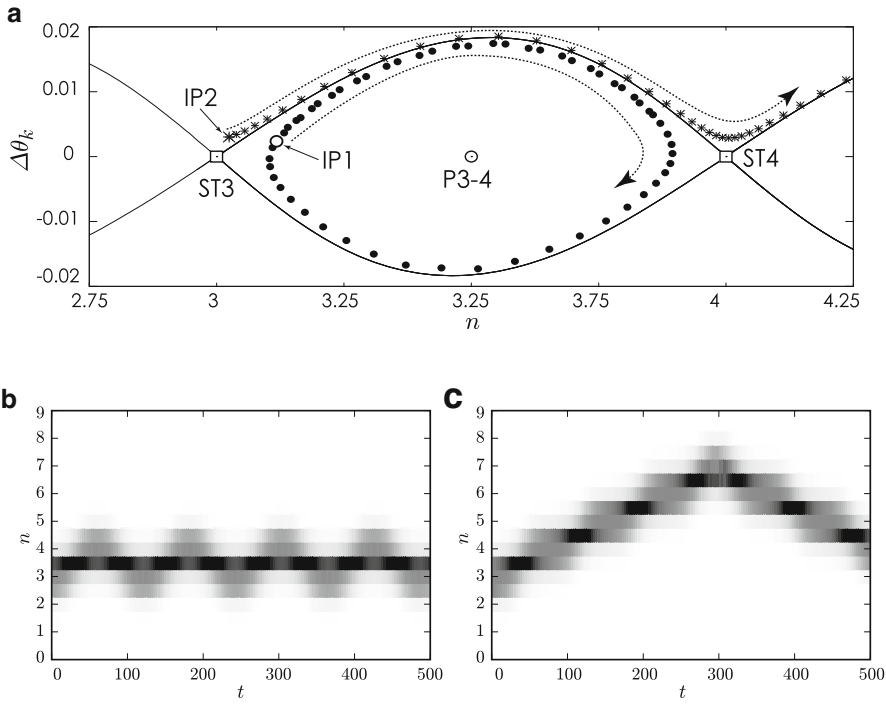

Fig. 6 Two different traveling ILMs generated from initial conditions which are close to each other. (**a**) Unstable manifolds of unstable ILMs. *Filled circle* and *asterisks* correspond to trajectories of traveling ILMs generated near ST3. (**b**) Reciprocally traveling ILM generated at IP1. (**c**) Traveling ILM initially started at IP2

of Fig. 5a). Other unstable manifolds show the same structure as the right branch of W^u(P3-4). Then Fig. 5a seems to be quite simple. The global phase structure at $\beta_2 = 0.006$ is shown in Fig. 5b. The structure is drastically changed from that at $\beta_2 = 0.005$. Although the connections between P-modes disappear, the vicinities of ST-modes are connected each other with unstable manifolds of themselves. The drastic change of phase structure is caused by the stability change which occurs between $\beta_2 = 0.005$ and 0.006. Unstable manifolds observed at $\beta_2 = 0.005$ is vanished with unstable P-modes by increasing β_2. Since ST-modes lose their stability by the stability change, invariant manifolds of ST-modes appear at $\beta_2 = 0.006$.

3.2 Sensitive Dependence on Initial Condition

The behaviors of traveling ILMs become completely different even if the initial points of the traveling ILMs are close each other. Here we take two initial points, IP1 and IP2, as shown in Fig. 6a, where $\beta_2 = 0.006$ and $H = 250$. IP1 is inside the

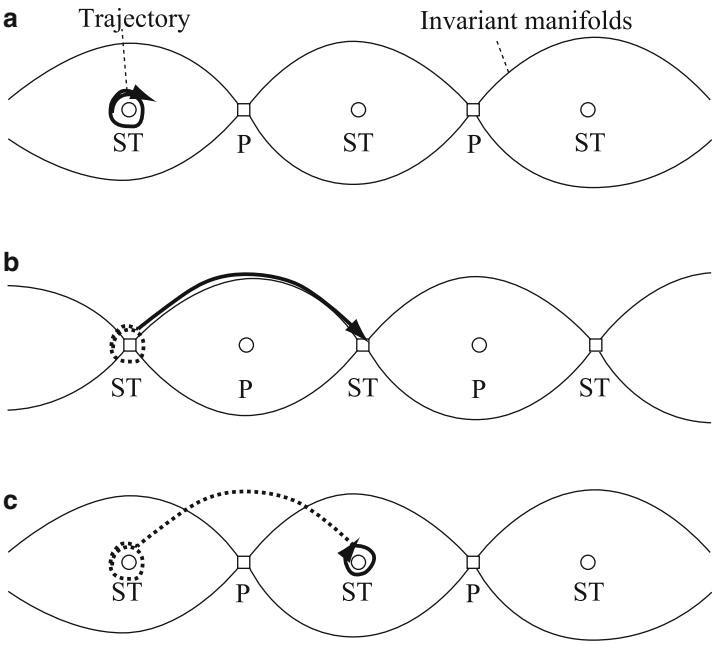

Fig. 7 Concept of ILM manipulation using stability change. *Squares* and *circles* correspond to unstable and stable ILMs, respectively. *Solid curves* indicate unstable manifolds of unstable ILMs. The *arrow* represents the trajectory of the traveling ILM. (**a**) Initial state. (**b**) Release. (**c**) Capture

cyclic structure formed by unstable manifolds of unstable ST-modes, whereas IP2 is outside the structure. The trajectory started at IP1 turns clockwise and the other trajectory moves to the right hand side. The corresponding time-development of energy concentrations is shown in Fig. 6b, c. For the case of IP1, the locus of the high energy concentration reciprocally moves between $n = 3$ and 4. On the other hand, a traveling ILM started from IP2 wanders beyond ST4. Although IP1 and IP2 are close to each other, the behavior of the ILMs show completely different feature. It suggests that the structure of unstable manifolds determines the behavior of traveling ILM.

3.3 Capture and Release Manipulation

As shown in the previous section, the behavior of traveling ILM is sensitively affected by the unstable manifolds. In addition, the drastic change of the global phase structure was observed with respect to the nonlinear inter-site coefficient β_2. These facts allow us to expect that the behavior of traveling ILM can be manipulated by adjusting β_2. Figure 7 depicts a concept to manipulate ILMs by changing the global phase structure. Here, it is assumed that a traveling ILM is initially excited

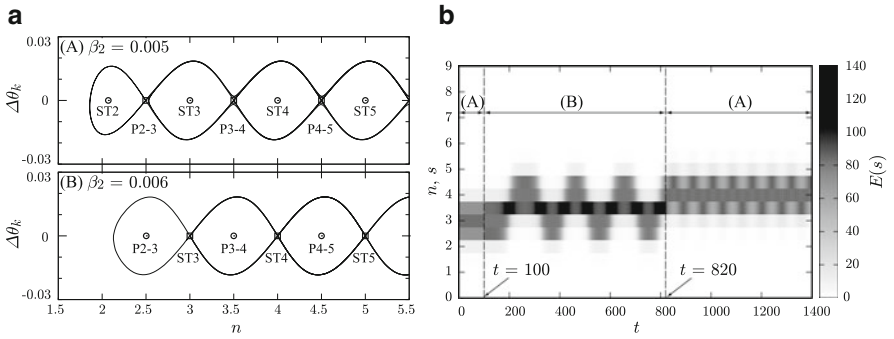

Fig. 8 Capture and release manipulation of traveling ILM. *Dashed-lines* indicate when the stability change is caused. (**a**) Coexisting ILMs and unstable manifolds at (*A*) $\beta_2 = 0.005$, (*B*) $\beta_2 = 0.006$. (**b**) Time-development of energy concentrations

near a stable ILM. Then the traveling ILM stays around the stable ILM as shown in Fig. 7a. When β_2 is rapidly varied, the stability of coexisting ILMs changes and the drastic change of the global phase structure occurs. As a result, the traveling ILM begins to move along unstable manifolds of the destabilized ILMs (Fig. 7b). That is to say, the traveling ILM is *released*. The released ILM will wander in the array. The wandering ILM will be *captured* by the secondary stability change of ILMs, when the wandering ILM approaches to the vicinity of an unstable ILM. The captured ILM stays around the stabilized ILM at a site as shown in Fig. 7c. As results, the traveling ILM is shifted from a site to the next.

A numerical simulation is shown for the capture and release manipulation as in Fig. 8. The structure of unstable manifolds is shown in Fig. 8a. The time development of energy distribution is shown by the tone in Fig. 8b. Here, an initial condition is set as stable ST3 at $\beta_2 = 0.005$. The locus of the energy concentration initially exists at $n = 3$. The first stability change at $t = 100$ is due to the discontinuous change of β_2. Then the global phase structure changes from Fig. 8a (A) to (B). ST3 loses its stability and begins to travel toward $n = 4$ for $100 < t < 820$. That is, ST3 is released. The nonlinear inter-site coefficient β_2 is changed to 0.005 again at $t = 820$. Then the traveling ILM is captured around $n = 4$. Consequently, the ILM is manipulated from the site at $n = 3$ to 4.

4 Experimental Manipulation in Macro-mechanical System

4.1 Macro-mechanical Cantilever Array

Intrinsic localized modes in a coupled cantilever array need nonlinearities in the array in order to exist (Kimura 2009). Then, a macro-cantilever is designed to have a nonlinearity in its restoring force. A static magnetic force is often employed to

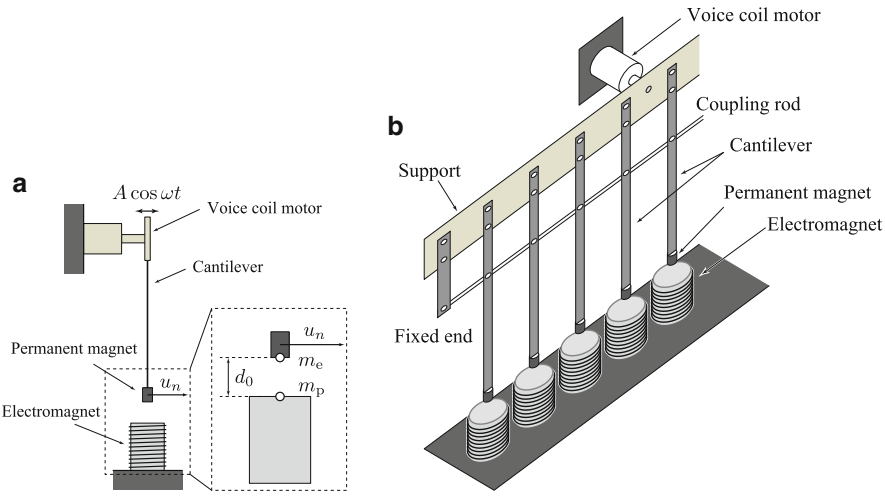

Fig. 9 The mechanically coupled cantilever array and the configuration of magnetic charges. (**a**) Side view of a cantilever with external exciter. (**b**) Overview of the cantilever array

induce the nonlinearity (Hikihara et al. 1997, 2001a,b; Moon et al. 1979). In this paper, a magnetic interaction between a permanent magnet and an electro magnet is applied. A schematic configuration is shown in Fig. 9a. The magnetic force between permanent magnet (PM) and electromagnet (EM) can approximately be described by Coulomb's law for magnetic charges. Then the interaction force is nonlinearly changed against the displacement of cantilever (Kimura and Hikihara 2009):

$$F(u_n) = \frac{m_p m_e(I_{EM})}{4\pi\mu_0} \frac{u_n}{\left(u_0^2 + d_0^2\right)^{\frac{3}{2}}} = \chi(I_{EM}) \frac{u_n}{\left(u_0^2 + d_0^2\right)^{\frac{3}{2}}}, \tag{4}$$

where m_p and $m_e(I_{EM})$ correspond to magnetic charges of PM and EM, respectively. Because the magnitude of $m_e(I_{EM})$ depends on the current flowing EM, which is denoted by I_{EM}, the coefficient of the interaction can be represented as a function of the current, namely, $\frac{m_p m_e(I_{EM})}{4\pi\mu_0} = \chi(I_{EM}) \simeq \chi_0 + \chi_1 I_{EM}$.

The overview of the cantilever array is shown in Fig. 9b. Each cantilever is coupled by an elastic rod and a voice coil motor is attached to excite the whole of the array. When the voice coil motor is driven by a sinusoidal signal, the motion of the cantilever is depicted by Kimura and Hikihara (2009)

$$\ddot{u}_n = -\omega_0^2 u_n - \gamma \dot{u}_n + F(u_n) + A\cos(\omega t) - C\left(u_n - u_{n+1}\right) - C\left(u_n - u_{n-1}\right), \tag{5}$$

where A and ω denote the magnitude and the angular frequency of the external force excited by the voice coil motor, respectively. The damping coefficient γ is due to the air resistance. Parameters which are experimentally estimated are listed in Table 1.

Table 1 List of symbols in Eq. (5)

Symbol	Value	Symbol	Value
ω_0	$2\pi \times 35.1$ rad/s	γ	$1.5\,\mathrm{s}^{-1}$
C	$284\,\mathrm{s}^{-2}$	χ_0	$-4.71 \times 10^{-5}\,\mathrm{m}^3/\mathrm{s}^2$
d_0	3.0 mm	χ_1	$-9.14 \times 10^{-3}\,\mathrm{m}^3/\mathrm{s}^2\mathrm{A}$
A	$3.0\,\mathrm{m/s}^2$	ω	$2\pi \times 36.1$ rad/s

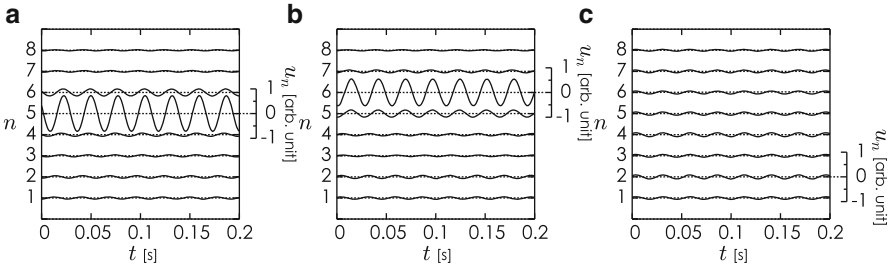

Fig. 10 Experimentally excited ILMs. The cantilever array was externally vibrated with 36.1 Hz. (**a**) ILM at $n = 5$. (**b**) ILM at $n = 6$. (**c**) No ILM

4.2 Observation of Localized Oscillations

Several ST-modes were observed in the coupled cantilever array by an external excitation. Figure 10a, b show wave forms of observed localized oscillations. One of the cantilevers has a quite large amplitude while the others are relatively small. The amplitude distribution is obviously localized.

We also observed localized oscillations at $n = 2$ and $n = 4$. However, a localized oscillation standing at $n = 3$ could not be excited. The reason seems a disorder of the array. The disorder is implied by symmetry of amplitude distribution. As shown in Fig. 10a, amplitude of 6th cantilever is larger than 4th cantilever. That is, the symmetry of observed localized oscillation is slightly broken. Since the asymmetricity of ILM is not observed in numerical simulations in which any disorders are not considered, the disorder of array seems to break the symmetry of localized oscillations.

P-modes could not be excited experimentally. It implies that the even symmetric oscillations are unstable. Floquet multipliers are obtained numerically for both ST4 and P4-5. Figure 11a, b show the Floquet multipliers. All multipliers of ST4 are located inside unit circle. Even if a small fluctuation around the ST4 is caused by a disturbance, the fluctuation is exponentially decreased in time. Then, the ST4 is stable. On the other hand, the P4-5 has two Floquet multipliers on the real axis. The right panel in Fig. 11b shows that one of the multipliers are outside unit circle. Thus, the P4-5 is unstable for the parameters in Table 1.

However, the absolute value of the Floquet multiplier which is outside unit circle is very close to $+1$. Thus, the multiplier will enter unit circle if the damping coefficient is slightly larger. It implies that there is possibility to excite P-modes experimentally.

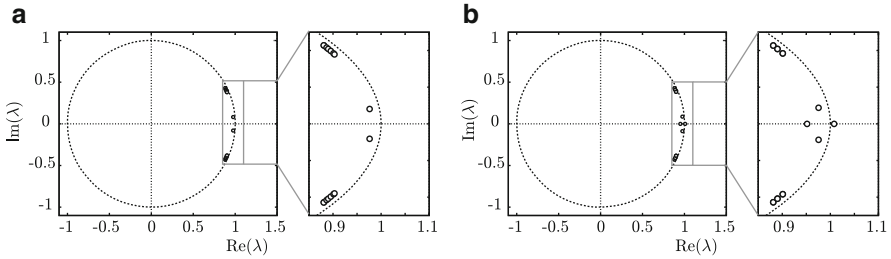

Fig. 11 Floquet multipliers of ST-mode and P-mode. The *left panel* of each case shows an enlarged figure around $+1$ on unit circle. Parameters are set to $\omega = 2\pi \times 36.1$ rad/s, $A = 3\,\mathrm{m/s^2}$, and $I_{\mathrm{EM}} = 24$ mA. (**a**) ST4. (**b**) P4-5

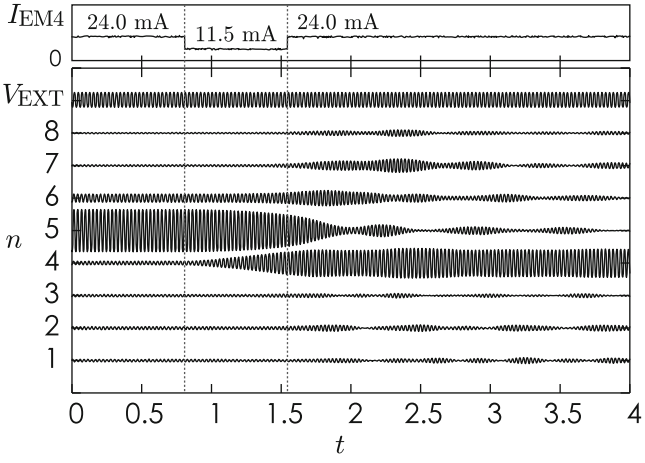

Fig. 12 Manipulation of an ILM by adding the impurity which is added at $n = 4$ by varying the current I_{EM4} from 24.0 to 11.5 mA. The manipulation starts at $t = 0.81$ s and ends at $t = 1.55$ s

4.3 Manipulations of ILM

Excitation of ILM is usually realized by causing the modulational instability (Flach and Willis 1998; Sato et al. 2003a). However, the position and the number of ILM cannot be controlled because the modulational instability causes a random behavior of traveling ILMs (Cretegny et al. 1998). On the other hand, it has been reported that ILM can be excited at a selected site by adding an impurity there (Sato et al. 2004). The manipulation using impurity is also realized (Sato et al. 2004). An excited ILM is attracted or repulsed by impurities. Here we consider the manipulation of ILM using an impurity in the macro-cantilever array.

An impurity on nth site is created by varying the current flowing nth EM, namely, $I_{\mathrm{EM}n}$. In this paper, the current I_{EM4} was decreased from 24.0 to 11.5 mA at the beginning of the manipulation, and was increased to 24.0 mA again at the end of the manipulation. Figure 12 shows the waveforms of individual cantilever

in the attractive manipulation. In the manipulation, ST5 is initially excited. After the impurity is added, the amplitude of 4th cantilever begins to increase. On the other hand, the amplitude of 5th cantilever is decreased. The impurity is removed when the amplitudes of 4th and 5th cantilever are almost same. The oscillation of 5th cantilever becomes smaller with spreading small traveling waves. However, the amplitude of 4th cantilever grows in large. As a result, the locus of ILM shifts from $n = 5$ to $n = 4$.

5 Conclusion

In this paper, manipulation for ILM in micro-cantilever array is discussed. At first, it was shown that several ILMs coexists in the array. The stability of the coexisting ILMs are flipped at a critical value of the nonlinear coupling coefficient. The global phase structure is investigated by computing the invariant manifolds of unstable ILMs. As results, it was revealed that the global phase structure is drastically changed with the nonlinear coupling coefficient. On the basis of the fact that the behavior of traveling ILM is governed by the global phase structure, the capture and release manipulation is proposed. The manipulation method was numerically confirmed.

Another method to manipulate ILM was experimentally demonstrated in a macro-cantilever array which was newly proposed for experimental investigation of ILM. For the manipulation, an artificial impurity was induced into the array. An initially excited ILM was attracted to the impurity and survived after removing the impurity. For confirming the capture and release manipulation in experiment, the proposed cantilever array has to be improved to have nonlinearity in coupling. We will attempt to improve the macro-cantilever array and to confirm the capture and release manipulation.

Acknowledgements We would like to show our appreciation to Professor M. Sato, Kanazawa University, Japan, for the discussion about the model of cantilever array. This research was partially supported by the Ministry of Education, Culture, Sports, Science and Technology (MEXT) in Japan, The 21st Century COE Program No. 14213201 and the Global-COE program. The experimental part was supported by Kyoto University Venture Business Laboratory, and MEXT (Grant-in-Aid for Young Scientists (B) No. 22760280).

References

Binder, P., Abraimov, D., Ustinov, A.V., Flach, S., Zolotaryuk, Y.: Phys. Rev. Lett. **84**, 745 (2000)
Campbell, D.K., Flach, S., Kivshar, Y.S.: Phys. Today **57**(1), 43 (2004)
Crespo da Silva, M.R.M.: Int. J. Solid Struct. **24**, 1225 (1988)
Crespo da Silva, M.R.M., Glynn, C.C.: J. Struct. Mech. **6**, 437 (1978)
Cretegny, T., Dauxois, T., Ruffo, S., Torcini, A.: Phys. D **121**, 109 (1998)

Eisenberg, H.S., Silberberg, Y., Morandotti, R., Boyd, A.R., Aitchison, J.S.: Phys. Rev. Lett. **81**, 3383 (1998)
Flach, S., Gorbach, A.: Chaos **15**, 15112 (2005)
Flach, S., Gorbach, A.V.: Phys. Rep. **467**, 1 (2008)
Flach, S., Willis, C.R.: Phys. Rep. **295**, 181 (1998)
Hikihara, T., Okamoto, Y., Ueda, Y.: Chaos **7**, 810 (1997)
Hikihara, T., Torii, K., Ueda, Y.: Phys. Lett. A **281**, 155 (2001a)
Hikihara, T., Torii, K., Ueda, Y.: Int. J. Bifurcat. Chaos **11**, 999 (2001b)
Houle, P.A.: Phys. Rev. E **56**, 3657 (1997)
Kimura, M.: Studies on the manipulation of intrinsic localized modes in coupled cantilever arrays. Ph.D. thesis, Kyoto University (2009)
Kimura, M., Hikihara, T.: Phys. Lett. A **372**, 4592 (2008)
Kimura, M., Hikihara, T.: Phys. Lett. A **373**(14), 1257 (2009)
Malatkar, P., Nayfeh, A.H.: Nonlinear Dyn. **31**, 225 (2003)
Marín, L.M., Aubry, S.: Nonlinearity **9**, 1501 (1996)
Moon, F.C., Holmes, P.J.: J. Sound Vib. **65**(2), 275 (1979)
Morandotti, R., Peschel, U., Aitchison, J.S., Eisenberg, H.S., Silberberg, Y.: Phys. Rev. Lett. **83**, 2726 (1999)
Sandusky, K.W., Page, J.B., Schmidt, K.E.: Phys. Rev. B **46**(10), 6161 (1992)
Sato, M., Hubbard, B.E., Sievers, A.J., Ilic, B., Czaplewski, D.A., Craighead, H.G.: Phys. Rev. Lett. **90**, 044102 (2003a)
Sato, M., Hubbard, B.E., English, L.Q., Sievers, A.J., Ilic, B., Czaplewski, D.A., Craighead, H.G.: Chaos **13**, 702 (2003b)
Sato, M., Hubbard, B.E., Sievers, A.J., Ilic, B., Craighead, H.G.: Europhys. Lett. **66**(3), 318 (2004)
Sato, M., Hubbard, B.E., Sievers, A.J.: Rev. Mod. Phys. **78**, 137 (2006)
Sato, M., Yasui, S., Kimura, M., Hikihara, T., Sievers, A.J.: Europhys. Lett. **80**, 30002 (2007)
Sievers, A.J., Takeno, S.: Phys. Rev. Lett. **61**, 970 (1988)
Takeno, S., Sievers, A.J.: Solid State Commun. **67**, 1023 (1988)
Trías, E., Mazo, J.J., Orlando, T.P.: Phys. Rev. Lett. **84**, 741 (2000)
Ustinov, A.V.: Chaos **13**, 716 (2003)
Waggoner, P.S., Craighead, H.G.: Lab Chip **7**, 1238 (2007)
Zueco, D., Martínez, P.J., Floría, L.M., Falo, F.: Phys. Rev. E **71**, 036613 (2005)

Dynamic Control and Ground-Based Experiments of a Tethered Satellite System

Haiyan Hu, H. Wen, and D.P. Jin

Abstract The paper presents the deployment and retrieval control of a tethered satellite system from both theoretical and experimental points of view. The ideas of online optimization and receding horizon control enable one to design a feedback controller for the tethered satellite system. The presented feedback control law is not in any closed-form, but can accounts for the nonlinearity in the system model and the mission-related constraints. Furthermore, the paper outlines a technically and economically feasible solution to verify the efficacy of the controller via a ground-based experiment. The two key issues concerning the design of the ground-based experiment are the principle of dynamic similarity and the idea of using thrusts for simulating the gravity gradient field and the Coriolis forces. Finally, the paper presents the experimental verification of proposed control scheme for the deployment and retrieval processes of the satellite simulator.

Keywords Tethered satellite system • Ground-based experiment • Receding horizon control

H.Hu (✉)
Department of Mechanics, Beijing Institute of Technology, 100081 Beijing, China

Institute of Vibration Engineering Research, Nanjing University of Aeronautics and Astronautics, 210016 Nanjing, China

H. Wen • D.P. Jin
Institute of Vibration Engineering Research, Nanjing University of Aeronautics and Astronautics, 210016 Nanjing, China
e-mail: hhyae@nuaa.edu.cn

M. Wiercigroch and G. Rega (eds.), *IUTAM Symposium on Nonlinear Dynamics for Advanced Technologies and Engineering Design*, IUTAM Bookseries (closed) 32, DOI 10.1007/978-94-007-5742-4_29,

1 Introduction

The concept of Tethered Satellite System (TSS), that is, two or more satellites connected by thin and long cables, promises to revolutionize many aspects of space exploration and exploitation (Wen et al. 2008a). Recent years have witnessed numerous important applications of such systems, ranging from propellant-less propulsion for satellites, gravity gradient stabilization, tether-assisted re-entry, electro-dynamic propulsion to debris mitigation, and so on (Wen et al. 2008a; Kumar 2006; Cartmell and Mckenzie 2008). However, the dynamics and control of any TSS are quite complex. Because of their overall flexibility, the tethers are strongly susceptible to undergoing a complicated set of librations and vibrations when they are placed into a space environment and coupled with satellites (Kumar 2006). Even in the station-keeping phase, the libration motions of the TSS may become chaotic when the orbit is eccentric (Fujii and Ichiki 1997). The problem becomes even more challenging when the deployment and retrieval parts of a TSS mission are taken into consideration because the librations and vibrations of the tether can grow dramatically due to the effect of the Coriolis accelerations. If the TSS is not carefully controlled, the large motion may result in an excessively high tensional stress beyond the strength of tether material and may lead to the failure of a whole TSS. In particular, the electro-dynamic TSS in an inclined orbit deserves special attention paid to the possible instability because of the continuous pumping of energy from electro-magnetic forces into the tether attitude motion (Peláez et al. 2000).

Over the past two decades, numerous attempts have been made to gain an insight into the complex dynamics and to solve the control problem of a TSS, mainly in the following two aspects: theoretical analyses and numerical simulations. For example, Yu presented a range-rate control scheme for the TSS model with a mass-distributed and flexible tether, and investigated the stability of the stationary (quasi-stationary) configurations (Yu 2002). Steindl et al. designed the optimal controllers to achieve force controlled deployment and retrieval of a TSS based on the multiple shooting method (Steindl and Troger 2003; Steindl et al. 2005). Peláez et al. identified a new kind of instability due to the pumping of energy from electro-dynamic forces and presented an in-depth analysis of the periodic motion of TSS (Peláez et al. 2000; Peláez and Andrés 2005). Jin and Hu proposed a control strategy based on the combination of quasi-linearization and truncated Chebyshev polynomials to solve the constrained nonlinear optimal control problem of the TSS with three degrees of freedom (Jin and Hu 2006). Wen et al. introduced two infinite-horizon control schemes to stabilize the three-dimensional retrieval process of an elastically tethered subsatellite (Wen et al. 2008b).

Recent studies on TSS reveal a growing trend towards the collaboration between theoretical and experimental researches. Especially, ground-based experiments have been recognized as a kind of very efficient means to verify the theoretical studies on the dynamics and control of a TSS in the initial stage of design before any costly and time consuming spaceflight experiments. Ground-based experimental systems for TSS roughly fall into three main categories, that is, rotating table (Higuchi et al. 1997), drop-tower (Taketiara et al. 2005), and air-bearing table (Mori and

Matunaga 2007; Chung et al. 2007). For example, Higuchi and Natori presented an experimental set-up where a piece of dry ice was placed on a slope on a rotating table to simulate the in-plane dynamics of a TSS (Higuchi et al. 1997). Takehara et al. presented a flexible multi-body model for simulating a TSS undergoing a large deformation and a large displacement, and performed drop-tower experiments to evaluate the validity of the numerical formulations (Taketiara et al. 2005). Mori and Matunaga presented a two-dimensional ground experiment system consisting of a ground station and three satellite simulators floating on a flat floor by using air-bearings. Soon-Jo et al. demonstrated the decentralized nonlinear control of tethered formations via ground experiments conducted at the Synchronized Position Hold, Engage, and Reorient Experimental Satellites (SPHERES) test-bed (Chung et al. 2007).

This study follows a research philosophy of balancing theoretical excellence and practical mission. Both theoretical and experimental investigations deal with the control problems concerning tether deployment and retrieval. The first objective of the study is to devise control strategies that are not only versatile in terms of system nonlinearity and constraints, but also efficient enough to be implemented on digital hardware. Therefore, the ideas of nonlinear optimization and receding horizon control (RHC) are introduced to design a feedback controller for the deployment and retrieval processes of the TSS. The second purpose of the study is to provide a technically and economically feasible solution for verifying the efficacy of the controller via a ground-based experiment, during which both the gravity gradient field and the Coriolis forces experienced by the TSS can be well simulated on the ground. These issues will be discussed more extensively in the remainder of the paper.

2 Model Descriptions

This section presents fundamental models governing the dynamics of the TSS and the proposed ground-based experiment system, and establishes a bridge between the two models based on the principle of dynamic similarity. Furthermore, it gives a brief introduction to the main subsystems and components of the ground-based experiment system.

2.1 Tethered Satellite System

Figure 1 shows an idealized 'dumbbell' model for the TSS consisting of a spaceship S_1 of mass M and a subsatellite S_2 of mass m connected by a tether of length l (Wen et al. 2008a). In the model, the tether is assumed as a rigid mass-less rod with variable length, while the spaceship and subsatellite are simplified as two lumped-masses. The in-plane position of the tether is given by the pitch angle θ whereas the out-of-plane motions are neglected because only the two-dimensional dynamics of a TSS can be simulated in the ground-based experiment. Furthermore, the assumption $m << M$ is made such that the orbit center of the system can be assumed to

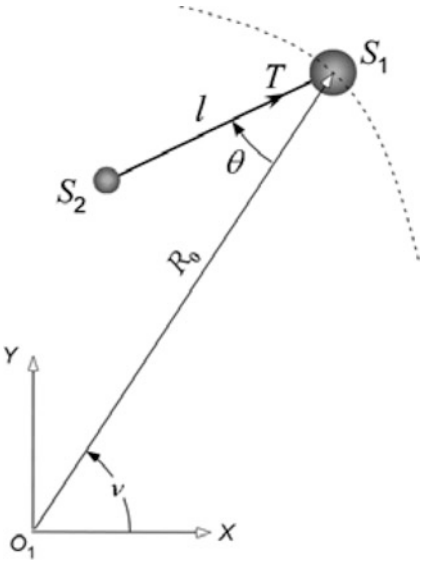

Fig. 1 The schematic view of the TSS on a circular orbit

coincide with the mass center of the spaceship moving on a circular orbit of radius R_0. The angular position ν of the TSS in its orbit is defined as $\nu = \Omega t$, where Ω represents the orbital angular velocity of the system. Under the above assumptions, the dynamic equation of the TSS reads

$$\begin{aligned} l\theta'' + 2l'\theta' &= 2\Omega l' - 3l\Omega^2 \sin\theta\cos\theta \\ l'' - l\theta'^2 &= -2\Omega l\theta' + 3l\Omega^2\cos^2\theta - T/m \end{aligned} \tag{1}$$

where the prime represents the derivative with respect to time t, T is the tensional force along the tether and serves as the control input.

2.2 Ground-Based Experiment System

This subsection presents a ground-based experiment system to simulate the in-plane motions of the TSS as shown in Fig. 1. The experiment features in a combination of air-bearing facilities and on-board thrusts to achieve the simulation of the gravity gradient field and the Coriolis forces experienced by the TSS. The ground experiment system consists of a flat table of 3.5 m long and 2.5 m wide, a satellite simulator floating on the flat table via air-bearings, and a tether connecting the satellite simulator to the Tether Control Unit (TCU), as shown in Fig. 2. In the figure, $\underline{S}_1$ is the towing point on the TCU side, $\underline{S}_2$ is the center of mass of the satellite simulator, and l represents the distance between $\underline{S}_1$ and $\underline{S}_2$. Two

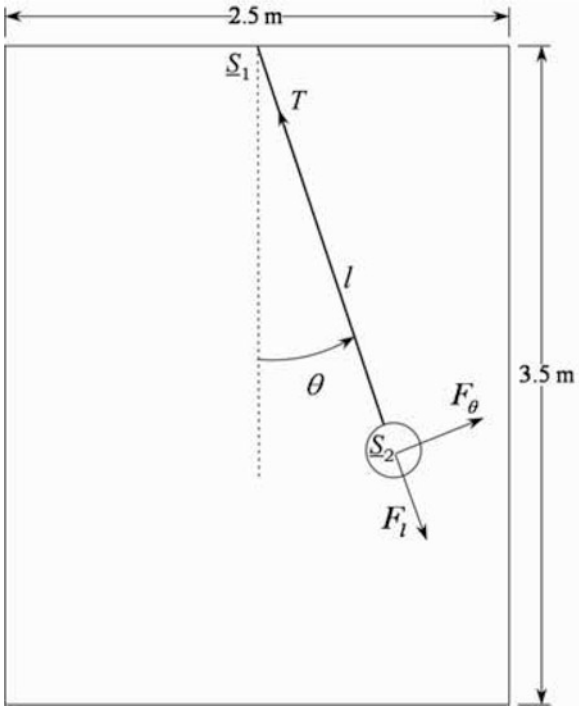

Fig. 2 The schematic view of the ground-based experiment system

groups of thrusters are installed along two mutually perpendicular axes of the satellite simulator, respectively. The resultant forces of all the thrusters can be resolved into two components, i.e., F_l along the tether and F_θ perpendicular to the tether, as shown in Fig. 2. By modeling the satellite simulator with a point-mass approximation and neglecting the mass and flexibility of the tether, the dynamic equation of the tethered satellite simulator reads

$$l\theta'' + 2l'\theta' = F_\theta/m, \quad l'' - l\theta'^2 = (F_l - T)/m \tag{2}$$

Based on the principle of dynamic similarity, Eq. (1) is equivalent to Eq. (2) if the following conditions hold true

$$F_\theta = m\Omega(2l' - 3l\Omega \sin\theta\cos\theta), \quad F_l = m\Omega l(3\Omega\cos^2\theta - 2\theta') \tag{3}$$

The "dynamic similarity" implies that the dynamic equation of the TSS on an orbit and the ground-based experimental system can be further transformed to the same dimensionless form. In addition, it is indicated by Eq. (3) that F_θ and F_l will be too small to be simulated precisely on the ground if the value of Ω is set to be the real orbital angular velocity of the TSS. Therefore, in the ground-based experiment, the orbital angular velocity Ω of the TSS is not directly used, but enlarged by many times based on the principle of dynamic similarity. As an example, the value of Ω is taken to be 0.03 rad/s in this study.

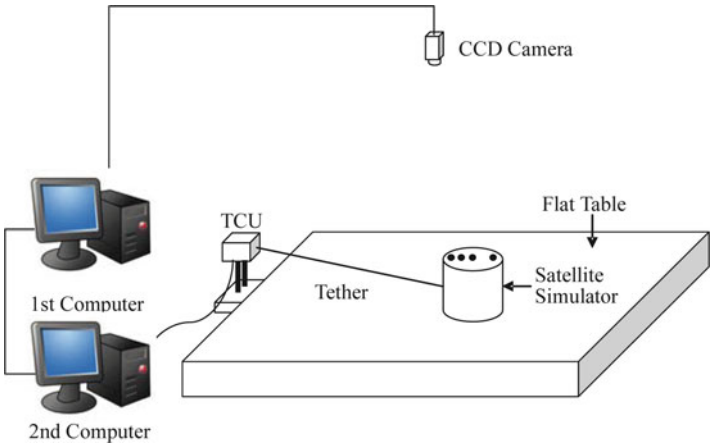

Fig. 3 The subsystems and components of the ground-based experiment system

Recent technologies of computer vision and wireless local network enable one to design the experimental facilities as shown in Fig. 3, where the main subsystems and components of the ground-based experiment system include the satellite simulator and the corresponding TCU, a Charge-Coupled Device (CCD) camera to sense the position of the satellite simulator, as well as two computers. There are four optical markers placed on the top surface of the satellite simulator such that the state information of the simulator can be acquired via the CCD camera. Figure 4 depicts the satellite simulator floating on the flat table. According to Eq. (3), the on-board thrusters of the satellite simulator are actively controlled to simulate the gravity gradient field and the Coriolis forces in real-time. The first computer in the system performs the tasks of computer vision from the CCD camera, wireless communication with the simulator and experiment supervision, whereas the second computer solves the control law online and sends the control commands of tether length to the TCU.

3 Controller Design

Optimal control is perhaps best-suited for the deployment and retrieval problems of the TSS because they can not only optimize the mission performance, but also account for the nonlinearity in the system model and the mission constraints. However, the classical strategies of closed-loop optimal control are generally ill-suited for such complex problems. Therefore, the idea of nonlinear optimization and RHC scheme are exploited to generate a feedback control for the TSS. The feedback control law is not analytically explicit, but determined via a rapid re-computation of the open-loop optimal trajectory online. In other words, the feedback control law is formed by gluing a sequence of open-loop control laws together (Wen et al. 2009a).

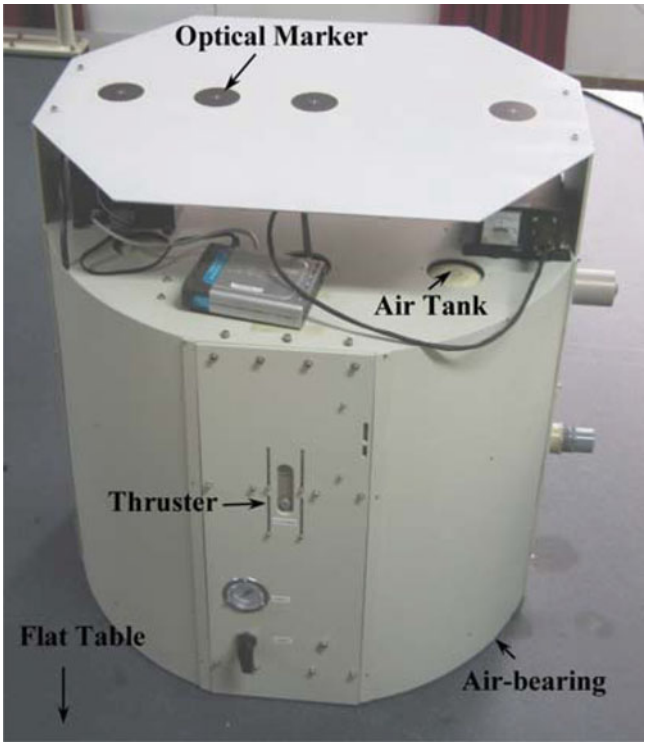

Fig. 4 The satellite simulator floating on the flat table

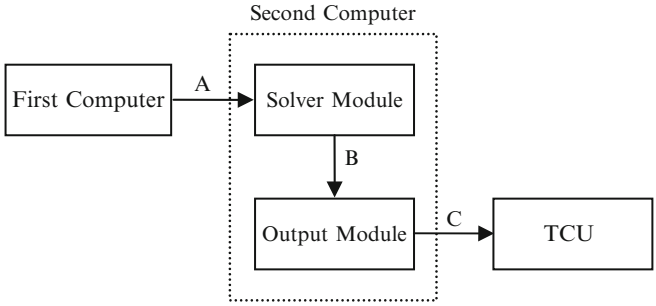

Fig. 5 The flow chart of the control system

Figure 5 illustrates the flow chart of the control system of the experiment. As shown in the figure, the software of second computer consists of two main modules running in parallel, namely a solver module and an output module. The solver module is responsible for re-solving the open-loop control problem every one second, according to the latest state information sent from the first computer. The output module determines the control commands of tether length by interpolating

the latest solution of the solver module, and sends the commands to the TCU every 20 ms. In Fig. 5, the arrow 'B' represents the procedure that the solution of the solver module is used to update the open-loop control law stored in the output module as soon as a new solution is available.

The optimal control problem involved in the i th online computation is to look for the continuous vector function $[\nu_i \quad \nu_i + T_p] \ni \nu \mapsto \mathbf{q}$ so as to minimize the following cost function

$$J(\Lambda(\cdot)) = E(\Lambda(\nu_i + T_p)) + \int_{\nu_i}^{\nu_i + T_p} F(\Lambda(\nu))\mathrm{d}\nu \tag{4}$$

which is subject to the end-point constraints $\mathbf{x}(\nu_i) = \tilde{\mathbf{x}}_i$, and the general state-control path constraints

$$\mathbf{h}^L \leq \mathbf{h}(\Lambda(\nu)) \leq \mathbf{h}^U \tag{5}$$

Here all the variables are in dimensionless form, the dot denotes the derivative with respect to the orbital angular position ν, T_p represents the control horizon of the RHC controller, ν_i corresponds to the instant when the i th online computation begins, $\tilde{\mathbf{x}}_i$ is the latest state feedback, $\mathbf{h}^L$ and $\mathbf{h}^U$ are the lower and upper bounds for $\mathbf{h}(\Lambda(\nu))$, $\Lambda = (\mathbf{q};\ \dot{\mathbf{q}};\ \ddot{\mathbf{q}})$, $\mathbf{x} = (\mathbf{q};\ \dot{\mathbf{q}})$, $\mathbf{q} = (\theta;\ \xi)^{\mathrm{T}}$, $\xi = l/l_c$, the semicolon denotes the vertical concatenation of vectors, and l_c is a reference length equal to $2,500$ mm. It is worth noticing that Eq. (5) is a more general form of Eq. (1), the second row of which can be transformed to the following formulation of a differential inclusion of the second order

$$-\bar{T}_{\mathrm{up}} \leq \ddot{\xi} - \xi\dot{\theta}^2 + 2\xi\dot{\theta} - 3\xi\cos^2\theta \leq -\bar{T}_{\mathrm{low}} \tag{6}$$

where $\bar{T}_{\mathrm{up}}$ and $\bar{T}_{\mathrm{low}}$ represent the upper and lower bounds of the dimensionless tension force $\bar{T} = T/(m\Omega^2 l_c)$, respectively.

The Legendre Pseudo-spectral (LP) method of the second order can be introduced to solve the problem of open-loop optimal control (Wen et al. 2009b). The basic idea is to discretize the optimal control problem first and then solve the resulting large-scale optimization problem via nonlinear programming. The presented algorithms are coded into a reusable general optimal control package in C++ language, and the computation efficiency is improved by using a symbolic preprocessor and putting the sparse structures of involved matrices into full use.

4 Experiments of Dynamic Control

This section presents the experimental verification of the proposed control scheme and the efficacy of the experiment system for the deployment and retrieval processes of the satellite simulator.

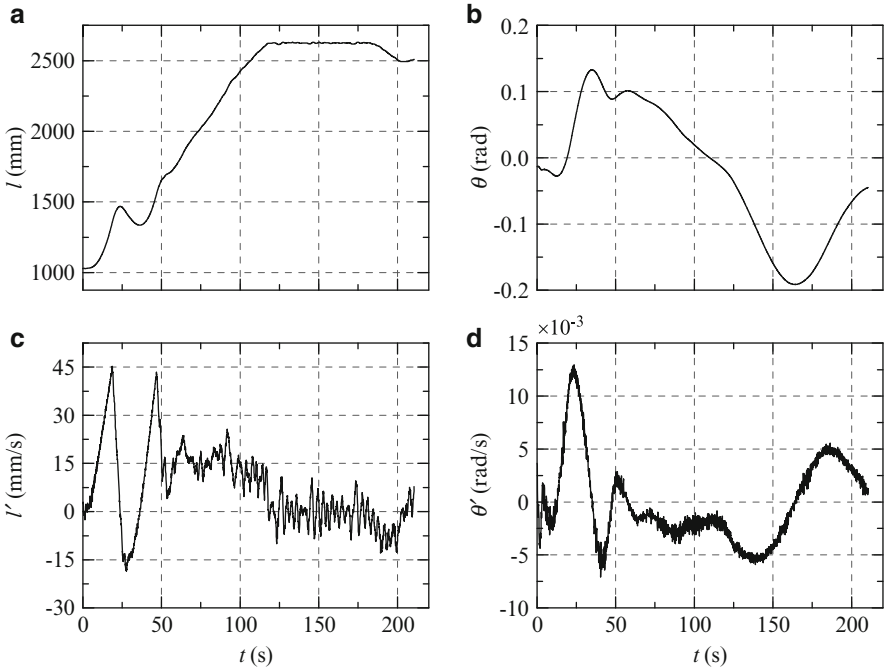

Fig. 6 Experimental results for the deployment control of the satellite simulator

4.1 Deployment Control

In the case study of deployment control, the cost function (4) is chosen to be

$$J = [100\theta^2 + 100(\xi - \xi_d)^2 + 20(\dot{\theta}^2 + \dot{\xi}^2)]\Big|_{\nu=\nu_i+T_p} + \int_{\nu_i}^{\nu_i+T_p} [5\theta^2 + (\xi - \xi_d)^2 + 10\dot{\theta}^2 + \dot{\xi}^2)]\mathrm{d}\nu \tag{7}$$

where $T_p = 3$, the desired tether length $l_d = l_c = 2,500$ mm (corresponding to $\xi_d = 1.0$), and the state-control constraints are set as

$$\theta \in [-1 \;\; 1], \quad \xi \in [0.35 \;\; 1.05], \quad \bar{T} \in [0.1 \;\; 6] \tag{8}$$

Figure 6 shows the experimental results for the deployment control. It takes about 100 s for l to reach the desired value $l_d = 2,500$ mm, and then l continues to increase until it reaches the upper bounds 2, 625 mm (corresponding to $\xi = 1.05$), as shown in Fig. 6a. After that, the tethered simulator demonstrates a pendulum-like movement for dozens of seconds, with l remaining almost unchanged at its

upper bounds, as shown in Fig. 6. In the final few seconds, l gradually decreases to the desired value l_d, and θ finally falls within the range from -0.05 to 0 rad. The angular velocity $\dot{\theta}$ and the length rate $\dot{l}$ are not directly obtained via computer vision, but estimated online based on the discretely measured values of θ and l. The experimental results show that there are two stages involved in the deployment process of the tether. In the first stage, the tether is deployed in a fast way with significant pitch motions induced, whereas the change in tether length becomes quite slow in the second stage and finally evolves into state-keeping motions.

4.2 Retrieval Control

In the case study of the retrieval control, the cost function is chosen to be

$$J = [10\theta^2 + 200(\xi - \xi_d)^2 + 10(\dot{\theta}^2 + \dot{\xi}^2)]\Big|_{\nu=\nu_i+T_p} + \int_{\nu_i}^{\nu_i+T_p} [4(\xi - \xi_d)^2 + 4\dot{\theta}^2)]\mathrm{d}\nu \tag{9}$$

where the desired tether length $l_d = 1,100$ mm (corresponding to $\xi_d = 0.44$), and T_p is gradually reduced from $T_p = 5$ in the beginning to $T_p = 3$ when $\xi < 0.8$ just holds to $T_p = 3$, and then to $T_p = 1.5$ when $\xi < 0.6$ just holds in order to improve the control performance. The system constraints are set as

$$\theta \in [-1 \;\; 1], \quad \xi \in [0.42 \;\; 1.2], \quad \bar{T} \in [1 \;\; 6] \tag{10}$$

Figure 7 shows the experimental results for the case study of retrieval control. The experiment of retrieval control yields more significant motions of the satellite simulator compared with the deployment control, especially when the simulator is close to the target position. There may be two reasons for the motions under retrieval control being more significant than that under deployment control. One is that the retrieval is always unstable because of the negative damping (Kumar 2006). The other is that the attitude of the satellite simulator puts more significant effects on the motions of the system in the final part of the retrieval experiment because the final length of the tether in the retrieval case is much shorter than that in the deployment case.

5 Conclusions

The paper presents both theoretical and experimental studies on the deployment and retrieval control of a tethered satellite system, and focuses on the planar case here because of the experimental limitations. However, the three-dimensional

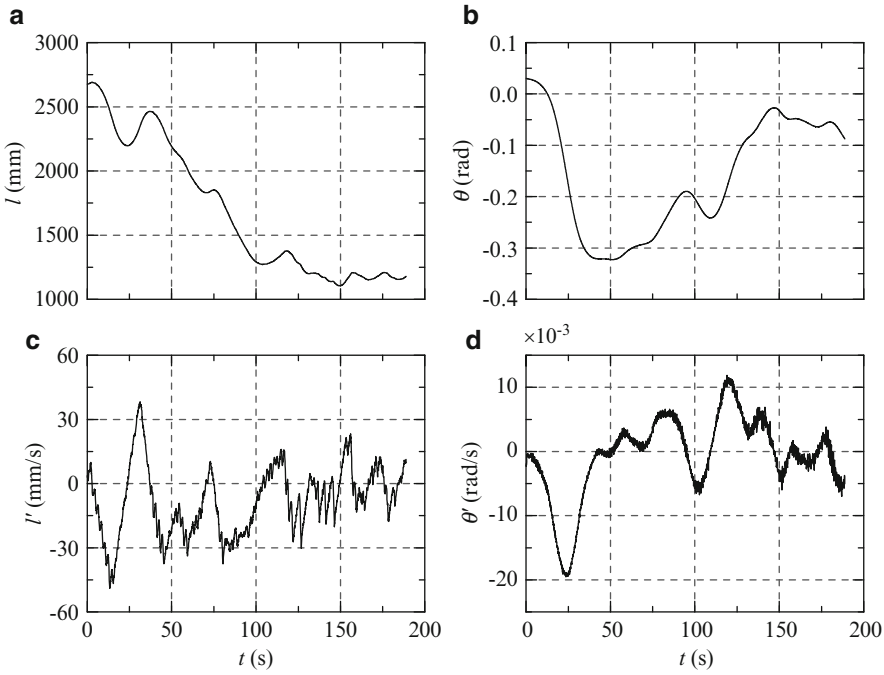

Fig. 7 Experimental results for the retrieval control of the satellite simulator

extension of the presented control strategy is straightforward. The experimental results well demonstrate the effectiveness of the experimental design and the real-time performance of the proposed control scheme. In this study, the subsatellite is simplified as a lumped-mass in controller design. One of the future studies is to take the attitude dynamics of the subsatellite into consideration.

Acknowledgements This work was supported in part by the National Natural Science Foundation of China under Grant 10672073 and 50875124, and in part by the China Postdoctoral Science Foundation and Jiangsu Postdoctoral Science Foundation.

References

Cartmell, M.P., Mckenzie, D.J.: A review of space tether research. Prog. Aerosp. Sci. **44**(1), 1–21 (2008)

Chung, S.J., Slotine, J.J.E., Miller, D.W.: Nonlinear model reduction and decentralized control of tethered formation flight. J. Guid. Control. Dyn. **30**(2), 390–400 (2007)

Fujii, H.A., Ichiki, W.: Nonlinear dynamics of the tethered subsatellite system in the station keeping phase. J. Guid. Control. Dyn. **20**(2), 403–406 (1997)

Higuchi, K., Natori, M.C.: Ground experiment of motion control of retrieving space tether. In: Proceedings of the AIAA/ASME/ASCE/AHS/ASC Structures, Structural Dynamics & Materials Conference, Kissimmee, Fl, USA (1997)

Jin, D.P., Hu, H.Y.: Optimal control of a tethered subsatellite of three degrees of freedom. Nonlinear Dyn. **46**(1–2), 161–178 (2006)

Kumar, K.D.: Review of dynamics and control of nonelectrodynamic tethered satellite systems. J. Spacecr. Rocket. **43**(4), 705–720 (2006)

Mori, O., Matunaga, S.: Formation and attitude control for rotational tethered satellite clusters. J. Spacecr. Rocket. **44**(1), 211–220 (2007)

Peláez, J., Andrés, Y.N.: Dynamic stability of electrodynamic tethers in inclined elliptical orbits. J. Guid. Control. Dyn. **28**(4), 611–622 (2005)

Peláez, J., Lorenzini, E.C., Lopez-Rebollal, O., et al.: A new kind of dynamic instability in electrodynamic tethers. J. Astronaut. Sci. **48**(4), 449–476 (2000)

Steindl, A., Troger, H.: Optimal control of deployment of a tethered subsatellite. Nonlinear Dyn. **31**(3), 257–274 (2003)

Steindl, A., Steiner, W., Troger, H.: Optimal control of retrieval of a tethered subsatellite. Solid Mech. Appl. **122**, 441–450 (2005)

Taketiara, S., Terumichi, Y., Nohmi, M., et al.: Numerical and experimental approaches on the motion of a tethered system with large deformation, rotation and translation. In: Proceedings of the ASME International Design Engineering Technical Conferences and Computers and Information in Engineering Conference, Long Beach, CA, USA (2005)

Wen, H., Jin, D.P., Hu, H.Y.: Advances in dynamics and control of tethered satellite systems. Acta Mechani. Sinica **24**(3), 229–241 (2008a)

Wen, H., Jin, D.P., Hu, H.Y.: Infinite-horizon control for retrieving a tethered subsatellite via an elastic tether. J. Guid. Control. Dyn. **31**(4), 899–906 (2008b)

Wen, H., Jin, D.P., Hu, H.Y.: Feedback control for retrieving an electro-dynamic tethered subsatellite. Tsinghua Sci. Technol. **14**(S2), 79–83 (2009a)

Wen, H., Jin, D.P., Hu, H.Y.: Costate estimation for dynamic systems of the second order. Sci. China Ser. E Technol. Sci. **52**(3), 752–760 (2009b)

Yu, S.H.: Dynamic model and control of mass-distributed tether satellite system. J. Spacecr. Rocket. **39**(2), 213–218 (2002)

Chaos Control Methods Applied to Avoid Bifurcations in Pendulum Dynamics

Aline S. de Paula, Marcelo A. Savi, Marian Wiercigroch, and Ekaterina Pavlovskaia

Abstract This paper deals with the application of chaos control methods in order to perform bifurcation control of a parametric pendulum-shaker system. The extended time-delayed feedback control method is employed to maintain stable rotational solution of the system avoiding bifurcation to chaos. The considered pendulum system is chosen due to its potential application for extracting energy from sea waves. This alternative concept of energy harvesting is based on exploiting the rotational unbounded solution of the pendulum dynamics. The bifurcation control proposed allows the system to keep the desired rotational solution over extended parameter range avoiding undesirable changes in system dynamics.

Keywords Pendulum dynamics • Delayed feedback control • Rotating solutions

1 Introduction

The idea of energy harvesting from various renewable sources has been gaining an increasing interest and importance in recent years. The sea waves though possessing the largest renewable energy source are practically untapped. Wiercigroch proposed

A.S. de Paula (✉)
Department of Mechanical Engineering, Universidade de Brasília, 70.910.900 Brasília, DF, Brazil
e-mail: alinedepaula@unb.br

M.A. Savi
Department of Mechanical Engineering, Universidade Federal do Rio de Janeiro, 21.941.972 Rio de Janeiro, RJ, P.O. Box 68.503, Brazil
e-mail: savi@mecanica.ufrj.br

M. Wiercigroch • E. Pavlovskaia
Centre for Applied Dynamics Research, School of Engineering, University of Aberdeen, Aberdeen AB24 3UE, UK
e-mail: m.wiercigroch@abdn.ac.uk; e.pavlovskaia@abdn.ac.uk

M. Wiercigroch and G. Rega (eds.), *IUTAM Symposium on Nonlinear Dynamics for Advanced Technologies and Engineering Design*, IUTAM Bookseries (closed) 32, DOI 10.1007/978-94-007-5742-4_30,

an energy generation concept from the sea waves using a pendulum system by converting the base oscillations of the structure into a rotational motion of the pendulum mass. In such case, the oscillations of the structure are caused by the sea waves, whereas the pendulum rotational motion provides a driving torque for an electrical generator (Xu 2005; Horton and Wiercigroch 2008). In order to explore potentials of this concept, the dynamics of the pendulum system has to be carefully considered and the means of maintaining the periodic rotational solutions have to be developed.

The dynamics of parametrically excited pendulum has been extensively investigated in the literature. Although rotating solutions of the pendulum are found and studied by different authors (Clifford and Bishop 1995; Szemplinska-Stupnicka and Tyrkiel 2002; Lenci et al. 2008), it should be pointed out that they only exist over limited parameters range and there are a lot of bifurcations of the system that destabilize this kind of motion. In this regard, the bifurcation control can be very useful in maintaining the rotational solution of the system and crucial in potential energy extraction applications.

Chaos control exploits the richness of chaotic behaviour and may be understood as the use of tiny perturbations for the stabilization of an unstable periodic orbit (UPO) embedded in a chaotic attractor. In this work continuous chaos control methods are employed in order to maintain the rotating solution of the pendulum system by stabilizing UPOs of the system. The main goal is to avoid bifurcations that destabilize the rotating motion.

2 Chaos Control Methods

Chaos control may be understood as the use of small perturbations in order to stabilise UPOs. Since UPOs belong to the system dynamics, the stabilisation of these orbits is associated with low energy consumption. Chaos control methods can be split into discrete and continuous methods. Continuous methods are based on continuous-time perturbations to perform stabilization. This approach was first proposed by Pyragas (1992) and deals with a dynamical system modelled by a set of ordinary nonlinear differential equations as follows:

$$\dot{\mathbf{x}}(t) = \mathbf{Q}(\mathbf{x}, t) + \mathbf{B}(t) \tag{1}$$

where t is time, $\mathbf{x}(t) \in \Re^n$ is the state variable vector, $\mathbf{Q}(\mathbf{x}, t) \in \Re^n$ defines the system dynamics, while $\mathbf{B}(t) \in \Re^n$ is associated with the control action.

Socolar *et al.* (1994) proposed a control law named as the extended time-delayed feedback (ETDF) control considering the information of time-delayed states of the system represented by the following equations:

$$\begin{aligned} \mathbf{B}(t) &= \mathbf{K}\left[(1-R)\mathbf{S}_\tau - \mathbf{x}\right] \\ \mathbf{S}_\tau &= \sum_{m=1}^{N_\tau} R^{m-1}\mathbf{x}_{m\tau}, \end{aligned} \tag{2}$$

where $\mathbf{K} \in \Re^{n \times n}$ is the feedback gain matrix, $0 \leq R < 1$ is a control gain, $\mathbf{S}_\tau = \mathbf{S}(t-\tau)$ and $\mathbf{x}_{m\tau} = \mathbf{x}(t - m\tau)$ are related to delayed states of the system and τ is the time delay. The UPO stabilisation can be achieved by a proper choice of $\mathbf{K}$ and R. Note that for any gain defined by $\mathbf{K}$ and R, perturbation of Eq. (1) vanishes when the system is on the UPO since $\mathbf{x}(t - m\tau) = \mathbf{x}(t)$ for all m if $\tau = T_i$, where T_i is the periodicity of the ith UPO. It should be pointed out that when $R = 0$, the ETDF turns into the original time-delayed feedback (TDF) control method proposed by Pyragas (1992).

The controlled dynamical system consists of a set of delay differential equations (DDEs). The solution of this system is obtained by establishing an initial function $\mathbf{x}_0 = \mathbf{x}_0(t)$ over the interval $(-N_\tau \tau, 0)$. By estimating this function by a Taylor series expansion, as proposed by Cunningham (1954), the following system is obtained:

$$\dot{\mathbf{x}} = \mathbf{Q}(\mathbf{x}, t) + \mathbf{K}\left[(1 - R)\mathbf{S}_\tau - \mathbf{x}\right]$$

$$\text{where} \quad \begin{cases} \mathbf{S}_\tau = \displaystyle\sum_{m=1}^{N_\tau} R^{m-1}\left[\mathbf{x} - m\tau\,\dot{\mathbf{x}}\right], & \text{for } (t - m\tau) < 0. \\ \mathbf{S}_\tau = \displaystyle\sum_{m=1}^{N_\tau} R^{m-1}\mathbf{x}_{m\tau}, & \text{for } (t - m\tau) \geqslant 0 \end{cases} \tag{3}$$

Note that DDEs contain derivatives that depend on the solution at delayed time instants. Therefore, besides the special treatment that must be given for $(t - N_\tau \tau) < 0$, it is necessary to deal with time-delayed states while integrating the system. A fourth-order Runge-Kutta method with linear interpolation on the delayed variables is employed in this work for the numerical integration of the controlled dynamical system (Mensour and Longtin 1997).

Before the control stage, where the desired UPOs are stabilised, it is necessary to identify the UPOs embedded in chaotic attractor, which is done by using the close-return method (Auerbach *et al.*1987), and to define proper controller parameters, $\mathbf{K}$ and R, for each one of the desired orbits. The controller parameter values for each UPO are defined by calculating the Lyapunov exponents of the correspondent orbit in such a way that the exponents become all negatives and the UPO becomes stable. A proper procedure to calculate these Lyapunov exponents is presented by De Paula and Savi (2009).

3 Parametric Pendulum-Shaker System

The idea that energy harvesting can be provided from sea waves was previously addressed in Xu (2005) and Horton and Wiercigroch (2008) that investigated the dynamics of a parametrically driven pendulum. Motivated by this idea, Xu *et al.* (2007)

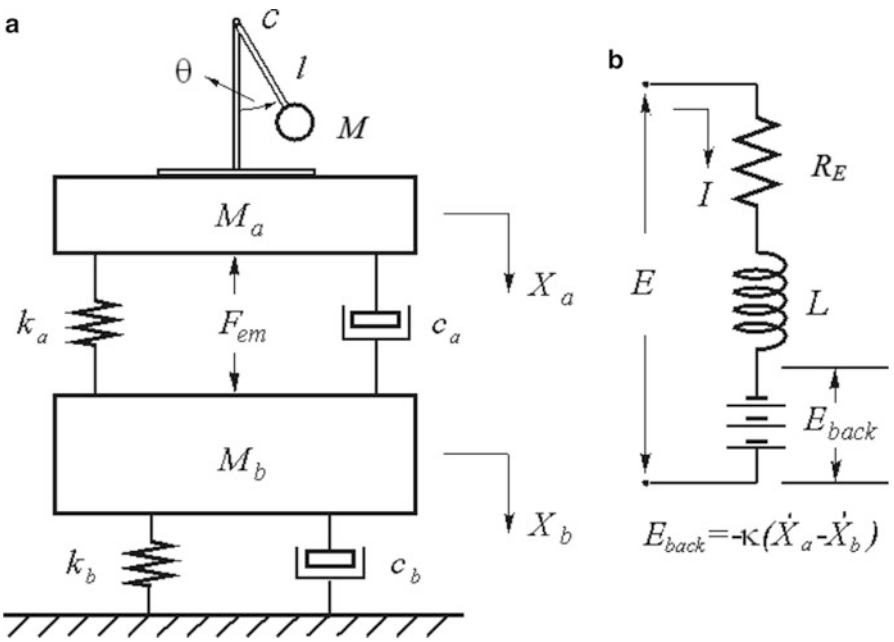

Fig. 1 Physical model of the pendulum-shaker system (Xu *et al.*2007) with mechanical and electrical components

analysed the behaviour of a parametric pendulum excited by electro-dynamical shaker, which is chosen to be studied in this work. Experimental studies undertaken at the University of Aberdeen have confirmed the validity of such model. Figure 1 presents a schematic picture of this system identifying mechanical and electrical parts. The mechanical system (Fig. 1a) is comprised of three masses: the pendulum mass, M, the armature assembly mass, M_a, and the body mass, M_b, that represents the mass of the magnetic structure containing the field coil. The excitation is provided by an axial electromagnetic force, F_{em}, which is generated by the alternating current in the constant magnetic field represented by the electrical system.

The mechanical part of the pendulum–shaker system is described by three generalized coordinates: angular displacement of the pendulum, θ, and the vertical displacements of the body and the armature, X_b and X_a, respectively. The electrical system is described by the electric charge q, that is related to the current I by its derivative: $I = dq/dt$. Equations of motion for each degree-of-freedom of the parametric pendulum-shaker system are given by (Xu *et al.*2007). Considering the state variables $\{x_1, x_2, x_3, x_4, x_5, x_6, x_7\} = \{\theta, \dot{\theta}, X_a, \dot{X}_a, X_b, \dot{X}_b, I\}$, the equations of motion are written as a set of first order differential equations:

Table 1 Pendulum-shaker system parameters

M	0.845 kg	L	0.3166 m	c	0.0475 kg/s
M_a	68.38 kg	k_a	86,175.9 kg/s^2	c_a	534.05 kg/s
M_b	820 kg	k_b	244,284 kg/s^2	c_b	679.35 kg/s
R_E	0.3 Ω	L	2.626×10^{-3} H	κ	130 N/A

$$
\begin{aligned}
\dot{x}_1 &= x_2 \\
\dot{x}_2 &= \frac{(T_C/l - clx_2)(M_a + M) - [c_a(x_4 - x_6) + k_a(x_3 - x_5) + \kappa x_7]M \sin x_1}{Ml(M_a + M - M\sin^2 x_1)} + \\
&\quad + \frac{M^2 l {x_2}^2 \cos x_1 \sin x_1}{Ml(M_a + M - M\sin^2 x_1)} \\
\dot{x}_3 &= x_4 \\
\dot{x}_4 &= \frac{(M_a + M)g + Ml{x_2}^2 \cos x_1 - \kappa x_7 - c_a(x_4 - x_6) - k_a(x_3 - x_5)}{M_a + M - M\sin^2 x_1} + \\
&\quad \frac{-clx_2 \sin x_1 - mg\sin^2 x_1}{M_a + M - M\sin^2 x_1} \\
\dot{x}_5 &= x_6 \\
\dot{x}_6 &= \frac{M_b g + \kappa x_7 - c_b x_6 + c_a(x_4 - x_6) - k_b x_5 + k_a(x_3 - x_5)}{M_b} \\
\dot{x}_7 &= \frac{E_0 \cos(\Omega t) - R_E x_7 + \kappa(x_4 - x_6)}{L}
\end{aligned}
\tag{4}
$$

where T_C corresponds to the control parameter actuation, which consists of a torque applied to the pendulum. By using the formalism presented for the extended time-delayed feedback control law, with $N_\tau = 3$, T_C may be expressed as follows:

$$
T_C = \frac{Ml(M_a + M - M\sin^2 x_1)}{(M_a + M)} K[(1 - R)(x_\tau + Rx_{2\tau} + R^2 x_{3\tau}) - x], \tag{5}
$$

where $x_\tau = x_2(t - \tau)$, $x_{2\tau} = x_2(t - 2\tau)$ and $x_{3\tau} = x_2(t - 3\tau)$. Moreover, matrix gain $\mathbf{K}$ becomes a scalar K once only component K_{22} is different from zero. This component influences time evolution equation related to x_2 and multiplies a term that depends on delayed states of x_2.

Xu et al. (2007) discussed experimental aspects of the pendulum-shaker dynamics. Here, we use the proposed model with experimentally determined parameters presented in Table 1.

At this point, let us briefly analyse the uncontrolled system behaviour. Bifurcation diagrams are constructed by assuming a quasi-static stroboscopically increase of the voltage amplitude E_0 with initial value of $E_0 = 60$ V. The first 200 periods

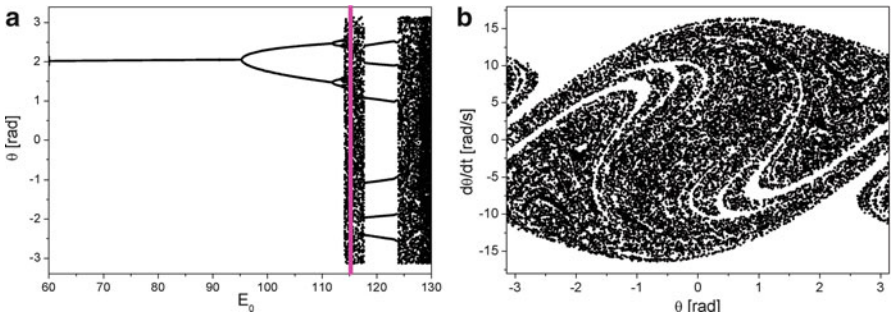

Fig. 2 (**a**) Bifurcation diagram constructed at $\Omega = 9$ rad/s and (**b**) Poincare section at $E_0 = 115$ V

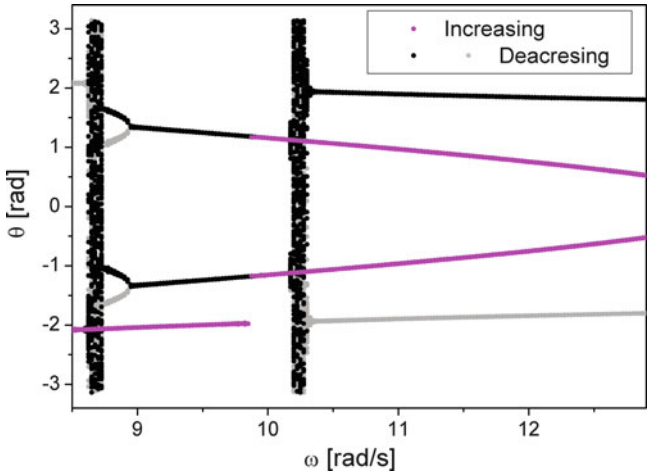

Fig. 3 Bifurcation diagram E0 = 85 V by increasing and decreasing the forcing frequency. Different coexisting solutions are *highlighted*

are neglected in order to reach steady state response. The diagram shows period doubling bifurcations that reach chaotic regions and then, periodic window related to a period-6 response. Figure 2a presents this bifurcation diagram for $\Omega = 9$ rad/s. A Poincaré section, whose cross-section is shown in Fig. 2a, is also presented in Fig. 2b for $E_0 = 115$ V considering the phase space bounded within $(-\pi, +\pi)$.

In order to explore some details of the dynamical behaviour of the pendulum-shaker system, a different bifurcation diagram is now constructed under the variation of frequency parameter Ω and $E_0 = 85$ V. Figure 3 presents three different situations: increasing the forcing frequency, in pink, and decreasing the frequency with different initial conditions, in black and in gray. The analysis of Fig. 3 shows that the system seems to have similar behaviour at $\Omega = 12.2$ rad/s and $\Omega = 10.25$ rad/s. Nevertheless, in the first case the system presents three co-existing periodic attractors, while at $\Omega = 10.25$ rad/s there are two quasi-periodic and one periodic attractors co-existing.

The analysis of the system dynamics shows that the parametric pendulum may present different kinds of solutions. Periodic, quasi-periodic and chaotic responses are all present in the system behaviour. Besides, it is important to highlight the coexisting attractors that can occur for the same set of parameters. Therefore, bifurcation control is important when we are thinking of the use of this pendulum system in some application. In terms of energy harvesting, it is of special interest to keep a period-1 rotating orbit avoiding any kind of bifurcation. In the same context, an interesting procedure could be the stabilization of a rotation solution immersed in chaotic attractor and not only a period-1 orbit. In this regard, we will apply control techniques for bifurcation control.

4 Controlling the Pendulum-Shaker System

In this section continuous chaos control method is employed in order to prevent bifurcation to chaos by stabilizing originally unstable period-1 rotating orbit.

Figure 4 presents some co-existing orbits identified in bifurcation diagram of Fig. 3. Figure 4a presents a phase space with three orbits: two orbits of period-1 and a period-2 orbit that coexist at $\Omega = 12.2$ rad/s and $E_0 = 85$ V. Figure 4b presents the phase space of the same orbits at $\Omega = 10.25$ rad/s and $E_0 = 85$ V showing the change of the two period-1 orbits to two quasi-periodic orbits. This picture also presents the Poincare sections of quasi-periodic responses.

It is considered the case where the forcing frequency is decreasing. The aim is to keep a rotating orbit, avoiding the bifurcation to chaos. Moreover, since the period-2 orbit is not a rotating orbit, this response is not desirable. Before the bifurcation to chaos the system presents a quasi-periodic behaviour, the period-1 "positive" orbit identified at $E_0 = 85$ V and $\Omega = 12.2$ rad/s is considered as the fiducial trajectory. Figure 5 shows the bifurcation diagram constructed at $E_0 = 85$ V with and without control action. Controller uses $R = 0.2$ and $K = 0.4$ with the objective of keep the rotating response of the system. It is important to mention that on the results

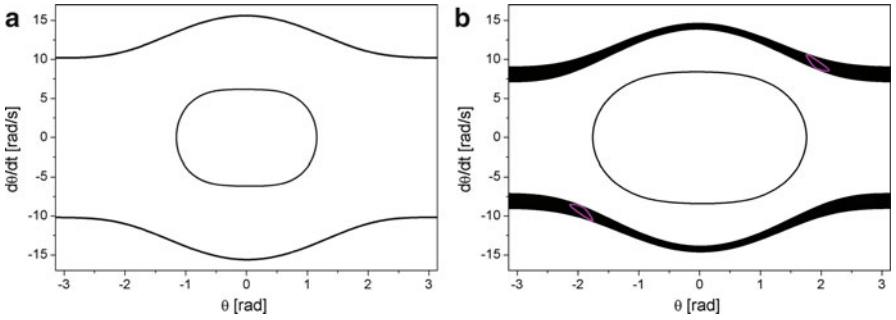

Fig. 4 Coexisting attractors at $E_0 = 85$ V: (a) $\Omega = 12.2$ rad/s; (b) $\Omega = 10.25$ rad/s

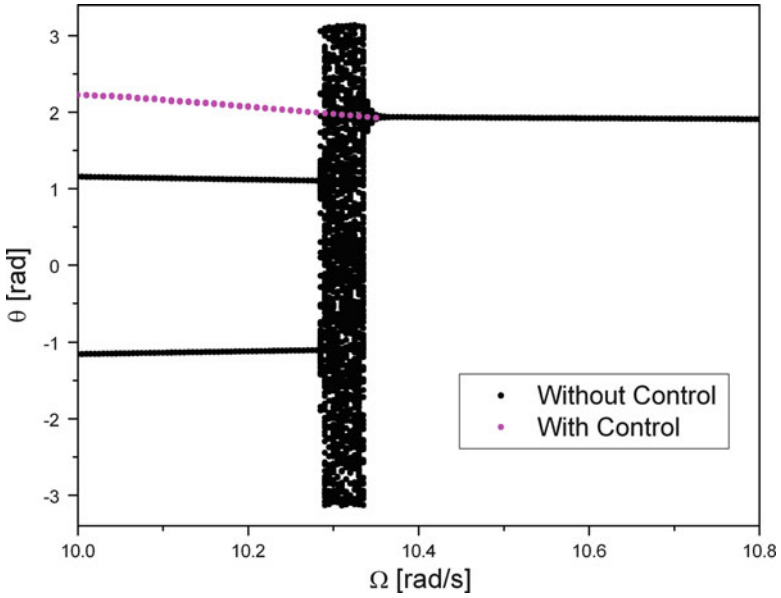

Fig. 5 Bifurcation diagram at $E_0 = 85$ V with and without control action

presented in Fig. 5 the controller waits until the system trajectory "falls" in the neighbourhood of the desired orbit before being in the control on mode. Moreover, the desired orbit is the period-1 orbit identified at $\Omega = 12.2$ rad/s. This wait time is necessary due to the quasi-periodic behaviour before the bifurcation. If there were a period-1 response before the bifurcation, instead of the quasi-periodic behaviour, the system would already be at the neighbourhood of the desired orbit and the wait time would not be necessary. This wait time is an essential characteristic of discrete chaos control method (Ott *et al.*1990) being not usually employed in continuous methods (Pyragas 1992).

5 Conclusions

This paper presents the analysis of bifurcation control of a pendulum-shaker system. This electric-mechanical system may be used to simulate the dynamics of the pendulum to explore the concept of energy harvesting from sea waves. This idea requires the rotating unbounded periodic response of the system to be maintained throughout significant parameters range. The bifurcation control is applied in order to stabilize desired rotational orbits for the parameters values where they are originally unstable. The continuous control methods known as extended time delayed feedback is employed to avoid bifurcation to chaos and stable rotating solution is successfully obtained.

Acknowledgments The authors would like to acknowledge the support of FINATEC and of the Brazilian Research Agencies CNPq, FAPERJ and through the INCT-EIE (National Institute of Science and Technology – Smart Structures in Engineering) the CNPq and FAPEMIG. The Air Force Office of Scientific Research (AFOSR) is also acknowledged.

References

Auerbach, D., Cvitanovic, P., Eckmann, J.-P., Gunaratne, G., Procaccia, I.: Exploring chaotic motion through periodic orbits. Phys. Rev. Lett. **58**(23), 2387–2389 (1987)

Clifford, M.J., Bishop, S.R.: Rotating periodic orbits of the parametrically excited pendulum. Phys. Lett. A **201**, 191–196 (1995)

Cunningham, W.J.: A nonlinear differential-difference equation of growth. Mathematics **40**, 708–713 (1954)

De Paula, A.S., Savi, M.A.: Controlling chaos in a nonlinear pendulum using an extended time-delayed feedback control method. Chaos Solitons Fract. **42**(5), 2981–2988 (2009)

Horton, B.W., Wiercigroch, M.: Effects of heave excitation on rotations of a pendulum for wave energy extraction. In: IUTAM Symposium on Fluid-Structure Interaction in Ocean Engineering, vol. 8, pp. 117–128, Springer, Dordrecht (2008)

Lenci, S., Pavlovskaia, E., Rega, G., Wiercigroch, M.: Rotating solutions and stability of parametric pendulum by perturbation method. J. Sound Vib. **310**, 243–259 (2008)

Mensour, B., Longtin, A.: Power spectra and dynamical invariants for delay-differential and difference equations. Phys. D **113**, 1–25 (1997)

Ott, E., Grebogi, C., Yorke, J.A.: Controlling chaos. Phys. Rev. Lett. **64**(11), 1196–1199 (1990)

Pyragas, K.: Continuous control of chaos by self-controlling feedback. Phys. Lett. A **170**, 421–428 (1992)

Socolar, J.E.S., Sukow, D.W., Gauthier, D.J.: Stabilizing unstable periodic orbits in fast dynamical systems. Phys. Rev. E **50**(4), 3245–3248 (1994)

Szemplinska-Stupnicka, W., Tyrkiel, E.: The oscillation-rotation attractors in the forced pendulum and their peculiar properties. Int. J. Bifurc. Chaos **12**, 159–168 (2002)

Xu, X.: Nonlinear dynamics of parametric pendulum for wave energy extraction. PhD thesis, University of Aberdeen (2005)

Xu, X., Pavlovskaia, E., Wiercigroch, M., Romeo, F., Lenci, S.: Dynamic interactions between parametric pendulum and electro-dynamical shaker. Z. Angew. Math. Mech. **87**(2), 172–186 (2007)

A Study on Swing up Control for Rotation of Parametric Pendulum

Yuichi Yokoi and T. Hikihara

Abstract A parametric pendulum inherently demonstrates a conversion from external vibration to rotational motion and this property is applicable to energy scavenging from vibration of external source in nature. The periodic rotation of the parametric pendulum has a benefit to convert the mechanical energy to electric energy through conventional electric machines. On the other hand, the onset of the periodic rotation depends on the initial condition. We propose a control method for starting up the parametric pendulum to the periodic rotations based on an external force input with time delay. The feasibility of proposed method is verified numerically and experimentally. The results show that there exists a certain range of control gain to achieve the control from any initial condition. This paper advocates that the proposed method is suitable for crossing over a separatrix which governs the dynamics.

Keywords Parametric pendulum • Delayed feedback control • Rotating solutions

1 Introduction

Parametrically excited pendulums have been widely investigated as a simple nonlinear dynamical system with complex behaviour. There appear a variety of steady motions for the parametric pendulum (McLaughlin 1981; Koch et al. 1983;

Y. Yokoi (✉)
Division of Electrical Engineering and Computer Science, Nagasaki University, Bunkyo, Nagasaki, 852-8521, Japan
e-mail: yyokoi@nagasaki-u.ac.jp

T. Hikihara
Department of Electrical Engineering, Kyoto University, Katsura, Nishikyo, Kyoto, 615-8510, Japan
e-mail: hikihara@kuee.kyoto-u.ac.jp

M. Wiercigroch and G. Rega (eds.), *IUTAM Symposium on Nonlinear Dynamics for Advanced Technologies and Engineering Design*, IUTAM Bookseries (closed) 32, DOI 10.1007/978-94-007-5742-4_31,

Clifford and Bishop 1995). The rotation corresponds to a conversion from external vibration to the rotational motion. This suggests that the parametric pendulum is applicable to energy scavenging from vibration of external source. The periodic rotation of the parametric pendulum is useful in this sense. This study was motivated by the previous work Xu and Wiercigroch (2007), Lenci et al. (2008), and Horton et al. (2008). Because the onset of the periodic rotation depends on the initial condition, the parametric pendulum has to be controlled for the desirable motion.

We propose a control method for starting up the parametric pendulum to the periodic rotation (Yokoi and Hikihara 2011) based on the external force control (Pyragas 1992). The onset to the inherent periodic rotation requires a null control input after the rotary motion is established. It is worth pointing out here that an exact model cannot be developed from a practical point of view. This paper shows that the external force control with delayed feedback is well suited for starting up.

The feasibility of the proposed control method is verified numerically and experimentally. The external force control has been used as a method for controlling chaos (Pyragas 1992), which stabilizes an unstable periodic orbit embedded in a chaotic attractor (Otto et al. 1990; Schuster 1999; Schöll and Schuster 2008). The controlling chaos is based on the properties of chaos such as the topological transitivity representing that the state accesses the vicinity of each one of the periodic orbits, and the sensitive dependence on small perturbation. It is obvious that the same properties as chaos are not observed in the periodic rotation of parametric pendulum. However, the periodic structure of the state space and a torque control makes it possible for the state to approach the periodic rotation instead of the topological transitivity. Since the desired motion is a stable periodic rotation, the sensitive dependence is not required. Thus the external force control can operate for the periodic rotation of parametric pendulum without the above chaotic properties. The reference signal needed in the control can be designed by using the delayed state. Additionally, the control method, called the delayed feedback control (Pyragas 1992), possesses the property that an exact model of the controlled system is not required (Pyragas and Tamaševičius 1993; Hikihara and Kawagoshi 1996).

2 Start-Up Control

Before introducing the start-up control, the target periodic rotation is introduced. The dynamics of parametric pendulum is described by the following differential equations with the angular displacement $\theta(t)$ and the velocity $v(t)$:

$$\begin{cases} \dfrac{\mathrm{d}\theta}{\mathrm{d}t} = v, \\ \dfrac{\mathrm{d}v}{\mathrm{d}t} = -\gamma v - (1 + p\cos\omega t)\sin\theta, \end{cases} \tag{1}$$

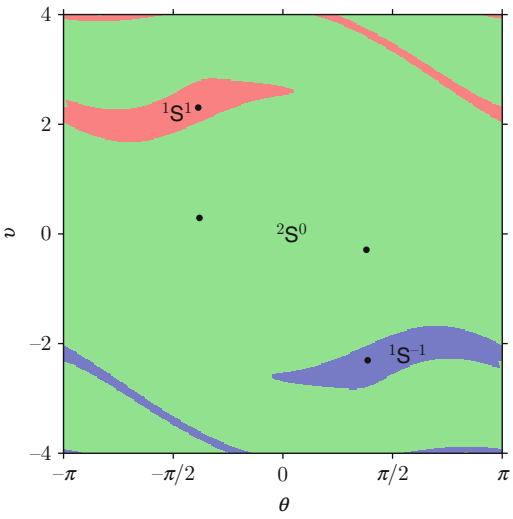

Fig. 1 Basins of attraction in the parametric pendulum (1) calculated for $\gamma = 0.1$, $p = 0.5$, and $\omega = 2$. The periodic states are depicted by the fixed points ${}^nS^r$, where n and r correspond to Eq. (2)

where γ is the viscous damping coefficient. The term $p \cos \omega t$ gives the parametric excitation with the amplitude p and the frequency ω. Steady states of a parametric pendulum can be expressed by a natural number n and an integer r as

$$\theta(t) := \theta(t - nT) + 2\pi r, \tag{2}$$

where T denotes the period of parametric excitation. A combination of n and r expresses that the pendulum rotates r times during n periods. The positive (negative) value of r represents that the pendulum rotates in the direction to increase (decrease) the angular displacement θ, respectively. Periodic oscillations are expressed as $r = 0$.

In the following, the parameter setting for Eq. (1) is fixed at $\gamma = 0.1$, $p = 0.5$, and $\omega = 2$ so that the parametric pendulum rotates once during the excitation period T (Clifford and Bishop 1995). The periodic rotation coexists with a periodic rotation in the inverse direction and a $2T$-periodic oscillation. Figure 1 shows the domain of attraction at the parameter setting. The periodic states are depicted by the fixed points ${}^nS^r$, where n and r correspond to Eq. (2). Here we focus on the periodic rotation in the positive direction ($r > 0$) as the target motion to control.

We propose a control method for starting up a periodic rotation inherent in the parametric pendulum based on the external force control (Pyragas 1992). The external force control requires the reference signal for the target motion. The expression (2) describes that the current angular displacement $\theta(t)$ is equivalent to the sum of the delayed displacement $\theta(t - nT)$ and the rotation angle $2\pi r$. The required reference signal can be designed by using a delayed angular displacement and a constant. Figure 2 shows the block diagram of the proposed start-up control. The proposed method regulates a torque applied to the parametric pendulum so

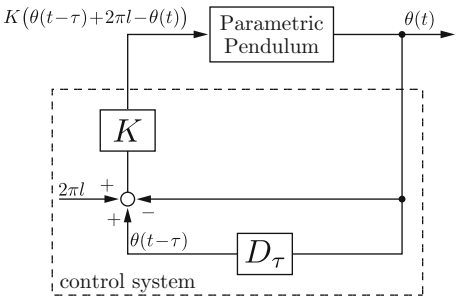

Fig. 2 Block diagram of the proposed control method for starting up a periodic rotation of parametric pendulum

that the pendulum follows the reference signal. The reference signal consists of the delayed angular displacement $\theta(t-\tau)$ memorized in the delay block D_τ and the constant $2\pi l$. Based on the external force control, the feedback loop constructs the control signal u from the current angular displacement θ, the reference signal $\theta(t-\tau)+2\pi l$, and the control gain K as shown in Fig. 2. In the case that the target motion is described by the expression (2), the control parameters are adjusted at $\tau = nT$ and $l = r$. Thus, the start-up control does not require an exact model of the parametric pendulum and any information about the target except n and r. The equations governing the controlled parametric pendulum are given as

$$\begin{cases} \dfrac{\mathrm{d}\theta}{\mathrm{d}t} = v, \\ \dfrac{\mathrm{d}v}{\mathrm{d}t} = -\gamma v - (1 + p\cos\omega t)\sin\theta + u(t), \\ u(t) = K\big(\theta(t-\tau) + 2\pi l - \theta(t)\big). \end{cases} \tag{3}$$

The characteristics of control method are determined by the control gain K, the delay time τ, and the rotation number l.

3 Numerical Study

We numerically examine the performance of the start-up control. Throughout this section, the start-up control is applied to the parametric pendulum (1) at the above parameter setting. The control parameters are fixed at $\tau = T = 2\pi/\omega$ and $l = 1$ for starting up the periodic rotation, at which the pendulum rotates once during the excitation period T.

Figure 3 shows the start-up control for the periodic rotation inherent in the parametric pendulum from the coexisting periodic oscillation. Onset of the control is $t = t_0 = 3T$. The initial condition of the delay component is set on the angular displacement before the onset of control, that is $\theta(t_0 + s)$ where $s \in [-T, 0)$. The points on the curves denote the stroboscopic points taken at every excitation

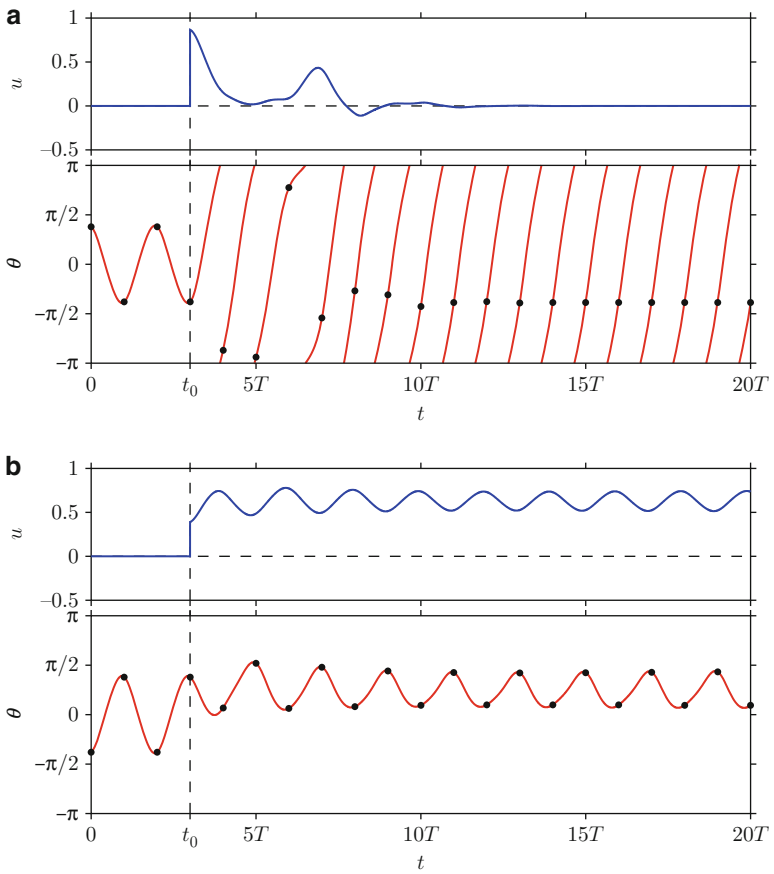

Fig. 3 Start-up control for the inherent periodic rotation from two initial conditions at $\gamma = 0.1$, $p = 0.5$, $\omega = 2$, $K = 0.1$, $\tau = 2\pi/\omega$, and $l = 1$. The initial conditions are selected on the periodic oscillation. Onset of the control is $t = t_0 = 3T$. The points on the curves denote the stroboscopic points at every excitation period T

period T. Figure 3a shows that the periodic rotation can be established by using the proposed control. After the onset of control, the null control input implies that the periodic rotation is inherent in the parametric pendulum. On the other hand, the proposed control cannot start the periodic rotation from the different initial condition as shown in Fig. 3. Therefore the performance of the start-up control depends on the initial condition.

The performance also depends on the control gain K (Pyragas 1992). In order to understand the characteristics of the proposed control, the domain of attraction in the controlled parametric pendulum (3) is investigated for the control gain. Figure 4 shows the domain of attraction at $K = 0.05$, 0.1, 0.15, and 0.2. The initial condition of the delay component is given as the inherent motion of the parametric

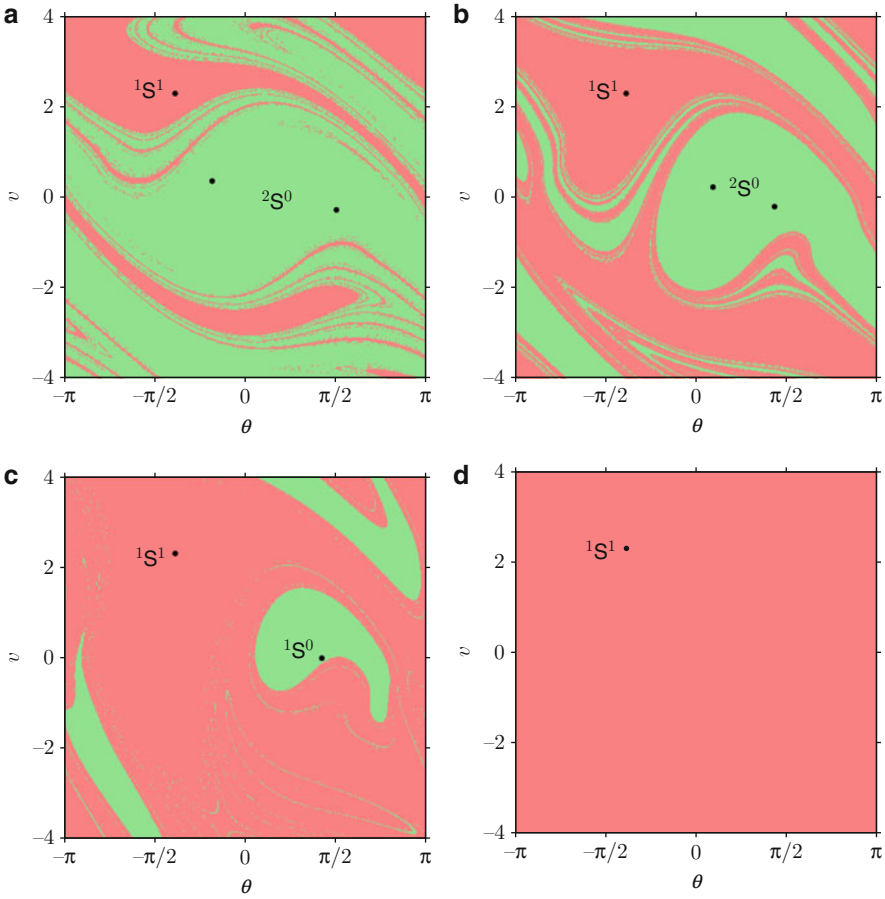

Fig. 4 Domain of attraction in the controlled parametric pendulum (3) at $\gamma = 0.1$, $p = 0.5$, $\omega = 2$, $\tau = 2\pi/\omega$, and $l = 1$. The initial condition of the delay component is given as the inherent motion of the parametric pendulum (1). The periodic states are depicted by the fixed points ${}^nS^r$, where n and r correspond to Eq. (2). (**a**) $K = 0.05$. (**b**) $K = 0.1$. (**c**) $K = 0.15$. (**d**) $K = 0.2$

pendulum (1). Increasing the control gain expands the basin of the target rotation, denoted by $^1S^1$ in Fig. 4. For small control gain, the achievement of the target rotation strongly depends on the initial condition. The target rotation becomes only one attractor on the domain at $K = 0.2$ as shown in Fig. 4d. At the control gain, the start-up control can establish the target periodic rotation from any initial condition. The result shows that the proposed method can start up the parametric pendulum to the inherent periodic rotation from any initial condition for a certain control gain.

4 Experimental Verification

The feasibility of the start-up control is verified experimentally. Figure 5 shows the experimental setup for parametric pendulum constructed by exciting a mechanical pendulum vertically. The mechanical pendulum consists of the mass 189.1 g and the length 138.3 mm by constructing a rod and a bob in Table 1. The pendulum is supported by a mechanical rig mounted on an electromagnetic shaker. The shaker generates a vertical excitation corresponding to the parametric excitation. The setup involves the angle sensor for the angular displacement of pendulum and the DC motor for the control input torque. The control loop can be implemented as a program in a computer with A/D and D/A converters.

The vertical excitation of the shaker is adjusted to the sinusoidal waveform having amplitude $1.1\,\mathrm{m/s^2}$ and frequency $2.0\,\mathrm{Hz}$ so that the periodic rotation coexists with a periodic oscillation. The control gain is set at $K = 0.072\,\mathrm{A/rad}$. This is equivalent to $0.013\,\mathrm{N \cdot m/rad}$ in terms of the control torque. The start-up control beginning from the periodic oscillation in the experimental pendulum is shown in Fig. 6. The result shows that the periodic rotation is achieved from the periodic oscillation. After the accomplishment of control, the control input $u(t)$ disappears. This suggests that the periodic rotation is inherent in the experimental setup at the parameters.

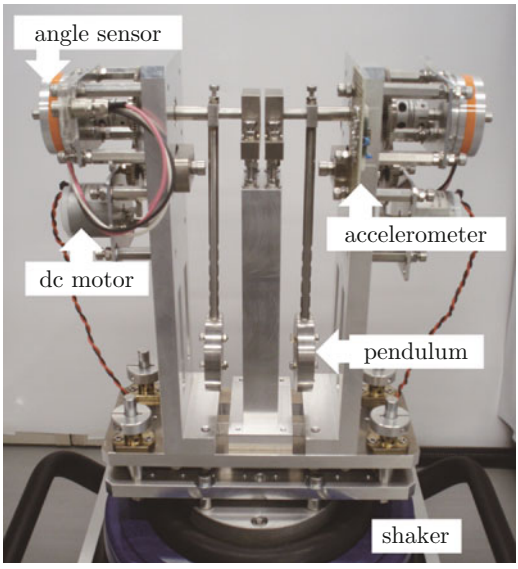

Fig. 5 Experimental setup of the parametric pendulum (Horton 2008)

Table 1 Size of mechanical pendulum

Rod		Bob	
Mass	39.6 g	Mass	144.9 g
Length	180.0 mm	Diameter	50.0 mm
Diameter	6.0 mm	Width	10.0 mm

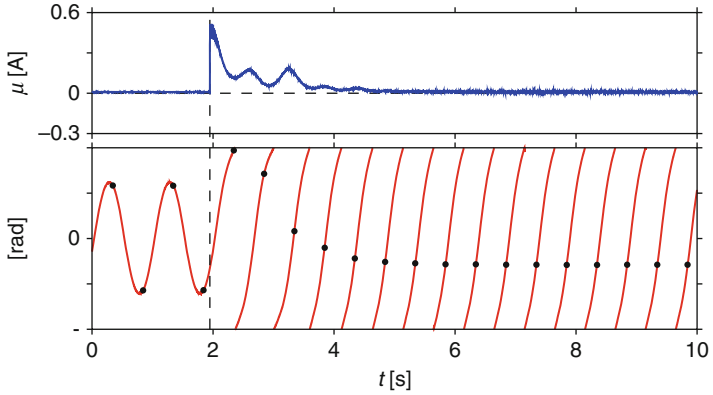

Fig. 6 Start-up control for the periodic rotation of the experimental pendulum from the periodic oscillation

5 Summary

In this paper, we proposed a control method for starting up the parametric pendulum to the periodic rotation and examined the feasibility numerically and experimentally. The proposed method with time delay works as a control to cross over separatrixes which form boundaries between basins of steady states. The control generates a path to the target state by adding dimensions to the inherent state space. For the delayed feedback control which is the framework of the proposed method, the extended and the generalized schemes have been reported (Schöll and Schuster 2008; Pyragas 1995). Since these concepts are essentially the same as that of the original method, we confined the discussion to the most fundamental control scheme in this paper. It is obvious that the extension and the generalization are valid for the proposed start-up control.

Acknowledgements The authors appreciate fruitful discussions with Dr. Kohei Yamasue, Assistant Professor of Research Institute of Electrical Communication in Tohoku University. In particular, one of the authors (YY) appreciates kind support and hospitality in research visit at the Centre for Applied Dynamics Research at the University of Aberdeen. This research was partially supported by the Global COE program of Kyoto University founded by the Ministry of Education, Culture, Sports and Technology of Japan.

References

Clifford, M.J., Bishop, S.R.: Rotating periodic orbits of the parametrically excited pendulum. Phys. Lett. A **201**, 191–196 (1995)

Hikihara, T., Kawagoshi, T.: An experimental study on stabilization of unstable periodic motion in magneto-elastic chaos. Phys. Lett. A **211**, 29–36 (1996)

Horton, B.: Nonlinear dynamics of pendula systems. PhD Thesis, University of Aberdeen (2008)
Horton, B., Wiercigroch, M., Xu, X.: Transient tumbling chaos and damping identification for parametric pendulum. Philos. Trans. R. Soc. A **366**, 767–784 (2008)
Koch, B.P., Leven, R.W., Pompe, B., Wilke, C.: Experimental evidence for chaotic behaviour of a parametrically forced pendulum. Phys. Lett. A **96**, 219–224 (1983)
Lenci, S., Pavlovskaia, E., Rega, G., Wiercigroch, M.: Rotating solutions and stability of parametric pendulum by perturbation method. J. Sound Vib. **310**, 243–259 (2008)
McLaughlin, J.B.: Period-doubling bifurcations and chaotic motion for a parametrically forced pendulum. J. Stat. Phys. **24**, 375–388 (1981)
Otto, E., Grebogi, C., Yorke, J.A.: Controlling chaos. Phys. Rev. Lett. **64**, 1196–1199 (1990)
Pyragas, K.: Continuous control of chaos by self-controlling feedback. Phys. Lett. A **170**, 421–428 (1992)
Pyragas, K.: Control of chaos via extended delay feedback. Phys. Lett. A **206**, 323–330 (1995)
Pyragas, K., Tamaševičius, A.: Experimental control of chaos by delayed self-controlling feedback. Phys. Lett. A **180**, 99–102 (1993)
Schöll, E., Schuster, H.G. (eds.): Handbook of Chaos Control, 2nd edn. Wiley-VCH, Weiheim (2008)
Schuster, H.G. (ed.): Handbook of chaos control. Wiley-VCH, Weinheim (1999)
Xu, X., Wiercigroch, M.: Approximate analytical solutions for oscillatory and rotational motion of a parametric pendulum. Nonlinear Dyn. **47**, 311–320 (2007)
Yokoi, Y., Hikihara, T.: Start control of parametric pendulum into periodic rotation (in Japanese). ISCIE J. (2011, to be published)

On Nonlinear Dynamics and Control Design in a "MEMS" Gyroscope System

Fábio Roberto Chavarette, José Manoel Balthazar, and Jorge Luis Palacios Felix

Abstract This paper deals with a (MEMS) Gyroscope nonlinear dynamical system, modeled with a proof mass constrained to move in a plane with two resonant modes, which are nominally orthogonal. We present some modifications to the governing equations of the considered system, taking into account the nonlinear interactions between the parts of the systems. We also develop a linear optimal control design, for reducing the oscillatory movement of the nonlinear system to a stable point.

Keywords Non-ideal vibrating MEMS gyroscope • Nonlinear dynamics and stability • Linear optimal control

1 Introduction

The technology of micro electro mechanical systems, called ("MEMS") has found numerous applications in recent years. It is also well known that the classical tuning-fork ("MEMS") gyroscope contains a pair of masses that are driven to oscillate with

F.R. Chavarette
Faculty of Engineering, Post Graduate Program in Mechanical Engineering, UNESP – Univ Estadual Paulista, DM, Avenida Brasil, 56, 15385-000, Ilha Solteira, SP, Brazil
e-mail: fabioch@mat.feis.unesp.br

J.M. Balthazar (✉)
Geoscience and Exact Science Institute, UNESP – Univ Estadual Paulista, DEMAC, PO BOX 178, Rio Claro 13500-230, SP, Brazil
e-mail: jmbaltha@rc.unesp.br

J.L.P. Felix
UNIPAMPA, Universidade Federal do Pampa, Rua Carlos Barbosa s/n°, 96412-420 CP 07 Bagé, RS, Brazil
e-mail: jorgelpfelix@yahoo.com.br

M. Wiercigroch and G. Rega (eds.), *IUTAM Symposium on Nonlinear Dynamics for Advanced Technologies and Engineering Design*, IUTAM Bookseries (closed) 32, DOI 10.1007/978-94-007-5742-4_32,

equal amplitude but in opposite directions. When rotating, the Coriolis force gives rise to an orthogonal vibration that can be sensed by a variety of mechanisms (see e.g., Oropeza-Ramos et al. 2007). The Draper Lab gyroscope uses a comb-type structure to drive the tuning fork into resonance. Rotation causes the proof masses to vibrate out of plane, and this motion is sensed capacitive with a custom CMOS ASIC. The micro-tuning fork gyroscope may be mathematically modeled (by a Macro Model) by two proof masses must be driven into oscillations which are opposite in directions (Oropeza-Ramos et al. 2007; Lee et al. 2008). Microscopic gyroscopes (Miller et al. 2008; Oropeza-Ramos et al. 2008) help to enable an emerging technology called electronic stability control.

By another hand, it is known that control problems consist of attempts to stabilize an unstable system to an equilibrium point, a periodic orbit, or more general, to a given reference trajectory (periodic or not).

In the last years, a significant interest in control of nonlinear systems exhibiting unstable behavior, has been observed and many of the techniques have been discussed in the literature (Ott et al. 1990; Sinhá et al. 2000; Rafikov and Balthazar 2008). Among strategies of control with feedback, the most popular is the OGY (Ott-Grebogi-Yorke) method (Ott et al. 1990). This method uses the Poincaré map of the system. Recently, a methodology, based on the application of the Lyapunov-Floquet transformation, was proposed by Sinha et al. (2000) in order to solve this kind of problem. This method allows directing the chaotic motion to any desired periodic orbit or to a fixed point. It is based on the linearization of the equations, which describe the error between the actual and the desired trajectories. Recently, a technique was proposed by Rafikov and Balthazar in (and 2008): The linear feedback control problem for nonlinear systems has been formulated, under the optimal control theory viewpoint. Asymptotic stability of the closed-loop nonlinear system is guaranteed by means of a Lyapunov function, which can clearly be seen as the solution of the Hamiton-Jacobi-Bellman equation, thus guaranteeing both stability and optimality. The formulated theorem (Rafikov and Balthazar 2008) expresses explicitly the form of the minimized functional and gives the sufficient conditions which allow using the linear feedback control for nonlinear systems.

The aim of this paper is to propose the application of the optimal linear control (Rafikov and Balthazar 2008) to the unstable movement of the non-ideal vibrating "MEMS" gyroscope. We organize the paper as follows: in Sect. 2, we present the mathematical model. In Sect. 3, we analyze the non-linear dynamics and stability of the non-linear "MEMS" gyroscope model. In Sect. 4, we discuss an optimal control design problem for the "MEMS" gyroscope. In Sect. 5, we end up with some concluding remarks.

2 "MEMS" Gyroscope Mathematical Model

Here, we consider the model for the "MEMS", with variable capacitor, (Fig. 1).

This model is based on the combination of the models, considered before in (Oropeza-Ramos et al. 2007; Luo and Wang Fei-Yue 2004; Luo 2002;

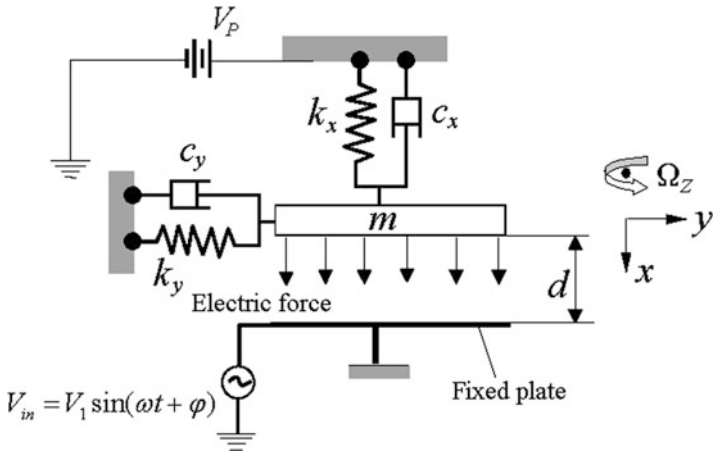

Fig. 1 A model of an electrostatically actuated micro-structure with variable capacitor

Wauer et al. 1009) with the inclusion of a kind of nonlinear interaction (Chavarette et al. 2010). The fixed plate of the capacitor is assumed to have area A. The other plate of the capacitor is a movable, rigid plate of mass m. The support of the moving plate is represented by a nonlinear spring with elastic restoring forces $F_r(x)$ and $F_r(y)$ in the x and y direction, respectively, and damping coefficients c_x and c_y. $V(t)$ is the voltage applied across the drives, with a polarization voltage V_{DC} and with an AC voltage $V_{AC} = V_A cos\ (wt)$, where V_A, w are the AC amplitude, and frequency, respectively. Without the electric force, the gap between the two plates of the capacitor in the "MEMS" is d. The coordinates of motion are x and y. The governing equations of the nonlinear "MEMS", with electrostatic force of the variable capacitor and by considering a conventional vibratory gyroscope, are:

$$m\ddot{x} + c_x\dot{x} + k_{x1}x + k_{x3}x^3 = F_e + 2m\Omega_z\dot{y}$$

$$m\ddot{y} + c_y\dot{y} + k_{y1}y + k_{y3}y^3 = -2m\Omega_z\dot{x} \tag{1}$$

where, F_e, the electrostatic force between the capacitor plates (the fixed plate and the movable plate) generated by applying a voltage V(t), can be expressed as:

$$F_e = \frac{\varepsilon_0 A V^2}{2(d-x)^2} \tag{2}$$

Note that the terms $2m\Omega_z\dot{x}$ and $2m\Omega_z\dot{y}$ represent the rotation-induced by Coriolis forces, the angular rotation is considered to be constant, and ε_0 is the

absolute dielectric constant of vacuum. The electric variable charge is adopted in the following form:

$$q = CV = \frac{\varepsilon_0 A V^2}{d - x} \tag{3}$$

and substituting it into the first Eq. (1), we will obtain

$$\begin{aligned} m\ddot{x} + c_x\dot{x} + k_{x1}x + k_{x3}x^3 &= \frac{q^2}{2\varepsilon_0 A} + 2m\Omega_z\dot{y} \\ m\ddot{y} + c_y\dot{y} + k_{y1}y + k_{y3}y^3 &= -2m\Omega_z\dot{x} \end{aligned} \tag{4}$$

Considering the equation of motion of the electric variable of the micro-structure

$$L\ddot{q} + R\dot{q} + \frac{1}{C(x)}q = V \tag{5}$$

the governing equations of the nonlinear micro-gyroscope are

$$\begin{aligned} m\ddot{x} + c_x\dot{x} + k_{x1}x + k_{x3}x^3 &= \frac{q^2}{2\varepsilon_0 A} + 2m\Omega_z\dot{y} \\ m\ddot{y} + c_y\dot{y} + k_{y1}y + k_{y3}y^3 &= -2m\Omega_z\dot{x} \\ L\ddot{q} + R\dot{q} + \frac{1}{C(x)}q &= V \end{aligned} \tag{6}$$

Using the following dimensionless variables

$$\tau = w_x t,\ w_x = \sqrt{\frac{k_x}{m}},\ X = \frac{x}{d},\ Y = \frac{y}{d},\ \Omega = \frac{w}{w_x},\ \beta_0 = \frac{V_{AC}}{Lq_0 w_x^2},\ \beta_1 = \frac{V_A}{Lq_0 w_x^2},$$

$$\mu_1 = \frac{c_x}{mw_x},\ \mu_2 = \frac{c_y}{mw_x},\ \gamma = \frac{2\Omega_z}{w_x},\ w_y = \sqrt{\frac{k_y}{m}},\ \delta = \frac{w_y}{w_x},\ r = \frac{R}{Lw_x},$$

$$\lambda_1 = \frac{q_0^2}{2\varepsilon_0 Amdw_x^2},\ \lambda_2 = \frac{d}{\varepsilon_0 ALw_x^2},\ \alpha_1 = \frac{k_{3x}d^2}{mw_x^2},\ \alpha_2 = \frac{k_{3y}d^2}{mw_x^2}$$

we may transform the equations of motion (6) to a dimensionless form

$$\begin{aligned} X'' + \mu_1 X' + X + \alpha_1 X^3 &= \lambda_1 Q^2 + \gamma Y' \\ Y'' + \mu_2 Y' + \delta^2 Y + \alpha_2 Y^3 &= -\gamma X' \\ Q'' + rQ' - \lambda_2 (1 - X)\, Q &= \beta_0 + \beta_1 \cos\Omega\tau \end{aligned} \tag{7}$$

3 Nonlinear Dynamics and Stability Analysis

The chosen numerical values for the parameters are: Ω=*1.0*, $\beta_0 = 0.15$, $\beta_1 = 0.1026$, $r = 0.015$, $\lambda_1 = 1.2$, $\lambda_2 = 0.5$, $\alpha_1 = \alpha_2 = 0.75$, $\mu_1 = \mu_2 = 0.01$, $\delta = 1.0$, whereas X' and γ = are varied. The Jacobian matrix J is:

$$J = \begin{bmatrix} 0 & 1 & 0 & 0 & 0 & 0 \\ -1 - 1.62X' & -0.01 & 0 & \gamma & 0.6 & 0 \\ 0 & 0 & 0 & 1 & 0 & 0 \\ 0 & -\gamma & -0.000164 & -0.01 & 0 & 0 \\ 0 & 0 & 0 & 0 & 0 & 1 \\ -0.125 & 0 & 0 & 0 & 0.5 - 0.5X' & -0.015 \end{bmatrix} \quad (8)$$

The eigenvalues of J, will provide the conditions for stability or instability of the equilibrium points: an equilibrium point is asymptotically stable if all the eigenvalues have negative real part and unstable if at least one of them has positive real part (Guckenheimer and Holmes 1983). The stability diagram for Eq. (7) is showed in Fig. 2.

The bifurcation diagram for Eq. (7), are showed in Fig. 3a (γ = varied) and the Lyapunov exponents are showed in Fig. 3b.

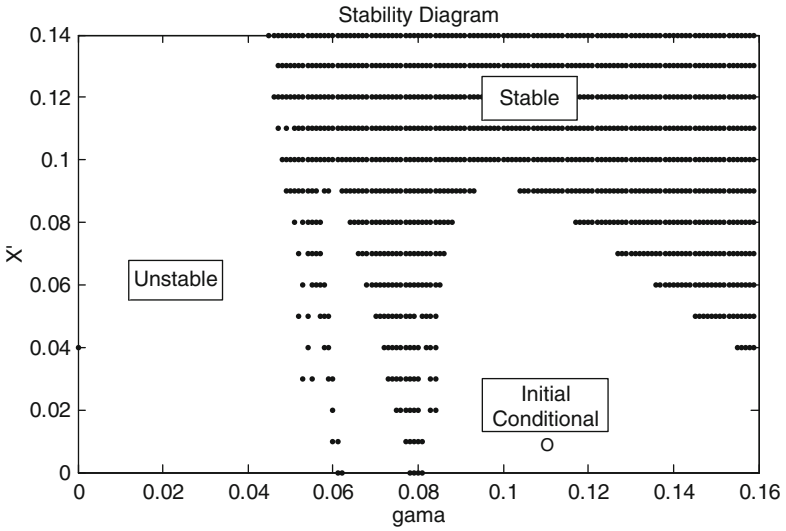

Fig. 2 Stability diagram – Chaos, $\gamma = 0.116$

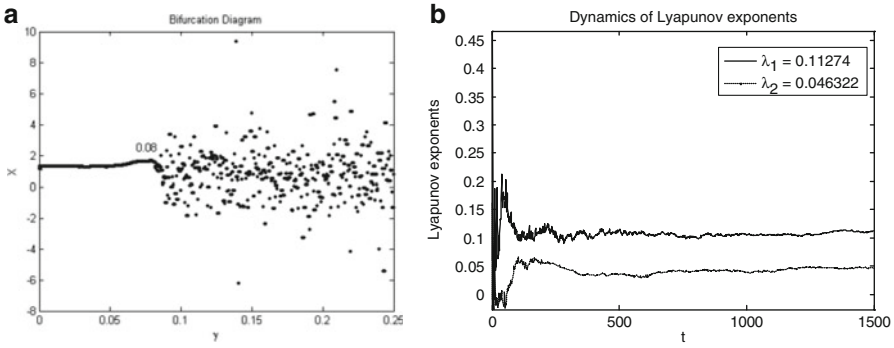

Fig. 3 (**a**) The bifurcation diagram – Chaos, $\gamma = 0.116$, (**b**) Lyapunov exponents – Chaos, $\gamma = 0.116$

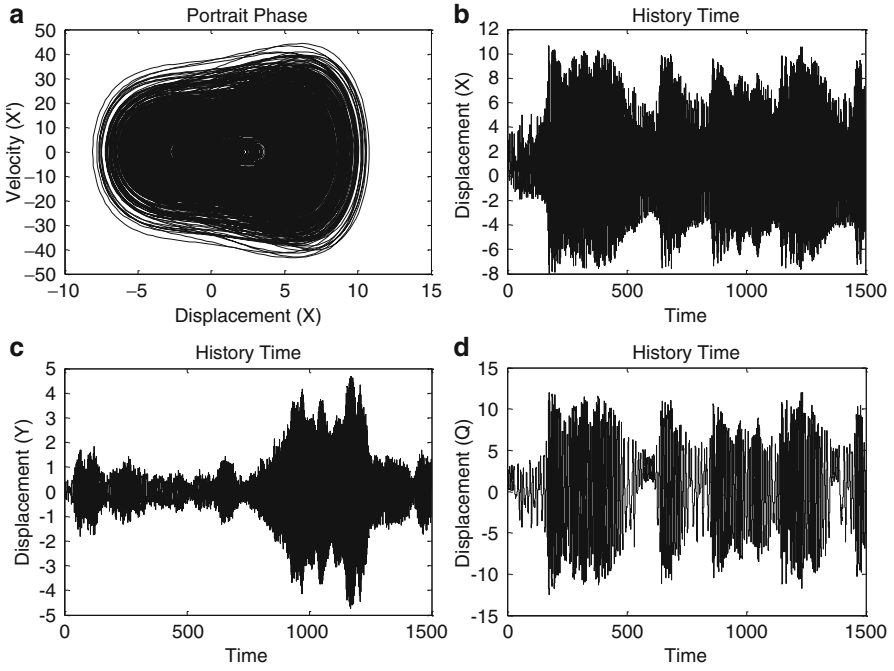

Fig. 4 (**a**) The projection of phase portrait (X', X) – Chaos, $\gamma = 0.116$; (**b**) Dynamical behavior of the time history (X), (**c**) The time history (Y), and (**d**) The time history (Q)

The phase portraits and the time history of Eq. (7), are showed in Fig. 4 and exhibit a chaotic behavior. This was obtained, by considering the following numerical values of the parameters: $\Omega = 1.0$, $\beta_0 = 0.15$, $\beta_1 = 0.1$, $r = 0.015$, $\lambda_1 = 1.2$, $\lambda_2 = 0.5$, $\alpha_1 = \alpha_2 = 0.75$, $\mu 1 = \mu_2 = 0.01$, $\delta = 1.0$ and $\gamma = 0.116$.

4 The Particular Case Including a Non-linear Cubic Term

Including the term $\lambda_3 Q^3$, the governing equations of motion are:

$$\begin{aligned} X'' + \mu_1 X' + X + \alpha_1 X^3 &= \lambda_1 Q^2 + \gamma Y' \\ Y'' + \mu_2 Y' + \delta^2 Y + \alpha_2 Y^3 &= -\gamma X' \\ Q'' + rQ' - \lambda_2 (1 - X) Q + \lambda_3 Q^3 &= \beta_0 + \beta_1 \cos \Omega \tau \end{aligned} \tag{9}$$

Figure 5 illustrates the dynamic behavior of the enriched model, by using the same values of the parameters as considered before and $\lambda_3 = 0.75$, $\gamma = 0.15$. The beating phenomenon is obtained, resulting from the superposition of two waves, propagating in the same direction, with slightly different frequencies. Figure 5 illustrates this behavior.

5 The Control Design

In this section, we develop an optimal linear control design, for the considered "MEMS" Gyroscope vibrating problem, reducing the oscillatory movement to a stable point. Next, we present a summary of the used methodology. Due to the simplicity of its configuration and implementation, the linear state feedback control, is especially attractive (Rafikov and Balthazar 2008). It was used before in (Chavarette et al. 2009a, b) based on the models proposed by Miller et al. (2008), Oropeza-Ramos et al. (2008). We remark that this approach analytical, and does not disregard any non-linear term.

Let's consider the nonlinear governing equations of motion (7), re-written in a state form

$$\dot{x} = Ax + g(x) + U \tag{10}$$

Here, we take into account a vector function $\tilde{x}$, that characterizes the desired trajectory, and consider the control U vector as consisting of two parts: $\tilde{u}$ is the feed forward and u_f a linear feedback, such that

$$u_t = Bu \tag{11}$$

where B is a constant matrix. Next, taking the deviation of the trajectory of system (10) to the desired one (11) $y = x - \tilde{x}$, the following equation is obtained

$$\dot{y} = Ay + g(x) - g(\tilde{x}) + Bu \tag{12}$$

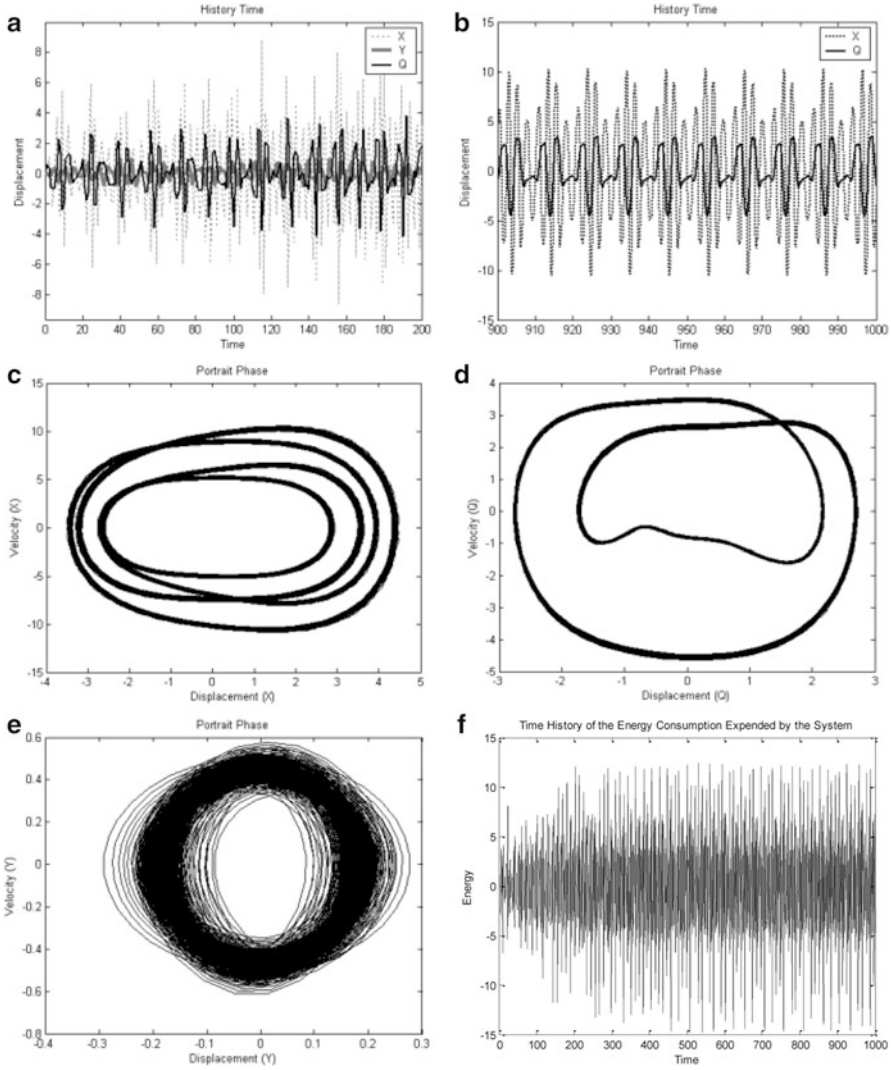

Fig. 5 (**a**) Time histories (*X, Y, Q*); (**b**) The time histories (*X, Q*); (**c**) The projection of portrait phase (X', X); (**d**) The projection of phase portrait (Y', Y), (**e**) The projection of phase portrait (Q', Q); and (**f**) The time history of the energy consumption of the system

where $G\,(x, \tilde{x})$ it is a limited matrix. We use the important result (Rafikov and Balthazar 2008): If there exits matrices $Q\ (t)$ and $R\ (t)$, positive definite, being Q symmetric, such that the matrix $\tilde{Q} = Q - G^T\,(y, \tilde{x})\,P(t) - P(t)G(y, \tilde{x})$ is positive definite for the limited matrix G, then the linear feedback control

$$u = -R^{-1}B^T P\ y \tag{13}$$

is optimal, in order to transfer the non-linear system (7) from any initial state to the final one $y(t_f) = 0$, by minimizing the functional $\tilde{J} = \int_0^\infty (y^T \tilde{Q}\, y + u^T R\, u) dt$. The symmetric matrix $P(t)$ is evaluated through the solution of the matrix Riccati differential equation

$$PA + A^T P - PBR^{-1}B^T P + Q = 0 \tag{14}$$

Satisfying the final condition $P(t_f) = 0$.

In addition, with the feedback control (13), there exists a neighborhood $\Gamma_0 \subset \Gamma$, $\Gamma \subset \Re^n$, of the origin such that if $x_0 \in \Gamma_0$, the solution $x(t) = 0, \quad t \geq 0$, of the controlled system (12) is locally asymptotically stable, and $J_{min} = x_0^T P(0)\, x_0$. Finally, if $\Gamma = \Re^n$ then the solution $y(t) = 0, \quad t > 0$, of the controlled system (12) is globally asymptotically stable.

Next, we will present an important result, concerning a control law that guarantees stability for the nonlinear system and minimizes a non quadratic performance functional (for details, see Rafikov and Balthazar 2008).

5.1 Application of the Control Design Theory to a "MEMS" Gyroscope

For the application of the control technique to the system, the Eq. (11), describing the controlled model, must be written in the following form

$$\begin{aligned} X'' + \mu_1 X' + X + \alpha_1 X^3 &= \lambda_1 Q^2 + \gamma Y' + U \\ Y'' + \mu_2 Y' + \delta^2 Y + \alpha_2 Y^3 &= -\gamma X' \\ Q'' + rQ' - \lambda_2 (1 - X)\, Q &= \beta_0 + \beta_1 \cos \Omega \tau \end{aligned} \tag{15}$$

Defining the state variables $\begin{pmatrix} x_1 \\ x_2 \\ x_3 \\ x_4 \\ x_5 \\ x_6 \end{pmatrix} = \begin{pmatrix} X \\ X' \\ Y \\ Y' \\ Q \\ Q' \end{pmatrix}$, the matrix A of Eq. (12) becomes

$$A = \begin{bmatrix} 0 & 1 & 0 & 0 & 0 & 0 \\ -1 - 1.62X^2 & -0.01 & 0 & 0.116 & 2.4Q & 0 \\ 0 & 0 & 0 & 1 & 0 & 0 \\ 0 & -0.116 & -1 - 1.62Y^2 & -0.01 & 0 & 0 \\ 0 & 0 & 0 & 0 & 0 & 1 \\ -0.5Q & 0 & 0 & 0 & 0.5 - 0.5X - 2.25Q^2 & -0.015 \end{bmatrix}.$$

Then, we will obtain $B = \begin{bmatrix} 1 \\ 1 \\ 0 \\ 0 \\ 0 \\ 0 \end{bmatrix}$, $y = \begin{bmatrix} x_1 - \tilde{x}_1 \\ x_2 - \tilde{x}_2 \\ x_3 - \tilde{x}_3 \\ x_4 - \tilde{x}_4 \\ x_5 - \tilde{x}_5 \\ x_6 - \tilde{x}_6 \end{bmatrix}$ and $\tilde{x} = \begin{bmatrix} 0.1 \\ 0.1 \\ 0.1 \\ 0.1 \\ 0.1 \\ 0.1 \end{bmatrix}$; the matrix

$Q = \begin{bmatrix} 1\,0\,0\,0\,0\,0 \\ 0\,1\,0\,0\,0\,0 \\ 0\,0\,1\,0\,0\,0 \\ 0\,0\,0\,1\,0\,0 \\ 0\,0\,0\,0\,1\,0 \\ 0\,0\,0\,0\,0\,1 \end{bmatrix}$ is positive definite, i.e. its eigenvalues are all positive, in this

case $\lambda_{1.6} = 1$, and $\mathrm{R} = [1]$, $A = \begin{bmatrix} 0 & 1 & 0 & 0 & 0 & 0 \\ -1.0162 & -0.01 & 0 & 0.116 & 0.0024 & 0 \\ 0 & 0 & 0 & 1 & 0 & 0 \\ 0 & -0.116 & -1 & -0.01 & 0 & 0 \\ 0 & 0 & 0 & 0 & 0 & 1 \\ -0.0005 & 0 & 0 & 0 & 0.45 & -0.015 \end{bmatrix}$;

when the matrix $M = \left|B|AB|A^2B \ldots |A^{2n}B\right| \neq 0$, then the dynamical system is controllable (Ogata 2003).

Using the command lqr in the software matlab® we will obtain the matrix *P(t)* as

$P = \begin{bmatrix} 2.731 & -2.683 & -1.638 & 1.801 & -3065.782 & -4519.386 \\ -0.283 & 1.084 & 0.787 & -0967 & -796.457 & -1174.090 \\ -1.638 & 0.787 & 16.900 & 0.137 & -683.557 & -1007.662 \\ 1.801 & -0.967 & 0.137 & 17.700 & -3743.479 & -5518.407 \\ -3065.782 & -796.457 & -683.557 & -3743.479 & 11243398 & 16574330 \\ -4519.386 & -1174.090 & -1007.662 & -5518.407 & 16574330 & 24432865 \end{bmatrix}$

and then we will obtain that the optimal control is given by $u = (0.0024x_1 + 0.0008x_2 - 0.0008x_3 + 0.0008x_4 - 3.8622x_5 - 5.6934x_6) * 10^3$.

The trajectories of the system with control may be seen, in Fig. 6.

According to the optimal control verification (Rafikov and Balthazar 2008), the function (12) is numerically calculated across $L(t) = y^T \tilde{Q} y$, where *L(t)* is defined positive and it is shown in Fig. 6e.

6 Conclusions

In this work, a model of "MEMS" gyroscope system with nonlinear and nonlinear interactions is proposed and its dynamics are investigated. We applied the optimal linear control technique to control "MEMS" Gyroscope. This control allows

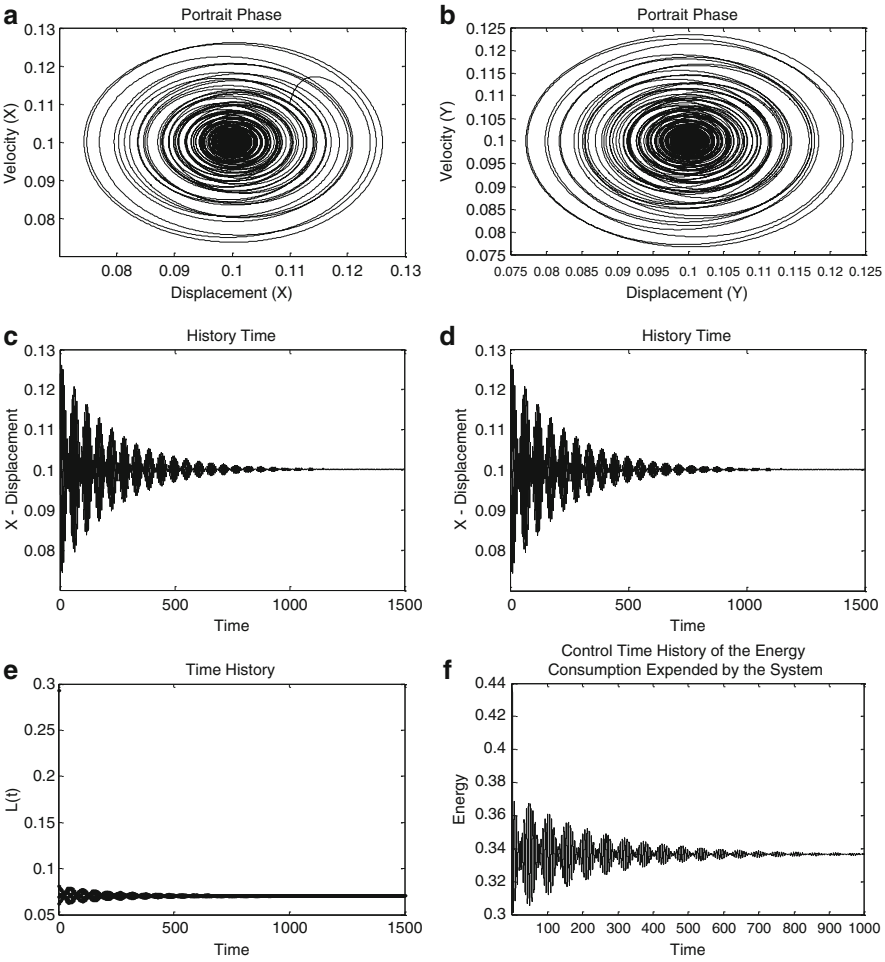

Fig. 6 (**a**) The projection of controlled phase portrait (X', X); (**b**) The projection of controlled phase portrait (Y', Y); (**c**) The controlled time history (X); (**d**) The controlled time history (Y); (**e**) The controlled time history (Q), and (**f**) The controlled time history of the energy consumption of the system

reduction of the chaotic oscillatory movement of the system to a desired stable point. Figures 6 and 7a illustrate the effectiveness of the control strategy applied to these problems. Figures 7a, b and 8a show that the optimal linear control reduces the energy consumption expended by the system and Figs. 7b, 8c, d illustrate the inclusion of the non-linear cubic term, which reduces the energy consumption.

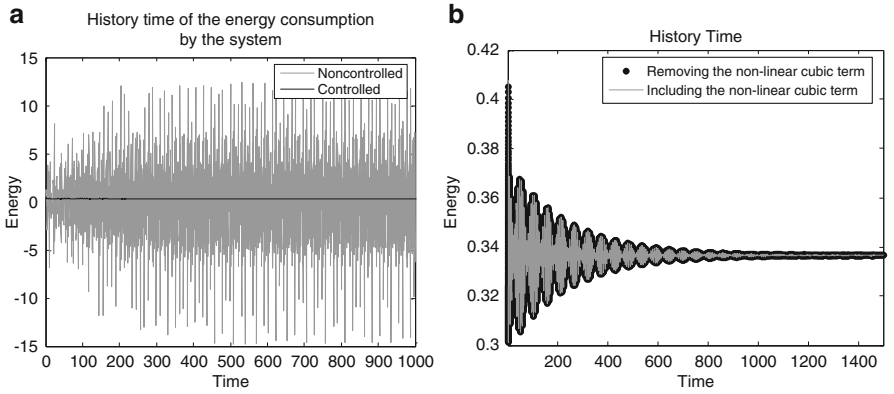

Fig. 7 (**a**) Non-controlled and controlled time history of the energy consumption, and (**b**) Controlled time history of the energy consumption, with and without non-linear cubic term

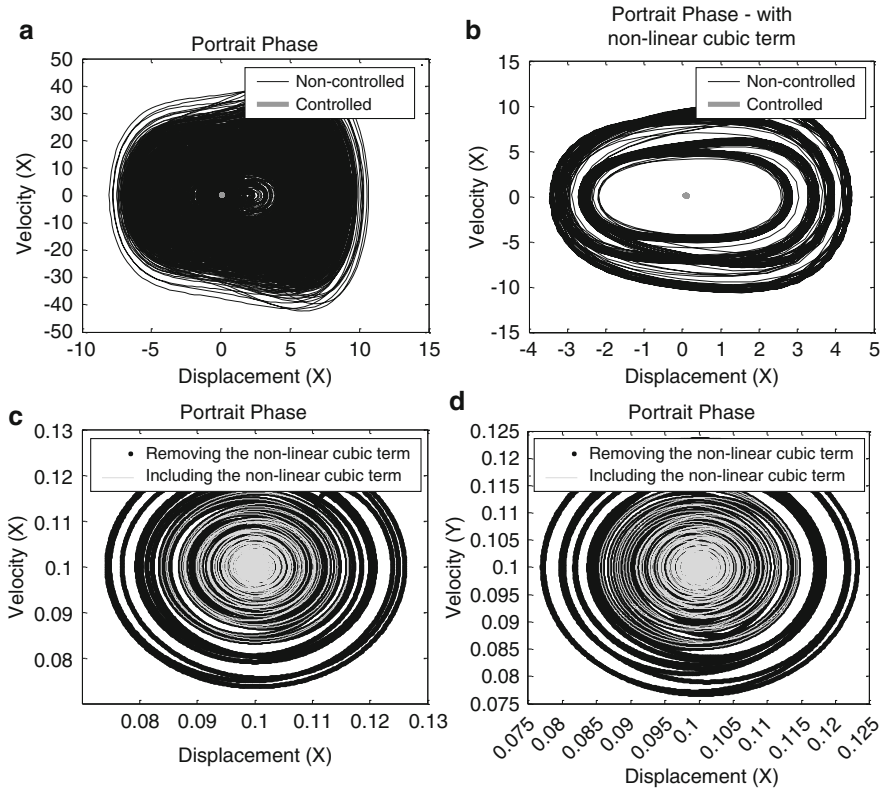

Fig. 8 (**a**) The projection of controlled and non-controlled phase portrait (X', X), (**b**) The projection of controlled and non-controlled phase portrait (X', X), without and with non-linear cubic term, (**c**) The projection of controlled phase portrait (X', X), without and with non-linear cubic term, and (**d**) The projection of controlled phase portrait (Y', Y), without and with non-linear cubic term

References

Chavarette, F.R., Balthazar, J.M., Felix, J.L.P., Rafikov, M.: Reducing a chaotic movement to a periodic orbit, in of a micro-electro-mechanical system, by using an optimal linear control design. Commun. Nonlinear Sci. Numer. Simul. **14**(5), 1844–1853 (2009a)

Chavarette, F.R., Balthazar, J.M., Rafikov, M.: On an energy pumping levels in a MEMS gyroscope vibrating problem, by using of an optimal (global and local) linear control design. In: Proceedings of the ASME 2009 IDETC/CIE, San Diego (2009b)

Chavarette, F.R., Balthazar, J.M., Felix, J.L.P.: Remarks on an optimal linear control design applied to a nonideal and an ideal structure coupled to an essentially nonlinear oscillator. J. Comput. Nonlinear Dyn. **5**, 24501–24508 (2010)

Guckenheimer, J., Holmes, P.: Nonlinear Oscillations, Dynamical System, and Bifurcation of Vector Fields. Springer, New York (1983)

Lee, Y., Pai, P.F., Feng, Z.C.: Nonlinear complex response of a parametrically excited tuning fork. Mech. Syst. Signal Process. **22**, 1146–1156 (2008)

Luo, A.C.J., Wang Fei-Yue: Chaotic motion in a micro-electro-mechanical system with nonlinearity from capacitors. Commun. Nonlinear Sci. Numer. Simul. **7**, 31–49 (2002)

Luo, A.C.J., Wang Fei-Yue: Nonlinear dynamics of a micro-electro-mechanical system with time-varying capacitors. J. Vib. Acoust. **126**, 77–83 (2004)

Miller, N.J., Shaw, S.W., Oropeza-Ramos, L.A., Turner, K.L.: Analysis of a novel MEMS gyroscope actuated by parametric resonance. In: Proceedings of the Sixth EUROMECH Nonlinear Dynamics Conference (ENOC 2008), Saint Petersburg, Russia, June 30–July 4 2008 (2008)

Ogata, K.: Engenharia de Controle Moderno, vol. 4, p. 788. Pearson Prentice Hall, São Paulo (2003)

Oropeza-Ramos, L., Burgner, C.B., Olroyd, C., Turner, K.: Characterization of a novel MEMGyroscope actuated by parametric resonance. In: Proceedings of the ASME 2007, IDETC/CIE 2007, pp. 1–6, Las Vegas, Nevada, 4–7 September 2007

Oropeza-Ramos, L., Burgner, C.B., Olroyd, C., Turner, K.: Inherently robust micro gyroscope actuated by parametric resonance. In: IEEE International Conference on Micro Electro Mechanical Systems, pp. 872–875, Tucson, AZ (2008)

Ott, B., Grebogi, C., Yorke, J.A.: Controlling chaos. Phys. Rev. Lett. **66**, 1196 (1990)

Rafikov, M., Balthazar, J.M.: On control and synchronization in chaotic and hyperchaotic systems via linear feedback control. Commun. Nonlinear Sci. Numer. Simul. **13**(7), 1246–1255 (2008)

Sinhá, S.C., Henrichs, J.T., Ravindra, B.A.: A general approach in the design of active controllers for nonlinear systems exhibiting chaos. Int. J. Bifur. Chaos **10**(1), 165 (2000)

Wauer, J.: On the dynamics of electrostatic transducer with distributed parameters. In: 9th Conference on Dynamical Systems Theory and Applications, pp. 1009–1016, Lódz, Poland, 17–20 December 2007

Control of Chains of Mass Points in a Frictional Environment

Carsten Behn and Klaus Zimmermann

Abstract This paper is devoted to the adaptive control of worm-systems, which are inspired by biological ideas. We introduce a certain type of mathematical models of finite DOF worm-like locomotion systems: modeled as a chain of k interconnected (linked) point masses in a common straight line (a discrete straight worm). We assume that these systems contact the ground via (1) spikes and then (2) stiction combined with Coulomb sliding friction (modification of a Karnopp friction model). In general, one cannot expect to have complete information about a sophisticated mechanical or biological system, only structural properties (known type of actuator with unknown parameters) are known. Additionally, in a rough terrain, unknown or changing friction coefficients lead to uncertain systems, too. The consideration of uncertain systems leads to the use of adaptive control. Gaits from the kinematical theory (preferred motion patterns to achieve movement) can be tracked by means of adaptive controllers (λ-trackers). Simulations are aimed at the justification of theoretical results.

Keywords Worm-like locomotion systems • Chains of mass points • Adaptive control • Friction

1 Introduction

The following is taken as the basis of our theory, Zimmermann et al. (2009): (i) A worm is a mainly terrestrial (or subterrestrial, possibly also aquatic) locomotion system characterized by one dominant linear dimension with no active (driving)

C. Behn (✉) • K. Zimmermann
Department of Technical Mechanics, Ilmenau University of Technology,
Max-Planck-Ring 12, 98693 Ilmenau, Germany
e-mail: carsten.behn@tu-ilmenau.de; klaus.zimmermann@tu-ilmenau.de

M. Wiercigroch and G. Rega (eds.), *IUTAM Symposium on Nonlinear Dynamics for Advanced Technologies and Engineering Design*, IUTAM Bookseries (closed) 32, DOI 10.1007/978-94-007-5742-4_33,

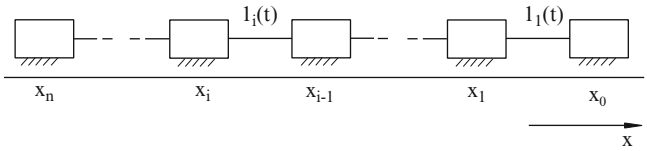

Fig. 1 Chain of point masses with spikes

legs or wheels; (ii) global displacement is achieved by (periodic) change of shape (in particular local strain: peristalsis) and interaction with the environment (undulatory locomotion); (iii) the model body of a worm is a 1-dimensional continuum that serves as the support of various physical fields. This interaction (mentioned in (ii)) could emerge from a surface texture or from a surface endowed with *spikes* which suppress or prevent backward displacements. It is responsible for the conversion of (mostly periodic) internal and internally driven motions into a change of external position (undulatory locomotion (Ostrowski et al. 1995)), see Steigenberger (1999). In contrast to (iii) only *discrete straight worms* shall be considered in this paper: chains of mass points moving along a straight line, Fig. 1.

First we focus on interaction via *spikes* (thorough kinematic theory), later on we introduce Coulomb friction as a ground contact.

2 Kinematics

Following Steigenberger (2004), the motions of the worm system, $t \longmapsto x_i(t)$, are investigated under the **general assumption** to be of differentiability class $D^2(\mathbb{R})$, i.e.,

$$x_i(\cdot) \text{ and } \dot{x}_i(\cdot) \text{ continuous, } \ddot{x}_i(\cdot) \text{ piecewise continuous } (\ddot{x}_i \in D^0(\mathbb{R})) \,. \quad (1)$$

The spikes (attached to each mass point) restrict the velocities of the contact points,

$$\dot{x}_i \geq 0\,, \quad i = 0, \ldots, n, \quad \forall\, t. \quad (2)$$

This is a system of **differential constraints** the system's motions are subject to.

Introducing the distances of consecutive mass points (= actual lengths of the links) $l_j := x_{j-1} - x_j$, $j = 1, \ldots, n$, and the actual distance of the mass point i from the head $S_i := x_0 - x_i = \sum_{j=1}^{i} l_j$ there holds for the velocities $\dot{x}_i = \dot{x}_0 - \dot{S}_i$, $i = 0, \ldots, n$, and the constraint (2) yields $\dot{x}_0 - \dot{S}_i \geq 0$, i.e., $\dot{x}_0 \geq \dot{S}_i$, $i = 0, \ldots, n$. This necessarily entails

$$\dot{x}_0 \geq V_0 := \max\{\dot{S}_i \mid i \in \{0\,, \ldots\,, n\}\}. \quad (3)$$

Consequently, the head velocity is $\dot{x}_0 = V_0 + w$, $w \geq 0$, and for the others it follows $\dot{x}_i = V_0 - \dot{S}_i + w$, $i = 0, \ldots, n$. Since w is a common additive term to *all* velocities $\dot{x}_i$, it describes a *rigid part of the motion* of the system.

The worm system is called to move under **kinematic drive** if by means of the actuators *all* distances l_j (or $\dot{l}_j$) are prescribed as functions of t. Then $\dot{S}_i$ and V_0 become known functions of t, and in the velocities $\dot{x}_i$ the rigid part w is now the only free variable. The rigid part w of the velocities keeps arbitrary in kinematics. So it seems promising to put it equal to zero, then all velocities of the mass points are known functions of t. Putting $w = 0$ locks the single degree of freedom. There remains a nicely simple ***Kinematical theory*:** (worm with kinematic drive and $w(t) = 0$)

Prescribe: $l_j(\cdot) \in D^2(\mathbb{R}) : t \mapsto l_j(t) > 0, \quad j = 1, \ldots, n.$
Determine: $S_i := \sum_{j=1}^{i} l_j, \quad V_0 := \max\{\dot{S}_i \mid \kappa \in \{0, \ldots, n\}\} \in D^1(\mathbb{R}).$
Result: $x_0(t) = \int_0^t V_0(s)ds, \quad x_j(t) = x_0(t) - S_j(t), \quad j = 1, \ldots, n.$

(4)

The kinematical theory is valid if and only if at any time at least one spike is active. In applications it might be necessary to use a kinematic drive that ensures a prescribed number of spikes to be active at every time.

Example 1. We consider a worm system with $n = 2$. We present (construction suppressed here) a kinematic drive such that at every time exactly one of the three spikes is active. Using the Heaviside function

$$h(t_0, t_1, \cdot) : \tau \mapsto h(t_0, t_1, \tau) := \begin{cases} 1, \text{ if } t_0 < \tau \leq t_1 \\ 0, \text{ else} \end{cases}$$

we define

$$l_1(t) := l_0 \Big[1 + a\, l_0 \big(1 - \cos(\pi\, t)\big)\Big] h(0, 2, t) + l_0\, h(2, 3, t)$$

$$l_2(t) := l_0 \Big[1 - a\, l_0 \big(1 - \cos(\pi\, t)\big)\Big] h(0, 1, t) + l_0 \left[1 - 2\, a\, l_0\right] h(1, 2, t)$$

$$+ l_0 \Big[1 - a\, l_0 \big(1 + \cos(\pi\, t)\big)\Big] h(2, 3, t) \tag{5}$$

on the primitive time interval $[0, T]$, $T := 3$, and then take their T-periodic continuation to $\mathbb{R}^+$. Here $l_0 = 2$ is the original length of the links, and $l_0 a$ with $a = 0.1$ is the amplitude of the length variation in time. Applying (4) we obtain the results sketched in Fig. 2. The cycle of active spikes is $\mathbf{1} \to \mathbf{0} \to \mathbf{2}$. Average speed of center of mass is $\overline{v} \approx 0.5333$.

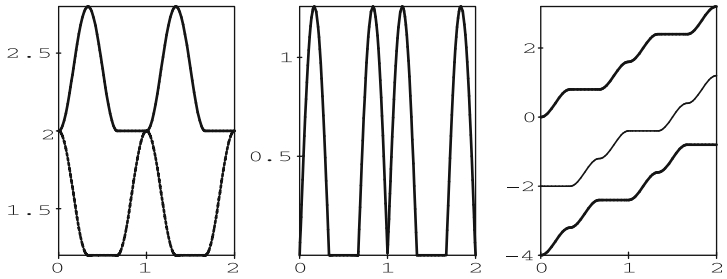

Fig. 2 *Left*: Gait l_1 (*upper curve*) l_2 (*lower curve*) vs. t/T; *middle*: V_0 vs. t/T, *right*: worm motion—x_0 (*upper curve*), x_1 (*middle curve*) and x_2 (*lower curve*) vs. t/T

3 Dynamics

The following forces are applied to mass point i, all acting in $x-$direction, see Fig. 3:

- g_i, the *external impressed* (physically given) *force* (e.g., resultant of viscous friction and weight component backward: $g_i = -k_0\,\dot{x}_i - \Gamma_i$).
- μ_i, the *stress resultant* (inner force) of the links (let, formally, $\mu_0 = \mu_{n+1} := 0$).
- $z_i, i \in \{0, \ldots, n\}$, the *external reaction force* caused by the constraint (2), acting on the spiked mass points.

The dynamics of the worm system are formulated by means of Newton's law for each of the mass points:

$$m\,\ddot{x}_i = g_i + \mu_i - \mu_{i+1} + z_i, \qquad i = 0, \ldots, n. \tag{6}$$

As the constraint (2) describes a **one-sided** restriction of $\dot{x}_i$, velocity and reaction force are connected by a **complementary-slackness condition**:

$$\dot{x}_i \geq 0, \quad z_i \geq 0, \quad \dot{x}_i\, z_i = 0, \quad i = 0, \ldots, n. \tag{7}$$

This means that $z_i(t)$ is zero if at time t the mass point i is moving forward, whereas $z_i(t)$ may have arbitrary non-negative values as long as $\dot{x}_i(t) = 0$ (reaction force at resting spike).

An *actuator* is, first, a multi-pole with input activation signal and energy (immanent energy source—e.g., electrical battery. Its output are forces, torques, displacements, twists, respectively. Often the internal dynamics of an actuator are not modeled, rather the output is connected with the input: the multi-pole remains a black box. We hint at four physical models of actuators from literature: (a) in Huang (2003) with output force, (b) in Steigenberger (2004) with output displacement, (c) in Steigenberger (1999) a mixed case, and (d) in Hirose (1993) with output torque or rotation.

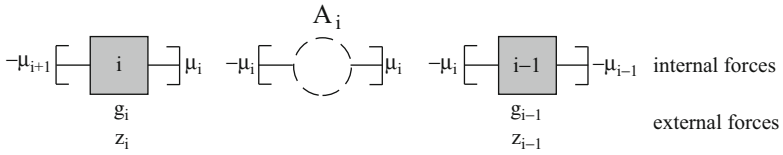

Fig. 3 Mass points with forces (A_i: actuator)

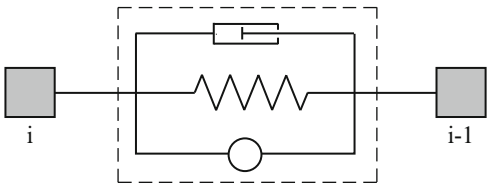

Fig. 4 Actuator, general physical model

Our starting-point for introducing an actuator is a given output law. Let μ_i be qualified as impressed forces:

$$\mu_i(t, x, \dot{x}) := c_i\left(x_{i-1} - x_i - l_i^0\right) + k_i(\dot{x}_{i-1} - \dot{x}_i) + u_i(t). \tag{8}$$

This mathematical relation describes the parallel arrangement of a linear-elastic spring (constant stiffness c_i, original length l_i^0), a Stokes damping element (constant coefficient k_i), and a time-dependent force $u_i(t)$. Figure 4 shows the corresponding physical model of this actuator (now a white box), where the circular box represents a non-modeled device generating the force $u_i(t)$.

Under the assumption that all actuators have the same data the equations of motions follow from (6) in the actual form

$$\begin{aligned}
m\ddot{x}_0 &= -c(x_0 - x_1 - l^0) - k_{00}(\dot{x}_0 - \dot{x}_1) - k_0\dot{x}_0 - u_1(t) - \Gamma_0 + z_0,\\
m\ddot{x}_j &= -c(2x_j - x_{j+1} - x_{j-1}) - k_{00}(2\dot{x}_j - \dot{x}_{j+1} - \dot{x}_{j-1}) +\\
&\quad + u_j(t) - u_{j+1}(t) - k_0\dot{x}_j - \Gamma_j + z_j,\\
m\ddot{x}_n &= c(x_{n-1} - x_n - l^0) + k_{00}(\dot{x}_{n-1} - \dot{x}_n) - k_0\dot{x}_n + u_n(t) - \Gamma_n + z_n.
\end{aligned} \tag{9}$$

The accompanying complementary slackness conditions can be satisfied through expressing the z_i by means of the "controller" (see Steigenberger (2004))

$$z_i(f_i, \dot{x}_i) = -\frac{1}{2}\big(1 - \operatorname{sign}(\dot{x}_i)\big)\big(1 - \operatorname{sign}(f_i)\big) f_i, \quad i \in \{0, \ldots, n\}, \tag{10}$$

where f_i is the resultant of all further forces acting on the mass point i.

Remark 1. Let us briefly discuss this controller (10). For brevity we dropped the index i here:

- If $\dot{x} > 0$ than (10) yields $z = 0$, and we have $\dot{x}\, z = 0$.
- If $\dot{x} = 0$ it follows $z = -\frac{1}{2}\,(1 - \mathrm{sign}(f))\, f$.
  - If now $f > 0$ then $z = 0$, that means, a movement of this mass point m starts immediately in positive direction.
  - If $f < 0$ we get $z = -f$ and the spikes cancel the resultant of all forces.
  - $f = 0$ implies $z = 0$ (no acting forces, no existence of a spike force).
- If $\dot{x} < 0$, Eq. (10) is ill defined, in other words, it breaks down. But this case does not happen:

  Let $\dot{x} < 0$, then by continuity of $\dot{x}$ and, as it has to be, initial condition $\dot{x}(0) \geq 0$, $\dot{x}$ has a zero, without loss of generality, at $t = t_0$. Then at $t = t_0 + 0$ ($f(t_0+0) =: f^0$) we have $m\,\ddot{x}(t_0+0) = f^0 + z = f^0 - \frac{1}{2}\,2\,(1-\mathrm{sign}(f^0))\, f^0 = f^0 - (f^0 - |f^0|) = |f^0| \geq 0$. If $f^0 \neq 0$ then $\ddot{x} \geq 0$ and it follows $\dot{x} > 0$ for some $t \in (t_0, t_1)$. Contradiction. If $f^0 = 0$ and $f = 0$ for $t \in (t_0, t_1)$ then $\dot{x} = 0$. Contradiction. If $f^0 = 0$ and $f \neq 0$ for $t \in (t_0, t_1)$ then $\ddot{x} > 0$ for these t and $\dot{x}$ goes to positive values. Contradiction. *Summarizing*, $\dot{x} < 0$ cannot occur.

At this stage, the u_i are to be seen as prescribed functions of t (*offline-controls*), later on they are handled as depending on the state $(x, \dot{x})$ (*feedback, online-controls*).

If the actuator data are known (l^0, c and k_{00}), and n is small ($n \leq 2$), then an actuator input $u_i(t)$ can be calculated which controls the system in such a way as to track a preferred motion-pattern constructed in kinematical theory like (5). But, as a rule, the actuator data are not known exactly.

4 Adaptive Control

The lack of precise knowledge of parameters (actuator data, worm system parameters, environmental contact) leads to the consideration of uncertain systems. Hence, it is impossible to calculate force inputs u to achieve a prescribed movement. We have to design a controller which on its own generates the necessary forces to track a prescribed kinematic gait. This leads us to an adaptive high-gain output feedback controller (learning controller). The aim is not to identify the some data, but to simply control this system in order to track a given reference trajectory (kinematic gait), i.e., to ensure a desired movement of the system. We do not focus on exact tracking, rather we focus on the **λ-tracking control objective** tolerating a prespecified tracking error of size λ.

Considering the worm system (9) we choose as outputs the actual lengths of the links, i.e., $y_j := x_{j-1} - x_j$, for $j = 1, \ldots, n$. λ-tracking now means, given $\lambda > 0$, a control strategy $y = (y_1, \ldots, y_n) \mapsto u = (u_1, \ldots, u_n)$ is sought which, when applied to this system (9), realizes tracking of any reference signal $y_{\mathrm{ref}} = (y_{\mathrm{ref}\,1}, \ldots, y_{\mathrm{ref}\,n})$ in the following way:

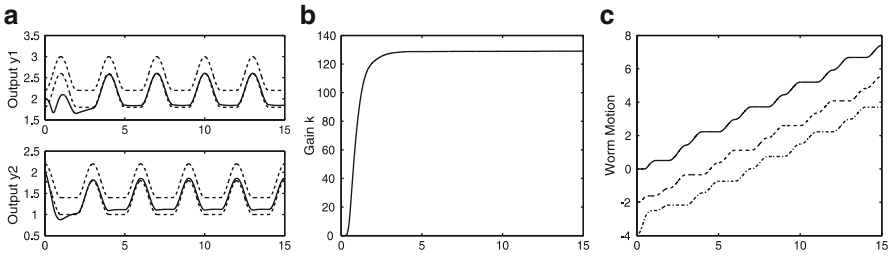

Fig. 5 (**a**) Outputs y_1 and y_2 with λ-tubes; (**b**) gain parameter $k(\cdot)$; (**c**) worm motion; all vs. time t

(i) Every solution of the closed-loop system is defined and bounded on $\mathbb{R}_{\geq 0}$, and
(ii) The output $y(\cdot)$ tracks $y_{\text{ref}}(\cdot)$ with asymptotic accuracy quantified by $\lambda > 0$ in the sense that $\max\left\{0, \left\|y(t) - y_{\text{ref}}(t)\right\| - \lambda\right\} \to 0$ as $t \to \infty$.

The following controller realizes our goal, for a mathematical proof (and a general system class where it works) see Behn (2005) and Behn and Zimmermann (2006):

$$\left.\begin{aligned} e(t) &:= y(t) - y_{\text{ref}}(t)\,, \qquad y_{\text{ref}}(\cdot) \in W^{2,\infty}(\text{a Sobolev} - \text{Space}) \\ u(t) &= \left(k(t)e(t) + \tfrac{d}{dt}\big(k(t)e(t)\big)\right), \\ \dot{k}(t) &= \gamma\, \max\left\{0, \left\|e(t)\right\| - \lambda\right\}^2, \qquad k(0) \in \mathbb{R}\,, \lambda > 0\,, \gamma > 1 \end{aligned}\right\}. \tag{11}$$

For simulations we consider a worm with $n = 2$ links, and $y_{\text{ref}\,1,2} := t \mapsto l_{1,2}(t)$ from (5). So the control $u_{1,2}$ is sought such that $y_{1,2}$ gets close to $l_{1,2}$ in the above precise sense. We choose the following data:

worm system: $m_0 = m_1 = m_2 = 1$, $c = 10$, $k_{00} = 5$; *initial conditions*: $x_0(0) = 0, x_1(0) = -2, x_2(0) = -4, \dot{x}_i(0) = 0\,(i = 1, 2, 3)$; *environment*: $k_0 = 0$, $\Gamma_{1,2,3} = 2.7$ (ensures kinematical theory to be dynamically feasible); *reference gait*: (5) with $l_0 = 2$, $a = 0.1$; *controller*: $k(0) = 0$, $\lambda = 0.2$, $\gamma = 300$. The actuator and environmental data $(c\,, k_{00}\,, k_0\,, \Gamma)$ are fixed just for doing the simulations. In general they could be understood as estimates the unknown values may vary about.

For numerical reasons we use the smooth approximation $\text{sign}(x) \approx \tanh(10000\,x)$.

Simulation 1. Worm with ideal spikes, i.e., (10) with controller (11).

The figures (compared with Fig. 2) show a good tracking behavior after a transient phase until $t \approx 3$. Average speed of center of mass is $\overline{v} \approx 0.4938$ (after transient process). Figure 5b shows a monotonic increase of $k(t)$ towards a limit k_∞. But if some perturbation repeatedly caused the output to leave the λ-strip then $k(t)$ would take larger values again and again. That is why we introduce an improved adaptation law, see Behn and Steigenberger (2009), that makes $k(t)$ decrease as long as further growth is not necessary. We distinguish three cases: (1) increasing

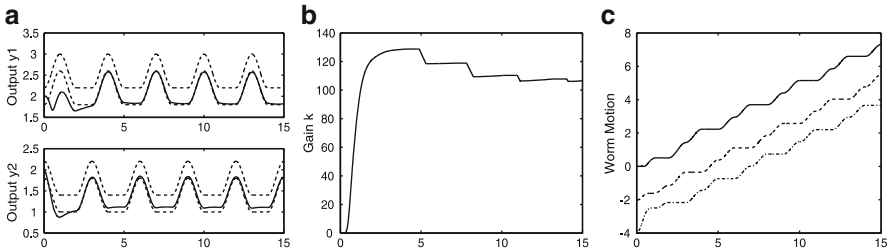

Fig. 6 (**a**) Outputs y_1 and y_2 with λ-tubes; (**b**) gain parameter $k(\cdot)$; (**c**) worm motion; all vs. time t

$k(\cdot)$ while e is outside the tube, (2) constant $k(\cdot)$ after e entered the tube—no longer than a pre-specified duration t_d of stay, and (3) decreasing $k(\cdot)$ after this duration has been exceeded. For instance:

$$\dot{k}(t) = \begin{cases} \gamma \left(\|e(t)\| - \lambda \right)^2, & \|e(t)\| \geq \lambda \,, \\ 0, & \left(\|e(t)\| < \lambda \right) \wedge (t - t_E < t_d) \,, \\ -\sigma\, k(t), & \left(\|e(t)\| < \lambda \right) \wedge (t - t_E \geq t_d), \end{cases} \tag{12}$$

with given $\sigma > 0$, $\gamma \gg 1$, and $t_d > 0$, whereas t_E is an internal time variable.

Simulation 2. Controller from (11) with adaptor (12) ($\sigma = 0.2$, $t_d = 1$).

Figure 6b indicates that the maximal value $k \approx 130$ is only due to the transient behavior (until e enters the λ-tube) whereas the minimum high gain is obviously $k^* \approx 100$. Average speed of center of mass is $\overline{v} \approx 0.4859$ (after transient process).

5 Friction

Now, we replace the worm-ground interaction via spikes by stiction combined with Coulomb sliding friction (a more realistic description of the interaction). First, we present a mathematical model for the Coulomb laws that is both theoretically transparent and handy in computing. It is by far simpler than various sophisticated laws in literature (e.g. Armstrong-Hélouvry et al. 1994; Awrejcewicz and Olejnik 2005; Canudas de Wit et al. 1995; Olsson et al. 1998) but similar to the model given in Karnopp (1985) and it well captures stick-slip effects in application to worm dynamics, see Behn et al. (2007) and (Steigenberger, 2006, unpublished). We note that this modeling makes friction a real-valued function of two arguments, and not a set-valued one depending solely on the velocity as preferred by most authors. Let

$$F(f,v) := \begin{cases} F^-, & v < -\varepsilon \vee \big(|v| \le \varepsilon \wedge f < -F_0^-\big), \\ -f, & |v| \le \varepsilon \wedge f \in \big[-F_0^-, F_0^+\big], \\ -F^+, & v > \varepsilon \vee \big(|v| \le \varepsilon \wedge f > F_0^+\big). \end{cases} \tag{13}$$

Think of F acting on a mass point whose dynamics in $\mathbb{R}^1$ are $\dot{x} = v, m\,\dot{v} = f + F$. Then (13) essentially indicates the mutual cancelation of forces if the point is at rest and $|f|$ is bounded by $F_0^{\pm}$, and a piecewise constant 'braking' of magnitude $F^{\pm}$ during motion. Different $F^{\pm}$ or $F_0^{\pm}$ values characterize a friction *anisotropy*. A suitable $\varepsilon > 0$ replaces the computer accuracy and mimics the vague processes at small velocities as well.

Using the Heaviside function h from Example 1 F can be given a closed form (disregarding its values at $v = \pm\varepsilon$). In order to avoid difficulties in computing caused by jumps of the h-function we turn to a smooth mathematical model (in the sense of an approximation). Basically, we use a tanh-approximation of the sign-function $\operatorname{sign}(x) \approx \tanh(A\,x)$ with some sufficiently large $A \gg 1$.

The smooth mathematical model then is

$$\begin{aligned} F(f,v) = &-f\; H(-\varepsilon,\varepsilon,v)\; H(-F_0^-, F_0^+, f) \\ &+F^-\left\{H(-\infty,-\varepsilon,v) + H(-\varepsilon,0,v)\; H(-\infty,-F_0^-,f)\right\} \\ &-F^+\left\{H(\varepsilon,+\infty,v) + H(0,\varepsilon,v)\; H(F_0^+,+\infty,f)\right\}, \end{aligned} \tag{14}$$

where F is now a $\mathscr{C}^\infty$-function in *closed analytical form* by means of

$$H(a,b,x) := \frac{1}{2}\Big\{\tanh\big(A\,(x-a)\big) + \tanh\big(A\,(b-x)\big)\Big\}, \tag{15}$$

the smooth approximation of $h(a,b,x)$.

We use $A = 10^5$ and $\varepsilon = 0.005$ in the sequel.

Mind that $F_0^- \gg 1$ essentially leads to the theory of ideal spikes, whereas a small F_0^- corresponds with a breakable or broken spike.

Again, adaptive control has to be used when considering uncertain or randomly changing friction data (rough terrain). Successful application is shown by the following simulation results: (1) stiction only, (2) sliding friction only, and (3) both.

Simulation 3. First, we consider only stiction, i.e., $F^+ = F^- = 0$ for (14). We choose $F_0^- = 16$ (guided by spikes-worm theory—not outlined here) and $F_0^+ = 3$. Applying controller (11) with adaptor (12) ($\sigma = 0.2$, $t_d = 1$) yields the results shown in Fig. 7:

There are some short backward motions at the beginning (see Fig. 7c), afterwards the motion coincides with that of Simulations 1 and 2. Average speed of center of mass is $\bar{v} \approx 0.4857$ (after transient process).

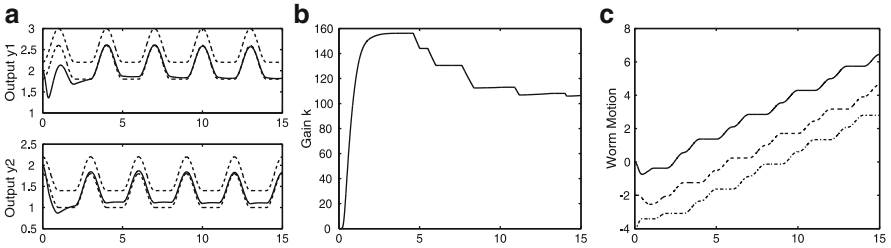

Fig. 7 (**a**) Outputs y_1 and y_2 with λ-tubes; (**b**) gain parameter $k(\cdot)$; (**c**) worm motion; all vs. time t

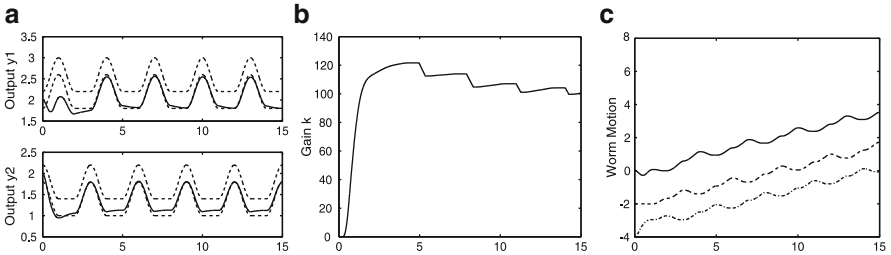

Fig. 8 (**a**) Outputs y_1 and y_2 with λ-tubes; (**b**) gain parameter $k(\cdot)$; (**c**) worm motion; all vs. time t

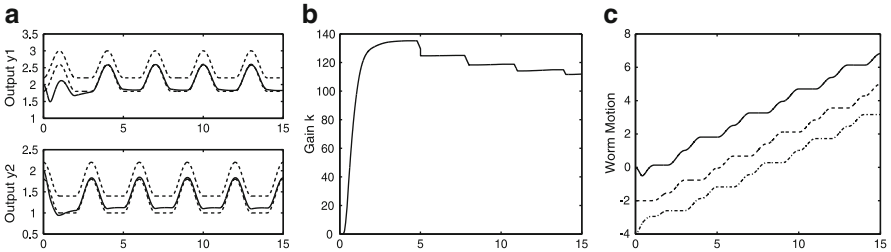

Fig. 9 (**a**) Outputs y_1 and y_2 with λ-tubes; (**b**) gain parameter $k(\cdot)$; (**c**) worm motion; all vs. time t

Simulation 4. Now, we replace stiction by sliding friction. We put $F_0^+ = F_0^- = 0$ and choose instead $F^- = 16$ and $F^+ = 3$. Again applying controller (11) with adaptor (12) ($\sigma = 0.2$, $t_d = 1$) yields (shown in Fig. 8):

Though there is again a good tracking of the desired gait from kinematical theory (see Fig. 8a), we observe an unsatisfactory external behavior of the worm (recurring negative velocities), see Fig. 8c, obviously owing to the cancelation of stiction. Average speed of center of mass is $\bar{v} \approx 0.2399$ (after transient process).

Simulation 5. At last, applying the friction model (14) with $F_0^- = 18$, $F_0^+ = 3$ (remind $F_0^- = 16$ in Simulation 3), $F^- = 8$, $F^+ = 1$ (additional sliding friction) and using the same control data as before we obtain the following results (shown in Fig. 9):

Good behavior (see Fig. 9a, c), comparable with that in Simulation 3, but now a bit smaller average speed $\overline{v} \approx 0.4793$ due to the sliding friction.

If $F_0^- = 16$ was used then the worm would run backwards. The need of $F_0^- = 16 + 2$ is caused by the forward sliding friction $F^+ = 1$. This is essentially the same effect as it would be caused by an increase of Γ from 2.7 to 4.7 since two mass points are sliding at every moment during the motion. So F^+ leads to an additional backward force of magnitude 2 that has to be compensated by stiction.

6 Conclusion and Outlook

In the foregoing examples the (adaptive) control has been directed to ensure a prescribed gait (i.e., a temporal pattern of shape—something internal!). It is intelligible that a changing environment or changing type of interaction influences the global movement and the driving forces u_i despite a good tracking of the gait.

A comparison of Simulations 3–5 points at stiction as the essential part of Coulomb interaction with the ground and gives a *warning of* a careless reducing of the interaction to pure sliding friction (Fig. 10).

Finally we sketch some current and future tasks:

- To track a prescribed global movement of the worm (first step: to track a reference head speed—a pure tracking of the prescribed gait is not sufficient to do this),
- To investigate tracking under friction which randomly changes online, possibly coupled with appropriate change of gaits ('gear shift'),
- To investigate tracking under randomly changing internal data (failing actuator),
- To validate the theory by experiments:
  For this purpose a locomotion system is developed (the 'TM-Robot II'). It is designed to have a better dynamical behavior than older systems. The drive is by motors, pulleys and springs. The adaptive control algorithms are prepared to be implemented in order to track reference motions.

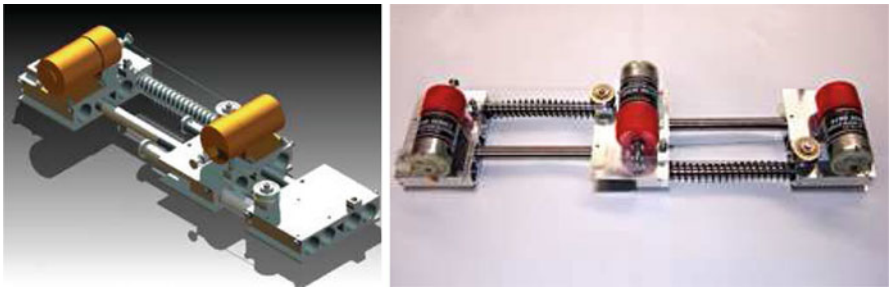

Fig. 10 CAD-model (left) and prototype (right) of the TM-Robot II.

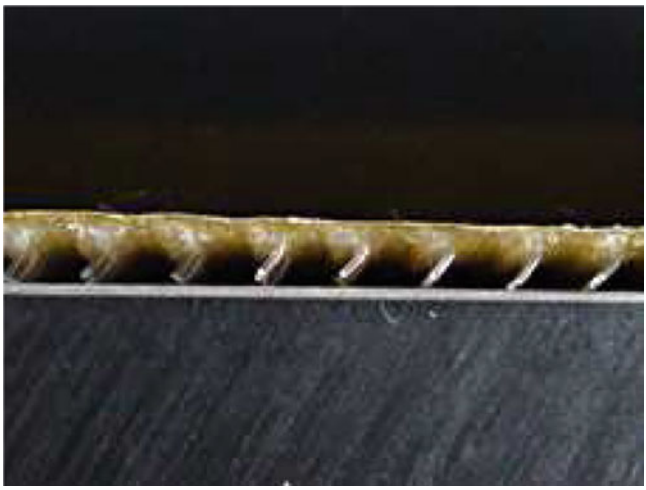

Fig. 11 The bristle-structure

Each mass point is equipped with a bristle-structure to prevent slipping backwards, see Fig.11.

References

Armstrong-Hélouvry, B., Dupont, P., Canudas de Wit, C.: A survey of models, analysis tools and compensation methods for the control of machines with friction. Automatica, **30**(7), 1083–1138 (1994)

Awrejcewicz, J., Olejnik, P.: Analysis of dynamic systems with various friction laws. Appl. Mech. Rev. **58**, 389–411 (2005)

Behn, C.: Ein Beitrag zur adaptiven Regelung technischer Systeme nach biologischem Vorbild. Cuvillier, Göttingen (2005)

Behn, C., Steigenberger, J.: Improved adaptive controllers for sensory systems – first attempts. In: Awrejcewicz, J. (ed.) Modeling, Simulation and Control of Nonlinear Engineering Dynamical Systems, pp. 161–178. Springer, New York (2009)

Behn, C., Zimmermann, K.: Adaptive λ-tracking for locomotion systems. Robot. Auton. Syst. **54**, 529–545 (2006)

Behn, C., Steigenberger, J., Zimmermann, K.: Biologically inspired locomotion systems – improved models for friction and adaptive control. In: Bottasso, C.L., Masarati, P., Trainelli, L. (eds.) Proceedings ECCOMAS Thematic Conference in Multibody Dynamics, Milano, Italy, 20p (2007). Electronical publication

Canudas de Wit, C., Olsson, H., Åström, K.J., Lischinsky, P.: A new model for control of systems with friction. IEEE Trans. Autom. Control **40**(3), 419–425 (1995)

Hirose, S.: Biologically Inspired Robots: Snake-Like Locomotors and Manipulators. Oxford University Press, Oxford (1993)

Huang, J.: Modellierung, Simulation und Entwurf biomimetischer Roboter basierend auf apedaler undulatorischer Lokomotion. ISLE, Ilmenau (2003)

Karnopp, D.: Computer simulation of stick-slip friction in mechanical dynamic systems. ASME J. Dyn. Syst. Meas. Control **107**(1), 100–103 (1985)

Olsson, H., Åström, K.J., Canudas de Wit, C., Gräfert, M., Lischinsky, P.: Friction models and friction compensation. Eur. J. Control **4**, 176–195 (1998)

Ostrowski, J.P., Burdick, J.W., Lewis, A.D., Murray, R.M.: The mechanics of undulatory locomotion: the mixed kinemtic and dynamic case. In: Proceedings IEEE International Conference on Robotics and Automation, Nagoya, Japan (1995)

Steigenberger, J.: On a class of biomorphic motion systems. Preprint No. M12/99. Faculty of Mathematics and Natural Sciences, TU Ilmenau (1999)

Steigenberger, J.: Modeling Artificial Worms. Preprint No. M02/04. Faculty of Mathematics and Natural Sciences, TU Ilmenau (2004)

Zimmermann, K., Zeidis, I., Behn, C.: Mechanics of Terrestrial Locomotion – With a Focus on Non-pedal Motion Systems. Springer, Berlin (2009)

Author Index

M. Wiercigroch and G. Rega (eds.), *IUTAM Symposium on Nonlinear Dynamics for Advanced Technologies and Engineering Design*, IUTAM Bookseries (closed) 32, DOI 10.1007/978-94-007-5742-4,

Subject Index

M. Wiercigroch and G. Rega (eds.), *IUTAM Symposium on Nonlinear Dynamics for Advanced Technologies and Engineering Design*, IUTAM Bookseries (closed) 32, DOI 10.1007/978-94-007-5742-4,

E

Q

R